

Photophysical and Biological Profiling of Ruthenium(II) Polypyridyl Complex-based Systems

Sandra Estalayo Adrián, M.Sc.

February 2019



**Trinity College Dublin
The University of Dublin**

**Based on research carried out under the direction of
Prof. Thorfinnur Gunnlaugsson and Prof. John M. Kelly**

*A thesis submitted to the School of Chemistry,
Trinity College Dublin, The University of Dublin, for the degree of Doctor of
Philosophy*

Declaration

I declare that this thesis has not been submitted as an exercise for a degree at this or any other university and it is entirely my own work. I agree to deposit this thesis in the University's open access institutional repository or allow the Library to do so on my behalf, subject to Irish Copyright Legislation and Trinity College Library conditions of use and acknowledgement.

Signed: _____

Sandra Estalayo Adrián

Acknowledgements

First, I would like to sincerely thank my supervisor Prof. Thorri Gunnlaugsson for giving me the opportunity to work in his research group, despite my English not being very good when we first talked. I am truly grateful for your trust in me and your continued support, advice and encouragement over the past four years. I would also like to thank my co-supervisor Prof. John M. Kelly for his boundless enthusiasm and invaluable guidance along the photoadduct mystery. “Curiouser and curiouser!”. I really learnt a lot from our discussions in countless meetings and emails. I feel privileged to have been co-supervised by you.

I must also thank all the collaborators without whom a big part of this work would not have been possible. Thank you to our TCD collaborators Prof. Clive Williams for giving me the opportunity to use the biochemistry facility, and Prof. Rachel Evans for letting me use her surface tensiometer with the kind help of Camille Blayo.

Among our international collaborators, I would like to thank Prof. Guillermo Orellana for all his help, discussions and advice not only for this thesis, but also during my time as an undergraduate student in Universidad Complutense de Madrid (UCM). I still remember the time when you offered me the chance to be a summer student in your research group. I probably started loving research from then. Thank you for teaching me about singlet oxygen photosensitisation and letting me use your many instruments at UCM, as well as replying my numerous emails that always contained thousands of questions. I will never be able to thank you enough for all your help over the last eight years! Also thank you to Prof. Andrée Kirsch-De Mesmaeker at Université Libre de Bruxelles (ULB) for the collaboration on the photoadduct project and our several discussions trying to understand the intriguing behaviour of the photoadduct, and to Dr Lionel Marcélis for his valuable help and advice during the synthesis and purification of the photoadduct.

Without the generous financial support from the Science Foundation Ireland (SFI) it would not have been possible to complete this PhD. Many thanks for all the funding throughout over the last four years.

I would also like to express my sincere thanks to all the technical staff in the School of Chemistry, especially Dr John O’ Brien for his help with the NMR characterisation, in particular for the thousands of scans in the tiny NMR tubes he had run to get good spectra on the photoadduct; Dr Manuel Ruether for coming to help me every time I had a problem

with any instrument in TCD (especially the Fluorolog and the HPLC); and Dr Martin Feeney and Dr Gary Hessman for their enormous help with Mass Spectrometry. Thank you to Dr Gavin McManus from the School of Biochemistry and Immunology for all the hours we spent together on level -2 doing the confocal imaging of my “weird” chemical samples. I really appreciate your uncountable biochemical advice and your strong encouragement in the last few weeks.

Thank you to all the past, current, and visiting members of the TG group I had the pleasure to work with (with special mention to all the English native speakers who have gone through this thesis and dealt with my long Spanish style sentences). Apart from being excellent chemists, you are all amazing people, always willing to help me every time I needed it. I couldn't have imagined better people to share my time in the TG group with.

To all the past members: Joe, Emma, Esther (I couldn't have made the gold nanoparticles without all your help!), Helen, Gearóid, Chris, Eoin, Niamh, Raju, Sam and Anna. I hope I don't miss anybody as we were a really big group!

A particular thanks to the TG members that composed the ruthenium team (before you all left me alone...), Salvador, Sandra, Fergus and Bjørn. Salvador, thank you for all the support you gave me from the day I came to the group until you left. Sandra Bright, I owe you all the biochemistry I learnt. Thank you for all your patience when teaching me and your biochemical assistance even after leaving the group. Fergus, you are as nice as you are tall! Thanks for all your help with my transient spectroscopy experiments and your advice and support throughout the years. You are probably the only person who can understand my pain during the sample preparation for the FTIR experiments (I think I became “bag-phobic”!). Bjørn, my ruthenium brother, my fumehood mate for three years. The fumehood was not the same since you left, even if Dermot tried quite hard to keep up your level of mess! Thank you for helping me with all the DNA binding studies (you will always be the DNA titrations master), and for your infinite Danish wisdom. Thanks to you I now know that, although a turtle can't turn into a race horse, it can turn into a very fast turtle. As a turtle or as a horse, I hope you are happy in Denmark.

To the current TG postdocs: Oxana, Dawn, Sachi and Adam. Oxana, the group is organised so well it is mainly thanks to all the invaluable and non-chemistry related work you do every day for us. We are all very lucky to work with you. Dawn, thanks a lot for your positivity and help over the years. Sachi, thank you for your calm spirit in these hard times of thesis writing. Adam, thanks for all the thesis reading you have done for me. Don't worry, you are in the right direction to become the best postdoc (after Oxana, I am sorry!). Also

thank you to the present PhD members of the TG group: Hannah, Isabel, Bruno, Emanuele, Jason, June, Shauna and Deirdre. Hannah, te quiero, amor mío, bailamos! Isabel, I will never forget that night we slept IN together in lovely Freemount. I really enjoyed the time we spent together girls. In particular, our girl trip to Madrid with sangria (I love you too my non TG girl Adriana!). The Italians Bruno and Emanuele, I hope you will keep delighting the group with your Italian food. Sorry Emanuele, I prefer the cannoli to the oranges. Jason Marcel Denis, my favourite French person in Ireland (after my beloved Charlyne, bien sûr!). I will try to miss you a little bit mon ami! June, your kindness is as big as your English accent is difficult to understand for me. I hope I am getting better with that! Shauna and Deirdre, I know it is just the beginning but keep strong! You can do it!

To my 4th year buddies: Elena, Dermot and Amy. I feel so lucky I spend these four years with the three of you! Elena, I probably owe half of the cells I used in the biological experiments discussed in this thesis to you. Apart from your help in biochemistry, I really appreciated our deep conversations at night time (including gym, sorry you couldn't get me to join you) and all your support, coffee and donuts over the last few months. I consider you as my friend and I hope we will keep in touch wherever we will be (forget the silly things sometimes I say). We can always meet in Madrid city centre and, if it is too crowded for you, you can be my tourist guide in Alcalá de Henares! Actually, I have never been there. Dermot, the pineapple of my ear, my tequila drinking buddy (with our Amy) and my grammar lover soulmate! You used to say: "We still have four years!" Where did they go?? Not a long time ago, during one of my existential crises, you told me that you didn't know if it was a good idea for me having moved to Ireland to do my PhD but it really was for you because you meet me. If I look back and think of the reasons why I feel happy about spending the last four years in this country, you are one of the main ones. I will always love you my Dermot (in Ireland, in Spain or in the moon). Amy, mi profesora de cosas irlandesas (like making tea for plumbers), my main English corrector (after reading more than 80 pages of this thesis I am sure you love ruthenium as much as I do), my flatmate for the last year and a half (the apartment was not the same since you left...), mi alma gemela (siempre) and I hope my friend for the rest of our life! You will always occupy a special place in my heart and, of course, on my photos wall! ¡Qué haría yo sin ti!

To all the flatmates I lived with for the last for years: Marie, Tim, Alberto, Linda, Anna, Amy (again) and Jenelle. All of you have always made my life much easier. To all the friends who came to Ireland to visit me and enjoy this lovely green country! Because, despite my "eventual" complaints about the weather and Dublin public transport, I really

like Ireland (yes, Amy, I do!). Clara, Sergio and Ana, the first people coming to visit! Miguel, you must really like Ireland to come twice! It doesn't matter if it is having carrot cake (because the coin said noodles) in Ireland, having dinner in the Indian restaurant in Valdemoro, walking on warm stones in Bolonia, having really "nice" ice-creams in Milan, talking about boots in the McDonald's McAuto, or spending a lovely time in Teruel paradise, I always enjoy spending time with you. I am really lucky I met you in December 2009, as you like to remember. Bea and Patricia Feijoo, I can wait to visit you both in San Sebastián and Castellón! Ana, my friend from the time I lived Bruxelles. Estefi, I am happy we are still in touch and you came to Dublin to visit me (with Laura, Sara and Julia). Soraya, we even celebrated my birthday together here last year! Ludo, my Belgian friend, even if you came to show your amazing work to the photochemistry community, I am really happy we saw each other again after more than three years! It is very easy to laugh when you are around (even if the most of your jokes are based on making fun of me!).

Finally, I would like to thank my parents, Mercedes and Antonio, and my beloved sister, Alicia. Se que no soy muy expresiva (solo hay que ver mis tarjetas de felicitación) y que a veces no tengo claro que sepa haceros ver lo importante que sois para mí. Nunca podré agradeceros lo suficiente por la confianza y el apoyo constante no solo en estos últimos cuatro años, si no en cada una de las decisiones que he tomado a lo largo de mi vida aunque hayan significado estar a miles de kilómetros de distancia. Esto también pasará... Os quiero muchísimo.

To everyone who has contributed to the accomplishment of this thesis: thank you, go raibh maith agat, gracias...

Abstract

Ruthenium(II) polypyridyl complexes have been shown to be promising compounds for the design of novel metal-based therapeutic and imaging agents due to their attractive and tuneable photochemical, photophysical and redox properties. This thesis, entitled “Photophysical and Biological Profiling of Ruthenium(II) Polypyridyl Complex-based Systems”, is focused on the development of new Ru(II) polypyridyl complexes with a view to exploiting their attractive photophysical properties for use in biological applications, specifically in the context of DNA binding and photodynamic therapy (PDT) for the treatment of cancer.

The research work presented here is divided into seven chapters. *Chapter 1*, the introduction, first provides a brief overview of the current therapies used in the treatment of cancer. The sections that follow focus on discussing in more detail the two therapeutic strategies most pertinent to this thesis: DNA binding and PDT. Therefore, a description of the DNA structure is given, as well as the different binding modes by which molecules can interact with DNA. The mechanism of action of PDT is then described, and some examples of photosensitisers approved for clinical use in the treatment of cancer are also provided. Following this, the applicability of metal-based compounds as anticancer agents is discussed with particular emphasis on the potential of certain ruthenium complexes. A description of the photophysical properties of Ru(II) polypyridyl complexes and their application as DNA binding, cellular imaging, and PDT agents is also given and supported by relevant examples from the literature. The remainder of the chapter provides a brief account of the properties of gold nanoparticles (AuNPs) and their potential use as platforms for applications in biomedicine. This chapter concludes by reviewing recent examples of Ru(II)-based systems developed in the Gunnlaugsson group and also includes a description of the aims of the research work conducted in each of the subsequent chapters.

In *Chapter 2*, the synthesis and photophysical evaluation of a series of Ru(II) polypyridyl complexes based on an extended aromatic ligand, dipyrido[3,2-*a*:2',3'-*c*][1,2,5]thiadiazolo[3,4-*h*]phenazine, or **dtp**, is presented. Their DNA binding properties are then evaluated using various spectroscopic techniques, such as UV-vis absorption and emission spectroscopy, DNA thermal denaturation, circular dichroism as well as viscosity measurements. In addition, their ability to produce singlet oxygen in DNA-free or -containing media is investigated, followed by their cellular uptake and phototoxicity against

HeLa cervical cancer cells. Part of this chapter has been published in *Dalton Transactions* (2016, **45**, 18208–18220).

Chapter 3 describes a detailed spectroscopic study on the photoadduct formed by covalent binding between the π -deficient complex $[\text{Ru}(\text{TAP})_3]^{2+}$ (**TAP** = 1,4,5,8-tetraazaphenanthrene) and the guanine-containing nucleotide guanosine 5'-monophosphate (GMP) under irradiation with visible light. The pH effect on the spectroscopic properties of such a photoadduct on both ground and excited states is probed with a view to gain further insight into the elusive mechanism by which this mono-photoadduct is capable of reacting with a second molecule of GMP under further irradiation and form a bi-photoadduct, despite its non-emissive character. This double photoreactivity is of particular interest in irreversible and photocontrolled DNA damage *via* crosslinking of the two DNA strands.

In *Chapter 4*, a family of water-soluble amphiphilic Ru(II) polypyridyl complexes is discussed. These complexes possess both a hydrophilic head-group (Ru(II) complex moiety) and different length hydrophobic tails (ten or twenty-one carbon alkyl chains). Ru(II) complexes containing only a methyl group and the parent complexes $[\text{Ru}(\text{phen})_3]^{2+}$ and $[\text{Ru}(\text{TAP})_2\text{phen}]^{2+}$ (**phen** = 1,10-phenanthroline) are also used for comparison. The formation of supramolecular micellar species from the complexes containing the longest alkyl chain is investigated with focus being paid towards determining the critical micelle concentration (cmc) and an estimation of their size. Moreover, the influence of the alkyl chain length in the photophysical properties, DNA binding and singlet oxygen generation is evaluated. Their alkyl chain length-dependent cellular internalisation and their ability to act as PDT agents in live cells is also examined.

Chapter 5 details the synthesis and photophysical characterisation of a series of alkyl disulphide functionalised dinuclear Ru(II) polypyridyl complexes and the conjugates resulting from their attachment onto the surface of AuNPs. Their suitability for use in a cellular environment is also assessed by preliminary cellular uptake and phototoxicity studies.

Finally, an overall conclusion of this work is presented in *Chapter 6*, while *Chapter 7* outlines the experimental procedures, and presents the synthesis and characterisation of the compounds discussed within this thesis. Subsequently, literature references and the Appendices are provided, the latter containing supplementary experimental data to support the work described in the main text.

Abbreviations

A	Adenine or Absorbance (as relevant)
Å	Ångstrom (1×10^{-10} m)
A549	Human lung cancer cell line
ABDA	9,10-Anthracenediyl-bis(methylene)dimalonic acid
AFM	Atomic force microscopy
<i>a priori</i>	From the earlier
aq.	Aqueous
ATR	Attenuated total reflectance
a.u	Arbitrary units
AuNP	Gold Nanoparticle
B78H1	Amelanotic melanoma cell line
BET	Back electron transfer
BHK	Baby hamster kidney cell line
bpy	2,2'-Bipyridine
c	Concentration
C	Cytosine
<i>ca.</i>	<i>Circa</i> ; approximately
calc.	Calculated value
ccc	Covalently closed circular form
CD	Circular dichroism
CDCl ₃	Deuterated chloroform
CD ₃ CN	Deuterated acetonitrile
CHO-K1	Chinese hamster ovarian cell line
CIDNP	Chemically induced dynamic nuclear polarisation
cmc	Critical micelle concentration
COD	1,5-cyclooctadiene
CPP	Cell-penetrating peptide
C_t	Total complex concentration
CT26.WT	Murine colon carcinoma cell line
d	Doublet
D	Doublet or Donor (as relevant)
DAPI	4',6-Diamidino-2-phenylindole
DCFH-DA	2,7-Dichlorofluorescein diacetate

DCF	Dichlorofluorescein
DCM	Dichloromethane
dd	Doublet of doublets
decomp.	Decomposition
DFT	Density functional theory
dip	4,7-Diphenyl-1,10-phenanthroline
DLS	Dynamic light scattering
DMAP	4-Dimethylaminopyridine
DMF	<i>N,N</i> -dimethylformamide
DMSO	Dimethyl sulfoxide
DMSO- <i>d</i> ₆	Deuterated dimethyl sulfoxide
DNA	Deoxyribonucleic acid
DNP	2,4-Dinitrophenol
D/P	Dye-to-DNA phosphate ratio
DPBF	1,3-Diphenylisobenzofuran
dppn	Benzo[<i>i</i>]dipyrido[3,2- <i>a</i> :2',3'- <i>c</i>]phenazine
dppz	Dipyrido[3,2- <i>a</i> :2',3'- <i>c</i>] phenazine
dpq	Dipyrido[3,2- <i>d</i> :2',3'- <i>f</i>]quinoxaline
dtp	Dipyrido[3,2- <i>a</i> :2',3'- <i>c</i>][1,2,5]thiadiazolo[3,4- <i>h</i>]phenazine
E	Energy
EC ₅₀	Half maximal effective concentration
EDC	1-Ethyl-3-(3-dimethylamino-propyl)carbodiimide
<i>e.g.</i>	<i>Exempli gratia</i> ; for example
<i>E</i> _{ox}	Oxidation potential
EPR	Enhance permeability and retention
eq.	Equivalent
<i>E</i> _{red}	Reduction Potential
ES	Excited state
ESI	Electrospray ionization
ET	Electron transfer
<i>et al.</i>	<i>Et alii</i> ; and co-workers
EtOH	Ethanol
<i>f</i> _Δ ^T	Fraction of excited triplet states quenched by O ₂ yielding ¹ O ₂
FBS	Fetal bovine serum
FDA	Food and Drug Administration

FET	Forward electron transfer
FTIR	Fourier transform infrared
G	Guanine
GMP	Guanosine 5'-monophosphate
GS	Ground state
h	Hour
HAT	1,4,5,8,9,12-Hexaazatriphenylene
HeLa	Human cervical cancer cell line
HL60	Human promyelocytic leukaemia cell line
HPLC	High-performance liquid chromatography
HRMS	High-resolution mass spectrometry
$h\nu$	Energy (photon)
Hz	Hertz (s^{-1})
I	Emission intensity
I_a	Apparent emission intensity
IC ₅₀	Half maximal inhibitory concentration
ICD	Induced circular dichroism
ICP-MS	Inductively coupled plasma mass spectrometry
<i>i.e.</i>	<i>Id est</i> ; in other words
IL	Intra-ligand
ILCT	Intra-ligand charge transfer
IVR	Intramolecular vibrational relaxation
<i>in vacuo</i>	Under vacuum
<i>in vitro</i>	In glassware
<i>in vivo</i>	In live samples
IR	Infrared
ISC	Intersystem crossing
J	Coupling constant
K_b	Binding constant
k_{Dec}	Dechelation constant
k_{MC}	MC state activation constant
k_{nr}	Non-radiative rate constant
k_q	Quenching rate constant
k_r	Radiative rate constant
L	Ligand

l	Path length
L1210	Murine leukemia cancer cell line
LC	Ligand-centred
LD	Linear dichroism
LD ₅₀	Median lethal dose
LED	Light-emitting diode
lit.	Literature value
LMCT	Ligand-to-metal charge transfer
log <i>P</i>	log of the octanol/H ₂ O partition coefficient
log <i>D</i>	log of the octanol/buffered solution distribution coefficient
m	Multiplet
<i>m</i>	Slope
M	Molar or molecular ion (as relevant)
MALDI	Matrix-assisted laser desorption/ionization
MC	Metal-centred
MCF-7	Human breast cancer cell line
mDeg	Millidegrees
MeCN	Acetonitrile
MeOH	Methanol
MLCT	Metal-to-ligand charge transfer
mθ	Ellipticity
m.p.	Melting point
MTD50	Maximum tolerated doses 50
<i>m/z</i>	Mass-to-charge ratio
<i>n</i>	Binding site size
NA	Numerical aperture
NaOMe	Sodium methoxide
NEt ₃	Triethylamine
NIR	Near-infrared
NLS	Nuclear localisation signal
NMR	Nuclear Magnetic Resonance
oc	Open circular form
OD	Optical density
ODN	Oligodeoxynucleotide
OPA	Optical parametric amplifier

PACT	Photoactivated chemotherapy
pbpn	4,9,16-Triazadibenzo[<i>a,c</i>]naphthacene
PCET	Proton-coupled electron transfer
PCP	Pentachlorophenol
pD	$-\log[D_3O^+]$
P/D	DNA phosphate-to-ruthenium dye ratio
Pd/C	Palladium on carbon
PDI	Polydispersity index
pdppz	Pyrazino[2,3- <i>h</i>]dipyrido[3,2- <i>a</i> :2',3'- <i>c</i>]phenazine
PDT	Photodynamic therapy
PEP	5-Pyren-1-ylethynyl-1,10-phenanthroline
PET	Photoinduced electron transfer
pH	$-\log[H_3O^+]$
phehat	1,10-Phenanthrolino[5,6- <i>b</i>]-1,4,5,8,9,12-hexaazatriphenylene
phen	1,10-Phenanthroline
PI	Phototoxic index
pip	2-Phenyl-1 <i>H</i> -imidazo[4,5- <i>f</i>][1,10]phenanthroline
p <i>K</i> _a	$-\log K_a$ where K_a is the acidity constant
ppm	Parts per million (Hz/MHz)
PS	Photosensitiser
PT	Proton transfer
$P_{O_2}^T$	Proportion of triplet excited states quenched by O ₂
PTT	Photothermal therapy
q	Quadruplet or quaternary carbon (as relevant)
qdppz	Naphtho[2,3- <i>a</i>]dipyrido[3,2- <i>h</i> :2',3'- <i>f</i>]phenazine-5,18-dione
rac	Racemic
Ref.	Reference
RNA	Ribonucleic acid
ROS	Reactive oxygen species
rpm	Revolutions per minute (1/60 Hz)
rt	Room temperature
s	Singlet
satd.	Saturated
SCE	Saturated calomel electrode
S.E.M.	Standard error of the mean

SK-MEL-28	Human malignant melanoma cell line
SOSG	Singlet oxygen sensor green
SPR	Surface plasmon resonance
SPS	Solvent purification system
SPT	Single photon counting
stDNA	Salmon testes DNA
t	Time or triplet (as relevant)
T	Thymine or temperature (as relevant)
TBACl	Tetrabutylammonium chloride
TAP	1,4,5,8-Tetraazaphenanthrene
TEM	Transmission electron microscopy
TFA	Trifluoroacetic acid
TLC	Thin layer chromatography
T_m	Melting temperature
TMRM	Tetramethylrhodamine methyl ester
TOAB	Tetraoctylammonium bromide
TOF	Time of flight
tpac	Tetrapyrido[3,2- <i>a</i> :2',3'- <i>c</i> :3'',2''- <i>h</i> :2''',3'''- <i>j</i>]acridine
tpphz	Tetrapyrido[3,2- <i>a</i> :2',3'- <i>c</i> :3'',2''- <i>h</i> :2''',3'''- <i>j</i>]phenazine
TrA	Transient absorption
TRIR	Time-resolved infrared
Trp	Tryptophan
Tyr	Tyrosine
U87	Human glioblastoma cell line
UV	Ultraviolet
<i>via</i>	By means of
Vis	Visible
VR	Vibrational relaxation
<i>vs</i>	Versus
δ	Chemical shift
Δ	Heat, increase or delta enantiomer (as relevant)
ϵ	Molar absorptivity
ϵ_a	Apparent molar absorption coefficient
ϵ_b	Molar absorption coefficient of bound complex
ϵ_f	Molar absorption coefficient of unbound (free) complex

η	Refractive index or viscosity (where relevant)
λ	Wavelength
λ_{exc}	Excitation wavelength
λ_{em}	Emission wavelength
λ_{max}	Wavelength of maximum absorbance/intensity
Λ	Lambda enantiomer
τ_{em}	Emission lifetime
τ_M	Pre-exponential weighted mean lifetime
ν	Frequency
Φ_{em}	Emission quantum yield
Φ_{Δ}	Quantum yield of singlet oxygen production
Φ_T	Quantum yield of triplet excited-state formation

“J’aurais aimé commencer cette histoire à la façon des contes de fées. J’aurais aimé dire: “Il était une fois un petit prince qui habitait une planète à peine plus grande que lui, et qui avait besoin d’un ami...” Pour ceux qui comprennent la vie, ça aurait eu l’air beaucoup plus vrai.”

Antoine de Saint-Exupéry, *Le Petit Prince*

Table of Contents

Acknowledgements	i
Abstract	v
Abbreviations	vii
Chapter 1 – Introduction	1
1.1 Introduction	3
1.2 Overview of Cancer Therapies.....	3
1.3 Deoxyribonucleic Acid as Target for Cancer Therapy	5
1.3.1 The Structure of DNA	5
1.3.2 DNA Binding Interactions.....	8
1.4 Photodynamic Therapy in the Treatment of Cancer	10
1.5 Metal Complexes as Anticancer Agents	12
1.6 Ruthenium(II) Polypyridyl Complexes.....	15
1.6.1 Photophysical Properties of Ru(II) Polypyridyl Complexes	16
1.6.2 Ru(II) Polypyridyl Complexes as DNA Binding and Cellular Imaging Agents .	20
1.6.3 π -Deficient Ru(II) Polyazaaromatic Complexes and their Photoreactivity with DNA	24
1.6.4 Ru(II) Polypyridyl Complexes as Photosensitisers for Photodynamic Therapy .	30
1.7 Gold Nanoparticles and their Anticancer Applications	33
1.8 Recent Advances within the Gunnlaugsson Group.....	36
1.9 Objectives of this Work	40
Chapter 2 – Ruthenium(II) Polypyridyl Complexes Containing an Extended ‘dppz’ like Ligand	43
2.1 Introduction	45
2.2 Synthesis and Characterisation of 63 and 64	47
2.3 Crystallographic Studies of 64	51
2.4 Photophysical Characterisation of 63 and 64	54

2.5 DNA Binding Interactions of 63 and 64	57
2.5.1 Spectroscopic Titrations of 63 and 64	57
2.5.2 Thermal Denaturation Studies of 63 and 64	62
2.5.3 Circular Dichroism of 63 and 64 in the Presence of DNA	63
2.5.4 Viscosity Studies of 63 and 64	65
2.6 Singlet Oxygen Photosensitisation of 63 and 64	66
2.7 <i>In vitro</i> Studies of 63 and 64	70
2.7.1 Cellular Uptake Studies of 63 and 64	70
2.7.2 Cellular Toxicity Studies of 63 and 64	71
2.7.3 Nuclear Localisation of 63 and 64 by Ethanol Membrane Permeabilisation	74
2.8 Conclusion and Future Perspectives.....	77
Chapter 3 – Spectroscopic Studies of the Photoadduct Formed between [Ru(TAP)₃]²⁺ and 5'-GMP	81
3.1 Introduction	83
3.2 Photoreaction between 38 and GMP	85
3.3 Purification of the Photoproducts by High-Performance Liquid Chromatography ...	90
3.4 Characterisation of the Isolated Photoproducts by High Resolution MALDI-TOF Mass Spectrometry and UV-vis Absorption and Emission Spectroscopy	91
3.5 Acid Hydrolysis of the Ribose-Phosphate Moiety in 43	95
3.6 Spectroscopic Studies of the Ground State of 43 at Different pH Values	97
3.6.1 UV-vis Absorption and Emission Spectroscopic Studies of 43	98
3.6.2 Fourier-Transform Infrared Spectroscopic Studies of 43	100
3.6.3 Circular Dichroism Studies of 43	103
3.6.4 Nuclear Magnetic Resonance Spectroscopic Studies of 43	106
3.7 Spectroscopic Studies of the Excited State of 43 at Different pH Values	115
3.7.1 ps-Transient Absorption Studies of 43	116
3.7.2 ps- and ns-Time-Resolved Infrared Studies of 43	119
3.8 Conclusion and Future Perspectives.....	126

Chapter 4 – Water-soluble Amphiphilic Ruthenium(II) Polypyridyl Complexes	131
4.1 Introduction	133
4.2 Synthesis and Characterisation of 78–83	135
4.3 Photophysical Characterisation of 78–83	139
4.4 Self-aggregation Ability of 78–83	143
4.4.1 Critical Micelle Concentration Determination of 80 and 83 by Surface Tension Studies	144
4.4.2 Dynamic Light Scattering Studies of 80 and 83	146
4.4.3 UV-vis Absorption and Emission Spectroscopic Studies of 80 and 83	147
4.4.4 Lifetimes versus Concentration Studies of 80 and 83	148
4.5 DNA Binding Interactions of 78–83	150
4.5.1 Spectroscopic Titrations of 78–83	150
4.5.2 Thermal Denaturation Studies of Complexes 78–83	155
4.5.3 Circular Dichroism of Complexes 78–83 in the Presence of DNA.....	157
4.6 Lipophilicity Studies of 78–83	159
4.7 Singlet Oxygen Photosensitisation of 78–83	161
4.7.1 Direct Detection of Singlet Oxygen Production by Time-Resolved Near-Infrared Phosphorescence	161
4.7.2 Indirect Detection of Singlet Oxygen Production by Chemical Photo-consumption of 9,10-anthracenediyl-bi(methylene)dimalonic acid (ABDA)	164
4.8 <i>In vitro</i> Studies of 78–83	169
4.8.1 Cellular Uptake Studies of 78–83	169
4.8.2 Cellular Toxicity Studies of 78–83	172
4.8.3 Intracellular ROS Generation Ability of 80 and 83	176
4.9 Conclusions and Future Perspectives.....	178
Chapter 5 – Ruthenium(II) Polypyridyl Functionalised Gold Nanoparticles for Cellular Imaging	181
5.1 Introduction	183

5.2 Synthesis of 90·AuNP and 91·AuNP	185
5.2.1 Synthesis and Characterisation of 90 and 91	185
5.2.2 Functionalisation of AuNPs with 90 and 91	190
5.3 Dynamic Light Scattering Studies of 90·AuNP and 91·AuNP	192
5.4 Transmission Electron Microscopy Studies of 90·AuNP and 91·AuNP	193
5.5 Photophysical Characterisation of 90 , 91 , 90·AuNP and 91·AuNP	195
5.6 <i>In vitro</i> Studies of 90 , 91 , 90·AuNP and 91·AuNP	200
5.6.1 Cellular Uptake Studies of 90 , 91 , 90·AuNP and 91·AuNP	200
5.6.2 Cellular Toxicity Studies of 90 and 91	204
5.7 Conclusion and Future Perspectives	205
Chapter 6 – Conclusions	209
Chapter 7 – Experimental	215
7.1 General Experimental Apparatus and Techniques	217
7.2 Photophysical and Photochemical Characterisation	219
7.3 DNA Binding Studies Techniques	225
7.4 General Biological Procedures	226
7.5 Materials	227
7.6 General Synthetic Procedures	228
7.6.1 Procedure 1: Synthesis of Polypyridyl Alkylamide Ligands	228
7.6.2 Procedure 2: Synthesis of [Ru(L) ₂ Cl ₂] Complexes	229
7.6.3 Procedure 3: Synthesis of [Ru(L) ₂ (L')] ²⁺ Complexes	229
7.6.4 Procedure 4: Synthesis of Ru(II) Stabilised AuNPs	229
7.7 Synthesis and Characterisation of Compounds Described in Chapter 2	230
7.7.1 Synthesis and Characterisation of Ligands TAP and dtp	230
7.7.2 Synthesis and Characterisation of Complexes 63 and 64	233
7.8 Synthesis and Characterisation of Compounds Described in Chapter 3	234
7.8.1 Synthesis and Characterisation of Complex 38	234

7.8.2 Photosynthesis of the Photoadduct 43	234
7.8.3 Acid Hydrolysis of the Ribose-Phosphate Moiety in the Photoadduct 43	235
7.9 Synthesis and Characterisation of Compounds Described in Chapter 4.....	236
7.9.1 Synthesis and Characterisation of Ligands 84, 85 and 86	236
7.9.2 Synthesis and Characterisation of Complexes 42, 39 and 78–83	238
7.10 Synthesis and Characterisation of Compounds Described in Chapter 5.....	243
7.10.1 Synthesis and Characterisation of the Ligand 89	243
7.10.2 Synthesis and Characterisation of Complexes 90 and 91	244
Chapter 8 – References	247
Appendices	273
Appendix 2.....	275
Appendix 3.....	281
Appendix 4.....	291
Appendix 5.....	311
Publications	315

Chapter 1

Introduction

1.1 Introduction

Small molecules with the ability to bind selectively to deoxyribonucleic acid (DNA) and exhibit photophysical properties sensitive to the binding event, have shown to be potential candidates as imaging probes, diagnostic tools and therapeutic agents.^{1,2} The work presented in this thesis focuses on the design of new ruthenium-based systems and the investigation of their potential in biological applications such as DNA photoprobes and anticancer agents with photocontrolled cytotoxicity. In this chapter a brief overview of the current therapies for the treatment of cancer will be first given, with particular interest in those using DNA as a therapeutic target and light as an external trigger to induce anticancer activity. This will be followed by an introduction of the structure of DNA and the different binding modes to target this biomolecule, as well as a description of the photodynamic therapy (PDT) mechanism. The use of metal complexes as anticancer agents will be then discussed, with a main focus on ruthenium(II) polypyridyl complexes and their attractive photophysical properties that provide them with the ability to be used as DNA targeting molecules and in cancer therapy as PDT agents. Recent developments in the anticancer applications of gold nanoparticles (AuNPs) will be also introduced. The remainder of this chapter will review some examples of previous work completed within the Gunnlaugsson group in the research areas of Ru(II) polypyridyl complexes and AuNPs followed by a description of the work carried out during this thesis.

1.2 Overview of Cancer Therapies

The term cancer is used to define a complex group of more than two hundred diseases which is one of the main causes of death in the world.³ Cancer arises from failures in the mechanisms that regulate cell growth and division resulting in an uncontrolled cell proliferation that can be lethal.⁴ Currently, the most common cancer treatments include surgery, radiotherapy or chemotherapy.⁵ While radiotherapy employs high doses of radiation to treat directly the tumour and kill cancer cells, chemotherapy is based on the use of chemicals with the ability to kill fast-growing and dividing cells.⁶ The mechanism of action of most of chemotherapeutic agents consists of interfering with cell division or DNA synthesis. Different class of chemotherapeutic agents are alkylating agents (*e.g.* chlorambucil (**1**)), anti-metabolites (*e.g.* 5-fluorouracil (**2**)), anthracyclines (*e.g.* doxorubicin (**3**)) or topoisomerase inhibitors (*e.g.* topotecan (**4**)), with some examples shown in Figure 1.1.⁶

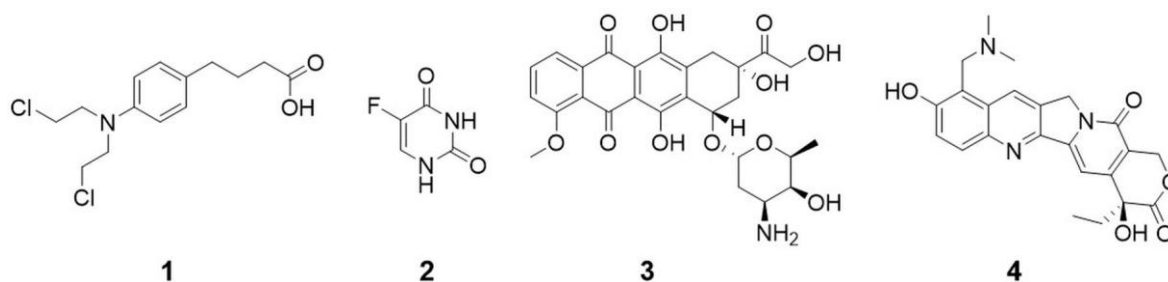


Figure 1.1. Chemical structures of chlorambucil (1), 5-fluorouracil (2), doxorubicin (3) and topotecan (4).

These types of therapies are often used together with a view to prevent cancer cells from acquiring resistance to either therapeutic technique. However, these treatments have been shown to be highly aggressive and non-selective as they destroy many non-cancerous cells resulting in severe side effects.⁷ Therefore, the research for new therapeutic agents able to treat cancer with lower drug toxicity in healthy tissues and more efficacy by targeting tumour angiogenesis has become one of the most important aims in the field of medicinal chemistry.⁸ In this context, targeted therapy has emerged as an alternative to conventional cancer treatment in which pharmacological agents are used to stop cancer from growing and spreading but, in contrast to chemotherapy, they interfere with specific genes or proteins involved in tumorigenesis.⁶ Monoclonal antibodies (*e.g.* bevacizumab) and small-molecule drugs (*e.g.* imatinib) are the two types of targeted cancer therapy.⁶

Other cancer treatments include photodynamic therapy (PDT) and hyperthermia. Both therapies use external triggers (light and heat, respectively) for inducing cancer cells death which results in a local control of the cytotoxicity.⁵ In PDT, a non-toxic molecule (termed photosensitiser) is activated by irradiation with visible or near infrared (NIR) light promoting a number of photochemical processes that lead to the generation of reactive oxygen species (*e.g.* singlet oxygen, free radicals or peroxides) which are highly toxic and cause irreversible photo-damage of tumour tissues.⁹⁻¹¹ On the other hand, hyperthermia uses microwaves, ultrasounds or radiofrequencies to heat a tumour and inhibit proliferation of cancer cells resulting in tumour thermal ablation.

Immunotherapy has also been shown as a promising strategy to treat cancer by using components of the immune systems such as antibodies to help the immune system to destroy tumours.⁵ The potential of this emerging cancer treatment has been recently highlighted when James P. Allison and Tasuku Honjo were awarded with the 2018 Nobel Prize in Physiology or Medicine for their research in cancer immunotherapy. Furthermore, gene therapy has experienced considerable advances in recent years.^{5,12,13} In this therapeutic strategy, DNA, RNA, small interfering RNA and antisense oligonucleotides are introduced

into specific target cancer cells to induce their death or restore normal cellular function.^{5,12,13} Although to date there are not too many examples of gene therapy products commercially available, GenidicineTM and OncorineTM are two adenoviral vectors approved in China for their clinical use.^{5,12,13}

Since the anticancer activity of the compounds that will be discussed along this thesis was aimed to be based on their ability to bind to DNA or becoming cytotoxic after light activation, the use of DNA as therapeutic target and the mechanism of action of PDT agents will be further reviewed in the next sections.

1.3 Deoxyribonucleic Acid as Target for Cancer Therapy

Deoxyribonucleic acid (DNA) is known to carry the genetic information essential to cell function and viability. Therefore, the development of molecules capable to target DNA and inducing cell damage by disruption of the replication and transcription processes has become the focus of research in various field of medicine. In this context, DNA binders have been revealed as promising drugs in the treatment of cancer.¹⁴ Thus, the understanding of the DNA structure is essential in order to develop compounds capable of interacting specifically with this biomolecule and will be presented next.

1.3.1 The Structure of DNA

The double helix structure of DNA was discovered in 1953 by Watson and Crick from Rosalind Franklin's X-ray data.^{15,16} DNA is a biopolymer usually consisting of two strands arranged in a right handed antiparallel double helix.¹⁵ Each strand is composed of a number of nucleosides which are consecutively joined by phosphate groups resulting in a poly-anionic chain.¹⁶ Nucleosides comprise a deoxyribose monosaccharide and a nitrogenous base. DNA contains four different nitrogenous bases: the purines, *adenine* (A) and *guanine* (G), and the pyrimidines, *thymine* (T) and *cytosine* (C). Hydrogen bonds are formed between the bases of complementary strands and are known as the Watson-Crick base pairing.¹⁵ Thus, adenine always pairs with thymine through two hydrogen bonding interactions and guanine always pairs with cytosine by three hydrogen bonding interactions as shown in Figure 1.2a. Alternative Hoogsteen base pairing can also occur in which the N7 face of adenine and guanine are hydrogen bonded to thymine or another adenine base, and cytosine or another guanine base, respectively. Such interactions result in the formation of secondary structures of DNA including triple-stranded DNA and G-quadruplex.

The nucleobases are partially stacked due to hydrophobic and electrostatic interactions which depend on the aromaticity and dipole moments. Thus, while the

hydrophobic bases are packed into the core, the hydrophilic phosphate backbone (Figure 1.2b) is positioned on the outside of the helical structure to interact with water molecules. The asymmetry in the base stacking results in the formation of two grooves of different size (major and minor grooves) in the double helix.¹⁵ Both hydrogen bonding between base pairs and base stacking provide stability to the double helix structure of DNA.¹⁷⁻¹⁹

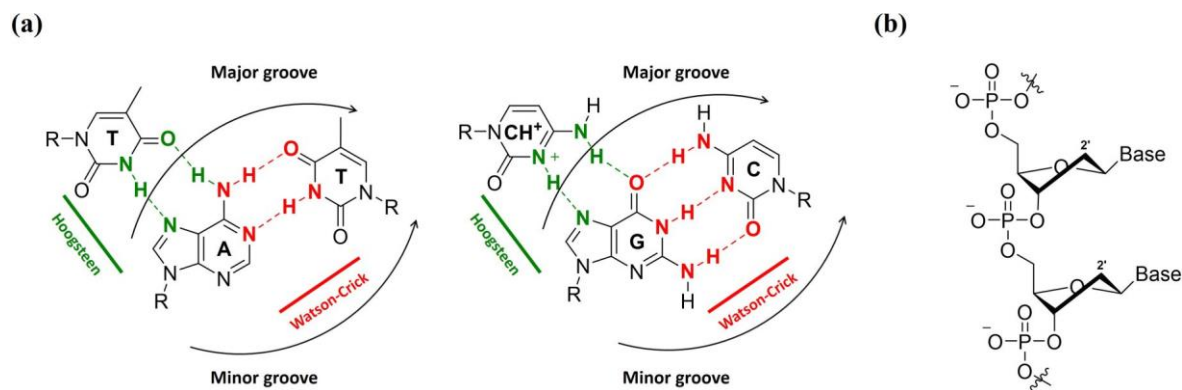


Figure 1.2. a) Chemical structure of the DNA base pairs showing the Watson-Crick and the Hoogsteen base pairing and the position of the minor and major groove. (b) The alternating deoxyribose-phosphate that form the DNA backbone.

B-DNA is the classic right-handed helical structure described by Watson and Crick and the most common DNA conformation. However, a number of other forms (*e.g.* A-DNA and Z-DNA) are also possible depending on environmental conditions such as humidity, pH, temperature, and salt concentration.²⁰⁻²⁴ The structures of B-DNA, A-DNA and Z-DNA are depicted in Figure 1.3.²⁵

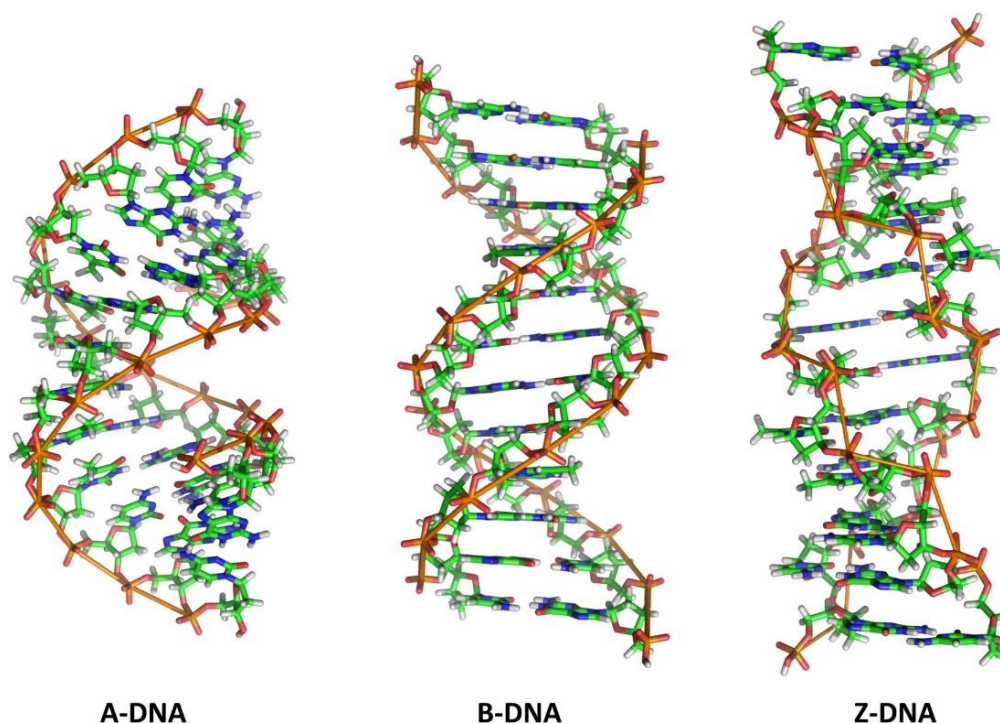


Figure 1.3. Representative crystal structures for A-DNA, B-DNA and Z-DNA.²⁵

The interactions of water molecules with the two DNA grooves are very important for the stabilisation of the B-DNA structure.^{24,26-28} Fibre and single crystal diffraction studies have shown a reversible conformation change of B-DNA to A-DNA when the relative humidity is reduced to 75%.^{29,30} A-DNA is also a right-handed helical structure but wider and flatter than B-DNA. A third conformation, Z-DNA, was also founded in sequences of alternating guanine and cytosine residues in the presence of high salt concentration as shown by fibre X-ray diffraction and Nuclear Magnetic Resonance (NMR) spectroscopy.^{31,32} This conformation shows a left-handed helical structure and a “zig-zag” arrangement of the phosphate backbone when compared to A- or B-DNA. A summary of the structural features of all three conformations is given in Table 1.1.¹⁵

Table 1.1. Average helix parameters for A-DNA, B-DNA and Z-DNA.¹⁵

	A-DNA	B-DNA	Z-DNA
Helix	Right-handed	Right-handed	Left-handed
Diameter	~26 Å	~20 Å	~18 Å
Base pairs per helical turn	11	10	12
Helical twist per base pair	32.7°	36°	-9°, -51°
Helix rise per base pair	2.56 Å	3.4 Å	3.7 Å
Base tilt to the helix axis	20°	-6°	-7°
Major groove	Narrow and deep	Wide and deep	Flat
Minor groove	Wide and shallow	Narrow and deep	Narrow and deep
Glycosidic bond	Anti	Anti	Anti for pyrimidines, syn for purines
Sugar pucker	C3'-endo	C2'-endo	C2'-endo for pyridines, C3'-endo for purines

In its B conformation as is the most prevalent in nature, the DNA double helix possesses a number of structural features that makes it chemically accessible for specific molecules that can act as DNA targeting drugs. Indeed, the mechanism of action of a large number of clinically important drugs has shown to occur *via* DNA interaction and subsequent inhibition of its biological function.¹ Thus, in the next section, the different existing ways by which potential DNA binders interact with the polynucleotide will be discussed.

1.3.2 DNA Binding Interactions

Based on the DNA structure described in the previous section, the interaction of small molecules with the double helix can take place by five major binding modes: (i) electrostatic binding, (ii) major groove binding, (iii) minor groove binding, (iv) intercalation and (v) covalent binding, as illustrated in Figure 1.4. It is not unusual that more than one binding mode is involved in the interaction of molecules with DNA.

The polyanionic nature of DNA makes the double helical structure suitable for electrostatic interactions with cationic molecules in a non-specific way.³³ For example, protonated polyamines such as spermidine (**5**) and spermine (**6**), which have shown to play an essential role in cell growth, bind to DNA by electrostatic interactions with the negatively charged phosphate backbone (Figure 1.5).³⁴

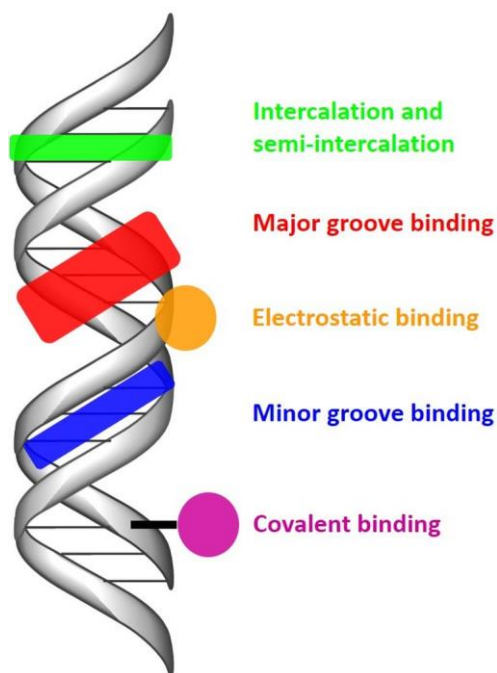


Figure 1.4. Schematic representation of the binding modes possible for double helical DNA.

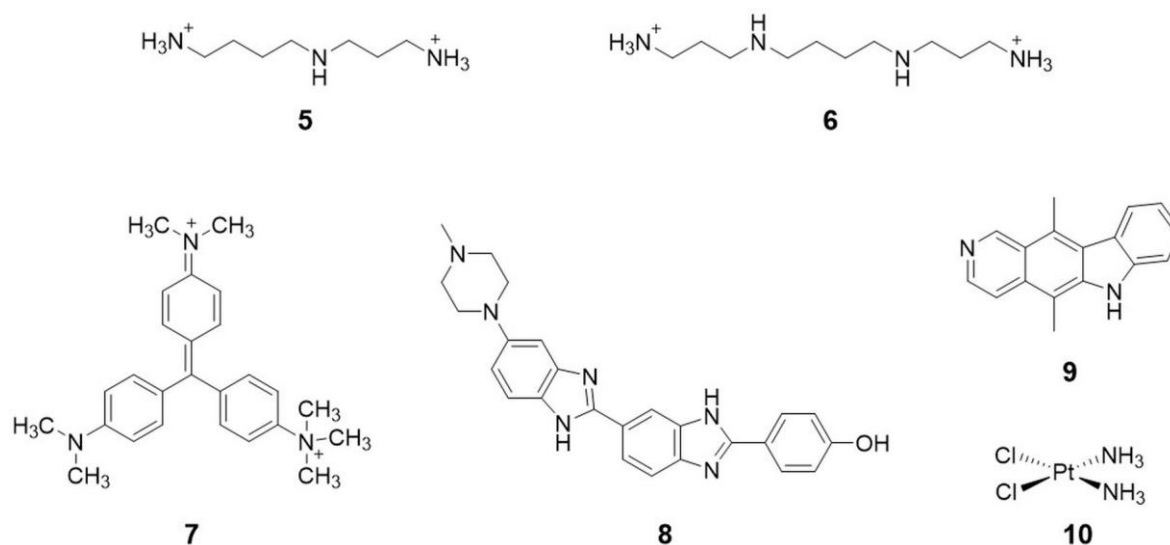


Figure 1.5. Chemical structures of spermidine (**5**), spermine (**6**), methyl green (**7**), Hoechst 33258 (**8**), ellipticine (**9**) and cisplatin (**10**).

On the other hand, the grooves are interesting areas within the DNA structure for binding of small molecules since it is at such locations that the functional groups of the nucleobases are exposed to the environment providing a series of hydrogen bond donors and

acceptors depending on the DNA sequence (Table 1.2). This makes the groove a potential region for sequence specificity of binding.^{35,36} Therefore, compounds possessing an adequate size and shape to be placed in the grooves and form hydrogen bonds with the functional groups of the bases will bind to either the major or minor grooves.^{35,37-39} The grooves also differ in electrostatic potential, steric effects and hydration.²² While large size molecules tend to bind to the major groove, minor groove binders are often characterised by being cationic due to an enhanced negative electrostatic potential in the minor groove, and containing several aromatic rings connected by bonds with torsional freedom.^{35,37-39} In addition, the displacement of the spine of well-ordered water molecules in the minor groove is the entropic driving force which promotes binding into this groove. Example of molecules that bind to the grooves are the DNA fluorescent dyes methyl green (**7**) and Hoechst 33258 (**8**) which bind to the major and minor grooves, respectively (Figure 1.5).^{40,41}

Table 1.2. The hydrogen bond donating and accepting functional groups of the nucleobases (A, T, G and C), which are exposed in the major and minor grooves of the DNA.

Hydrogen Bond Site	Major Groove	Minor Groove
Donor	N ₆ amino (A), N ₄ amino (C)	N ₂ amino (G)
Acceptor	N ₇ (A), O ₄ (T), N ₇ (G), O ₆ (G)	N ₃ (A), O ₂ (T), N ₃ (G), O ₂ (C)

Furthermore, molecules containing extended aromatic moieties may also bind to DNA by π -stacking interactions with the hydrophobic nitrogenous bases of DNA. Such intercalative binding mode requires the stacked base pairs to separate by an additional 3.4 Å to accommodate the intercalating ligand which results in an unwinding and lengthening of the DNA double helix.⁴²⁻⁴⁴ In addition to the intercalating planar moiety, many intercalators possess a positive charge which provides them with an electrostatic contribution to their binding to DNA. Inhibition of the topoisomerases involved in DNA replication and transcription is known as the mechanism of action of DNA intercalators.^{45,46} For example, the natural plant alkaloid ellipticine (**9**) and its derivatives exert their anticancer activity by intercalation into the DNA and inhibition of topoisomerase II (Figure 1.5).^{47,48}

Finally, covalent bonds can also be formed between the DNA and molecules with the ability to react with some of the DNA structure functionalities. Alkylating agents such as nitrogen mustard, previously mentioned in Section 1.2, are known as the first class of molecules showing such reactivity with DNA.⁴⁹ These chemotherapeutic drugs cause DNA damage by addition of alkyl groups to the nitrogen atoms of the guanine and adenine

nucleotides resulting in cell apoptosis.^{6,50} In addition to this type of alkylating agents, platinum-based therapeutics such as cisplatin (**10**) and its analogues are commonly used in the treatment of several types of cancer, being particularly effective against testicular cancer (Figure 1.5).^{51,52} The antitumor activity of cisplatin is based on its ability to covalently bind to DNA after displacement of the two chloride ligands and coordination to the N7 position of purine bases from the same or different strands resulting in DNA inter- and intra-strand crosslinking.^{52,53} This results in the distortion of the DNA structure causing the inhibition of gene expression and, eventually, leading to cellular apoptosis.^{52,54-56}

DNA binding is not the only therapeutic strategy attempted in this thesis to induce cell death. In order to increase selectivity of the compounds presented in this work, the use of light to trigger the anticancer activity of such molecules will be also investigated. Therefore, the use of PDT as anticancer therapy will be next discussed.

1.4 Photodynamic Therapy in the Treatment of Cancer

Since its inception in early 1900s and later demonstration in the 1970s, photodynamic therapy has emerged as a complementary cancer treatment to conventional therapies such as surgery, radiotherapy or chemotherapy.^{11,57,58} This anticancer strategy involves the administration of a photosensitiser (PS) that, ideally, is not non-toxic in the dark (Figure 1.6). After uptake and accumulation into cancer cells, the PS is activated by localised visible

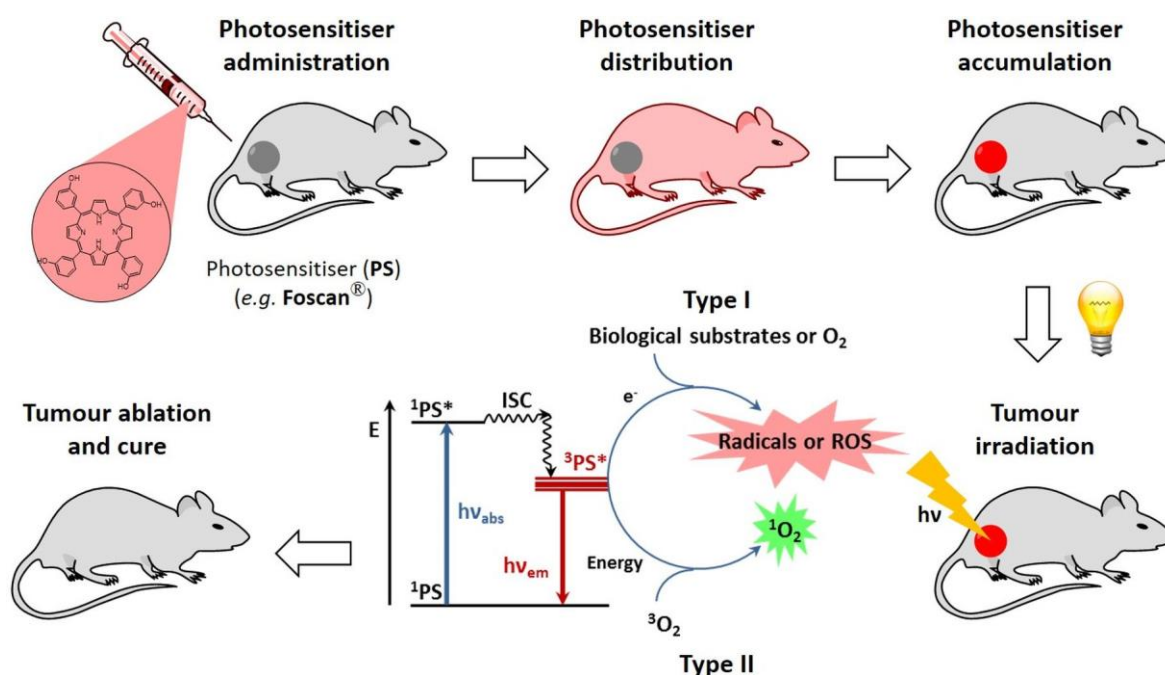


Figure 1.6. Schematic representation of the mechanism of action of PDT for a photosensitiser (PS) expressed using a modified Jablonski diagram.

or NIR light. It should be noted that, although visible light cannot penetrate deep into tissues, the recent developments in light sources and light delivery technologies (*e.g.* fiber optic light guides) overcome the limitation of the use of visible light for diseases affecting the surface of the body.⁵⁹ Thus, absorption of a photon of light at a particular wavelength by the singlet ground state of the PS (^1PS) results in the formation of its short-lived singlet excited state ($^1\text{PS}^*$) which subsequently undergoes intersystem crossing and the long-lived triplet excited state of the PS ($^3\text{PS}^*$) is generated. Two different oxidative mechanisms, named Type I and Type II, can then occur. The Type I mechanism consists of a hydrogen or electron transfer from the $^3\text{PS}^*$ to the surrounding biological substrates, resulting in radical formation which can further react with molecular oxygen and generate reactive oxygen species (ROS) such as the superoxide anion, hydroxyl radical or hydrogen peroxide. Alternatively, the Type II mechanism involves the energy transfer from the $^3\text{PS}^*$ to molecular oxygen in its ground triplet state ($^3\text{O}_2$) releasing singlet oxygen ($^1\text{O}_2$). These generated species are highly toxic and induce irreversible tissue damage, leading to apoptosis.^{9,60-63} Therefore, the therapeutic activity of PDT agents relies on the cell damage caused by reactions with oxygen upon light exposure.

Both PDT pathways can occur simultaneously, and the ratio between these two processes depends on the properties of PS, the concentration of biomolecules and molecular oxygen present, and the binding affinity of PS for a particular biomolecule.¹⁰ However, Type II mechanism is considered as the primary mode of action for most PDT agents.^{64,65} Interestingly, $^1\text{O}_2$ has a short half-life (*ca.* 40 ns) and only diffuses a short distance within the cells (*ca.* 100 nm) and as such it will rapidly react with the surrounding biomolecules resulting in a PS subcellular localisation dependence of the cell damage.⁶⁶⁻⁶⁸ Thus, PDT allows a spatial and temporal photocontrol resulting in a powerful strategy to minimise the toxic side effects to non-cancerous cells shown by many chemotherapeutic drugs nowadays.⁶⁹

A hematoporphyrin derivative, Photofrin[®] (**11**), was the first PS approved by the U. S. Food and Drug Administration (FDA) for clinical use in the treatment of cancer in the 1990's and belongs to the first generation of PSs (Figure 1.7).^{70,71} Since then, other porphyrin-based PS have been developed as an attempt to overcome the drawbacks exhibited by the first generation of PS such as poor light absorption, water insolubility, poor bioavailability, prolonged photosensitivity or tumour selectivity.⁷⁰ The second generation of PSs includes the protoporphyrin prodrug Levulan[®] (**12**), the chlorin Foscan[®] (**13**) and the benzoporphyrin Visudyne[®] (**14**).⁷⁰⁻⁷²

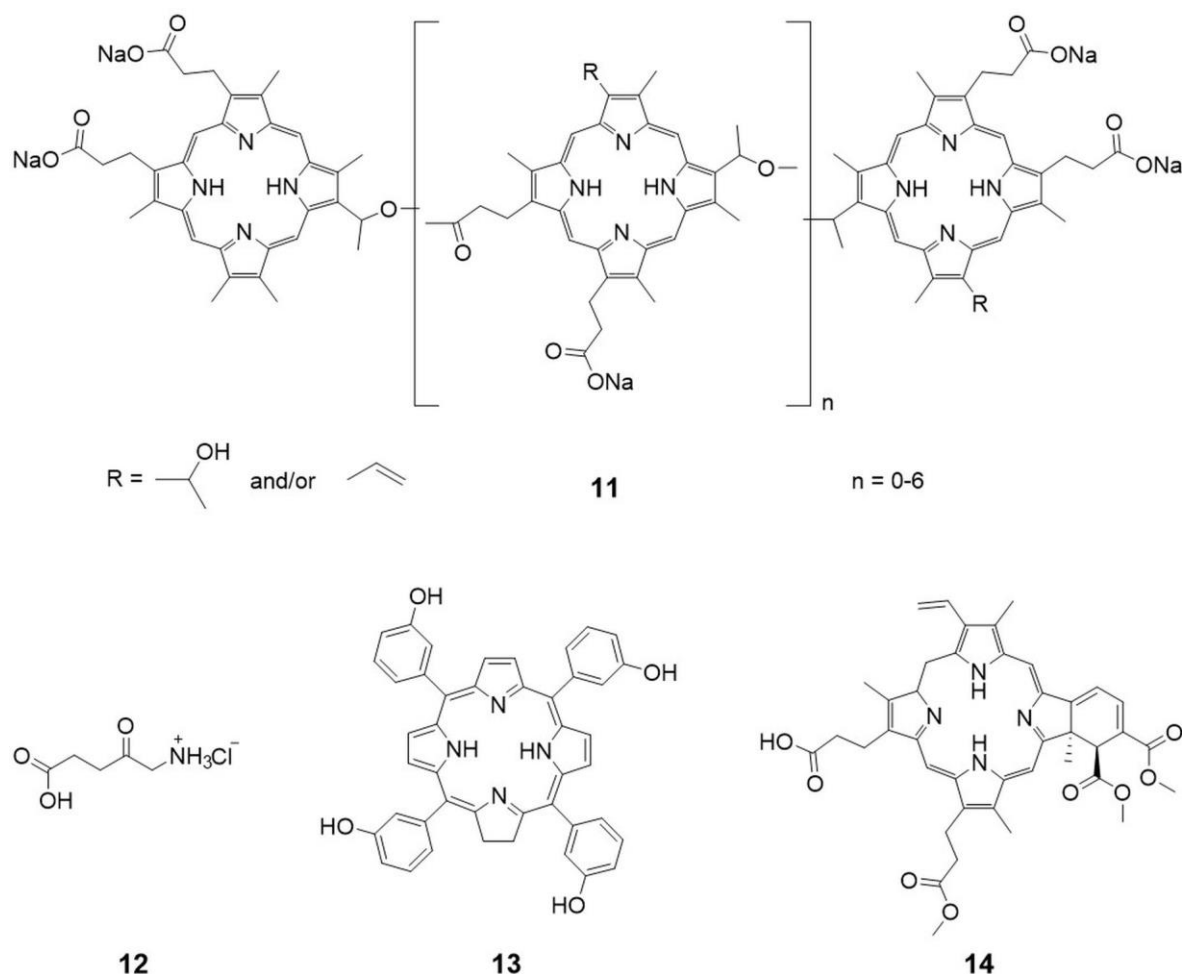


Figure 1.7. Chemical structures of Photofrin[®] (11), Levulan[®] (12), Foscan[®] (13) and Visudyne[®] (14).

However, despite its potential application in the treatment of cancer, PDT remains underused as a first-line oncological therapy, most likely due to the difficulty in finding an ideal photosensitizer. Therefore, there is still a need to develop new classes of non-porphyrin-based photosensitizers and it will be one of the aims of the work presented in this thesis.

1.5 Metal Complexes as Anticancer Agents

The use of metal-based compounds in the treatment of diseases dates back to times of ancient Assyrians, Egyptians and Chinese. For example, Chinese medical practitioners used arsenic trioxide as antiseptic and to treat psoriasis, syphilis and rheumatoid diseases.⁷³ Gold and copper were also known by the Egyptians and Chinese for their potential in the treatment of certain diseases such as syphilis.⁷³ More recently, the serendipitous discovery of the antitumor properties of cisplatin (10) in the 1960's by Rosenberg *et al.* was a landmark in the history of the treatment of cancer with metal-based compounds.^{74,75} Since then, the development of new metal-based drugs for use as anticancer agents has become a promising

research field in medicinal chemistry.^{73,76-81} The mechanism of action of cisplatin was previously discussed in Section 1.3.2. Despite its FDA approval and current use for the treatment of testicular, ovarian and bladder cancers, cisplatin displays several side effects derived from the lack of selectivity as well as resistance.⁸² Therefore, the next step in this research field was the design of new metallic compounds able to overcome these disadvantages. In this context, many Pt(II)-based complexes have been synthesised with the aim of improving the anticancer and pharmacokinetic properties of cisplatin, some of which have shown promising anticancer activity.^{73,77,83} Examples of successful cisplatin derivatives are carboplatin (**15**) and oxaliplatin (**16**), that were approved by the FDA for the treatment of several cancers (Figure 1.8).^{73,84}

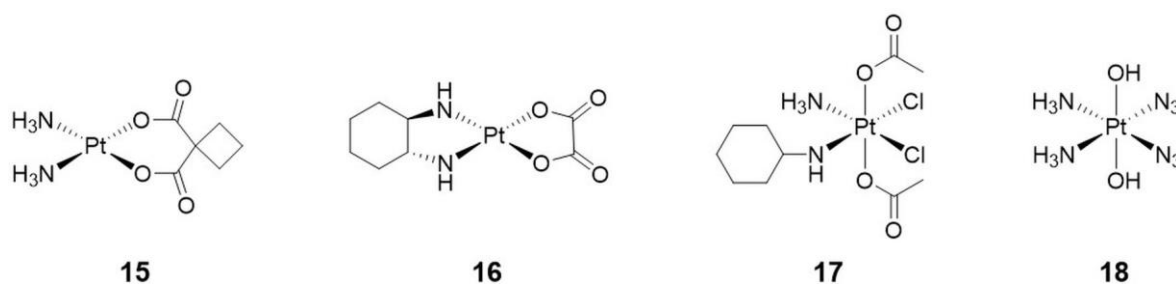


Figure 1.8. Chemical structures of platinum complexes: carboplatin (**15**), oxaliplatin (**16**), satraplatin (**17**) and Pt(IV) azide complex (**18**).

However, the lack of superior advantage of some platinum drugs over cisplatin and the remaining toxicity towards normal cells led to the development of new strategies to reduce the side effects of Pt(II)-based compounds. In this context, Pt(IV) complexes can be used as prodrugs to overcome some of the shortcomings showed by cisplatin and Pt(II) derivatives.⁸³ A prodrug is an inactive compound that becomes active after metabolization. In this case, Pt(IV) complexes have been shown to confer drug stability when compared to the Pt(II) complex analogues due to the two extra ligands coordinated to the octahedral metal centre. Intracellular reduction of Pt(IV) to Pt(II) leads to activation of the cytotoxicity of the Pt-based compound and provides a way to control its anticancer activity. Satraplatin (**17**) is an example of Pt(IV) prodrug of cisplatin (Figure 1.8) and, although it has not been approved by the FDA, it was the first orally active Pt-based chemotherapeutic drug developed.⁸⁵ Furthermore, photoactivation of Pt(IV) prodrugs by incorporation of two azide ligands (**18**) has also been investigated by Sadler *et al.* (Figure 1.8).⁸⁶ Thus, the active antitumour agent is released upon light irradiation resulting in a localised cancer treatment.

The anticancer application of metals is not limited to Pt-based complexes. Despite the reluctance of pharmaceutical industry to use “heavy metals” as therapeutic agents, a wide

range of transition metals have shown promising properties as chemotherapeutic drugs, including charge variation, redox activity and several coordination geometries that give them different shapes.⁷³ In this area, numerous metal compounds have been investigated as antitumour agents. For example, gold complexes have emerged as a potential anticancer alternative to cisplatin. Auranofin (**19**), a gold complex used to treat rheumatoid arthritis (Figure 1.9), was also found to be active against tumour cells by inhibition of DNA, RNA and protein synthesis.⁷⁶ On the other hand, titanium complexes such as titanocene C (**20**) have been shown to exhibit antiproliferative activity against several human cancer cell lines (Figure 1.9).^{73,87}

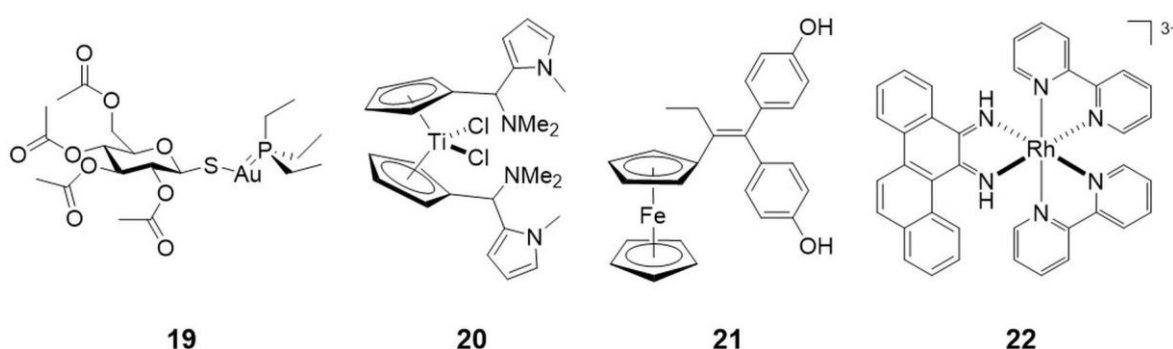


Figure 1.9. Chemical structures of several metal complexes: Auranofin (**19**), titanocene C (**20**), ferrocifen (**21**) and rhodium metalloinsertor (**22**).

Another example of a metal complex with anticancer properties is ferrocifen (**21**), an organometallic iron complex derived from the anti-estrogen tamoxifen (Figure 1.9), which has been found to display antitumour effects on breast cancer cells.^{76,88} Furthermore, a series of rhodium metalloinsertors (e.g. **22**) developed by Barton *et al.* (Figure 1.9) have shown to exert antiproliferative activity against human colorectal carcinoma cell lines through DNA base mismatch binding.^{89,90} Other metal-containing anticancer agents described in the literature include copper, silver, cobalt, osmium or iridium compounds.^{73,76,80,81}

Ruthenium complexes are also a promising alternative to platinum-derived drugs.^{8,91} In addition to their tuneable photophysical properties, these complexes show interesting features for use in biological applications.^{62,63,91-94} For instance, they exhibit activity against some cell lines that are resistant to cisplatin, low side effects, selective uptake by cancer cells when compared with healthy tissue, and binding to some biological structures such as transferrin as it has similar chemical properties to iron.⁹¹ There are a few ruthenium complexes that have entered clinical trials including two Ru(III) complexes NAMI-A (**23**) and KP1339 (**24**) (Figure 1.10).^{95,96} The mechanism of action of these compounds involves the activation by reduction of the Ru(III) complexes into a more active Ru(II) form when

they are localised in the characteristic hypoxic environment of tumours allowing a localised toxicity control. Furthermore, the Ru(II)-arene complex RAPTA-C (**25**) in combination with erlotinib has shown efficient anticancer action (Figure 1.10).⁹¹ In addition, ruthenium half-sandwich complexes (*e.g.* **26**) designed by Meggers *et al.* (Figure 1.10) as mimics of the natural product staurosporine were found to act as kinase inhibitors.^{97,98} The selective inhibition of kinases activity is a potential strategy in the treatment of cancer as certain kinases have shown to be more active in some types of cancer cells.

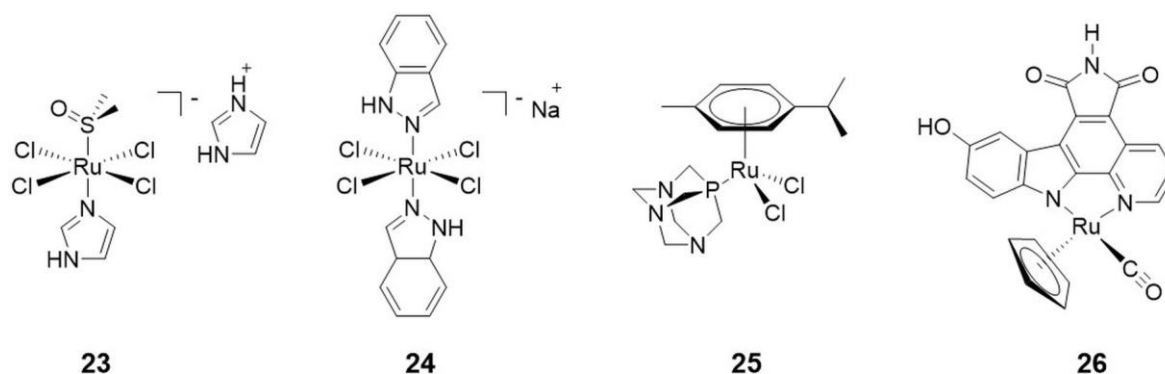


Figure 1.10. Chemical structures of ruthenium complexes: NAMI-A (**23**), KP1339 (**24**), RAPTA-C (**25**) and half-sandwich kinase inhibitor (**26**).

Another class of ruthenium complexes that have shown promising results against cancer cells are Ru(II) polypyridyl complexes.^{62,63,92,93} As they are the type of complexes the work described in this thesis will be focused on, their photophysical and photochemical properties as well as their biological applications, in particular as DNA probes and anticancer agents, will be presented in detail in the next section.

1.6 Ruthenium(II) Polypyridyl Complexes

Over the last number of decades, Ru(II) polypyridyl complexes have received an increasing interest due to their extraordinary photochemical, photophysical and redox properties.^{99,100} Such complexes are characterised by the absorption of light in the visible region (λ_{MLCT} of *ca.* 450 nm), luminescence in the red spectral range (λ_{max} of *ca.* 600 nm or greater), large Stokes shift and relatively long luminescence lifetimes (typically from hundreds of nanoseconds to a few microseconds). These properties make Ru(II) polypyridyl complexes very attractive candidates for applications in several research fields such as in light harvesting antenna systems, in artificial photosynthesis, as catalysts for the oxidation of water to molecular oxygen or as light-emitting devices.¹⁰¹⁻¹⁰⁵ Furthermore, the study of these complexes as potential DNA photoprobes (for cellular imaging) or as phototherapeutic agents has received particular attention.^{2,62,63,93} Since the Ru(II) complexes discussed in this

thesis have been designed for their use in biological applications, a more detailed explanation regarding their biological relevance will be given in the following sections of this chapter after first discussing their photophysical properties.

1.6.1 Photophysical Properties of Ru(II) Polypyridyl Complexes

The properties of Ru(II) polypyridyl complexes can be modulated by the nature of the ligands coordinated to the metal centre. Thus, an understanding of the photophysical behaviour of these complexes is necessary in order to select the appropriate ligands for the design of compounds with specific applications. Ruthenium is a transition metal with electronic configuration $[\text{Kr}]4d^75s^1$. In complexes with organic ligands, the most common oxidation states of ruthenium are II or III. For the purpose of this work, the focus will be on ruthenium complexes in the oxidation state II and, in particular, those containing polypyridyl ligands. Ru(II) has six d electrons in its valence shell and commonly forms octahedral complexes. The polypyridyl ligands reported here are bidentate ligands which possess σ -donor orbitals localised on the nitrogen atoms and π -donor and π^* -acceptor orbitals delocalised on the aromatic rings. A simplified molecular orbital diagram for a Ru(II) polypyridyl complex and the main electronic transitions is shown in Figure 1.11.^{99,106}

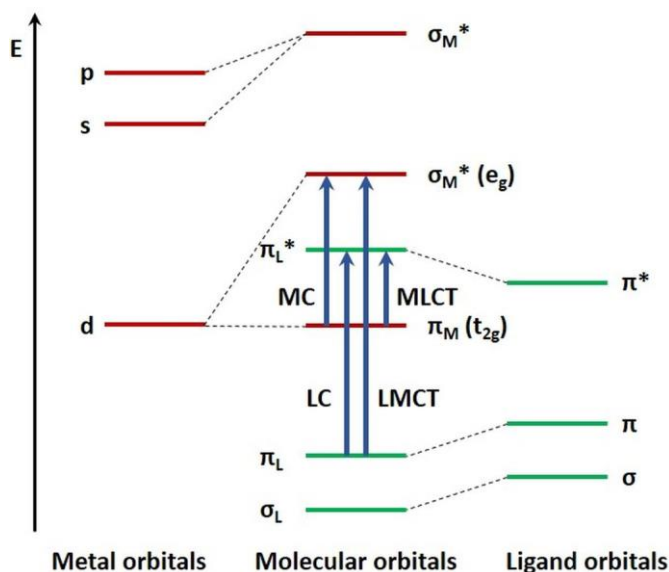


Figure 1.11. Molecular orbital diagram for a $[\text{Ru}(\text{L-L})_3]^{2+}$ complex (L-L = polypyridyl ligand, e.g. **bpy**) in octahedral symmetry showing the electronic transitions: metal-centred (MC), ligand-centred (LC), ligand-to-metal charge transfer (LMCT) and metal-to-ligand charge transfer (MLCT). The energy of orbitals depend on the ligands that form the Ru(II) complex.¹⁰⁷

Three fundamental types of electronic transitions occur in these complexes and can be observed in their characteristic UV-vis absorption spectra:

- 1) *Metal-to-ligand charge transfer (MLCT)*: spin-allowed electronic transitions between the nonbonding metal-centred orbitals (π_M) and antibonding ligand-centred orbitals (π_L^*). These transitions are observed in the visible region between 400 and 500 nm.
- 2) *Ligand-centred (LC)*: spin-allowed electronic transitions between bonding (π_L) and antibonding (π_L^*) ligand-centred orbitals. Such transitions can be detected in the UV region between 200 and 400 nm.
- 3) *Metal-centred (MC) or d-d transitions*: Laporte forbidden electronic transitions between the nonbonding (π_M) and antibonding (σ_M^*) metal centred orbitals. These transitions are weak in intensity and are usually hidden beneath the LC and MLCT bands.

One of the most studied Ru(II) polypyridyl complexes is $[\text{Ru}(\text{bpy})_3]^{2+}$ (**27**) (**bpy** = 2,2'-bipyridine, Figure 1.12a). Since this compound was first synthesised in 1936, its photophysical properties have been extensively investigated and it has been used as a reference model for other Ru(II) polypyridyl complexes.^{99,108}

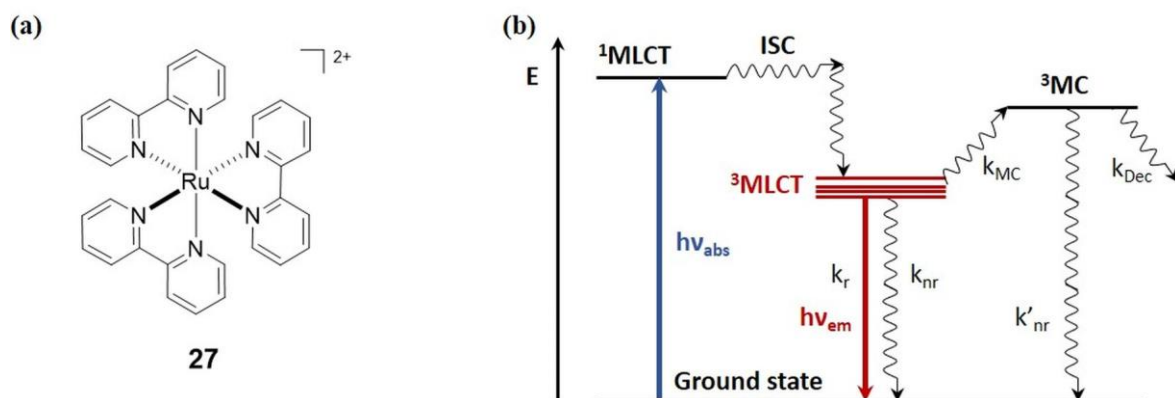


Figure 1.12. (a) Chemical structure of $[\text{Ru}(\text{bpy})_3]^{2+}$ (**27**). (b) Simplified Jablonski diagram for **27**. k_r = radiative constant, k_{nr} = non-radiative constant, k_{Dec} = dechelation constant, k_{MC} = MC state activation constant

The photophysical model accepted in the literature for **27** is shown in Figure 1.12b.^{109,110} When the complex absorbs a photon, a singlet metal-to-ligand charge transfer ($^1\text{MLCT}$) excited state is generated. Although singlet to triplet transitions are formally spin-forbidden, extremely rapid (less than 1 ps) intersystem crossing (ISC) results in the population of a triplet metal-to-ligand charge transfer ($^3\text{MLCT}$) excited state. This $^3\text{MLCT}$ excited state has been shown to consist of three excited states that are very close in energy and a fourth state that is slightly higher in energy.¹¹¹⁻¹¹⁴ Deactivation of this $^3\text{MLCT}$ excited state can then occur through three different processes:

- 1) Radiative decay through the emission of a photon which explains the luminescence observed for several ruthenium complexes in the wavelength region between 600 and 900 nm. This radiative transition is spin-forbidden as it occurs from a triplet excited state to a singlet ground state and is known as phosphorescence. The radiative rate constant (k_r) of phosphorescence is much lower than that observed in fluorescence, where the radiative transition is allowed, and takes place between a ground and an excited state with the same spin multiplicity (singlet-singlet). This explains the longer-lived excited states observed for these complexes when compared with organic fluorophores.
- 2) Non-radiative decay through a loss of energy generally released as heat to the solvent. For some Ru(II) polypyridyl complexes it has been shown that the non-radiative rate constant (k_{nr}) decreases when the energy gap between the excited and ground states is bigger.^{113,115-119}
- 3) Population of a triplet metal-centred (^3MC) state by thermal activation which is typically deactivated by a non-radiative process because of the large structural distortion of this state with respect to the ground state.¹²⁰ In addition, population of the ^3MC states can result in the loss of a ligand from the complex (ligand photo-ejection) due to the strong antibonding character of this excited state that makes the Ru-N bond longer and weaker.^{121,122} Although, this photochemical reaction is responsible for the photoinstability of some Ru(II) polypyridyl complexes, it has also been exploited as a therapeutic tool through the development of complexes that are capable of inducing toxicity after photoinduced loss of a ligand where the biological activity is either in the resulting ruthenium complex or in the released ligand.¹²³⁻¹³⁵

However, this model cannot explain the photophysical behaviour of all Ru(II) polypyridyl complexes particularly in the case of complexes containing extended aromatic ligands such as $[\text{Ru}(\text{bpy})_2\text{dppz}]^{2+}$ (**28**) where **dppz** is [2,3-*h*]dipyrido[3,2-*a*:2',3'-*c*]phenazine. This complex was synthesised for the first time in 1985 by Sauvage and co-workers and has been widely studied ever since.¹³⁶ In contrast to $[\text{Ru}(\text{bpy})_3]^{2+}$, neither $[\text{Ru}(\text{bpy})_2\text{dppz}]^{2+}$ nor $[\text{Ru}(\text{phen})_2\text{dppz}]^{2+}$ (**29**) (**phen** = 1,10-phenanthroline, Figure 1.13a) show any luminescence in aqueous solution upon excitation of the MLCT band. However, in aprotic solvents they do. This particular behaviour can be explained with an alternative photophysical model (Figure 1.13b) which proposes the existence of two $^3\text{MLCT}$ states centred on the **dppz** ligand; a luminescent state where the charge transfer occurs from the ruthenium centre to the 1,10-phenanthroline moiety of the **dppz**, and a non-luminescent

"dark state" corresponding to the charge transfer from the metal centre to the phenazine functionality on the extended ligand.^{137,138} The relative energy of both states depends on the solvent employed. Thus, in protic solvents such as water, the "dark state" will be stabilised due to the formation of hydrogen bonds with the nitrogen atoms of the phenazine moiety. Therefore, the "dark state" will be lower in energy than the luminescent state and will be more populated. However, in aprotic solvents, such hydrogen bonds cannot be formed and thus the "dark state" will be less stabilised. The luminescent state will be more accessible causing the $[\text{Ru}(\text{bpy}/\text{phen})_2\text{dppz}]^{2+}$ complex to become emissive.

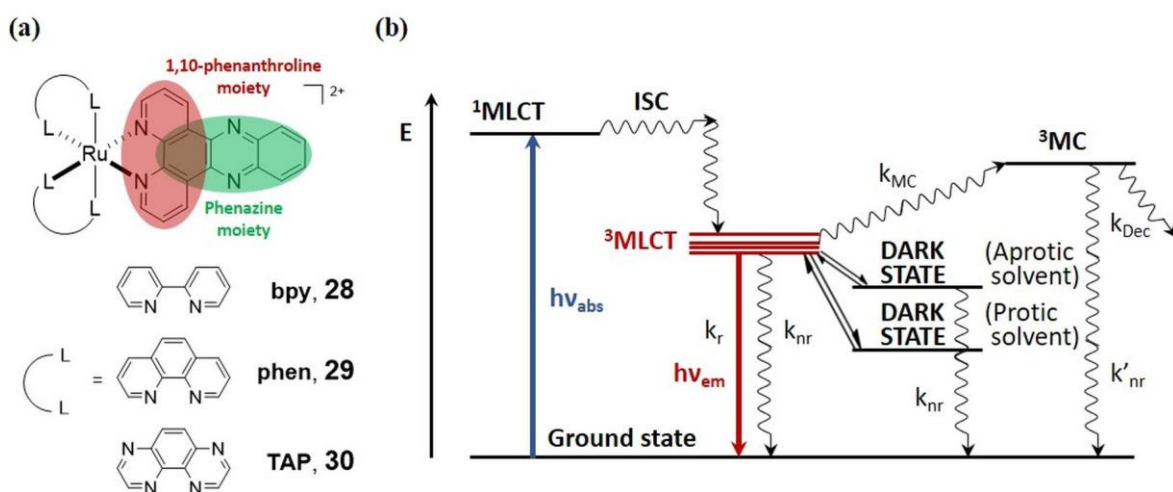


Figure 1.13. (a) Chemical structure of $[\text{Ru}(\text{bpy})_2\text{dppz}]^{2+}$ (**28**), $[\text{Ru}(\text{phen})_2\text{dppz}]^{2+}$ (**29**) and $[\text{Ru}(\text{TAP})_2\text{dppz}]^{2+}$ (**30**). (b) Simplified Jablonski diagram for **28** and **29**. k_{r} = radiative constant, k_{nr} = non-radiative constant, k_{Dec} = dechelation constant, k_{MC} = MC state activation constant.

This unusual behaviour is exhibited by Ru(II) complexes containing **bpy** or **phen** as ancillary ligands. However, when these ligands are replaced by 1,4,5,8-tetraazaphenanthrene (**TAP**) ligand, the resulting complex $[\text{Ru}(\text{TAP})_2\text{dppz}]^{2+}$ (**30**) (Figure 1.13a) shows luminescence in both water and organic solvents.¹³⁹ This is attributed to the more π -acceptor character of the **TAP** in contrast to either **bpy** or **phen** ligands; therefore, the $^3\text{MLCT}$ excited state is now localised on the **TAP** ligand and not on the **dppz**. Thus, the lower excited state $^3\text{MLCT}$ corresponds to $[\text{Ru}^{\text{III}}(\text{TAP})(\text{TAP}^{\cdot-})\text{dppz}]^{2+*}$ instead of $[\text{Ru}^{\text{III}}(\text{TAP})_2\text{dppz}^{\cdot-}]^{2+*}$ as it is the case for $[\text{Ru}(\text{bpy}/\text{phen})_2\text{dppz}]^{2+}$ complexes.¹⁰⁵

As illustrated in this section, Ru(II) polypyridyl complexes possess very attractive photophysical properties that make them promising molecules for use in biological applications. Based on these photophysical properties, the potential of Ru(II) polypyridyl complexes as DNA binding and cellular imaging agents will be discussed next.

1.6.2 Ru(II) Polypyridyl Complexes as DNA Binding and Cellular Imaging Agents

As was previously mentioned in Section 1.3, one way to induce cell damage is through DNA binding. DNA interacting drugs can display cytotoxicity in cancer cells by inhibition of DNA relaxation, gene expression or DNA replication.¹⁴ Indeed, this is one of the most common mechanisms of action of chemotherapeutic agents. As described in Section 1.3.2, there are different DNA binding modes such as intercalation, electrostatic, groove or covalent binding. Since Ru(II) complexes are positively charged, an electrostatic binding is favoured due to the poly-anionic nature of the phosphate backbone of DNA. However, depending on the ligands coordinated to the ruthenium centre, other binding modes can occur. For example, complex **27** is known to bind to DNA mainly electrostatically (probably in one or both of the grooves) but, when Ru(II) polypyridyl complexes contain extended aromatic ligands, an intercalative binding mode is possible because these ligands can stack in between the DNA base pairs.¹⁴⁰ This is the case with complexes containing the **dppz** ligand such as **28** and **29**, as demonstrated by several techniques including UV-vis absorption and emission spectroscopy,¹⁴¹⁻¹⁴⁶ NMR spectroscopy,^{147,148} resonance Raman spectroscopy,¹⁴⁹⁻¹⁵¹ linear dichroism (LD) spectroscopy,^{143,152-154} DNA viscosity measurements and X-ray crystallographic studies.^{30,155-162} Furthermore, the two enantiomers of these Ru(II)-**dppz** complexes resulting from the octahedral coordination geometry of the chelating ligands around the Ru(II) centre (denoted Δ and Λ), were found to bind to DNA with a different orientation by luminescence spectroscopy and crystallographic studies (Figure 1.14).^{142,143,159,162-164}

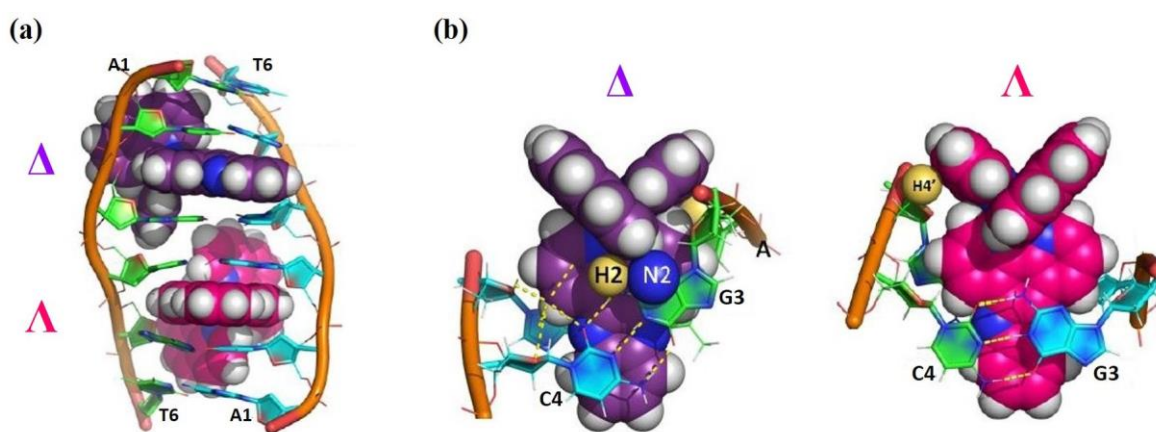


Figure 1.14. (a) X-ray crystal structure of the Δ - and Λ -enantiomers of *rac*-**29** bound to the DNA duplex *d*(ATGCAT)₂ when viewed into the major groove. (b) The different binding geometries of Δ -**29** (purple) and Λ -**29** (pink) when bound to this DNA duplex by intercalation of the **dppz** ligand. Images from reference 159.

As previously mentioned, the luminescence of complexes **28** and **29** is quenched in water but not in aprotic solvents. In the presence of DNA, these **dppz**-based complexes

recover their luminescence similar to that seen in aprotic solvents. This "light switch" effect was first described by Barton *et al.* in 1990 for **28**; a landmark in the development of novel DNA photoprobes.¹⁶⁵ Similar behaviour was reported later for the **phen** analogue **29** by Hartshorn *et al.*¹⁴² The origin of this effect arose from protection of the intercalating **dppz** moiety by the hydrophobic microenvironment of DNA in which the phenazine nitrogen atoms of **dppz** are unreachable by water.¹⁶³ Hydrogen bonds are not formed and the "dark state" is not stabilised. Furthermore, complex **30**, resulting from the replacement of the **bpy** or **phen** ancillary ligands by the **TAP** ligand, exhibits an enhancement of its emission intensity when bound to DNA containing no guanine bases but its luminescence is quenched in the presence of DNA containing guanine bases.¹⁶⁶ The origin of this particular behaviour observed for Ru(II) polypyridyl complexes containing π -deficient ligands such as **TAP** will be discussed in the next section.

A large number of the Ru(II) polypyridyl complexes that have been studied as DNA binders contain extended aromatic ligands based on the **dppz** ligand scaffold. Some of these ligands are benzo[*i*]dipyrido[3,2-*a*:2',3'-*c*]phenazine (**dppn**),¹⁴² tetrapyrido[3,2-*a*:2',3'-*c*:3'',2''-*h*:2''',3'''-*j*]phenazine (**tpphz**),¹⁶⁷ tetrapyrido[3,2-*a*:2',3'-*c*:3'',2''-*h*:2''',3'''-*j*]acridine (**tpac**),¹⁶⁸ 1,10-phenanthrolino[5,6-*b*]-1,4,5,8,9,12-hexaazatriphenylene (**phehat**),¹⁶⁷ naphtho[2,3-*a*]dipyrido[3,2-*h*:2',3'-*f*]phenazine-5,18-dione (**qdppz**)¹⁶⁹ or pyrazino[2,3-*h*]dipyrido[3,2-*a*:2',3'-*c*]phenazine (**pdppz**)¹⁷⁰ and are shown in Figure 1.15. Another

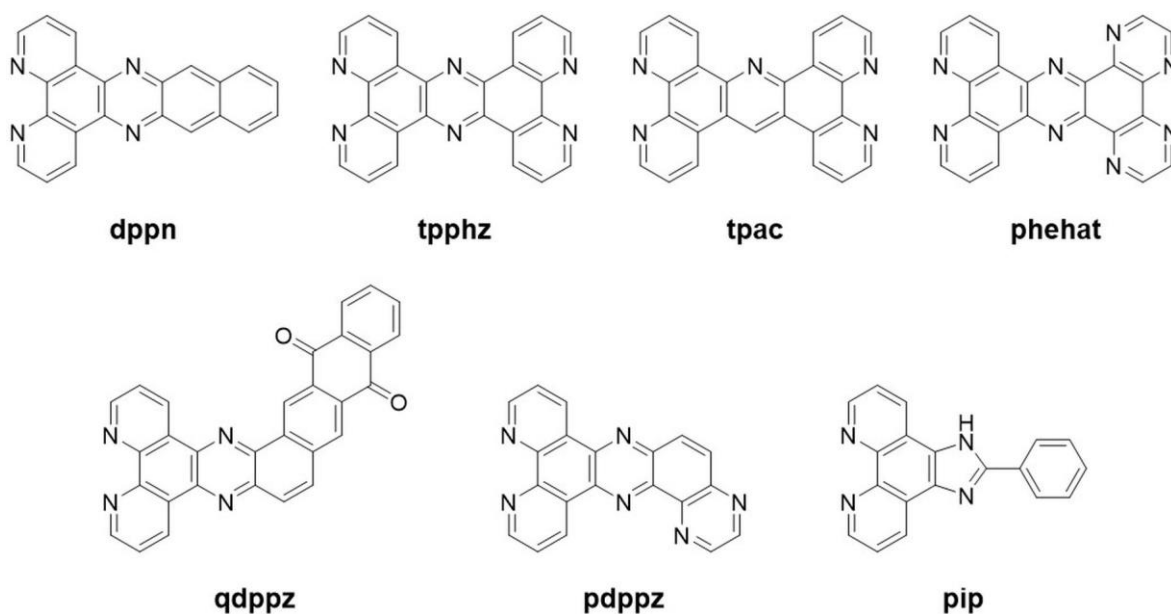


Figure 1.15. Chemical structures of a number of ligands used in the study of DNA binding of Ru(II) polypyridyl complexes.

example of a ligand employed for DNA binding is 2-phenyl-1*H*-imidazo[4,5-*f*][1,10]phenanthroline (**pip**).¹⁷¹ The Ru(II) complexes resulting from the coordination of these **dppz**-like ligands to the metal centre have shown high affinity for DNA and binding to the double helix by intercalation.

The ability of these complexes to bind strongly to DNA and as such disrupt the DNA replication and transcription processes can be exploited in therapeutic applications. Therefore, in a cellular environment, there is a need for these complexes to reach the cell nucleus to exert cell damage by interaction with the genetic material. However, only a few Ru(II) complexes have shown nuclear localisation in live cells.¹⁷²⁻¹⁷⁷ Localisation in other cell regions, such as the cell membrane, cytoplasm, mitochondria, endoplasmic reticulum, lysosomes and nucleoli, have been observed for many Ru(II) complexes.^{63,93} To reach the nucleus and other organelles, complexes must first be taken up by the cells, but this is not the case of **28**, **29** and **30** which have shown poor cellular uptake most likely due to their low lipophilic character.^{170,178} With a view to improve the ability of these complexes to be internalised into the cells, chemical modifications of the **dppz** ligand have been carried out by different research groups. For example, incorporation of a fluorine, amino or methoxy group at the 11-position of the **dppz** ligand was found to increase the lipophilicity and cellular uptake of the resulting [Ru(bpy)₂(L)]²⁺ complex, where L is the chemically modified **dppz** ligand. Moreover, nuclear localisation was observed for these complexes as shown in Figure 1.16a for the fluorine-containing **dppz** derivative (**31**).^{173,179} Studies performed by

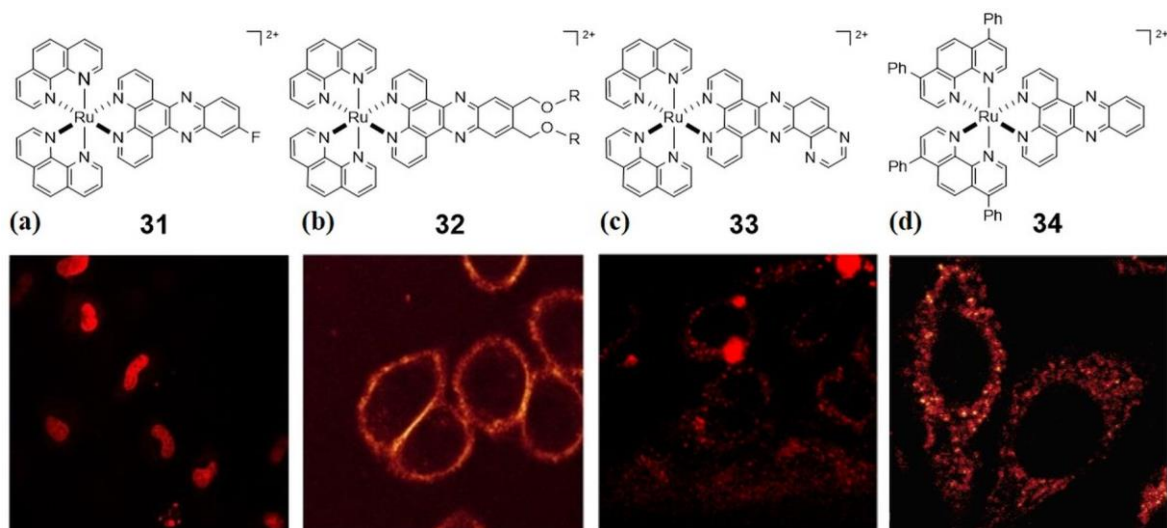


Figure 1.16. Chemical structures and confocal microscopy images of (a) HeLa cells incubated with **31** (red, 10 μ M) for 2 h, (b) CHO-K1 cells incubated with **32** (red, 10 μ M) immediately after addition, (c) HeLa cells incubated with **33** (red, 100 μ M) for 24 h, and (d) HeLa cells incubated with **34** (red, 5 μ M) for 2 h. Images from references 170, 173, 178 and 180.

Lincoln and co-workers have also demonstrated that modification of the **dppz** ligand by attachment of alkyl ether chains resulted in preferential localisation of the resulting Ru(II) complex (**32**) in the cellular membrane (Figure 1.16b).^{180,181} Furthermore, extension of the surface area of the **dppz** ligand (**dppn** and **pdppz** ligands) was shown to confer lipophilicity to the resulting Ru(II) complexes (**33**) and thus enhanced their cellular uptake (Figure 1.16c).^{170,182} The variation of the ancillary ligands of Ru(II)-**dppz** complexes was also found to have an effect in their cellular internalisation. In particular, Puckett *et al.* have shown that the replacement of the **bpy** ancillary ligands in **28** by two 4,7-diphenyl-1,10-phenanthroline (**dip**) ligands resulted in the high lipophilic complex $[\text{Ru}(\text{dip})_2\text{dppz}]^{2+}$ (**34**) which was rapidly taken up by live cells (Figure 1.16d).¹⁷⁸

The introduction of a second ruthenium moiety has also been shown to provide the resulting dinuclear complex not only with a stronger affinity for DNA when compared to the mononuclear analogues, but also with an enhancement of its cellular uptake. In this area, O'Reilly *et al.* have demonstrated that the complex obtained from linking two $[\text{Ru}(\text{bpy})_3]^{2+}$ or $[\text{Ru}(\text{phen})_2\text{bpy}]^{2+}$ units with flexible polyalkyl chains of various lengths (**35** and **36**) (Figure 1.17a) displayed a 100-fold increase in the affinity for DNA.¹⁸³⁻¹⁸⁵ Further biological studies carried out by Keene and co-workers have shown that the cellular uptake of such dinuclear Ru(II) complexes was improved by increasing the chain length of the flexible linker and as such the overall lipophilicity.¹⁸⁶⁻¹⁸⁸ Moreover, these complexes were found to localise in the mitochondria or in the nucleoli depending on the cell line, highlighting the importance of the cell line to the subcellular localisation of the complexes (Figure 1.17b).¹⁸⁹

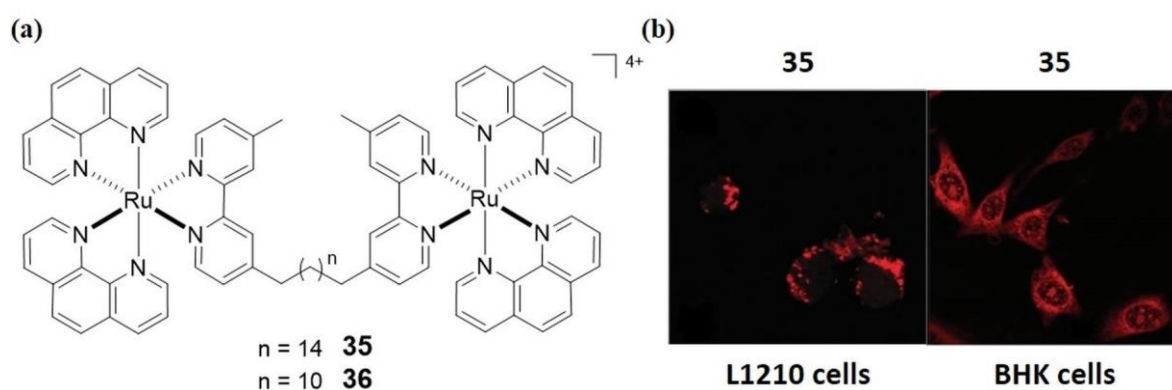


Figure 1.17. (a) Chemical structures of the dinuclear complexes **35** and **36**. (b) Confocal microscopy images of L1210 cells incubated with **35** (red, 50 μM) for 4 h and BHK cells incubated with **35** (red, 55 μM) for 4 h. Images from references 186 and 189.

A more rigid dinuclear Ru(II) polypyridyl complex based on the **tpphz** ligand (**37**) has been developed by the Thomas research group (Figure 1.18a).^{172,190} This complex was shown to display very attractive properties for use in biological applications. In addition to

a high affinity for both duplex and quadruplex DNA, complex **37** was found to be successfully taken up by the cells and selectively stained their nuclei (Figure 1.18b).^{172,190} Its DNA binding ability together with its nuclear localisation makes this complex a potential *in cellulo* DNA structural probe.¹⁷²

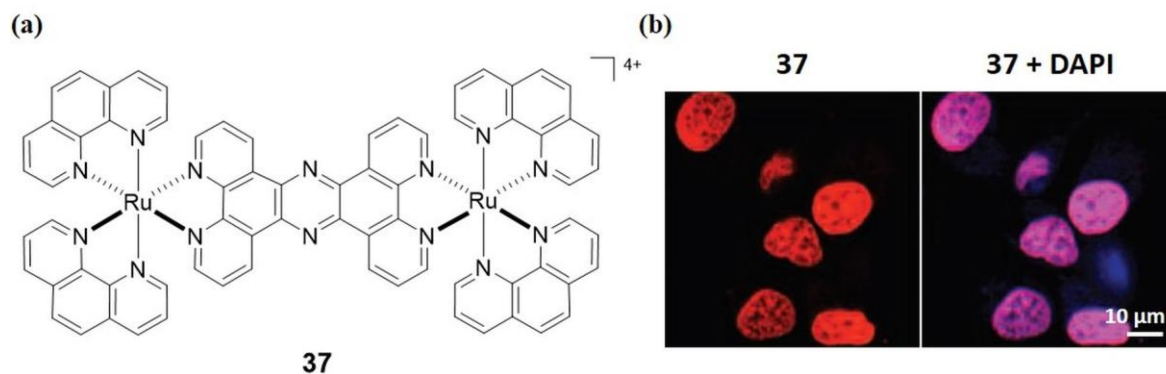


Figure 1.18. (a) Chemical structure of the dinuclear Ru(II) *tpphz* complex (**37**) developed by the Thomas group. (b) Co-staining of **37** (red) with the nuclear stain DAPI (blue) in MCF-7 cells showing the localisation of **37** in the cell nucleus. Images from reference 172.

Another strategy to improve the cellular uptake and control the subcellular distribution of Ru(II) polypyridyl complexes is their conjugation to cell-penetrating peptides (CPPs) such as nuclear localisation signal (NLS) sequences.¹⁹¹⁻¹⁹⁹ These peptides provide the resulting complexes with the ability to penetrate the cell membrane by a protein transduction process and localise in the cell nucleus. Furthermore, Ru(II) polypyridyl complexes can also display selectivity since they are easily conjugated to oligodeoxynucleotides (ODN) that recognise specific DNA sequences.²⁰⁰ However, modification of the complex structure can have a dramatic effect in its DNA binding affinity and cytotoxicity.^{195,201}

The use of ruthenium complexes to target DNA is not limited to non-covalent interactions. In the next section, the ability of Ru(II) polypyridyl complexes containing π -deficient ligands to react with DNA upon light irradiation and form covalent photoadducts will be presented as an alternative mechanism to induce cell damage through photocontrolled DNA covalent binding.

1.6.3 π -Deficient Ru(II) Polyazaaromatic Complexes and their Photoreactivity with DNA

Ru(II) polypyridyl complexes show an enhancement of their redox activity in the excited state. In particular, the research group of Kirsch-De Mesmaeker demonstrated that Ru(II) complexes containing at least two π -deficient ligands, such as **TAP** or 1,4,5,8,9,12-

hexaazatriphenylene (**HAT**), exhibited extremely oxidising $^3\text{MLCT}$ excited states (Figure 1.19).^{202,203}

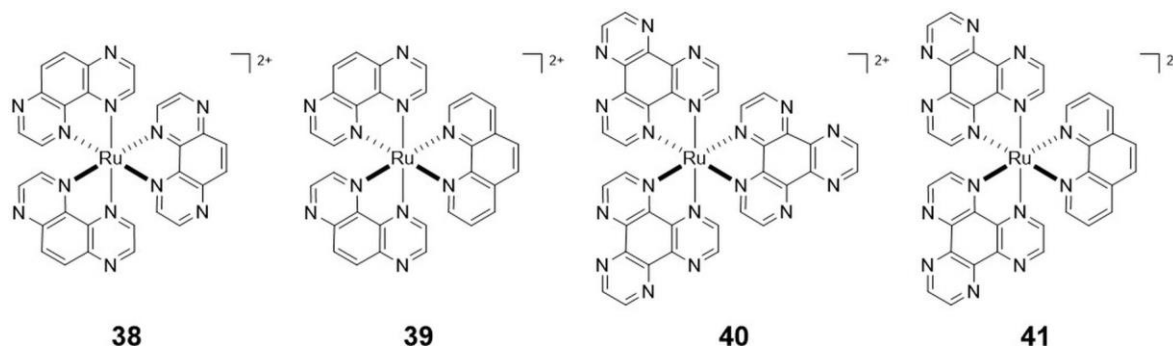


Figure 1.19. Chemical structures of the π -deficient ligands-containing Ru(II) complexes $[\text{Ru}(\text{TAP})_3]^{2+}$ (**38**), $[\text{Ru}(\text{TAP})_2\text{phen}]^{2+}$ (**39**), $[\text{Ru}(\text{HAT})_3]^{2+}$ (**40**) and $[\text{Ru}(\text{HAT})_2\text{phen}]^{2+}$ (**41**).

The high photooxidation power of the excited states of these complexes is in contrast to their **bpy** and **phen** analogues as highlighted by the very positive reduction potentials of their $^3\text{MLCT}$ excited states (E_{red}^*) reported in Table 1.3. Therefore, complexes such as $[\text{Ru}(\text{TAP})_3]^{2+}$ (**38**) ($E_{\text{red}}^* = +1.30$ V/SCE) and $[\text{Ru}(\text{HAT})_3]^{2+}$ (**40**) ($E_{\text{red}}^* = +1.49$ V/SCE) are strong enough oxidising agents to extract an electron from weakly reducing biomolecules such as the nucleotide guanosine-5' monophosphate (GMP) ($E_{\text{ox}} = +1.07$ V/SCE) or the amino acids tryptophan (Trp) ($E_{\text{ox}} = +0.77$ V/SCE) and tyrosine (Tyr) ($E_{\text{ox}} = +0.69$ V/SCE) due to the exergonicity (ΔG^0) of the process (Table 1.3).^{202,204,205}

Table 1.3. The reported reduction potentials (vs SCE) determined by cyclic voltammetry in acetonitrile for a number of Ru(II) polypyridyl complexes in the ground (E_{red}) and excited states (E_{red}^*). Exergonicity of the PET process (ΔG^0) of the corresponding complexes with the electron donor (D) either GMP ($E_{\text{ox}}(\text{G}/\text{G}^+) = 1.07$ V/SCE),²⁰⁴ Trp ($E_{\text{ox}}(\text{Trp}/\text{Trp}^+) = 0.77$ V/SCE)²⁰⁵ or ($E_{\text{ox}}(\text{Tyr}/\text{Tyr}^+) = 0.69$ V/SCE)²⁰⁵ estimated according to $\Delta G^0_{\text{PET}} = -nF[E_{\text{ox}}(\text{D}) - E_{\text{red}}(\text{RuL}_3^{2+*}/\text{RuL}_3^{2+})]$. Note that the ΔG^0 values reported here do not take into account proton transfer (PT), as a proton-coupled electron transfer (PCET) is expected to be more exergonic than a simple electron transfer (ET).²⁰³

Complex	E_{red} (V/SCE) (ground state)	E_{red}^* (V/SCE) (excited state)	ΔG^0 (eV)	ΔG^0 (eV)	ΔG^0 (eV)
			GMP	Trp	Tyr
$[\text{Ru}(\text{bpy})_3]^{2+}$ (27) ^[a]	-1.35	+0.65	+0.42	+0.12	+0.04
$[\text{Ru}(\text{phen})_3]^{2+}$ (42) ^[a]	-1.35	+0.70	+0.37	+0.07	-0.01
$[\text{Ru}(\text{phen})_2\text{dppz}]^{2+}$ (29) ^[b]	-1.00	+0.96	+0.11	-0.19	-0.27
$[\text{Ru}(\text{HAT})_3]^{2+}$ (40) ^[a]	-0.62	+1.49	-0.42	-0.72	-0.80
$[\text{Ru}(\text{HAT})_2\text{phen}]^{2+}$ (41) ^[a]	-0.66	+1.25	-0.18	-0.48	-0.56
$[\text{Ru}(\text{TAP})_3]^{2+}$ (38) ^[a]	-0.75	+1.30	-0.23	-0.53	-0.61
$[\text{Ru}(\text{TAP})_2\text{phen}]^{2+}$ (39) ^[a]	-0.83	+1.15	-0.08	-0.38	-0.46
$[\text{Ru}(\text{TAP})_2\text{dppz}]^{2+}$ (30) ^[a]	-0.80	+1.20	-0.13	-0.43	-0.51

^[a] From reference 202.

^[b] From reference 206.

As a result, two types of photophysical behaviours are observed for such complexes possessing π -deficient ligands in the presence of DNA. Thus, in contrast to effects described for **28** and **29** in the previous section, the emission and the $^3\text{MLCT}$ lifetime of **30** were enhanced only in the presence of DNA containing no guanine bases (*e.g.* homopolymers $[\text{poly}(\text{dA-dT})]_2$) as DNA prevents quenching of the luminescence by oxygen.^{33,166,207} However, in the presence of DNA containing guanine (*e.g.* homopolymers $[\text{poly}(\text{dG-dC})]_2$ or GMP) the emission of the complex was quenched and an increase in the $^3\text{MLCT}$ excited-state lifetime was observed.²⁰⁷⁻²¹¹ This luminescence quenching has been attributed to a photoinduced electron transfer (PET) between the guanine residues and the highly oxidising $^3\text{MLCT}$ excited state of the complex.^{166,211-213} For example, laser flash photolysis experiments performed on **38** in phosphate buffer at pH 7 have shown the appearance of a transient band at *ca.* 500 nm only in the presence of GMP, which was assigned to the reduced metal complex.^{211,212,214} The proposed mechanism of such PET process between **38** and GMP is illustrated in Figure 1.20.

Irradiation of **38** with visible light results in the promotion of an electron from the Ru(II) centre to an ancillary TAP ligand and a $^3\text{MLCT}$ excited state corresponding to $[\text{Ru}^{\text{III}}(\text{TAP})_2(\text{TAP}^{\bullet-})]^{2+*}$ is generated. In the presence of GMP, a forward electron transfer (FET) process takes place between the guanine base and the excited state of the complex resulting in the formation of two radical species, that is the reduced metal complex $[\text{Ru}^{\text{II}}(\text{TAP})_2(\text{TAP}^{\bullet-})]^+$ and the guanine radical cation $\text{GMP}^{\bullet+}$. This guanine radical cation has shown to be more acidic than its unoxidized form ($\text{p}K_{\text{a}}$ of GMP and $\text{GMP}^{\bullet+}$ are 9.5 and 3.9, respectively)²¹⁵⁻²¹⁷ and thus, deprotonation of the radical is expected in aqueous solution at pH 7.²¹⁸ Furthermore, a $\text{p}K_{\text{a}}$ of 7.6 has been reported for the reduced metal complex **38** and therefore is protonated in aqueous solution at pH 7.²¹² This proton transfer (PT) has also been proposed to take place simultaneously to the electron transfer (*i.e.* proton-coupled electron transfer), as the oxidation potential of the nucleobase would decrease.^{208,212,218-220} However, it still remains unclear if the PT occurs before, at the same time or after the PET.^{221,222} Three possible reaction pathways can then take place:

- 1) Back electron transfer (BET) from the reduced metal complex to the oxidised guanine moiety resulting in the regeneration of the starting species, that is complex **38** and GMP.^{139,212,218}
- 2) Recombination of the two generated radical species which results in the formation of the photoadduct $[\text{Ru}^{\text{II}}(\text{TAP})_2(\text{TAP-GMP})]^{2+}$ through a covalent bond between the

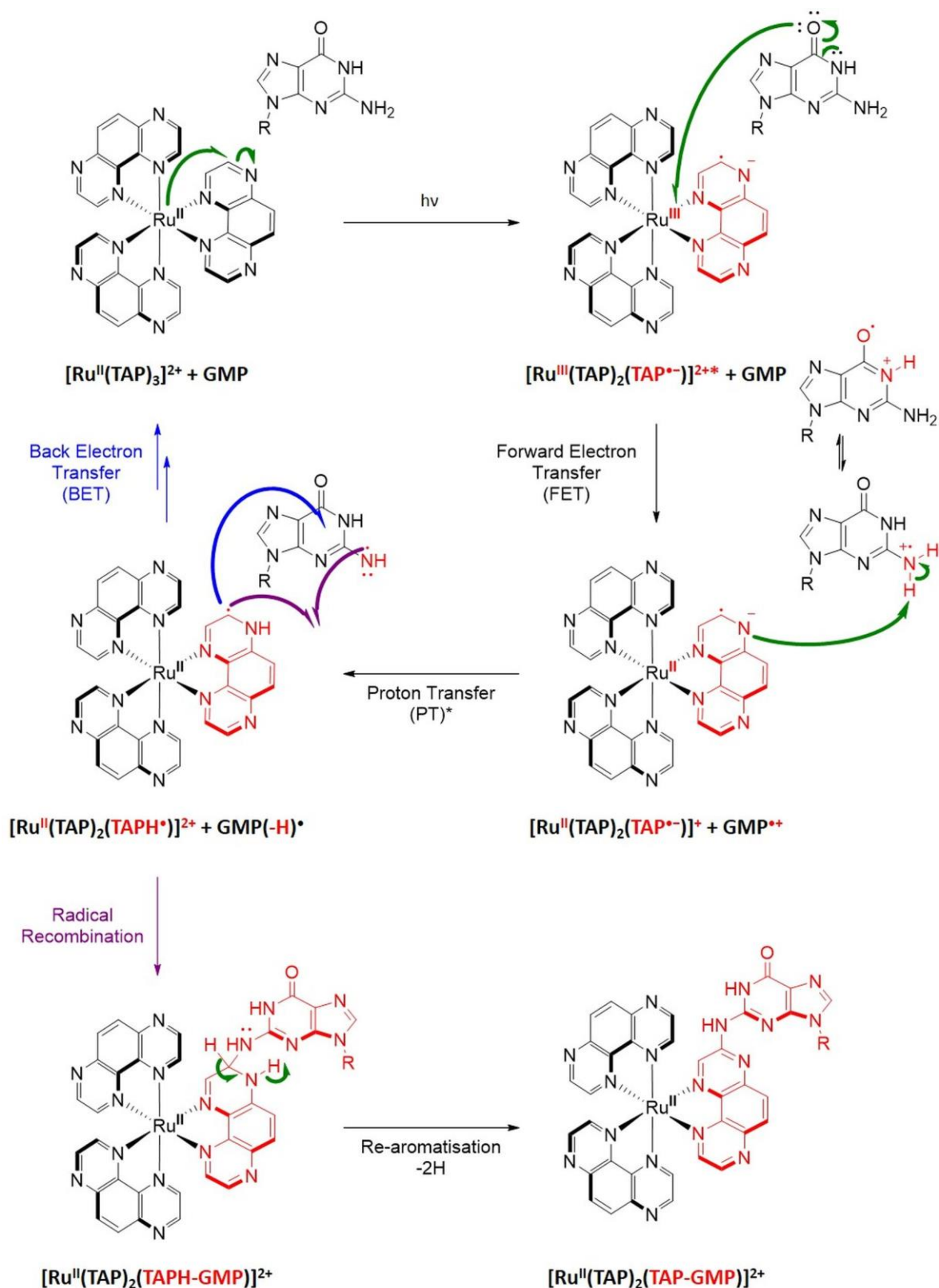


Figure 1.20. Proposed mechanism of the photoinduced electron transfer reaction between **38** and GMP (R = ribose-phosphate). *Deprotonation of the guanine radical cation may occur simultaneously to the oxidation reaction (i.e. PCET).²⁰⁸ Note that, although the most stable guanosine radical tautomer corresponds to that with the electron on the oxygen, the guanosine radical tautomer represented here corresponds to that with the electron on the exocyclic amino group as has been demonstrated that such tautomer is the reactive species that reacts with the protonated reduced complex $[Ru^{II}(TAP)_2(TAPH^*)]^{2+}$. The explanation of such behaviour still remains unknown.

carbon in the β -position to the chelating N of one of the **TAP** ligands and the exocyclic nitrogen of the guanine moiety.^{203,213,219,223} Thus, photoadduct formation does not disrupt the coordination sphere around the metal ion. It must be noted that the charge of such photoadduct will depend on the pH of the solution.²¹³

- 3) Photo-cleavage of guanine-containing DNA in which the guanine radical cation or its deprotonated derivative, produced by oxidation by the excited state of the complex, escapes from the BET process and abstracts an H-atom from the sugar moiety of DNA and, after several reactions, gives rise to strand breaks.^{208,224,225} For example, photo-induced cleavage of the DNA plasmid has been observed when it was irradiated in solution in the presence of **38**.^{202,212,226} Atomic force microscopy (AFM) experiments have shown transformation of the supercoiled covalently closed circular form (ccc) of the plasmid into its open circular form (oc).^{202,212,226} Despite its interesting biological applications, DNA photo-cleavage will not be discussed in this thesis and only the reaction pathway leading to photoadduct formation will be further examined.

The described PET mechanism should be similar for other π -deficient ligands-containing Ru(II) complexes and with the reducing amino acids Trp and Tyr, although it has been shown that the electron transfer is not kinetically coupled to a proton transfer in the presence of these amino acids.²²⁷ This is most likely due to the increased exergonicity of the forward PET process in the presence of Trp and Tyr (Table 1.3). In addition, photoadduct formation with the **HAT** derivative $[\text{Ru}(\text{HAT})_2\text{phen}]^{2+}$ (**41**) has been found to occur *via* the O-6 atom of the guanine moiety instead of the exocyclic amino group (Figure 1.21).²²⁸

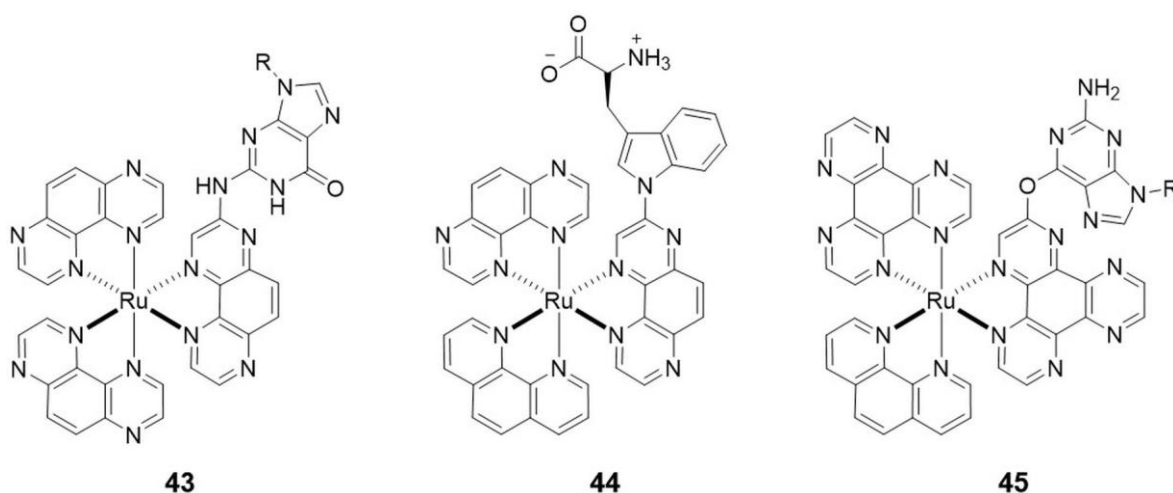


Figure 1.21. Chemical structures of the photoadducts formed between **38** and GMP (**43**), **39** and Trp (**44**), and **41** and GMP (**45**). In the GMP moiety, R = ribose-phosphate.

The formation of a covalent photoadduct between the oxidising Ru(II) complex and either a guanine or tryptophan moiety has been demonstrated by different techniques, including denaturing polyacrylamide gel electrophoresis,^{202,203,209,219} dialysis experiments,^{202,203,219} UV-vis absorption spectroscopy and mass spectrometry.^{202,203,209,219,223,229} In addition, ¹H, ¹H–¹H and ¹H–¹³C NMR spectroscopy unveiled the structure of such photoadducts which was further confirmed by steady-state ¹H photo-chemically induced dynamic nuclear polarisation (CIDNP).^{223,229,230} Furthermore, the ability of these complexes to photoreact with biomolecules is not restricted to the formation of mono-adducts. Bi-adduct formation has also been observed by addition of two guanine or tryptophan residues to the same Ru(II) complex. This is of particular interest as it provides these complexes with the ability to irreversibly photocrosslink the two strands of DNA containing guanine residues or two proteins with tryptophan amino acids *via* two consecutive PET reactions.^{203,231} Indeed, homo- and hetero-photocrosslinkings of guanine-containing oligonucleotides and tryptophan-containing peptides with an oxidising Ru(II) complex acting as photobridging agent has also been demonstrated (Figure 1.22).^{203,231}

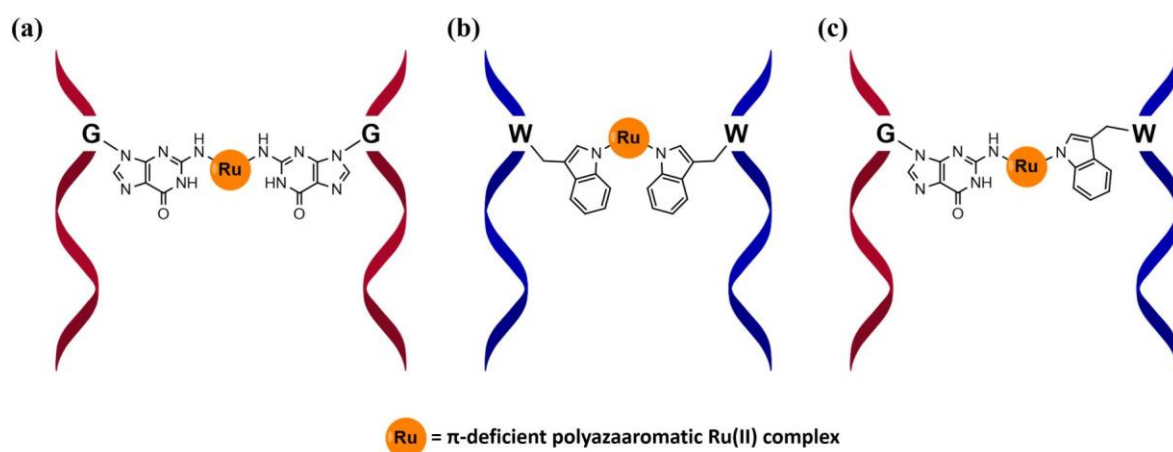


Figure 1.22. Schematic representation of the homo-photocrosslinking between (a) two guanine-containing oligonucleotides (red) or (b) two tryptophan-containing peptides (blue), and (c) hetero-photocrosslinking between one guanine-containing oligonucleotide (red) and one tryptophan-containing peptide (blue).

As discussed in Section 1.3.2, the anti-cancer activity of cisplatin results from covalent adduct formation with adenine and guanine nucleobases of DNA, yielding inter- or intra-strand crosslinks.⁵⁵ Therefore, the ability of π -deficient polyazaaromatic Ru(II) complexes to form covalent photoadducts with biomolecules in a spatially and temporally controlled manner is very attractive for the development of new photoactivated chemotherapeutic agents. This can induce irreversible photodamage to biomolecules resulting in gene expression inhibition or protein dysfunction. In addition, photoadduct

formation provides this type of complex with the ability to exert their phototherapeutic activity in the absence of O₂. This additional mechanism of action, known as photoactivated chemotherapy (PACT), is an alternative to that displayed by conventional PDT agents and may overcome one of the limitations of PDT, that is, its ineffectiveness in hypoxic environments which are often present in tumour tissues. Indeed, a Ru(II) polyaaromatic complex (**46**) has been recently delivered into the nucleus of mammalian cell lines for the first time by Keyes and co-workers by conjugation to a NLS sequence (Figure 1.23). Complex **46** was found to selectively destroy the treated cells upon light irradiation *via* an oxygen-independent mechanism such as direct DNA oxidation by a PET process between the guanine bases and the π -deficient polyaaromatic Ru(II) complex and possibly photoadduct formation.¹⁹⁸

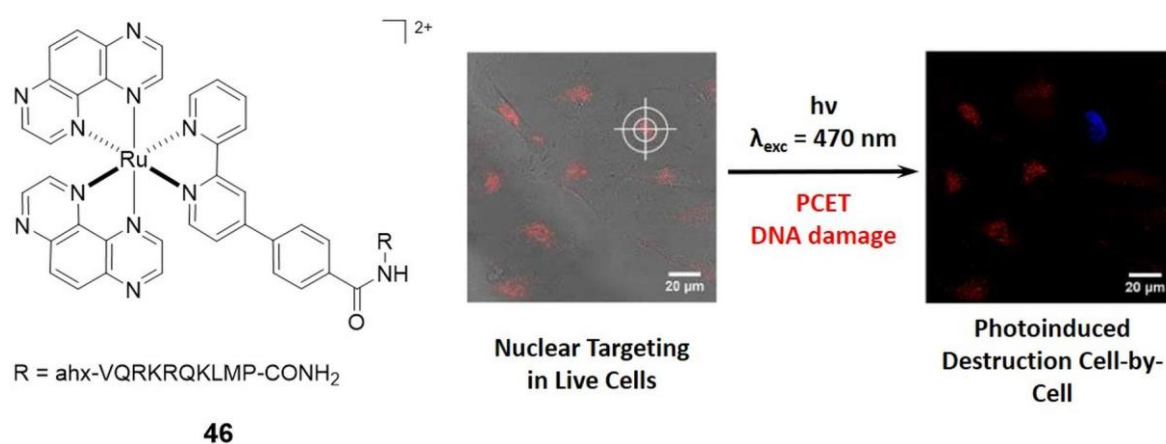


Figure 1.23. Chemical structure of **46** and confocal microscopy images of HeLa cells incubated with **46** (red, 100 μM) for 5 h showing the phototoxic effect of **46** by irradiating a single HeLa cell at 470 nm (0.13 mW cm^{-2}) for 15 min in the presence of DRAQ7 (blue), a nuclear stain that only enters the nucleus of dead cells. Images from reference 198.

In the next section, the potential of Ru(II) polypyridyl complexes to be light activated and induce control cell death *via* oxygen-dependent mechanisms, that is, as PDT agents, will be presented.

1.6.4 Ru(II) Polypyridyl Complexes as Photosensitisers for Photodynamic Therapy

As previously discussed in Section 1.6.2, the therapeutic activity of Ru(II) polypyridyl complexes in a cellular environment is not always possible through DNA interaction (non-covalent and covalent binding), as they are not often able to reach the cell nucleus where the genetic material is contained. However, the attractive excited-state properties of these complexes make them versatile molecules to exert their biological potential *via* other cytotoxic pathways. In this context, Ru(II) polypyridyl complexes have emerged as promising photoactivatable chemotherapeutic agents, that is, transition metal complexes that

show light-triggered anticancer activity.^{62,63,92,93,232} The use of light provides this therapeutic strategy with a spatial and temporal control over the cytotoxicity of the drug. Photoactivated chemotherapy can occur through oxygen-dependent and -independent mechanisms. In oxygen-independent mechanisms the presence of oxygen is not necessary for the drug to exert its therapeutic activity upon light activation. For example, this is the case of the therapeutic effect arising from photoadduct formation examined in the previous section. On the other hand, oxygen-dependent pathways require the presence of oxygen and are those that define PDT. The potential of PDT in the treatment of cancer as an alternative to the conventional anticancer therapies as well as the mechanism of action of such strategy was earlier discussed in Section 1.4. As was highlighted, most of the photosensitisers approved by the FDA are porphyrin-based molecules. However, due to the several drawbacks displayed by this class of PSs, research efforts have been made with a view to develop new PSs. Ru(II) polypyridyl complexes have been extensively studied as potential PDT candidates for their photophysical, photochemical and photobiological properties that can be tuned to optimise their PDT activity.^{62,63,92,93} Indeed, a number of Ru(II)-based photosensitisers have shown quantum yields of $^1\text{O}_2$ production (Type II PDT) close to unity.^{121,233} The use of Ru(II) polypyridyl complexes in PDT has been recently reviewed by several research group and as such, only some representative examples will be presented here.^{62,63,92,93,232}

In 2016, Sainuddin *et al.* reported the Ru(II) complex $[\text{Ru}(\text{bpy})_2(\text{pbpn})]^{2+}$ (**47**, **pbpn** = 4,9,16-triazadibenzo[*a,c*]naphthacene) (Figure 1.24a), a cyclometalated version of a Ru(II)-**dppn** based complex obtained by exchanging one of the coordinating nitrogen atoms of the **dppn** polypyridyl ligand for an isoelectronic carbon anion (the chemical structure of the **dppn** ligand was depicted previously in Figure 1.15).¹³² The replacement of diimine ligands by their cyclometalated counterparts has been shown to influence the properties of the resulting complex. Thus, cyclometalated Ru(II) complexes usually display red-shifted absorption, increased photostability and a significantly greater cytotoxicity when compared to their Ru(II) diimine analogues.²³⁴⁻²³⁶ Interestingly, cytotoxicity studies in human malignant melanoma cells (SK-MEL-28) showed that complex **47** was not toxic in the dark with a half maximal effective concentration (EC_{50}) value of more than 300 μM . However, after visible-light treatment (100 J cm^{-2}), complex **47** was found to be extremely phototoxic towards cells ($\text{EC}_{50} = 0.206 \mu\text{M}$) resulting in a large phototoxic index (PI, *i.e.* the ratio of the EC_{50} value in the dark to the EC_{50} value upon light irradiation) of more than 1400 (Figure 1.24a). The origin of such photoactivity was not due to Type II PDT, as complex **47**

displayed a low quantum yield of $^1\text{O}_2$ production ($\Phi_{\Delta} = 0.0056$ in air-saturated MeCN at 298 K), but to direct photoreduction of biological molecules as well as dioxygen to produce the ROS superoxide (Type I PDT).¹³²

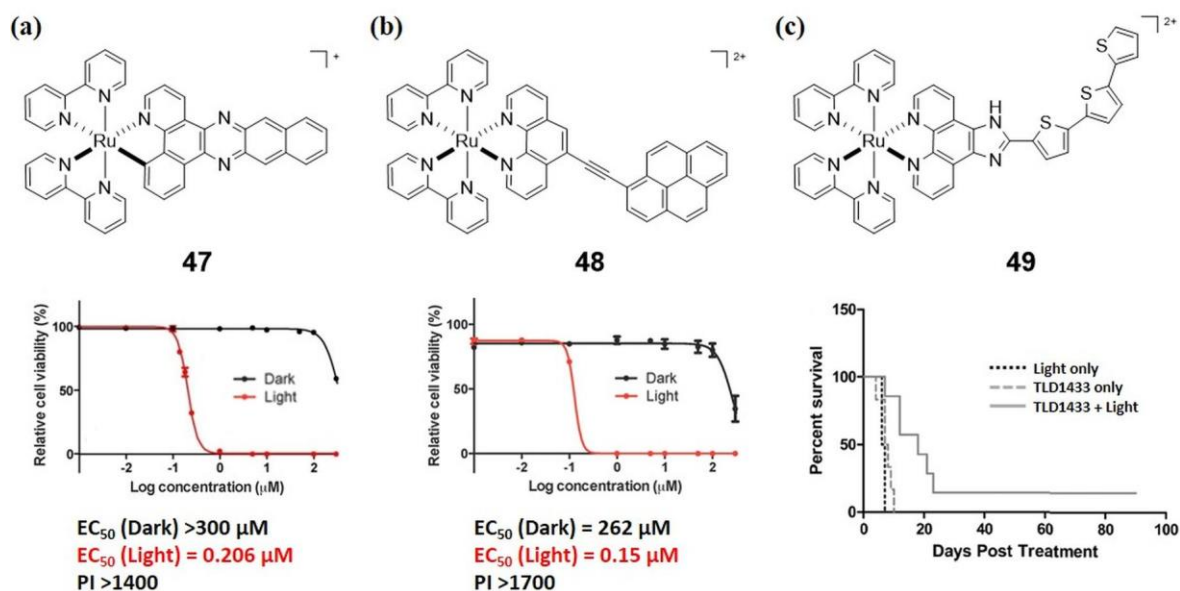


Figure 1.24. (a) Chemical structure of $[\text{Ru}(\text{bpy})_2(\text{pbpn})]^{2+}$ (**47**) and *in vitro* dose-response curves for **47** in SK-MEL-28 cells with (red) and without (black) visible-light activation (100 J cm^{-2}). (b) Chemical structure of $[\text{Ru}(\text{bpy})_2(5\text{-PEP})]^{2+}$ (**48**) and *in vitro* dose-response curves for **48** in HL60 cells with (red) and without (black) visible-light activation (100 J cm^{-2}). (c) Chemical structure of TLD1433 (**49**) and Kaplan-Meier survival curves of mice bearing CT26.WT colon adenocarcinoma tumours post **49**-mediated PDT using a continuous wave light source ($\lambda_{\text{exc}} = 525\text{--}530 \text{ nm}$, 192 J cm^{-2}). Graphs from references 132, 233 and 237.

Another Ru(II) polypyridyl complex that has shown biological potential to act as PDT agent was developed by Lincoln *et al.* in 2013.²³³ This Ru(II)-appended pyrenylethynylene complex $[\text{Ru}(\text{bpy})_2(5\text{-PEP})]^{2+}$ (**48**, **5-PEP** = 5-pyren-1-ylethynyl-1,10-phenanthroline) (Figure 1.24b) was found to possess long-lived ^3IL -based excited states that were sensitive to trace amounts of oxygen ($\Phi_{\Delta} = 0.68$ in air-saturated MeCN at 298 K). Furthermore, complex **48** showed a potent phototoxic effect in human promyelocytic leukaemia cells (HL60) with EC_{50} values of 262 and $0.15 \mu\text{M}$ with and without light treatment, respectively, resulting in a PI of more than 1700 (Figure 1.24b).²³³

One of the most exciting Ru(II)-based compounds developed to date is a complex derived from α -terthienyl appended to imidazo[4,5-*f*][1,10]-phenanthroline, designated TLD1433 (**49**) (Figure 1.24c).²³⁷⁻²³⁹ This complex was designed by McFarland and co-workers and is the first Ru(II) polypyridyl complex entered into clinical trials for PDT treatment of non-muscle invasive bladder cancer.²⁴⁰ The potential of **49** as PDT agent was evaluated *in vitro* in colon carcinoma and glioblastoma cell lines.²³⁷ Low dark toxicity was observed in cells treated with less than $10 \mu\text{M}$ concentration of **49** for 6 h. However, when

murine colon carcinoma (CT26.WT) and human glioblastoma (U87) cells were incubated with 1 μM concentration of **49** and irradiated with green light ($\lambda_{exc} \approx 525 \text{ nm}$, 45 J cm^{-2}), 100% cell death was induced by complex **49**, which corresponds to median lethal dose (LD_{50}) values of 21 and 51 nM in CT26.WT and U87 cell lines, respectively. A $^1\text{O}_2$ quantum yield close to unity and the ineffectiveness of **49** under hypoxic conditions ($<0.5\% \text{ O}_2$) demonstrated the dependence of the photodynamic effect on the presence of oxygen.^{237,238,241} Furthermore, *in vivo* studies were also assessed in 8-10-week-old BALB/C mice subcutaneously injected with CT26.WT murine colon carcinoma and maximum tolerated doses 50 (MTD50) were found to be 103 mg kg^{-1} . PDT treatment of the mouse model was shown to be effective in causing tumour growth delay resulting in a significant increase in animal survival (Figure 1.24c).²³⁷ These studies showed the potential of **49** as photosensitiser in both *in vitro* and *in vivo* models.

As illustrated in the examples presented above, Ru(II) polypyridyl complexes are promising light-activatable agents with theranostic PDT potential in anticancer applications. Their conjugation to other functional species may result in an improvement of their biological properties. In this context, gold nanoparticles (AuNPs) have become the research focus in many fields of medicinal chemistry. In the next section, the potential applications of these nanomaterials in cancer therapy, with particular attention to AuNPs conjugated to photoactive species for use in PDT, will be discussed.

1.7 Gold Nanoparticles and their Anticancer Applications

In recent years, gold nanoparticles conjugates have been extensively explored for use in biology and medicine.²⁴²⁻²⁴⁶ Defined as submicroscopic particles with sizes between 1 and 100 nm, they display unique and tuneable optoelectronic properties which can be exploited in diagnostic and therapeutic applications. For instance, AuNPs absorb light strongly at a particular wavelength due to a phenomenon called surface plasmon resonance (SPR) resulting from the collective oscillation of free electrons on the gold nanoparticle surface.²⁴⁵⁻²⁴⁸ The wavelength where this occurs is dependent on the size and shape of the gold nanomaterial. In addition, the AuNP surface offers a stable and easily functionalised platform for conjugation with ligands containing functional groups that exhibit affinity for gold, as is the case of thiols, phosphines and amines.^{244-246,248} Furthermore, AuNPs have shown attractive properties for use in biological systems. For example, they are biocompatible, with any toxicity arising being associated with the chemical composition of the ligands attached to the gold surface.²⁴⁵ They also have a large surface area to volume

ratio which provides them with the ability to achieve high loading of ligands and thus high concentrations of cargo can be delivered into cells while maintaining a lower overall concentration of AuNPs.²⁴⁹ Intracellular penetration of most gold nanoconjugates has also been confirmed by several research groups, although differences in their surface chemistry, particle size, charge and lipophilicity have been shown to play a crucial role in the cellular uptake mechanism.^{250,251} On the other hand, nanodrugs have been found to exhibit size-selective accumulation at tumours, presumably because of the enhance permeability and retention (EPR) effect, a phenomenon caused by the abnormal leaky tumour vasculature and poor lymphatic drainage by which the diffusion and retention of molecules of a certain size within tumour tissue are facilitated (Figure 1.25).²⁴⁵ However, it must be noted that the realibility of the EPR effect remains a controversial topic in nanomedicine.

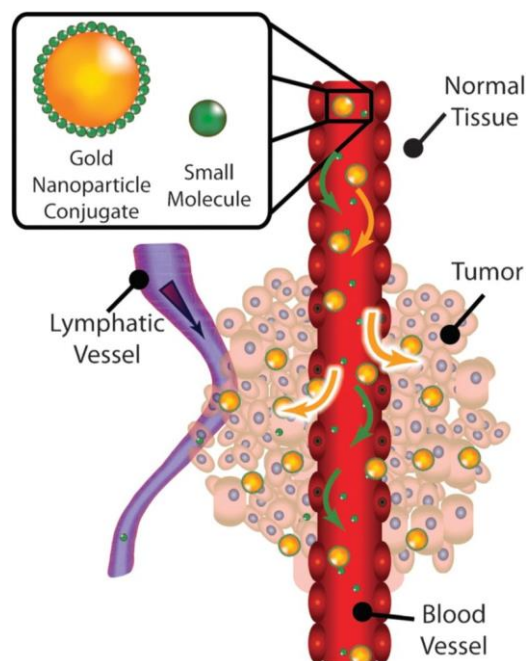


Figure 1.25. Graphic illustration of the size-selective preferential accumulation of circulating gold nanoparticle conjugates at tumour sites by the EPR effect. Image from reference 245.

The above-described properties make gold nanoparticles potential platforms for use in a wide range of biomedical applications such as cancer therapy.^{245,249} In this area, AuNPs have been employed as delivery scaffolds of anticancer drugs.²⁵² For example, the research groups of Mirkin and Lippard attached a Pt(IV) complex (**50**), that acted as prodrug of the

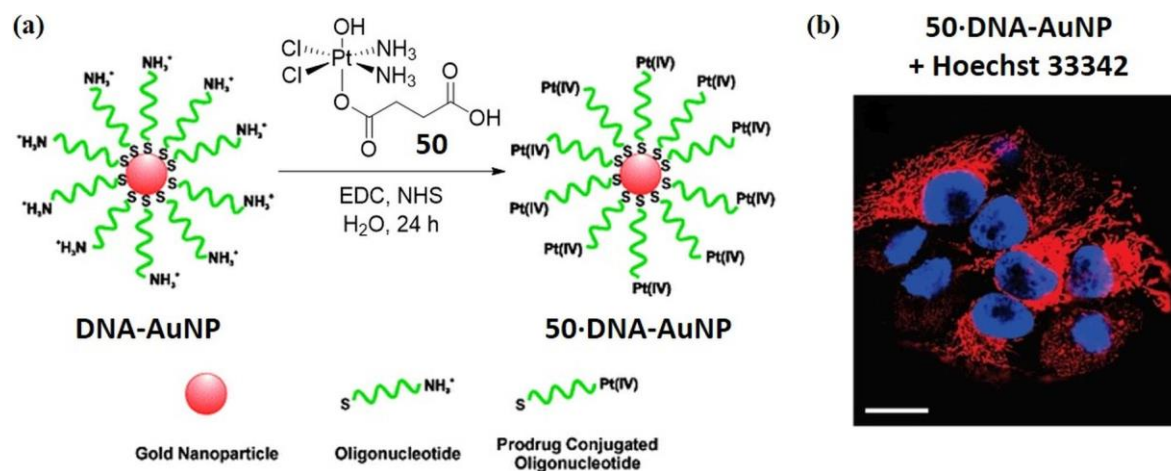


Figure 1.26. (a) Conjugation of a Pt(IV) cisplatin prodrug (**50**) to amine-terminal oligonucleotide-functionalised AuNPs. (b) Live cell imaging of HeLa cells upon incubation with **50-DNA-AuNP** (red) for 12 h. The nucleus is stained blue with Hoechst 33342. Image from reference 253.

chemotherapeutic cisplatin, to DNA-AuNPs (Figure 1.26a). The resulting conjugates (**50•DNA-AuNP**) were efficiently internalised by HeLa cervical cancer cells (Figure 1.26b) with subsequent reduction of the Pt(IV) prodrug and release of the cytotoxic cisplatin, which entered the cell nucleus and formed intra-strand crosslinks with nuclear DNA.²⁵³ Gold nanoparticles have also shown promising opportunities in gene therapy for the delivery of small interfering RNA (siRNA) and subsequent knockdown of the tumorigenic proteins expression.^{254,255} Furthermore, the efficient light-to-heat conversion capability of AuNPs has been explored for their use in photothermal therapy (PTT) for cancer treatment in which exogenously applied light is converted into heat in order to induce cancer cells death.^{256,257}

As previously mentioned, one aim of the work presented in this thesis is the development of new Ru(II)-based systems with PDT activity. Within this field, AuNP conjugates have been revealed as emerging nanomaterials for use in PDT that can overcome some of the limitations of the classic photosensitisers.^{258,259} In this area, Russell and co-workers functionalised AuNPs with phthalocyanines (**51•AuNP**) and using the phase transfer reagent tetraoctylammonium bromide (TOAB) to stabilise the photosensitisers on the gold surface (Figure 1.27a).²⁶⁰ An enhancement of the quantum yield of $^1\text{O}_2$ production was observed for the resulting 2–4 nm system compared to the free phthalocyanine (**51**). Furthermore, the AuNP conjugates were found to be effectively taken up by HeLa cells (Figure 1.27b) and induced greater photodynamic efficacy than the free photosensitiser after irradiation with 690 nm light.²⁶¹ Subsequent *in vivo* studies in amelanotic melanoma (B78H1 cells) subcutaneously transplanted on mice revealed that **51•AuNP** conjugates were able to selectively target cancer tissue and display a great PDT response resulting in the inhibition of tumour growth.²⁶²

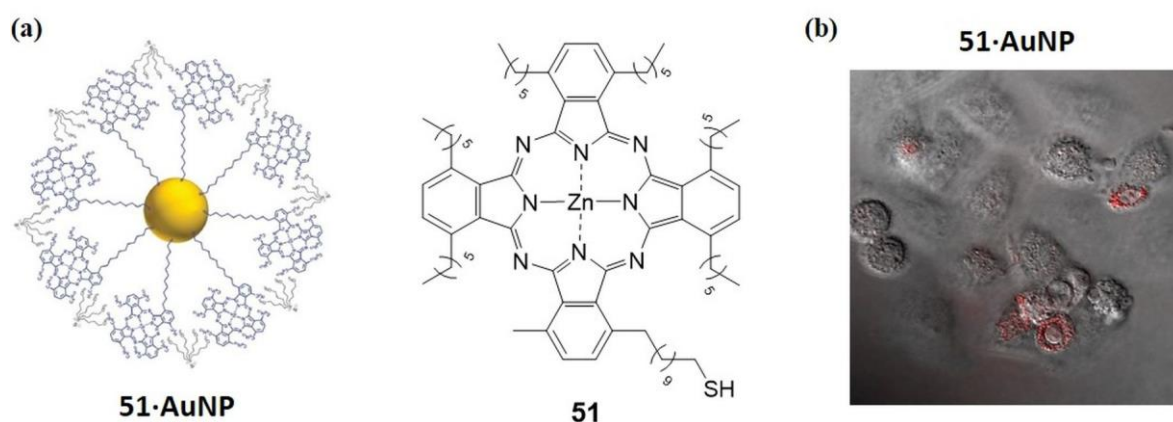


Figure 1.27. (a) Schematic representation of phthalocyanine (**51**) functionalised AuNPs and with the phase transfer reagent TOAB (**51•AuNP**). (b) Combined confocal fluorescence and Differential Interference Contrast images of HeLa cells after incubation with **51•AuNP** (red) for 16 h. Image from reference 261.

In the particular case of Ru(II) polypyridyl complexes, only a few examples of AuNPs functionalised with these metal complexes have been reported in the literature, being the cases where the Ru(II)-AuNP conjugates are used in PDT even more limited.²⁶³⁻²⁷¹ For example, Rogers *et al.* investigated the cellular imaging of 100 nm diameter AuNPs functionalised with a Ru(II) polypyridyl complex (**52**) previously coated with a non-ionic fluorinated surfactant (Figure 1.28a).²⁶⁶ Single particles were visualised within A549 human lung cancer cells with no significant toxicity towards cells highlighting the potential of **52·AuNP** as cellular imaging probes (Figure 1.28b).

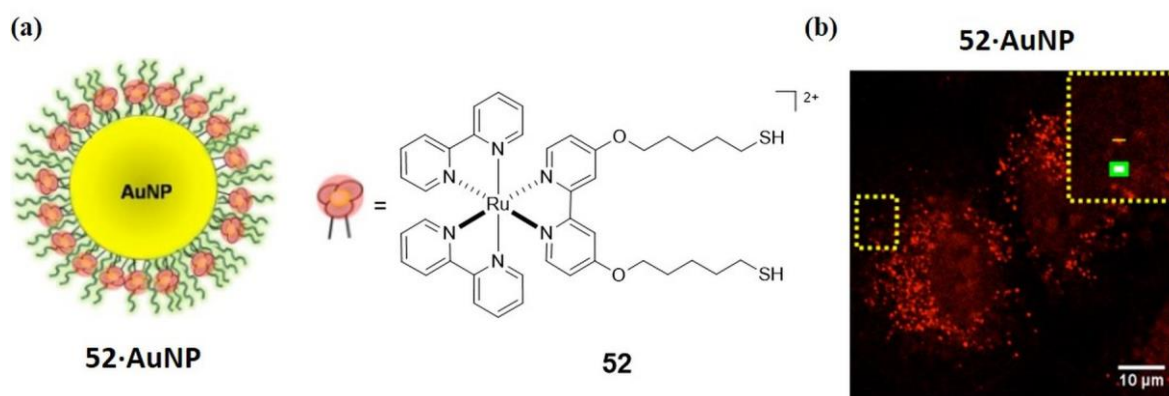


Figure 1.28. (a) Schematic representation of Ru(II) polypyridyl (**52**) functionalised AuNPs previously coated with a non-ionic fluorinated surfactant (**52·AuNP**). (b) Confocal images of single **52·AuNP** (red) in A549 cells. Image from reference 266.

Some of the most representative examples of Ru(II) polypyridyl functionalised AuNPs have been developed within the Gunnlaugsson group over the past few years and will be presented in the next section among other Ru(II)-based structures achieved in the group.^{264,271}

1.8 Recent Advances within the Gunnlaugsson Group

The excellent photophysical properties and potential biological applications of Ru(II) polypyridyl complexes have been the focus of extensive studies in the Gunnlaugsson group. Therefore, many new ruthenium-based structures were developed and their ability to be used as therapeutic agents and DNA imaging probes was investigated in detail in collaboration with Prof. D. Clive Williams in the School of Biochemistry and Immunology and Prof. John M. Kelly in the School of Chemistry at Trinity College Dublin.^{63,170,264,271-278}

Within the Gunnlaugsson group, Dr Elmes and collaborators developed Ru(II) polypyridyl complexes containing pyrazino[2,3-*h*]dipyrido[3,2-*a*:2',3'-*c*]phenazine (**pdppz**), a new extended aromatic ligand resulting from the combination of both **TAP** and **dppz** functionalities.¹⁷⁰ The expansion of the aromaticity in the **dppz** ligand was expected to

enhance the DNA binding of the resulting complexes because of a "hook effect". For this purpose, the properties of Ru(II) complexes containing **pdppz** and either **phen** or **TAP** as ancillary ligands (**33** and **53**, respectively) were investigated. Both complexes displayed high affinity for DNA in competitive media and active or facilitated cellular uptake with localisation in the cytoplasm (Figure 1.29a). In addition, cytotoxicity assays in several

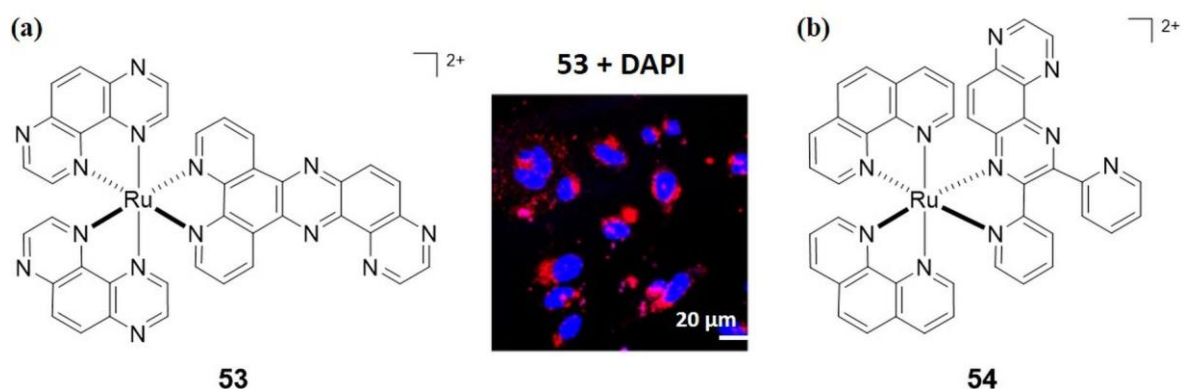


Figure 1.29. (a) Chemical structure of **53** and confocal microscopy image of HeLa cells incubated with **53** (red, 100 μM) for 24 h. The nucleus is stained blue with DAPI. Images from reference 170. (b) Chemical structure of **54**.

malignant cell lines demonstrated that complex **53** was able to induce apoptosis after photoactivation using low energy irradiation, thus revealing this compound as a promising candidate to be used in PDT.¹⁷⁰ However, most of Ru(II) polypyridyl complexes show MLCT absorption and emission maxima shorter than 500 and 650 nm, respectively, a drawback for their use as imaging agents and cancer phototherapeutics due to the deeper tissue penetration of NIR light (700–1100 nm). Therefore, long-wavelength excitation and emitting compounds are advantageous for such biological applications. With this in mind, Elmes *et al.* synthesised a Ru(II) polypyridyl complex (**54**) based on the 2,3-di(pyridin-2-yl)pyrazino[2,3-*f*]quinoxaline ligand.²⁷⁴ This complex showed a MLCT emission band centred at *ca.* 800 nm and binding affinity for DNA, features that makes complex **54** a potential NIR emitting DNA probe (Figure 1.29b).²⁷⁴

The Gunnlaugsson group is a multidisciplinary research group where several research areas are developed simultaneously. Taking advantage of this fact, much effort has been made to incorporate ruthenium complexes into other structures being studied in the Gunnlaugsson group in order to create more complex systems which combine the properties of both motifs. In this context, Ru(II) polypyridyl complexes have been conjugated to 1,8-naphthalimide derivatives by Dr Ryan and Dr Elmes in collaboration with Prof. Susan J. Quinn at University College Dublin (UCD), using both rigid and flexible linkers to separate

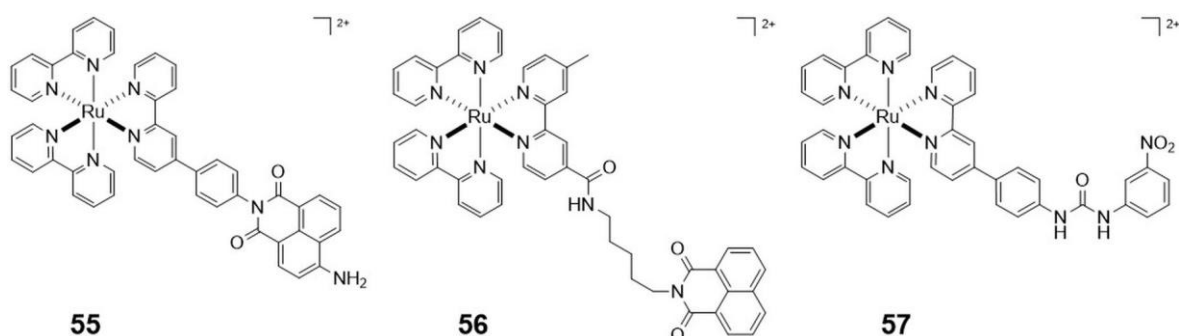


Figure 1.30. Chemical structures of the 1,8-naphthalimide Ru(II) polypyridyl conjugates **55** and **56**, and the Ru(II) polypyridyl complex featuring an aryl urea derivatised 2,2'-bpy auxiliary ligand **57**.

the ruthenium and naphthalimide functionalities (Figure 1.30).^{272,277} Interestingly, the incorporation of the naphthalimide moiety resulted in an enhancement in the binding affinity of the resulting conjugates (**55** and **56**) for DNA. Both derivatives **55** and **56** displayed efficient cleavage of DNA upon photo-irradiation. In addition, the Ru(II)-naphthalimide conjugate **56** was found to be successfully internalised by HeLa cells with localisation in the cytoplasm, and photo-toxic towards cells.^{272,277}

This work was further extended by Dr Elmes and co-workers who developed a dinuclear analogue of **55** by incorporation of a Tröger's base functionality (Figure 1.31a).²⁷⁵

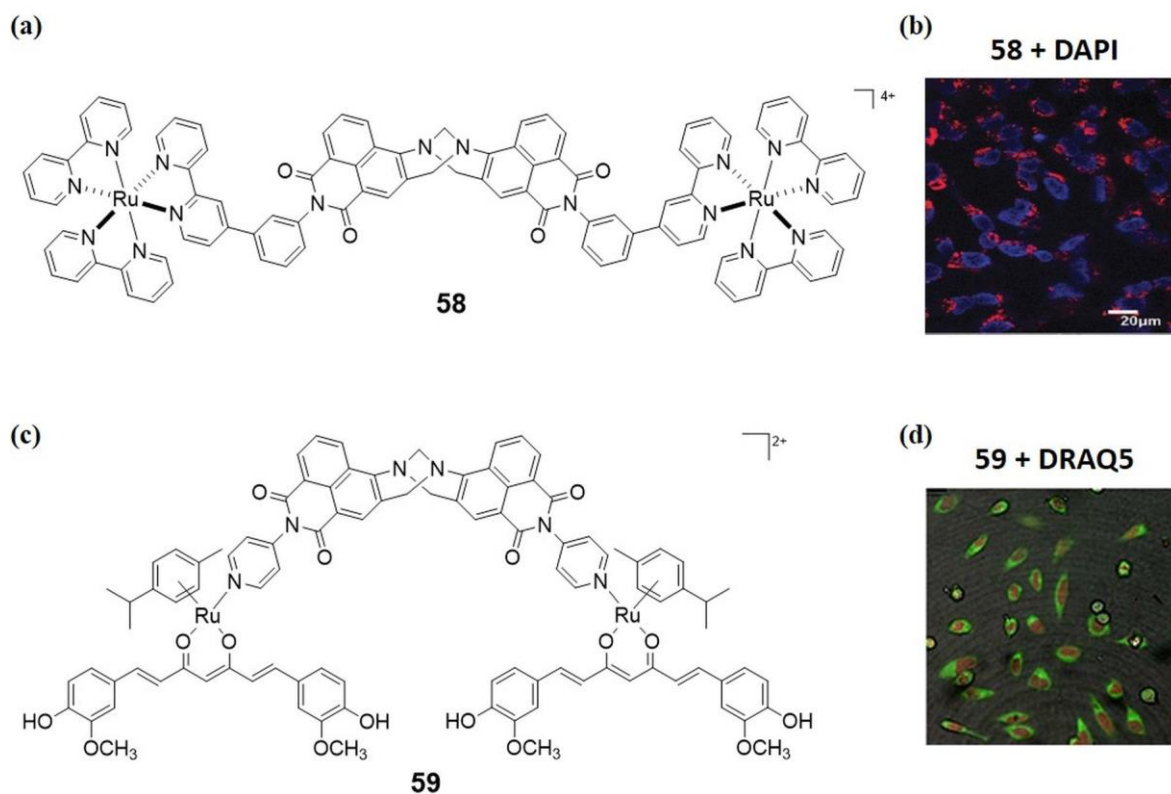


Figure 1.31. (a) Chemical structure of **58**. (b) Confocal microscopy image of HeLa cells incubated with **58** (red, 10 μ M) for 24 h. The nucleus is stained blue with DAPI. (c) Chemical structure of **59**. (d) Confocal microscopy image of HeLa cells incubated with **59** (green, 1 μ M) for 30 min. The nucleus is stained red with DRAQ5. Images from references 275 and 278.

The resulting complex (**58**) was found to undergo rapid cellular uptake in HeLa cells and displayed good luminescence inside the cells without affecting cell viability after 24 h incubation (Figure 1.31b). More recently, Shanmugaraju *et al.* showed the fast-cellular uptake and antiproliferative activity against HeLa cells of the 4-amino-1,8-naphthalimide Tröger's base-Ru(II)-curcumin organometallic conjugate **59** (Figures 1.31c and 1.31d).²⁷⁸ Other examples of Ru(II) polypyridyl based-structures explored in the Gunnlaugsson group include a Ru(II) polypyridyl complex containing urea (**57**) (Figure 1.30) that has been shown to be useful for luminescent anion sensing.²⁷⁶

Gold nanoparticles have also been functionalised with Ru(II) polypyridyl complexes by Elmes *et al.* (Figure 1.32a).²⁶⁴ As was previously discussed, AuNPs are known to have interesting properties such as biocompatibility, low cytotoxicity and high solubility in water which make them suitable platforms to be used in biological applications. The mentioned ruthenium polypyridyl decorated AuNPs (**60**·AuNP_{5 nm}, **61**·AuNP_{5 nm} and **62**·AuNP_{5 nm}) (hydrodynamic diameter of *ca.* 5 nm) displayed DNA affinity and non-toxicity in HeLa cells.

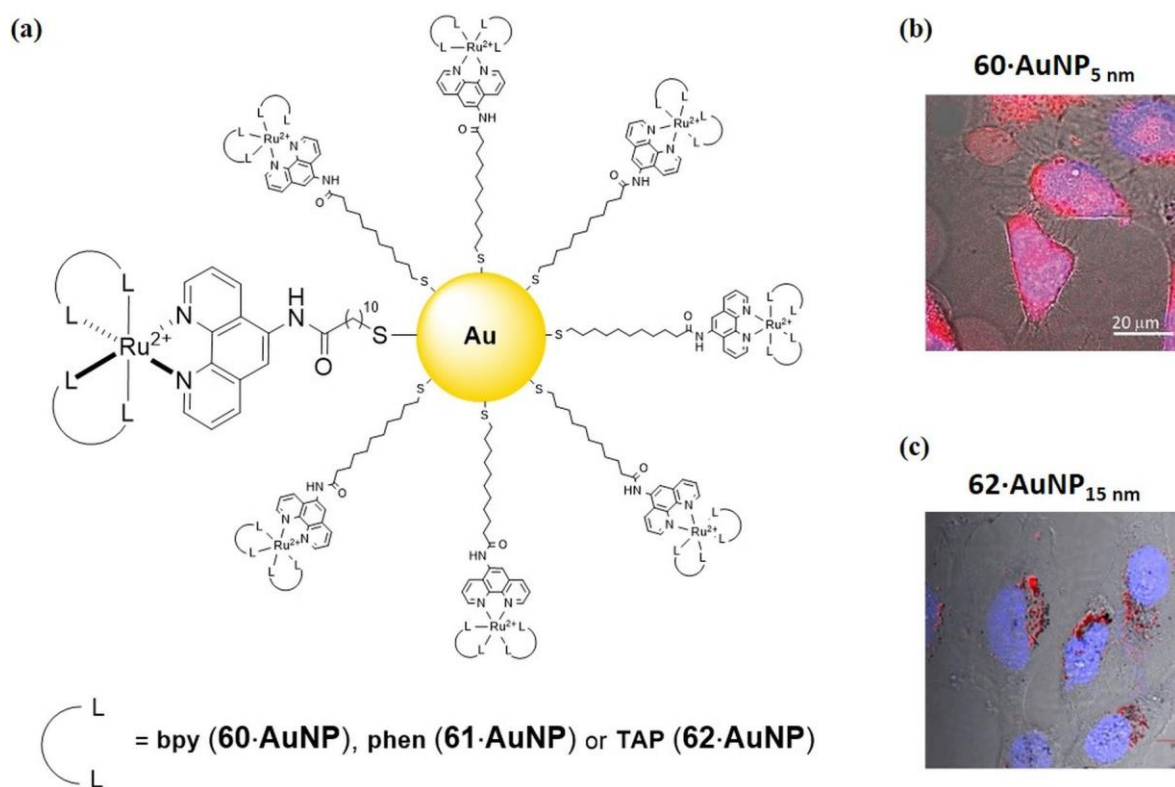


Figure 1.32. (a) Chemical structures of Ru(II) polypyridyl functionalised AuNPs ($L-L = \text{bpy}$ (**60**·AuNP), phen (**61**·AuNP) or TAP (**62**·AuNP)). (b) Confocal microscopy images of HeLa cells incubated with (a) **60**·AuNP_{5 nm} (red, ~16 nM gold concentration) for 4 h or (c) **62**·AuNP_{15 nm} (red, 20 μM) for 24 h. The nucleus is stained blue with DAPI. Images from reference 264 and 271.

Confocal microscopy (Figure 1.32b) and transmission electron microscopy (TEM) imaging showed that these systems were taken up into HeLa cells and they were localised within the

cytoplasm and nuclei of cells, demonstrating the potential of such nanomaterials to deliver high concentrations of Ru(II) polypyridyl complexes into live cells and act as cellular imaging agents.²⁶⁴ Later on, larger Ru(II) functionalised AuNPs were synthesised by Dr Martínez-Calvo and co-workers (**60**·AuNP_{15 nm}, **61**·AuNP_{15 nm} and **62**·AuNP_{15 nm}) (hydrodynamic diameter of *ca.* 15 nm) with a view to overcome the difficulties shown by small size AuNPs when investigating their cellular uptake mechanism (Figure 1.32a).²⁷¹ Similarly to the previously synthesised 5 nm Ru(II) functionalised AuNPs, these systems were found to display high binding affinity for DNA, rapid cellular uptake (Figure 1.32c) and non-phototoxicity against HeLa cells, which highlighted once again their promising applicability in biological systems.

Finally, the recent work carried out by Dr Poynton in collaboration with Prof. John M. Kelly based on the elucidation of the influence of the DNA sequence nature in PET using both transient absorption (TrA) and time-resolved infrared (TRIR) spectroscopy both in solution and in crystal structures should be highlighted.²⁷⁹⁻²⁸⁴ This research gives further insight into the photophysical properties of Ru(II) polypyridyl complexes.

1.9 Objectives of this Work

Following the investigation into the photophysical properties and potential biological applications of Ru(II) polypyridyl complexes, the objective of this research project is concerned with the design of novel ruthenium-based DNA probes and photoactivated anticancer drugs.

In *Chapter 2*, we aim to synthesise and photophysical characterise two new Ru(II) polypyridyl complexes containing the extended aromatic ligand dipyrido[3,2-*a*:2',3'-*c*][1,2,5]thiadiazolo[3,4-*h*]phenazine (**dtp**). We hypothesise that the extension of the well-known **dppz** ligand with the thiadiazole heterocycle will improve the binding properties of the Ru(II) complex to DNA and, therefore, enhance the potential of the resulting molecules to induce DNA damage through disruption of replication and transcription processes. Furthermore, based on the ability of many Ru(II) polypyridyl complexes to generate ¹O₂, it is envisaged that these compounds will be ideal candidates as PDT agents in cancer therapy. Therefore, in addition to their DNA binding properties, cellular uptake and phototoxicity studies will be pursued.

In *Chapter 3*, we will examine the mono-photoadduct formed from the photoreaction between a π -deficient Ru(II) polyyzaaromatic complex with a guanine-based nucleotide on both its ground and excited states by a number of spectroscopic techniques. It is foreseen

that additional spectroscopic studies to those already reported in the literature for this compound will contribute to gain a more comprehensive understanding of the photochemical mechanism by which this mono-photoadduct is able to react with a second guanine moiety and participate in DNA photocrosslinking.

In *Chapter 4*, we will prepare and study a series of water-soluble Ru(II) complexes based on polypyridyl ligands containing long alkyl chains. Their ability to self-assemble in aqueous solution into micellar species and act as luminescent surfactants as well as the aggregation effect on their photophysical properties will be analysed. Furthermore, the potential of these systems to bind to DNA and be used as DNA targeting species will be investigated. In addition, it can be anticipated that the coordination of lipophilic ligands to the ruthenium centre will result in an enhancement of the cellular uptake of the complexes due to their more favourable internalisation arising from the localisation in the cellular membrane. *In vitro* studies are expected to give information about the influence of the alkyl chain length on the cellular uptake and in the ability of these complexes to reduce cellular viability *via* photoactivation pathways.

Finally, in *Chapter 5*, we aim to synthesise two dinuclear Ru(II) polypyridyl complexes attached onto the surface of AuNPs. The combination of the advantageous properties of both the ruthenium moiety and the gold nanomaterial is expected to extend the applicability of the resulting conjugate in biological systems. Photophysical studies as well as cellular uptake investigations will be pursued.

Chapter 2
Ruthenium(II) Polypyridyl Complexes
Containing an Extended ‘dppz’ like
Ligand

2.1 Introduction

Ruthenium(II) polypyridyl complexes containing the extended aromatic ligand **dppz** have been the focus of extensive research efforts by a wide number of research groups since **28** was synthesised in 1985 and the subsequent discovery in 1990 of its particular environment-dependent photophysical properties.^{136-138,142,143,145,146,150,151,163,165,174,285-293} As described in Section 1.6.2, this complex has shown to be weakly emissive in aqueous solution, but it emits strongly in non-protic solvents and when bound to DNA. The same behaviour is observed for the **phen** analogue **29** that displays a luminescence lifetime of *ca.* 250 ps in aqueous solution but it becomes 174 ns in acetonitrile.^{137,163} Although the photophysical processes responsible of this effect are still the object of several studies, it seems to be generally accepted that H bond formation between the nitrogen atoms of the phenazine moiety of the **dppz** ligand and the water molecules present is the reason for the weak emission of these complexes in aqueous solution.^{137,138} However, in the presence of DNA, intercalation of complexes **28** and **29** between the base pairs *via* the **dppz** ligand results in a protection of the phenazine part from H-bonding causing them to become emissive.^{137,138} This phenomenon, known as the “light-switch effect”, makes these complexes suitable for DNA imaging.^{142,143,163,294,295}

Furthermore, the replacement of the **bpy** and **phen** ancillary ligands in such complexes by the π -deficient **TAP** ligand confers a strongly oxidising character on the excited state of the resulting ruthenium complex **30** and provides it with the ability to photo-react with reducing biomolecules such as tryptophan and guanine residues *via* a photoinduced-electron transfer (PET) mechanism from the nucleobase or amino acid to the ³MLCT excited state of the complex.^{166,203,231} Therefore, Ru(II) complexes containing polyazaaromatic ligands show potential applications as photoactivated therapeutic drugs as they can induce controlled and irreversible damage to biomolecules using light as an external trigger. Simultaneously, cell damage can also be induced through ROS generation. In this context, a large number of Ru(II) polypyridyl complexes have shown promising excited-state properties for their use in PDT with significant quantum yields values of singlet oxygen production.^{62,63,93,296} However, despite their interesting photophysical properties that make them suitable for biological applications, these **dppz** complexes show a low ability to be taken up by the cells thus limiting their use in a cellular level. Therefore, the development of new Ru(II) polypyridyl complexes containing chemically modified **dppz** derivatives with the capacity to overcome this issue has become an active research field.^{170,173,179,181,297}

Taking the therapeutic potential of Ru(II) polypyridyl complexes into account,⁶³ the aim of the research presented in this chapter will be the development of two new Ru(II) polypyridyl complexes based on an extended **dppz** ‘like’ ligand, dipyrido[3,2-*a*:2',3'-*c*][1,2,5]thiadiazolo[3,4-*h*]phenazine (**dtp**), synthesised for the first time by Miranda *et al.*²⁹⁸ This ligand results from the extension of the **dppz** aromatic structure with a 1,2,5-thiadiazole ring (Figure 2.1). As mentioned in Section 1.8, previously in the Gunnlaugsson group, a series of Ru(II) polypyridyl complexes containing the **dppz** derivative pyrazino[2,3-*h*]dipyrido[3,2-*a*:2',3'-*c*]phenazine (**pdppz**) were synthesised and their DNA binding properties as well as their biological applications were investigated.¹⁷⁰ In this case, the original **dppz** ligand was modified by incorporation of a pyrazine heterocycle (Figure 2.1).

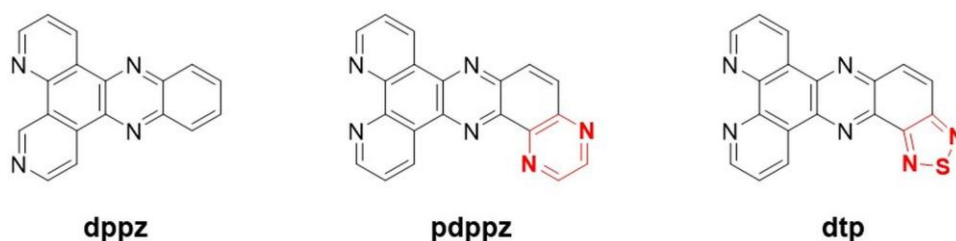


Figure 2.1. Chemical structures of the extended aromatic ligands **dppz**, **pdppz** and **dtp**.

In the same way as with the **pdppz** ligand, it was expected that the extension of the planar structure of **dppz** would increase the intercalation of the complexes into the DNA structure and enhance their cellular uptake.^{178,299} In addition, thiadiazoles have been widely used in medicinal chemistry in the development of new drugs for the treatment of cancer, inflammation, hypertension, depression, or epilepsy, among others, as they are bioisosteres of several heterocycles such as pyrimidine, oxadiazole or oxazole.³⁰⁰

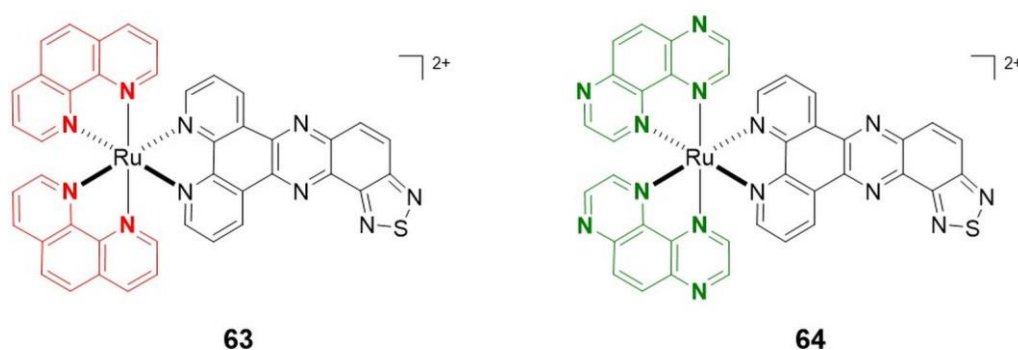


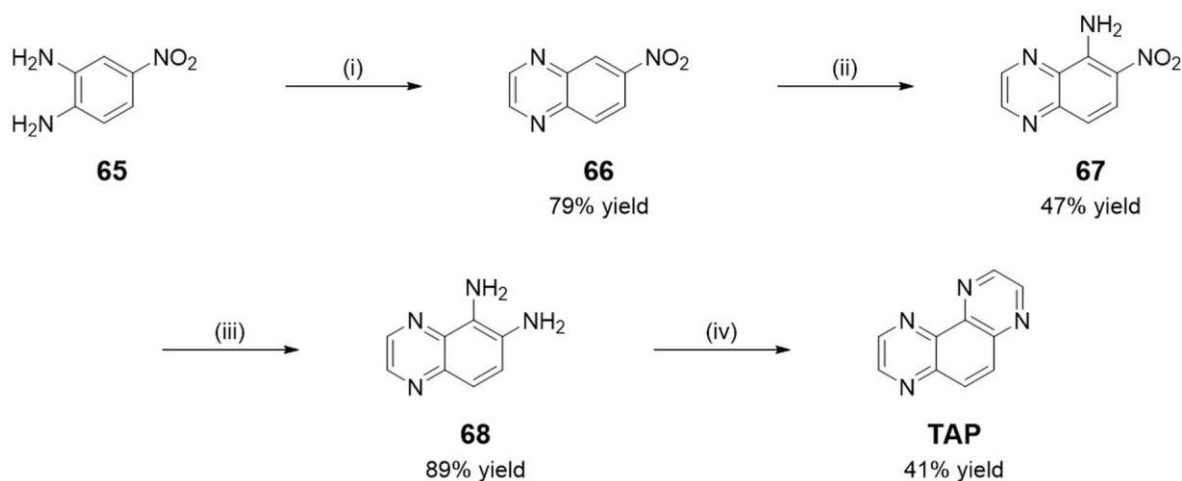
Figure 2.2. Chemical structures of the Ru(II) polypyridyl complexes **63** and **64** studied in this chapter.

The main purpose of this chapter is the design of new ruthenium **dppz**-based compounds and the evaluation of their potential as DNA photoprobes and anticancer drugs. First, the synthesis and characterisation of complexes **63** and **64** is described. In the

following sections, their photophysical properties are discussed and their DNA binding behaviour is investigated using different spectroscopic techniques such as UV-vis absorption and emission spectroscopic titrations, thermal denaturation studies and circular dichroism as well as viscosity. Finally, their ability to produce singlet oxygen is evaluated and biological studies including cellular uptake and phototoxicity are presented.

2.2 Synthesis and Characterisation of **63** and **64**

Synthesis of complexes **63** and **64** was achieved adapting literature procedures which were previously used in our group for similar complexes.^{170,301,302} First, 1,4,5,8-tetraazaphenanthrene (**TAP**) and dipyrido[3,2-*a*:2'.3'-*c*][1,2,5]thiadiazolo[3,4-*h*]phenazine (**dtp**) ligands were synthesised according to two different four step procedures described in the literature.^{298,303} The synthetic pathway of the **TAP** ligand is outlined in Scheme 2.1.

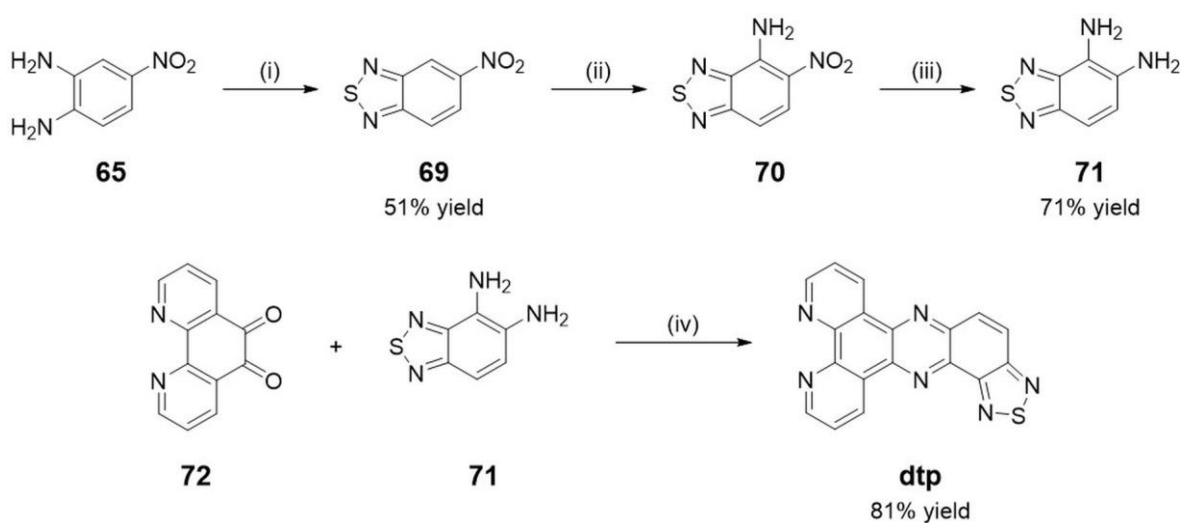


Scheme 2.1. Synthetic pathway for **TAP**: (i) glyoxal (40 wt. % in H₂O), EtOH, reflux, 16 h; (ii) NH₂OH.HCl, NaOMe, MeOH, reflux, 16 h; (iii) N₂H₄·H₂O, 10% Pd/C, EtOH, reflux, 1 h; (iv) glyoxal, EtOH, reflux, 2 h.

The first step involved condensation of 4-nitro-1,2-benzenediamine (**65**) with glyoxal (40 wt. % in H₂O) in EtOH under reflux for 16 h. After cooling down the reaction mixture, the resulting precipitate was filtered and washed with cold MeOH to give 6-nitroquinoxaline (**66**) as a grey solid in 79% yield. Direct amination of **66** at position 5 was achieved by nucleophilic aromatic substitution using hydroxylamine in the presence of freshly prepared NaOMe. The reaction mixture was refluxed for 16 h before being cooled in the freezer for two days followed by filtration yielding 5-amino-6-nitroquinoxaline (**67**) as an orange solid in 47% yield. Subsequent reduction of the nitro group of **67** was carried out using hydrazine in the presence of 10% Pd/C in EtOH under reflux for 1 h. Filtration of the reaction mixture through celite followed by solvent removal under reduced pressure gave 5,6-diaminoquinoxaline (**68**) as a red solid in 89% yield. Glyoxal (40 wt. % in H₂O) was

then condensed with **68** in EtOH under reflux for 2 h. The reaction mixture was cooled and filtered to give a brown solid which was subsequently suspended in CH₂Cl₂ and passed through silica using a mixture CH₂Cl₂/acetone (8:2) as eluent. Removal of the solvent under reduced pressure and recrystallization from EtOH yielded **TAP** as beige needles in 41% yield. Further synthetic details as well as full characterisation of **TAP** ligand by ¹H NMR, ¹³C NMR, HRMS, melting point analysis and IR spectroscopy can be found in Section 7.7.1 of Chapter 7 and Figures A2.1 and A2.2 of the Appendices.

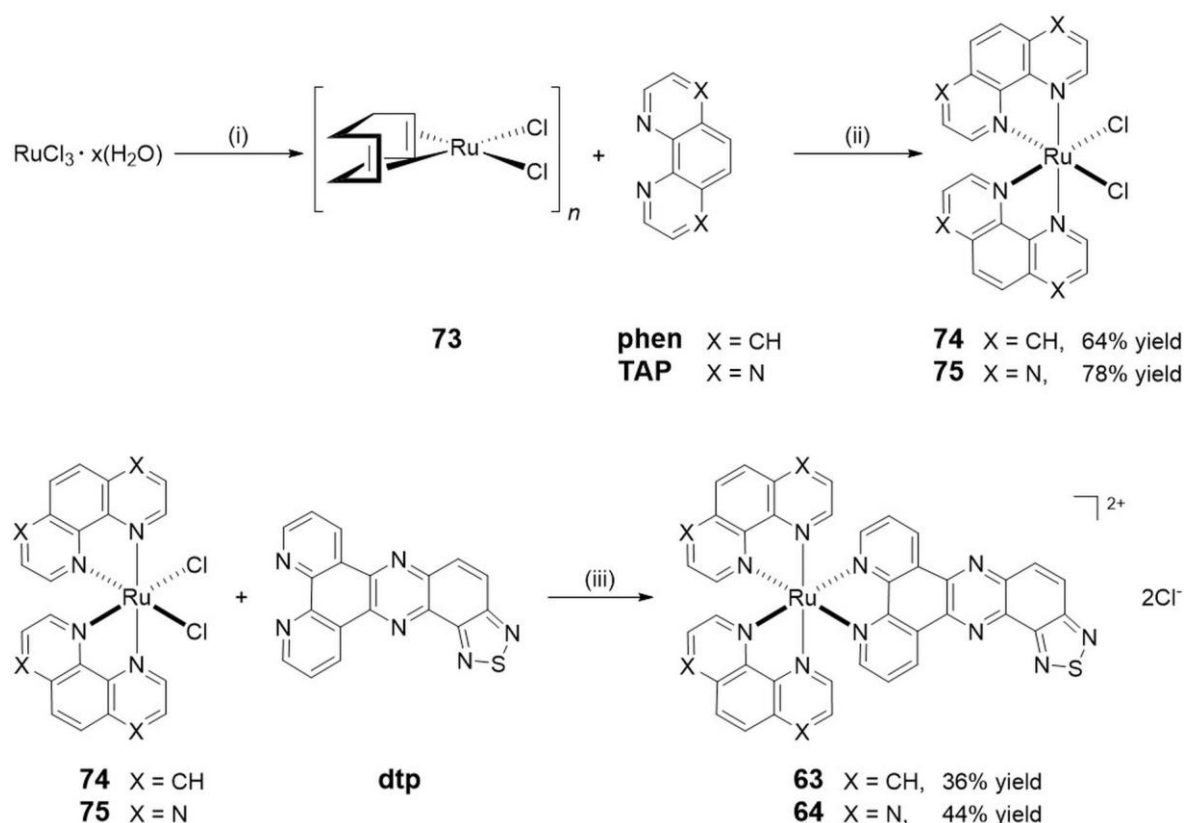
The synthesis of **dtp** ligand is shown in Scheme 2.2. Firstly, **65** was converted into 5-nitro-2,1,3-benzothiadiazole (**69**) using thionyl chloride in the presence of triethylamine in DMF at 0 °C for 2 h. After quenching of the reaction mixture with H₂O, the organic layer was washed with a saturated solution of NaHCO₃, H₂O and brine and the CH₂Cl₂ removed under reduced pressure, after which the resulting solid was purified by silica chromatography using a mixture of CH₂Cl₂/hexane (1:1) as eluent to give **69** as a yellow solid in 51% yield. Direct amination of **69** at position 4 was carried out by nucleophilic aromatic substitution with hydroxylamine in the presence of ethanolic KOH at 0 °C. The reaction mixture was stirred for 2 h before being quenched with 36% HCl to give 4-amino-5-nitro-2,1,3-benzothiadiazole (**70**) as a yellow precipitate which was filtered, washed with EtOH and subsequently reduced to 4,5-diamine-2,1,3-benzothiadiazole (**71**) using Na₂S₂O₄ in boiling H₂O. The reaction mixture was boiled for 20 min, filtered and cooled at room temperature for 16 h yielding **71** as a red solid in 71% yield. The final step involved condensation of **71** with 1,10-phenanthroline-5,6-dione (**72**), kindly prepared by Dr Bjørn la Cour Poulsen, in a



Scheme 2.2. Synthetic pathway for **dtp**: (i) SOCl₂, NEt₃, DMF, 0 °C, 2 h; (ii) NH₂OH·HCl, KOH, EtOH, 0 °C, 2 h; (iii) Na₂S₂O₄, H₂O, reflux, 20 min; (iv) H₂O/EtOH (1:1), pressure tube, 140 °C, 16 h.

mixture of EtOH/H₂O (1:1) in a high-pressure tube at 140 °C for 16 h. After cooling to room temperature, filtration of the resulting precipitate and further washing with H₂O, EtOH and Et₂O gave **dtp** a yellow powder in 81% yield. The **dtp** ligand was then characterised by ¹H NMR, ¹³C NMR, HRMS, melting point analysis and IR spectroscopy (see Section 7.7.1 of Chapter 7 and Figures A2.3 and A2.4 of the Appendices for details).

Precursor bispolypyridyl dichloride complexes were synthesised in two steps as shown in Scheme 2.3. First, [Ru(η⁴-COD)Cl₂]_n (**73**) was prepared by refluxing RuCl₃·x(H₂O) in the presence of 1,5-cyclooctadiene (COD) in EtOH for three days to give **73** as a dark brown solid in 97% yield. The second step involved reaction of **73** with the corresponding polypyridyl ligand (1,10-phenanthroline (**phen**) or 1,4,5,8-tetraazaphenanthrene (**TAP**), for **63** and **64**, respectively) in degassed DMF using microwave irradiation at 140 °C for 40 min. Addition of acetone and cooling of the reaction mixture at -15 °C for 2 days resulted in the precipitation of the precursors *cis*-[Ru(phen)₂Cl₂] (**74**) and *cis*-[Ru(TAP)₂Cl₂] (**75**) as dark purple solids in 64% and 78% yield, respectively.



Scheme 2.3. Synthetic pathway for **63** and **64**: (i) 1,5-cyclooctadiene, EtOH, reflux, 3 days; (ii) DMF, microwave reaction, 140 °C, 40 min; (iii) EtOH/H₂O (1:1), microwave reaction, 140 °C, 40 min.

This procedure ensured that the two remaining chlorides are coordinated to the ruthenium centre in a *cis* orientation, which was essential for subsequent incorporation of the final

bidentate ligand **dtp**. Complexation of the extended **dtp** ligand with the appropriate Ru(II) bispolypyridyl dichloride was subsequently carried out by microwave reaction in a degassed EtOH/H₂O mixture (1:1) at 140 °C for 40 min. The crude complexes were purified by column chromatography using neutral alumina and MeCN/H₂O (10:0 to 9:1) as eluent, yielding the chloride salts of the di-heteroleptic complexes **63** and **64** as red solids in 36% and 44% yield, respectively.

Complexes **63** and **64** were characterised by ¹H NMR, ¹³C NMR, Elemental Analysis, HRMS, melting point analysis and IR spectroscopy. The ¹H NMR spectrum (400 MHz, CD₃CN) of **64** is shown in Figure 2.3 with that of **63** given in Figure A2.5 of the Appendices. Additional 2D NMR experiments allowed the identification of all signals. Twenty-four protons and twenty protons were observed between 7.6 and 10.0 ppm for **63** and **64**, respectively, which was consistent with the molecular formula of each compound.

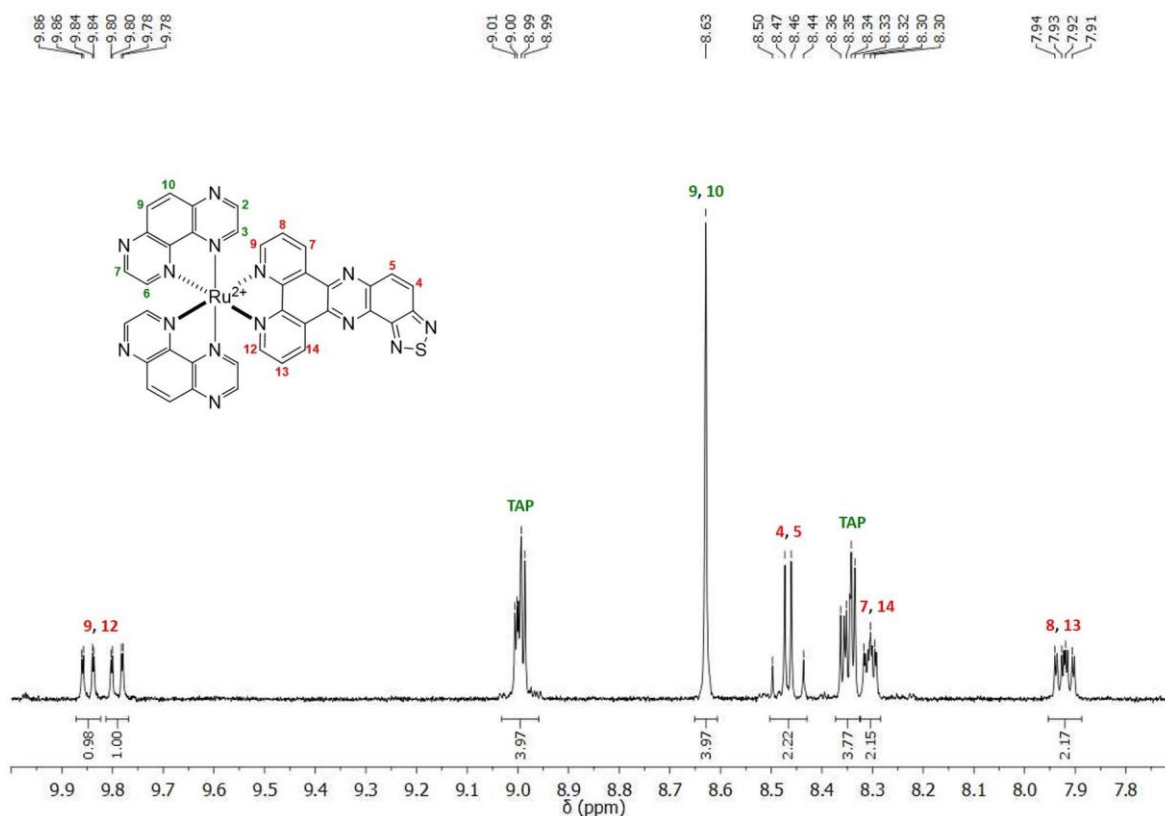


Figure 2.3. ¹H NMR (400 MHz, CD₃CN) spectrum of **64**. Signals corresponding to TAP ligands are in green and signals assigned to the **dtp** ligand are in red.

MALDI⁺- or ESI⁺-HRMS also confirmed successful formation of both complexes **63** and **64** showing peaks at *m/z* 802.0945 and 403.0387 corresponding to their [M]⁺ and [M]²⁺ ions, respectively. Furthermore, comparison of the theoretical and experimental isotopic

distribution pattern of both complexes showed the typical isotopic profile of ruthenium complexes (Figure 2.4).

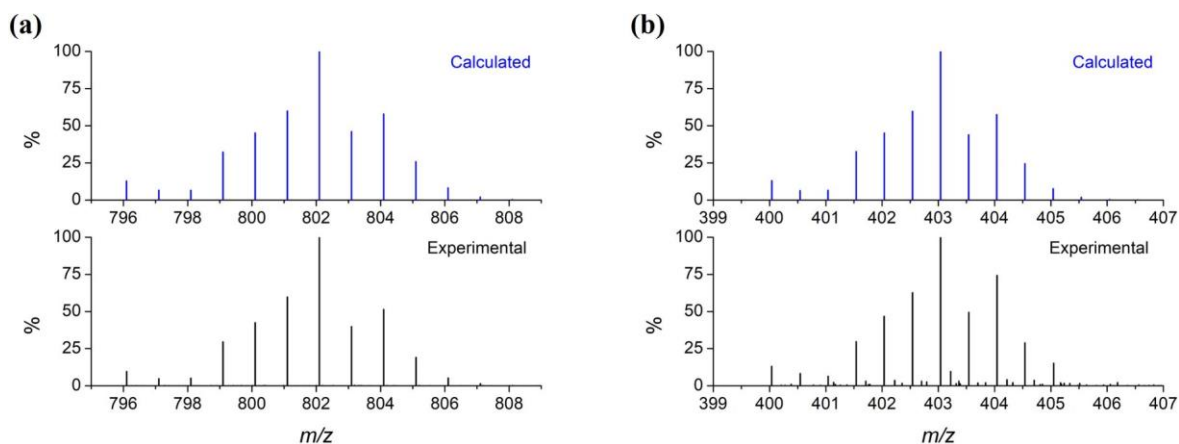


Figure 2.4. Comparison between the calculated (blue) and experimental (black) isotopic distribution pattern for (a) **63** and (b) **64** from matrix-assisted laser desorption/ionisation (positive mode) and electrospray ionisation (positive mode) high resolution mass spectrometry analysis, respectively.

Additional details of synthetic procedures and the full characterisation of both complexes and **TAP** and **dtP** ligands can be found in Section 7.7 of Chapter 7 and Figures A2.1–A2.7 of the Appendices.

2.3 Crystallographic Studies of **64**

Having synthesised and characterised complexes **63** and **64**, investigation into the solid-state structure of complex **64** was carried out. Therefore, red plate shaped crystals of the racemic mixture of complex **64**, were obtained by slow evaporation from a solution of the chloride form of the complex in methanol. Unfortunately, despite several attempts to grow crystals of the **phen** analogue complex, they were not found to be suitable for crystallographic studies.

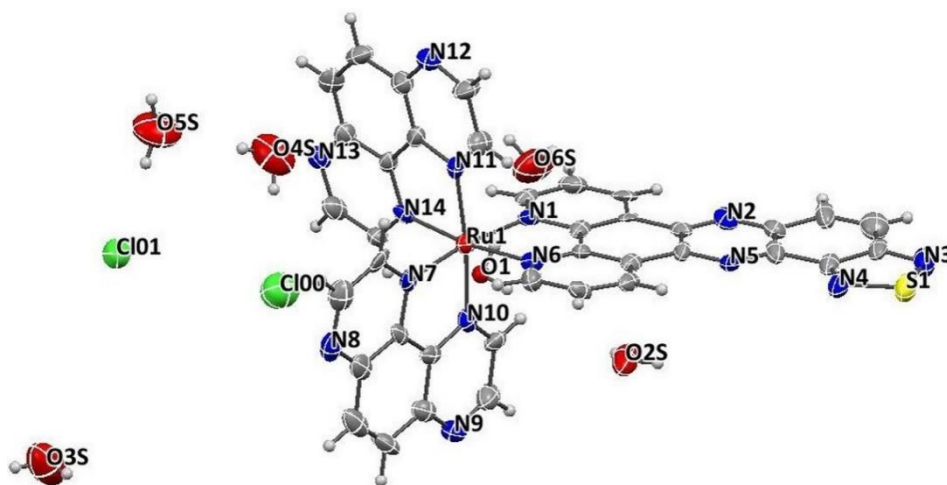


Figure 2.5. Ellipsoid plot of the asymmetric unit of the unit cell of **64**. Ellipsoids are shown at 50% probability.

Crystals of **64** were then analysed by single crystal X-ray diffraction. The crystallographic information was collected and refined by Dr Salvador Blasco and can be found at Table A2.1 of the Appendices. The single crystal diffraction data were solved and refined in the monoclinic space group *C2/c*. The asymmetric unit contains one molecule of **64**, two chloride counter ions and six solvent water molecules (Figure 2.5). The unit cell contains eight asymmetric units. The coordination environment of the ruthenium atom exhibits a fairly regular octahedral geometry. The metallic centre is coordinated to the nitrogen atoms of two **TAP** ligands and one **ntp** ligand, with N-Ru-N angle values between 80.1(3) and 95.0(3)°, and Ru-N bond distances between 2.052(10) and 2.075(10) Å (Table 2.1). These bond lengths are typical for other Ru(II) polypyridyl complexes reported in the literature.^{170,304-306}

Table 2.1. Selected bond lengths (Å) and angles (°) for **64**.

Atoms	Bond lengths (Å)	Atoms	Angles (°)	Atoms	Angles (°)
Ru1-N1	2.075(10)	N10-Ru1-N7	82.1(4)	N11-Ru1-N6	92.9(3)
Ru1-N6	2.067(9)	N10-Ru1-N14	94.9(3)	N14-Ru1-N7	89.6(3)
Ru1-N7	2.068(10)	N10-Ru1-N1	91.0(4)	N14-Ru1-N11	80.7(3)
Ru1-N10	2.052(10)	N10-Ru1-N6	91.8(3)	N14-Ru1-N1	95.9(3)
Ru1-N11	2.060(9)	N11-Ru1-N7	93.8(4)	N6-Ru1-N7	95.2(3)
Ru1-N14	2.055(9)	N11-Ru1-N1	93.4(3)	N6-Ru1-N1	80.1(3)

A network of hydrogen bonds is formed by the six water molecules and the two chloride counter ions which constitute the asymmetric unit, whereas none of the external nitrogen atoms of the complex seems to participate in the hydrogen bonding except for N9 which receives hydrogen bonding from O6.

The extended aromatic **ntp** ligand was found to be quite flat and displays π - π interactions resulting in the stacking of the **ntp** moiety of one complex molecule with another **ntp** ligand of a neighbouring complex with the same absolute configuration (Figure 2.6). The stacking distances, defined as the distance between the mean plane of the **ntp** ligand of one **64** molecule and one individual atom of the **ntp** moiety of a stacked **64** molecule, are in the range of 3.113 to 3.642 Å. The mean planes of each **ntp** units are almost parallel with a narrow angle of 4.14° and the offset distance is 1.415 Å.

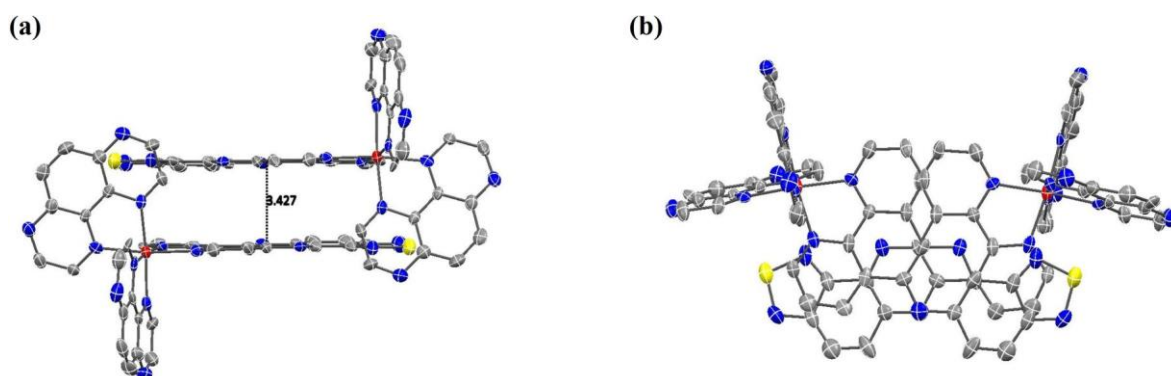


Figure 2.6. Ellipsoid plot of the paired structure of two neighbouring Λ -**64** enantiomers; view down crystallographic (a) *b* and (b) *a* axis. Ellipsoids are shown at 50% probability. Distance between the mean plane of the **dtp** ligand of one Λ -**64** molecule and the C12 atom of the **dtp** ligand of the stacked Λ -**64** molecule is shown. Hydrogen atoms, solvent molecules and counter ions are omitted for clarity.

The particular π - π stacking interactions between **dtp** ligands from different molecules of **64** with the same absolute configuration result in the packing of these pairs of $\Lambda\Lambda$ or $\Delta\Delta$ complexes in enantiopure layers along the (001) plane (Figure 2.7).

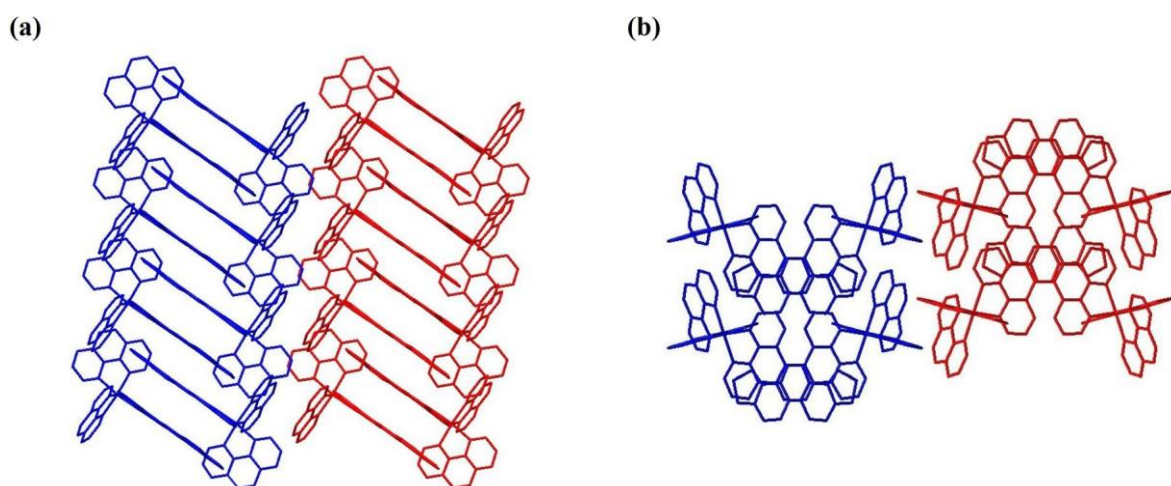


Figure 2.7. Capped stick view of the arrangement of the Λ -**64** (blue) and Λ -**64** (red) domains; view down crystallographic (a) *b* and (b) *a* axes. Hydrogen atoms, solvent molecules and counter ions are omitted for clarity.

No positional disorder was observed. However, the solvent molecules exhibited some degree of thermal disorder and therefore they were refined using suitable ISOR restraints. An ISOR command was also used to refine C19 atom which was not positive definite. Hydrogen atoms from water molecules were placed with help of DFIX and DANG restraints.

The maximum 2θ value is 108.42° , which provides a mediocre resolution in the crystal structure of 0.94 \AA . The collection of data took two days in order to collect as many reflections as possible. Both R1 and wR2 values from the “Final R indexes [$I \geq 2\sigma(I)$]” and “Final R indexes [all data]” are larger than 5 and 10% values, respectively, required for a

good structure. That is due to the poor quality of the crystals which were quite small. On the other hand, this kind of ruthenium complexes are light sensitive and this could result in a degradation of the compound which would make the data collection difficult.

In the next section, characterisation of the photophysics of both complexes **63** and **64** in solution will be undertaken as such information will be essential in the understanding of the interaction of these systems with DNA which will be studied in further sections.

2.4 Photophysical Characterisation of **63** and **64**

The photophysical properties of complexes **63** and **64** were initially investigated in 10 mM sodium phosphate-buffered aqueous solution at pH 7.4 (complex **64**) and in acetonitrile (for both **63** and **64**) at room temperature, since the solvent plays a key role in the luminescent behaviour of Ru(II) complexes based on **dppz** and containing **phen** as ancillary ligands (see Section 1.6.1 for further discussion).^{141,163} Therefore, it can be anticipated that, in the same manner that it occurs for **29** and **30**, the ³MLCT excited state will be localised on the extended **dtp** ligand of complex **63** and on one of the **TAP** ligands of complex **64**, making them non-emissive and emissive in aqueous solution, respectively. The origin of the lack of luminescence of **63** is due to hydrogen bonding with the nitrogen atoms of the phenazine moiety of the extended ligand as discussed previously in detail in Section 1.6.1 for **dppz** analogues.^{137,138}

Hence, the UV-vis absorption, excitation and emission spectra of **63** and **64** were recorded in acetonitrile and in 10 mM sodium phosphate-buffered aqueous solution, respectively, and are shown in Figure 2.8.

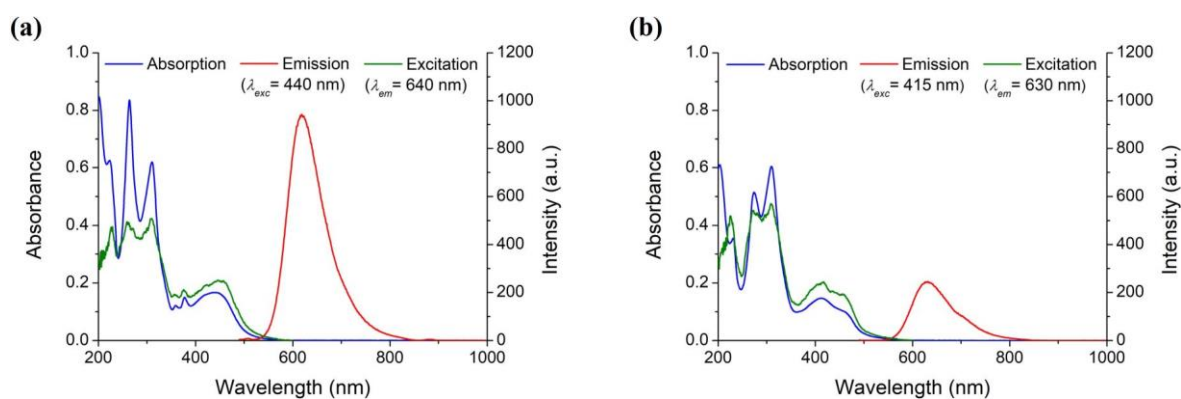


Figure 2.8. UV-vis absorption, excitation and emission spectra of (a) **63** in acetonitrile and (b) **64** in 10 mM sodium phosphate-buffered aqueous solution at pH 7.4, at room temperature (rt).

As previously reported in the literature for other Ru(II) polypyridyl complexes containing extended aromatic ligands, similar characteristic bands were observed in the UV-vis absorption and in the emission spectra of **63** and **64**.^{142,167} Complex **63** showed two

absorption bands at 223 and 262 nm which can be assigned to π - π^* intra-ligand transitions of the ancillary **phen** ligands; a band at 310 nm characteristic of π - π^* transitions within the extended aromatic ligand **dtp**; two less intense bands at 359 and 377 nm corresponding to n - π^* transition within the phenazine part of **dtp**; and a broad band centred at 439 nm attributed to the MLCT transition involving an electron transfer from the metal centre to the extended ligand. Complex **64** showed an absorption band at 274 nm characteristic of π - π^* intra-ligand transitions of the ancillary **TAP** ligands; a band at 309 nm corresponding to π - π^* transition within the ligand **dtp**; and a band at 413 nm attributed to the typical MLCT transition of this kind of complexes where an electron transfer occurs from the metal centre to the **TAP** ligands. Values for the molar absorptivity of some of these absorption bands in 10 mM sodium phosphate-buffered aqueous solution at pH 7.4 are shown in Table 2.2.

Table 2.2. Absorption properties of **63** and **64** in 10 mM sodium phosphate-buffered aqueous solution at pH 7.4, at rt.

Complex	Absorbance λ_{max} , nm (ϵ , $10^4 \text{ M}^{-1}\text{cm}^{-1}$) ^[a]		
	π - π^* IL	π - π^* dtp	π - π^* MLCT
63	262 (9.0 \pm 0.2)	310 (6.4 \pm 0.1)	439 (1.83 \pm 0.04)
64	274 (6.79 \pm 0.07)	309 (7.9 \pm 0.1)	413 (1.96 \pm 0.02)

^[a] Molar absorptivity values correspond to the mean \pm SEM.

The emission properties of **63** and **64** are summarised in Table 2.3 and they revealed a similar behaviour to **dppz** Ru(II) complexes described in the literature.^{142,167} Thus, upon excitation of the MLCT bands, characteristic luminescence bands of radiative deactivation from the ³MLCT excited state were observed at 619 nm for **63** ($\lambda_{exc} = 440$ nm) in acetonitrile, and at 631 nm for **64** ($\lambda_{exc} = 415$ nm) in 10 mM sodium phosphate-buffered aqueous solution at pH 7.4. As expected, the emission spectrum of complex **63** recorded in 10 mM sodium phosphate-buffered aqueous solution at pH 7.4 confirmed the non-emissive character of **63** in aqueous solution (Figure A2.8 of the Appendices). Similarly, the excitation spectra recorded for **63** and **64** were found to be identical to their absorption spectra.

Quantum yields (Φ_{em}) of **63** and **64** were determined using the optically dilute solution method with [Ru(bpy)₃]Cl₂ as a reference compound and the reported values correspond to the average of a minimum of three independent measurements.^{307,308} Thus, **63** and **64** showed values of 0.016 and 0.029, in air-saturated acetonitrile and 10 mM sodium phosphate-buffered aqueous solution, respectively; Φ_{em} of **63** is higher than the value

recorded for **29**, while Φ_{em} of **64** is comparable to the corresponding value for **30** in aqueous solution.^{166,286}

Table 2.3. Emission properties of **63** in acetonitrile and **64** in both 10 mM sodium phosphate-buffered aqueous solution at pH 7.4 and acetonitrile, at rt. Complexes **29** and **30** are included for comparison.

Complex	λ_{max}^{em} (nm) buffer	λ_{max}^{em} (nm) MeCN	$\Phi_{em}^{[a]}$ buffer (air)	$\Phi_{em}^{[a]}$ MeCN (air)	τ_{em} (ns) ^[b] buffer (air)	τ_{em} (ns) ^[b] buffer (N ₂)	τ_{em} (ns) ^[b] MeCN (air)	τ_{em} (ns) ^[b] MeCN (N ₂)
29 ^[c]	-	607	-	0.0073	-	-	177	663
30 ^[d]	636	621	0.035	-	820	1090	-	-
63	-	619	-	0.016	-	-	169	590
64	631	614	0.029	0.036	697	864	683	1122

^[a] Air-saturated aqueous solution of [Ru(bpy)₃]Cl₂ as reference ($\Phi_{em} = 0.028$).³⁰⁸ Estimated errors $\pm 5\%$.

^[b] The luminescence decays are monoexponential. Estimated errors $\pm 10\%$.

^[c] From reference 286.

^[d] From reference 166. The reported values are in aqueous solution.

Furthermore, luminescence lifetimes (τ_{em}) of **63** and **64** were also recorded using single-photon timing (SPT) ($\lambda_{exc} = 458$ nm, $A_{MLCT} = 0.05$) and taking the average of a minimum of three measurements for each complex. In all the cases, the data was best fitted to a single exponential decay function, with χ^2 values close to 1. Therefore, in air-saturated acetonitrile solution, complex **63** showed a luminescence lifetime of 169 ns, while in deaerated acetonitrile solution a lifetime of 590 ns was observed. On the other hand, complex **64** exhibited luminescence lifetimes of 697 and 864 ns in air-saturated and deaerated 10 mM sodium phosphate-buffered aqueous solution, respectively. When the solution is not deaerated, lifetimes are considerably lower due to the quenching of the excited state from dissolve oxygen in solution. Lifetimes values of **63** are very close to reported lifetimes of **29**.²⁸⁶ However, lifetimes values of **64** are slightly smaller than the corresponding reported values of the **30** in aqueous solution but indicate that the excited-state character of **64** is similar to the **dppz** analogue.¹⁶⁶

In summary, complexes **63** and **64** have revealed interesting photophysical properties which are sensitive to the environment. Therefore, their interaction with DNA can be studied by monitoring changes in the MLCT absorption band upon addition of DNA. Additionally, emission of both complexes is expected to be altered in the presence of DNA in aqueous solution. Thus, recovery of the emission can be anticipated for **63** due to the ‘light switch’ effect upon binding to the nucleic acid. In contrast, a quenching of the luminescence of **64** can be expected as a result of a photo-induced electron transfer (PET) between the guanine

nucleobase and the π deficient Ru(II) complex. Hence, in the following section the nature of the interaction of such complexes with DNA will be studied in order to assess their applications as novel luminescent probes for targeting DNA.

2.5 DNA Binding Interactions of **63** and **64**

Over the last decades, the ability of Ru(II) polypyridyl complexes to bind to DNA has been extensively investigated in the literature as was discussed in Section 1.6.2.² The preferred binding mode of such complexes can be controlled by selection of the suitable ligands coordinated to the metal centre. As complexes **63** and **64** reported here are cationic and contain the extended aromatic ligand **dtp**, they are expected to bind to DNA essentially by a combination of electrostatic and intercalation modes.¹⁶⁵ However, other binding modes such as groove binding are possible. In order to study the nature and binding affinity of **63** and **64** with the DNA, several spectroscopic techniques have been used; namely, absorption and emission DNA titrations, thermal denaturation and circular dichroism (CD). Furthermore, viscosity studies have also been carried out to understand the types of binding mode of these complexes. DNA studies of complex **63** were carried out by Dr Bjørn la Cour Poulsen and the results are included here only for comparison.

2.5.1 Spectroscopic Titrations of **63** and **64**

The interaction of **63** and **64** with salmon testes DNA (stDNA) was first examined by UV-vis absorption and emission spectroscopic titrations. DNA titrations were carried out by gradual addition of stDNA to a 10 mM sodium phosphate-buffered aqueous solution (pH 7.4) containing the racemic mixture of the corresponding Ru(II) complex and either in the presence or in the absence of 160 mM NaCl (low and high ionic strength, respectively). Changes in the absorption and the emission spectra were monitored until no significant change was observed at further increases in the concentration of DNA indicating that almost all the complex was bound to DNA. All titrations were repeated at least three times to ensure reproducibility of the obtained results.

The overall changes in the UV-vis absorption spectra of both **63** and **64** are shown in Figure 2.9 (low ionic strength) and Figure 2.10 (high ionic strength). As reported for similar Ru(II) complexes, a decrease in the absorption was observed upon increasing DNA concentration.¹⁷⁰ Complex **63** showed a 18% and 16% hypochromism in the MLCT band at 439 nm (low and high ionic strength, respectively) along with a 48% and 45% hypochromism in the band corresponding to the π - π^* transition within the **dtp** ligand at

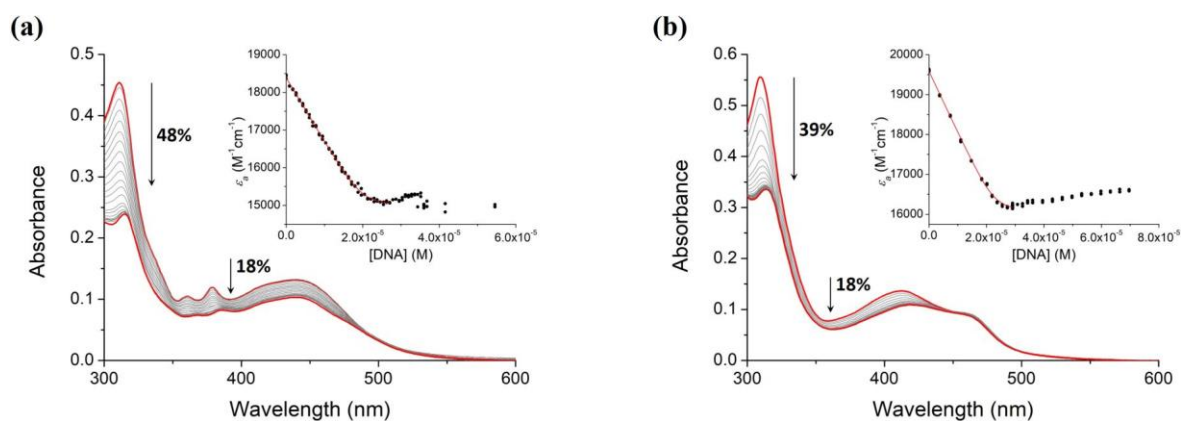


Figure 2.9. Changes in the UV-vis absorption spectra of (a) **63** (7.35 μM) and (b) **64** (6.95 μM) with increasing concentration of stDNA (0–55 μM and 0–70 μM, respectively) in 10 mM sodium phosphate-buffered aqueous solution at pH 7.4. Inset: Plot of ϵ_a (M⁻¹cm⁻¹) vs. [DNA] (M, bases) using data from absorbance at (a) 439 nm and (b) 413 nm and the best fit of the data using a modification of the Bard Equation.

310 nm (low and high ionic strength, respectively). On the other hand, a 18% and 15% hypochromism in the MLCT band at 413 nm (low and high ionic strength, respectively) in addition to a 39% and 35% hypochromism in the **dtp** band at 310 nm (low and high ionic strength, respectively) were found for complex **64**. This hypochromic effect and, in particular, the large decrease in the absorbance at 310 nm, can be attributed to an intercalative binding resulting from the π - π stacking between the chromophore of the extended aromatic ligand and the chromophores of the DNA base pairs.³⁰⁹

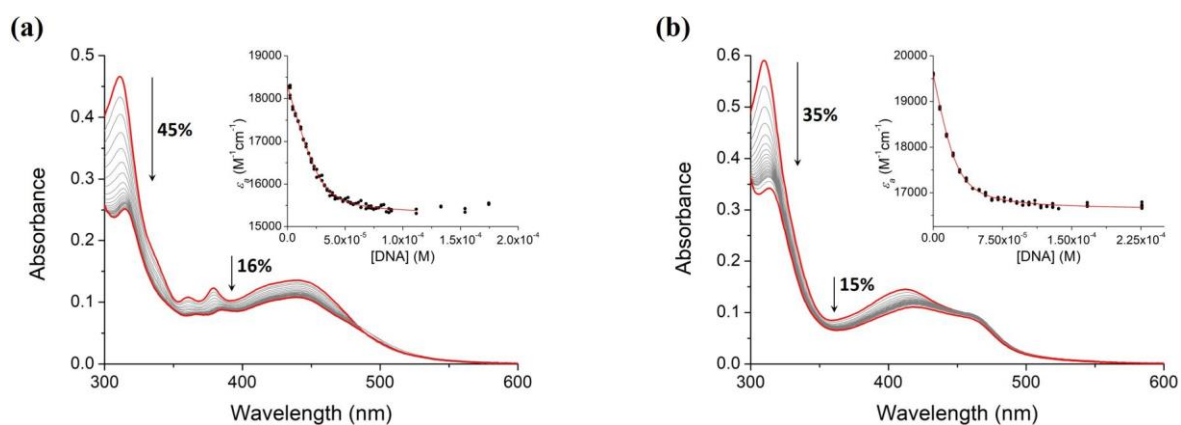


Figure 2.10. Changes in the UV-vis absorption spectra of (a) **63** (7.41 μM) and (b) **64** (7.39 μM) with increasing concentration of stDNA (0–175 μM and 0–230 μM, respectively) in 10 mM sodium phosphate-buffered aqueous solution containing 160 mM NaCl at pH 7.4. Inset: Plot of ϵ_a (M⁻¹cm⁻¹) vs. [DNA] (M, bases) using data from absorbance at (a) 439 nm and (b) 413 nm and the best fit of the data using a modification of the Bard Equation.

Regarding the changes in the emission spectra upon addition of stDNA then, different behaviours were observed for both complexes **63** and **64**, as shown in Figure 2.11 (low ionic strength) and Figure 2.12 (high ionic strength). Complex **63** containing **phen** as ancillary ligands exhibited the well-known “light-switch” effect as expected from the structural

similarity between **dppz** and **dtp**. Therefore, where the emission was fully quenched in aqueous solution, it became emissive in the presence of DNA. This effect is attributed to a

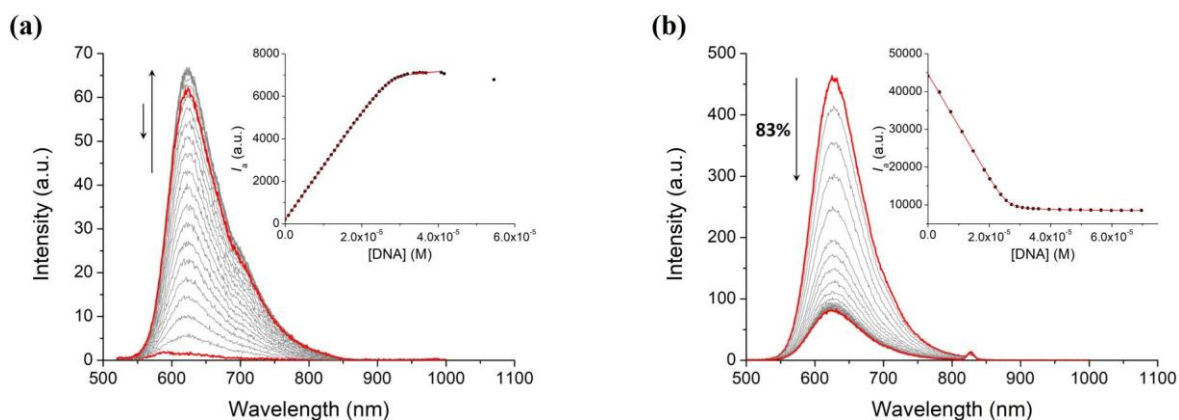


Figure 2.11. Changes in the emission spectra of (a) **63** ($7.35 \mu\text{M}$, $\lambda_{exc} = 439 \text{ nm}$) and (b) **64** ($6.95 \mu\text{M}$, $\lambda_{exc} = 413 \text{ nm}$) with increasing concentration of stDNA ($0\text{--}55 \mu\text{M}$ and $0\text{--}70 \mu\text{M}$, respectively) in 10 mM sodium phosphate-buffered aqueous solution at pH 7.4. Inset: Plot of I_a (a.u.) vs. $[\text{DNA}]$ (M, bases) using data from integrated MLCT emission intensity and the best fit of the data using a modification of the Bard Equation.

change in the environment as a result of the intercalation of the extended aromatic ligand into the DNA base pairs and, thus, protection of the N-atoms of the phenazine moiety from interaction with solvent molecules that is known as the reason of the quenching of the emission.^{137,138,157,159,165} Upon addition of stDNA, the emission showed a biphasic behaviour at low and high ionic strength. A strong emission enhancement was first observed followed

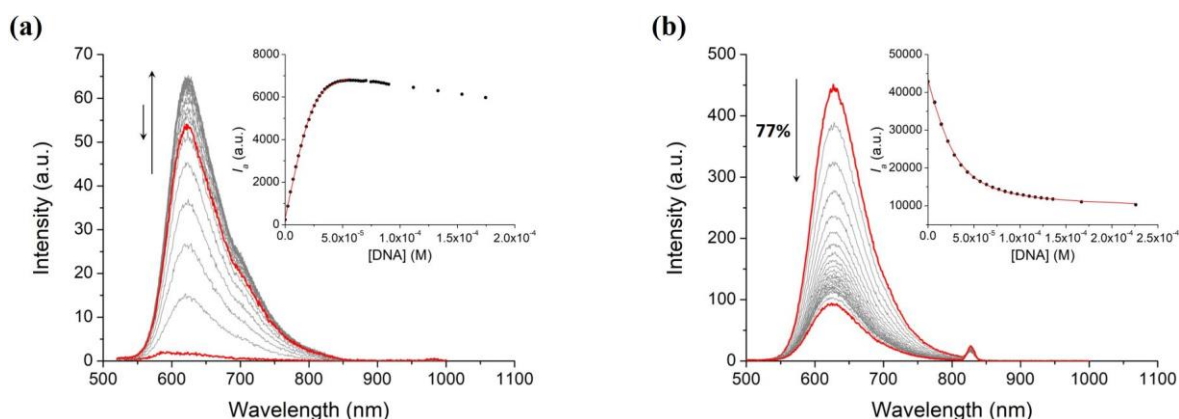


Figure 2.12. Changes in the emission spectra of (a) **63** ($7.41 \mu\text{M}$, $\lambda_{exc} = 439 \text{ nm}$) and (b) **64** ($7.39 \mu\text{M}$, $\lambda_{exc} = 413 \text{ nm}$) with increasing concentration of stDNA ($0\text{--}175 \mu\text{M}$ and $0\text{--}230 \mu\text{M}$, respectively) in 10 mM sodium phosphate-buffered aqueous solution containing 160 mM NaCl at pH 7.4. Inset: Plot of I_a (a.u.) vs. $[\text{DNA}]$ (M, bases) using data from integrated MLCT emission intensity and the best fit of the data using a modification of the Bard Equation.

by a slow decrease of the emission intensity (insets in Figures 2.11a and 2.12a). In contrast, an 83% and 77% decrease in the MLCT emission intensity at 631 nm (low and high ionic strength, respectively) was observed for complex **64** with **TAP** as ancillary ligands (insets

in Figures 2.11b and 2.12b), which is explained by the ability of Ru(II) complexes containing at least two **TAP** ligands to oxidize the guanine leading to a luminescence quenching (see Section 1.6.3 for further discussion).^{166,203,212}

The binding constant (K_b) and the binding site size (n) for both **63** and **64** were determined using a modification of the model of Bard *et al.* that consists in the reorganisation of the original equation (2.1) in equation (2.3), where ε_a , ε_f and ε_b correspond to the apparent molar absorption coefficient, the molar absorption coefficient for the free Ru(II) complex and the molar absorption coefficient for the Ru(II) complex in the bound form, respectively, while C_t is the total complex concentration, and $[DNA]$ is the concentration of DNA in bases.^{310,311} With introducing this modification, an estimation of ε_b from the titration data is no longer necessary as it can be fitted together with K_b and n . In this way, ε_a is the dependent variable and $[DNA]$ and C_t are the independent variables. It has to be noticed that, although the dependence of C_t was also considered in the fitting, only the dependence of $[DNA]$ was shown in the plots presented in this section. This reorganisation of the Bard equation was introduced for the first time by Dr Bjørn la Cour Poulsen with a view to get more accurate values of the binding parameters.^{284,311}

$$\frac{(\varepsilon_a - \varepsilon_f)}{(\varepsilon_b - \varepsilon_f)} = \frac{b - (b^2 - 2K_b^2 C_t [DNA]/n)^{1/2}}{2K_b C_t} \quad (2.1)$$

$$b = 1 + K_b C_t + K_b [DNA]/2n \quad (2.2)$$

$$\varepsilon_a = \frac{b - (b^2 - 2K_b^2 C_t [DNA]/n)^{1/2}}{2K_b C_t} \times (\varepsilon_b - \varepsilon_f) + \varepsilon_f \quad (2.3)$$

Hence, changes in the MLCT band at 439 and 413 nm for **63** and **64**, respectively, and the integrated emission were fitted according to equation (2.3) and using a non-linear regression fitting with OriginPro 8.5. For the fitting of the emission titrations ε was substituted by emission intensity (I). Plots of ε_a or I_a vs $[DNA]$ and the corresponding best fit of the data to the reorganised Bard equation are shown as insets in Figures 2.9, 2.10, 2.11 and 2.12 and the values of the binding parameters obtained for **63** and **64** from absorption and emission data at low and high ionic strength are given in Table 2.4. At low ionic strength, **63** and **64** exhibited K_b values in the order of 10^7 M^{-1} suggesting both complexes bind strongly to DNA. Note that both absorption and emission data yielded comparable results within the error. Emission spectroscopy seems to provide more precise K_b values as this technique is more sensitive than absorption spectroscopy. Similar binding values have been reported in the literature for **29** and **30** complexes which are known to have a high affinity

for DNA.^{143,166} Values of n were estimated to be close to two base pairs and thus an intercalation binding mode can be presumed.¹⁴⁰

Table 2.4. DNA binding parameters of **63** and **64** calculated from fits to absorbance and emission data at low (no NaCl) and high ionic strength (160 mM NaCl) in 10 mM sodium phosphate-buffered aqueous solution at pH 7.4, at 298 K.

Complex		Low ionic strength			High ionic strength		
		$K_b^{[a]}$ (10^6 M^{-1})	n (base pairs) ^[a]	R^2	$K_b^{[a]}$ (10^6 M^{-1})	n (base pairs) ^[a]	R^2
Absorption	63	13 ± 5	1.35 ± 0.04	0.99	1.8 ± 0.4	1.99 ± 0.05	0.99
	64	6 ± 1	1.63 ± 0.01	0.99	0.58 ± 0.08	1.63 ± 0.03	0.99
Emission	63	11 ± 1	1.8 ± 0.1	0.99	1.4 ± 0.1	1.6 ± 0.1	0.99
	64	27.7 ± 0.4	1.9 ± 0.1	0.99	0.33 ± 0.07	1.8 ± 0.2	0.99

^[a] Results correspond to the mean ± SEM.

Furthermore, DNA binding parameters were also calculated at high ionic strength in the presence of 160 mM NaCl. This is expected to reduce the electrostatic binding derived from the interaction between the positively charged complex and the anionic phosphate backbone of DNA. K_b values decreased an order of magnitude with respect to values obtained at low ionic strength conditions but was still higher than 10^6 M^{-1} for both complexes (absorption and emission data). These results indicate that, even though the electrostatic contribution to the binding is important, a high affinity for DNA is conserved, supporting the existence of non-electrostatic interactions with DNA, such as intercalation. However, it should be noted that, due to the complexity of the interaction of these complexes with DNA, the values obtained for the binding parameters and its interpretation have to be taken as an estimation. For example, it was assumed that both enantiomers displayed a similar binding, that the affinity for each two base-pair binding sites is the same, and that only one of the groove participate in the binding event.³¹² Crystal structure determination and solution studies have shown, however, that both enantiomers of **29** and **30** does not bind with the same strength to the DNA and that they display preference for particular sequences.^{146,164} The crystal structures of these complexes with DNA have also shown that the complex intercalates *via* the minor groove,^{156-159,218} although entry from major group was also possible according to some solution studies.¹⁴⁷ Therefore, it is important that caution is

exercised when taking into consideration the values presented here. Further investigation of the binding of these complexes to DNA was then accomplished by using additional techniques and these studies will be discussed in the following sections.

2.5.2 Thermal Denaturation Studies of **63** and **64**

DNA denaturation is the process by which double-stranded DNA unwinds and separates into single-stranded DNA due to the breaking of the hydrogen bonds between the base pairs that hold the native duplex structure of the nucleic acid.^{313,314} Denaturation of DNA can occur when it is subjected to extreme conditions such as high temperature, very basic pH or low ionic strength. The denaturation process is characterised by an increase of the absorbance of the DNA at 260 nm due to unstacking of the nucleobases which are able to absorb more light. The melting temperature of DNA (T_m) refers to the temperature at which half of the DNA exists in the double-stranded state and the other half in the single-stranded state.³¹⁵ Evidence that a compound is bound to DNA is an increasing in the melting temperature of the double-stranded structure as a result of stabilisation of the double helix structure and, therefore, this technique has been extensively used in the literature for classical DNA-binding molecules.^{316,317}

In this section, thermal denaturation studies were conducted to evaluate the ability of complexes **63** and **64** to bind to DNA. For this purpose, the change in the absorption of stDNA at 260 nm was monitored at different concentrations of ruthenium complex as the temperature was gradually increased from 30 °C to 90 °C. Experiments were repeated at least three times to ensure reproducibility. The resulting thermal denaturation curves of stDNA (150 μ M) in the presence of **63** and **64** in 10 mM sodium phosphate-buffered aqueous

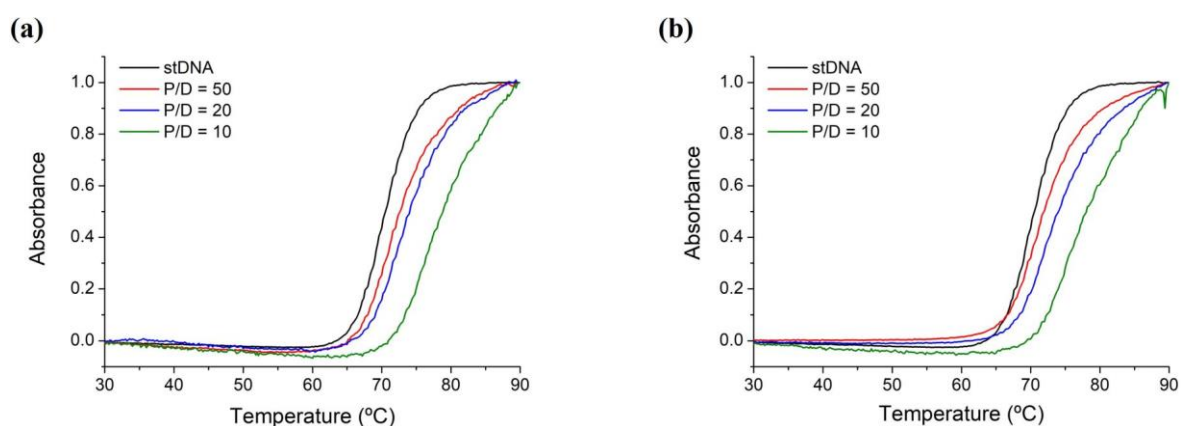


Figure 2.13. Thermal denaturation curves of stDNA (150 μ M) in 10 mM sodium phosphate-buffered aqueous solution at pH 7.4, in the absence and presence of (a) **63** and (b) **64** at different P/D ratios.

solution at DNA phosphate-to-ruthenium dye ratios (P/D) of 50, 20 and 10 are shown in Figure 2.13.

In the absence of Ru(II) complexes, stDNA exhibited a T_m value of 69.8 °C. As the complex concentration is increased, higher T_m values of stDNA are obtained, indicating stabilisation of the DNA helix by DNA-Ru complex interaction (Table 2.5). Thus, at P/D of 50, both complexes **63** and **64** increased slightly the T_m of stDNA by 1.2 °C and 0.8 °C, respectively. At P/D ratio of 20, complexes **63** and **64** displayed an increase of stDNA T_m of 1.5 °C and 2.3 °C, respectively, being this increase of 6.7 °C and 6.5 °C at P/D ratio of 10. For P/D ratios lower than 5, melting temperature values were higher than 90 °C and as such could not be accurately determined. These values are smaller than that observed for **29** (9.1 °C) with calf thymus DNA but similar to T_m values determined for other Ru(II) complexes that bind to DNA *via* an intercalative mode.^{318,319}

Table 2.5. Variation of the melting temperature values for thermal denaturation of stDNA (150 μ M) in 10 mM sodium phosphate-buffered aqueous solution at pH 7.4, in the presence of **63** and **64** at different P/D ratios. T_m value of stDNA without complex is 69.8 °C.

Complex	ΔT_m (°C) ^[a]		
	P/D = 50	P/D = 20	P/D = 10
63	1.2 ± 0.8	1.5 ± 0.9	6.7 ± 0.4
64	0.8 ± 0.0	2.3 ± 0.5	6.5 ± 0.5

^[a] Results correspond to the mean ± SEM.

In summary, **63** and **64** were found to stabilise the double helix structure of stDNA, suggesting interaction of both complexes with the biomolecule, although a particular binding mode cannot be determined through this technique. Hence, in order to further investigate the DNA binding of these compounds, circular dichroism studies were performed, and they will be discussed in the next section.

2.5.3 Circular Dichroism of **63** and **64** in the Presence of DNA

Circular dichroism (CD) is also a powerful spectroscopic technique to study the interaction of potential binding molecules with DNA.³²⁰ CD probes the asymmetry of a system and it is defined as the difference in the absorption of left- and right-handed circularly polarised light that occurs when a molecule contains one or more chiral chromophores.³²¹ Heterocyclic bases of DNA do not show any chirality. However, the asymmetric sugar-phosphate backbone makes the DNA an optically active molecule which then displays CD signals. In contrast, racemic mixtures of metal complexes do not give CD, but upon interaction with

DNA, an induced CD (ICD) of the optically inactive *rac*-metal complexes can be acquired. Therefore, any observation of ICD signals is indicative of DNA conformational changes and reveals a metal complex-DNA binding.^{322,323}

With a view to evaluate the ability of **63** and **64** to bind to DNA, CD titrations were carried out in 10 mM sodium phosphate-buffered aqueous solution. In order to avoid dilution effects, independent solutions containing 150 μM concentration of stDNA ($A_{260} \approx 1$) and varying the complex concentration to get P/D ratios of 50, 20, 10 and 5 were prepared. CD titrations were repeated at least three times to ensure reproducibility. The CD spectra of stDNA in the presence of the racemic mixture of both **63** and **64** at different P/D ratios are shown in Figure 2.14. B-DNA form exhibits a typical CD spectrum characterised by a positive band at about 280 nm, due to the interaction between the π - π^* transitions of the stacked bases, and a negative band around 245 nm, due to right handed helicity. In the presence of **63** and **64** significant changes in the stDNA spectrum were identified. At low wavelength, the evolution of a strong negative band was observed with a maximum at about 275 nm for **63** and 295 nm for **64**. These bands can be attributed to π - π^* intra-ligand transitions of the ancillary **phen** and **TAP** ligands, respectively. At high P/D ratio, a small negative ICD signal was observed for both complexes at about 415 nm corresponding to the typical MLCT absorption band of the Ru(II) polypyridyl complexes. These changes are indicative of intercalation of the **dtp** extended ligand or groove binding of the ancillary ligands.³²²

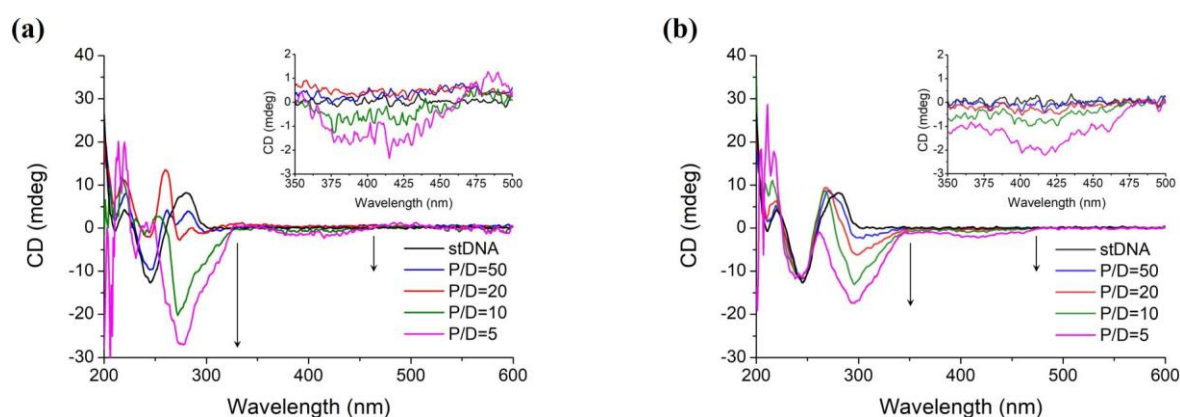


Figure 2.14. Circular dichroism spectra of stDNA (150 μM) in 10 mM sodium phosphate-buffered aqueous solution at pH 7.4, in the absence and presence of racemic mixtures of (a) **63** and (b) **64** at different P/D ratios. Inset: Zoom of the region between 350 and 500 nm showing the ICD signal corresponding to the MLCT absorption band of the corresponding Ru(II) polypyridyl complex.

Although the exact binding mode cannot be determined from these observations, the existence of an interaction between **63** and **64** and the DNA molecule can be concluded. These results are consistent with experiments previously discussed for these complexes and

are similar to other Ru(II) complexes reported in the literature.^{154,320,324} To complete the DNA studies and shed light on the particular binding mode by which both complexes bind to DNA, viscosity studies will be discussed in the following section.

2.5.4 Viscosity Studies of **63** and **64**

In order to investigate in more detail the DNA binding interactions of complexes **63** and **64**, viscosity measurements were carried out. It is well known that the intercalation of a molecule between the DNA base pairs requires the double helix to be lengthened.⁴³ Since viscosity of DNA increases with the length of duplex, viscometry is a suitable method to study whether complexes **63** and **64** interact with DNA through intercalation. Therefore, viscosity of stDNA (1.2 mM) at increasing ruthenium dye-to-DNA phosphate ratios (D/P) in 10 mM sodium phosphate-buffered aqueous solution was measured using a Cannon-Manning semimicro viscometer at 298 K. Viscosity of DNA alone (η_0) and in the presence of ruthenium complex (η) was calculated according to equation (2.4):

$$\eta = t - t_0 \quad (2.4)$$

Where t is the flow time of DNA containing solutions and t_0 is the flow time of the buffer alone. Plotting $(\eta/\eta_0)^{1/3}$ vs D/P (Figure 2.15) resulted in a straight line with positive slope values of 1.27 and 1.12 for **63** and **64**, respectively.

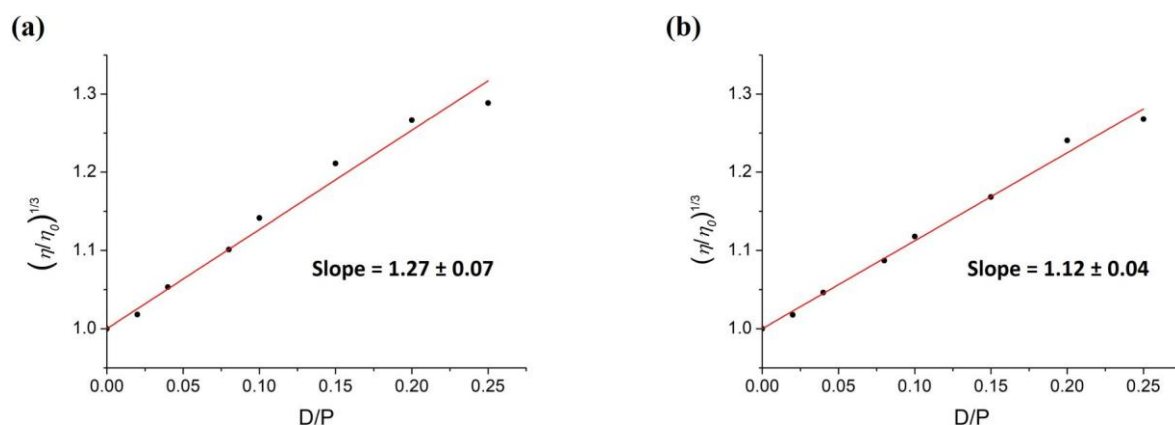


Figure 2.15. Viscosity measurements of stDNA (1.2 mM) in the presence of complexes (a) **63** and (b) **64** at different D/P ratios in 10 mM sodium phosphate-buffered aqueous solution at pH 7.4, at 298 K.

The observed increase in stDNA viscosity can be considered as a positive proof of intercalation of both **63** and **64**. This results are not unexpected and are consistent to the behaviour exhibited by the structural analogue and well-known DNA intercalator ruthenium complex **29** for which both enantiomers Δ and Λ have shown to increase DNA viscosity in contrast to **42** that does not length the double helix and, therefore, does not intercalate into DNA in the classical way.³²⁵ On the other hand, similarity in the slope values obtained for

both complexes **63** and **64** suggests that the intercalation of the complexes takes place preferentially through the extended aromatic moiety **dtp**, being independent of the ancillary ligands **phen** and **TAP**.

In summary, the DNA studies presented above confirm that **63** and **64** are capable to bind to DNA. UV-vis absorption and emission spectroscopic titrations allowed quantification of the strength of the binding between both ruthenium complexes and DNA through determination of the binding constants using a modification of Bard equation. Evaluation of the contribution of the electrostatic interaction between the positively charged ruthenium complexes and the negatively charged DNA phosphate backbone to the binding mode was possible due to comparison of the K_b values in both low and high ionic strength 10 mM sodium phosphate-buffered aqueous solutions. In addition, while thermal denaturation and circular dichroism studies supported the binding affinity of these complexes for the DNA, viscosity studies suggested intercalation as the main DNA binding mode employed by both complexes **63** and **64**.

Having demonstrated the potential of complexes **63** and **64** as spectroscopic probes for DNA, their ability to produce singlet oxygen will be next examined in order to assess their suitability to be used as photodynamic therapy agents before undertaking cellular studies.

2.6 Singlet Oxygen Photosensitisation of **63** and **64**

As discussed in Section 1.4, singlet oxygen ($^1\text{O}_2$) photosensitisation is one of the possible modes of action (Type II mechanism) of the molecules developed for their use in photodynamic therapy (PDT). This mechanism involves the energy transfer from the long-lived triplet excited state of such molecules to the triplet ground state of molecular oxygen resulting in the generation of the highly reactive $^1\text{O}_2$ species. Many Ru(II) polypyridyl complexes have been shown to display excellent quantum yields of $^1\text{O}_2$ production, in some cases even close to unity.^{121,233}

In this context, evaluation of the ability of a molecule to generate $^1\text{O}_2$ is very useful for the design of new PDT agents. Different methods have been developed for singlet oxygen quantification. Among them, direct detection of $^1\text{O}_2$ phosphorescence emission at 1265 nm is one of the most common techniques.^{326,327} Other indirect methods involve the use of chemical probes such as singlet oxygen sensor green (SOSG), 1,3-diphenylisobenzofuran (DPBF) or 9,10-anthracenediyl-bis(methylene)dimalonic acid (ABDA).³²⁸ In the presence of $^1\text{O}_2$, these chemical probes undergo photooxidation and the resulting products exhibit

different absorption and fluorescence properties. Thus, the ability of a molecule to produce $^1\text{O}_2$ can be evaluated by monitoring the changes in the absorption and emission spectra of such chemical probes and under light irradiation. Indirect methods for $^1\text{O}_2$ detection will not be used in this chapter.

Quantum yields of $^1\text{O}_2$ production (Φ_{Δ}) of complexes **63** and **64** in O_2 -saturated D_2O solutions have been determined by time-resolved near-infrared (NIR) phosphorescence from $^1\text{O}_2$ in collaboration with Prof. Guillermo Orellana at Universidad Complutense de Madrid (UCM). As was previously demonstrated that **63** and **64** bind to DNA and their photophysical properties are expected to change when bound to the biomolecule, $^1\text{O}_2$ production studies were carried out both in the absence and in the presence of stDNA. Absorbance-matched ($A_{532} \approx 0.40$) solutions of the ruthenium complex (with or without stDNA) and the reference photosensitiser $[\text{Ru}(\text{phen})_3]\text{Cl}_2$ ($\Phi_{\Delta} = 0.39 \pm 0.03$ in O_2 -saturated D_2O at room temperature)³²⁷ were prepared in D_2O . Deuterated water was used as solvent instead of regular water due to $^1\text{O}_2$ lifetime being longer in deuterated solvents, thus facilitating its detection. After saturation of the solutions containing the photosensitiser by sparging with O_2 for 30 min, singlet oxygen emission was monitored at 1265 nm ($\lambda_{exc} = 532$ nm) at different laser energies. The $^1\text{O}_2$ luminescence decays were fitted to a single exponential function after excluding the fast (sub- μs) decay due to the residual Ru(II) sensitiser emission even under O_2 saturation of the solution. After extrapolating the intensities of the $^1\text{O}_2$ signal at zero time within each exponential decay curve, the intercept values were plotted as a function of the laser energy. The slope values (m) obtained from the linear regression plots of the sample and reference sensitiser dyes were used to calculate the quantum yields of singlet oxygen production (Φ_{Δ}) of **63** and **64**, in the presence or in the absence of stDNA, in O_2 -saturated D_2O according to equation (2.5):

$$\Phi_{\Delta, \text{D}_2\text{O}, \text{O}_2}^{\text{complex}} = \Phi_{\Delta, \text{D}_2\text{O}, \text{O}_2}^{\text{ref}} \frac{m_{\text{complex}}}{m_{\text{ref}}} \quad (2.5)$$

Conversion of the Φ_{Δ} values obtained in O_2 -saturated D_2O into those in air-saturated H_2O is possible by considering equations (2.6) and (2.7):³²⁶

$$P_{\text{O}_2}^T = \tau k_q [\text{O}_2] = 1 - \frac{\tau}{\tau_0} \quad (2.6)$$

$$\Phi_{\Delta} = \Phi_T P_{\text{O}_2}^T f_{\Delta}^T \quad (2.7)$$

Where $P_{O_2}^T$ is the proportion of triplet excited states quenched by O_2 , k_q is the O_2 quenching rate constant, τ and τ_0 are the emission lifetimes in the presence and in the absence of O_2 , respectively, Φ_T is the quantum yield of triplet excited-state formation (intersystem crossing), and f_{Δ}^T is the fraction of excited triplet states quenched by O_2 yielding 1O_2 .

Knowing that Φ_T is considered to be equal to 1 for this type of complex,³²⁶ assuming that the fraction of quenched Ru(II) triplet that yields 1O_2 is the same in D_2O and H_2O as well as having determined the lifetimes of the complexes in O_2 - and argon-saturated D_2O , and air- and argon-saturated H_2O , Φ_{Δ} values in air-equilibrated H_2O were calculated according to equation (2.8):

$$\Phi_{\Delta,H_2O,air}^{complex} = \Phi_{\Delta,D_2O,O_2}^{complex} \left(1 - \frac{\tau_{H_2O,air}}{\tau_{H_2O,Ar}}\right) / \left(1 - \frac{\tau_{D_2O,O_2}}{\tau_{D_2O,Ar}}\right) \quad (2.8)$$

The 1O_2 luminescence decay profiles of **63** and **64** in O_2 -saturated D_2O are shown in Figure 2.16 and a summary of τ_{em} and Φ_{Δ} values at different conditions obtained for both

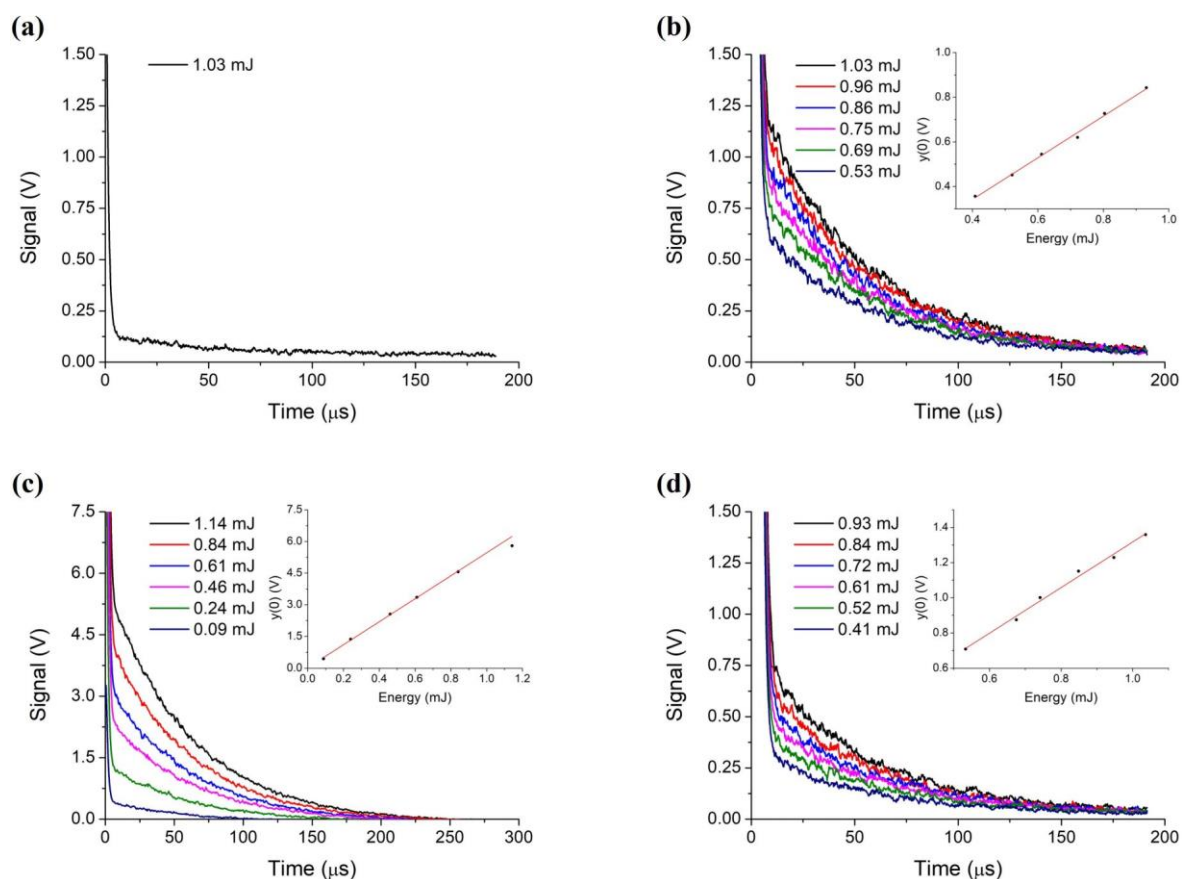


Figure 2.16. Singlet oxygen emission decays at 1270 nm produced by (a) **63**, (b) **63** bound to stDNA (25 eq. base pairs), (c) **64**, and (d) **64** bound to stDNA (25 eq. base pairs), at different laser energies ($\lambda_{exc} = 532$ nm) in O_2 -saturated D_2O solution at 298 K. Inset: Plot of intercept values (V) vs. laser energy (mJ) and the best linear fit of the data.

complexes in the absence of stDNA or when bound to stDNA can be found in Table 2.6. Complex **63** showed no singlet oxygen production in the absence of stDNA and as such the Φ_A value could not be determined for this compound (Figure 2.16a). This observation was not unexpected as **63** is not emissive in aqueous solution and as such the lifetime of its excited state will not be long enough to react with molecular oxygen and form $^1\text{O}_2$.¹⁷⁹ However, when complex **63** was bound to stDNA, some $^1\text{O}_2$ phosphorescence could be observed (Figure 2.16b). As was previously discussed in Section 1.6.2, Ru(II) complexes containing ‘dppz’ like ligands become emissive when bound to DNA. This is due to protection of the intercalating extended aromatic ligand by the hydrophobic microenvironment of DNA preventing phenazine nitrogen atoms from forming hydrogen bonds and stabilising the “dark state”. Thus, the increase of the excited-state lifetime of the complex allows its reaction with molecular oxygen resulting in $^1\text{O}_2$ formation. A small Φ_A value of 0.02 was, however, determined in air-saturated H_2O . A double protection of both solvent and dissolved molecular oxygen from DNA could explain the observed behaviour. This interpretation is supported by comparison of the τ_{em} observed for **63** in the presence of stDNA in O_2 - and argon-saturated D_2O or in air- and argon-saturated H_2O . Solution deoxygenation resulted only in a small increase of the τ_{em} (from 504 to 554 ns in D_2O , and from 301 to 319 ns in H_2O) suggesting that the complex is already protected by DNA from the dissolved molecular oxygen making difficult for both molecules to get together and form $^1\text{O}_2$. In addition, it is well known that in high viscosity media such as solutions containing large concentrations of DNA, oxygen quenching efficiency is lower due to it is a diffusion-controlled process.⁶⁸

Table 2.6. Emission lifetimes (τ_{em}) measured in O_2 - and argon-saturated D_2O , and in air- and argon-saturated H_2O , and quantum yields of singlet oxygen production (Φ_A) in O_2 -saturated D_2O and air-saturated H_2O for complexes **63** and **64**, both in the absence and in the presence of stDNA (25 eq. base pairs).

Complex	τ_{em} (ns) ^[a] (O_2 , D_2O)	τ_{em} (ns) ^[a] (Ar, D_2O)	τ_{em} (ns) ^[a] (Air, H_2O)	τ_{em} (ns) ^[a] (Ar, H_2O)	Φ_A (D_2O , O_2 -satd.) ^[b]	Φ_A (H_2O , Air-satd.)
63	-	-	-	-	-	-
63 + DNA	504 ^[c]	554 ^[c]	301 ^[c]	319 ^[c]	0.03	0.02
64	361	719	876	947	0.64	0.19
64 + DNA	374 ^[c]	777 ^[c]	232 ^[c]	377 ^[c]	0.04	0.03

^[a] If not otherwise indicated, the luminescence decays are monoexponential. Estimated errors $\pm 5\%$.

^[b] O_2 -saturated D_2O solution of $[\text{Ru}(\text{phen})_3]\text{Cl}_2$ as reference ($\Phi_A = 0.39$).³²⁷ Estimated errors $\pm 10\%$.

^[c] The luminescence decays are tri-exponential; reported data correspond to the pre-exponential weighted mean lifetimes (τ_M).³²⁹ See Section 7.2 of Chapter 7 and Table A2.2 of the Appendices for further information.

Complex **64** showed a Φ_A value of 0.19 in air-saturated H₂O and in the absence of DNA. In contrast to **63**, complex **64** is emissive in aqueous solution as explained previously in Section 1.6.2. Furthermore, Φ_A value of the complex when bound to stDNA decreased to 0.03. In this case, the luminescence of the complex is expected to be quenched by guanine nucleobases in DNA resulting in a shorter excited-state lifetime therefore reducing the chance of reacting with molecular oxygen to produce ¹O₂. These results suggest that, unsurprisingly, localisation within the cell can play a key role in the phototoxicity exhibited by this type of complex.¹⁷⁹ Hence, in the case of **63** and **64**, localisation into the cell nucleus would not be suitable for light-mediated toxicity *via* a ¹O₂ production mechanism due to their strong DNA binding and, thus, low ¹O₂ photosensitisation.

Considering the ability to generate ¹O₂ observed for **64** when it is not bound to DNA, biological studies were carried out on both complexes **63** and **64** with a view to elucidate their cellular uptake and their photoinduced cytotoxicity for their application as PDT agents.

2.7 *In vitro* Studies of **63** and **64**

To investigate the ability of **63** and **64** to be internalised in HeLa cervical cancer cells and reduce viability, cellular uptake and toxicity studies were carried out in collaboration with Dr Bjørn la Cour Poulsen, Dr Sandra Bright and Dr Salvador Blasco.

2.7.1 Cellular Uptake Studies of **63** and **64**

The uptake and localisation of complexes **63** and **64** in live HeLa cells was studied using confocal fluorescence microscopy. Thus, HeLa cells were incubated with 100 μM concentration of **63** and **64** at 37 °C for 24 h. After being treated with the fluorescent nuclear stain Hoechst 33258, cells were imaged using an Olympus FV1000 point scanning microscope with a 60x oil immersion lens with an NA (numerical aperture) of 1.42. Experiments were repeated on three independent days to ensure reproducibility. Confocal microscopy images of these experiments are shown in Figure 2.17. Results demonstrated that both complexes were successfully taken up into the cells at these conditions. The increased lipophilic character associated to the extension of the size of the **dppz**-based ligand could explain the cellular uptake observed for these compounds when compared with the **dppz** analogues **29** and **30**.^{170,178,299} Complexes appeared to be localised within the cytoplasm of cells as evidenced by red luminescent emission from the complexes observed around the nucleus. These results agree with previous studies achieved in our group for similar Ru(II) polypyridyl complexes.¹⁷⁰ Some toxicity against the cells was observed during confocal imaging, probably because of singlet oxygen production by **64**, as discussed in the

previous section. The punctate appearance of the compounds inside the cells suggests endocytosis as the mechanism by which the complexes are internalised by the cells. This hypothesis is supported by previous studies in our group with similar Ru(II) **dppz**-based complexes for which their cellular internalisation was found to be temperature-dependent and thus to occur *via* an energy-dependent mechanism.¹⁷⁰ However, further studies must be performed to confirm endocytosis as the uptake mechanism employed by **63** and **64** to be cellularly internalised.

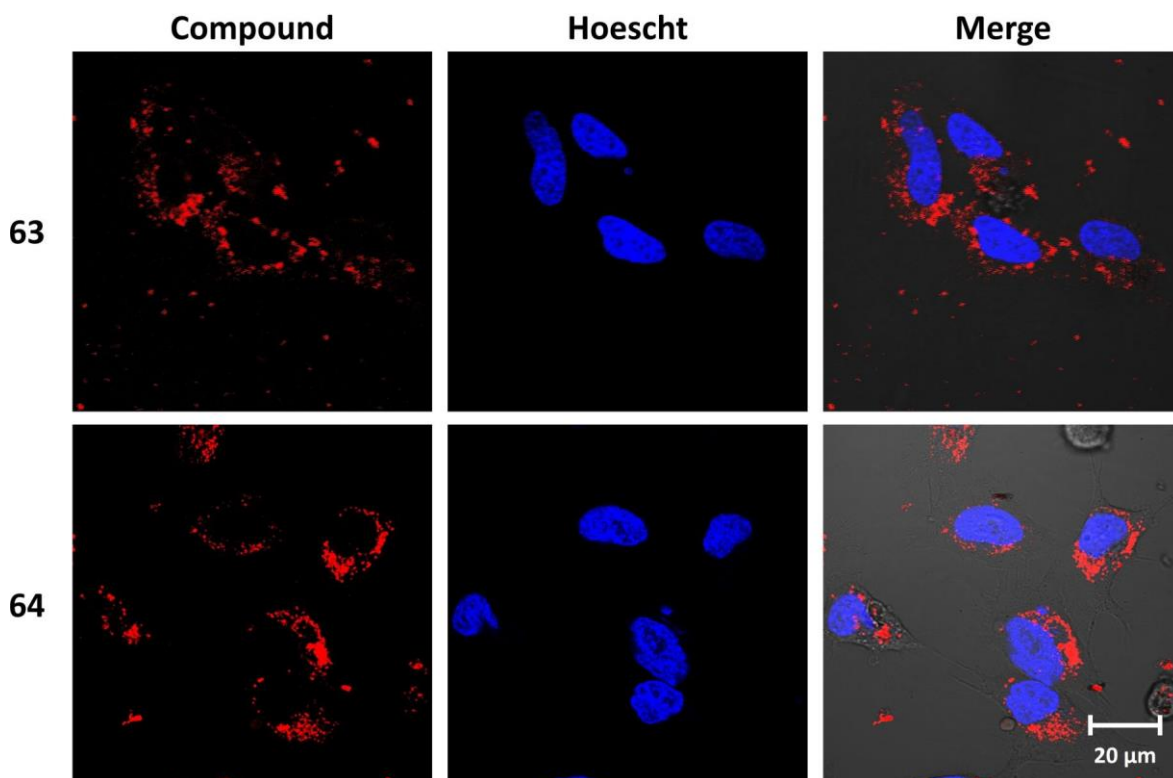


Figure 2.17. Confocal fluorescence microscopy images of HeLa cells showing the uptake of **63** and **64** (red) at 100 μ M after 24 h incubation. The nucleus is stained blue with Hoechst 33258.

Once complexes **63** and **64** were found to be taken up by the cells and localise in the cytoplasm, cytotoxicity studies were performed in both dark and light conditions to assess the potential of both complexes to photoinduce cell death.

2.7.2 Cellular Toxicity Studies of **63** and **64**

As described in Sections 1.4 and 1.6.4, the development of new photodynamic therapy agents capable to overcome the side effects of those currently existing is desirable. Ruthenium complexes have previously exhibited PDT potential with increased cytotoxicity upon light activation of the ruthenium complex photosensitiser.^{62,63,93,170} In this context, based on the results presented previously in this chapter, it can be anticipated the potential of **64** as a Ru(II) based PDT candidate due to its ability to be internalised in HeLa cells and

photosensitise $^1\text{O}_2$. Although complex **63** was also found to be taken up by the cells, it was not expected to display or show phototoxicity *a priori* due to lack of $^1\text{O}_2$ production.

Cellular viability of **63** and **64** in HeLa cells was investigated under both dark and visible light conditions using the Alamar Blue cytotoxicity assay. The Alamar Blue reagent contains the cell permeable non-fluorescent resazurin dye, which becomes highly fluorescent when reduced to the pink coloured resorufin. The fluorescent intensity produced when resazurin is converted to resorufin due to cellular metabolic reduction is proportional to the number of living cells respiring and, thus, a way to measure cell viability. Therefore, HeLa cells were incubated with different concentrations of **63** and **64** for 24 h at 37 °C. The treated cells were then either irradiated with 18 J cm⁻² of light for 1 h using a UV-filtered Hg-Xe arc lamp or kept in the dark. After further 24 h incubation, cells were treated with Alamar Blue and incubated for 4 h before the toxicity was assessed by measuring the fluorescence intensity of resorufin at 590 nm upon excitation at 544 nm. The activity of the complexes was expressed as percentage cell viability compared to untreated control cells. Cytotoxicity assays were performed in triplicate on three independent days to ensure reproducibility.

Toxicity profiles of both complexes in HeLa cells under the mentioned conditions are shown in Figure 2.18 with the corresponding IC₅₀ values presented in Table 2.7.

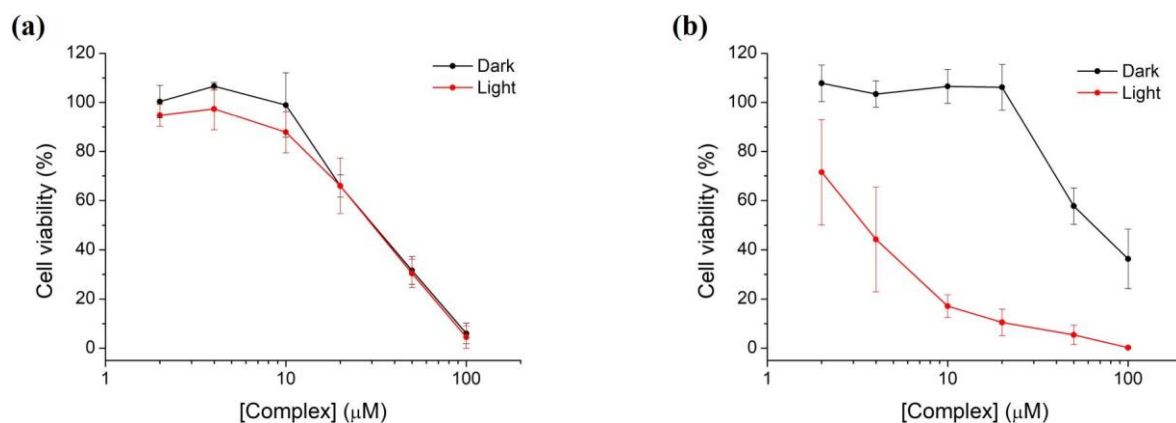


Figure 2.18. Toxicity profiles of (a) **63** and (b) **64** in HeLa cells. HeLa cells were treated with the indicated concentrations of the required complexes and incubated for 24 h followed by either exposure to light for 1 hour or maintenance in the dark and followed by further 24 h incubation. Cells were then incubated with the Alamar Blue dye for 4 h and assessed for cellular viability.

Results revealed that **63** containing **phen** as ancillary ligands did not show light-dependent cytotoxicity (phototoxic index (PI) of approx. 1) with similar IC₅₀ values obtained in the dark and after light irradiation. However, complex **64** containing **TAP** instead of **phen** displayed IC₅₀ values of 63 μM in dark and 4 μM after exposure to light irradiation, resulting in a toxicity of the photoactivated complex with a PI of *ca.* 16. This behaviour was in agreement with the $^1\text{O}_2$ photosensitisation studies discussed previously in this chapter. Thus,

the lack of phototoxicity shown by **63** is likely related to the fact that this complex was found to produce no $^1\text{O}_2$. While, the effective photoactivation of complex **64** can be explained by its ability to produce $^1\text{O}_2$ with a Φ_A value of 0.19 determined in air-saturated H_2O . However, other alternative mechanisms such as DNA photocleavage or photoreaction with biomolecules are also possible for **64** due to its π deficient nature. On the other hand, the higher toxicity observed for **63** (when compared with **64**) in the dark can be due to complexes containing **phen** as ancillary ligands being more lipophilic than their **TAP** analogues. This lipophilicity difference between **phen** and **TAP** containing Ru(II) complexes will be discussed in detail in Section 4.6 of Chapter 4.

Table 2.7. IC_{50} values for the cytotoxicity of **63** and **64** in HeLa cells in the dark and exposed to light.

Complex	IC_{50} dark (μM) ^[a]	IC_{50} light (μM) ^[a]	PI ^[c]
30 ^[b]	>100	12 ± 7	-
63	34 ± 3	33 ± 6	1
64	63 ± 8	4.0 ± 1.5	16

^[a] IC_{50} values correspond to the mean \pm SEM.

^[b] From reference 170.

^[c] Phototoxic index (PI) is defined as the ratio of the IC_{50} value in the dark to the IC_{50} value upon light irradiation.

Comparison with the well-known complex **30** reported in Table 2.7 as a reference showed that both complexes **63** and **64** exhibited higher IC_{50} values in dark conditions. After light activation, complex **64** also appeared to be considerably more toxic than this reference compound. Thus, whereas **63** seems to be more suitable for being used as an *in vitro* fluorescent DNA probe, complex **64** revealed interesting phototoxic properties than can be employed in PDT.

However, it must be noted that the cytotoxicity exhibited by **63** and **64** is based on their cytoplasm localisation. This could be different if they were localised into the cell nucleus since it was previously demonstrated in Sections 2.5 and 2.6 of this chapter that these complexes bind to stDNA *via* intercalation and, moreover, they do not produce $^1\text{O}_2$ when bound to stDNA. With a view to explore the phototoxicity of complexes **63** and **64** when reached the cellular DNA, efforts have been devoted to achieving nuclear localisation of such complexes and preliminary results will be presented in the next section.

2.7.3 Nuclear Localisation of **63** and **64** by Ethanol Membrane Permeabilisation

Despite the DNA affinity shown by **63** and **64**, their localisation in the cell cytoplasm makes no possible to take advantage of their affinity for the genetic material in a cell environment. As discussed in Section 1.6.2, different strategies such as using lipophilic ligands or conjugation to cell-penetrating peptides (CPPs) and nuclear localisation signal (NLS) sequences have been developed to improve the cellular uptake of Ru(II) polypyridyl complexes and, in particular, to localise them into the cell nucleus.^{178,181,191,192,195,197-199} However, modification of the chemical structure of such complexes could be complicated and result in a change in their photophysical and photochemical properties. In this context, Zhu *et al.* have described another strategy to enhance the cellular uptake and a nuclear localisation of **dppz**-based Ru(II) complexes using biochemical agents such as pentachlorophenol (PCP) *via* formation of a stable lipophilic ion-pair.³³⁰ With this in mind, numerous attempts were performed in order to localise **63** and **64** into the nucleus by co-incubation in HeLa cells with PCP and the structural analogue 2,4-dinitrophenol (DNP).

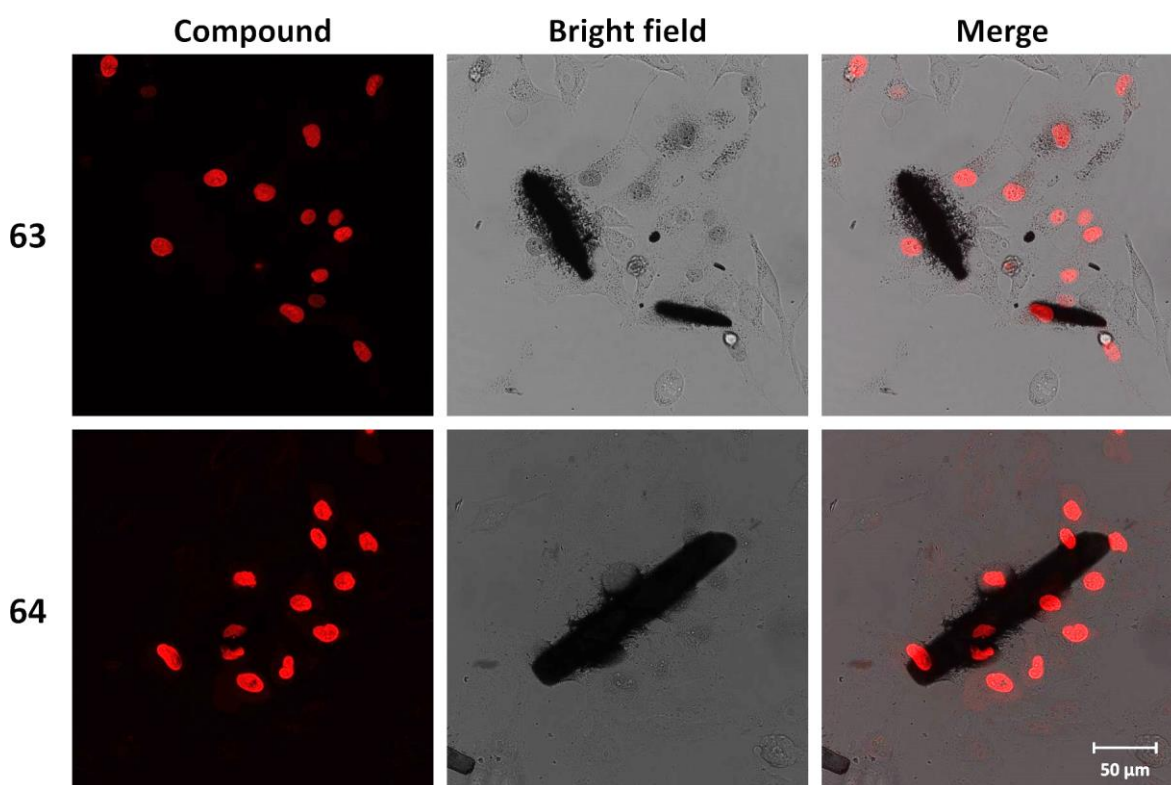


Figure 2.19. Confocal fluorescence microscopy images of HeLa cells showing the uptake of **63** and **64** (red) at 100 μM in the presence of PCP at 200 μM after 1 h incubation.

However, the low water solubility of both PCP and DNP meant aqueous solutions containing these compounds could not be prepared. Even then, the cellular uptake of aqueous suspensions containing either **63** or **64** (100 μM) in the presence of PCP or DNP (200 μM)

was investigated using a Leica SP8 scanning confocal microscope with a 40x oil objective with an NA (numerical aperture) of 1.30. However, nuclear localisation was only observed in those cells where a significant amount of PCP and DNP precipitated after 1 h of incubation as shown for PCP in Figure 2.19. It must be noticed that in the work published by Zhu *et al.* cells were incubated with the Ru(II) complex in the presence of 300 μM concentration of PCP for 3 h.³³⁰ A lower PCP concentration and a shorter incubation time was used since toxicity studies of PCP were carried out using the Alamar Blue cytotoxicity assay which revealed an IC_{50} value of 114 μM (Figure A2.9a of the Appendices). In contrast, the IC_{50} value determined for DNP was shown to be larger than 300 μM (Figure A2.9b of the Appendices). However, similar results were obtained when larger PCP concentrations and longer incubation times were tested.

In an attempt to fully solubilise PCP and DNP, a mixture of $\text{H}_2\text{O}/\text{EtOH}$ (1:1) was employed to prepare the stock solutions containing the appropriate phenol derivative and **63** and used to treat the cells. Complex **64** was not tested in the following experiments. Therefore, HeLa cells were treated with 40 μL of a $\text{H}_2\text{O}/\text{EtOH}$ (1:1) solution containing **63** (100 μM) and PCP (200 μM) and incubated for 3 min. Following this, the cells were washed with fresh medium to remove the EtOH and the excess of complex then subsequently imaged using confocal fluorescence microscopy. A 40 μL aliquot was used to cover a larger area of cells since it was shown that only a small group of cells were able to internalise the complex when smaller volumes were tested. Although nuclear localisation was achieved in these conditions, the same results were observed in the absence of PCP or DNP, suggesting that the nuclear localisation of **63** was due to the EtOH.

Experiments were then carried out to investigate the role of the EtOH in the nuclear localisation of **63** using a Leica SP8 gated STED confocal microscope with a 10x dry objective with an NA (numerical aperture) of 0.30 (Figure 2.20). Firstly, it was demonstrated that the minimum amount of EtOH required to localise the ruthenium complex into the nucleus was 50% of the total volume of the aliquot (3.7% of the final volume) added to the cells as no nuclear localisation of **63** was observed when 30%, 10% or 0% of EtOH was used. Interestingly, complex **63** was taken up by a defined group of cells that corresponded to the area in direct contact with the 40 μL aliquot when added to the cells.

Furthermore, it has been described in the literature that organic solvents such as DMSO or EtOH can perturb the lipid bilayer that constitutes the cell membrane increasing its fluidity and reducing its rigidity.³³¹ In this context, EtOH has been used for reversible intracellular delivery of cargo molecules. Therefore, ethanol membrane permeabilisation

could be the cause of the fast uptake of the complex and nuclear localisation. On the other hand, it has been shown that Ru(II) complexes can be internalised by cells with damaged cell membrane and used as probes for cell viability measurement by flow cytometry, confocal microscopy and time-resolved luminescence.³³² In order to evaluate if the ethanol

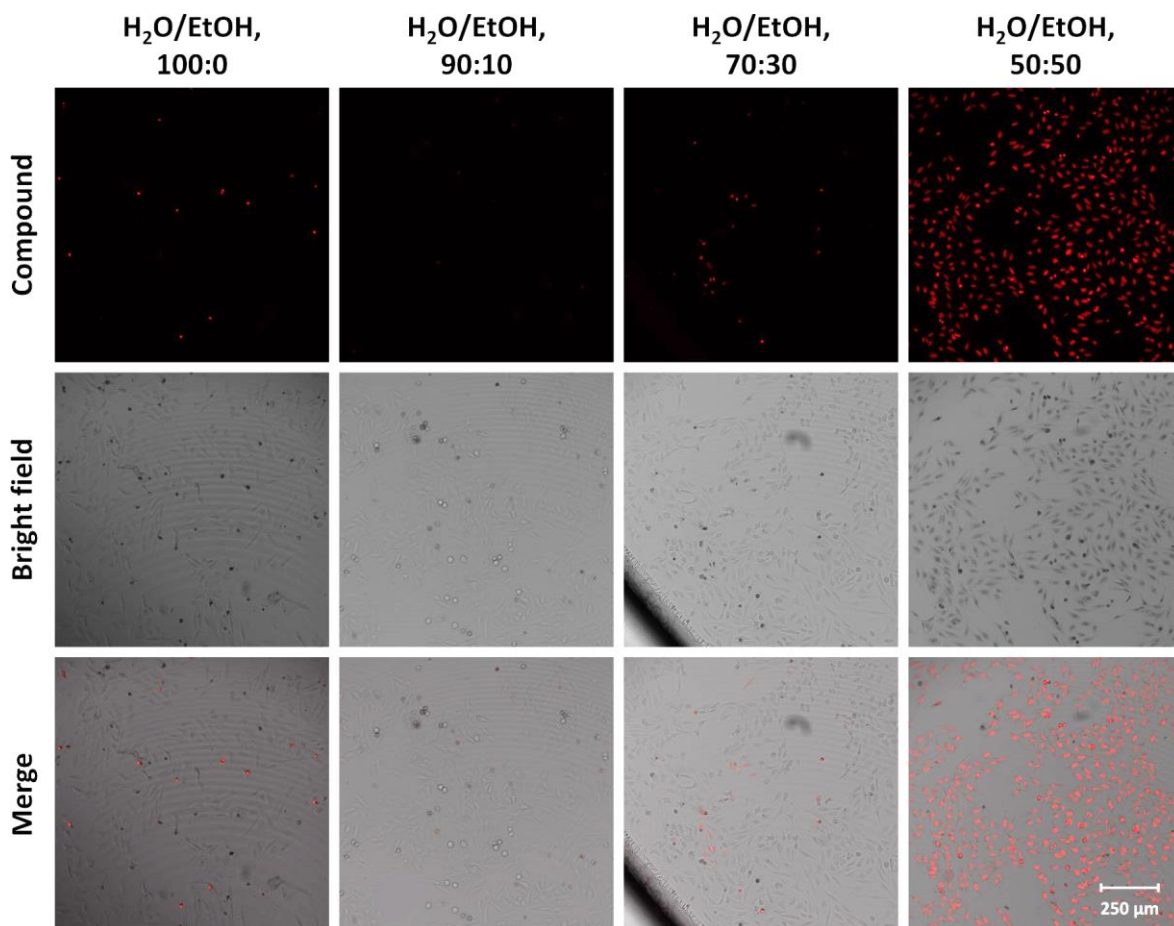


Figure 2.20. Confocal fluorescence microscopy images of HeLa cells showing the minimum amount of EtOH required to localise **63** (100 μ M, red) into the nucleus after 3 min incubation.

treatment was causing irreversible cell damage, tetramethylrhodamine methyl ester (TMRM) was used to evaluate cell viability through mitochondrial functionality. TMRM is a cell-permanent fluorescent dye that only accumulates in mitochondria with intact membrane potentials being able to selectively distinguish between apoptotic and non-apoptotic cells. Therefore, TMRM (20 nM) was added to HeLa cells previously treated with 40 μ L of a solution containing **63** (50 μ M) in H₂O/EtOH (1:1) for 3 min. After 30 min incubation, cells were washed with fresh medium and imaged by confocal fluorescence microscopy using a Leica SP8 gated STED confocal microscope with a 10x dry objective with an NA (numerical aperture) of 0.30 (Figure 2.21). Nuclear localisation of complex **63** in a well-defined area was again observed, probably where the solution containing the

complex in a mixture of H₂O/EtOH (1:1) was dropped. Interestingly, TMRM fluorescence was not observed in those cells that were able to internalise **63** into the nucleus suggesting loss of their mitochondrial membrane potential due to their unhealthy condition. Therefore, these results could be considered as an evidence that the localisation of **63** into the nucleus of HeLa cells is due to cell membrane permeabilization by the presence of EtOH which would facilitate the cell membrane crossing by the ruthenium complex and its reach of the cell nucleus.

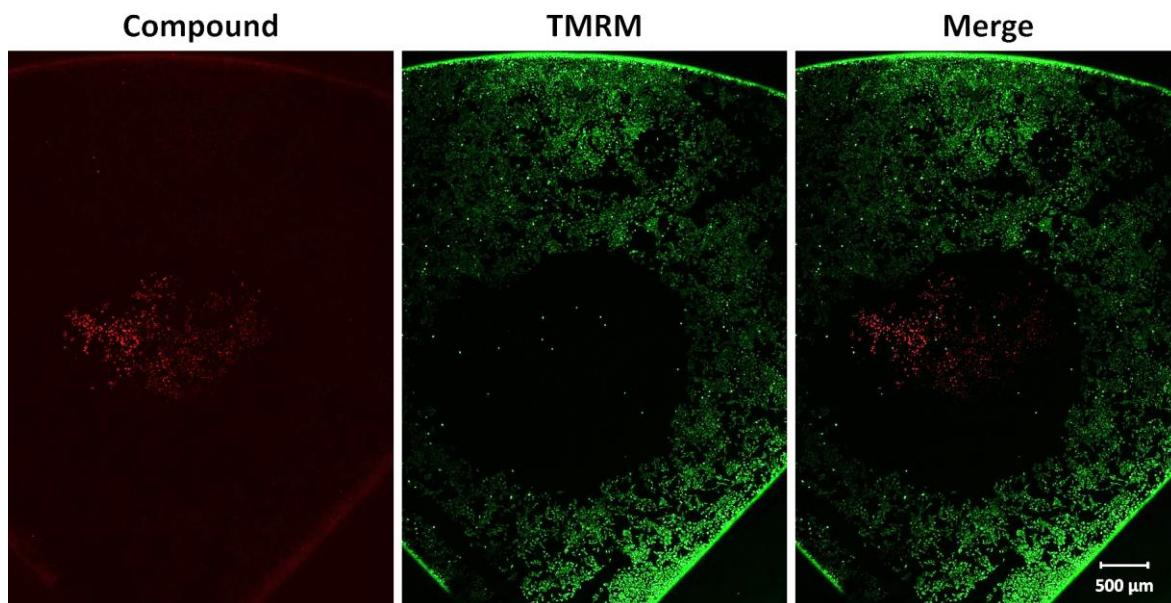


Figure 2.21. Confocal fluorescence microscopy images showing the viability of HeLa cells using the mitochondrial fluorescence dye TMRM (green, 20 nM) after being treated with 40 μ L of a solution containing **63** (red, 50 μ M) in H₂O/EtOH (1:1) for 3 min.

Current studies are being carried out to localise Ru(II) polypyridyl complexes into the cell nucleus through controlled and reversible cell membrane permeabilization. Thus, after recovering of the temporal damaged cell membrane, the phototoxicity of such complexes will be investigated when localised into the cell nucleus as this contains the genetic material of the cell which is an interesting target to induce cell death.

2.8 Conclusion and Future Perspectives

With the goal of designing new Ru(II) polypyridyl complexes with the ability to bind to DNA by intercalation and act as PDT agents, in this chapter two novel Ru(II) **dppz**-based complexes have been synthesised and characterised and their photophysical properties have been investigated. The DNA-binding affinity of **63** and **64**, which contain the **ntp** extended aromatic ligand, was explored in aqueous solution using a variety of spectroscopic techniques. DNA titrations in absorption and emission spectroscopy indicated high affinity

of both complexes for DNA with K_b values being *ca.* 10^7 and 10^6 M^{-1} at low and high ionic strength, respectively. These results supported the co-existence of electrostatic and non-electrostatic interactions, suggesting intercalation of complexes into the DNA structure. Thermal denaturation and circular dichroism (CD) studies were consistent with the ability of these complexes to bind to DNA. Viscosity experiments confirmed intercalation into DNA of both complexes as the main binding mode.

Subsequently, the capability of complexes **63** and **64** to sensitise 1O_2 was investigated in the absence and in the presence of DNA and thus Φ_{Δ} values were determined through direct measurement of 1O_2 phosphorescence at 1265 nm in O_2 -saturated D_2O . Lack of 1O_2 production was observed for **63** in air-saturated H_2O and in the absence of DNA while **64** showed a Φ_{Δ} value of 0.19 in the same conditions. In addition, low 1O_2 production was observed for both complexes when bound to DNA suggesting that their ability to act as Type-II photosensitisers in a cellular environment will depend on their localisation.

Furthermore, cell studies using confocal fluorescence microscopy revealed that both complexes **63** and **64** were taken up into HeLa cells and localised in the cytoplasm, making them promising candidates as photoprobes. In agreement with their ability to produce 1O_2 , toxicity assays showed that the toxicity properties of **63** did not change upon photoactivation, while **64** became considerably more toxic and as such can be potentially used as PDT agent. Most of the work presented here has been published in *Dalton Transactions* and can be found in the Publications section.

Finally, several attempts were carried out to localise **63** and **64** into the cell nucleus *via* cell membrane permeabilization using EtOH as co-solvent when treating the cells with the complexes. However, such an intracellular delivery strategy has been shown to damage the cells permanently. Thus, further perspectives of this work will be focus on achieving nuclear localisation of Ru(II) polypyridyl complexes without irreversibly disrupting the cell membrane integrity. This will be essential to study their phototoxicity when localised in the cell nucleus and bound to DNA based on preliminary 1O_2 production studies performed in the presence of the genetic material with a view to investigate the cell localisation dependence of the photoactivation of such complexes.

Moreover, the development of Ru(II) polypyridyl complexes analogues such as **76** (Figure 2.22) by replacement of the sulphur atom in the **dtp** ligand by selenium may result interesting with the aim to study the impact of such modification in the cytotoxicity of the resulting complexes compared to **63** and **64** since a wide number of selenium-containing molecules have shown potential applications in cancer therapy.³³³⁻³³⁷

On the other hand, taking advantage of the presence of the sulphur atom in the **dtp** ligand and in relation with previous work in the Gunlaugsson group and with further chapters in this thesis, complexes **63** and **64** could be employed to functionalise gold nanoparticles (**64·AuNP**) (Figure 2.22) in order to study their DNA binding as well as their biological properties when attached to the nanomaterial surface.^{264,271}

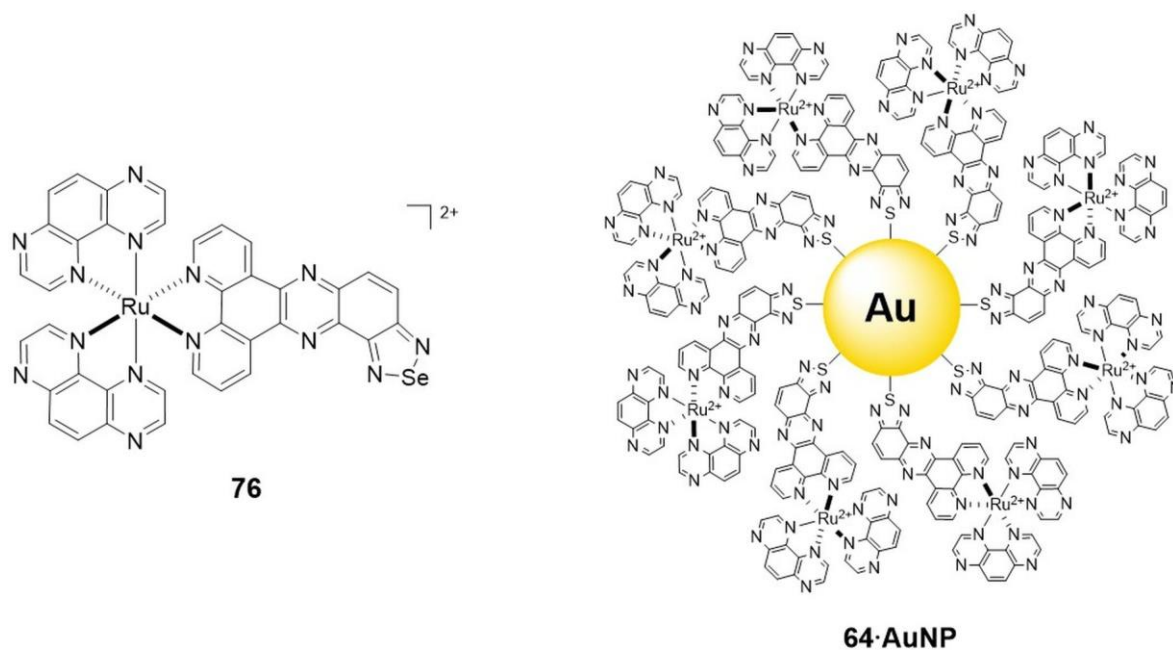


Figure 2.22. Chemical structures of the Ru(II) polypyridyl systems **76** and **64·AuNP** resulting from the replacement of the sulphur atom in **dtp** ligand by selenium and functionalisation of AuNPs with **64**, respectively.

In the next chapter, the system resulting from the photoreaction between **38** and guanosine 5'-monophosphate (GMP) will be investigated as a model to complete the current knowledge about the reactivity of Ru(II) polypyridyl complexes containing π -deficient ligands such as **TAP** with biomolecules. Particularly focusing on their ability to covalently bind to DNA as another way to induce photo-controlled damage of the genetic material. Thus, spectroscopic studies of both ground and excited states of such photoadduct will be next presented.

Chapter 3
Spectroscopic Studies of the
Photoadduct Formed between
 $[\text{Ru}(\text{TAP})_3]^{2+}$ and 5'-GMP

3.1 Introduction

The design of molecules capable of binding to DNA is of particular interest in the field of medicinal chemistry. For example, most of the chemotherapeutic drugs have been shown to exert their anticancer activity by the inhibition of DNA relaxation, gene expression or DNA replication.¹⁴ As was discussed in Section 1.6.2 and shown in the previous chapter, many Ru(II) polypyridyl complexes have been shown to act as powerful DNA binders.² However, the DNA binding ability of Ru(II) complexes is not limited to non-covalent binding modes such as electrostatic, groove binding or intercalation. In this context, the coordination of π -deficient ligands such as **TAP** to the Ru(II) centre has been shown to confer a high oxidising ³MLCT excited state to the resulting complex.^{202,203} Therefore, in the presence of reducing molecules such as guanine, a photoinduced electron transfer (PET) can occur from the DNA nucleobase to the Ru(II) complex in its excited state.^{166,211-213} This process results in the generation of radical species that can lead to the formation of photoproducts with DNA.^{203,213,219,223} A more detailed explanation of the mechanism by which these photoproducts (more commonly known as photoadducts) are formed was given in Section 1.6.3.

Over the last number of decades, photoadduct formation and their impact on biological applications have been extensively studied by the research group of Kirsch-De Mesmaeker.^{168,202,203,208,211,213,219,223,225,229,230,338} In particular, complex **38** (Figure 1.19) is among the most used π -deficient Ru(II) polyaazaromatic complexes as an oxidising entity in the photoreaction with guanine-containing molecules, including the nucleotide guanosine 5'-monophosphate (GMP), oligonucleotides or DNA.^{211,213,219,223,230} Despite its photoinstability,¹²² complex **38** shows advantageous properties such as a significant reduction potential of its ³MLCT excited state ($E_{red}^* = +1.30$ V/SCE)²⁰² as well as a symmetric structure that reduces the amount of possible photoproducts formed after irradiation in the presence of guanine-containing molecules.

Importantly, it has also been demonstrated that further illumination of such mono-photoadducts in the presence of guanine-containing molecules gives rise to the incorporation of a second guanine unit to the Ru(II) polypyridyl complex resulting in the formation of bi-photoadducts.^{202,203,213} This is of particular interest as two complementary guanine-containing oligonucleotides can be irreversibly photocrosslinked, most likely due to two consecutive PET reactions with a single π -deficient Ru(II) polyaazaromatic complex.^{168,202,203,338} Indeed, the mechanism of action of the well-known chemotherapeutic agent cisplatin has been shown to occur *via* DNA inter- or intra-strand crosslinking.⁵⁵

More recently, a great effort has been made by Kirsch-De Mesmaeker and co-workers to elucidate the photophysical mechanism by which the formation of bi-photoadducts occurs.²¹³ For this purpose, the photoadduct formed between the previously mentioned complex **38** and GMP (**43**) (Figure 3.1) was used as a model system. Interestingly, the isolated photoadduct **43** is not emissive suggesting that the lifetime of its excited state is shortened by an intramolecular quenching process. However, despite the lack of emission, the addition of a second GMP molecule to **43** was found to occur at acidic pH but not at basic pH showing that the properties of **43** ($pK_a = 6.8$) are

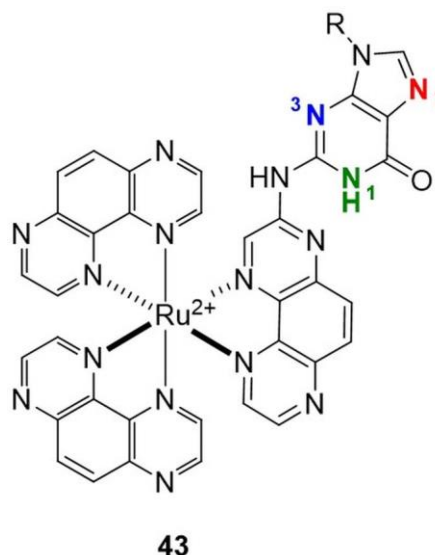
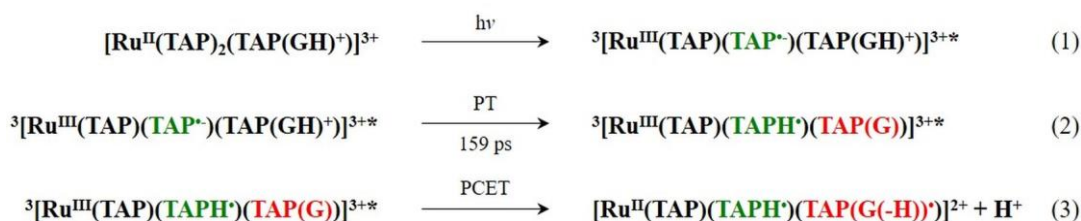


Figure 3.1. Chemical structure of the photoadduct formed between **38** and GMP (**43**).

affected by the solution pH. Based on different spectroscopic techniques (including visible transient absorption (TrA)) and density functional theory (DFT) calculations, the authors of this study have proposed different protonation states of **43** depending on the solution pH which would result in the existence of different nature excited states. Thus, at pH 5.9, **43** would be protonated and reactive 3MLCT excited states would be populated after excitation (Scheme 3.1 (1)). These excited states would then undergo proton transfer (PT) from the protonated guanine moiety to the TAP^{*+} motif (Scheme 3.1 (2)). This would be followed by an intramolecular electron transfer (ET) from the guanine moiety to the Ru(III) centre of the 3MLCT excited state, most likely accompanied by proton transfer (PCET), giving rise to the



Scheme 3.1. Proposed mechanism of the dynamic processes that occur after excitation of **43** in aqueous solution at pH 5.9 proposed by Marcellis et al.²¹³ Note that this mechanism could also occur through a 3MLCT excited state where the electron would be placed on the GMP modified TAP ligand.

formation of a long-lived biradical species (Scheme 3.1 (3)). This species could further react with a second GMP molecule and form a bi-photoadduct. In contrast, at pH 8, the non-protonated **43** would have unreactive ligand-to-ligand charge transfer/intra-ligand charge transfer (LLCT/ILCT) excited states. These LLCT/ILCT excited states would not lead to intramolecular PT and ET processes and as such, long-lived species with the ability to react

with another GMP unit would not be formed. Furthermore, according to DFT calculations, the N7 position of the guanine moiety in **43** has been proposed to be the protonation site (Figure 3.1). However, such protonation results are surprising due to (i) the pK_a of the N7 position in free GMP is 2.48; thus, a much lower pH than 5.9 is required to protonate this position;^{339,340} and (ii) protonation of the imidazole ring of GMP has been shown to have a negative effect on the exergonicity of the ET.³⁴¹ Therefore, there is still a need to further analyse this system through additional techniques.

The main goal of the work described in this chapter is to provide more information on the photophysical scheme by which the mono-photoadduct **43** can react with a second molecule of GMP and yield a bi-photoadduct, despite its non-emissive character. In particular, we proposed to study the mechanism using time-resolved infrared (TRIR) spectroscopy as this technique should provide greater insight into the structure of the transient species, including excited states, involved. In this context, TRIR has been used extensively for investigating photosensitised oxidation of guanine by Ru(II) polypyridyl complexes.^{279-283,342,343} Therefore, the photosynthesis, isolation and characterisation of **43** will be first presented. Investigations into the effect of the pH on its ground state will then be performed using several spectroscopic techniques, including UV-vis absorption and emission spectroscopy, Fourier-transform infrared (FTIR), circular dichroism (CD) and NMR spectroscopy. Furthermore, TrA and, as previously mentioned, TRIR spectroscopy will be employed to probe the different pH-dependent excited states that exist in **43**. It was envisioned that TRIR would be useful to study the pH-dependent excited states of **43** as the specific vibrations within this photoadduct are expected to be sensitive to changes in the electronic structure of the complex resulting from differences in the solution acidity. The studies described here were conducted under the supervision of Prof. John M. Kelly at Trinity College Dublin (TCD) and in collaboration with Prof. Andrée Kirsch-De Mesmaeker at Université Libre de Bruxelles (ULB).

3.2 Photoreaction between **38** and GMP

The photoadduct **43** was photosynthesised based on previous protocols developed by the research group of Prof. Andrée Kirsch-De Mesmaeker at Université Libre de Bruxelles (ULB).^{213,223,228,229} A photoreactor containing diode lasers as excitation sources was used for the first time in order to replace the traditional Xenon lamp previously employed for this kind of photoreaction involving π -deficient Ru(II) polypyridyl complexes and biomolecules.^{168,211,213,219,223,227-229,344,345} The LightBATH-405 advanced laser photoreactor

(Figure 3.2) was designed and manufactured by Prof. Guillermo Orellana and Dr Maximino Bedoya at Universidad Complutense de Madrid (UCM).

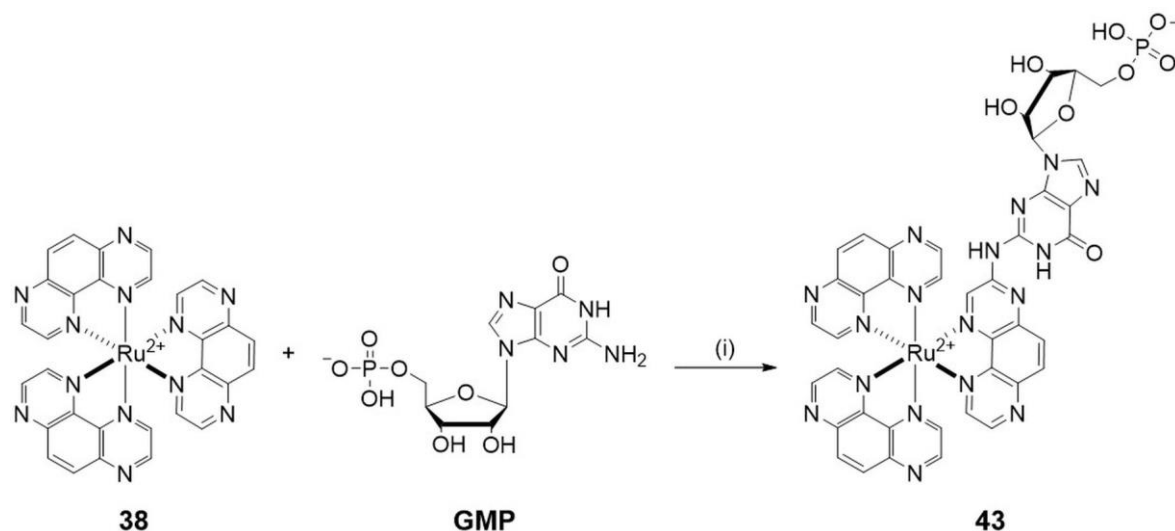


Figure 3.2. (a) LightBATH-405 advanced laser photoreactor manufactured by the UCM Optical Chemosensors & Applied Photochemistry Group (GSOLFA) of Universidad Complutense de Madrid (UCM) and used for photoproducing the photoadduct **43**. (b) Optical glass bottle reactor containing the photoreaction mixture.

This unique device provides several advantages when compared with Xenon lamps: (i) high selectivity for performing photochemical reactions as the diode laser illumination of the LightBATH-405 is centred at *ca.* 405 nm; (ii) versatility of the system since the original 405-nm diode lasers can be easily replaced by lasers of different wavelengths; (iii) the diode lasers are inserted into an aluminium block for passive cooling of the system and thus no water flow is needed; (iv) two switches located on both sides of the LightBATH-405 allow half or full radiant power from the eight diode laser sources the device is equipped with, with each having an average radiant power of (33 ± 4) mW; (v) the LightBATH-405 photoreactor is fitted with a standard SMA-905 port for front-face fiber-optic monitoring of the photochemical reaction progress by luminescence or reflectance measurements using a fiber-optic spectrometer.

Thus, for the synthesis of the photoadduct **43**, a 25 mL aqueous solution of a mixture of complex **38** (100 μ M) and GMP (3 mM) was prepared. Synthetic and characterisation details of **38** can be found in Section 7.8.1 of Chapter 7 and Figures A3.1-A3.3 of the Appendices. The pH of the solution was adjusted to pH 5 by addition of 0.1 M HCl and transferred to the optical glass bottle reactor (Figure 3.2b). Indeed, it has been previously demonstrated that for the photoreaction between **38** and GMP to occur a pH lower than 7 was necessary.^{213,219} The optical glass bottle reactor, provided with a rubber septum, was placed in the tailored pit between the illumination sources of the LightBATH-405 photoreactor. Before irradiation, the solution was purged with argon for 30 min to remove

any dissolved oxygen and to avoid the formation of secondary oxidised products.^{213,219,228} The mixture was then irradiated for 8 h at full radiant power under continuous stirring (Scheme 3.2).



Scheme 3.2. Synthetic pathway for the photoreaction between **38** and GMP to form the photoadduct **43**: (i) deaerated aqueous solution, pH 5, 8 h irradiation with 405 nm light.

The progress of the photoreaction was monitored every hour by UV-vis absorption spectroscopy (Figure 3.3a) and a shift of the MLCT band maximum to slightly shorter wavelengths could be observed. This behaviour has been already reported in the literature for the formation of a photoadduct with the GMP.^{213,219,223} However, the hyperchromic effect at *ca.* 390 nm typically observed in the formation of **43** could not be detected.^{213,219,223} It has to be noted that the photoreaction conditions employed here do not result in the best reaction yield but rather favour the purity of the photoproducts obtained. Thus, at the GMP

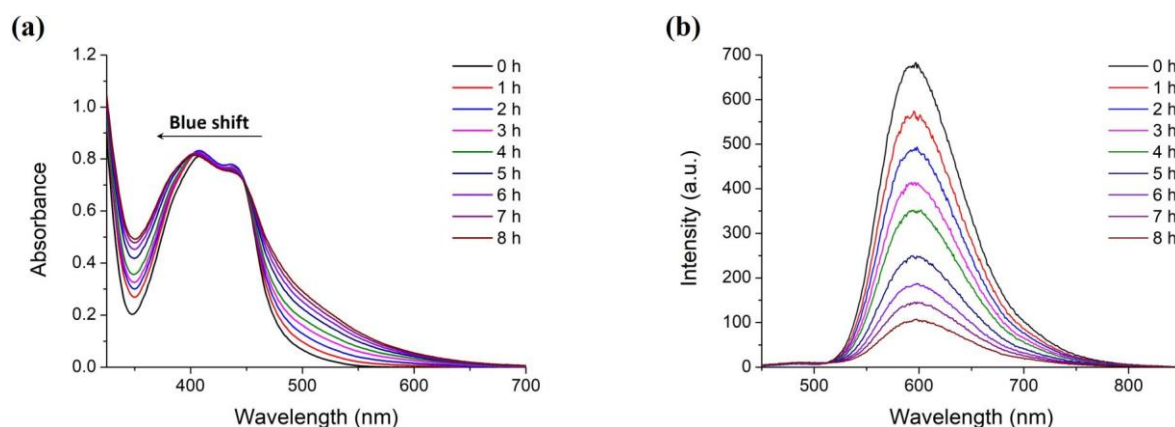


Figure 3.3. Monitoring of the photoreaction progress between **38** (100 μ M) and GMP (3 mM) in deaerated aqueous solution at pH 5 by (a) UV-vis absorption and (b) emission spectroscopy ($\lambda_{exc} = 407$ nm) at different irradiation times, at 298 K.

concentration used and knowing that the luminescence lifetime of **38** in water is 220 ns and the rate constant (k_q) for the quenching of the excited state of such complex by GMP is $2.2 \times 10^9 \text{ M}^{-1} \text{ s}^{-1}$,²¹² only *ca.* 60% of the excited states are quenched. Therefore, competition with other processes such as photodechelation of the ruthenium complex is expected. This is supported by the appearance of a shoulder at *ca.* 500 nm. Illumination of the complex **38** in the presence of 10 mM GMP concentration was also carried out (*ca.* 80% quenching of the excited states). The progress of the photoreaction was monitored by UV-vis absorption spectroscopy (Figure A3.4 of the Appendices) and showed the expected hyperchromic effect. This again confirmed a greater competition for other process when lower GMP concentrations are used. Unfortunately, as previously pointed out, 3 mM GMP concentration had to be used in order to facilitate the subsequent purification of the photoproducts. The use of large GMP concentrations resulted in gel formation when, once illumination was complete, the crude product of the photoreaction was concentrated, making the purification step difficult.

Emission spectroscopy was also employed to monitor the photoreaction progress (Figure 3.3b). A decrease in emission intensity with the illumination time was observed and can be attributed to the consumption of the emissive starting material **38**, either because of the formation of the non-emissive **43** photoadduct and other photoproducts or due to photodechelation. In order to exclude the photodechelation of the complex **38** as the main photoproduct, illumination of **38** (50 μM) in the absence of GMP was carried out and monitored by UV-vis absorption and emission spectroscopy, with the corresponding spectra shown in Figure A3.5 of the Appendices. An isosbestic point at *ca.* 460 nm was clearly observed indicating the superposition of the absorption spectra of two different species. These species would correspond to the disappearing starting material **38** and the formation of the dechelated complex by replacement of one of the **TAP** ligands by H_2O molecules or chloride ions which results in the appearance of a typical absorption band at *ca.* 500 nm.²¹⁹ A decrease in emission intensity was also observed with the illumination time. The dechelation appeared complete after 4 h irradiation. From this experiment it can be concluded that, even if some dechelation occurs when the complex **38** is illuminated in the presence of GMP, the loss of a **TAP** ligand is more dramatic in the absence of the guanine nucleotide. This suggests that another process is also taking place, that is, photoadduct formation.

To further confirm the formation of photoproducts, the photoreaction progress was also monitored by High-Performance Liquid Chromatography (HPLC). Chromatograms at

different illumination times are shown in Figure 3.4. Before irradiation, two peaks could be detected at retention times of *ca.* 3.1 and 8.6 min corresponding to the starting materials GMP and **38**, respectively. Independent analyses of the pure starting materials allowed identification of their retention times (Figure A3.6 of the Appendices). It must be noted that small differences in retention times between injections are expected as no reference compound was used. Once irradiation of the reaction mixture began, the appearance of three main peaks at retention times of *ca.* 6.4, 10.7 and 12.2 min was observed as well as the

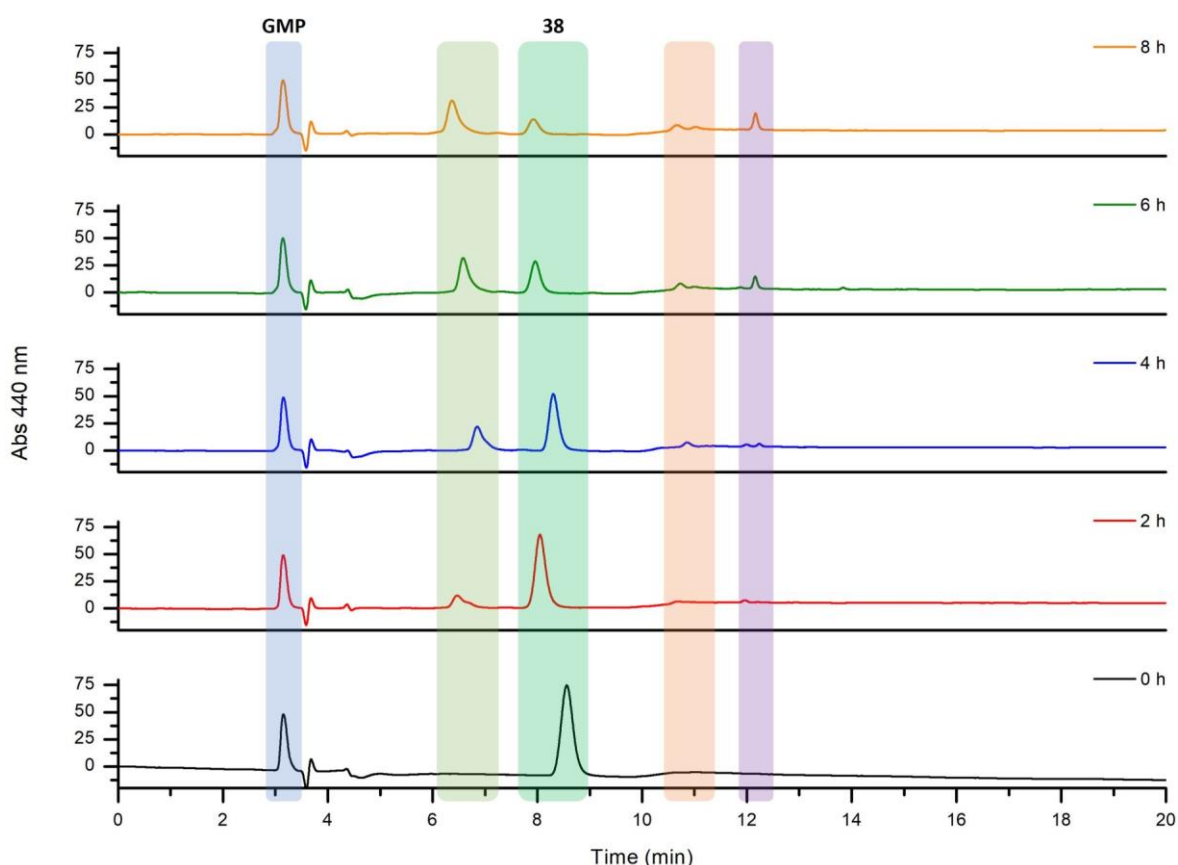


Figure 3.4. Monitoring of the photoreaction between **38** and GMP by analytical HPLC measuring the absorption at 440 nm at different irradiation times. Column: Jupiter[®] 5 μ m C18 300 Å, LC Column 250 \times 4.6 mm. Gradient: 0–5 min 85% A, 10% B and 5% C; 5–25 min from 85% A, 10% B and 5% C to 0% A, 95% B and 5% C (A = H₂O, B = MeCN and C = TFA (2%)).

decrease of the peak attributed to **38** due to the consumption of this starting material. A decrease of the peak corresponding to GMP was not observed as this reagent was in large excess. Therefore, it can be concluded that at least three new photoproducts were formed in the course of the photoreaction. In the next section the isolation of each peak by HPLC will be discussed.

3.3 Purification of the Photoproducts by High-Performance Liquid Chromatography

After repeating the photoreaction a minimum of five times and concentrating the combined crudes obtained, the different photoproducts were isolated by HPLC. Three different purification steps were needed to obtain them in high purity. The first purification consisted on removing the high excess of GMP by semi-preparative HPLC using a Jupiter[®] 5 μ m C18 300 Å, LC Column 250 \times 10.0 mm (Phenomenex) with a 4 mL/min flow and a gradient elution of 90% H₂O, 5% MeCN and 5% TFA(2%) for 10 min, from 90% H₂O, 5% MeCN and 5% TFA(2%) to 70% H₂O, 25% MeCN and 5% TFA(2%) for 10 min, and 70% H₂O, 25% MeCN and 5% TFA(2%) for 10 min (Figure 3.5).

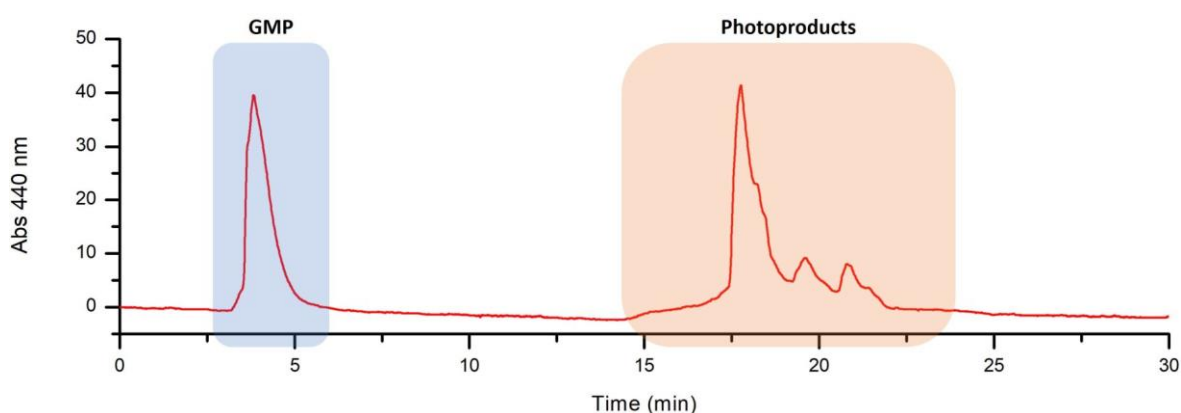


Figure 3.5. HPLC chromatogram ($\lambda_{abs} = 440$ nm) of the crude photoreaction mixture showing the conditions used to remove the GMP. Column: Jupiter[®] 5 μ m C18 300 Å, LC Column 250 \times 10.0 mm. Gradient: 0–10 min 90% A, 5% B and 5% C; 10–20 min from 90% A, 5% B and 5% C to 70% A, 25% B and 5% C; 20–30 min 70% A, 25% B and 5% C (A = H₂O, B = MeCN and C = TFA (2%)).

Once the GMP was removed from the crude photoreaction mixture, the second purification step involved analytical HPLC purification using a Jupiter[®] 5 μ m C18 300 Å, LC Column 250 \times 4.6 mm (Phenomenex) with a 1 mL/min flow and a gradient elution of 85% H₂O, 10% MeCN and 5% TFA(2%) for 5 min, from 85% H₂O, 10% MeCN and 5% TFA(2%) to 0% H₂O, 95% MeCN and 5% TFA(2%) for 20 min, and 0% H₂O, 95% MeCN and 5% TFA(2%) for 6 min (Figure 3.6). Note that purification by semi-preparative HPLC could not be carried out due to a poor resolution of the peaks, most likely due to the limited amount of photoproducts.

Four fractions with retention times of *ca.* 6.4 (*a*), 7.9 (*b*), 10.7 (*c*) and 12.2 (*d*) min were isolated. Finally, fraction *a* was identified as the fraction containing the photoadduct of interest by high resolution MALDI-TOF mass spectrometry (see next section for further details) and was further repurified by analytical HPLC using the same column and flux as

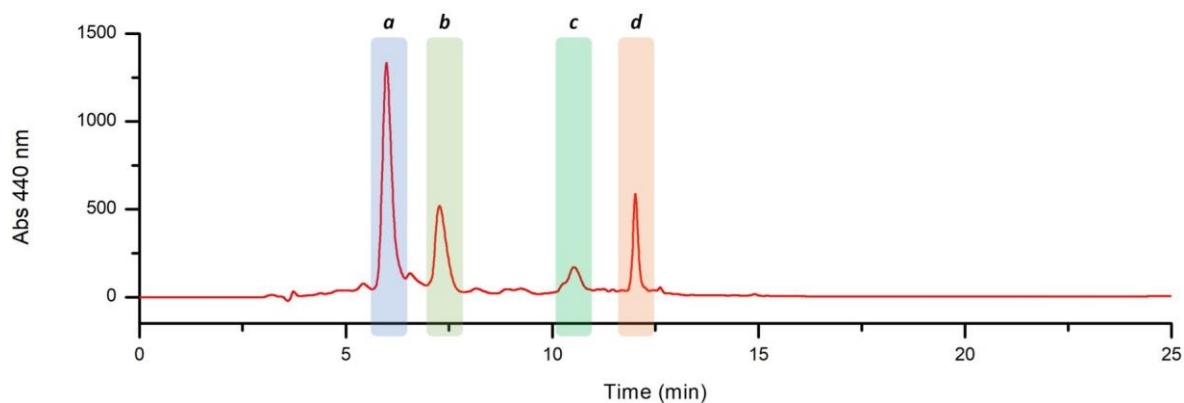


Figure 3.6. HPLC chromatogram ($\lambda_{abs} = 440$ nm) of the crude photoreaction mixture after removing the GMP showing the conditions used to isolate the different photoproducts. Column: Jupiter[®] 5 μ m C18 300 Å, LC Column 250 \times 4.6 mm. Gradient: 0–5 min 85% A, 10% B and 5% C; 5–25 min from 85% A, 10% B and 5% C to 0% A, 95% B and 5% C (A = H₂O, B = MeCN and C = TFA (2%)).

before but with a different gradient elution: 90% H₂O, 5% MeCN and 5% TFA(2%) for 5 min, from 90% H₂O, 5% MeCN and 5% TFA(2%) to 85% H₂O, 10% MeCN and 5% TFA(2%) for 20 min, and 85% H₂O, 10% MeCN and 5% TFA(2%) for 5 min (Figure 3.7). A peak with a retention time of *ca.* 19.3 min corresponding to the photoadduct **43** was isolated.

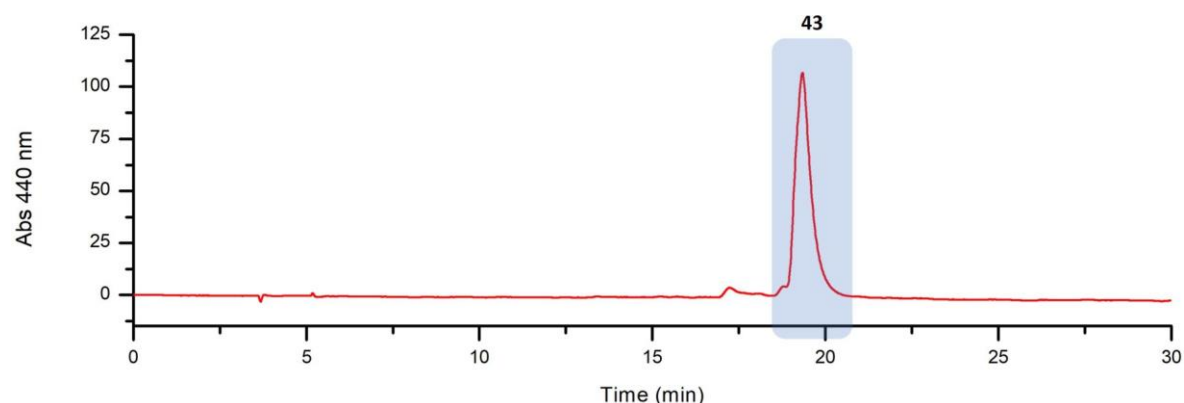


Figure 3.7. HPLC chromatogram ($\lambda_{abs} = 440$ nm) of fraction a after being isolated from the starting materials and other photoproducts showing the conditions used to get the photoadduct of interest in high purity. Column: Jupiter[®] 5 μ m C18 300 Å, LC Column 250 \times 4.6 mm. Gradient: 0–5 min 90% A, 5% B and 5% C; 5–25 min from 90% A, 5% B and 5% C to 85% A, 10% B and 5% C; 25–30 min from 85% A, 10% B and 5% C (A = H₂O, B = MeCN and C = TFA (2%)).

After purification, the four fractions isolated were characterised by high resolution MALDI-TOF mass spectrometry and UV-vis absorption and emission spectroscopy. Such characterisation will be described in the next section.

3.4 Characterisation of the Isolated Photoproducts by High Resolution MALDI-TOF Mass Spectrometry and UV-vis Absorption and Emission Spectroscopy

The different photoproducts isolated by HPLC were first analysed by high resolution MALDI-TOF mass spectrometry in order to identify which fraction corresponded to the

desired photoadduct. An analysis of the crude photoreaction mixture after removing the starting material GMP was also carried out and the mass spectrum is shown in Figure 3.8. A peak at m/z 1009.1295 corresponding to the photoadduct of interest **43** was observed and confirmed the formation of this compound during the course of the photoreaction. Other

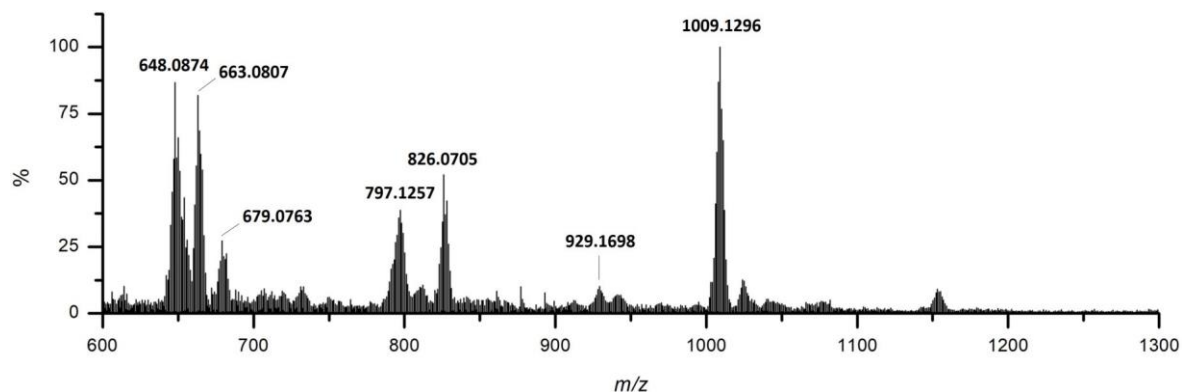


Figure 3.8. Mass spectrum of the crude photoreaction mixture after removing the starting material GMP obtained by MALDI-TOF (α -cyano-4-hydroxycinnamic acid (α -CHCA) matrix, molecular weight 189.17 Da).

peaks at m/z 929.1698 and 797.1257 were identified as being the photoadduct after losing the phosphate group and the ribose-phosphate moiety, respectively. Likewise, a peak at m/z 648.0874 corresponding to the remaining starting material **38** was observed. In addition, the mass spectrum displayed a peak at m/z 663.0807 that was attributed to the complex **38** containing an amino group which supports the formation of the photoadduct *via* the exocyclic amino group of the GMP as reported in the literature.^{223,229} Furthermore, a peak at m/z 826.0705 was identified as another photoproduct obtained by the replacement of one of the **TAP** ligands by GMP. The observation of a peak at m/z 679.0763 corresponding to this photoproduct after losing the guanine base suggests the coordination of the GMP to the ruthenium centre *via* the phosphate group.

Mass spectrometry analysis of the four fractions isolated by HPLC was then performed. The mass spectrum of fraction *a* is shown in Figure 3.9 and revealed that this fraction contained the desired photoadduct **43** (m/z 1009.1289). A comparison of the theoretical and experimental isotopic distribution pattern of the photoadduct **43** is shown in Figure 3.10. It must be noted that the typical isotopic profile exhibited by ruthenium complexes was not observed for this compound. This phenomenon has previously been described in the literature and is due to the coexistence of two different singly charged species: (i) a one-electron capture by the doubly charged photoadduct, which results in a radical cation at m/z 1009 (reduced form), and (ii) a one proton loss from the phosphate

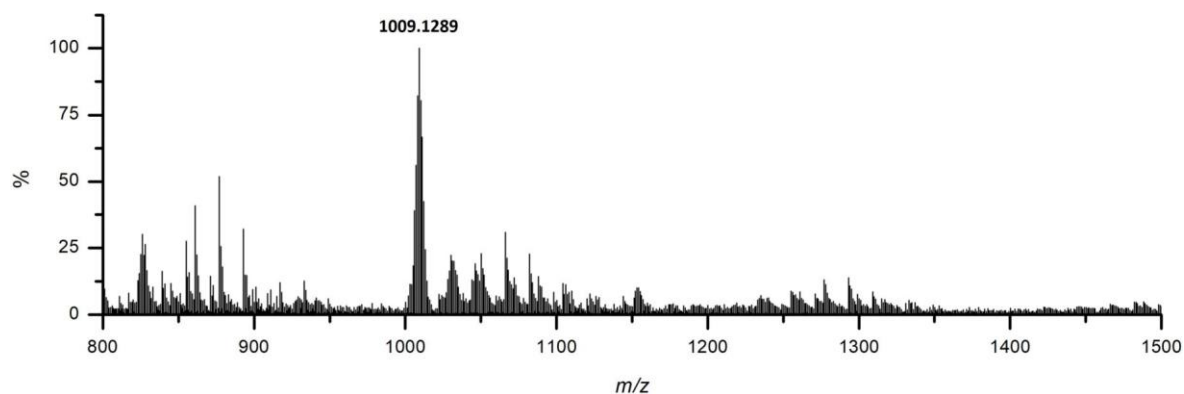


Figure 3.9. Mass spectrum of fraction *a* obtained by high resolution MALDI-TOF mass spectrometry analysis (α -cyano-4-hydroxycinnamic acid (α -CHCA) matrix, molecular weight 189.17 Da) and corresponding to **43** ($m/z = 1009.1289$).

moiety, which generates a cation at m/z 1008 (deprotonated form).³⁴⁶ Thus, the isotopic distribution pattern experimentally observed for the isolated photoadduct would correspond to the overlap of those displayed by the two existing species.

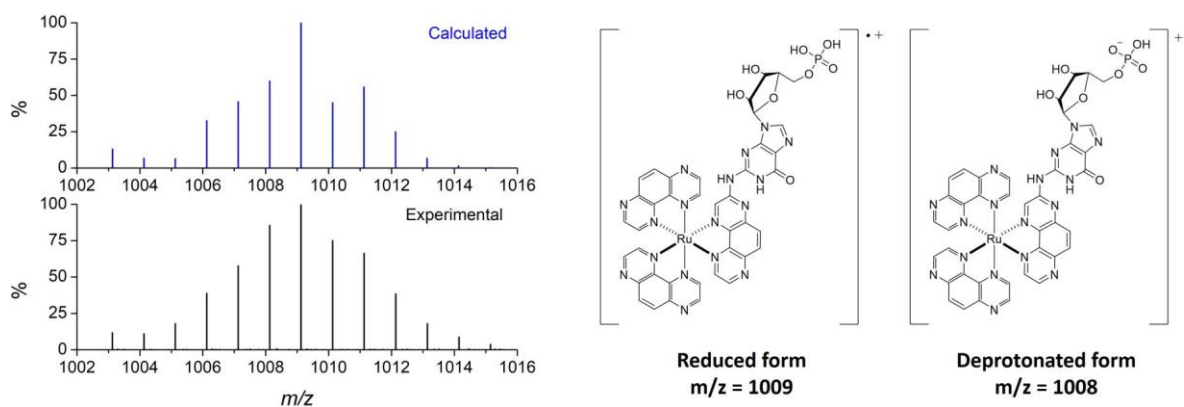


Figure 3.10. Comparison between the calculated (blue) and experimental (black) isotopic distribution pattern for fraction *a* containing the photoadduct of interest and obtained by high resolution MALDI-TOF mass spectrometry analysis.

To further analyse the fraction containing the photoadduct of interest **43**, tandem mass spectrometry (MS/MS) analysis was carried out on the peak at m/z 1009.1289 (Figure 3.11). The main fragmentations corresponded to the loss of the ribose-phosphate group followed by the loss of one and two **TAP** ligands (m/z 614.0408 and 431.9928, respectively). Other fragmentations, such as the loss of the **TAP** ligand where the GMP moiety was attached, were also observed (m/z 466.0243).

Concerning the analysis of the other three photoproducts isolated by mass spectrometry, fraction *b* was identified as the unreacted starting material **38** from the peak at m/z 648.0914 displayed in the mass spectrum recorded for this fraction and shown in Figure A3.7 of the Appendices. In addition, the mass spectrum of fraction *c* (Figure A3.8 of

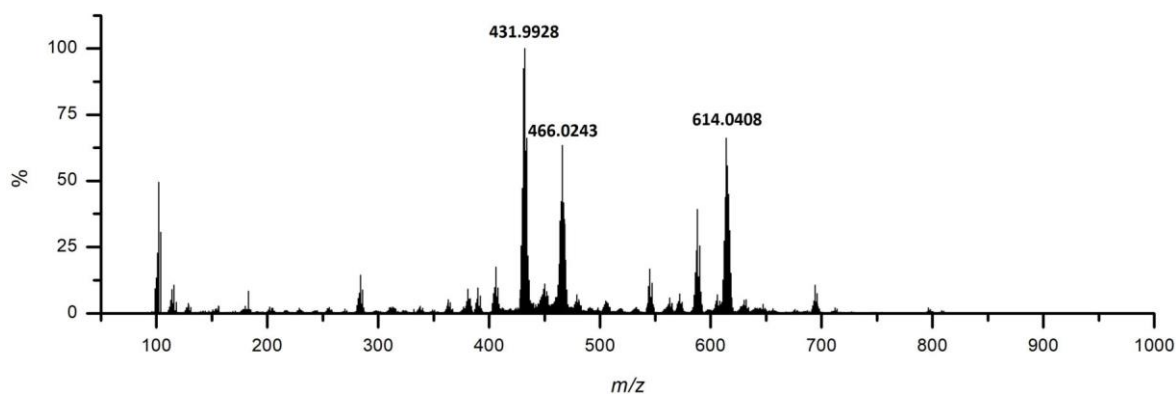


Figure 3.11. MS/MS spectrum of fraction *a*.

the Appendices) displayed peaks at m/z 825.1410 and 679.0788 that corresponded to the photoproducts formed by the substitution of a **TAP** ligand in complex **38** by a GMP, and the loss of the guanine base by such photoproduct, respectively. Finally, fraction *d* contained the complex **38** bearing an amino group on one of its **TAP** ligands (m/z 663.0779, Figure A3.9 of the Appendices), probably resulting from the breakdown of the bond between the exocyclic amino group and the purine heterocycle of the GMP moiety attached to **38** in the photoadduct **43**.

Additionally, UV-vis absorption and emission spectra of the four isolated fractions were recorded and are shown in Figure 3.12. Importantly, the UV-vis absorption spectrum of the isolated fraction *a*, which was identified as that containing the photoadduct of interest **43** by high resolution MALDI-TOF spectrometry, showed the typical features previously reported for this compound, that is an important hyperchromic and hypsochromic shift (*ca.* of 10 nm) of the MLCT absorption maximum compared to **38**.^{213,219,223} Moreover, no emission from the photoadduct **43** was detected due to an intramolecular electron transfer from the guanine moiety to the ruthenium centre resulting in the luminescence quenching of the ³MLCT excited states of such photoadduct.²¹³ On the other hand, as expected, the UV-vis absorption spectrum of fraction *b* corresponded to the remaining starting material **38**, showing a MLCT band maximum at 407 nm, as well as the emission spectrum with a maximum centred at *ca.* 600 nm.³⁴⁷ Fractions *c* and *d* showed different UV-vis absorption spectra than both the photoadduct **43** and the starting material **38**. In particular, the MLCT band maximum of fraction *d*, which was attributed to complex **38** containing an amino group, exhibited a shift to slightly longer wavelengths when compared with **38**. As was the case for the photoadduct, any photoproducts found in fractions *c* and *d* seemed to be significantly emissive.

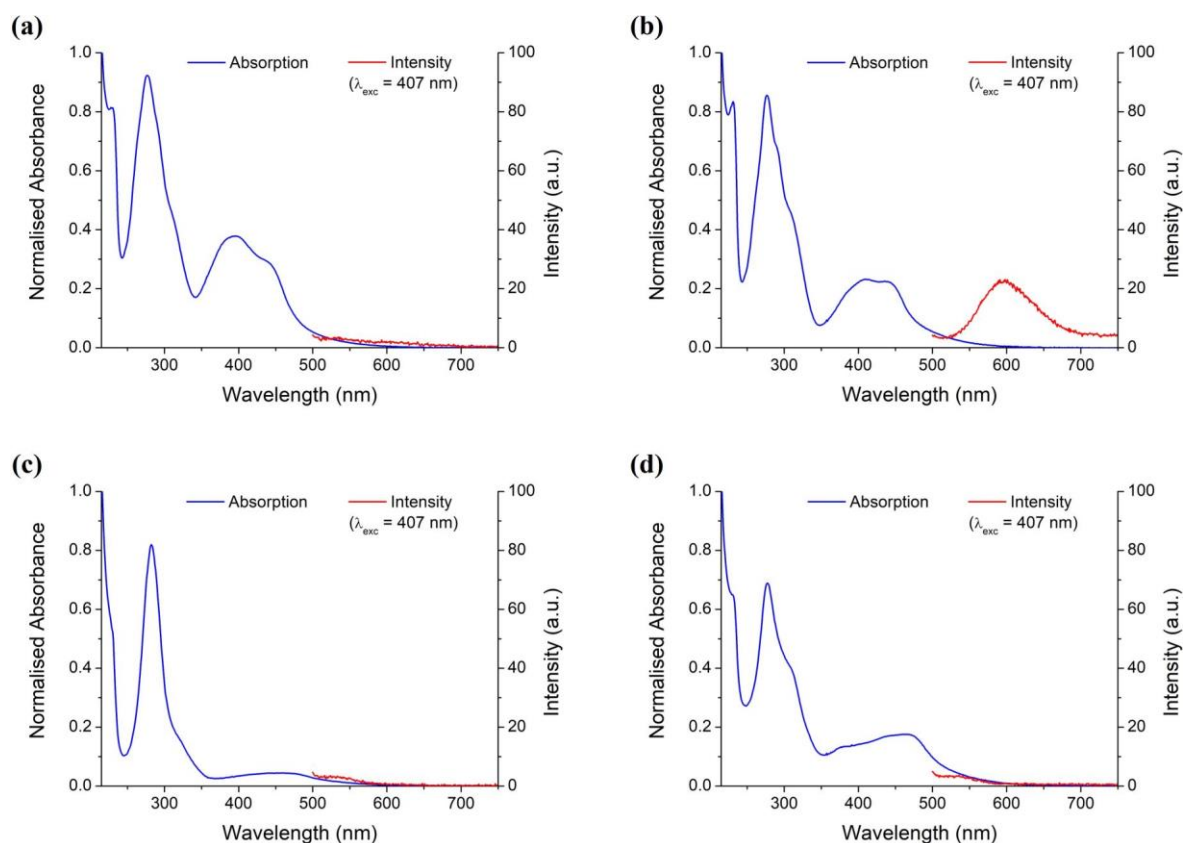


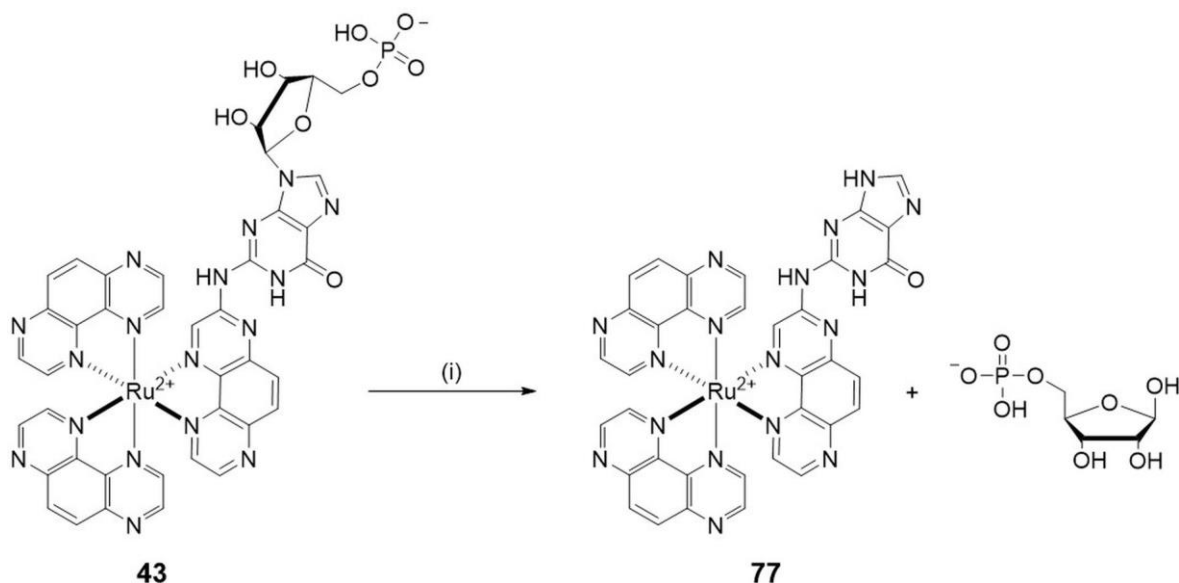
Figure 3.12. UV-vis absorption and emission spectra of (a) fraction a, (b) fraction b, (c) fraction c and (d) fraction d isolated by analytical HPLC from the crude photoreaction mixture.

It must be taken into account that, as was recently demonstrated, the hyperchromic and hypsochromic shift observed for the photoadduct **43** depends on the pH of the solution and such changes are only expected at acidic pH.²¹³ As the UV-vis absorption spectrum was recorded directly after HPLC purification without further workup and TFA was present in the eluent gradient used, the solution is expected to be acidic. At the same time, depending on the acidity of the solution, the hyperchromic and hypsochromic shifts of the MLCT absorption band are more significant. Thus, the MLCT absorption band would be more blue shifted at pH 1 than at pH 5. This pH effect on the photophysical properties of the photoadduct **43** will be further analysed in the following sections of this chapter. Firstly, in order to construct a more simple model that allows understanding the influence of the phosphate group in this particular behaviour, the nucleobase derivative **77** was isolated by hydrolysis of the ribose-phosphate group in **43** as will be next described.

3.5 Acid Hydrolysis of the Ribose-Phosphate Moiety in **43**

Cleavage of the of the ribose-phosphate moiety in the photoadduct **43** was performed by acid hydrolysis based on the protocols previously employed by Jacquet *et al.*^{223,229} Thus, **43** was dissolved in 2 M HCl aqueous solution and heated at 95 °C for 2 h (Scheme 3.3). After

vacuum distillation of the acidic solvent, the resulting orange hydrolysate was purified by analytical HPLC using a Jupiter[®] 5 μ m C18 300 Å, LC Column 250 \times 4.6 mm (Phenomenex)



Scheme 3.3. Synthetic pathway for the acid hydrolysis of the photoadduct **43** to form **77**: (i) 2 M HCl aqueous solution, 95 °C, 2 h.

with a 1 mL/min flow and a gradient elution of 90% H₂O, 5% MeCN and 5% TFA(2%) for 5 min, from 90% H₂O, 5% MeCN and 5% TFA(2%) to 85% H₂O, 10% MeCN and 5% TFA(2%) for 25 min, 85% H₂O, 10% MeCN and 5% TFA(2%) for 5 min, and from 85% H₂O, 10% MeCN and 5% TFA(2%) to 0% H₂O, 95% MeCN and 5% TFA(2%) for 5 min (Figure 3.13). Three main peaks at retention times of *ca.* 18.8, 26.3 and 27.4 min were

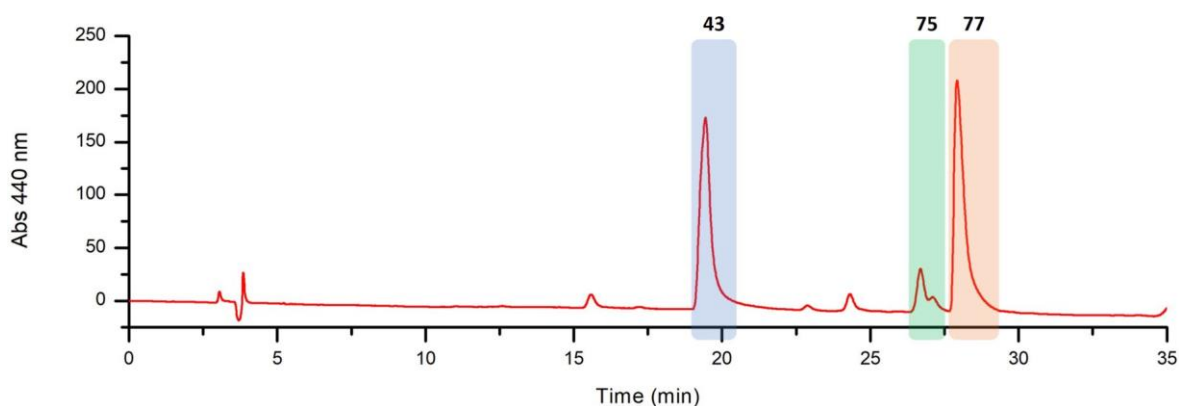


Figure 3.13. HPLC chromatogram ($\lambda_{abs} = 440$ nm) of the crude acid hydrolysis mixture of the ribose-phosphate moiety in **43** showing the conditions used to isolate the different photoproducts. Column: Jupiter[®] 5 μ m C18 300 Å, LC Column 250 \times 4.6 mm. Gradient: 0–5 min 90% A, 5% B and 5% C; 5–25 min from 90% A, 5% B and 5% C to 85% A, 10% B and 5% C; 25–30 min 85% A, 10% B and 5% C; 30–35 min from 85% A, 10% B and 5% C to 0% A, 95% B and 5% C (A = H₂O, B = MeCN and C = TFA (2%)).

observed in the HPLC chromatogram. By comparison with the HPLC chromatogram recorded before **43** was subjected to acid hydrolysis, the peak with the lowest retention time

corresponded to the remaining unhydrolysed photoadduct **43**. This assignment was confirmed by analysis of the isolated peak by high resolution MALDI-TOF mass spectrometry. On the other hand, the peak with a retention time of *ca.* 26.3 min was attributed to $[Ru(TAP)_2Cl_2]$ (**75**), obtained by replacement of the **TAP-GMP** ligand in **43** by two chlorides, most likely due to the poor stability of the photoadduct at high temperature.

Finally, mass spectrometry allowed the identification of the peak with a retention time of *ca.* 27.4 min as being the desired nucleobase derivative **77** (Figure 3.14). Once again, the typical isotopic pattern of ruthenium complexes was not observed for the hydrolysed photoadduct and, as was previously proposed for **43**, the coexistence of two different singly charged species could be an explanation for this phenomenon (Figure A3.10 of the Appendices).

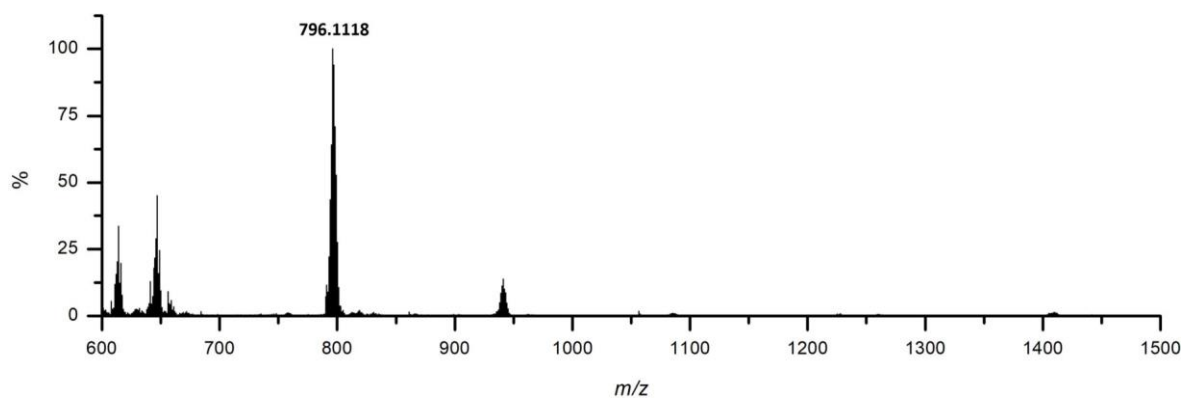


Figure 3.14. Mass spectrum of the peak with a retention time of *ca.* 27.4 min obtained by high resolution MALDI-TOF mass spectrometry analysis (α -cyano-4-hydroxycinnamic acid (α -CHCA) matrix, molecular weight 189.17 Da) and corresponding to **77** ($m/z = 796.1118 [M-H]^+$).

In the next sections of this chapter, the pH dependence of the spectroscopic properties of the photoadduct **43** in both its ground and excited states, and using **77** as a comparative compound in some of the studies, will be discussed in detail.

3.6 Spectroscopic Studies of the Ground State of **43** at Different pH Values

In order to investigate the photoreactivity of the excited state of the photoadduct **43** and its pH dependence, an understanding of its ground state is necessary. Therefore, the ground state of the photoadduct in acidic and basic aqueous solution was studied using several spectroscopic techniques including UV-vis absorption, Fourier-transform infrared (FTIR), circular dichroism (CD) and NMR spectroscopy. It should be noted that, despite most of the experiments were carried out in D_2O , the term pH will be used instead of pD. Details about the composition of the potassium-buffered D_2O solutions used here and their corresponding experimental pH and calculated pD values are provided in Section 7.5 of Chapter 7.

3.6.1 UV-vis Absorption and Emission Spectroscopic Studies of **43**

The UV-vis absorption and emission spectra of the photoadduct **43** were recorded in D₂O and in 10 mM potassium phosphate-buffered D₂O solution at acidic and basic pH and are shown in Figure 3.15a. As expected from previous studies performed by Marcélis *et al.*,²¹³ the UV-vis absorption spectrum of the photoadduct was pH sensitive. Thus, at pH 5, **43** exhibited an absorption maximum in the visible region which was blue shifted (*ca.* 15 nm) and displayed a hyperchromic effect when compared to the MLCT band of its parent complex **38**. A similar effect was found at pH 1, although in this case the blue shift (*ca.* 30 nm) of the absorption maximum in the visible region was more dramatic (Figure A3.11a of the Appendices). These observations are in agreement with the typical spectral changes reported in the literature during the photoadduct formation, as discussed in previous sections of this chapter.^{213,219,223} However, in D₂O and at pH 8, a different UV-vis absorption spectrum was recorded with the appearance of a shoulder at approximately 500 nm. Marcélis

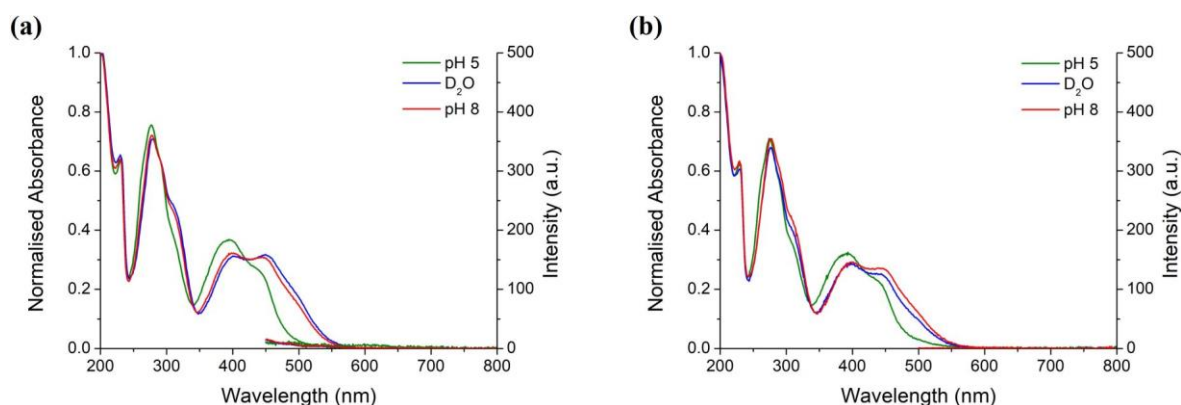


Figure 3.15. UV-vis absorption and emission spectra of (a) **43** and (b) **77** in D₂O (blue) and 10 mM potassium phosphate-buffered D₂O solution at pH 5 (green) and 8 (red), at 298 K.

et al. found that the pK_a of **43** was 6.8 and thus a protonation of the photoadduct at pH values lower than its pK_a was proposed to explain the pH dependence of the absorption properties of this compound.²¹³ Therefore, a protonated form of the photoadduct would exist at pH 5 while a non-protonated form would be expected to dominate at pH 8.

It is more complicated, however, to find out the exact site where this protonation takes place. It would be expected that protonation will not occur in the **TAP** ligands since a pK_a value of -2.7 has been reported in the literature for the complex **38**.³⁴⁸ Thus, protonation is expected to take place in the GMP moiety (GMP has pK_a values of 0.3, 2.48, 6.25 and 9.49 corresponding to the first OH of the phosphate group, N7 position, second OH of the phosphate group and N1 position, respectively).³³⁹ From these pK_a values for free GMP, it could be presumed that the phosphate would be the group protonated in **43** at pH 5. However,

it has been proposed that the N7 position of the GMP moiety in the complex is the protonation site according to DFT calculations performed on this photoadduct.²¹³ As shown above, the phosphate group was found to make no contribution to the absorption spectra changes observed for **43** at acidic and basic pH. This was confirmed by recording the UV-vis absorption spectrum of the photoadduct **77** (*i.e.* after sugar-phosphate cleavage from **43**) under the same conditions, that is D₂O and pH 5 and 8 (Figure 3.15b). Similar behaviour to that exhibited by **43** was observed for **77** and thus it can be concluded that only the guanine moiety is involved in this particular pH dependence of the photoadduct. In addition, as expected from previous observations, neither **43** or **77** were emissive at the pH tested. This could be a result of an intramolecular electron transfer from the guanine moiety to the ruthenium centre that causes the luminescence quenching of the ³MLCT excited states of the photoadduct.²¹³ It must also be noted that no significant changes were observed when the UV-vis absorption spectrum of **43** was recorded at 400 μ M concentration (Figure 3.16), indicating that there is no concentration dependence of the absorption properties of **43**.

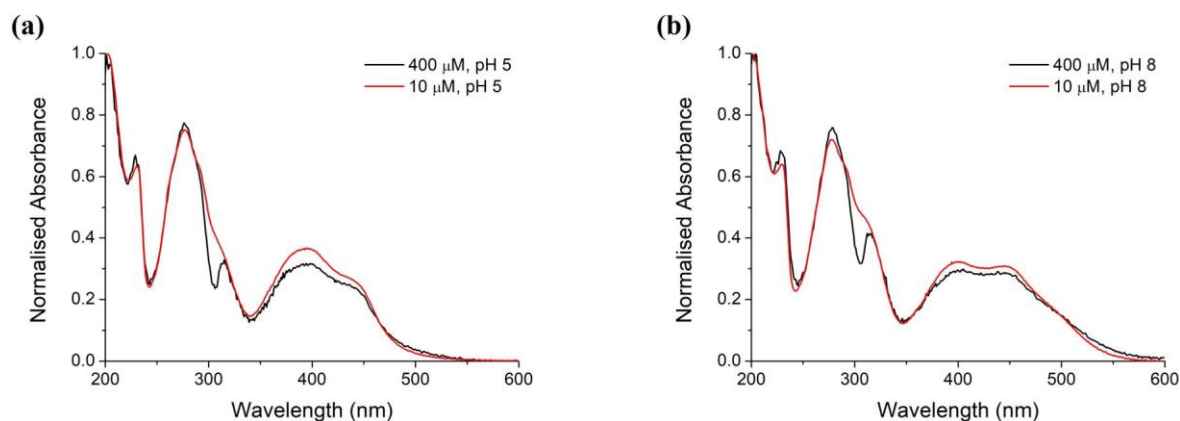


Figure 3.16. UV-vis absorption spectra of **43** at 400 μ M (black) and 10 μ M (red) in 50 mM (400 μ M concentration of **43**) or 10 mM (10 μ M concentration of **43**) potassium phosphate-buffered D₂O solution at (a) pH 5 and (b) pH 8, at 298 K. Note that the absorption spectrum of the sample at 400 μ M concentration was recorded in a Harrick cell with CaF₂ plates and as such, the absorption band observed between 300 and 320 nm is caused by a defect in the CaF₂.

For comparative purposes, the UV-vis absorption and emission spectra of both starting materials **38** and GMP were recorded in the same conditions employed for **43** (Figure 3.17). The absorption properties of neither of the compounds showed to be pH sensitive and confirmed that such behaviour is unique to the photoadduct resulting from the covalent bond between **38** and GMP. Only when the UV-vis absorption spectrum of GMP was recorded at pH 1 and 12, changes in the absorption maximum were observed (Figure A3.11b of the Appendices). Thus, at pH 1, when the N7 position of GMP is expected to be protonated, a red shift of the absorption band was observed. Moreover, at pH 12, for which

the N1 position of GMP should be deprotonated, the characteristic band of this nucleotide centred at about 260 nm and its shoulder became a single band. These results revealed that

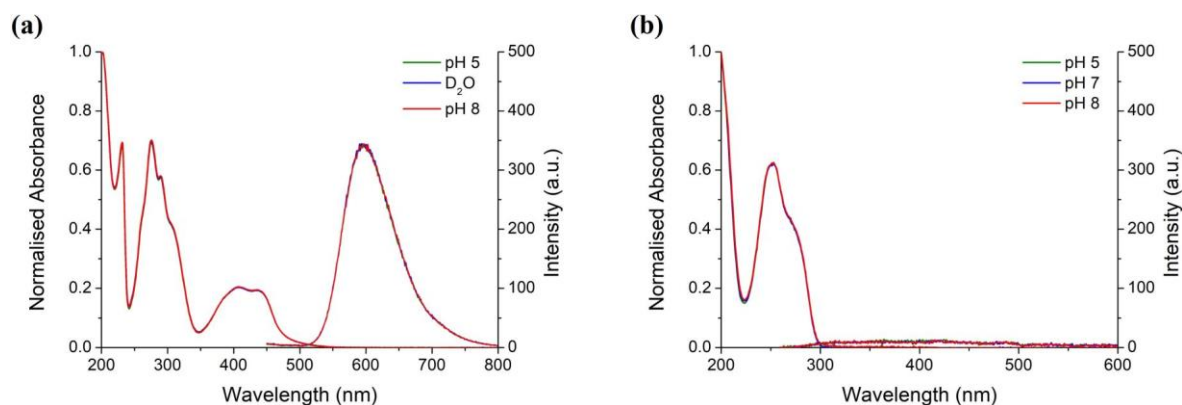


Figure 3.17. UV-vis absorption and emission spectra of (a) **38** and (b) GMP in D_2O (blue) and 10 mM potassium phosphate-buffered D_2O solution at pH 5 (green) and 8 (red), at 298 K.

it is only at extreme acidic and basic pH, where changes in its protonation state are expected, that GMP exhibits a pH dependent UV-vis absorption spectrum. Concerning the emission spectrum, while **38** was found to be emissive independent of the pH, emission of GMP was only observed at pH 1 as it is well-known that the protonated form of the GMP is significantly more luminescent than the neutral nucleobase.³⁴⁰

In the next section, infrared spectroscopic studies of the photoadduct **43** will be presented with the aim of gaining more information about the ground state of this molecule by looking at the transitions within the vibrational levels.

3.6.2 Fourier-Transform Infrared Spectroscopic Studies of **43**

The ground state of the photoadduct **43** was also studied by IR spectroscopy. Thus, the Fourier-transform infrared (FTIR) spectrum of **43** (800 μ M) was recorded in 10 mM potassium phosphate-buffered D_2O solution at pH 5 and 8 (Figure 3.18a). Special care was taken to avoid moisture and thus sample preparation was carried out in a glove bag continuously filled with N_2 . At pH 5, a sharp and strong band was observed at 1673 cm^{-1} and can be attributed to the carbonyl $C=O$ stretching (denoted ν_{CO}) localised in the guanine moiety. In addition, a series of weak bands were detected between 1350 and 1550 cm^{-1} and most likely correspond to vibrations within the polypyridyl ligands **TAP**.

Interestingly, at pH 8, the carbonyl band was also found at 1673 cm^{-1} . The absence of change in the position of the carbonyl band at both pH 5 and 8 is similar to the behaviour exhibited by free GMP at the same pH values (see below). By contrast, FTIR studies on the free GMP at pD 2 reported in the literature showed a shift of this band to a larger

wavenumber. This is due to protonation of the N7 position of the guanine base in acidic D₂O solution (pD 2).³⁴⁰ Furthermore, the weak bands at lower wavenumbers found at pH 5 and

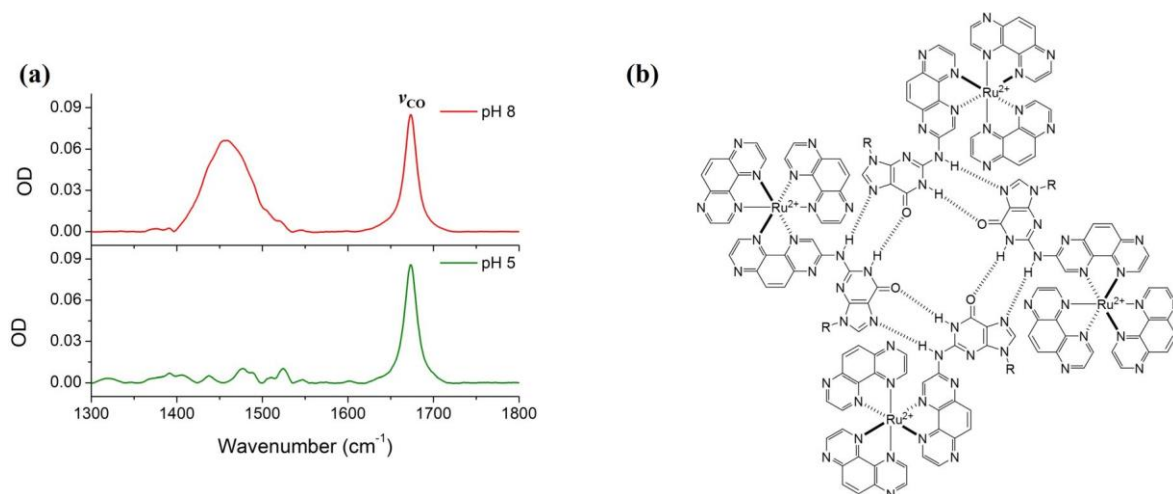


Figure 3.18. (a) FTIR spectra of **43** in 10 mM potassium phosphate-buffered D₂O solution at pH 5 (green) and 8 (red), and (b) chemical structure of a G-quartet by **43** (R = ribose-phosphate).

attributed to the **TAP** ligands were replaced by a broad and strong band centred at 1459 cm^{-1} when the FTIR spectrum of **43** was recorded at pH 8. The origin of this particular band could correspond to some intrinsic vibration of the photoadduct at such pH. It should be noted that it could also be assigned to the HOD bending ($\delta_{\text{HOD}} = 1443\text{ cm}^{-1}$)³⁴⁹ due to the presence of some water despite the great care taken in the sample preparation.

In order to gain a better understanding of the infrared features displayed by the photoadduct **43** at both pH 5 and 8, FTIR spectra of **38** and GMP were also recorded in the same conditions and are shown in Figure 3.19. Several bands of different intensity were detected between 1350 and 1650 cm^{-1} for complex **38** at both pH (Figure 3.19a) confirming the identification of the bands observed in that range in the FTIR spectrum of **43** at pH 5 as

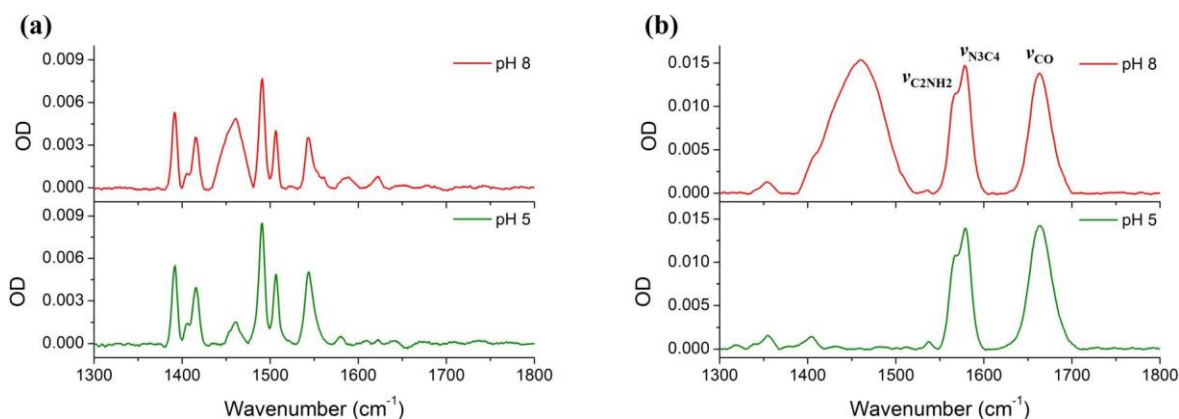


Figure 3.19. FTIR spectra of (a) **38** and (b) GMP at $800\text{ }\mu\text{M}$ in 10 mM potassium phosphate-buffered D₂O solution at pH 5 (green) and 8 (red).

vibrations from the **TAP** ligands. No significant changes were observed in the FTIR spectrum of **38** at pH 5 and 8, indicating that there is no influence of the pH on the IR properties of this complex in the conditions tested. This was not unexpected since **38** possesses a pK_a value of -2.7 , and thus neither protonation or deprotonation would occur at the pH values investigated in these experiments.³⁴⁸ Concerning the FTIR spectrum of GMP (Figure 3.19b), the band corresponding to the carbonyl C=O stretching (ν_{CO}) was found at 1664 cm^{-1} at both pH 5 and 8. A strong second band was also observed at 1579 cm^{-1} with a shoulder at 1567 cm^{-1} at both pH, and these have been assigned to purine ring vibrations, that is N3-C4 and C2-NH2 stretching (denoted ν_{N3C4} and ν_{C2NH2} , respectively), within the guanine moiety.³⁵⁰ At pH 8, GMP showed an additional strong and broad band at 1460 cm^{-1} as previously noticed for the photoadduct at that pH. Once again, no shift in the carbonyl band position was observed suggesting no protonation of the N7 position of the guanine nucleobase in the GMP at pH 5 as expected from its pK_a value of 2.48 .³³⁹ Furthermore, it has been described in the literature that protonation of the GMP in the N7 position has a dramatic impact in the band corresponding to the ring vibrations and thus the shoulder observed for that band disappears and a new band at higher frequency appears.^{340,350} This is not the case in the FTIR spectrum of the GMP recorded at pH 5 and gives further evidence of its non-protonated state at such pH which is not surprising according to its pK_a value.

FTIR has also been shown to be a powerful technique to identify guanine secondary structures that exist in solution, since the characteristic IR bands of GMP are expected to change in frequency and intensity when the nucleotide forms ordered structures.³⁵¹⁻³⁵³ In this context, significant differences were observed when the FTIR spectra described above of both **43** and GMP were compared. Thus, the carbonyl band in the GMP was found to be broad which is characteristic of solvated carbonyl groups that do not participate in Hoogsteen-type hydrogen bonding with nearby guanine molecules.³⁵³ However, this band narrowed by about 40% and shifted from 1663 in GMP to 1673 cm^{-1} in the photoadduct **43**. These changes imply more specific interactions of the carbonyl group and might be an indication of the guanine moiety being involved in Hoogsteen base-pairing or stacked tetrads formation (Figure 3.18b).^{340,353} Furthermore, the strong band at 1579 cm^{-1} corresponding to the ring vibrations in the GMP is typical of non-assembled guanines. Ring bands are, however, negligible in the FTIR of the photoadduct at both pH. A hypochromic effect on the intensity of the ring bands has been found to occur when the exocyclic NH_2 group is participating in hydrogen bonding and is considered as another evidence of guanine self-assembly.^{340,353} However, caution must be exercised when considering self-assembly as a

possible process occurring in the guanine-based ruthenium complex **43**. Guanine self-assembly has been shown to be concentration dependent and thus such process could not be extrapolatable to the results obtained by other spectroscopic techniques where much lower photoadduct concentrations were used. It must be noted that, although efforts have been made to record the FTIR spectrum of **43** at lower complex concentrations, the poor signal-to-noise ratio did not allow to clear identification of the compound IR bands and as such photoadduct concentrations lower than 800 μ M could not be employed in these studies.

The presented FTIR studies of the ground state of **43** will be particularly valuable when studying its excited state by TRIR further in this chapter. To gain further insight into the nature of **43**, the ground state of the photoadduct and its pH dependence was also investigated by circular dichroism and such studies will be discussed in the following section.

3.6.3 Circular Dichroism Studies of **43**

Tris(bidentate) octahedral Ru(II) complexes are chiral owing to the configuration of the chelating ligands around the metal centre which results in the existence of two enantiomers, that is the left-handed Λ enantiomer and the right-handed Δ enantiomer (Figure 3.20a). Despite a racemic mixture of **38** being used in the photoreaction with GMP, the resulting complex was expected to be optically active due to the incorporation of the chiral D-ribose into the molecule. Therefore, it could be anticipated that the two enantiomers that form rac-**38** would become a mixture of diastereomers after reaction with GMP (Figure 3.20b).

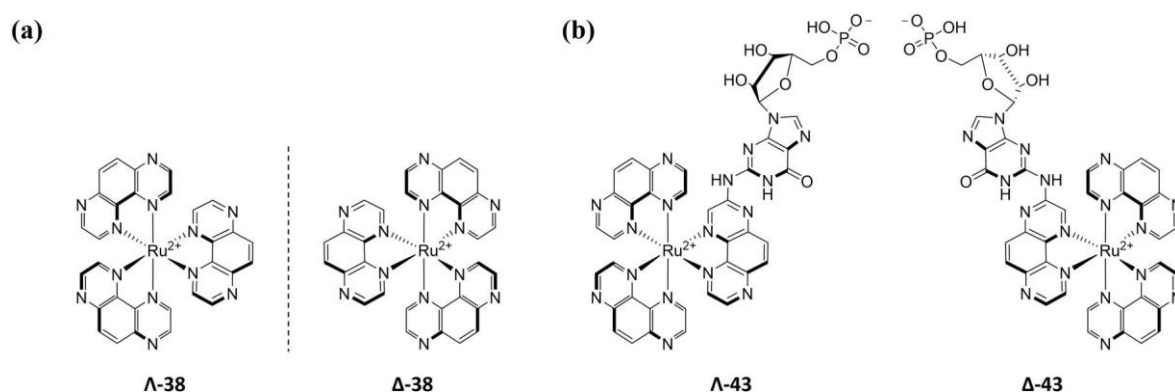


Figure 3.20. Chemical structure of (a) the left-handed Λ -38 and the right-handed Δ -38 enantiomers and (b) the Λ -43 and the Δ -43 diastereomers resulting from the photoreaction between rac-38 and GMP. Note that the ribose keeps the D configuration in both diastereomers.

As was already discussed in Section 2.5.3, circular dichroism (CD) is a spectroscopic technique based on the differential absorption of left- and right- circularly polarised light by optically active molecules and it is extensively used to study structural changes of chiral

molecules. Thus, in order to investigate the conformation adopted by the resulting diastereomeric photoadduct mixture and the influence of the solution pH on the structure, the CD spectra of **43** (9 μ M) were recorded in 10 mM potassium phosphate-buffered D₂O solution at pH 5 and 8 as shown in Figure 3.21a. At pH 5, two strong bands of opposite sign were observed in the UV-region at 280 and 300 nm that correspond to the π - π^* electronic transitions within the polypyridyl ligands, that is the two unmodified **TAP** and the GMP functionalised **TAP** ligands. In addition, another negative CD band of moderate intensity was found in the visible region at 390 nm and can be attributed to MLCT transitions. A comparable CD spectrum was observed at pH 8, although the band described above was shown to decrease in intensity.

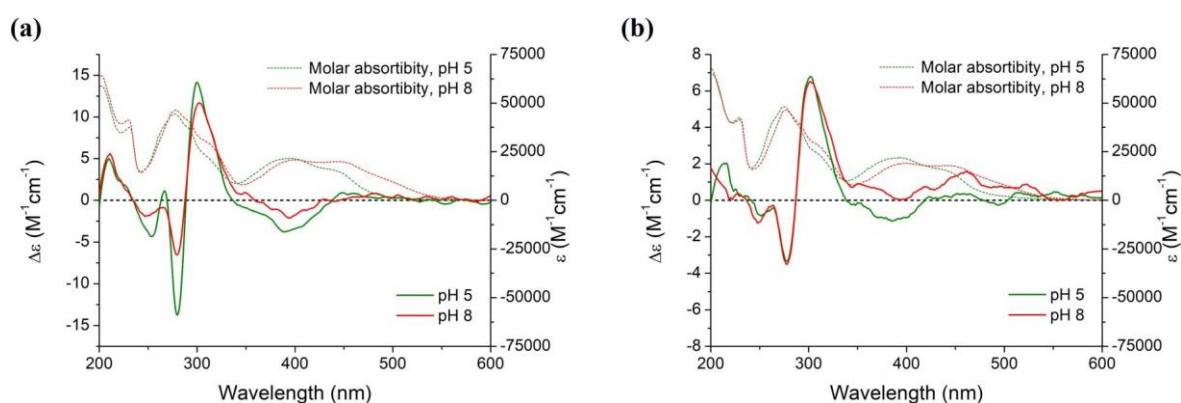


Figure 3.21. CD and molar absorption spectra of (a) **43** and (b) **77** at 9 μ M in 10 mM potassium phosphate-buffered D₂O solution at pH 5 (green) and 8 (red).

In order to confirm that the optical activity displayed by **43** was due to the presence of the chiral sugar, the CD spectrum of the photoadduct obtained after cleavage of the ribose-phosphate moiety was also recorded using the same conditions (Figure 3.21b). Surprisingly, **77** showed similar CD spectra to those found for **43** and thus, bands at 278 and 302 nm in the UV-region and at 385 nm in the visible region corresponding to π - π^* intra-ligand and MLCT transitions, respectively, were detected. It can then be concluded that the D-ribose moiety is afterwards not participating in the optical activity observed for **43** and thus another reason must be the origin of such behaviour. For example, the existence of enantioselectivity of the photoreaction occurring between rac-**38** and GMP would not be incongruous. Thus, the reaction of the guanosine radical cation (or neutral guanosine radical) with one of the enantiomers of the reduced metal complex (or protonated reduced complex) to form the photoadduct would be somewhat favoured in the encounter complex formed when both molecules approach each other through diffusion prior to the photoinduced electron transfer reaction. Furthermore, as was already mentioned in the previous section, the optical activity

exhibited by both **43** and **77** might be the result of the self-assembly of the guanine-based ruthenium complex molecules into ordered structures. Several examples have been reported in the literature about induced chirality from achiral molecules occurring after their self-assembly.³⁵⁴⁻³⁵⁷ Indeed, circular dichroism is particularly sensitive to the formation of nucleic acid secondary structures and recent studies have shown that the topologies of some G-quadruplexes displayed a positive CD band at *ca.* 300 nm.^{358,359} This interpretation would be in agreement with the FTIR experiments discussed previously although it must be taken into account that the concentration of complex used in such experiments is much larger than the concentration used to record the CD spectra and thus aggregation could be a concentration effect.

CD spectra of GMP and **38** were also recorded for comparison in 10 mM potassium phosphate-buffered D₂O solution at pH 5 and 8 and are shown in Figure 3.22. As expected, rac-**38** did not show any optical activity and proved that the photoadduct was synthesised through an unambiguously racemic mixture of the starting ruthenium complex. On the other hand, due to the chirality provided by the D-ribose, GMP showed CD signals in the UV region at 213 and 254 nm which are comparable with the CD spectrum reported in the literature for the nucleotide.³⁶⁰ No pH dependence on the CD spectra of either **38** or GMP was observed.

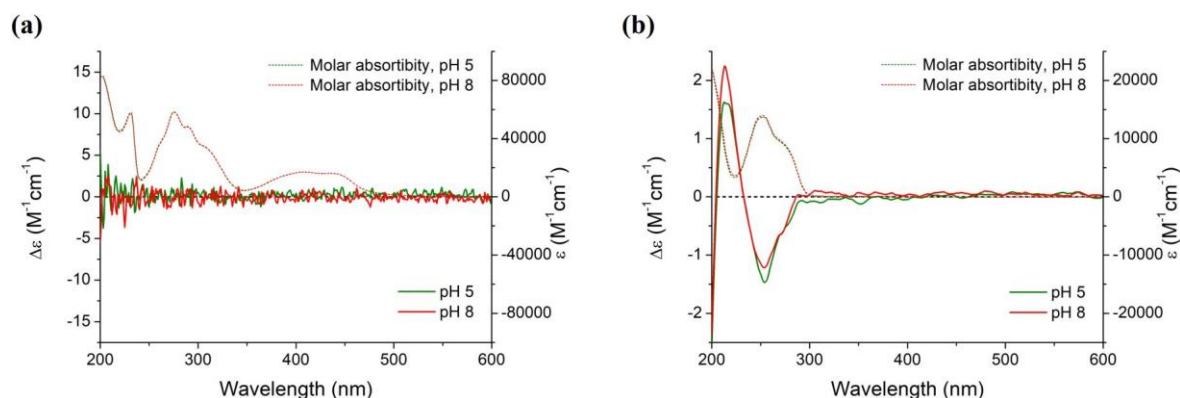


Figure 3.22. CD and molar absorption spectra of (a) **38** (9 μ M) and (b) GMP (74 μ M) in 10 mM potassium phosphate-buffered D₂O solution at pH 5 (green) and 8 (red).

Although the origin of the optical activity observed for the photoadduct (with or without the ribose-phosphate moiety) could not be precisely explained, these studies gave further evidence of the particular and intriguing behaviour of such a molecule in its ground state. In order to further investigate the ground state of **43** using a different spectroscopic technique, NMR studies at different pH and concentration conditions were conducted and are presented next.

3.6.4 Nuclear Magnetic Resonance Spectroscopic Studies of **43**

NMR spectroscopy was also employed to study the influence of the pH on the ground state of the photoadduct **43**, as the protons signals of this molecule are expected to be sensitive to changes in the environment, for example solution acidity. To date, the 1H NMR spectrum of the photoadduct (after sugar-phosphate cleavage) has only been reported once in the literature by Jacquet *et al.* and using DMSO- d_6 as a solvent.²²³ To allow comparison with the conditions for the excited-state experiments discussed in the next section, the 1H NMR (800 MHz) spectrum of **43** was recorded at 400 μ M concentration in 10 mM potassium phosphate-buffered H₂O/D₂O (95:5) solution at both pH 5 (Figure 3.23) and 8 (Figure 3.24). The sample concentration chosen for these experiments corresponds to that used in the transient spectroscopic studies that will be discussed in the following sections. It should be noted that, for clarity reasons, only the aromatic region is shown in the 1H NMR spectra presented here though the spectra corresponding to the sugar protons between 3.0 and 6.0 ppm can be found in Figures A3.12 and A3.13 of the Appendices. Assignment of the proton signals was done through 2D NMR experiments (Figures A3.14–A3.17 of the Appendices) and by comparison with the NMR spectrum of the photoadduct in DMSO- d_6 previously reported in the literature by Jacquet *et al.*²²³

At pH 5, seventeen protons were observed between 8.0 and 9.0 ppm and were assigned to the unmodified TAP ligands (green) and to the GMP functionalised TAP moiety (red). Furthermore, the proton found at 7.90–7.91 ppm was attributed to the guanine nucleobase G8 proton. Interestingly, this signal appeared to be split into two peaks with similar contribution but different shape. This feature was also observed by Jacquet *et al.* for **77** in the 1H NMR spectrum in DMSO- d_6 and was attributed to the presence of a dynamic process in the molecule due to a slow rotation of the guanine moiety about the linking N atom.²²³ Another important observation was the presence of two different species in solution and as such all the proton signals were doubled. This is particularly evident when looking at the two singlets at 8.06 and 8.04 ppm corresponding to proton 3 of the GMP modified TAP ligand. The coupling constant would be too large to assign these two signals to a doublet and they should be attributed to two independent singlets with similar chemical shift and intensity. Thus, it must be noted that, in fact, the signal integration shown in this 1H NMR spectrum only corresponds to half of the protons present in the sample solution. The two species observed could be due to the existence of two diastereomers formed after addition of the GMP containing the D-ribose to the racemic mixture of **38** as discussed in the previous section. Although the two enantiomeric forms present in rac-**38** must have protons with

identical chemical shifts, when they become diastereomers they should be easily distinguished by NMR spectroscopy. This explanation was supported by the ^{31}P NMR spectrum of **43** (inset in Figure 3.23) recorded in the same conditions where two phosphorus signals of similar intensity were found at -0.93 and -1.16 ppm.

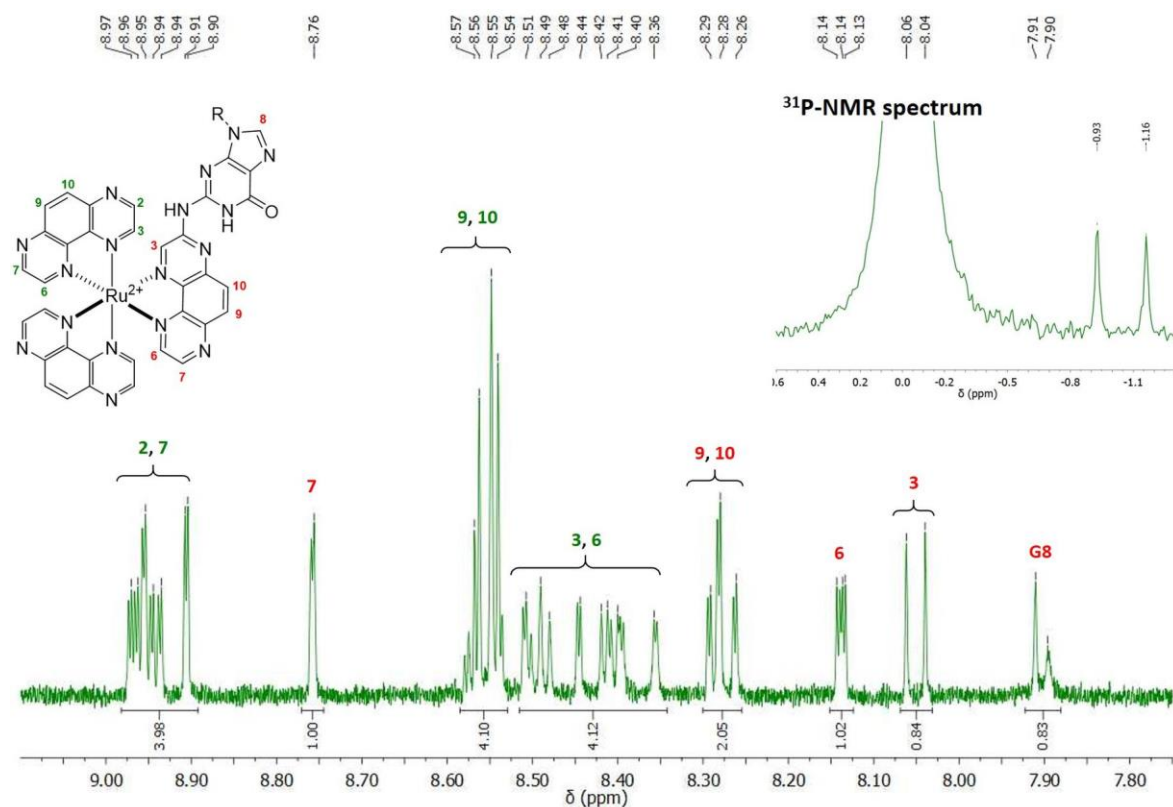


Figure 3.23. 1H NMR (800 MHz) spectrum of **43** (400 μM , R = ribose-phosphate) in 10 mM potassium phosphate-buffered H_2O/D_2O (95:5) solution at pH 5 and 293 K. Signals corresponding to TAP ligands are in green and signals assigned to TAP-GMP ligand are in red. Inset: ^{31}P NMR (162 MHz) spectrum of **43** (400 μM) in 10 mM potassium phosphate-buffered H_2O/D_2O (95:5) solution at pH 5 and 298 K.

Dramatic changes were observed in the 1H NMR spectrum of **43** recorded at pH 8 when compared to that obtained at pH 5. The overlapping, splitting and broadening of some of the signals (almost until they disappeared) make it impossible to completely assign the protons signals at this pH. Interestingly, the protons most affected by the increase of the basicity of the solution were G8 in the guanine moiety and 3, 9 and 10 in the GMP modified TAP ligand which are the protons closest to the nucleobase. Several NMR studies on the self-assembly of GMP have shown that evidence of the formation of ordered structures is the splitting of the G8 proton into four non-equivalent major signals between 7.0 and 8.5 ppm known as H_α , H_β , H_γ and H_δ .³⁶¹⁻³⁶⁶ These signals have been attributed to the existence of different aggregates, that is G-quartets (H_α and H_δ), stacking of GMP dimers (H_β) and stacking of monomers (H_γ).³⁶⁶ Although the overlapping with the signals corresponding to

the **TAP** ligands makes it difficult to identify the G8 proton that was clearly observed when the 1H NMR spectrum of **43** was recorded at pH 5, the appearance of a number of small broad signals could be a sign of the splitting of the G8 signal at pH 8. In addition, four phosphorus signals were found at 3.21, 3.10, -7.54 and -9.38 ppm at basic pH (inset in Figure 3.24) in contrast to pH 5 where only two were observed. The presence of more than one phosphorus signal has already been reported in the literature for the self-association of GMP into ordered structures in neutral or basic solution.^{363,364,366,367} In particular, Wu *et al.* have attributed this observation to the formation of two different right-handed helical structures by GMP depending on the solution acidity.^{366,367} Since the phosphate group of GMP has a pK_a of 6.25, it could be expected that it will be singly protonated at pH 5.³³⁹ The authors have proposed that the singly charged phosphate groups of the GMP would form a continuous hydrogen-bonded chain along the helical strand where the sugar moiety would be exclusively in C3'-*endo* conformation where all the phosphate groups are equivalent.³⁶⁷ Therefore, a single phosphorus signal is observed in the ^{31}P NMR spectrum of the GMP at acidic pH. On the other hand, doubly charged phosphate group can be presumed at pH 8.

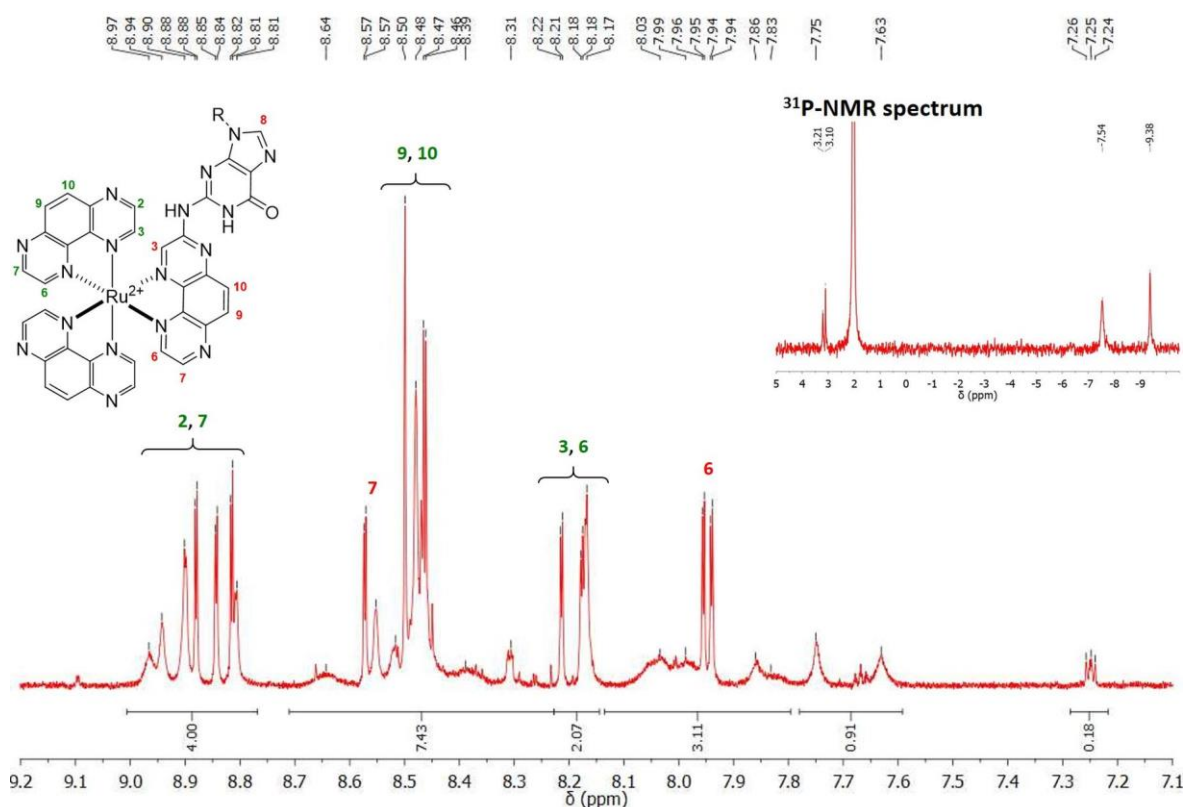


Figure 3.24. 1H NMR (800 MHz) spectrum of **43** (400 μM , R = ribose-phosphate) in 10 mM potassium phosphate-buffered H_2O/D_2O (95:5) solution at pH 8 and 293 K. Signals corresponding to **TAP** ligands are in green and signals assigned to **TAP-GMP** ligand are in red. Inset: ^{31}P NMR (162 MHz) spectrum of **43** (400 μM) in 10 mM potassium phosphate-buffered H_2O/D_2O (95:5) solution at pH 8 and 298 K.

The helical structure proposed in such conditions consists of individual GMP molecules with alternating $C2'$ -endo and $C3'$ -endo sugar pucker conformation and connected through hydrogen bonding between the deprotonated phosphate group of one GMP molecule and the hydroxyl group in the 2' or 3' position of the sugar moiety of the next GMP molecule.³⁶⁶ The existence of the ribose phosphate group in two magnetically different environments result in the presence of two ^{31}P NMR signals at pH 8. In the case of the photoadduct **43**, the presence of two different diastereomers in solution could be the reason for the appearance of four phosphorus signals at basic pH since they are expected to be doubled.

Self-assembly of the guanine moiety was also proposed as a possible explanation for some of the results of the experiments carried out on the ground state of **43** presented in previous sections. To further study the concentration effect on the photoadduct aggregation at acidic and basic pH, 1H NMR (800 MHz) dilution studies were performed at 400, 200 and 100 μM concentrations in 10 mM potassium phosphate-buffered H_2O/D_2O (95:5) solution at both pH 5 and 8 and are shown in Figures 3.25 and 3.26, respectively. At pH 5, changes in the chemical shifts of the protons of **43** were observed upon dilution and, in particular, for

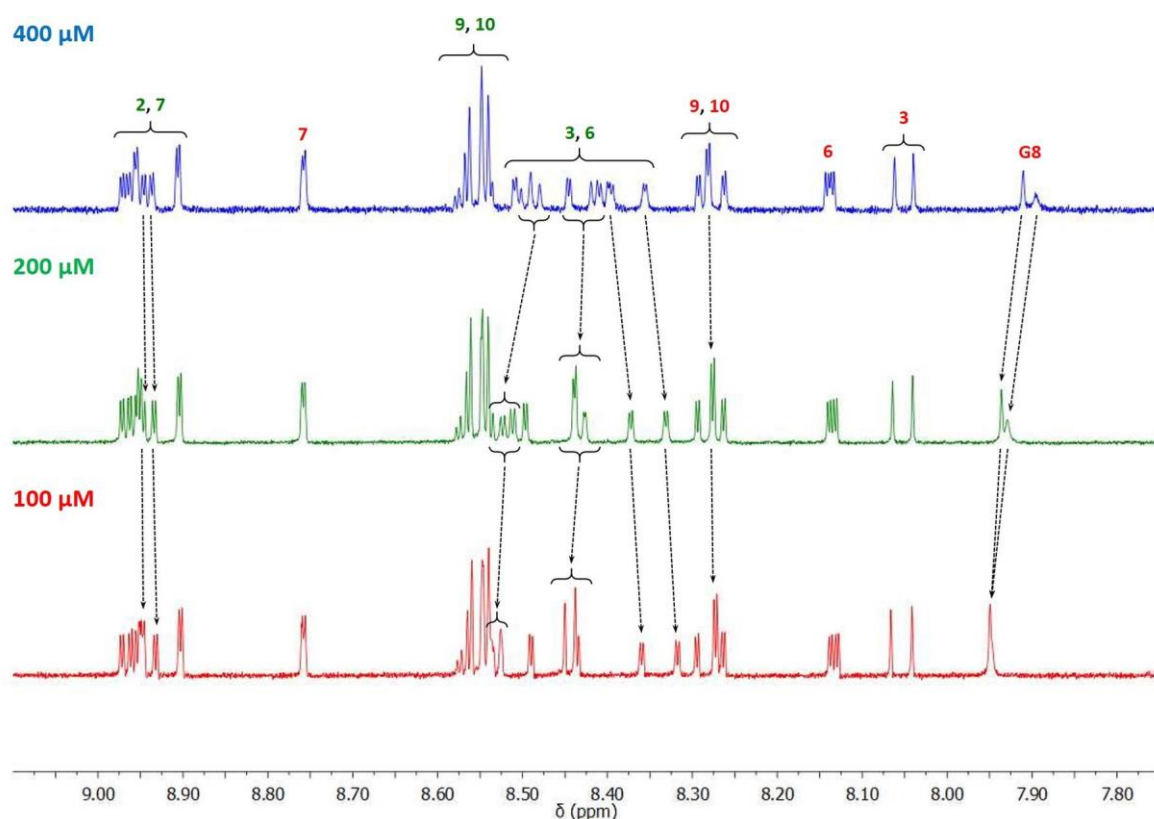


Figure 3.25. 1H NMR (800 MHz) spectrum of **43** at 400, 200 and 100 μM in 10 mM potassium phosphate-buffered H_2O/D_2O (95:5) solution at pH 5, at 293 K. Signals corresponding to TAP ligands are in green and signals assigned to TAP-GMP ligand are in red.

those corresponding to protons 3 and 6 of the unmodified **TAP** ligands. Thus, the group of signals attributed to protons 3 and 6 below 8.40 ppm showed a decrease in their chemical shifts. Furthermore, those between 8.40 and 8.45 ppm, which were well resolved at 400 μ M concentration, coalesced at lower photoadduct concentrations. Finally, some of the signals above 8.45 ppm were found to move upfield until overlapping with the signals identified as protons 9 and 10 in the unmodified **TAP** ligands. In addition, at high concentration, the two peaks found for the G8 proton of the guanine moiety at 400 μ M coalesced upon decreasing the concentration of **43** resulting in a single singlet at 100 μ M. Minor changes were observed in the group of doublets corresponding to protons 2 and 7 localised in the ancillary **TAP** ligands upon dilution, with some of the signals moving to higher chemical shifts. Furthermore, at lower photoadduct concentrations, a slight decrease in the chemical shift was found for the signal at 8.28 ppm from the group of doublets assigned to protons 9 and 10 in the GMP-functionalised **TAP** ligand. No noticeable changes were observed in the chemical shift of the protons 9 and 10 in the central phenyl ring of the unmodified **TAP** ligands, as well as in protons 7, 6 and 3 in the GMP functionalised **TAP** ligand. From this study, it can be concluded that there is aggregation of **43** at 400 μ M concentration and at pH 5 and the observed changes in the chemical shift of some of the signals would suggest that protons 3, 6 and G8 are the most likely to take part in such aggregation. It must be noted that no concentration effect was observed in the phosphorus signals (Figure A3.18 of the Appendices), indicating that the phosphate group is not affected by the aggregation of the photoadduct at acidic pH.

Changes in the chemical shift of the protons were also observed upon dilution in the 1H NMR spectrum of **43** recorded at pH 8 and pointed to aggregation of the photoadduct also occurring at basic pH. Thus, the chemical shift of signals above 8.9 ppm and identified as protons 2 and 7 in the **TAP** ancillary ligands moved slightly downfield at decreasing concentrations. Small changes with the concentration were also observed in the chemical shift of proton 7 in the **TAP-GMP** ligand and the non-identified signals between 8.5 and 8.55 ppm. Concerning protons 9 and 10 in the unmodified **TAP** ligands, minor changes were also detected in their chemical shifts. Furthermore, some of the signals attributed to the protons 3 and 6 in the **TAP** ancillary ligands were better resolved at lower concentrations. Decrease in the chemical shift of proton 6 in the **TAP-GMP** ligand was also observed upon dilution. Finally, the most drastic changes were found in the chemical shift of some of the broad and low intensity peaks that appeared between 7.6 and 8.0 ppm and could potentially correspond to the unassigned protons 3 in **TAP-GMP** and G8. Interestingly, the chemical

shifts of the protons seem to be less affected by the change in the sample concentration at basic pH than at acidic pH and could suggest that the aggregation state of **43** at both pH is different in the concentration range tested.

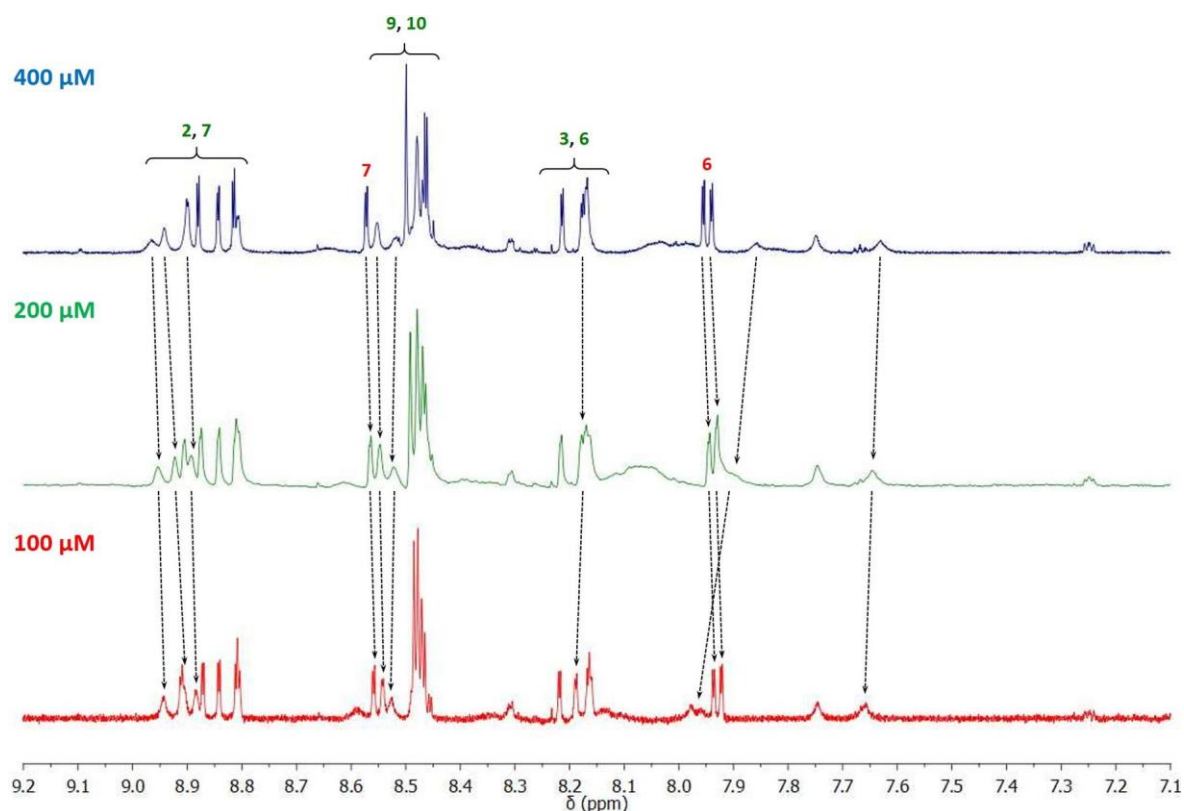


Figure 3.26. 1H NMR (800 MHz) spectrum of **43** at 400, 200 and 100 μM in 10 mM potassium phosphate-buffered H_2O/D_2O (95:5) solution at pH 8, at 293 K. Signals corresponding to **TAP** ligands are in green and signals assigned to **TAP-GMP** ligand are in red.

In addition, the 1H NMR spectrum of **43** was also recorded at 5 $^{\circ}C$, at 400 μM concentration and at both pH 5 and 8 (Figures A3.19 and A3.20 of the Appendices), as association of guanine moieties is expected to increase with decreasing temperature. At pH 5, the decrease in temperature resulted in major effects on the group of signals attributed to protons 3 and 6 in the **TAP** ancillary ligands, with dramatic broadening and overlapping of these signals observed. Changes were also evident in the signals corresponding to protons 9 and 10 in the **TAP-GMP** ligand with coalescence of some of the peaks at low temperature. Furthermore, the signals assigned to proton G8 moved downfield when the temperature was decreased while those attributed to proton 6 in the **TAP-GMP** ligand moved to higher chemical shifts. No significant changes were observed for protons 2, 7, 9 and 10 in the unmodified **TAP** ligands and protons 3 and 7 in GMP functionalised **TAP** ligand.

Concerning the temperature effect in the 1H NMR spectrum of **43** at pH 8, a decrease in temperature resulted in the broadening of all the signals. An increase of the chemical shift

of the signal attributed to proton 6 in the **TAP-GMP** ligand was observed. The broad and low intensity peaks found between 7.6 and 8.0 ppm that potentially correspond to the unassigned protons 3 in **TAP-GMP** and G8, were also found to move upfield, with no major changes observed in the chemical shift for the rest of the signals. Thus, the effect resulting from temperature variation in the 1H NMR spectrum of **43** at acidic and basic pH provides further evidence of the aggregation state of the photoadduct at 400 μM concentration and such aggregation is more likely to occur through the guanine moiety.

In the same manner as in previous sections, NMR spectroscopic studies on free GMP were also performed for comparison. The 1H NMR spectrum of GMP was recorded at 400 μM concentration in 10 mM potassium phosphate-buffered H_2O/D_2O (95:5) solution at pH values between 1 and 12 as shown in Figure 3.27. The sugar region between 3.0 and 5.0 ppm is not shown for clarity. The main changes were observed in the chemical shift of the G8 proton and the anomeric proton at the most extreme pH values 1 and 12, where the N7 position of the guanine nucleobase is expected to be protonated and the N3 position deprotonated, respectively, according to the pK_a values reported in the literature for GMP.³³⁹ Furthermore, less dramatic changes were found for these protons at pH 5, 7 and 8 where

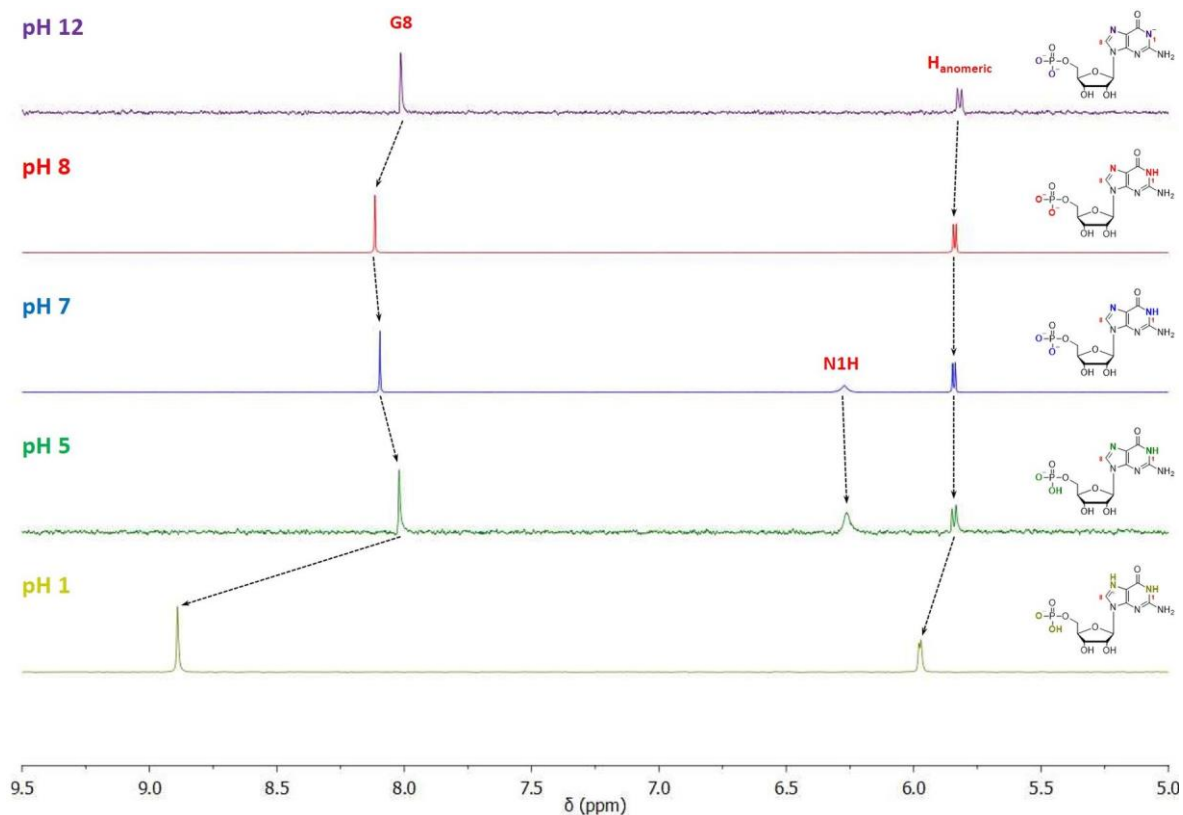


Figure 3.27. 1H NMR (400 and 600 MHz) spectrum of GMP (400 μM) in 10 mM potassium phosphate-buffered H_2O/D_2O (95:5) solution at pH 12, 8, 7, 5 and 1, at 298 K.

only deprotonation of the phosphate group is expected. Thus, the chemical shift of the signals corresponding to the G8 and anomeric protons moved slightly upfield and downfield, respectively, when decreasing the pH from 8 to 5. Interestingly, the N1H was visible at pH 5, decreased in intensity at pH 7 and finally disappeared at pH 8.

In addition, the ^{31}P NMR spectrum of the GMP was recorded in the same concentration, solvent and pH conditions (Figure 3.28). It must be noted that chemical shift values at different pH could not be compared as an internal reference was not used when recording the NMR spectra. No phosphorus signal was observed at pH 1 maybe due to acidic hydrolysis of the phosphate group in the GMP. Furthermore, while only one phosphorus signal was detected at pH 5 at a positive chemical shift, a second phosphorus signal started to appear at a negative chemical shift as the basicity of the solution was increased to pH 7, 8 and 12. As it was already observed for **43**, different number of phosphorus signals at

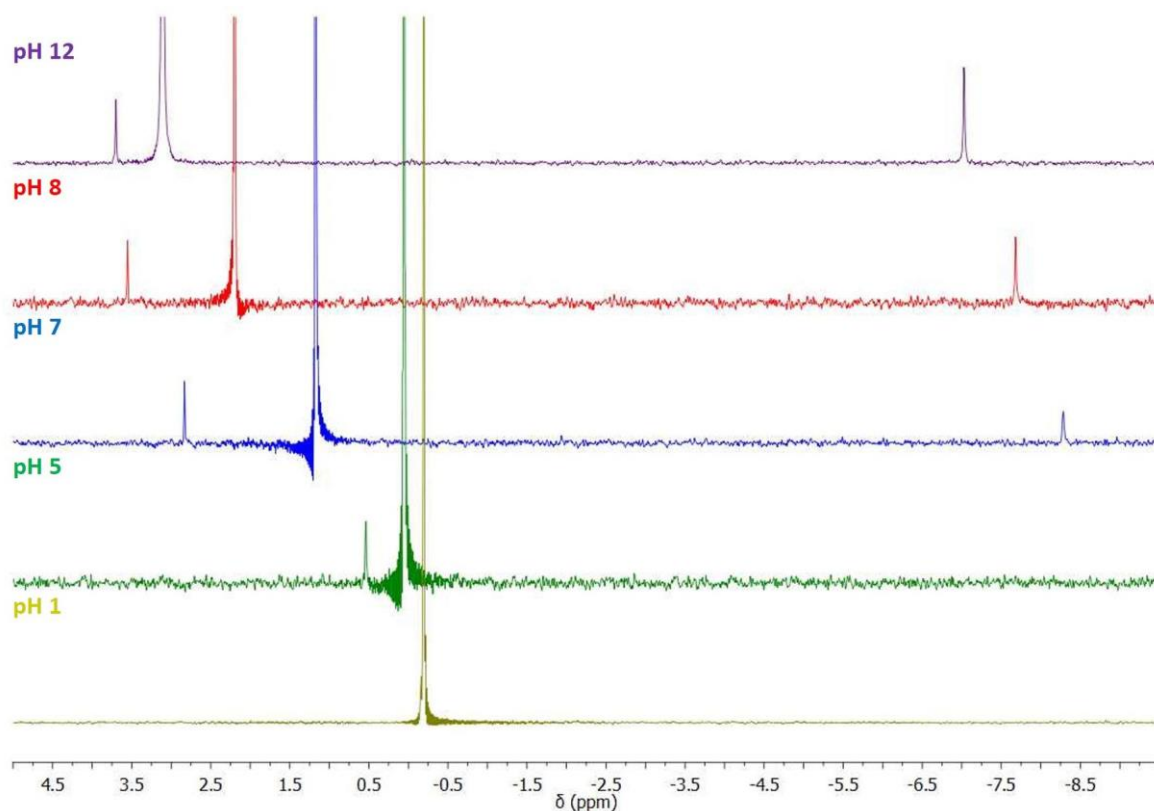


Figure 3.28. ^{31}P NMR (162 MHz) spectrum of GMP (400 μ M) in 10 mM potassium phosphate-buffered H_2O/D_2O (95:5) solution at pH 12, 8, 7, 5 and 1, at 298 K.

different pH values could be due to a different self-assembly of the GMP at acidic or basic pH resulting in different helical structures.^{366,367} However, at the concentration used in the present study, self-assembly of free GMP is not expected as it only occurs at much higher concentration according to the literature.³⁶⁸ Therefore, gradual deprotonation of the

phosphate group in the GMP when increasing the basicity of the solution could result in the existence of two magnetically different phosphorus, that is protonated phosphate GMP and deprotonated phosphate GMP, and explains the appearance of a second phosphorus signal as the pH is increased. Same interpretation could also be applied to **43**. However, in that case, aggregation of the photoadduct at 400 μ M concentration was demonstrated by dilution studies and such guanine-based aggregation could be favoured by the covalently attached metallic complex.

The NMR studies presented here again highlighted the complexity of the system resulting from the covalent attachment of the guanine-based nucleotide to the complex **38**, even in its ground state. Thus, taking previous spectroscopic studies into consideration, it is evident that the ground state of the photoadduct **43** is pH-dependent, as shown by UV-vis absorption and NMR spectroscopy. Furthermore, although the pH effect on the vibrational transitions still remains unclear, FTIR experiments suggested no protonation of the N7 position of the GMP moiety in the photoadduct at pH 5, as was previously proposed by Marcélis *et al.*²¹³ This hypothesis is based on the absence of a shift in the carbonyl band position when the FTIR spectrum of the photoadduct was recorded at pH 5 and 8, which has been reported in the literature as an indication of protonation of the N7 position in free GMP at much lower pH.³⁴⁰ Indeed, preliminary theoretical IR spectra calculated by Dr Vincent Lemaurat at Université de Mons (not shown here) have shown different positions of the carbonyl band of the GMP moiety in the photoadduct when the N7 position was protonated or deprotonated, in agreement with that observed for protonated/deprotonated free GMP.

The combined spectroscopic studies performed on the ground state of the photoadduct have also shown that this pH dependence is unique for the system resulting from a combination of both **38** and GMP (or G), as a pH effect was not observed for the unbound moieties. In addition, CD experiments have shown that the photoadduct **43** was optically active, independent of the presence of the ribose-phosphate moiety, although the origin of this chirality still remains unknown. Furthermore, NMR dilution studies indicated that aggregation of the photoadduct **43** occurs at 400 μ M at both pH 5 and 8. According to the spectroscopic studies presented above, aggregation does not have an effect on the UV-vis absorption spectrum of the photoadduct, although it may influence the IR properties of this compound. If this aggregation occurs through stacking of the GMP moieties or G-tetrads formation is still uncertain, but this is particularly relevant to the spectroscopic studies conducted on the excited state of the photoadduct **43** and described in the following section, as aggregation can have dramatic consequences on the photophysical properties of this

molecule. However, the original authors of this work did not consider aggregation in their studies and as such it will be assumed that aggregation of the photoadduct does not have a significant effect on the results obtained from the spectroscopic studies carried out on the excited state and presented next.

3.7 Spectroscopic Studies of the Excited State of **43** at Different pH Values

As was previously mentioned in Section 3.1, the main purpose of this research work was to build upon the previous studies conducted by Andrée Kirsch-De Mesmaeker and co-workers to further understand the mechanism by which the photoadduct **43** is able to react with a second molecule of GMP, despite its non-emissive character.²¹³ These researchers found that the bi-photoadduct could only be generated at slightly acidic pH (pH 5–6), while addition of a second GMP to the mono-photoadduct **43** was not observed at basic pH. This pH-dependent photoreactivity was proposed to be due to the existence of two different excited states, that is, reactive MLCT states at pH 5–6 and unreactive LLCT/ILCT states at pH 8. Therefore, this section will be focused on gaining more information about these excited states using different spectroscopic techniques. In this context, time-resolved spectroscopy has proved to be a useful technique in elucidating the excited-state processes occurring in Ru(II) polypyridyl complexes.^{166,211-213,227,279-284,341,344,369-377} In particular, transient absorption (TrA) and time-resolved infrared (TRIR) spectroscopy are the two ultrafast techniques employed in this section to investigate the electronic and vibrational transitions within the excited state of the photoadduct **43** at different pH values.

Both TrA and TRIR uses pump-probe spectroscopy in which sample molecules are excited with a short pulse (pump) of light and, after a particular period of time, sample changes induced by the pump (*e.g.* formation of excited states or short-lived reaction intermediates) are monitored by a second pulse (probe) of visible light (400–800 nm) in TrA or mid-IR (1200–1800 cm^{-1}) in TRIR. The intensity of the probe light transmitted by the sample is measured before and after photo-excitation. The ground-state spectrum is subtracted from that of the excited state, resulting in a difference spectrum in which the negative bands (bleach bands) correspond to regions of the spectrum where the ground state absorbs more strongly than the excited state and the positive bands (transient bands) are attributed to the excited state absorbing more strongly than the ground state. Varying the time delay between the pump and the probe pulses provides valuable kinetic information about the recovery time of the ground state and the lifetime of the transient species and any other intermediates formed.

Therefore, based on the potential of the time-resolved spectroscopic techniques, TrA and TRIR studies in the picosecond (both TrA and TRIR) and nanosecond (TRIR) time domains were performed on the photoadduct **43** in buffered D₂O solution at different pH values and will be next discussed. It must be noted that, for reasons of signal to noise ratio, transient studies were carried out at 400 μ M sample concentration. These experiments were conducted at the Central Laser Facility of the Science & Technology Facilities Council in the Rutherford Appleton Laboratory (UK).

3.7.1 ps-Transient Absorption Studies of **43**

The main purpose of this project was to investigate the nature and the pH-dependence of the excited state of **43** and transient photoproducts by TRIR spectroscopy. In addition, TrA spectroscopy was also employed in order to directly compare these results with those from previously reported by Marcélis *et al.*²¹³ The ps-TrA spectra of **43** (400 μ M) were recorded in 50 mM potassium phosphate-buffered D₂O solution at pH 5, 6, 7 and 8 and at various time delays after excitation at 373 nm. The TrA spectra at a short (10 ps) and a long (1500 ps) time delay after excitation of the photoadduct at the four pHs under investigation are shown in Figure 3.29 and confirm the influence of pH on the excited state of **43**. A negative bleach

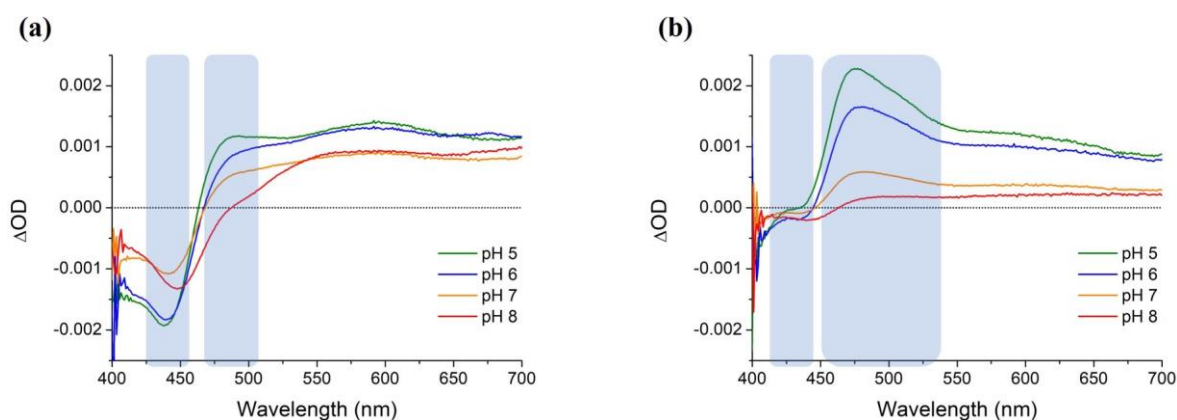


Figure 3.29. ps-TrA spectra recorded at (a) 10 ps and (b) 1500 ps after 373 nm excitation of **43** (400 μ M) in 50 mM potassium phosphate-buffered D₂O solution at different pH values.

band centred at wavelengths between 435 and 450 nm (depending on the pH) was observed in the TrA spectra recorded at 10 ps after excitation at the four pH conditions tested (Figure 3.29a) and corresponds to the loss of the MLCT absorbance of the ground state of **43**. The pH-dependent shift observed in this bleach band was due to the changes in the UV-vis absorption spectra showed by the ground state of **43** at different pHs, as previously discussed in Section 3.6.1. In addition, a transient band at *ca.* 480 nm was present at acidic pHs, but less evident at neutral pH and absent at basic pH. This band overlapped with a second broad

transient band at wavelengths above 550 nm, which is assigned to the excited-state species generated after excitation of **43**. A growth of the transient band at *ca.* 480 nm was observed at 1500 ps after excitation at acidic pH, while no significant changes were found for the second broad transient band (Figure 3.29b). However, at pH 7 and 8 the decay of the excited state to the ground state of **43** was observed, being almost complete by 1500 ps at basic pH, as evidence from the recovery of the bleach and the transient bands.

Having shown that the TrA spectrum of **43** is sensitive to the pH, the rest of the discussion of this section will be focused only on the TrA spectra of **43** at both pH 5 and 8, as the photoadduct behaviour in its excited state was found to be very similar at pH 5 and 6, and the TrA spectrum at pH 7 seemed to be intermediate between acidic and basic pH. Thus, the ps-TrA spectra of **43** in the conditions described above at various time delays after excitation at 373 nm and at both pH 5 and 8 are shown in Figure 3.30 (with those at pH 6 and 7 given in Figure A3.21 of the Appendices) and were found to be similar to those reported by Marcélis *et al.*²¹³ The corresponding UV-vis absorption spectra of **43** in its ground state are also included for comparison.

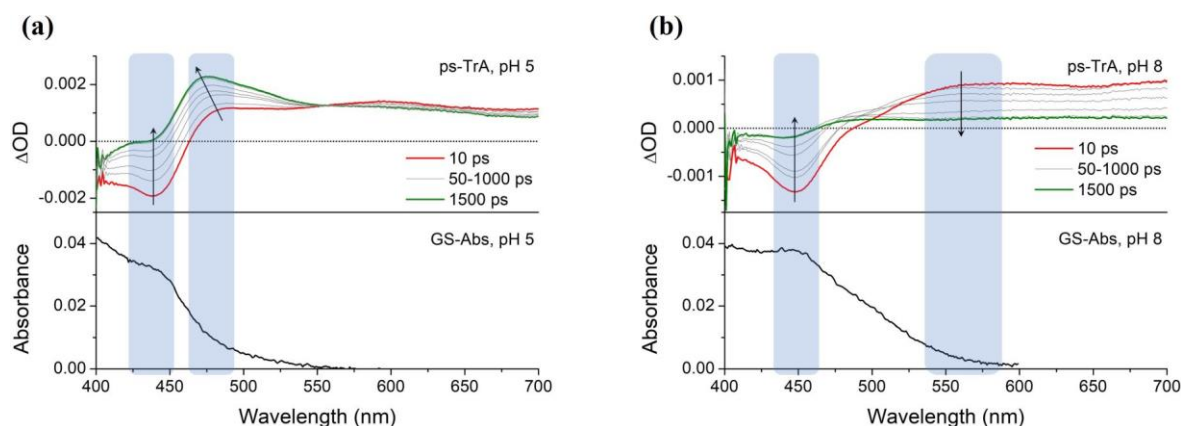


Figure 3.30. ps-TrA spectra recorded at the stated time delays after 373 nm excitation of **43** (400 μ M) in 50 mM potassium phosphate-buffered D_2O solution at (a) pH 5 and (b) pH 8, and the corresponding ground-state absorption (GS-Abs) spectra.

As was previously mentioned, the ps-TrA spectra of the photoadduct at pH 5 was characterised by a bleach band at 437 nm and a transient band at 477 nm with a broad shoulder from 550 nm (Figure 3.30a). This transient band was found to grow and blue shift to 470 nm over the timescale of the experiment, suggesting that the processes involved in the appearance of this band are not simple. The origin of this positive band was attributed to the presence of the GMP moiety in the photoadduct structure by Marcélis *et al.*, as this band was absent in the reported TrA spectrum of the parent complex **38**.²¹³ Interestingly, no recovery of the ground state of **43** was observed during the timescale of the measurement,

which indicated the existence of a long-lived species at pH 5. The nature of this new species formed will be further discussed in the following section from TRIR measurements. It must be mentioned that, despite its long-lived character, this species is non-emissive and as such, no luminescence from the photoadduct is observed, as previously discussed in Section 3.6.1. Bi-exponential fit of the ΔOD at 437 nm gave lifetime values of 63 ± 16 ps (52%) and 348 ± 82 ps (48%) (Figure 3.31a). Furthermore, the kinetics of the grow-in of the transient band at 477 nm was fitted to a bi-exponential function and yielded a short lifetime value of 86 ± 33 ps (31%) and a long lifetime value of more than 1500 ps (69%) (Figure 3.31b). It must be noted that, due to the complexity of the system and because the primary interest of this study was to analyse the long-lived species, kinetics were fitted from 10 ps. Before 10 ps a combination of cooling processes (intramolecular vibrational relaxation (IVR) and vibrational relaxation (VR)) were proposed to occur by Marćelis *et al.*²¹³

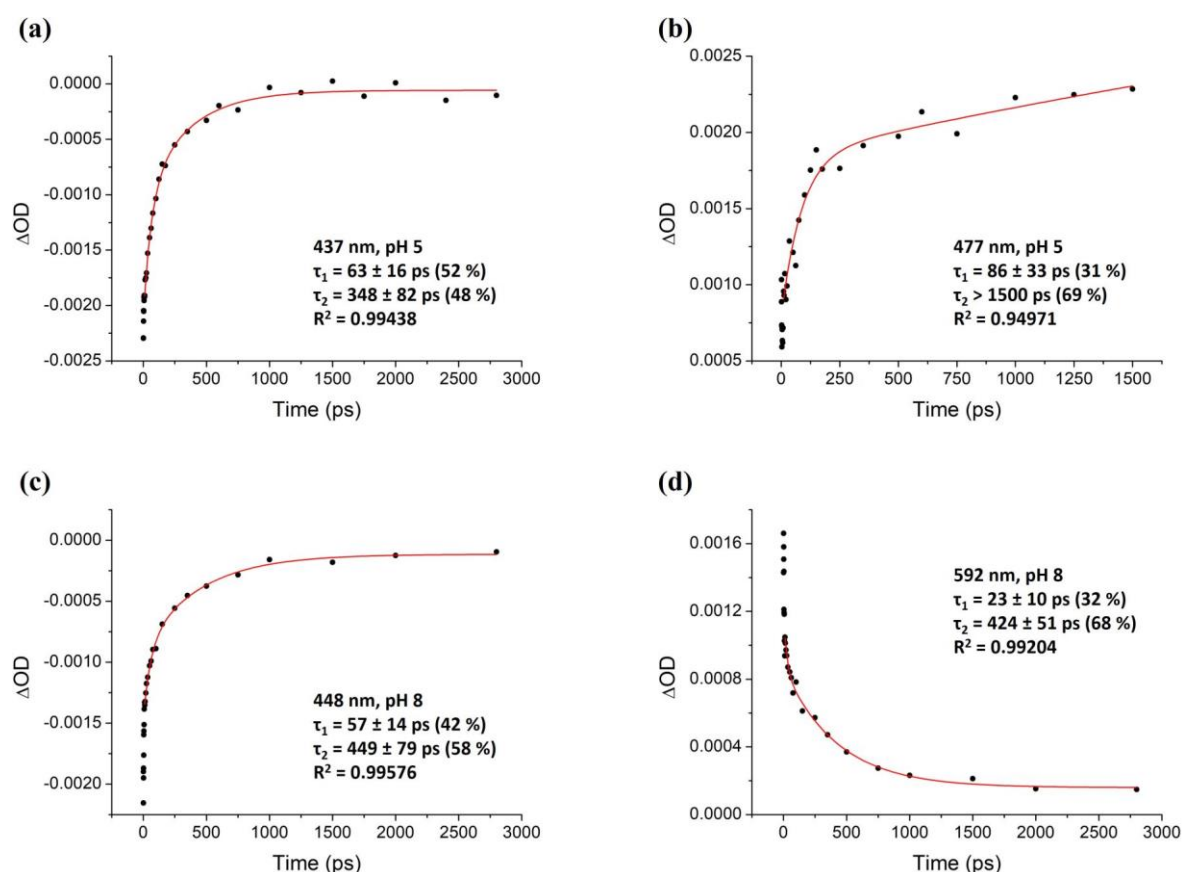


Figure 3.31. Bi-exponential fit to the ΔOD at (a) 437 nm, (b) 477 nm, (c) 448 nm and (d) 592 nm in the corresponding ps-TrA spectra ($\lambda_{exc} = 373$ nm) of **43** (400 μM) in 50 mM potassium phosphate-buffered D_2O solution at pH 5 (a, b) and 8 (c, d). Note that data were fitted between 10–2800 ps (a, c, d) and 10–1500 ps (b).

The ps-TrA spectra of the photoadduct **43** at pH 8 exhibited a bleach band at 448 nm and a broad transient band centred at *ca.* 590 nm (Figure 3.30b). In contrast to spectra

observed at pH 5, a decay of the transient band with a concomitant recovery of the bleach band was observed over the timescale of the experiment, which indicated that the ground state was reformed within the experimental timescale. Bi-exponential fit of the bleach band at 448 nm resulted in lifetime values of 57 ± 14 ps (42%) and 449 ± 79 ps (58%) (Figure 3.31c), while the transient band at 590 nm was also observed to decay bi-exponentially with similar lifetime values of 23 ± 10 ps (32%) and 424 ± 51 ps (68%) (Figure 3.31d).

As was previously demonstrated for the ground state, these results clearly show the influence of the solution pH on the nature of the excited state of the photoadduct **43** with the formation of long-lived species only at acidic pH. Further investigation into the excited state of **43** by ps- and ns-TRIR will be next discussed.

3.7.2 ps- and ns-Time-Resolved Infrared Studies of **43**

The ps-TRIR spectra of **43** were recorded in the mid-IR ($1300\text{--}1800\text{ cm}^{-1}$) using the same conditions as in the ps-TrA spectra described above, that is, at $400\text{ }\mu\text{M}$ sample concentration, in 50 mM potassium phosphate-buffered D_2O solution at pH 5, 6, 7 and 8, and at various time delays after photo-excitation at 373 nm . The spectral range chosen for this experiment corresponds to the region where the aromatic ring breathing modes of the polypyridyl ligands appear as well as the carbonyl stretching and purine ring vibrations in the guanine moiety.^{340,378} Since H_2O absorbs strongly in this region, D_2O was required for the study.

The TRIR spectra at a short (10 ps) and a long (1500 ps) time delay after excitation of **43** at the four pHs under investigation are shown in Figure 3.32. As was already noticed in the TrA experiments, a pH-dependence of the excited state of the photoadduct was also evidenced by TRIR measurements. At the time delay of 10 ps four main bands were observed

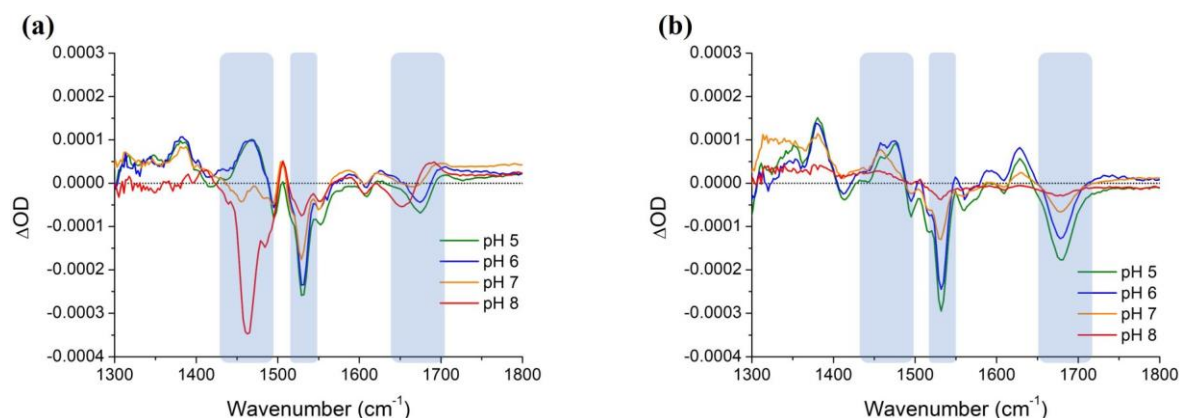


Figure 3.32. ps-TRIR spectra recorded at (a) 10 ps and (b) 1500 ps after 373 nm excitation of **43** ($400\text{ }\mu\text{M}$) in 50 mM potassium phosphate-buffered D_2O solution at different pH values.

in the TRIR spectrum of **43** recorded at acidic pH (Figure 3.32a), two positive bands at *ca.* 1465 and 1700 cm^{-1} corresponding to new vibrations of the transient species, and two negative bands at *ca.* 1530 and 1675 cm^{-1} assigned to the depopulation of the ground state. Interestingly, the transient band at *ca.* 1465 cm^{-1} observed at acidic pH appears as a strong bleach band when the TRIR spectrum of **43** was recorded at pH 8. Furthermore, the bleach band at *ca.* 1530 cm^{-1} was found to be weaker in intensity at basic pH than at acidic pH. Moreover, the bands at *ca.* 1675 and 1700 cm^{-1} present at acidic pH shifted to shorter wavenumbers at pH 8. In addition, the TRIR spectrum of **43** recorded at neutral pH was found to display an intermediate behaviour between those recorded at acidic and basic pHs.

The TRIR spectra of **43** recorded at 1500 ps after excitation at acidic pH showed that the two bleach bands at *ca.* 1530 and 1675 cm^{-1} were stronger in intensity (Figure 3.32b). Moreover, no significant changes were observed for the transient band at *ca.* 1465 cm^{-1} while the weak positive band at *ca.* 1700 cm^{-1} was found to disappear at this time delay. However, a recovery of the ground state was observed at pH 8 after 1500 ps, while the TRIR spectrum of **43** recorded at pH 7 showed intermediate features from both acidic and basic pH.

Having demonstrated that the TRIR spectrum of **43** is strongly influenced by pH, further analysis will focus on the TRIR spectra of the photoadduct at both pH 5 and 8, as these are the most representative values to study the pH-dependent behaviour of **43** in its excited state. The ps-TRIR spectra of **43** recorded in the conditions described above, at various time delays after excitation at 373 nm and at both pH 5 and 8 are shown in Figure 3.33 (those at pH 6 and 7 are given in Figure A3.22 of the Appendices), with the corresponding ground-state FTIR spectra included for comparison. As previously

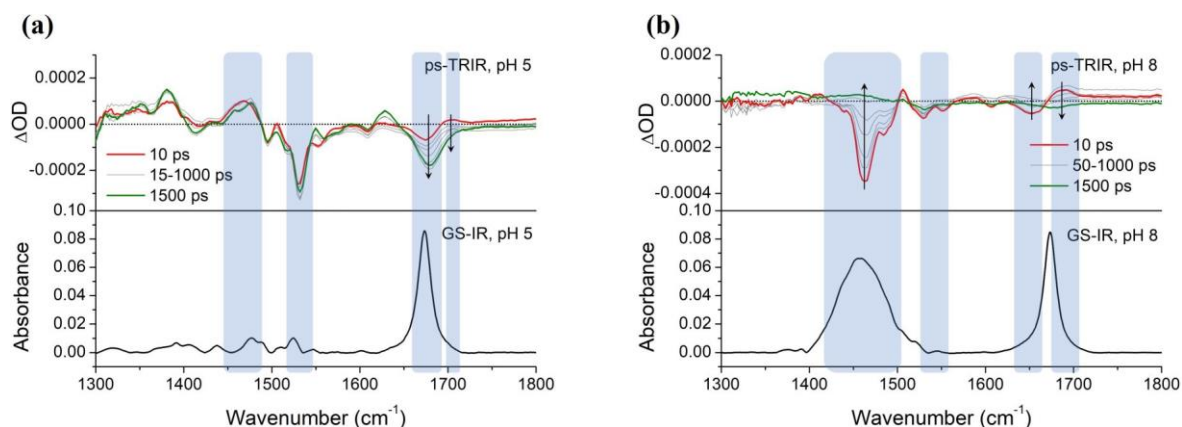


Figure 3.33. ps-TRIR spectra recorded at the stated time delays after 373 nm excitation of **43** (400 μM) in 50 mM potassium phosphate-buffered D_2O solution at (a) pH 5 and (b) pH 8, and the corresponding ground-state FTIR (GS-IR) spectra at 800 μM .

mentioned, at pH 5, two transient bands at 1468 and 1706 cm^{-1} , and two bleach bands at 1532 and 1678 cm^{-1} were mainly observed within 10 ps after photo-excitation (Figure 3.33a). By comparison with the ground-state FTIR spectrum of **43**, the bleach band observed at 1678 cm^{-1} was assigned to the carbonyl stretching in the guanine moiety. In addition, according to the literature, the appearance of a species absorbing at *ca.* 1700 cm^{-1} is consistent with the formation of the guanine radical cation ($G^{\bullet+}$).³⁷⁹⁻³⁸² If this is the case, it means that, even within 10 ps, the **TAP** complex has already oxidised the guanine moiety. The intramolecular electron transfer in this system is faster than that occurring between the excited state of **38** and free GMP due to the intermolecular reaction between these two free molecules is diffusion limited.²¹²

The transient band at 1706 cm^{-1} was found to decay mono-exponentially with a lifetime of 128 ± 13 ps (Figure 3.34a). Interestingly, as this species disappeared, the bleach band corresponding to the guanine carbonyl stretching became more apparent with a similar lifetime of 110 ± 7 ps (Figure 3.34c) and indicated the formation of a long-lived species in which $G^{\bullet+}$ is not forming G when it decays. This behaviour suggests the existence of some structural change in G when forming the long-lived species which results in the loss of its carbonyl character. To further examine the nature of this long-lived species, the system was also investigated on the nanosecond timescale, which will be discussed later in this section. Furthermore, no significant changes were observed in the transient band at 1468 cm^{-1} within the first 1500 ps after excitation and only minor changes were observed by the strong bleach band at 1532 cm^{-1} , which was found to increase in magnitude with a lifetime of 111 ± 21 ps (Figure 3.34e). This suggests minimal perturbation of the Ru(TAP) moiety while this new species is being formed within the first 1500 ps. Although the exact origin of these bands still remains unknown, according to the ground-state FTIR spectrum of **43**, they could be assigned to vibrations within the **TAP** ligands. It must be noted that mono-exponential fits to the data were done from 10 ps (unless otherwise stated) in order to exclude very fast process and facilitate the analysis.

Concerning the ps-TRIR spectra of **43** recorded at pH 8 (Figure 3.33b), one transient band at 1688 cm^{-1} and three bleach bands at 1463, 1529, and 1654 cm^{-1} appeared at 10 ps after photo-excitation. Similar to what was observed at pH 5, bands at 1688 cm^{-1} (transient) and 1654 cm^{-1} (bleach) were attributed to the formation of $G^{\bullet+}$ and to the guanine carbonyl stretching, respectively. However, these bands were shifted to shorter wavenumbers, when compared with those of the complex at pH 5. Furthermore, the decay to the ground state was

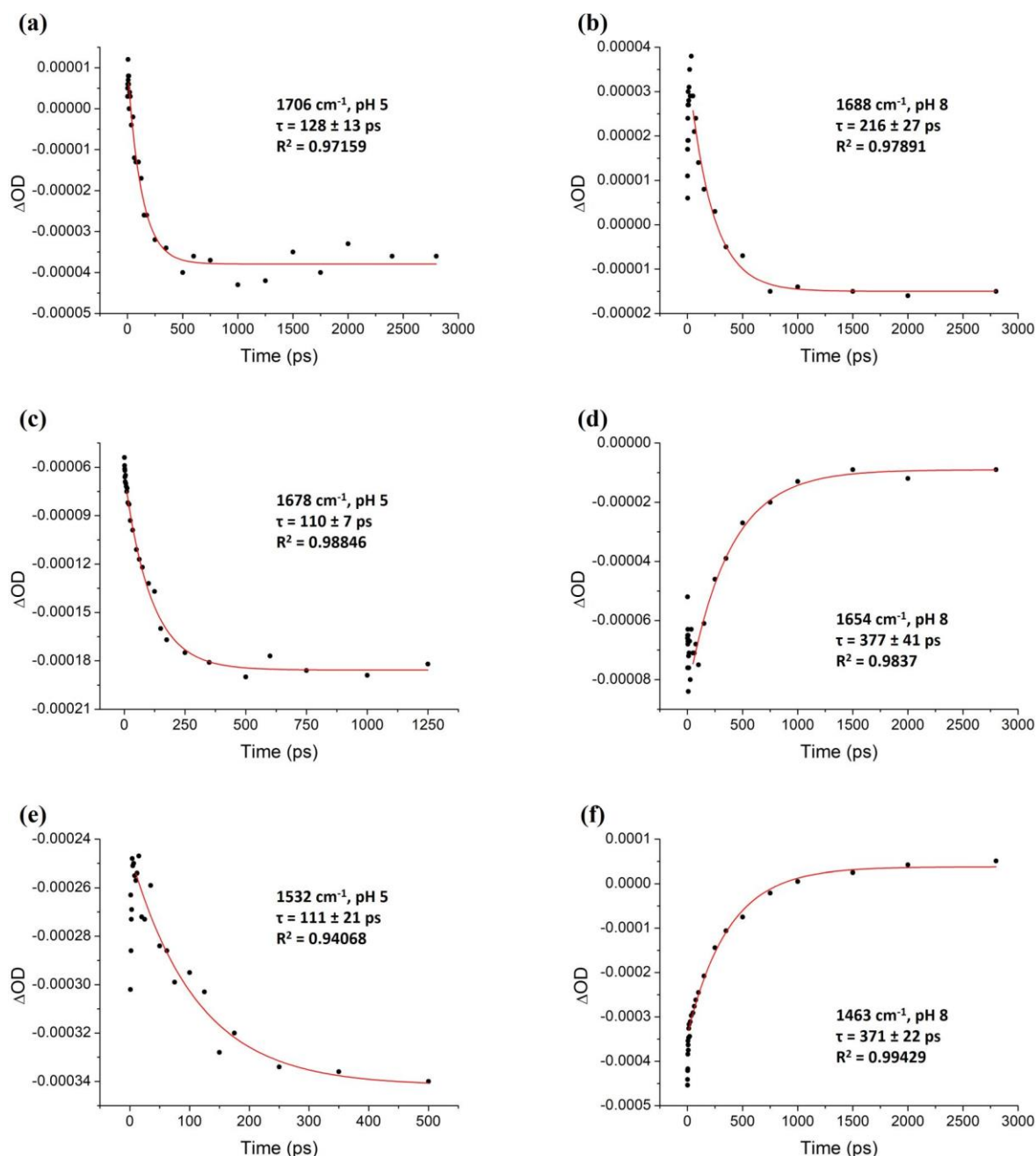


Figure 3.34. Mono-exponential fit to the ΔOD at (a) 1706 cm^{-1} , (b) 1688 cm^{-1} , (c) 1678 cm^{-1} , (d) 1654 cm^{-1} , (e) 1532 cm^{-1} and (f) 1463 cm^{-1} in the corresponding ps-TRIR spectra ($\lambda_{exc} = 373$ nm) of **43** (400 μM) in 50 mM potassium phosphate-buffered D_2O solution at pH 5 (a, c, e) and 8 (b, d, f). Note that data were fitted between 10–2800 ps (a), 10–2800 ps (c), 10–1250 ps (e), 50–2800 ps (b, d) and 10–2800 ps (f). For a better fit of the data, the baseline was corrected in the kinetics analysis of (a)–(d) by subtracting the ΔOD at 1749 cm^{-1} from the ΔOD at 1706 cm^{-1} (a), 1678 cm^{-1} (c), 1688 cm^{-1} (b) and 1654 cm^{-1} (d) in the same spectrum.

observed to occur in 216 ± 27 ps for the transient band at 1688 cm^{-1} (Figure 3.34b), and in 377 ± 41 ps for the bleach band at 1654 cm^{-1} (Figure 3.34d). These results suggest that, in contrast to pH 5, G^{*+} converts to G without formation of a long-lived species, in agreement with the ps-TrA experiments previously discussed. The reason that the lifetime value determined by mono-exponential fit to the ΔOD at 1688 cm^{-1} was shorter than that calculated for the decay of the band at 1654 cm^{-1} is still unknown. Moreover, as was previously noted,

the transient band observed at 1468 cm^{-1} at pH 5 was replaced by a strong bleach band centred at 1463 cm^{-1} when the TRIR spectra were recorded at pH 8. This bleach band was found to decay with a lifetime of $371 \pm 22\text{ ps}$ (Figure 3.34f), which was very similar to that determined for the bleach band at 1654 cm^{-1} , and presumably correspond to a vibration within the **TAP** ligands. Interestingly, this strong bleach band appeared at the same wavenumber as the broad and strong band observed in the FTIR spectrum of **43** recorded at pH 8. Finally, the bleach band at 1529 cm^{-1} was found to be much weaker than the analogue bleach band recorded at pH 5.

To further investigate the long-lived species formed at pH 5, TRIR measurements in the nanosecond time domain were conducted. Thus, the ns-TRIR spectra of **43** ($400\text{ }\mu\text{M}$) were also recorded in 50 mM potassium phosphate-buffered D_2O solution at pH 5 and at various time delays after photo-excitation at 400 nm (Figure 3.35a). The corresponding ns-TRIR spectra at pH 6 and 7 are given in Figure A3.23 of the Appendices and, as previously mentioned, those recorded at pH 6 showed to be similar to pH 5 while the ns-TRIR spectra at pH 7 seemed to be intermediate between acidic and basic pH and as such, they are not discussed here.

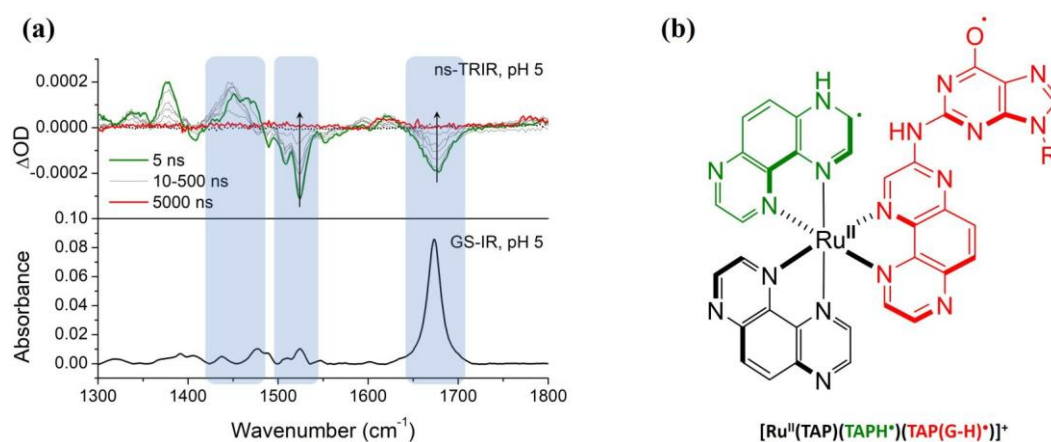


Figure 3.35. (a) ns-TRIR spectra recorded at the stated time delays after 400 nm excitation of **43** ($400\text{ }\mu\text{M}$) in 50 mM potassium phosphate-buffered D_2O solution at pH 5 and the corresponding ground-state FTIR (GS-IR) spectra at $800\text{ }\mu\text{M}$. (b) Proposed chemical structure of the long-lived biradical species formed after photo-excitation of **43** at pH 5.

The decay of the long-lived species to the ground state was found to occur within 5000 ns after photo-excitation of **43**, as evidenced from the recovery of the transient band at *ca.* 1460 cm^{-1} as well as the bleach bands at 1524 and 1676 cm^{-1} during this timescale. Bi-exponential fit to the kinetics of the bleach band at 1676 cm^{-1} that corresponds to the guanine carbonyl stretching yielded a short lifetime of $29 \pm 5\text{ ns}$ (37%) and long lifetime of $545 \pm 118\text{ ns}$ (63%) (Figure 3.36a). Similar lifetimes of $38 \pm 14\text{ ns}$ (49%) and $526 \pm 148\text{ ns}$ (51%)

were obtained from the decay of the bleach band at 1524 cm^{-1} (Figure 3.36b). Therefore, an average lifetime of *ca.* 535 ns can be estimated for the long-lived species formed after photoexcitation of **43** in acidic solution.

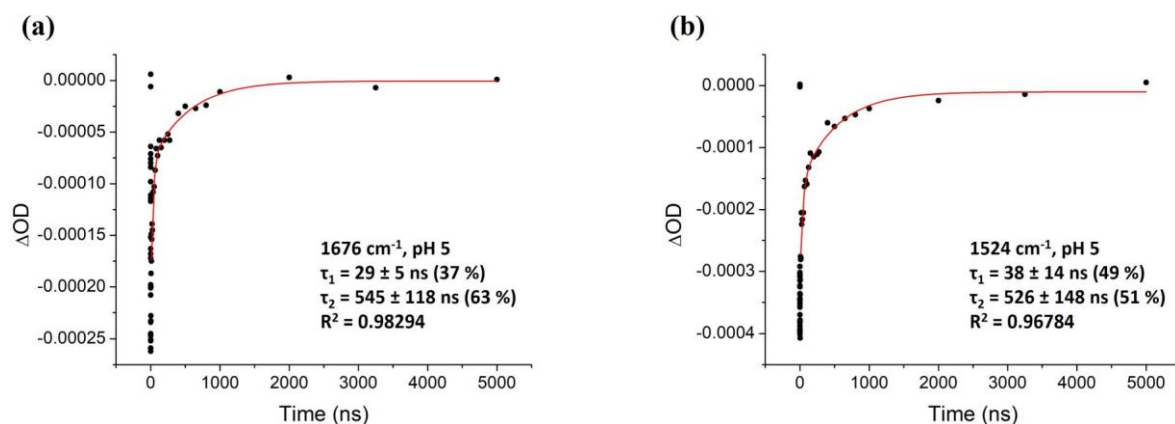
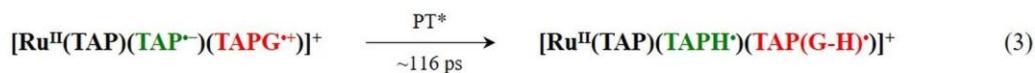
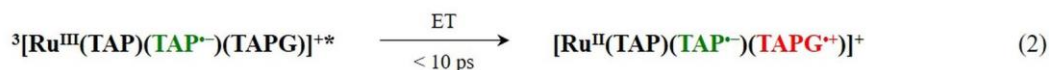
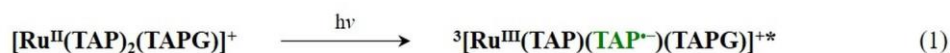


Figure 3.36. Bi-exponential fit to the ΔOD at (a) 1676 cm^{-1} and (b) 1524 cm^{-1} in the corresponding ps-TRIR spectra ($\lambda_{exc} = 400\text{ nm}$) of **43** ($400\text{ }\mu\text{M}$) in 50 mM potassium phosphate-buffered D_2O solution at pH 5. Note that data were fitted between 10–5000 ns.

Based on the results described above, two different mechanism can be proposed to occur at pH 5 and 8 (Schemes 3.4 and 3.5, respectively):

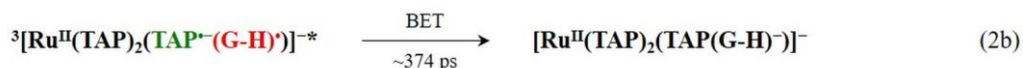
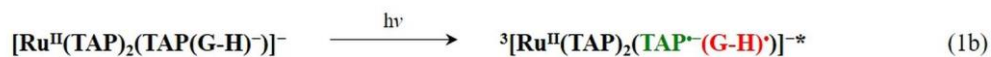
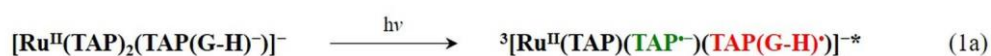
- At pH 5 it is assumed that the ground state of **43** existed in its non-protonated form at pH 5 (*i.e.* $[Ru^{II}(TAP)_2(TAPG)]^+$), as previous studies performed on the photoadduct in its ground state gave no evidence of protonation of the guanine moiety. Therefore, after excitation of the non-protonated **43** a 3MLCT excited state was generated (*i.e.* $^3[Ru^{III}(TAP)(TAP^{\bullet-})(TAPG)]^{+*}$; Scheme 3.4 (1)). Within 10 ps, oxidation of the guanine moiety *via* an intramolecular electron transfer (ET) from the



Scheme 3.4. Proposed mechanism of the dynamic processes that occur after excitation of **43** in deuterated aqueous solution at pH 5. *Deprotonation of the guanine radical cation may occur simultaneously to the oxidation reaction (*i.e.* PCET).²⁰⁸ Note that the lifetime values reported correspond to the average of those obtained by exponential fit to the different bands data. Only the long components of the bi-exponential fit to the bands data from ns-TRIR experiments were considered. It must be also noted that the overall charge of **43** in its ground state at pH 5 corresponds to the GMP moiety having a mono-protonated (neutral) phosphate group in agreement with the pK_a values reported for this group in free GMP ($pK_{a1} = 0.3$, $pK_{a2} = 6.25$).³³⁹

reducing guanine moiety to the oxidising Ru(III) centre in its 3MLCT excited state resulted in the formation of the guanine radical cation (*i.e.* $[Ru^{II}(TAP)(TAP^{\bullet-})(TAPG^{+\bullet})]^+$; Scheme 3.4 (2)). As the pK_a of $GMP^{+\bullet}$ has been shown to be 3.9,²¹⁵⁻²¹⁷ proton transfer (PT) could take place from the guanine moiety to the $TAP^{\bullet-}$ motif in *ca.* 116 ps giving rise to a long-lived biradical species (*i.e.* $[Ru^{II}(TAP)(TAPH^{\bullet})(TAP(G-H)^{\bullet})]^+$; Scheme 3.4 (3)). The existence of a PT process is in agreement with the isotopic effect reported by Marcélis *et al.* at pH 5.9.²¹³ As has been proposed for the system **38** and GMP, this PT could occur simultaneously to the ET (*i.e.* proton-coupled electron transfer (PCET)) as the oxidation potential of the guanine would decrease making the ET process more exergonic.^{208,218-220,383} The proposed structure of the biradical species in which the guanine has lost its carbonyl character is shown in Figure 3.35b. This biradical species lived for *ca.* 535 ns before decaying to the ground state (Scheme 3.4 (4)). It must be noted that this mechanism could also occur through a 3MLCT excited state where the electron would be placed on the GMP modified TAP ligand.

- 2) At pH 8 a deprotonation of the ground state **43** could be proposed as a pK_a of 6.8 was determined for the photoadduct by Marcélis *et al.* using UV-vis absorption spectroscopy.²¹³ The deprotonation site is still unknown but it should involve the guanine moiety and not the sugar-phosphate group, as the same pH effect was observed in the UV-vis absorption spectrum of the hydrolysed photoadduct **77**. Thus, after excitation, the excited state of the deprotonated form of **43** was formed (*i.e.* a LLCT excited state $^3[Ru^{II}(TAP)(TAP^{\bullet-})(TAP(G-H)^{\bullet})]^{-*}$; Scheme 3.5 (1a); or an



Scheme 3.5. Proposed mechanism of the dynamic processes that occur after excitation of **43** in deuterated aqueous solution at pH 8. Note that the lifetime values reported correspond to the average of those obtained by exponential fit to the data of the bands at 1654 and 1463 cm^{-1} . It must be also noted that the overall charge of **43** in its ground state at pH 8 corresponds to the GMP moiety having a fully deprotonated phosphate group in agreement with the pK_a values reported for this group in free GMP ($pK_{a1} = 0.3$, $pK_{a2} = 6.25$).³³⁹

ILCT excited state $^3[Ru^{II}(TAP)_2(TAP^-(G-H))]^-*$; Scheme 3.5 (1b)). The nature this excited state is still unclear although Marcélis *et al.* have suggested that it has LLCT or ILCT characteristics. As the guanine radical was already deprotonated, a second deprotonation was not expected to take place and as such a proton transfer did not occur at basic pH, in agreement with the absence of isotopic effect shown by Marcélis *et al.* at pH 8.²¹³ The generated radical species decayed then after *ca.* 374 ps (Scheme 3.5 (2a and 2b)).

It must be noted that the mechanisms suggested here are only hypothesis and represent an alternative to those proposed by Marcélis *et al.* and discussed in Section 3.1.²¹³ While the processes by which **43** reacts with a second GMP molecule to form bi-photoadducts have not been fully understood yet, the time-resolved spectroscopic studies presented here gives a plausible explanation about how the second photoreaction can take place at pH 5 but not at pH 8. Thus, different excited states would exist depending on the solution pH, in agreement with previous investigations performed by Marcélis *et al.*²¹³ The 3 MLCT excited state of **43** generated at pH 5 would give rise to the formation of a long-lived biradical species capable of reacting with a second GMP molecule and form bi-photoadducts involved in DNA strands photocrosslinking. However, at pH 8, a long-lived species would not be formed due to a different excited state of **43** (LLCT or ILCT) and as such, bi-photoadducts could not be produced at this pH. Further experiments will be required to gain more precise information about this system.

3.8 Conclusion and Future Perspectives

The initial rationale behind the work discussed in this chapter was to further investigate the photophysical processes occurring in the photoadduct formed between the complex **38** and the guanine-containing nucleotide GMP, with a view to elucidate the mechanism by which such photoadduct can react with a second GMP unit only at slightly acidic pH, despite its non-emissive character. Understanding this system is of particular relevance as **43** represents a model to study the ability of π -deficient Ru(II) polyaazaromatic complexes to induce photocontrolled cell damage *via* irreversible crosslinking of the two DNA strands. Therefore, the photosynthesis of **43** was first achieved using a unique advance laser photoreactor specially designed and manufactured by Prof. Guillermo Orellana and Dr Maximino Bedoya at Universidad Complutense de Madrid (UCM) for its use in this photoreaction. To the best of our knowledge, this is the first time that diode lasers have been employed as illumination sources for photoreactions involving π -deficient Ru(II) polypyridyl complexes and biomolecules, replacing the traditional Xenon lamps previously used for these

systems.^{168,211,213,219,223,227-229,344,345} A series of consecutive HPLC purification steps allowed the isolation of **43** in high purity. Successful production and isolation of this photoadduct was corroborated by MALDI-TOF mass spectrometry.

Spectroscopic studies were then conducted on **43** at different pH in order to further examine the pH effect on the spectroscopic properties of **43** in its ground state, previously reported by Kirsch-De Mesmaeker and co-workers.²¹³ UV-vis absorption spectroscopy showed that, in contrast to the parent compounds **38** and GMP, the absorption spectrum of **43** recorded at both pH 5 and 8 was influenced by the solution pH, indicating the existence of an acid-base reaction. This pH effect was found to be independent of the protonation/deprotonation of the phosphate group in the GMP moiety as the same pH dependence was observed for the hydrolysed photoadduct **77**. Based on DFT calculations, Marcélis *et al.* proposed the protonation of the N7 position in the GMP moiety of **43** at pH 5.9 as the origin of such particular behaviour.²¹³ However, our FTIR studies did not show significant changes in the carbonyl band position when the FTIR spectrum of **43** was recorded at pH 5 and 8. Previous FTIR investigations on free GMP have shown that a shift of the carbonyl band position is expected when the N7 position of the guanine moiety is protonated.³⁴⁰ Taking this into consideration, the FTIR studies presented in this chapter suggest that the guanine moiety of **43** is not protonated, or at least not in the N7 position. Other observations supporting this hypothesis are the low pK_a value reported for the N7 position in free GMP ($pK_a = 2.48$)³³⁹ to be protonated at pH 5, and the negative effect that the protonation of the imidazole ring of GMP would have on the exergonicity of the electron transfer, making the formation of a bi-photoadduct very difficult.³⁴¹ This means that another explanation for the pH-dependent spectroscopic properties exhibited by **43** needs to be found.

Furthermore, when the FTIR spectrum of **43** was compared to that obtained for free GMP in the same conditions, an absence of purine ring vibrations, as well as shifting and narrowing of the carbonyl band were observed. These features have been described in the literature as evidence of GMP self-assembly.^{340,353} Aggregation of **43** was further confirmed by ¹H NMR dilution studies. However, if such aggregation occurs *via* stacking of the GMP moieties or formation of G-tetrads is still uncertain. These NMR studies have also proved the existence of **43** in different ground states depending on the solution pH. In addition, ³¹P NMR experiments have shown that the phosphorus signals are also sensitive to the solution pH, although their implication in the photoadduct ground state structure also remains unknown. Finally, CD experiments performed on the ground state of **43** revealed the chirality

of the molecule, which was found to be independent of the presence of the chiral ribose moiety as similar optical activity was observed for the hydrolysed photoadduct **77**.

Time-resolved spectroscopic studies were conducted in order to gain further information about the excited state of **43**. TrA spectra were found to be similar to those reported previously by Marcélis *et al.* and showed the formation of a long-lived species only at pH 5.9.²¹³ The authors proposed this species to be responsible for the reactivity of the photoadduct with a second GMP molecule at slightly acidic pH. Furthermore, TRIR experiments showed that the electron transfer occurred at pH 5, as was evidenced from the formation of the guanine radical cation. However, while at pH 8 the generated radical species decayed to the ground state after *ca.* 374 ps, the biradical species formed at pH 5 were found to live for *ca.* 535 ns. These results confirmed the existence of a long-lived biradical species at pH 5 which could further react with a second guanine-containing molecule. Therefore, it can be concluded that different nature excited states (*i.e.* reactive MLCT or unreactive LLCT/ILCT) will be generated at pH 5 and 8, and this fact would explain the pH-dependent photoreactivity of **43**.

Although the exact mechanism by which the formation of a bi-photoadduct occurs could not yet be proved due to the complexity of the system, the results presented here represent a contribution to the understanding of the underlying photophysical processes taking place in **43**. However, further experiments are required to confirm the proposed mechanism of bi-photoadduct formation at pH 5. Therefore, future work will be focused on elucidating the protonation state of **43** in its ground state at

different pH. For example, recording the FTIR of **43** at pH 1 could corroborate the non-protonated state of the N7 position in the GMP moiety as at pH 1 this position would certainly be protonated and as such a shift of the carbonyl band would be expected.³⁴⁰ In addition, preliminary pK_a calculations on the **TAP-GMP** ligand using the free software MarvinSketch (ChemAxon) gave a pK_a value of *ca.* 7 for the N3 position in a different guanine tautomer (Figure 3.37). Indeed, it has been shown that the presence of water could promote the formation of some rare guanine enantiomers by reducing the energy barrier of tautomeric conversion.³⁸⁴ This pK_a value is very close to that experimentally determined for

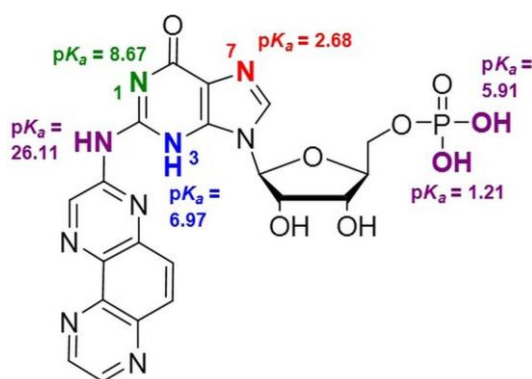


Figure 3.37. Chemical structures of the ligand **TAP-GMP** containing guanine in a different tautomer and showing the pK_a values for different positions in the GMP moiety calculated using the free software MarvinSketch (ChemAxon).

43 by Marcélis *et al.* ($pK_a = 6.8$)²¹³ and, therefore, deprotonation of the N3H group in the GMP moiety could be envisioned. DFT calculations could also provide more information about the exact protonation/deprotonation site in this photoadduct.

Concerning the optical activity observed for **43**, CD experiments performed at different temperatures would prove if the chirality of the photoadduct is due to an enantioselectivity of the photoreaction or because of a self-assembly process. CD could be also employed in the monitoring of the photoreaction to study the enantioselective character of the process.

In the last two chapters, the ability of Ru(II) polypyridyl complexes to bind to DNA *via* both non-covalent and covalent binding modes for use in a biological context has been extensively investigated for single complex molecules. With a view to extend the biological potential of these complexes, the following two chapters will concentrate on the development of systems involving more than one Ru(II) complex molecule. In particular, in the next chapter the synthesis of a family of amphiphilic Ru(II) polypyridyl complexes which contain alkyl chains of different lengths will be described along with studies of their ability to self-assembly into micelles and act as luminescent surfactants. The influence of such alkyl chain on their DNA binding ability as well as on their cellular internalisation and phototoxicity will be also evaluated in the interest of developing new DNA binders and PDT agents.

Chapter 4

Water-soluble Amphiphilic

Ruthenium(II) Polypyridyl Complexes

4.1 Introduction

As has been highlighted in previous chapters, Ru(II) polypyridyl complexes have attracted much interest in the last number of decades for their interesting photophysical and photochemical properties. These properties make them suitable for application as therapeutic agents and imaging probes, especially for targeting DNA but also in a cellular environment.^{2,62,63,91,93,134,296,385} Therefore, the design of ruthenium-based systems with the ability to be taken up by the cells has become a crucial matter for such biological applications. Among other factors such as molecule size and charge, lipophilicity has been shown to play a key role in the cellular uptake and localisation of Ru(II) polypyridyl complexes and thus, as previously discussed in Section 1.6.2, different strategies have been developed over the years with the aim of improving the cellular uptake of these complexes. Among them, coordination of lipophilic ligands such as 4,7-diphenyl-1,10-phenanthroline (**dip**) or alkyl chain-based derivatives to the Ru(II) centre has been shown to increase the intracellular internalisation when compared to their more hydrophilic analogues.^{178,180}

The incorporation of lipophilic tails to the hydrophilic ruthenium-based core also provides the resulting molecule with an amphiphilic character and a general structural resemblance to biological lipids thus facilitating their insertion into the lipid bilayer that constitutes the cell membrane.³⁸⁶ Therefore, their lipid similarity makes them suitable molecules to be used as luminescent membrane probes for structural and biophysical analysis of the cellular membrane of live cells. In this research area, several fluorescent dyes such as rhodamine, fluorescein or coumarin derivatives (Figure 4.1) have been functionalised with lipophilic chains, which are commercially available, and used to stain lipid membranes by insertion of the lipophilic tail into the membrane and with the polar fluorophore remaining

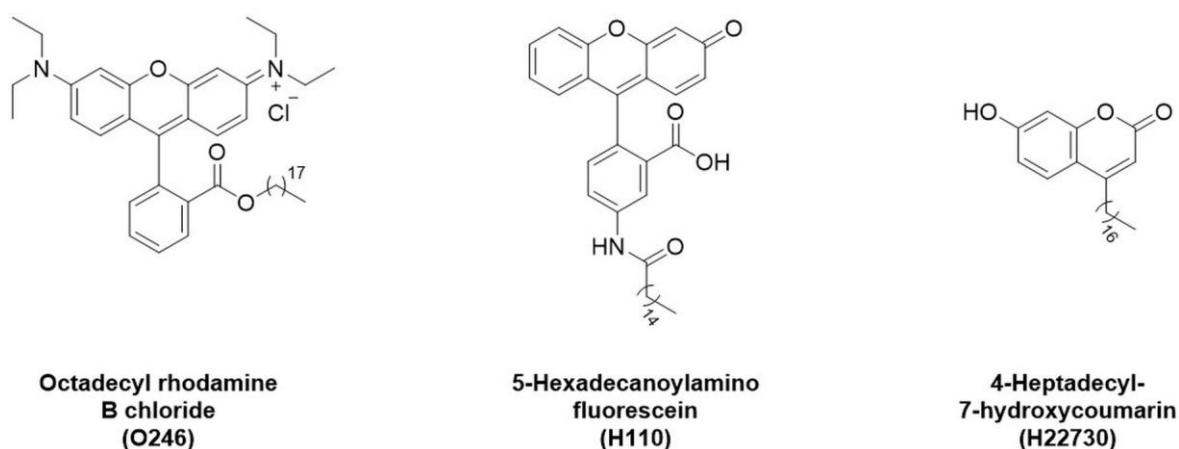


Figure 4.1. Chemical structures of several commercially available fluorescent dyes used to stain lipid membranes.

on the surface.³⁸⁶ In addition, lipid mimetic luminescent Ru(II) polypyridyl complexes have also been developed for their potential use in labelling liposomes and phospholipid membranes.³⁸⁷⁻³⁸⁹

On the other hand, the incorporation of hydrophobic alkyl chains into the water-soluble ruthenium moiety will have an effect not only on their lipophilicity, but also on their ability to form supramolecular structures in aqueous solution because of their spontaneous self-assembly in order to lower the solution free energy. Such structures are known as metallosurfactants and their simplest aggregation is the formation of spherical-shaped micelles which have been extensively used in recent years in imaging and drug delivery applications.³⁹⁰⁻³⁹² Furthermore, the presence of metals in the headgroup of these amphiphilic structures confers them with advantageous properties that are concentrated at the interface.³⁹³ In this context, surfactants containing lanthanides and transition metals have received special attention due to their tuneable magnetic, luminescent and photooxidant properties which make them suitable for use in a number of applications such as luminescent probes, thin film optoelectronic devices, homogeneous catalysis, templating of mesoporous materials or antibiotic drugs.^{181,394-399} In particular, ruthenium-based metallosurfactants have shown great potential in several biological applications such as in the imaging of physiological hypoxia, phospholipid membranes labelling, gene therapy or anticancer agents.^{389,400-402}

With the aim of exploring the properties of amphiphilic molecules and their resulting supramolecular structures, the work presented in this chapter will be focused on the

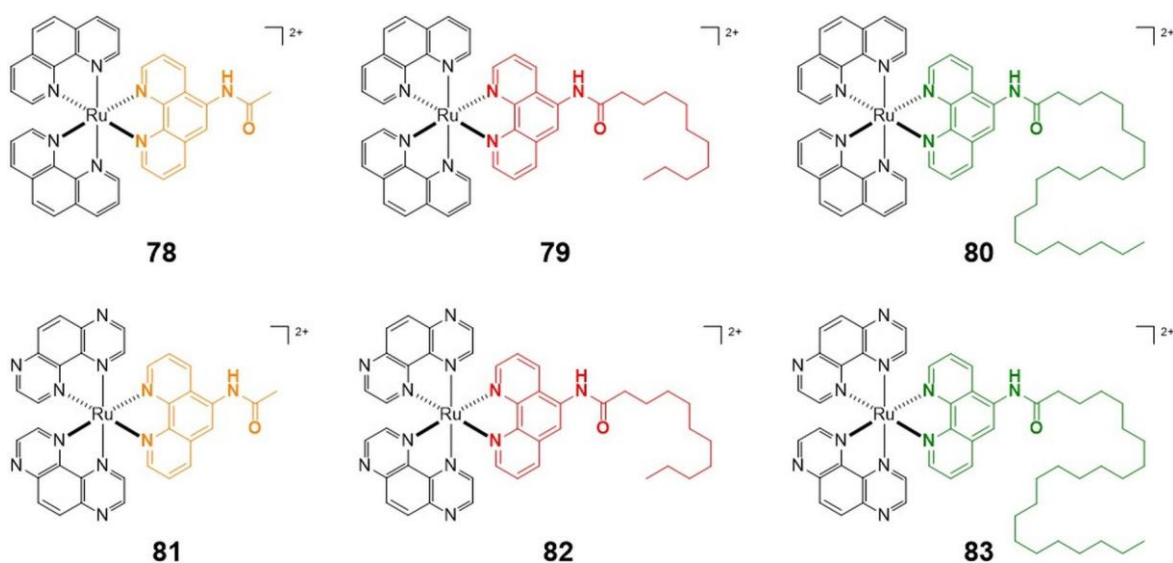


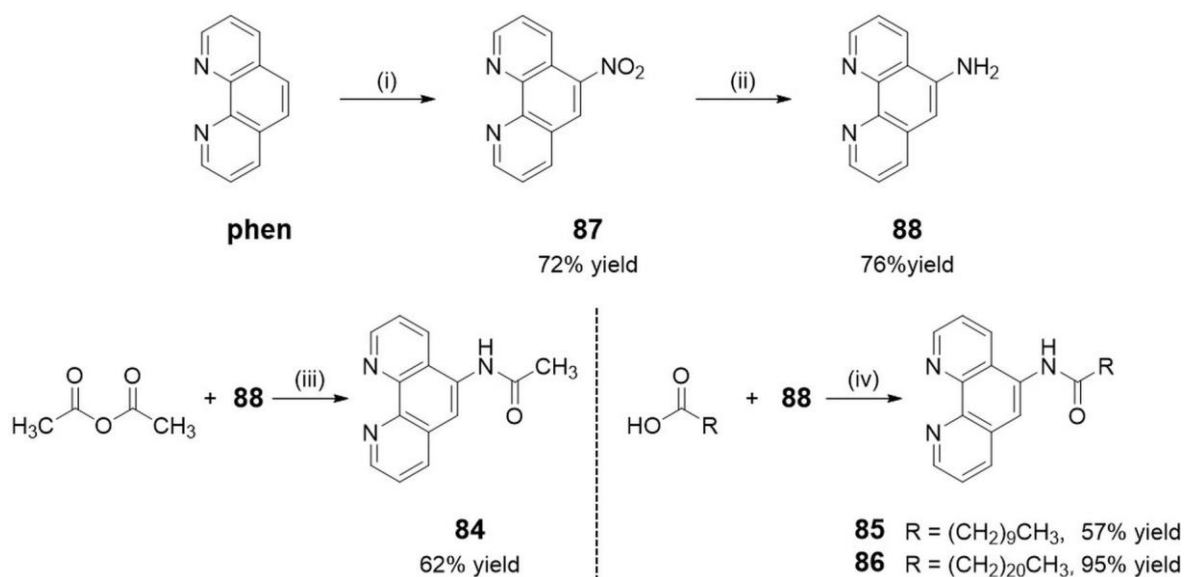
Figure 4.2. Chemical structures of the water-soluble amphiphilic Ru(II) polypyridyl complexes 78–83 studied in this chapter.

synthesis, characterisation and photophysical evaluation of a new family of Ru(II) polypyridyl complexes containing different lengths of alkylamide functionalised phenanthroline ligands and **phen** and **TAP** as ancillary ligands (**78–83**) (Figure 4.2).

Their ability to self-assemble and form aggregates such as micelles will be also evaluated by using different techniques including surface tension, dynamic light scattering (DLS) and luminescence lifetimes measurements. Furthermore, the influence of the alkyl chain length on their applicability in a biological environment will be investigated. UV-vis absorption and emission spectroscopy, thermal denaturation and circular dichroism (CD) will be employed to assess their DNA binding response. Finally, their ability to be used as PDT agents will be examined by determining their quantum yields of singlet oxygen production followed by cellular uptake and photoactivated toxicity studies in live cells.

4.2 Synthesis and Characterisation of 78–83

Ruthenium(II) polypyridyl complexes **78–83** were synthesised according to literature procedures for $[\text{Ru}(\text{L})_2(\text{L}')^{2+}]$ di-heteroleptic complexes, where L = 1,10-phenanthroline (**phen**) or 1,4,5,8-tetraazaphenanthrene (**TAP**), and L' = *N*-1,10-phenanthroline-5-yl-alkylamide (**84–86**).^{301,302} First, synthesis of ligands **84–86** was achieved according to a three step synthetic route as shown in Scheme 4.1. The synthesis of the **TAP** ligand was performed as described in Section 2.2.



Scheme 4.1. Synthetic pathway for **84–86**, where R = CH₃ (**84**), (CH₂)₉CH₃ (**85**) and (CH₂)₂₀CH₃ (**86**): (i) H₂SO₄, HNO₃, 160 °C, 4 h; (ii) N₂H₄·H₂O, 10% Pd/C, EtOH, reflux, 16 h; (iii) CH₃CN, r.t., 2 days; (iv) EDC, DMAP, CH₂Cl₂, r.t., 2 days.

The first step involved nitration of 1,10-phenanthroline using a mixture of concentrated H₂SO₄ and fuming HNO₃ at 160 °C for 4 h. Neutralisation of the reaction

mixture with NaOH yielded 5-nitro-1,10-phenanthroline (**87**) as a pale-yellow solid in 72% yield. Reduction of **87** with hydrazine in the presence of 10% Pd/C in EtOH under reflux for 16 h followed by filtration of the reaction mixture through celite and solvent removal under reduced pressure gave 5-amino-1,10-phenanthroline (**88**) as a yellow solid in 76% yield. The final step consisted of a coupling reaction between 5-amino-1,10-phenanthroline (**88**) and the appropriate carboxylic anhydride (**84**) in MeCN or carboxylic acid (**85** and **86**) in DCM using *N*-ethyl-*N'*-(3-dimethylaminopropyl)carbodiimide hydrochloride (EDC) in the presence of 4-dimethylaminopyridine (DMAP).⁴⁰³ Ligands **84–86** were obtained as beige solids in 62%, 57% and 95% yield, respectively, after solvent removal under reduced pressure (**84**) or H₂O precipitation followed by washing with MeCN (**85** and **86**).

The three ligands **84–86** were characterised by ¹H NMR, ¹³C NMR, HRMS, melting point analysis and IR spectroscopy. The ¹H NMR spectrum (600 MHz, DMSO-*d*₆) of **85** is shown in Figure 4.3 with those of **84** and **86** given in Figures A4.1 and A4.4 of the

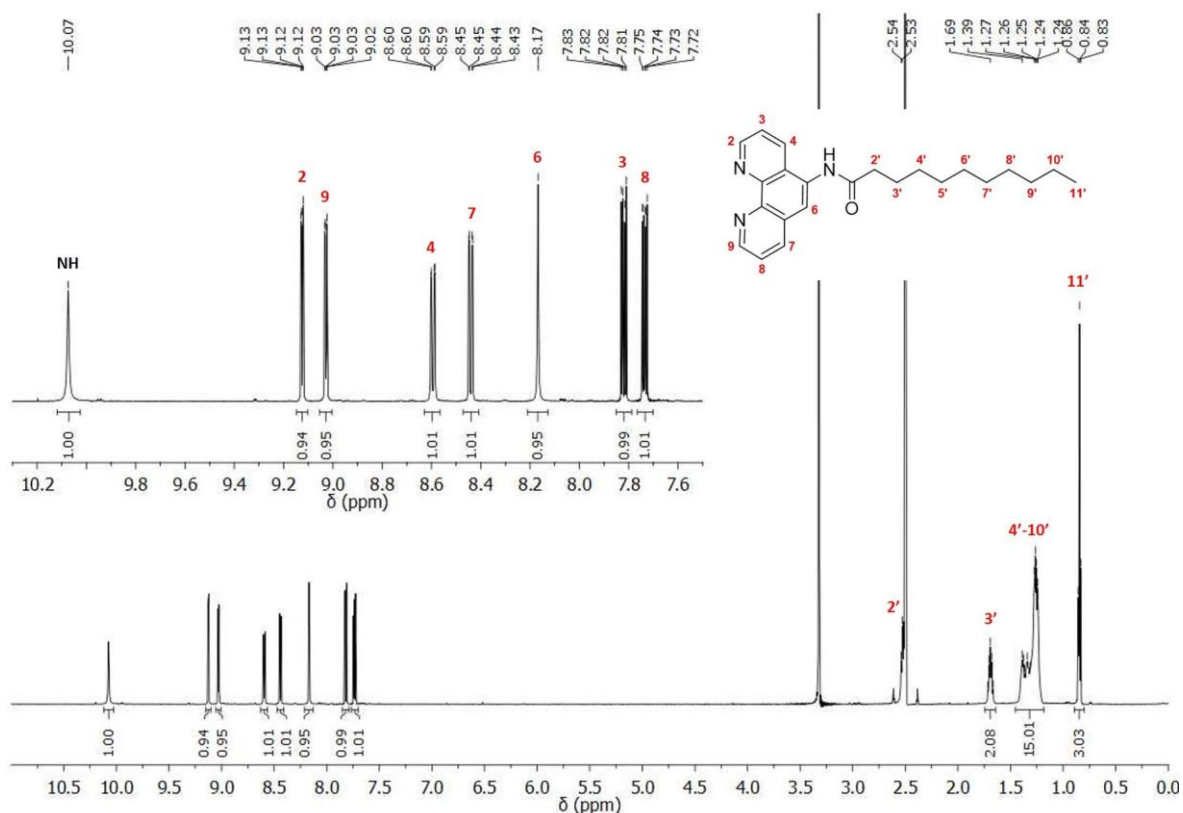


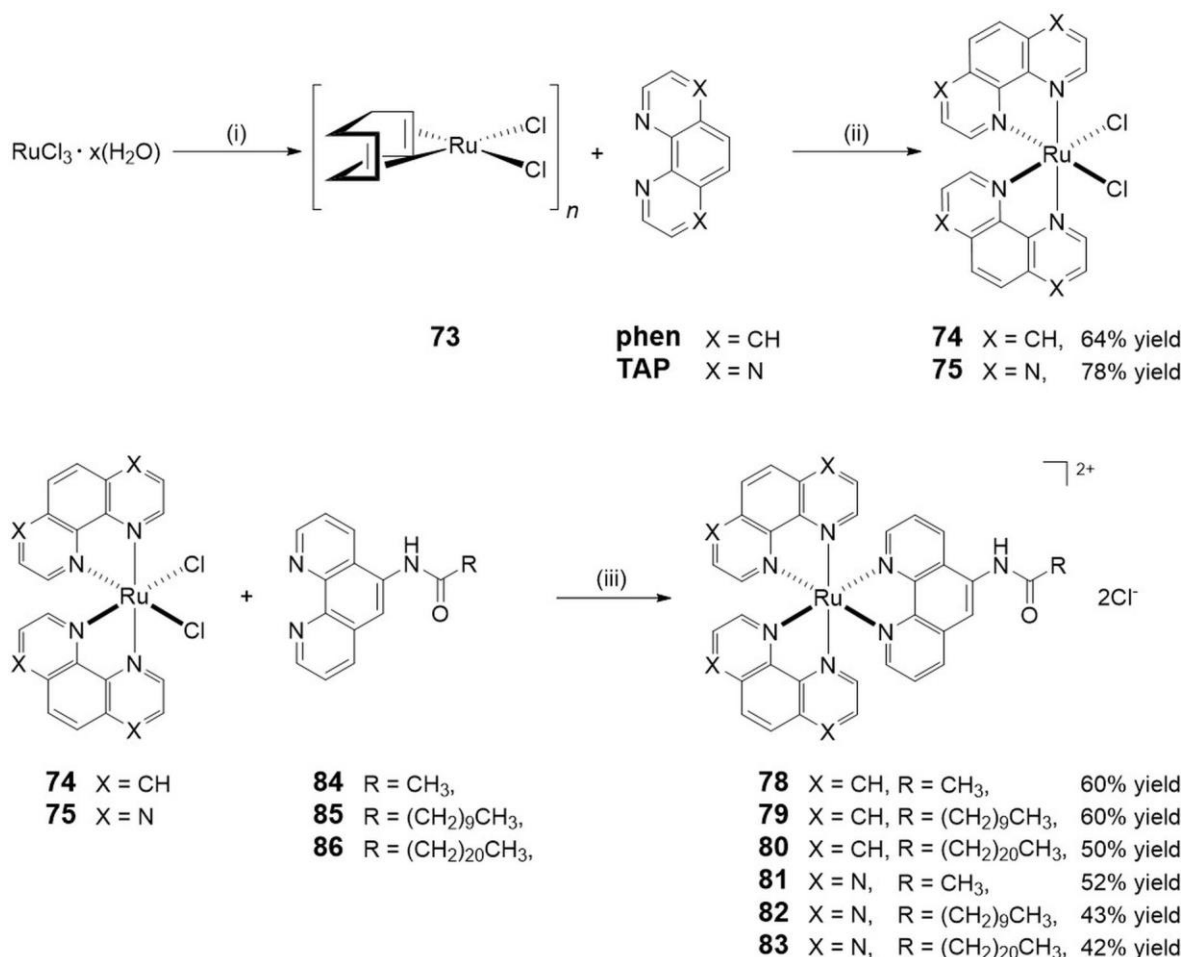
Figure 4.3. ¹H NMR (600 MHz, DMSO-*d*₆) spectrum of **85**.

Appendices. The successful formation of the amide bond was confirmed by the characteristic NH signal at 10.07 ppm in DMSO-*d*₆. Seven proton signals were observed in the aromatic region between 7.6 and 10.2 ppm and were assigned to the **phen** moiety of the ligand.

Likewise, the twenty-one protons corresponding to the ten carbon alkyl chain in ligand **85** were observed in the aliphatic region of the $^1\text{H-NMR}$ spectrum between 0.5 and 3.0 ppm.

Evidence of successful formation of ligands **84–86** was also observed by ESI⁺-HRMS which showed peaks at m/z 238.0973, 386.2206 and 540.3915 corresponding to the $[\text{M}+\text{H}]^+$, $[\text{M}+\text{Na}]^+$ and $[\text{M}+\text{Na}]^+$ ions, respectively.

In a similar way to that described in Section 2.2, complexes **78–83** were then prepared by microwave-assisted synthesis using the appropriate Ru(II) bispolypyridyl dichloride (**74** and **75**) as a precursor complex and the corresponding *N*-1,10-phenanthroline-5-yl-alkylamide as ligand in a mixture of H₂O/EtOH (1:1) at 140 °C for 40 (**78–80**) or 10 min (**81–83**) (Scheme 4.2). The chloride salts of **78–83** were obtained as red solids in 60%, 60%, 50%, 52%, 43% and 42% yield, respectively, after purification by column chromatography using neutral alumina and MeCN/H₂O (10:0 to 9:1) as eluent.



Scheme 4.2. Synthetic pathway for **78–83**: (i) 1,5-cyclooctadiene, EtOH, reflux, 3 days; (ii) DMF, microwave reaction, 140 °C, 40 min; (iii) EtOH/H₂O (1:1), microwave reaction, 140 °C, 40 min (**78–80**) or 10 min (**81–83**).

Complexes **78–83** were characterised by ^1H NMR, ^{13}C NMR, elemental analysis, HRMS, melting point analysis and IR spectroscopy. The ^1H NMR spectrum (400 MHz, CD_3CN) of **79** is shown in Figure 4.4 and those of **78**, **80** and **81–83** in Figures A4.10, A4.17, A4.12, A4.15 and A4.19 of the Appendices. Additional 2D NMR experiments allowed the identification of most of the signals. Twenty-one protons were observed between 0.5 and 3.0 ppm corresponding to the alkyl chain protons in ligand **85**. The twenty-three protons observed between 7.0 and 10.0 ppm were assigned to the **phen** moieties and the signal at 11.33 ppm was attributed to the amide proton. A total of forty-five protons was consistent with the molecular formula of the compound. However, the overlap of proton resonances in the **phen** ligands and in ligand **85** did not allow for a complete identification of all the signals.

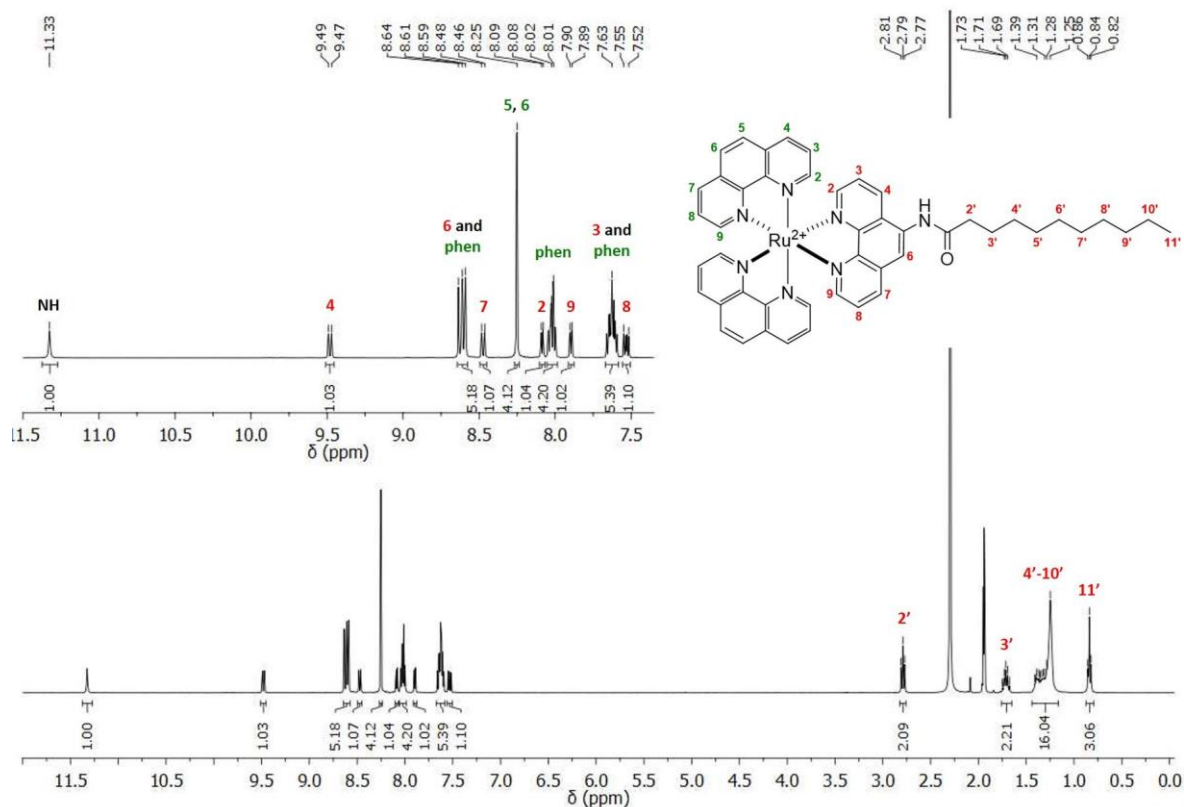


Figure 4.4. ^1H NMR (400 MHz, CD_3CN) spectrum of **79**. Signals corresponding to **phen** ligands are in green and signals assigned to ligand **85** are in red.

Successful formation of complexes **78–83** was also observed by ESI $^+$ - or MALDI $^+$ -HRMS displaying peaks at m/z 349.5676, 412.6378, 489.7232, 703.1135, 414.6258 and 983.4290, respectively, corresponding to their $[\text{M}]^{2+}$ or $[\text{M}]^+$ ion depending on the mass spectrometry technique used. A comparison of the theoretical and experimental isotopic distribution pattern of complexes **79** and **82** are shown in Figure 4.5 and those of **78**, **80**, **81**

and **83** in Figure A4.21 of the Appendices, with each showing the typical isotopic profile of ruthenium complexes.

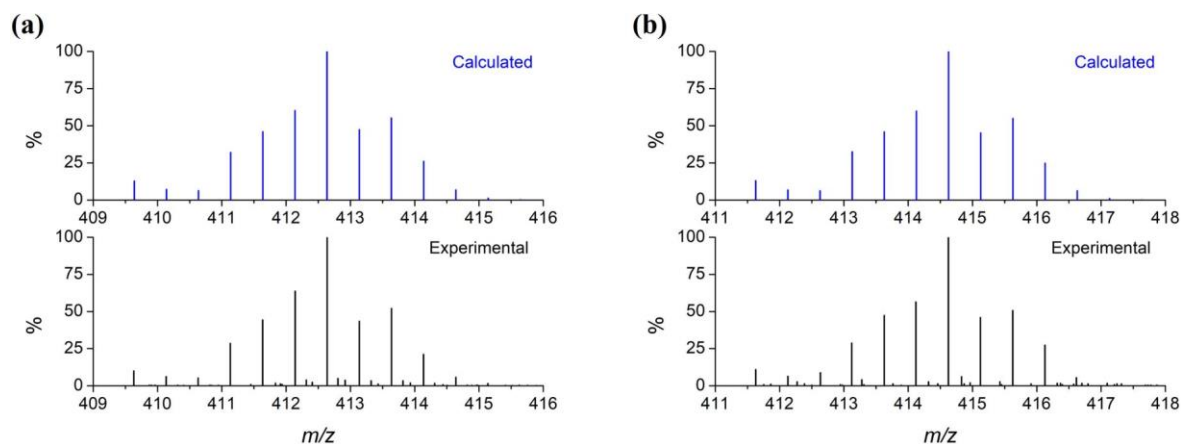


Figure 4.5. Comparison between the calculated (blue) and experimental (black) isotopic distribution pattern for (a) **79** and (b) **82** from electrospray ionisation (positive mode) high resolution mass spectrometry analysis.

Further details of synthetic procedures and the full characterisation of the six ruthenium complexes and the three ligands can be found in Section 7.9 of Chapter 7 and Figures A4.1–4.20 of the Appendices.

These complexes were synthesised as their chloride salts and despite the long alkyl chains present in some of the complexes, all were water-soluble and their photophysical behaviour was next studied in 10 mM sodium phosphate-buffered aqueous solution at pH 7.4.

4.3 Photophysical Characterisation of **78–83**

The photophysical properties of the six complexes were investigated in 10 mM sodium phosphate-buffered aqueous solution at pH 7.4. UV-vis absorption, excitation and emission

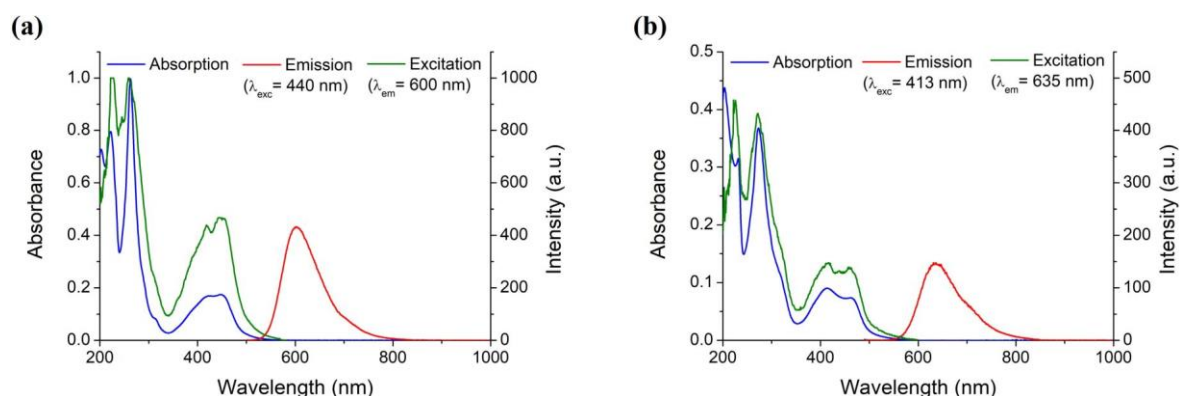


Figure 4.6. UV-vis absorption, excitation and emission spectra of (a) **79** and (b) **82** in 10 mM sodium phosphate-buffered aqueous solution at pH 7.4, at 298 K.

spectra of **79** and **82** are shown in Figure 4.6. Spectra for **78**, **80**, **81** and **83** can be found in Figures A4.22 of the Appendices.

Complexes containing **phen** as ancillary ligands (**78–80**) showed similar absorption spectra to that reported in the literature for the complex **42**.³⁴⁸ The π - π^* intra-ligand transitions of the **phen** ligand are localised at *ca.* 220 and 260 nm, while the broad band centred at *ca.* 440 nm is attributed to the characteristic MLCT transition in the metallic complexes. Likewise, similar absorption maxima to those reported for **39** were observed for complexes containing **TAP** as ancillary ligands (**81–83**).¹⁶⁶ Thus, intense bands at *ca.* 230 and 270 nm are attributed to π - π^* intra-ligand transitions in the **TAP** ligand, and the broad band centred at *ca.* 410 nm corresponded to the MLCT transition of the Ru(II) centre. The molar absorptivity values determined at these absorption maxima for these complexes are shown in Table 4.1.

Table 4.1. Absorption properties of **78–83** in 10 mM sodium phosphate-buffered aqueous solution at pH 7.4, at 298 K.

Complex		Absorbance λ_{max} , nm (ϵ , $10^4 \text{ M}^{-1} \text{ cm}^{-1}$) ^[a]		
		π - π^* IL	π - π^* IL	π - π^* MLCT
phen	78	221 (7.83 \pm 0.09)	262 (9.9 \pm 0.1)	447 (1.67 \pm 0.02)
	79	221 (7.9 \pm 0.1)	262 (10.0 \pm 0.1)	448 (1.76 \pm 0.02)
	80	222 (6.60 \pm 0.02)	263 (7.60 \pm 0.03)	451 (1.601 \pm 0.003)
TAP	81	232 (5.78 \pm 0.06)	272 (6.64 \pm 0.07)	414 (1.56 \pm 0.02)
	82	232 (6.07 \pm 0.08)	273 (7.08 \pm 0.09)	413 (1.74 \pm 0.02)
	83	230 (5.18 \pm 0.02)	274 (6.06 \pm 0.02)	418 (1.590 \pm 0.002)

^[a] Molar absorptivity values correspond to the mean \pm SEM.

Upon excitation into the MLCT bands of each complex, broad bands centred at 606 and 603 nm were observed for **78** and **79**, respectively. These values are very close to the emission maximum observed for the complex **42**.³⁴⁸ However, **80** showed a slightly red shifted emission band at 614 nm. Similarly, the emission spectra of **81** and **82** exhibited broad bands centred at 636 nm, while the emission maximum at 643 nm of complex **83** was found to be slightly red shifted compared to that observed for **39**, this being in agreement with the emission behaviour exhibited by the analogous **phen** complex **80** with the twenty-one carbon alkyl chain.¹⁶⁶ The excitation spectra recorded for the six complexes were found to be identical to their absorption spectra.

Luminescence quantum yields and lifetimes were determined in air-saturated or deaerated 10 mM sodium phosphate-buffered aqueous solution at pH 7.4 (Table 4.2) using the optically dilute solution method with $[\text{Ru}(\text{bpy})_3]\text{Cl}_2$ as a reference compound and single-photon timing (SPT) ($\lambda_{exc} = 458 \text{ nm}$, $A_{\text{MLCT}} = 0.05$), respectively.^{307,308} The reported values are the result of the average of a minimum of three independent measurements. The different alkyl chain length of ligands **84–86** were shown to influence the emission properties. Thus, quantum yield values of 0.040, 0.042 and 0.049 were observed for **78–80** with one, ten and twenty-one carbon alkyl chains, respectively. Similarly, **TAP** analogous complexes **81–83** showed quantum yields values of 0.023, 0.024 and 0.012, respectively. The values observed

Table 4.2. Emission properties of complexes **78–83** in 10 mM sodium phosphate-buffered aqueous solution at pH 7.4, at 298 K. Complexes **42** and **39** are included for comparison.

Complex		λ_{max}^{em} (nm) buffer	$\Phi_{em}^{[a]}$ buffer (air)	τ_{em} (ns) ^[b] buffer (air)	τ_{em} (ns) ^[b] buffer (N ₂)	$P_{O_2}^T$ buffer (Air-satd.)
phen	42	604 ^[c]	0.035	480 ^[c]	990 ^[c]	0.52
	78	606	0.040	644	1300	0.50
	79	603	0.042	650	1270	0.49
	80	614	0.049	1085 ^[d]	1354 ^[d]	0.20
TAP	39	645 ^[e]	0.020	690 ^[e]	835 ^[e]	0.17
	81	636	0.023	538	636	0.15
	82	636	0.024	570	674	0.15
	83	643	0.012	587 ^[d]	696 ^[d]	0.16

^[a] Air-saturated aqueous solution of $[\text{Ru}(\text{bpy})_3]\text{Cl}_2$ as reference ($\Phi_{em} = 0.028$).³⁰⁸ Estimated errors $\pm 5\%$.

^[b] If not otherwise indicated, the luminescence decays are mono-exponential. Estimated errors $\pm 10\%$.

^[c] From reference 348. The reported values are in aqueous solution.

^[d] The luminescence decays are bi-exponential; reported data correspond to the pre-exponential weighted mean lifetimes (τ_M).³²⁹

^[e] From reference 166. The reported values are in aqueous solution.

for complexes **78** and **79** and for **81** and **82** are similar to those reported in the literature for **42** and **39** in pure water, respectively.^{166,348} Interestingly, when compared to the quantum yield values displayed by the one and ten carbon alkyl chain derivatives containing **phen** and **TAP** (**78**, **79**, **81** and **82**), the **phen** complex **80**, containing the twenty-one carbon alkyl chain, exhibited a slightly higher value, while the twenty-one carbon alkyl chain-containing **TAP** complex **83** showed the opposite effect and a lower quantum yield value was observed, revealing the influence of alkyl chain length on the quantum yield. Thus, long lipophilic chains could exercise an auto-protection of the excited state of the complex from oxygen

quenching and deactivation by the solvent, thus explaining the behaviour observed for **80**. However, it is known that for **TAP** complexes the quenching of their excited states by dissolved oxygen is less significant.^{197,211,212,404} Thus, in the case of complex **83**, the lower quantum yield could be caused by a self-quenching process, that is a deactivation of the excited state of a complex molecule by interaction with the ground state of another complex molecule in close proximity possibly due to their association as a result of the amphiphilic character of these complexes.⁴⁰⁵

Concerning luminescence lifetimes, **78** and **79** showed values of 644 and 650 ns in air-saturated 10 mM sodium phosphate-buffered aqueous solution at pH 7.4, respectively. Similarly, luminescence lifetimes values of 538 and 570 ns were observed for the **TAP** analogue complexes **81** and **82**, respectively, in the same conditions. In addition, deaerated solutions of **78** and **79** resulted in a significant increase in the excited-state lifetimes with values of 1300 and 1270 ns, respectively. In contrast, only slightly longer lifetimes were observed for the deaerated solutions of **81** and **82** (636 and 674 ns, respectively). As already mentioned, these results demonstrated that the luminescence of the excited state of **TAP** complexes is less affected by the presence of dissolved oxygen than for complexes containing **phen** as ancillary ligands, in which the luminescence quenching by oxygen is more evident.^{197,211,212,404} This behaviour was corroborated through calculation of the values of the proportion of triplet excited states quenched by O₂ ($P_{O_2}^T$) for both **phen** and **TAP** complexes using equation (2.6) described in Section 2.6.³²⁶ Hence, **phen** derivatives displayed $P_{O_2}^T$ values of *ca.* 0.50 while the **TAP** analogues exhibited smaller values of *ca.* 0.15 and thus showed a larger efficiency of quenching of the excited states of the **phen** complexes by oxygen than of the **TAP** ones.

Furthermore, whereas luminescence lifetime data for complexes **78**, **79**, **81** and **82** could be fitted to a mono-exponential function, emission decay curves for **80** and **83** required bi-exponential fits, and as such the values reported in Table 4.2 correspond to the pre-exponential weighted mean lifetimes (τ_M) while τ_1 and τ_2 values and the corresponding pre-exponential factors are given in Table A4.1 of the Appendices.³²⁹ Since these compounds contain long alkyl chains, aggregates can be formed and different emitting species can co-exist in solution. Thus, the **phen** complex **80** showed τ_M values of 1085 and 1354 ns in aerated and deaerated aqueous solutions, respectively, which are longer than those reported for complexes **78** and **79** and where the shorter lifetime (τ_1) would correspond to the isolated molecules of a Ru(II) complex and the longer lifetime (τ_2) could be attributed to aggregates

formed in which the excited state would be protected from oxygen quenching and solvent deactivation.

This behaviour has previously been reported in the literature for similar Ru(II) complexes.⁴⁰⁶ The lower $P_{O_2}^T$ value exhibited by this complex when compared to **78** and **79** also supports the protection of the excited state of the complex from oxygen quenching by the long alkyl chain. On the other hand, τ_M values of 587 and 696 ns were observed for the **TAP** analogue **83** in both aerated and deaerated aqueous solutions, respectively, being similar to the values measured for **81** and **83**. Furthermore, the $P_{O_2}^T$ value displayed by complex **83** was comparable to those determined for **81** and **82** again confirming the negligible contribution of dissolved oxygen to the quenching of their excited state and thus the long alkyl chain did not have a significant effect on the protection of the luminescence of complex **83**. Additional lifetimes studies of **80** and **83** carried out at different complex concentrations will be discussed further later in this chapter.

The photophysical study of complexes **78–83** presented above allowed a better understanding of the impact the alkyl chains could have on the absorption and emission properties of the resulting Ru(II) complexes. Thus, although no significant effect was observed for complexes **78**, **79**, **81** and **82** when compared to the well-known **42** and **39**, respectively, the extension of the alkyl chain to twenty-one carbons seemed to affect the luminescence quantum yields and lifetimes of complexes **80** and **83**, most likely due to their ability to self-assemble in solution as a result of their amphiphilic character. Therefore, with a view to further investigate the capacity of complexes **80** and **83** to form aggregates in solution and study the influence of such behaviour on their photophysical properties, surface tension and dynamic light scattering (DLS) experiments were performed, followed by additional UV-vis absorption and emission spectroscopic studies as well as luminescence lifetime measurements at different concentrations of Ru(II) complex. Results from such experiments will be discussed in the next section.

4.4 Self-aggregation Ability of 78–83

As explained in Section 4.1 of this chapter, complexes **79**, **80**, **82** and **83** show an amphiphilic nature as they contain both a hydrophilic head-group (luminescent ruthenium core) and a hydrophobic tail (ten or twenty-one carbon alkyl chains) within their structure and so they are expected to self-assemble and form aggregates such as micelles. In this section, the ability of these complexes to act as luminescent surfactants will be investigated using different techniques such as surface tension, UV-vis absorption and emission spectroscopy,

luminescent lifetimes measurements and dynamic light scattering (DLS). It must be mentioned that the studies presented in this section are only focused on complexes **80** and **83** (twenty-one carbon alkyl chain). Preliminary studies carried out on complexes **79** and **82** (ten carbon alkyl chain) suggested incomplete micelle formation as might be expected because of the shorter alkyl chains.

4.4.1 Critical Micelle Concentration Determination of **80** and **83** by Surface Tension Studies

Critical micelle concentration (cmc) is one of the most significant parameters when studying the self-assembly process of surfactant molecules in aqueous solution. The cmc is defined as the concentration above which surfactant monomers self-organise into micellar species.⁴⁰⁷ Typically, micelles have cmc values in the μM to mM range depending on the surfactant structure (*i.e.* hydrophilic head charge and hydrophobic tail nature) and such values are affected by a large number of factors including temperature, pH or ionic strength of the aqueous solution.^{408,409} Several methods to determine the cmc of different types of surfactants have been described in the literature, including tensiometry, conductometry, and fluorimetry.^{407,410,411} However, not all the methods mentioned are always suitable, it being necessary to consider the surfactant properties when choosing a cmc determination technique.⁴⁰⁷ For example, popular spectroscopic methods based on fluorescent probes such as pyrene are not convenient for luminescent molecules and thus, their use will depend on the photophysical properties of the surfactant. Tensiometry is, however, one of the most classical methods for determining the cmc with high sensitivity for a wide range of cmc values and does not interfere with the surfactant photophysical properties. In this context, the critical micelle concentration of complexes **80** and **83** has been calculated through surface tension measurements carried out in collaboration with Prof. Rachel Evans group at Trinity College Dublin. The procedure consists on measuring the changes in the absolute surface tension of water in the presence of different concentrations of the surfactant for which the cmc is being determined. This often used a Wilhelmy plate method but here a cylindrical rod (0.5 mm diameter) made of an inert metal alloy was employed instead of a plate as this allows measurements to be carried out in smaller samples volumes.^{412,413} The force between the cylindrical rod of the tensiometer and the aqueous sample solution is measured and is proportional to the surface tension exerted by the surfactant solution according to equation (4.1):

$$\gamma = \frac{F}{l \times \cos\theta} \quad (4.1)$$

Where γ is the surface tension, F is the force measured, l is the wetted length, and θ is the contact angle. When complete wetting is assumed, the contact angle is 0° , and no correction factors have to be applied to calculate the surface tension.

Therefore, individual aqueous solutions at different concentrations were prepared for both complexes and left to equilibrate overnight before the surface tension of each concentration was measured. The variation of the surface tension of **80** and **83** as a function of the metal complex concentration is shown in Figure 4.7.

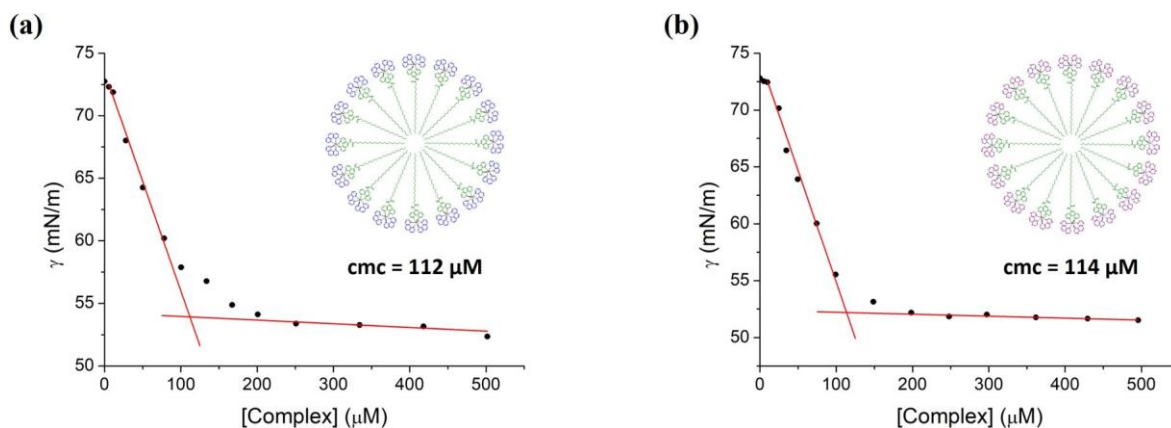


Figure 4.7. Determination of the critical micelle concentration by surface tension measurements of aqueous solutions of (a) **80** and (b) **83** at different concentrations, at 293 K.

As expected for tensioactive molecules, below the cmc when surfactant monomers exit in solution, the surface tension decreased gradually with the surfactant concentration, until a plateau was reached above the cmc indicating micelle formation. The cmc values for both complexes were determined by linear fitting of these two well-defined parts of the graph followed by calculation of the intersection of the two obtained lines. Thus, self-aggregation of complexes **80** and **83** was found to occur at 112 and 114 μM , respectively. These cmc values are in the hundred μM range and in agreement with those reported in the literature for structurally similar Ru(II) polypyridyl complexes-based surfactants.^{414,415} The similarity of the cmc values determined for both complexes shows that replacement of the **phen** ligands by the **TAP** ones that comprise the polar head of the surfactant has no influence on the self-assembly process and suggests that the cmc value is determined by the length of the alkyl chain.

Once the cmc was determined for both **80** and **83**, the size of the resulting aggregates at concentrations about and above the cmc was investigated through dynamic light scattering (DLS) measurements and such results will be presented in the next section.

4.4.2 Dynamic Light Scattering Studies of **80** and **83**

In order to further characterise the **80** and **83** based aggregates, the size of such as micellar species was estimated using dynamic light scattering (DLS) measurements. DLS is a non-invasive photon-based technique employed for measuring the size and size distribution of molecules and particles in solution.^{416,417} The principle of this technique is based on the Brownian motion that particles undergo as a result of their bombardment by solvent molecules.⁴¹⁷ When the particles are illuminated with a light source such a laser, the light is scattered at different intensities due to the size dependent Brownian motion of the particles. Particle size can then be determined from the analysis of the intensity fluctuations that yields the velocity of the Brownian motion. The diameter measured by using DLS refers therefore to how a particle diffuses within a fluid and it is called hydrodynamic diameter.⁴¹⁷

Thus, DLS measurements were carried out on filtered samples of **80** and **83**, at concentrations about and above their respective cmc values (Figure 4.8 and Figure A4.23 of the Appendices, respectively).

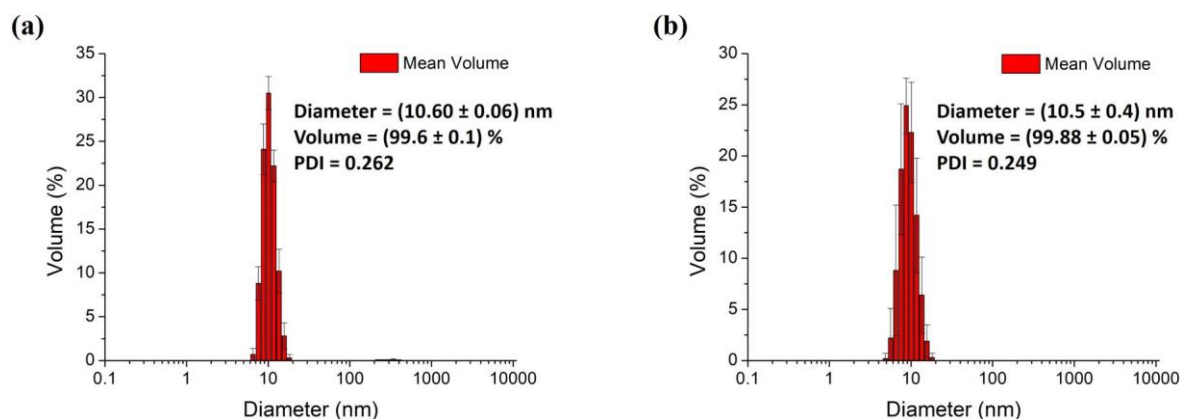


Figure 4.8. Micelle size distribution determined by DLS analysis for (a) **80** at 116 μM (about the cmc) and (b) **83** at 130 μM (about the cmc) in aqueous solutions at 298 K.

Complexes **80** and **83** showed hydrodynamic diameters of 10.6 and 10.5 nm, respectively, at approximately the cmc. In both cases, peak distributions corresponded to more than 99% in the volume distribution profiles and displayed a narrow size distribution within the range of 7.5–15.7 nm and 5.6–18.2 nm for **80** and **83**, respectively. Furthermore, slightly smaller hydrodynamic diameters values of 9.4 and 8.2 nm for **80** and **83**, respectively, were found at a concentration higher than the cmc. These small size differences suggest the stability of the micellar aggregates and, in particular, for the **phen** derivative for which the diameter difference at both concentrations is lower, indicating that the micellar species do not collapse into larger species at higher concentration, which has been shown for certain surfactants.

In the following sections, additional spectroscopic studies carried out at different surfactant concentrations of **80** and **83** will be discussed.

4.4.3 UV-vis Absorption and Emission Spectroscopic Studies of **80** and **83**

In order to further investigate the effect of aggregation on the photophysical properties of **80** and **83**, the normalised UV-vis absorption and emission spectra of these compounds were recorded in aqueous solution at concentrations below and above the cmc values determined previously for both ruthenium complexes and are shown in Figures 4.9 and 4.10.

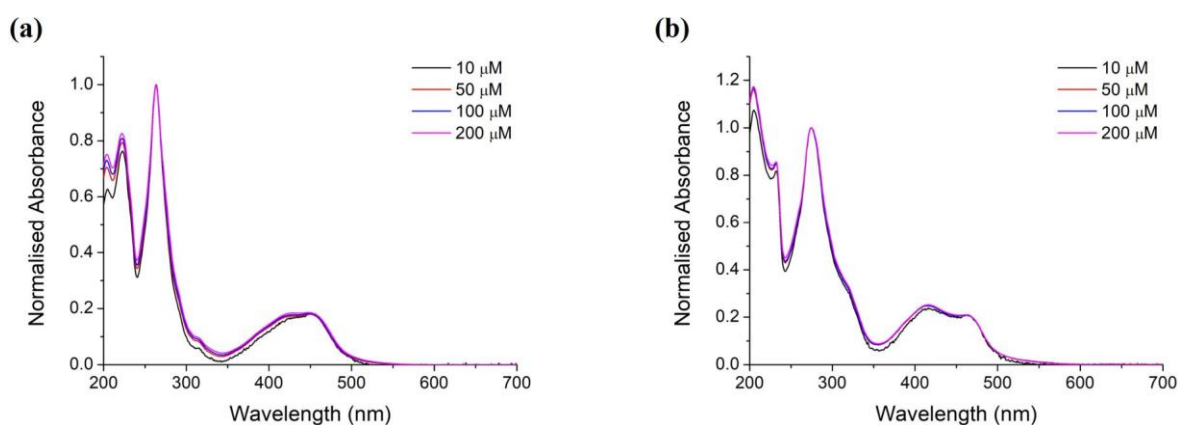


Figure 4.9. Normalised UV-vis absorption spectra of aqueous solutions of (a) **80** and (b) **83** at 10, 50, 100 and 200 μM concentrations, at 298 K. A quartz cuvette with an optical path length of 0.1 cm was used.

The UV-vis absorption spectra of both complexes **80** and **83** showed to be concentration independent as no shift of the absorption bands was observed at concentrations below and above the cmc.

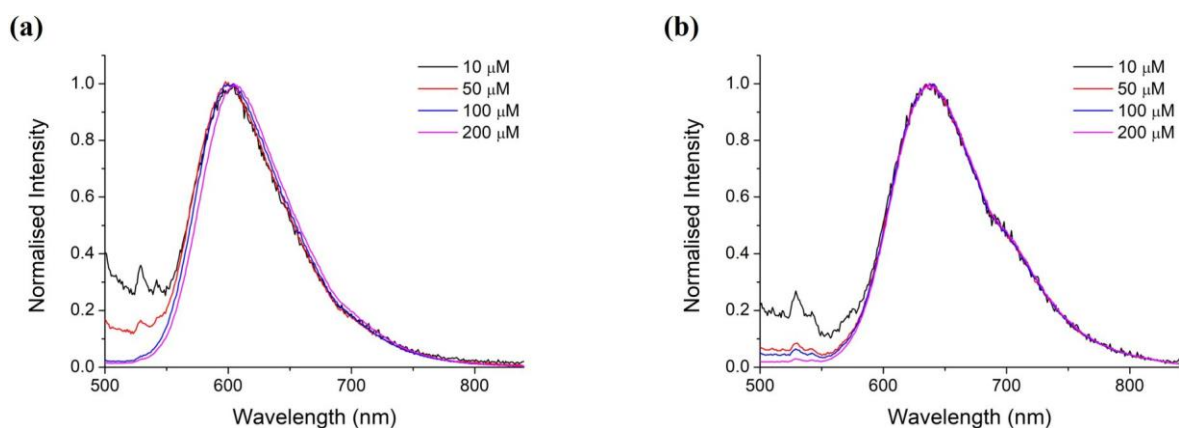


Figure 4.10. Normalised emission spectra of aqueous solutions of (a) **80** and (b) **83** at 10, 50, 100 and 200 μM concentrations, at 298 K. A quartz cuvette with an optical path length of 0.1 cm was used and it was placed diagonally in the spectrophotometer holder.

Concerning the emission spectra obtained upon excitation into the MLCT bands of each complex, while no significant change was observed for complex **83**, the maximum of

emission intensity of complex **80** at concentrations below the cmc (*ca.* 602 nm) is shifted slightly toward the red at a concentration above the cmc (*ca.* 605 nm).

Despite the self-aggregation of complexes **80** and **83** does not seem to significantly affect their UV-vis absorption and emission spectra, the influence on the surfactant concentration in the luminescent lifetimes was next examined.

4.4.4 Lifetimes versus Concentration Studies of **80** and **83**

Luminescence lifetime is an intrinsic property of a luminophore that is very often independent of the luminescence intensity and luminophore concentration. Ideally, a pure luminophore should exhibit a single exponential luminescence decay. However, as was shown earlier in Section 4.3, the luminescence decays of both complexes **80** and **83** required a bi-exponential fit, suggesting that more than one species is involved for both systems. It was previously discussed at the beginning of this section that these complexes were expected to spontaneously self-aggregate due to their amphiphilic nature. In addition, surface tension measurements allowed the determination of the concentration at which these complexes form aggregates. In order to further investigate this phenomenon, luminescence lifetimes of aerated aqueous solutions of complexes **80** and **83** at different concentrations (below and above their cmc) were measured using single-photon timing ($\lambda_{exc} = 405$ nm) in collaboration with Prof. Guillermo Orellana at Universidad Complutense de Madrid (UCM). As expected, bi-exponential fits were needed for the luminescence decay kinetics and thus pre-exponential weighted mean lifetimes (τ_M)³²⁹ were calculated according to equation (4.2) and plotted as a function of the complex concentration (Figure 4.11).

$$\tau_M = \sum_{i=1}^n \frac{a_i}{\sum_{i=1}^n a_i} \tau_i \quad (4.2)$$

Values of τ_1 and τ_2 and the corresponding pre-exponential factors at each complex concentration used to determine the τ_M values are given in Tables A4.2 and A4.3 of the Appendices.

Interestingly, the increase of the complex concentration had an opposite effect on the τ_M values of both **80** and **83**. Thus, while the **phen** complex showed larger τ_M values when the concentration of complex was increased, the τ_M values of the **TAP** analogue were shorter at larger complex concentrations. As previously mentioned in Section 4.3, the behaviour observed for complex **80** can be explained by a protection of its excited state from oxygen quenching and solvent deactivation that resulted from aggregation of the complex at

increasing concentrations.⁴⁰⁶ However, it has been shown that oxygen quenching is less efficient in complexes containing **TAP** as ancillary ligands.^{197,211,212,404} Therefore, it can be assumed that the formation of aggregates does not have any influence on the protection of the excited state of **83** from oxygen quenching. The decrease of the luminescence lifetime with the concentration could then be due to a self-quenching process by which the excited state of a complex molecule would be deactivated by interaction with the ground state of a nearby molecule of complex, and such effect would be more significant at larger concentrations of luminophore.⁴⁰⁵ Although self-quenching could also be expected for **80**, the oxygen quenching protection effect seems to have a greater impact in the luminescence lifetime of the complex.

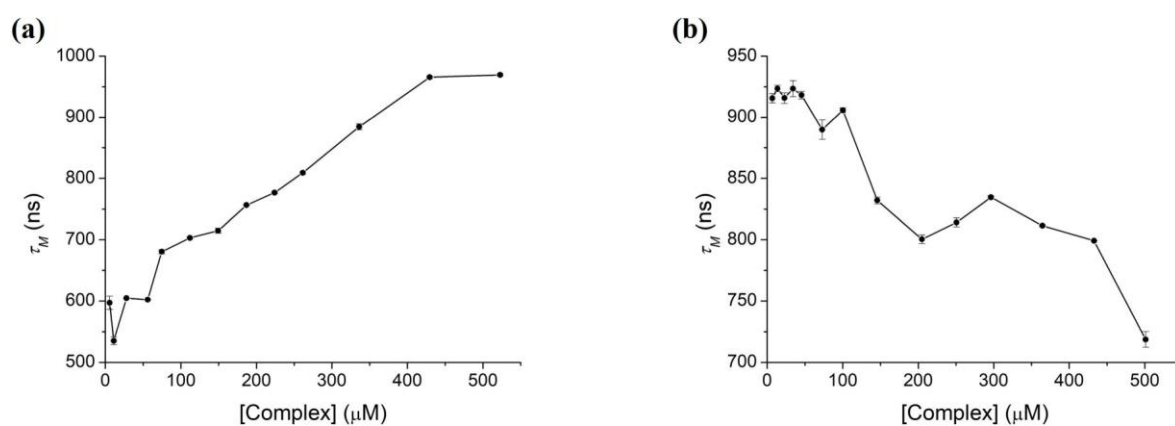


Figure 4.11. Evolution of the pre-exponential weighted mean lifetime (τ_M) of aerated aqueous solutions of (a) **80** and (b) **83** at different concentrations, at 298 K.

To summarise this section, it was demonstrated that complexes **80** and **83** are able to self-assemble and form micelles above a particular concentration that was determined by surface tension measurements. The size of such aggregates was estimated by DLS. Furthermore, while no significant differences were found in the UV-vis absorption and emission spectra of **80** and **83** at concentrations below and above the cmc, a concentration effect was observed in the lifetime values of such complexes suggesting the existence of different aggregation states.

Therefore, having photophysically characterised complexes **78–83** and after demonstrating that **80** and **83** have the ability to aggregate and form micelles, the following sections will be focused on their applicability in biological systems. As was shown in Chapter 2 for complexes **63** and **64**, the photophysical properties of complexes **78–83** are expected to be sensitive to their interaction with DNA. Therefore, the affinity of such complexes for DNA will next be evaluated using different spectroscopic techniques with the

aim of exploring their use as DNA targeting molecules for both therapeutic and imaging applications.

4.5 DNA Binding Interactions of 78–83

Despite complexes **78–83** not containing extended aromatic ligands that can intercalate between the DNA base pairs such as complexes presented in Chapter 2, their cationic nature still makes them suitable to electrostatically interact with the negatively charged phosphate backbone in the nucleic acid. Furthermore, groove binding or partial intercalation of the polypyridyl ancillary ligands **phen** and **TAP** could also be possible as well as hydrophobic interactions with the double helix provided by the long alkyl chains for some of the complexes. In the following sections, the nature and binding affinity of complexes **78–83** for DNA will be examined using several spectroscopic techniques such as absorption and emission DNA titrations, thermal denaturation and circular dichroism (CD).

4.5.1 Spectroscopic Titrations of 78–83

The interaction of complexes **78–83** with stDNA was first investigated using UV-vis absorption and emission spectroscopy. Thus, DNA titrations were performed in a similar way to that described in Section 2.5.1 by gradual addition of aliquots of stDNA to a 10 mM sodium phosphate-buffered aqueous solution (pH 7.4) containing the corresponding Ru(II) complex. Changes in the MLCT absorption band as well as in the emission intensity were monitored spectroscopically until no significant changes were detected at increasing stDNA concentrations. It should be noticed that at the complex concentration used in the DNA titrations (from 5 to 10 μM), self-aggregation of **80** and **83** is not expected according to previous experiments. All titrations were repeated at least three times to ensure reproducibility.

The changes in the UV-vis absorption and emission spectra of complexes containing **phen** as ancillary ligand (**78–80**) upon addition of stDNA are shown in Figure 4.12. Complexes **78** and **79** exhibited a 14% and 33% decrease of the absorption in the MLCT band at 447 and 448 nm, respectively, upon addition of stDNA. However, a more complex behaviour was observed for complex **80**. A decrease of the absorption in the MLCT band at 451 nm was first observed after addition of 0.5 eq. of stDNA followed by a strong increase when stDNA was added up to 2.2 eq. ending in a slight decrease until the absorption plateau was reached. Concomitantly, a red shift of *ca.* 15 nm of the MLCT band was observed.

Concerning the changes observed in the emission spectra upon addition of stDNA, complex **78** displayed an enhancement in the MLCT emission intensity centred at 603 nm,

together with a blue shift of *ca.* 6 nm. A triphasic behaviour was, however, exhibited by complex **79** for which the emission intensity at 604 nm enhanced upon the addition of 2.1 eq. of stDNA followed by a decrease up to 7.4 eq. of stDNA, and an increase again until emission intensity did not experience significant changes upon further increasing in the stDNA concentration. Complex **80** also showed a triphasic behaviour starting with a

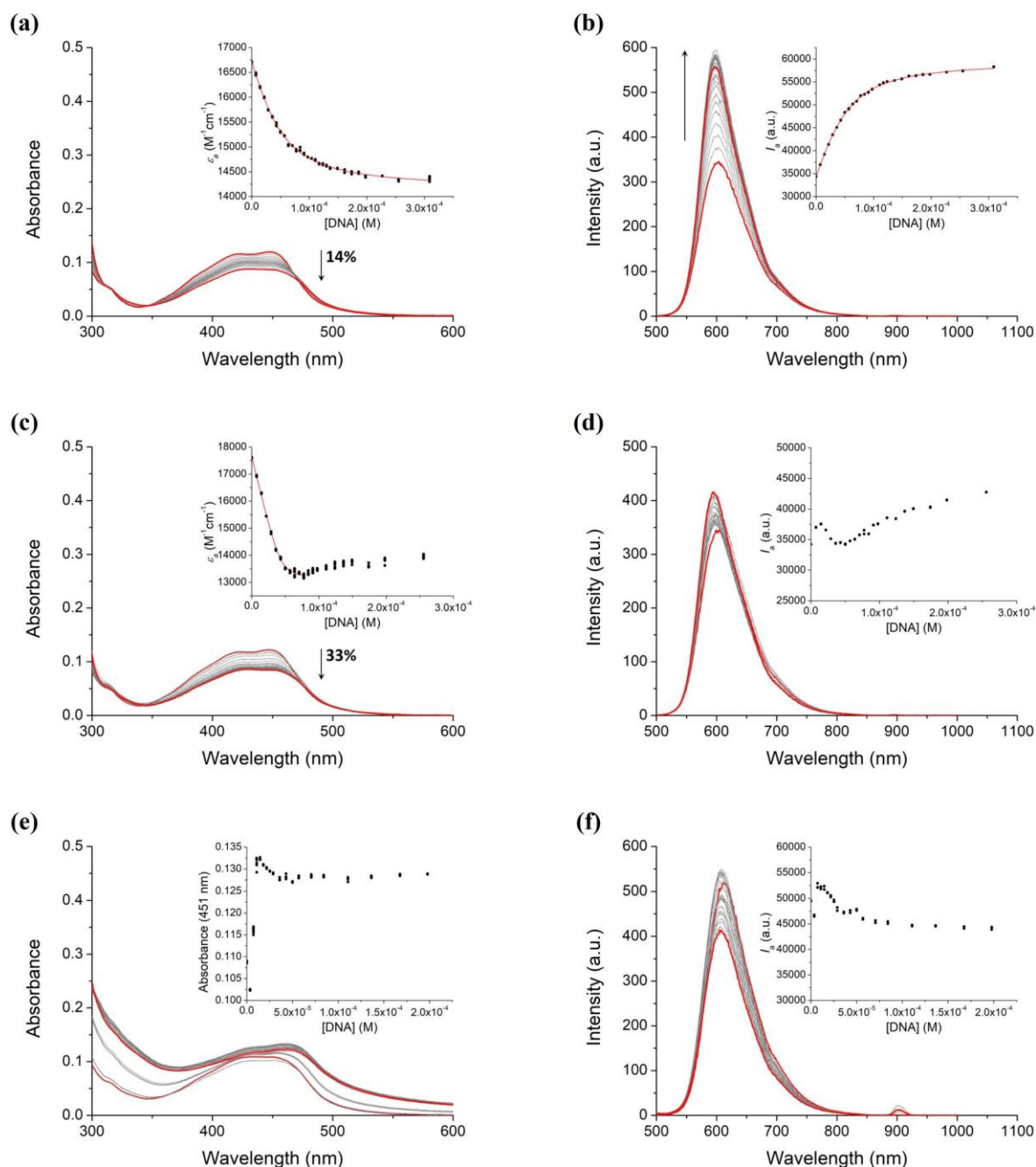


Figure 4.12. Changes in the UV-vis absorption and emission spectra of (a, b) **78** ($7.16 \mu\text{M}$, $\lambda_{\text{exc}} = 447 \text{ nm}$), (c, d) **79** ($6.94 \mu\text{M}$, $\lambda_{\text{exc}} = 448 \text{ nm}$) and (e, f) **80** ($6.79 \mu\text{M}$, $\lambda_{\text{exc}} = 451 \text{ nm}$) with increasing concentration of stDNA ($0\text{--}309 \mu\text{M}$, $0\text{--}256 \mu\text{M}$ and $0\text{--}198 \mu\text{M}$, respectively) in 10 mM sodium phosphate-buffered aqueous solution at $\text{pH } 7.4$. Inset: Plot of ϵ_a ($\text{M}^{-1}\text{cm}^{-1}$) or I_a (a.u.) vs. $[\text{DNA}]$ (M, bases) using data from absorbance at (a) 447 nm (c) 448 nm and (e) 451 nm or integrated MLCT emission intensity (b, d, f) and the best fit of the data, when possible, using a modification of the Bard Equation.

a decrease of the emission intensity at 612 nm after the addition of 0.5 eq. of stDNA, and then an increase up to 1.1 eq. of stDNA. This was then followed by a decrease in the emission intensity until a plateau was reached. For both complexes, the maximum of emission intensity was blue shifted *ca.* 7 nm.

Complexes containing the **TAP** moiety as ancillary ligands (**81–83**) also exhibited significant changes in their UV-vis absorption and emission spectra upon addition of stDNA,

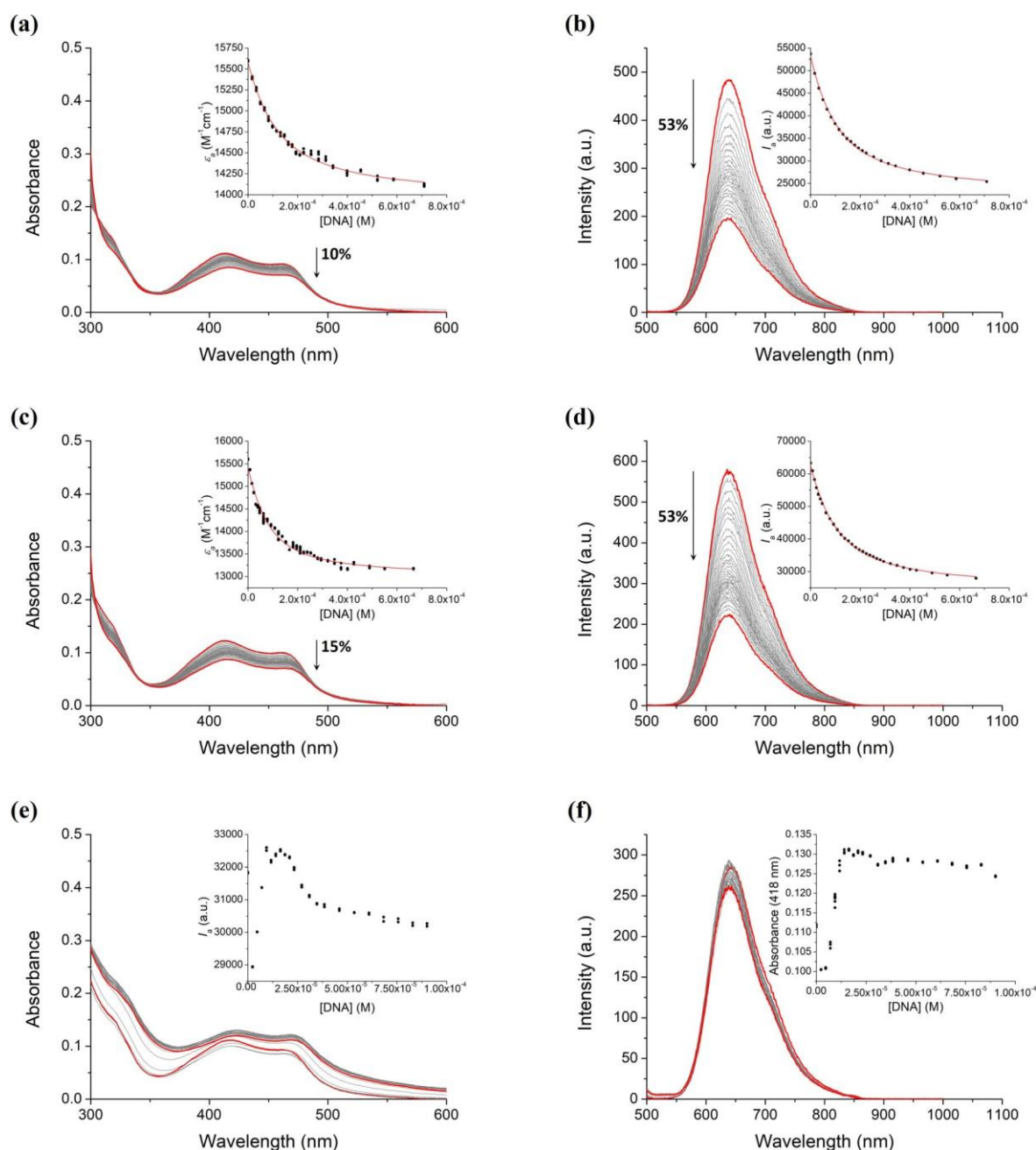


Figure 4.13. Changes in the UV-vis absorption and emission spectra of (a, b) **81** ($7.16 \mu\text{M}$, $\lambda_{exc} = 414 \text{ nm}$), (c, d) **82** ($7.85 \mu\text{M}$, $\lambda_{exc} = 413 \text{ nm}$) and (e, f) **83** ($7.03 \mu\text{M}$, $\lambda_{exc} = 418 \text{ nm}$) with increasing concentration of stDNA ($0\text{--}710 \mu\text{M}$, $0\text{--}666 \mu\text{M}$ and $0\text{--}90 \mu\text{M}$, respectively) in 10 mM sodium phosphate-buffered aqueous solution at $\text{pH } 7.4$. Inset: Plot of $\epsilon_a \text{ (M}^{-1}\text{cm}^{-1}\text{)}$ or $I_a \text{ (a.u.)}$ vs. $[\text{DNA}] \text{ (M, bases)}$ using data from absorbance at (a) 414 nm (c) 413 nm and (e) 418 nm or integrated MLCT emission intensity (b, d, f) and the best fit of the data, when possible, using a modification of the Bard Equation.

as shown in Figure 4.13. Here, complexes **81** and **82** displayed a 10% and 15% hypochromism in the MLCT band at 414 nm and 413 nm, respectively. As was seen for the **phen** analogue, complex **83** containing the twenty-one carbon alkyl chain, showed an initial decrease of the absorption at the MLCT band upon the addition of 0.3 eq. of stDNA, followed by a strong increase up to 2.0 eq. of stDNA and a slight decrease until reaching the absorption plateau. A red shift of *ca.* 6 nm of the MLCT band was simultaneously observed.

Furthermore, emission titrations of complexes **81** and **82** with stDNA showed a quenching of the MLCT emission intensity at 636 nm by 53% for both complexes, following the trend observed for ruthenium complexes containing at least two π -deficient **TAP** ligands for which their excited state is quenched as a consequence of a photo-electron transfer between the guanine moieties contained by the DNA and the MLCT excited state of the complex.^{166,203,212} Unexpectedly, the typical quenching of the emission intensity was not observed for complex **83**. In contrast, **83** exhibited a triphasic behaviour consisting of a strong decrease in the MLCT emission intensity centred at 643 nm after the addition of 0.3 eq. of stDNA, followed by an emission enhancement up to 2.3 eq. of stDNA. A decrease was seen again until no more changes were observed upon further addition of stDNA. A less obvious blue shift of *ca.* 4 nm was exhibited by this complex.

From the spectroscopic changes monitored upon addition of stDNA, binding parameters such as the binding constant (K_b) and the binding size (n) for some of these complexes were calculated using a modified Bard *et al.* model and in a similar way to that described in Section 2.5.1.^{310,311} Plots of ϵ_a vs. [DNA] and the corresponding best fit of the data, when possible, to the reorganised Bard equation are shown as insets in Figures 4.12a, 4.12c, 4.12e, 4.13a, 4.13c and 4.13e with those of I_a vs. [DNA] given in Figures 4.12b, 4.12d, 4.12f, 4.13b, 4.13d and 4.13f. The values of the obtained binding parameters are summarised in Table 4.3. A first observation of the values presented above revealed a higher affinity of the **phen** complexes for DNA when compared with their **TAP** analogues and a difference of one order of magnitude was found for complexes containing the same *N*-1,10-phenanthroline-5-yl-alkylamide ligand and either **phen** or **TAP** as ancillary ligands. Thus, **78** and **81** exhibited K_b values in the order of 10^5 and 10^4 M⁻¹, respectively, while **79** and **82** showed K_b values in the order of 10^6 and 10^5 M⁻¹, respectively. This behaviour could be anticipated from the fact that **TAP** complexes displayed a smaller hypochromic effect in their MLCT band upon addition of stDNA than the **phen** complexes, and a lower curvature of the titration curve (Figures 4.12 and 4.13). This might be due to partial intercalation of the **phen** ligands between the DNA base pairs or their insertion into the minor groove, as was reported in the

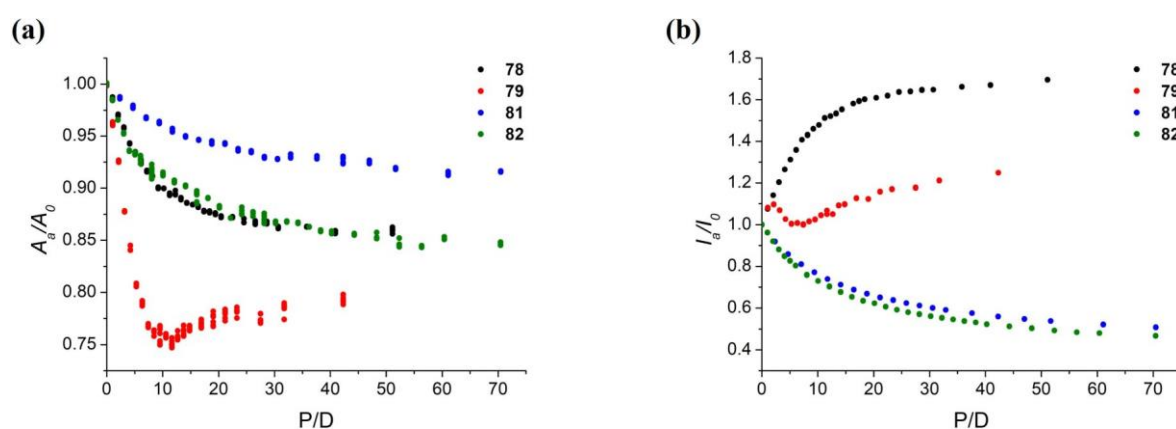
Table 4.3. DNA binding parameters of **78–83** calculated from fits to absorbance and emission data in 10 mM sodium phosphate-buffered aqueous solution at pH 7.4, at 298 K.

Complex		Absorption			Emission		
		$K_b^{[a]}$ (10^4 M^{-1})	n (base pairs) ^[a]	R^2	$K_b^{[a]}$ (10^4 M^{-1})	n (base pairs) ^[a]	R^2
phen	78	42 ± 8	3.6 ± 0.3	0.99	34 ± 2	3.4 ± 0.1	0.99
	79	553 ± 99	3.5 ± 0.3	0.99	-	-	-
	80	-	-	-	-	-	-
TAP	81	8.1 ± 0.4	$3.5^{[b]}$	0.99	9.4 ± 0.5	3.5	0.99
	82	15 ± 2	$3.5^{[b]}$	0.98	9.7 ± 0.3	3.5	0.99
	83	-	-	-	-	-	-

^[a] Results correspond to the mean \pm SEM.

^[b] n (base pairs) is fixed to 3.5, as the weak binding of the complex to DNA did not allow to keep n as a free parameter.

literature for **42**.^{418,419} Plots of the change in both MLCT absorption and emission of complexes **78**, **79**, **81** and **82** upon addition of stDNA are shown in Figure 4.14 and highlighted that the largest changes were observed for the **phen** based complexes.

**Figure 4.14.** Plot of (a) A_d/A_0 and (b) I_d/I_0 of **78**, **79**, **81** and **82** upon addition of stDNA in 10 mM sodium phosphate-buffered aqueous solution at pH 7.4, at 298 K.

Furthermore, the presence of the alkyl chain was found to improve the affinity of the complexes for DNA since larger K_b values were observed for **79** and **82** when compared with their short chain analogues **78** and **81**. These results suggest that additional hydrophobic interaction could also occur and contribute to the DNA binding event of such complexes as it was previously discussed in the literature for cationic surfactants.⁴²⁰⁻⁴²²

In addition, comparable results were obtained from both absorption and emission data within the range of the error, although the triphasic behaviour exhibited by **79** did not allow determination of the binding parameters using the emission data. Furthermore, values

of n were estimated to be of *ca.* 3.5 base pairs for complexes containing **phen** as ancillary ligands. It must be noted that, in the case of **TAP** complexes, due to their weak DNA binding, n could not be kept as a free parameter when the data were fitted and it was fixed to 3.5 assuming that both **phen** and **TAP** containing complexes have similar binding sizes. However, caution must be exercised when taking such K_b values into consideration as the replacement of the CH in positions 4 and 7 in the **phen** ligand by N in the **TAP** ligand is expected to have consequences in the binding event and, therefore, n values can be different. Unfortunately, DNA binding parameter for complexes **80** and **83** containing the twenty-one carbon alkyl chain could not be determined as a result of their complicated spectroscopic behaviour in the presence of stDNA.

After having obtained information about the interaction occurring between **78–83** and DNA through UV-vis absorption and emission titrations, the following sections will focus on gaining a further understanding of the DNA binding ability of such complexes by using various other spectroscopic techniques.

4.5.2 Thermal Denaturation Studies of Complexes 78–83

Thermal denaturation studies were also carried out to further investigate the interaction of **78–83** with stDNA in 10 mM sodium phosphate aqueous buffer at pH 7.4, as described in Section 2.5.2. Therefore, the absorbance at 260 nm of stDNA (150 μ M) in the presence of **78–83** at P/D ratios of 50, 20 and 10 was monitored as the temperature was gradually increased from 30 $^{\circ}$ C to 90 $^{\circ}$ C. Experiments were repeated at least three times to ensure reproducibility. Thermal denaturation curves recorded in the presence of **78–83** at a P/D ratio of 10 are shown in Figure 4.15 and those at P/D ratios of 50 and 20 for each complex in Figure A4.24 of the Appendices.

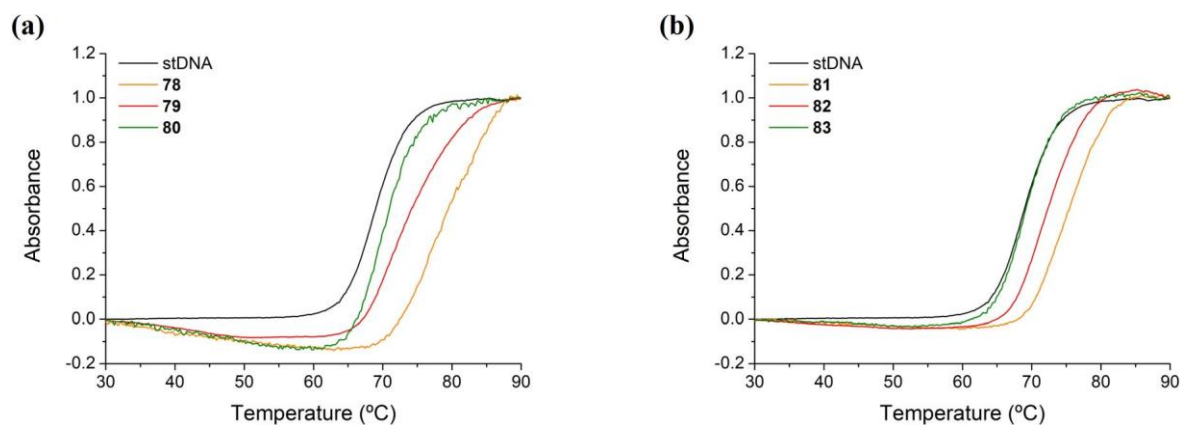


Figure 4.15. Thermal denaturation curves of stDNA (150 μ M) in 10 mM sodium phosphate-buffered aqueous solution at pH 7.4, in the absence and presence of (a) **78–80** and (b) **81–83** at a P/D ratio of 10.

In the absence of Ru(II) complexes, the T_m value determined for stDNA was 69.1 °C. In the presence of DNA binding species, this value might increase due to stabilisation of the DNA helical structure as shown in Chapter 2 for the DNA intercalators **63** and **64**. Complexes **78–83** do not contain π -extended aromatic ligands that make them suitable to bind to DNA by intercalation. However, as discussed in the previous section, other binding modes such as groove binding or partial intercalation are still possible. Variation of the T_m values for thermal denaturation of stDNA in the presence of complexes **78–83** at P/D ratios of 50, 20 and 10 are shown in Table 4.4. At a P/D of 50, complexes **78** and **81** containing the acetamide functionalised phenanthroline ligand were shown to slightly increase the T_m of stDNA. At a P/D of 20, more appreciable changes in the stDNA T_m were observed. Furthermore, at a P/D ratio of 10, these complexes were found to increase the T_m of stDNA by 10.4 and 6.2 °C, respectively, demonstrating their binding to DNA. No significant changes in the stDNA T_m were observed for complexes **79**, **80**, **82** and **83** at P/D ratios of 50 and 20. However, at a P/D of 10, while complexes **79** and **82** containing a ten carbon alkyl chain displayed a slight increase of stDNA T_m of 2.1 and 2.6 °C, respectively, complexes **80** and **83** containing twenty-one carbon alkyl chain did not induce a significant increase in the stDNA T_m and, therefore, they do not stabilise the DNA double helix structure.

Table 4.4. Variation of the melting temperature values for thermal denaturation of stDNA (150 μ M) in 10 mM sodium phosphate-buffered aqueous solution at pH 7.4, in the presence of **78–83** at different P/D ratios. T_m value without complex is 69.1 °C.

Complex		ΔT_m (°C) ^[a]		
		P/D = 50	P/D = 20	P/D = 10
phen	78	0.9 ± 0.1	5.0 ± 0.3	10.4 ± 0.9
	79	0.2 ± 0.1	0.7 ± 0.2	2.1 ± 0.2
	80	0.2 ± 0.1	0.2 ± 0.1	0.4 ± 0.2
TAP	81	0.8 ± 0.1	2.6 ± 0.1	6.2 ± 0.2
	82	0.2 ± 0.1	0.9 ± 0.1	2.6 ± 0.2
	83	-0.1 ± 0.1	0.0 ± 0.0	0.1 ± 0.1

^[a] Results correspond to the mean ± SEM.

These results suggest that the ability of these complexes to stabilise the DNA helix decrease with increasing alkyl chain length and are in contrast with the DNA binding studies performed by UV-vis absorption and emission spectroscopy discussed in the previous

section where complexes **79** and **82** with the ten carbon alkyl chain showed a greater affinity for DNA than their analogues **78** and **81** which contain the acetamide functionalised phenanthroline ligand. Thus, in order to shed more light on the binding of these complexes to DNA, circular dichroism studies were carried out and they will be discussed in the next section.

4.5.3 Circular Dichroism of Complexes 78–83 in the Presence of DNA

In an attempt to further study the interaction of **78–83** with DNA, circular dichroism titrations were performed in 10 mM sodium phosphate aqueous buffer at pH 7.4, in the same way as described in Section 2.5.3 for complexes **63** and **64**. Thus, the concentration of stDNA was kept constant (150 μ M) and that of the racemic mixture of complexes was varied with P/D ratios of 50, 20, 10 and 5. CD titrations were repeated at least three times to ensure reproducibility. CD spectra of **79** and **82** are shown in Figure 4.16 with those of **78**, **80**, **81** and **83** shown in Figure A4.25 of the Appendices.

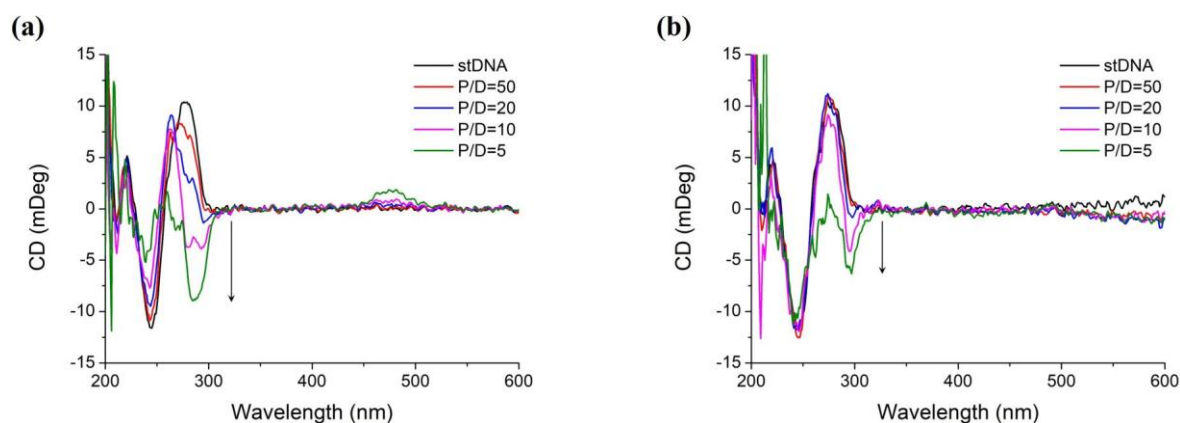


Figure 4.16. Circular dichroism spectra of stDNA (150 μ M) in 10 mM sodium phosphate-buffered aqueous solution at pH 7.4, in the absence and presence of (a) **79** and (b) **82** at different P/D ratios.

In the presence of **78** and **81**, the appearance of a negative band was observed in the DNA absorption region with a maximum at approximately 293 nm for both **78** and **81**, which corresponds to π - π^* intra-ligand transitions of the ancillary **phen** and **TAP** ligands. As these transitions from both complexes are in the UV region and overlap with the DNA absorption bands, it is difficult to discern if these bands result from an ICD or from structural changes in the DNA as a result of complexes interacting with the double helix structure. Similarly, the CD spectra of stDNA obtained in the presence of complexes **79** and **82** showed the evolution of a negative band at 285 and 296 nm for **79** and **82**, respectively. In addition, the **phen** derivative **79** also exhibited a small positive ICD signal at about 475 nm that can be attributed to the typical MLCT absorption band of the Ru(II) polypyridyl complexes. These

changes normally indicate the existence of an interaction between the complex and the DNA by intercalation or groove binding.³²² However, minor changes were observed upon addition of complexes **80** and **83** to stDNA with only a small negative band in the UV region, resulting in an almost complete disappearance of the characteristic DNA CD signal at a P/D ratio of 5. Once again, the **phen** derivative **80** showed a small positive ICD signal at *ca.* 480 nm in the charge-transfer region.

Overall, these results show that in all cases the CD spectrum of DNA was affected by the presence of the complexes. However, these changes are mainly in the UV region, where the absorption bands of complexes and DNA overlap, and are less dramatic than those observed for the intercalating Ru(II) complexes **63** and **64** studied in Chapter 2. Although these observations point to the existence of an interaction between the metallic complexes and the biomolecule, a further confirmation of this conclusion needs to be supported by other DNA binding studies. Thus, taking previous spectroscopic studies into consideration, it can be concluded that complexes **78**, **79**, **81** and **82** bind to DNA and such interactions are likely to occur by a combination of electrostatic attraction between the cationic Ru(II) complex and the negatively charged phosphate backbone of DNA, and partial intercalation into the DNA base pairs or insertion into the grooves of the ancillary ligands, as has been demonstrated in the literature for systems such as **42**.^{418,419} Furthermore, additional hydrophobic interactions between **79** and **82** and the nucleic acid are expected. Interestingly, the DNA binding strength seems to be affected by the alkyl chain length and such effect was different depending on the spectroscopic technique used to study the binding event. Thus, while complexes **79** and **82** containing a ten carbon alkyl chain displayed larger K_b values than their analogues **78** and **81** with an acetamide functionalised phenanthroline ligand, an increase of the alkyl chain length had a negative impact on the stabilisation of the double helix as established by DNA melting temperature studies. Therefore, it is not conclusive whether the DNA binding strength of these complexes increases or decreases with lengthening the alkyl chain. In addition, overall results indicate that **TAP** complexes have a lower affinity for DNA than the **phen** analogues. Both **80** and **83**, containing the longest alkyl chains, exhibited complicated spectroscopic behaviour upon addition of DNA, as such K_b values could not be determined for these compounds and thus the strength of their interaction with DNA could not be quantified. However, DNA denaturation and circular dichroism studies with both complexes have shown no significant stabilisation and changes in the conformation of the DNA helical structure suggesting a low affinity of complexes **80** and **83** for DNA.

Once the DNA binding of complexes **78–83** was evaluated, lipophilicity studies were then performed with a view to test their ability to cross the cell membrane and be used in live cell imaging and therapeutic applications.

4.6 Lipophilicity Studies of 78–83

Evaluation of the lipophilicity of molecules designed to be used in a cellular context is very important as this parameter plays a key role in the cellular uptake mechanism of such molecules and can influence their toxicity and cellular localisation. In this context, complexes containing long alkyl chains discussed in this chapter were expected to be highly lipophilic and be able to cross the cell membrane. In order to evaluate the lipophilicity of complexes **42**, **39** and **78–83**, the logarithm of their partition coefficient ($\log P$) was determined by using the “shake-flask” method.⁴²³ It must be noted that since the complexes studied in this chapter do not contain ionisable groups, they are not expected to be protonated/deprotonated at physiological pH, and as such $\log P$ values were calculated instead of the logarithm of their distribution coefficient ($\log D$). Thus, the complexes were dissolved in water (previously presaturated with 1-octanol) and mixed with an equal volume of 1-octanol (previously presaturated with water). The resulting mixture was shaken overnight before the two layers were carefully separated by centrifugation. The concentration of ruthenium in the aqueous phase was then determined by UV-vis absorption

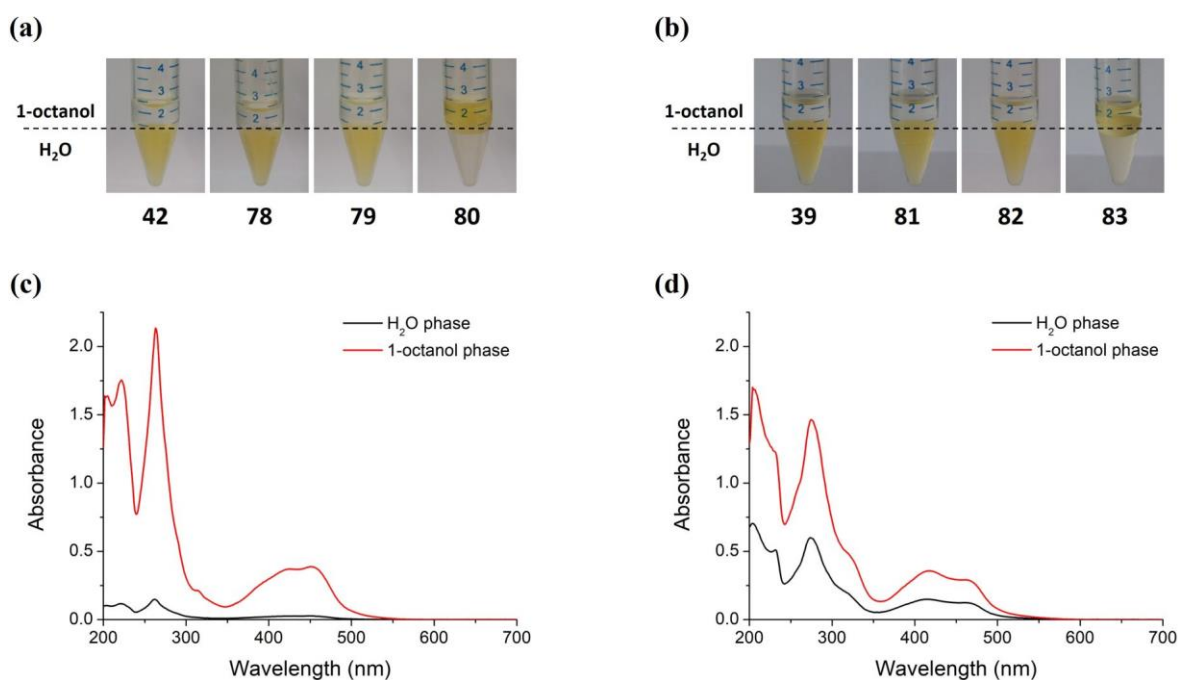


Figure 4.17. Partition studies of (a) **42** and **78–80** ($50 \mu\text{M}$) and (b) **39** and **81–83** ($50 \mu\text{M}$) between 1-octanol and water phases. UV-vis absorption spectra of (c) **80** and (d) **83** in water (black) and 1-octanol (red) phases at 298 K, showing the preference of both complexes by the 1-octanol phase.

spectroscopy and the $\log P$ values for each complex were calculated by taking into account the initial concentration of ruthenium complex in the water phase before the shaking step with 1-octanol. Preference of complexes **80** and **83** by the 1-octanol phase can be observed in Figure 4.17. UV-vis absorption spectra of complexes **42**, **78**, **79**, **39**, **81** and **82** in both aqueous and 1-octanol phases are shown in Figure A4.26 of the Appendices.

The $\log P$ values determined for complexes **42**, **39** and **78–83** are shown in Table 4.5 and reveal that the alkyl chain length as well as the ancillary ligands coordinated to the ruthenium centre have an influence on the lipophilicity of the complexes.

Table 4.5. The $\log P$ values of **42**, **39** and **78–83** at 298 K, showing the influence of the alkyl chain length and the ancillary ligands of the complex in their lipophilicities.

Complex		Alkyl chain (R)	$\log P^{[a]}$
phen	42	-	-2.28 ± 0.12
	78	CH ₃	-2.52 ± 0.08
	79	(CH ₂) ₉ CH ₃	-1.40 ± 0.05
	80	(CH ₂) ₂₀ CH ₃	1.07 ± 0.08
TAP	39	-	-2.76 ± 0.02
	81	CH ₃	-2.76 ± 0.22
	82	(CH ₂) ₉ CH ₃	-1.97 ± 0.05
	83	(CH ₂) ₂₀ CH ₃	0.49 ± 0.07

^[a] Results correspond to the mean \pm SEM.

The $\log P$ values obtained for complexes **78–80** containing **phen** as ancillary ligands showed an increase of the lipophilicity with the increasing alkyl chain length. In this manner, complex **80**, containing a twenty-one carbon alkyl chain, displayed the highest lipophilicity with a $\log P$ value of 1.07, followed by **79**, with a ten carbon alkyl chain and a $\log P$ value of -1.40 . On the other hand, the reference complex **42** and complex **78**, containing the acetamide functionalised phenanthroline ligand, were found to be the least lipophilic complexes with $\log P$ values of -2.28 and -2.52 , respectively. Modulation of the lipophilicity of Ru(II) polypyridyl complexes by varying the number of methylene groups contained by the polypyridyl ligands have already been reported by researchers.¹⁸⁸

A similar behaviour was observed for the **TAP** analogues (**81–83**). Thus, while complexes **83** and **82**, with twenty-one and ten carbon alkyl chains, respectively, showed the highest $\log P$ values, 0.49 and -1.97 , respectively, both the reference complex **39** and

complex **81** containing only one methyl group, displayed the lowest log P values, -2.76 in both cases. However, when compared **phen** and **TAP** derivatives, complexes containing **phen** as ancillary ligands were shown to be more lipophilic than those containing **TAP**. It has been demonstrated that substitution of **phen** ancillary ligands by **bpy** results in a significant reduction in the lipophilicity of the complex.¹⁷² However, to the best of our knowledge, log P values of **TAP** containing complexes have not been reported in the literature. Although lipophilicity of **TAP** complexes has not been quantified, it has been demonstrated that the complex **42** tethered to the cell-penetrating peptide TAT exhibited a greater uptake in HeLa cells than its **TAP** analogue, as shown by ICP-MS measurements.¹⁹⁷ This suggests that **TAP** complexes are more hydrophilic than their **phen** analogues, in agreement with the results presented here for complexes **42**, **39** and **78–83**.

These observations are significant for the biological evaluation of these complexes and to further understand their cellular uptake, which will be discussed later in this chapter. The results also suggest that the most lipophilic complexes **80** and **83** are expected to be the best candidates to be able to cross the cell membrane and be internalised into cells. In the next section, the ability of these complexes to be activated by production of singlet oxygen using light as trigger agent will be examined which will give an indication on their suitability to be used as PDT agents.

4.7 Singlet Oxygen Photosensitisation of 78–83

As discussed previously in Section 1.4 and in Section 2.6, singlet oxygen generation is involved in the Type II mechanism of PDT and so quantifying the amount of this reactive oxygen species produced by a molecule can be very useful for evaluating its ability to act as photosensitiser in PDT.⁶³ Therefore, quantum yields of $^1\text{O}_2$ production of complexes **78–83** have been determined by direct measurement of $^1\text{O}_2$ phosphorescence at 1265 nm and monitoring the fluorescence disappearance of the water-soluble $^1\text{O}_2$ chemical probe, 9,10-anthracenediyl-bi(methylene)dimalonic acid (ABDA).

4.7.1 Direct Detection of Singlet Oxygen Production by Time-Resolved Near-Infrared Phosphorescence

Quantum yields of $^1\text{O}_2$ production (Φ_A) of complexes **78–83** in O_2 -saturated D_2O solutions were first determined by time-resolved near-infrared (NIR) phosphorescence from $^1\text{O}_2$ in collaboration with Prof. Guillermo Orellana at Universidad Complutense de Madrid (UCM) and using the experimental procedure described in Section 2.6. Complexes **42** and **39** were included in this study as reference complexes. As was highlighted previously, using D_2O as

solvent instead of regular H₂O is due to the shorter ¹O₂ lifetime in H₂O compared to its deuterated analogue. However, knowing the Φ_{Δ} values in H₂O and in air conditions seems more reasonable when extrapolating to biological systems. Thus, conversion of the Φ_{Δ} values obtained in O₂-saturated D₂O into the ones in air-saturated H₂O was achieved using equations (2.6) and (2.7) of Chapter 2 and assuming that the fraction of quenched Ru(II) triplet that yields ¹O₂ is the same in D₂O and H₂O and knowing the lifetimes of the complexes in O₂- and argon-saturated D₂O, and air- and argon-saturated H₂O.

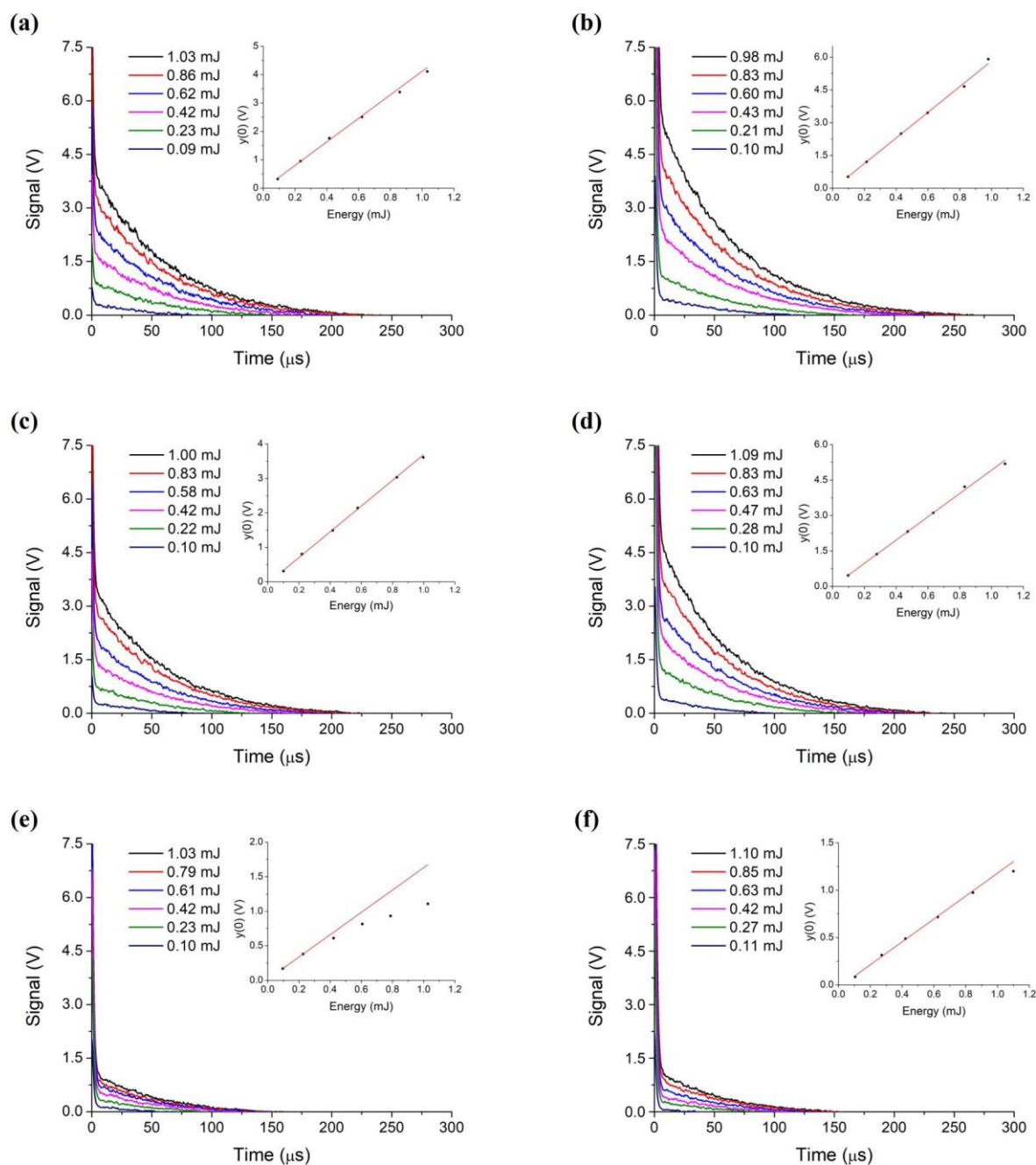


Figure 4.18. Singlet oxygen emission decays at 1270 nm produced by (a) **78**, (b) **81**, (c) **79**, (d) **82**, (e) **80** and (f) **83** at different laser energies ($\lambda_{exc} = 532$ nm) in O₂-saturated D₂O solution at 298 K. Inset: Plot of intercept values (V) vs. laser energy (mJ) and the best linear fit of the data.

The $^1\text{O}_2$ luminescence decay profiles of complexes **78–83** in O_2 -saturated D_2O are shown in Figure 4.18 with those in the presence of complexes **42** and **39** given in Figure A4.27 of the Appendices. τ_{em} and Φ_A values at different conditions are outlined in Table 4.6. Singlet oxygen production was shown to be dependent on the nature of the ancillary ligands (**phen** or **TAP**) and on the alkyl chain length. Thus, complexes **39** and **81–83** containing **TAP** as ancillary ligands displayed higher Φ_A values than their **phen** analogues in O_2 -saturated D_2O . This behaviour can be explained by the fact that the excited-state oxidation potentials of **TAP** complexes are significantly higher than those of **phen** analogues resulting in a considerable slowing down of the superoxide competing route that requires photoinduced electron transfer from the ruthenium complex to O_2 .³²⁶ However, when Φ_A values were converted from O_2 -saturated D_2O to air-saturated H_2O conditions the opposite behaviour was observed, that is, complexes containing **phen** as ancillary ligands displayed higher Φ_A values than their **TAP** analogues. This is due to a lower efficiency of quenching of the excited states of **TAP** complexes by oxygen in H_2O when compared with the **phen** complexes as can be observed from the calculated values of the proportion of triplet excited

Table 4.6. Emission lifetimes (τ_{em}) measured in O_2 - and argon-saturated D_2O , and in air- and argon-saturated H_2O , and quantum yields of singlet oxygen production (Φ_A) and proportion of triplet excited states quenched by O_2 ($P_{\text{O}_2}^T$) in O_2 -saturated D_2O and air-saturated H_2O for complexes **42**, **39** and **78–83**.

Complex		τ_{em} (ns) ^[a] (O_2 , D_2O)	τ_{em} (ns) ^[a] (Ar, D_2O)	τ_{em} (ns) ^[a] (Air, H_2O)	τ_{em} (ns) ^[a] (Ar, H_2O)	Φ_A (O_2 - satd. D_2O) ^[b]	Φ_A (Air- satd. H_2O)	$P_{\text{O}_2}^T$ (O_2 - satd. D_2O)	$P_{\text{O}_2}^T$ (Air- satd. H_2O)
phen	42	180 ^[c]	1154 ^[c]	505 ^[d]	933 ^[d]	0.39	0.21	0.84	0.46
	78	195	1358	596	1198	0.52	0.31	0.86	0.50
	79	201	1495	640	1242	0.44	0.24	0.87	0.48
	80	361 ^[e]	719 ^[e]	876 ^[e]	947 ^[e]	0.18 ^[f]	0.03	0.50	0.08
TAP	39	480	1724	724 ^[d]	840 ^[d]	0.72	0.14	0.72	0.14
	81	480	1868	740	919	0.69	0.18	0.74	0.19
	82	495	1947	760	954	0.59	0.16	0.75	0.20
	83	326 ^[e]	985 ^[e]	770 ^[e]	825 ^[e]	0.14	0.01	0.50	0.08

^[a] If not otherwise indicated, the luminescence decays are monoexponential. Estimated errors $\pm 5\%$.

^[b] O_2 -saturated D_2O solution of $[\text{Ru}(\text{phen})_3]\text{Cl}_2$ as reference ($\Phi_A = 0.39$).³²⁷ Estimated errors $\pm 5\%$.

^[c] From reference 326.

^[d] From reference 197.

^[e] The luminescence decays are bi- or tri-exponential; reported data correspond to the pre-exponential weighted mean lifetimes (τ_M).³²⁹ See Section 7.2 in Chapter 7 and Table A4.4 of the Appendices for further information.

^[f] Calculated from the linear fit of the data at low laser energy due to deviation from linearity of the data at high laser energy.

states quenched by O_2 ($P_{O_2}^T$) for both **phen** and **TAP** complexes reported in Table 4.6. Further details about the equation used to calculate the $P_{O_2}^T$ values can be found in Section 2.6 and Section 7.2 of Chapter 7.³²⁶

On the other hand, while complexes **78** and **81** containing the acetamide functionalised phenanthroline ligand showed the highest Φ_{Δ} value followed by **79** and **82** with the ten carbon alkyl chain, complexes **80** and **83** containing the twenty-one carbon alkyl chain exhibited the lowest ones. At first, this behaviour could be expected assuming that complexes containing long alkyl chains will be more protected from molecular oxygen preventing the interaction with the ruthenium centre to generate 1O_2 . However, it was demonstrated in previous sections of this chapter that complexes **80** and **83** are able to self-organise into micellar species. As direct measurement of the 1O_2 phosphorescence is a method that requires a high concentration of photosensitiser ($A_{532} \approx 0.4$, which corresponds to 331 μM and 304 μM concentration of **80** and **83**, respectively) for detecting 1O_2 signal, micelle formation by **80** and **83** can be expected at these conditions according to the cmc values calculated in Section 4.4.1 of this chapter. The ability of these complexes to produce 1O_2 could be different depending on whether the monomers are free in solution or forming micelles. In order to study the influence of the self-assembly state on the Φ_{Δ} values, an indirect method that requires lower concentrations of photosensitiser, at which it would behave as a free monomer, was also employed and it will be discussed in the next section.

4.7.2 Indirect Detection of Singlet Oxygen Production by Chemical Photoconsumption of 9,10-Anthracenediyl-bi(methylene)dimalonic Acid (ABDA)

As previously described in Section 2.6, another way to evaluate the ability of a molecule to produce 1O_2 is through indirect methods where changes in the absorption or in the emission

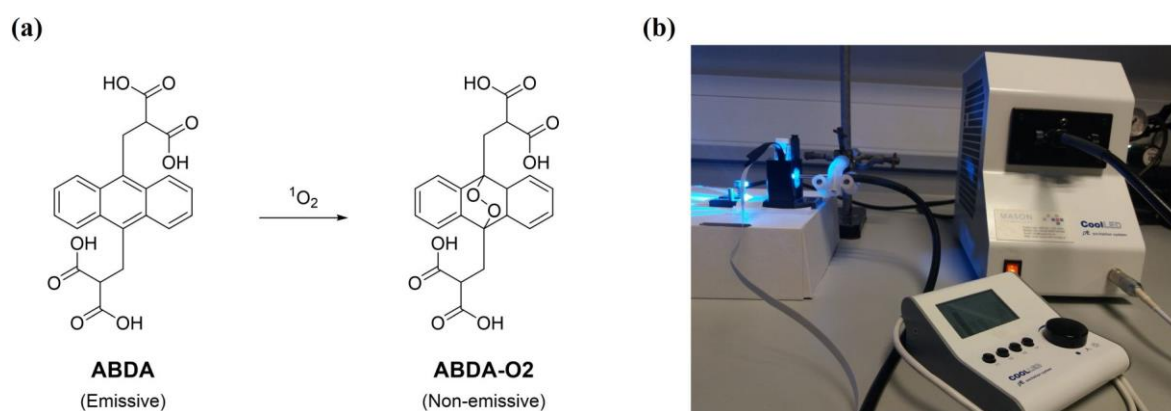


Figure 4.19. (a) Schematic illustration of the photooxidation of the 1O_2 chemical probe ABDA by 1O_2 . (b) pE-2 fluorescence LED used as illumination source.

properties of a chemical probe that undergoes photooxidation in the presence of $^1\text{O}_2$ are monitored. In this context, 9,10-anthracenediyl-bi(methylene)dimalonic acid (ABDA) was employed as a water-soluble $^1\text{O}_2$ probe for further investigation of the $^1\text{O}_2$ generation by complexes **42**, **39** and **78–83**, as this molecule is known to convert into a non-emissive endoperoxide product upon reaction with $^1\text{O}_2$ (Figure 4.19a).⁴²⁴ Thus, aqueous solutions containing ABDA (2 μM) in the presence of the reference photosensitiser $[\text{Ru}(\text{bpy})_3]\text{Cl}_2$ ($\Phi_{\Delta} = 0.18$ in air-saturated H_2O at room temperature)⁴²⁵ and the ruthenium complex ($A_{470} \approx 0.01$),

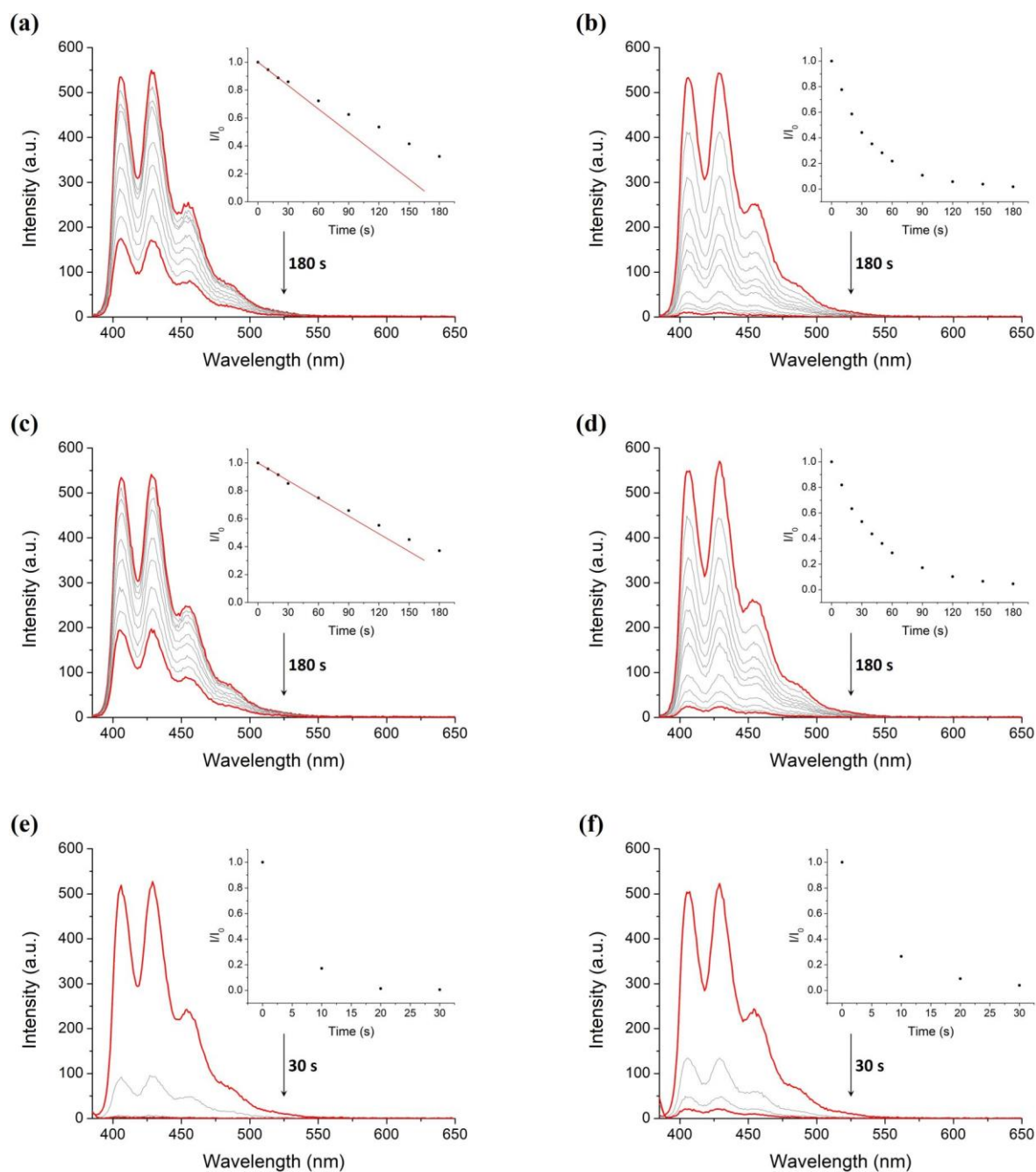


Figure 4.20. Emission spectra of ABDA ($\lambda_{\text{exc}} = 380 \text{ nm}$) in the presence of (a) **78**, (b) **81**, (c) **79**, (d) **82**, (e) **80** and (f) **83** ($A_{470} \approx 0.01$) in H_2O at different irradiation times using a 470 nm pE-2 LED illumination system (100% intensity), at 298 K. Inset: Plot of I/I_0 vs. irradiation time (s) and the best linear fit of the data.

for which its ability to act as photosensitiser was evaluated, were irradiated using a 470 nm pE-2 fluorescence LED (100% intensity) as illumination source (Figure 4.19b) to ensure no light absorption by the ABDA. The emission spectra of ABDA in the presence of complexes **78–83** upon increasing irradiation times are shown in Figure 4.20 with those in the presence of complexes **42** and **39** given in Figure A4.28 of the Appendices. In order to exclude any degradation of ABDA upon irradiation and make sure that the changes observed are due to the $^1\text{O}_2$ production by the ruthenium complexes, the emission spectra of ABDA in the absence of photosensitiser were also recorded and are shown in Figure A4.29 of the Appendices. No change in the emission intensity of ABDA at 405 nm was observed with the irradiation time. However, in the presence of complexes **42**, **39** and **78–83**, a decrease in the emission intensity of ABDA was observed as the irradiation time increased, indicating the formation of the non-fluorescent endoperoxide product of the ABDA and, therefore, generation of $^1\text{O}_2$ by all the complexes tested.

Emission intensity of ABDA at 405 nm was plotted as a function of the irradiation time and, from the linear regression of the obtained plots, slope values (m) were determined when possible. Quantum yields values of singlet oxygen production of complexes **42**, **39** and **78–83** were calculated according to equation (2.5) of Chapter 2 and are summarised in Table 4.7, as well as the corresponding percentages of photobleaching of the ABDA emission band at 405 nm after 10 s irradiation ($\lambda_{exc} = 470$ nm).

Table 4.7. Percentage of photobleaching of ABDA (emission band at 405 nm) in the presence of complexes **78–83** ($A_{470} \approx 0.01$) after 10 s irradiation ($\lambda_{exc} = 470$ nm) and quantum yields of singlet oxygen production (Φ_A) in air-saturated H_2O for complexes **42**, **39** and **78–83**.

Complex		%Photobleaching (405 nm, 10 s irradiation)	Φ_A (Air-satd. H_2O) ^[a,b]
phen	42	5	0.22
	78	5	0.29
	79	4	0.23
	80	83	-
TAP	39	19	-
	81	22	-
	82	18	-
	83	73	-

^[a] Calculated using equation (2.5) outlined in Section 7.2 of Chapter 7.

^[b] Air-saturated H_2O solution of $[\text{Ru}(\text{bpy})_3]\text{Cl}_2$ as reference ($\Phi_A = 0.18$).⁴²⁵

Interestingly, the disappearance of the ABDA emission is much slower in the presence of complexes **42**, **78** and **79** than with complex **80**, resulting in a 5%, 5%, 4% and 83% of photobleaching, respectively. The same behaviour was observed for the **TAP** analogues **39**, **81** and **82** that exhibited a 19%, 22% and 18% of photobleaching, respectively, while **83** displayed a decrease in the emission intensity of the ABDA at 405 nm of 73%. Plots of the change in the emission intensity of ABDA at 405 nm in the presence of complexes **42**, **39** and **78–83** and upon increasing irradiation times are shown in Figure 4.21 and highlighted that the fastest decreases are observed for complexes **80** and **83** containing the twenty-one carbon alkyl chain.

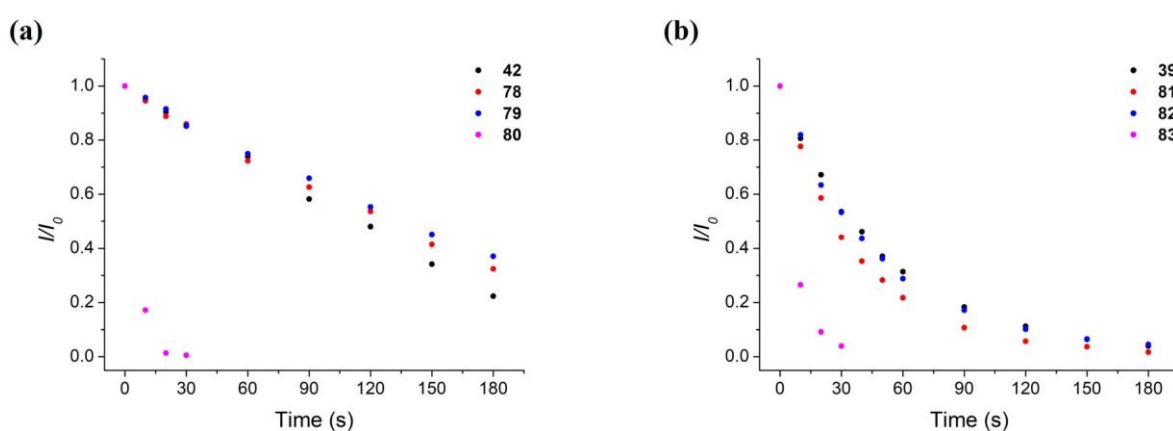


Figure 4.21. Rate of decay of ABDA emission intensity at 405 nm photosensitised by complexes (a) **42** and **78–80** and (b) **39** and **81–83** in air-saturated aqueous solution at 298 K.

Concerning the Φ_A values determined for these complexes in air-saturated H_2O , **42**, **78** and **79** displayed similar values to those obtained by time-resolved NIR phosphorescence from $^1\text{O}_2$ in the previous section. However, it must be noticed that while the evolution of the ABDA emission intensity with the irradiation time showed a linear trend, a slightly biphasic behaviour was observed for complexes **78** and **79** and only the first points could be used for the fitting and subsequent calculation of their Φ_A values. This could be explained by the existence of an interaction between the Ru(II) complex and the $^1\text{O}_2$ chemical probe. It can be assumed that the nature of such interaction is not electrostatic as biphasic behaviour was not observed for the reference $[\text{Ru}(\text{bpy})_3]^{2+}$ and the complex **42** which have the same double positive charge as **78** and **79**. Therefore, this interaction is more likely to be hydrophobic due to the presence of the alkyl chain in **79** although an additional interaction between the amide of the complex and the carboxylate of the ABDA cannot be dismissed. In addition, hydrophobic interactions with the $^1\text{O}_2$ chemical probe showed to be more important for

complex **80** and, as a consequence, although $^1\text{O}_2$ production can be assumed due to the fast decrease of the ABDA emission with the irradiation time, quantification was not possible.

Interestingly, **TAP** derivatives **39** and **78–83** exhibited a different behaviour as the consumption of the $^1\text{O}_2$ chemical probe decreased exponentially over time in contrast to the linear decrease observed for the **phen** complexes, that is first- and zero-order reaction kinetics, respectively. Thus, while the rate of disappearance of ABDA depends on the chemical probe concentration when the **TAP** analogues were used as photosensitisers, this is ABDA concentration independent in the presence of **phen** complexes. This behaviour could be explained by the remarkably photooxidant character of the excited state of Ru(II) complexes containing **TAP** as ancillary ligands providing them with the ability to directly photooxidise the ABDA. Thus, the co-existence of two competitive processes, that is oxidation of the chemical probe by $^1\text{O}_2$ production and/or by the **TAP** complex, can be presumed. This hypothesis is supported by the redox potentials reported in the literature for the species involved. The reduction potential of **39** in the excited state is +1.15 V/SCE while the oxidation potential of 9,10-dimethylanthracene is +1.09 V/SCE.^{166,426} Unfortunately, the oxidation potential of ABDA has not been previously determined and the value reported for 9,10-dimethylanthracene was used instead, assuming that the malonic acid moiety in ABDA did not have a strong effect in the oxidation potential of the anthracene derivative. From these values it can be concluded that direct photooxidation of ABDA is slightly thermodynamically favourable ($\Delta G^0 = -0.06$) although the exact oxidation potential of ABDA would be necessary to obtain a more accurate value. Therefore, Φ_{Δ} values for these complexes could not be determined through this method.

Despite it not being possible to quantify Φ_{Δ} values of both **80** and **83**, if it is assumed that singlet oxygen generation is involved in the fast consumption of the ABDA under irradiation in the presence of such complexes, the dramatic increase of $^1\text{O}_2$ production by these complexes when using ABDA as $^1\text{O}_2$ chemical probe in contrast to direct measurement of $^1\text{O}_2$ phosphorescence can be explained by the fact that this method requires a lower photosensitiser concentration. Complexes **80** and **83** have been shown to self-aggregate at concentrations above 112 and 114 μM , respectively. As explained in the previous section, the complex concentrations used for quantifying their $^1\text{O}_2$ production by direct measurement of the $^1\text{O}_2$ phosphorescence are above their cmc values and, therefore, **80** and **83** are expected to form aggregates. However, the use of chemical probes such as ABDA to determine the quantum yields of singlet oxygen production by these complexes required a very low concentration of photosensitiser ($A_{470} \approx 0.01$, which corresponds to 0.77 μM and 0.78 μM

for **80** and **83**, respectively). In these conditions, complexes **80** and **83** are expected to behave as free monomers making it easier for the interaction between the metallic centre and molecular oxygen to form $^1\text{O}_2$ to occur. Hence, it can be concluded that these complexes containing the twenty-one carbon alkyl chain display Φ_{Δ} values that are concentration dependent due to their ability to self-assemble into micelles. Thus, at concentrations below their cmc, complexes **80** and **83** would produce more $^1\text{O}_2$ than at concentrations above their cmc.

These results highlight the importance of the chemical properties of a potential photosensitiser when selecting a method to quantify its singlet oxygen production. Thus, although direct measurement of $^1\text{O}_2$ phosphorescence is often suitable to determine the Φ_{Δ} values of most photosensitisers, caution must be exercised with those possessing the ability to self-aggregate as this method required larger photosensitiser concentrations. Furthermore, the photooxidant character of the excited state of a photosensitiser has to be taken into account when investigating its $^1\text{O}_2$ production by photooxidation of a particular chemical probe as it seems that this method is not adequate for complexes containing **TAP** as ancillary ligands due to their strong oxidant excited state that can result in a competitive via to the $^1\text{O}_2$ photooxidation of the chemical probe.

Having evaluated the ability of complexes **78–83** to produce $^1\text{O}_2$ by two different methods, that is direct detection of $^1\text{O}_2$ phosphorescence and photooxidation of the $^1\text{O}_2$ trap ABDA, cellular studies were subsequently undertaken with a view to investigate their cellular uptake as well as their potential as PDT agents through the study of their cytotoxicity in both dark and exposed to light.

4.8 *In vitro* Studies of **78–83**

Cellular uptake and viability studies of **78–83** in HeLa cervical cancer cells were next carried out in order to investigate their ability to be internalised in live cells and reduce viability. These studies were achieved in collaboration with Dr Sandra Bright.

4.8.1 Cellular Uptake Studies of **78–83**

Confocal fluorescence microscopy was used in order to evaluate the cellular uptake and localisation of **78–83** in live cells. Thus, HeLa cells were incubated with **78** and **81** (50 μM) at 37 °C for 24 h and **79**, **82**, **80** and **83** (10 μM) at 37 °C for 2, 4 and 24 h before being treated with the fluorescent nuclear stain Hoechst 33258 and imaged using an Olympus FV1000 point scanning microscope with a 60x oil immersion lens with an NA (numerical aperture) of 1.42. Complexes **42** and **39** were used as references at 50 μM concentration and

incubated in HeLa cells for 24 h. Experiments were repeated on three independent days to ensure reproducibility. The results obtained from these experiments are shown in Figure 4.22 and demonstrated that **78** and **81** were not taken up into the cells (Figures 4.22c and 4.22g). Luminescence from these complexes could be imaged in the medium under high powered lasers, with little or no luminescence being observed inside the cells. The same behaviour was observed for the reference complexes **42** and **39** (Figures 4.22a and 4.22e).

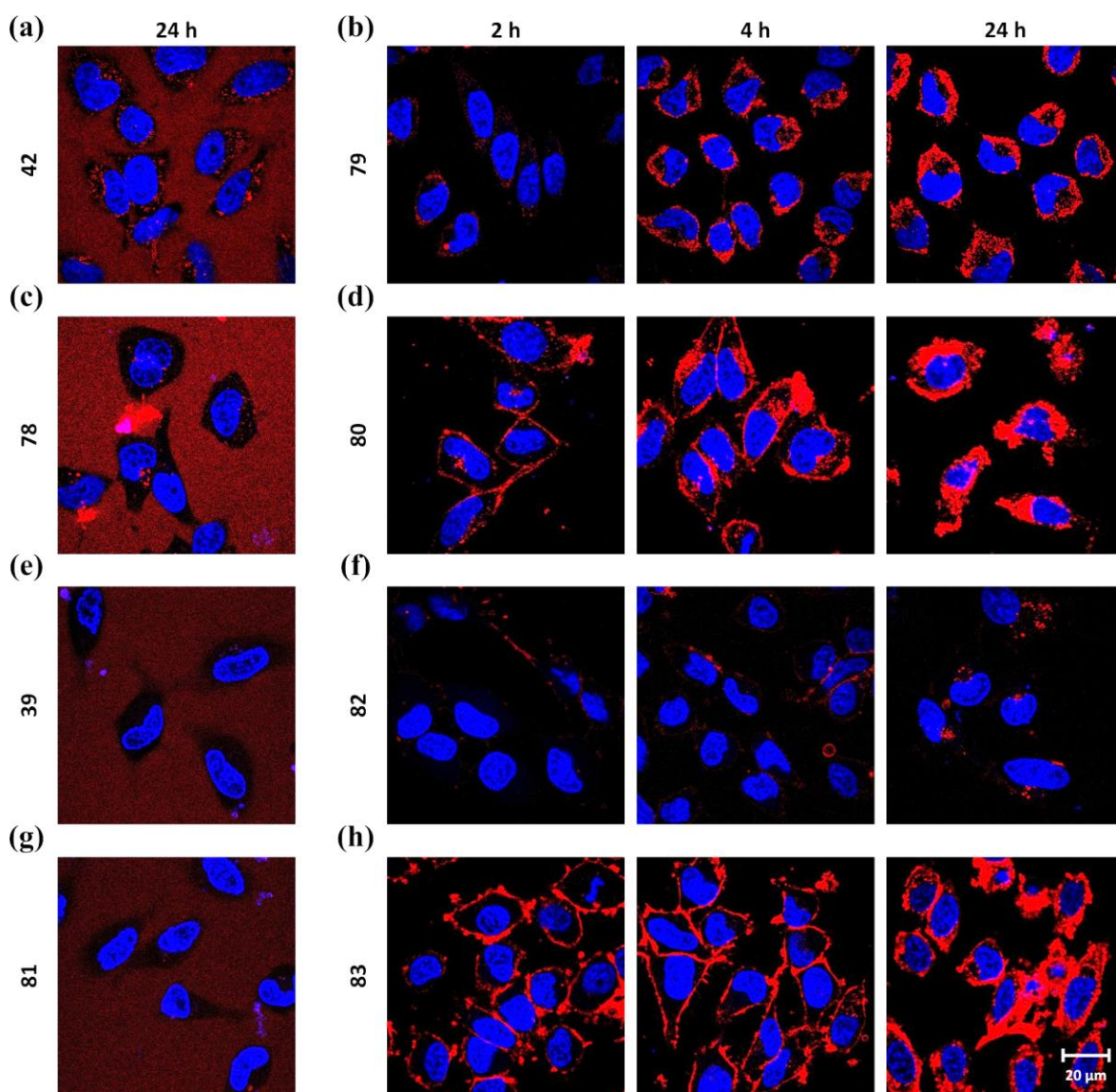


Figure 4.22. Confocal fluorescence microscopy images of HeLa cells showing the uptake of (a) **42** (red, 50 μM), (b) **79** (red, 10 μM), (c) **78** (red, 50 μM), (d) **80** (red, 10 μM), (e) **39** (red, 50 μM), (f) **82** (red, 10 μM), (g) **81** (red, 50 μM) and (h) **83** (red, 10 μM) after different incubation times. The nucleus is stained blue with Hoechst 33258.

However, time dependant cellular uptake was shown for complexes **79**, **82**, **80** and **83** and, in particular, for **80** and **83** which were rapidly taken up into the cells after 2 h incubation with initial localisation in the cell membrane (Figures 4.22b, 4.22d, 4.22f and 4.22h). This behaviour was not unexpected due to the amphiphilic character of these

complexes resulting in the insertion of the lipophilic tail into the cell membrane while the luminescent polar head resides on the surface acting as a luminescent membrane probe. Similar cell membrane localisation has already been described in the literature for other ruthenium complexes containing hydrophobic alkyl chains.^{180,181,427}

Uptake increased after 4 and 24 h incubation, as evidenced by increasing red luminescent emission from these complexes within cells and they appeared to be localised within the cytoplasm of cells. At this concentration, cell morphology suggested that **79**, **82** and **83** were well tolerated. However, the morphology of cells treated with **80** suggested this complex was highly toxic, with evidence of the cells undergoing apoptosis and necrosis. On the other hand, the weak luminescence of complex **82** inside the cells has to be pointed out. A reduction of the emission intensity of Ru(II) complexes containing **TAP** as ancillary ligands when compared to their **phen** analogues has also been reported in the literature.^{197,198} As has been discussed in Section 1.6.3, it is well known that Ru(II) complexes containing at least two π -acceptor ligands such as **TAP** are strong enough oxidising agents to extract an electron from weakly reducing biomolecules (*e.g.* guanine, tryptophan or tyrosine) through a photoinduced electron transfer process, resulting in a quenching of the luminescence of the metallic complex. In this context, it can be presumed that the luminescence of **82** is quenched by a PET process between the ruthenium moiety and the amino acids residues of the proteins existing within the cell. Although the same behaviour could be expected for complex **83** inside the cells, the longer alkyl chain could prevent the metallic centre from being in close proximity to the reducing species and protect its luminescence from being quenched. This explanation is supported by the DNA binding studies carried out in Section 4.5 of this chapter. As shown in the emission spectroscopic titrations performed on both complexes **82** and **83** in the presence of stDNA, while a dramatic quenching of luminescence was observed for complex **82** upon addition of the guanine containing biomolecule, no significant change in the emission of complex **83** was detected in the presence of increasing concentrations of stDNA.

In addition, to further understand the luminescence properties of these complexes in a biological environment and taking into account that luminescence quenching by the guanine would not be expected as the complexes do not seem to reach the cell nucleus, emission studies of complexes **82** and **83** in the presence of tryptophan were carried out and are shown in Figure A4.30 of the Appendices. Same studies were conducted for complexes **79** and **80** for comparison. Thus, emission spectra of the four complexes (10 μ M) in the absence or in the presence of L-tryptophan (5 mM) were recorded. Emission intensity of

complexes **79** and **80** decreased by 9% and 35% at 603 and 614 nm, respectively, in the presence of tryptophan. Surprisingly, both **82** and **83** showed similar luminescence quenching in the presence of tryptophan with an 89% and 91% decrease in emission at 636 and 643 nm, respectively. Therefore, it could be presumed that, although both complexes exhibited a decrease of the emission in the presence of the reducing amino acid, complex **83** displayed a higher lipophilicity than complex **82**, resulting in a larger intracellular concentration and, consequently, in a higher emission intensity despite the luminescence quenching by the tryptophan.

These results demonstrated that the successful cellular uptake of **79**, **82**, **80** and **83** is due to the presence of the long alkyl chain since complexes **78** and **81** containing only one methyl group were not taken up into the cells. In addition, these results are also in agreement with the lipophilicity studies discussed in Section 4.6 as complexes **79**, **82**, **80** and **83** and, in particular, **80** and **83**, showed to be more lipophilic than **78** and **81** and the reference complexes **42** and **39** making them more suitable to cross the lipid bilayer that forms the cell membrane probably by passive diffusion as observed before for other highly lipophilic Ru(II) polypyridyl complexes.^{178,428} Further experiments will need to be carried out in order to fully understand the cellular uptake mechanism and localisation of these compounds.

Having studied the cellular uptake and localisation of complexes **78–83** in HeLa cells, their cytotoxic potential in the same cell line and their ability to be photoactivated will be discussed in the next section.

4.8.2 Cellular Toxicity Studies of **78–83**

In order to evaluate the cytotoxic anticancer potential of **78–83** in HeLa cells, Alamar Blue assays were carried out, as described in Chapter 2. As mentioned in Section 1.6.4, ruthenium complexes have previously exhibited strong PDT potential.^{62,63,93,170} Additionally, their increased lipophilicity as well as their ability to produce singlet oxygen make **79**, **82**, **80** and **83** interesting compounds to be tested as PDT agents. Therefore, cells were treated with the reference compounds **42** and **39** and **78–83** for 24 h followed by either irradiation with 18 J cm⁻² of light for 1 h using a UV-filtered Hg-Xe arc lamp or kept in the dark and a further 23 h incubation before the Alamar Blue dye was added and the cytotoxicity assessed. Experiments were performed in triplicate on three independent days to ensure reproducibility. The IC₅₀ values of these complexes in HeLa cells incubated in the dark or exposed to light are shown in Table 4.8 and the respective toxicity profiles can be found in Figure A4.31 of the Appendices. The log *P* and Φ_{Δ} (air-saturated aqueous solution) values

are included in Table 4.8 in order to facilitate the discussion and the interpretation of the results.

Table 4.8. IC_{50} values for the cytotoxicity of **42**, **39** and **78–83** in HeLa cells in the dark and exposed to light and their respective $\log P$ values and quantum yields of singlet oxygen production (Φ_{Δ}) in air-saturated H_2O determined by time-resolved NIR 1O_2 phosphorescence.

Complex		IC_{50} dark (μM) ^[a]	IC_{50} light (μM) ^[a]	PI ^[b]	$\log P$ ^[a]	Φ_{Δ} (H_2O , Air-satd.)
phen	42	> 100	> 100	1	-2.28 ± 0.12	0.21
	78	> 100	> 100	1	-2.52 ± 0.08	0.31
	79	38 ± 7	9 ± 4	4	-1.40 ± 0.05	0.24
	80	13 ± 2	0.47 ± 0.01	27	1.07 ± 0.08	0.03
TAP	39	> 100	31 ± 3	> 3	-2.76 ± 0.02	0.14
	81	> 100	15 ± 2	> 7	-2.76 ± 0.22	0.18
	82	14 ± 4	9 ± 2	2	-1.97 ± 0.05	0.16
	83	11 ± 3	2 ± 1	6	0.49 ± 0.07	0.01

^[a] IC_{50} and $\log P$ values correspond to the mean \pm SEM.

^[b] Phototoxic index (PI) is defined as the ratio of the IC_{50} value in the dark to the IC_{50} value upon light irradiation.

As expected from the lack of cellular uptake observed by confocal microscopy, the reference compounds and the derivatives **78** and **81**, containing the acetamide functionalised phenanthroline ligand, did not induce any cytotoxicity in the HeLa cells in the dark up to a concentration of 100 μM , and as such IC_{50} values could not be determined for these compounds. However, both TAP-containing complexes **39** and **81** were found to be slightly toxic after light activation with IC_{50} values of 31 and 15 μM , respectively. It has been shown that the cellular internalization of Ru(II) complexes can be different upon light exposure.^{180,429-431} Their ability to act as 1O_2 photosensitisers can result in an increase of the cell membrane permeability which facilitates the complexes penetration into cells. To further study the effect of light in the cellular uptake, HeLa cells were treated with complexes **39** and **81** before being irradiated for 1 hour and incubated for a further 2 h (Figure 4.23). HeLa cells incubated with both complexes in the dark for 3 h were used as a control. The same experiment was carried out with the phen derivative **42** for comparison. No change in cellular uptake was observed upon light activation. However, while HeLa cells containing complexes **42** and **39** remained unaltered, evidence of increased toxicity of complex **81** after treatment with light were found in cell morphology changes compared to the ones in dark

conditions. This was in agreement with the lower IC_{50} value observed for this complex after light activation when compared with those obtained for **42** and **39**. It can be concluded then that a photoinduced cell membrane permeabilisation is not the reason of the phototoxicity observed for complexes **39** and **81**. Furthermore, both derivatives **42** and **78**, containing **phen** as ancillary ligands, were shown to generate more 1O_2 but did not display any toxicity in HeLa cells after light irradiation. This could suggest that the phototoxicity observed for complexes **39** and **81**, compared to their **phen** analogues, would not be related to the Type-II photosensitization effect as they produce less 1O_2 , but maybe related to their additional Type-I photosensitization mechanism (photoinduced electron transfer) due to their highly oxidizing character in the excited state. Further studies should be carried out to confirm this explanation.

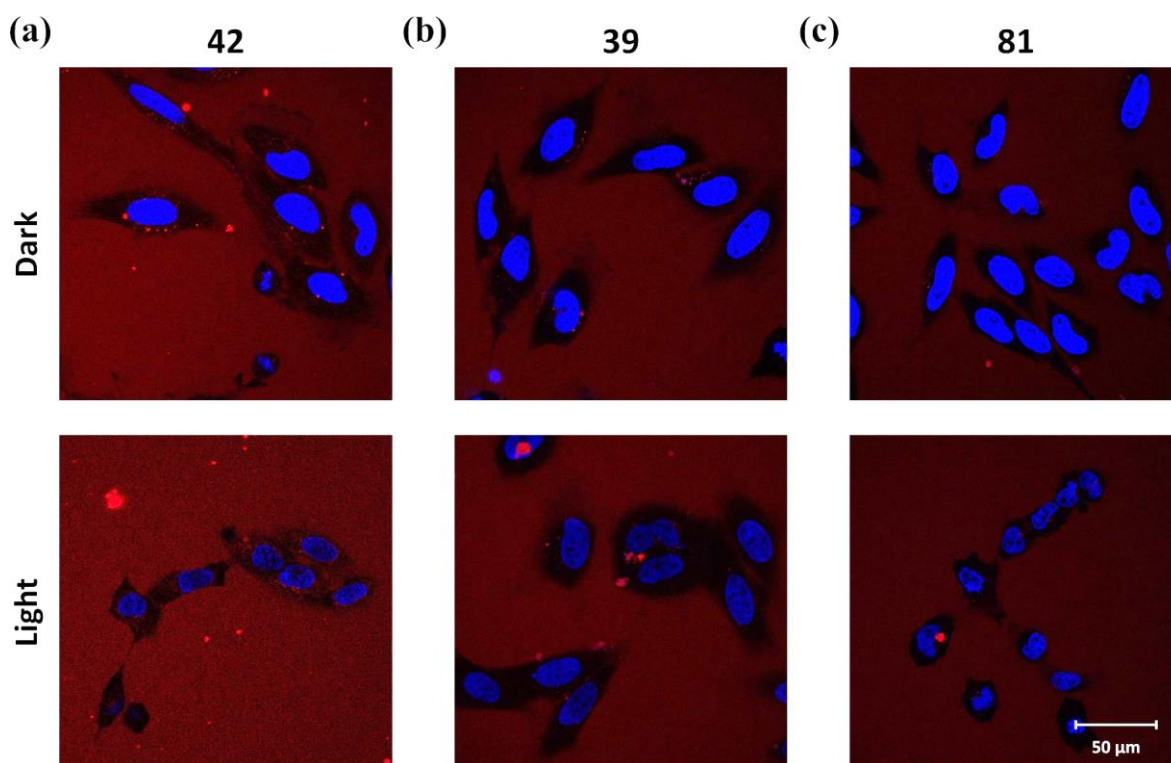


Figure 4.23. Confocal fluorescence microscopy images of HeLa cells showing the uptake of complexes (a) **42**, (b) **39** and (c) **81** (red) at $50 \mu\text{M}$ after 3 h incubation in the dark (top) or 1 h of light activation followed by 2 h incubation in the dark. The nucleus is stained blue with Hoechst 33258.

On the other hand, complexes **79** and **82**, with the ten carbon alkyl chain, displayed modest IC_{50} values against the cancer cell line of 38 and $14 \mu\text{M}$ after 48 h incubation in the absence of light, respectively. Some increase in cytotoxicity was observed after they were exposed to visible light showing both complexes IC_{50} values of $9 \mu\text{M}$ which corresponds to PIs of *ca.* 4 and 2, respectively. Similarly, IC_{50} values of 13 and $11 \mu\text{M}$ were observed in dark conditions for complexes **80** and **83** containing the twenty-one carbon alkyl chain.

However, after photoactivation, results demonstrated a significant increase in cytotoxicity, in particular for the **phen** complex, with IC_{50} values of 0.47 and 2 μ M for **80** and **83**, respectively. This corresponds to a PI of *ca.* 27 and 6, respectively, disclosing a good therapeutic window for **80**, which is the complex with the lowest IC_{50} value studied in the Gunnlaugsson group to date. As demonstrated in previous Sections 4.6 and 4.8.1, having a long alkyl chain increases the lipophilicity of these complexes and provides them with the ability to be efficiently internalised into cells. This results in a larger intracellular concentration of ruthenium complex which explains the increase of IC_{50} values with the length of the alkyl chain. Likewise, the photoactivation observed for complexes **79** and **82** was in agreement with their ability to produce 1O_2 . Particular cases are complexes **80** and **83** which have shown concentration dependant 1O_2 generation, showing potential production of the highly reactive oxygen species at concentrations below their cmc and negligible Φ_A values at concentrations above their cmc. Although the intracellular concentration of complexes **80** and **83** has not been determined, the high phototoxicity exhibited by these complexes and, especially by complex **80**, suggests that they behave as free monomers inside the cells being able to produce a significant amount of 1O_2 that would explain their ability to be efficiently photoactivated. Therefore, these results provide evidence that, while the ruthenium moiety is responsible for the light activated decrease in viability, the overall toxicity (in the dark) is likely due to the increasing length of the alkyl chain that provides the Ru(II) complex with the ability to be internalised into the cell.

Interestingly, only a few examples of Ru(II) polypyridyl complexes reported in the literature have shown IC_{50} values in the nanomolar range as is the case for **80** after light activation.^{132,234,238,432-435} However, the experimental conditions employed for each particular compound should be carefully considered, *e.g.* incubation time, cell line and, in the case of photoactivation, irradiation time and light dose. Furthermore, although **80** has also shown dark toxicity, it must be noticed that at the concentration at which this complex showed 50% cell viability after light treatment, about 100% cell viability was observed in dark conditions (Figure A4.31 of the Appendices), suggesting no toxicity against the cells at this concentration when they are not exposed to light and thus revealing this compound as a promising PDT agent.

In the next section, the ability of the most phototoxic complexes **80** and **83** to produce reactive oxygen species (ROS) inside live cells will be explored with a view to further confirm ROS generation as the main mechanism by which such complexes become more toxic after light irradiation in a cellular environment.

4.8.3 Intracellular ROS Generation Ability of **80** and **83**

Intracellular ROS generation by complexes **80** and **83** was investigated using the ROS indicator 2,7-dichlorofluorescein diacetate (DCFH-DA) which has been widely used as a probe for detecting intracellular oxidative stress.^{80,430} The non-fluorescent DCFH-DA probe diffuses through the cell membrane and is hydrolysed by intracellular esterases to the also non-fluorescent DCFH carboxylate anion (Figure 4.24). In the presence of ROS, DCFH is oxidised resulting in the formation of dichlorofluorescein (DCF), a highly fluorescent molecule that can be detected by fluorescence-based techniques such as confocal microscopy. Therefore, the ability of a compound to produce $^1\text{O}_2$ or other ROS can be evaluated by monitoring the appearance of the DCF fluorescence after irradiation.

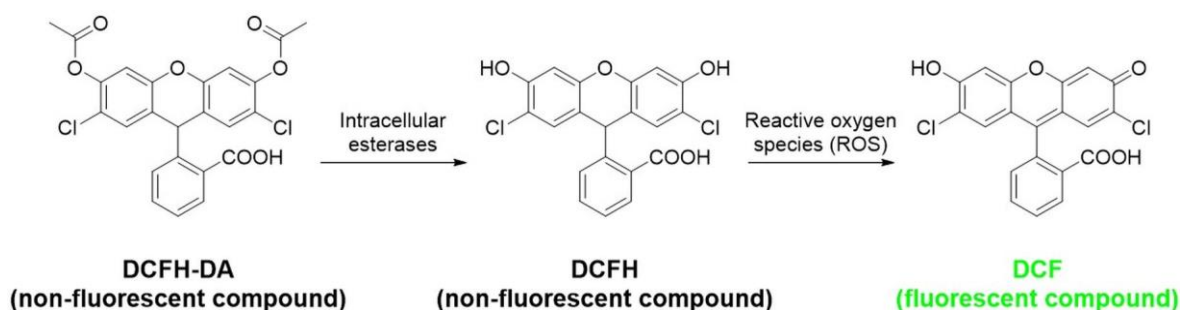


Figure 4.24. Schematic illustration of the formation of the fluorescent compound DCF by hydrolysis of DCFH-DA followed by ROS-induced oxidation.

Therefore, HeLa cells were incubated with complexes **80** and **83** ($5\ \mu\text{M}$) at $37\ ^\circ\text{C}$ for 30 min followed by treatment with DCFH-DA ($20\ \mu\text{M}$) and incubation at $37\ ^\circ\text{C}$ in the dark for a further 30 min. Cells were then irradiated using a 405 nm diode laser (1.6% intensity) attached to a real-time confocal microscope and images were taken every 1.3 s over a 3 min period. The evolution of the formation of the fluorescent DCF in the presence of complexes **80** and **83** upon increasing the irradiation time is shown in Figure 4.25. An increase of the green signal corresponding to the DCF fluorescence over the irradiation time was observed in the presence of both **80** and **83**, suggesting that oxidation of DCFH was taking place and thus ROS were generated within cells by such complexes. This process seems to be faster in the presence of complex **83** than with complex **80** as it can be presumed from the comparison of Figures 4.25b and 4.25c where the appearance of green signal was already evident after one minute of light irradiation in the presence of the **TAP** complex, while DCF formation was not significant when the **phen** complex was used as ROS generator under the same conditions. Simultaneously, a control experiment in the absence of ruthenium complex was performed (Figure 4.25a) in order to probe that the increase of the emission intensity by formation of DCF is due to the ability of both ruthenium complexes to produce ROS

intracellularly. No green signal appearance could be detected under the same experimental conditions.

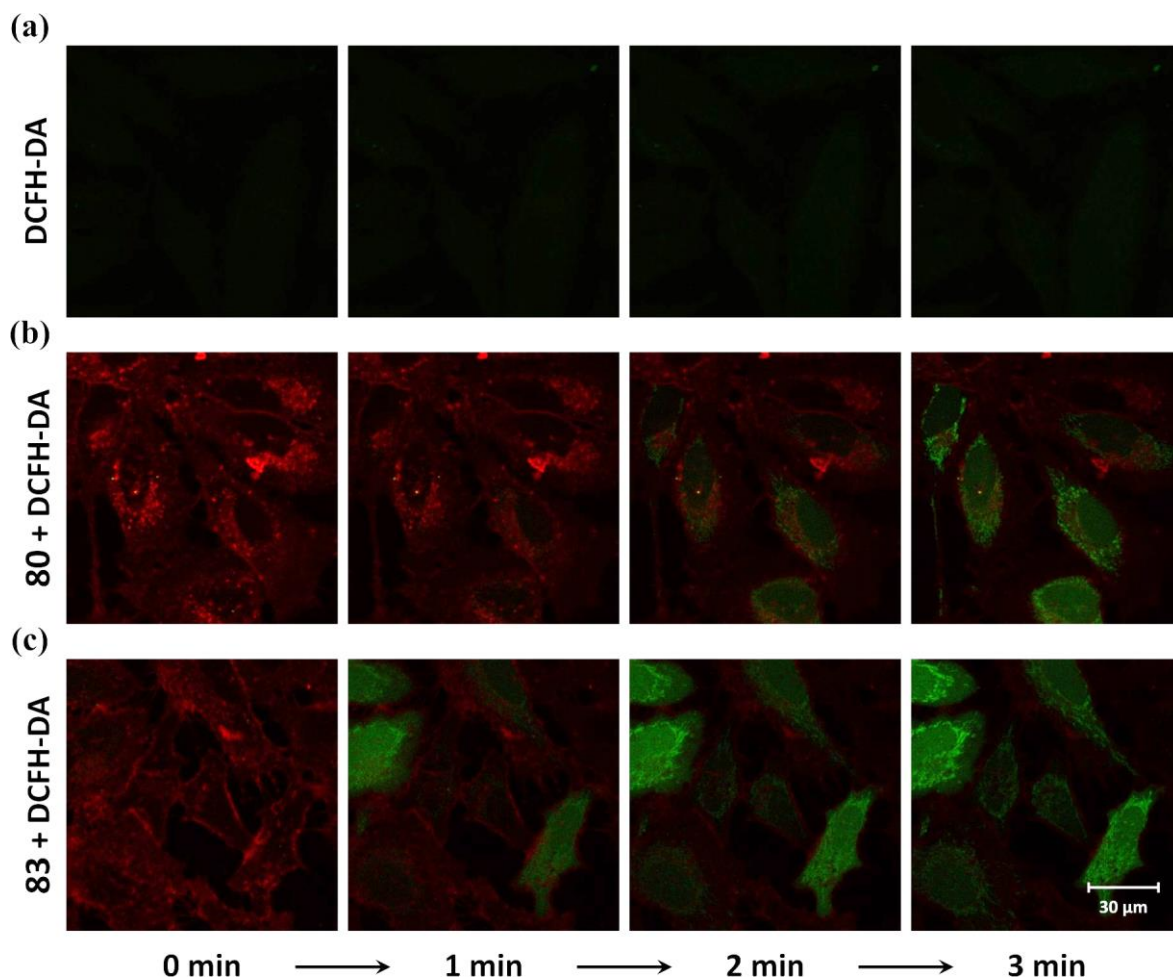


Figure 4.25. Confocal fluorescence microscopy images of HeLa cells treated with (a) DCFH-DA (20 μ M), (b) **80** (5 μ M, red) and DCFH-DA (20 μ M) and (c) **83** (5 μ M, red) and DCFH-DA (20 μ M) before and after irradiation with a 405 nm diode laser (1.6% intensity) for different periods of time showing the ROS generation by formation of the fluorescent probe DCF (green).

Furthermore, fluorescence from DCF seemed to be brighter within mitochondria, clearly recognisable by its typical reticulated morphology (Figure 4.26a).^{436,437} This was not unexpected as mitochondria are the cell organelles where all the redox processes take place. In addition, emission intensity of DCF in the absence (control) and in presence of **80** and **83** was plotted as a function of the irradiation time (Figure 4.26b). As was already observed in the confocal microscopy images, the fluorescence intensity of DCF over the irradiation time increased in the presence of both **80** and **83** but was not significant in the absence of ruthenium complex. Interestingly, while in the presence of the **phen** complex the DCF emission intensity underwent a linear increase, it increased logarithmically in the presence of the **TAP** analogue. However, it is important to take these observations just as an indication

of ROS production by both complexes as quantification in such cell environment would not be very accurate.

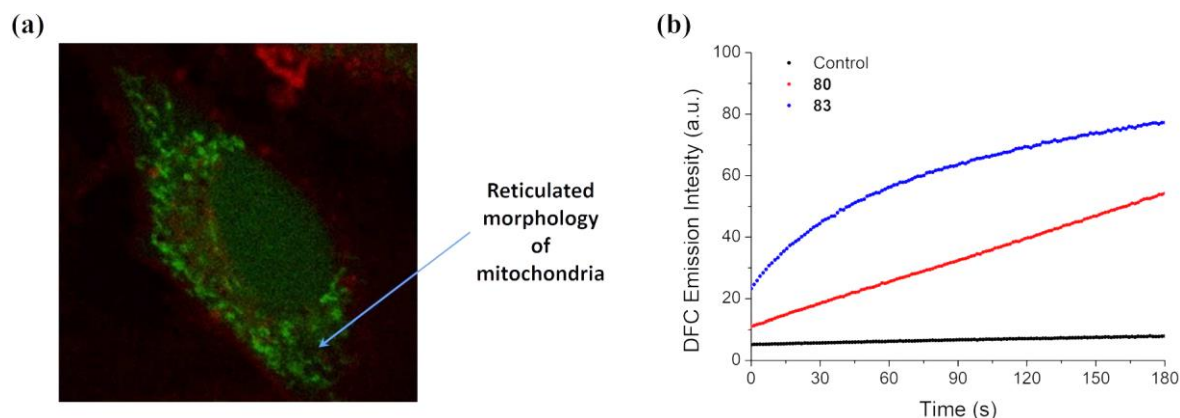


Figure 4.26. (a) Confocal fluorescence microscopy image of a HeLa cell treated with DCFH-DA (20 μM) after irradiation with a 405 nm diode laser (1.6% intensity) for 3 min in the presence of **80** (5 μM) showing the typical reticulated morphology of mitochondria. (b) Change of the DCF emission intensity in the absence of ruthenium complex (black) and in the presence of **80** (5 μM , red) and **83** (5 μM , blue) at different irradiation times.

In conclusion, these results are in agreement with the phototoxicity exhibited by complexes **80** and **83** in HeLa cells and can be considered as a confirmation of their ability to produce $^1\text{O}_2$ or other ROS not only in solution-based studies but also in a cellular context.

4.9 Conclusions and Future Perspectives

The study undertaken in this chapter has been focused on the development of new Ru(II) polypyridyl complexes containing lipophilic ligands with a view to investigate the potential of the resulting amphiphilic species as biological imaging and therapeutic agents. Thus, complexes **78–80** and **81–83** in which the ruthenium centre was coordinated to either **phen** or **TAP** as ancillary ligands, respectively, and where the third ligand consisted of a different length of alkylamide functionalised phenanthrolines (**84–86**), were synthesised and characterised followed by their photophysical evaluation. The ability of the two complexes containing the longest alkyl chain **80** and **83** to spontaneously self-assemble within aqueous solution and form micellar supramolecular aggregates was demonstrated by determination of their cmc values through surface tension measurements. Both complexes showed similar cmc values of *ca.* 110 μM suggesting that, in this case, the self-assembly process is determined by the alkyl chain length and not by the nature of the ancillary ligands (**phen** and **TAP**). Hydrodynamic diameters of *ca.* 10.5 nm were obtained by DLS analysis of both micellar systems. Although no significant changes were observed in the UV-vis absorption and emission spectra of **80** and **83** at concentrations above and below the cmc, luminescence lifetimes of these complexes showed to be concentration dependent giving further evidence

of the co-existence of different emitting species in solution. However, while luminescence lifetimes increased with the formation of aggregates of complex **80**, the opposite effect was observed for **83** where shorter lifetimes were observed upon increasing the complex concentration indicating different photophysical responses to the self-assembly process by **phen** and **TAP** complexes, that is, oxygen quenching protection and self-quenching of their excited states, respectively.

The potential of complexes **78–83** to be used in biological applications was first explored through evaluation of their DNA-binding affinities in aqueous solution using a variety of techniques such as UV-vis absorption and emission titrations, thermal denaturation experiments and CD studies. DNA binding constants of the order of 10^5 and 10^6 M^{-1} were obtained for **78** and **79**, respectively, and of 10^4 and 10^5 M^{-1} for the **TAP** analogues **81** and **82**, respectively, revealing an influence of the type of ancillary ligand and the alkyl chain length in the DNA binding strength of such complexes. Significant changes were also observed in the melting temperature and CD spectra of DNA in the presence of these complexes confirming their affinity for the nucleic acid. It was concluded that complexes **78**, **79**, **81** and **82** are capable of binding to the DNA helical structure by a combination of electrostatic attraction due to the positive and negative charge of the Ru(II) complexes and the DNA phosphate backbone, respectively, and partial intercalation into the nucleobase pairs or insertion into the grooves of the ancillary ligands. Additional hydrophobic interactions are also expected for complexes **79** and **82**. Unfortunately, K_b values could not be determined for complexes **80** and **83** due to their complicated photophysical behaviour in the presence of DNA although the modest changes observed in the T_m values and CD spectra of DNA in the presence of these complexes suggested weak DNA binding.

Subsequently, lipophilicity studies were accomplished using the “shake-flask” method and revealed positive $\log P$ values for the complexes **80** and **83**, containing the longest alkyl chain, and negative ones for the rest of the complexes **78**, **79**, **81** and **82**, confirming an increase of the lipophilicity with the alkyl chain length. Furthermore, singlet oxygen photosensitisation by complexes **78–83** was first investigated through direct measurement of 1O_2 phosphorescence at 1265 nm in O_2 -saturated D_2O . While complexes **78**, **79**, **81** and **82** showed moderate 1O_2 generation in air-saturated H_2O , very low Φ_A values were obtained for **80** and **83** suggesting no 1O_2 production by such complexes. However, due to the ability of such complexes to self-assemble, a concentration-dependent 1O_2 photosensitisation would not be unexpected. Therefore, efforts were made to indirectly

quantify their $^1\text{O}_2$ production by monitoring the fluorescence disappearance of the water-soluble $^1\text{O}_2$ chemical probe ABDA, as this method allowed to work in a concentration range where the complexes are expected to behave as free monomers facilitating their interaction with molecular oxygen. However, no conclusive results were obtained from these experiments probably due to hydrophobic interaction between the highly lipophilic complexes and the probe.

Finally, *in vitro* studies of complexes **78–83** in HeLa cervical cancer cells were performed in order to probe the applicability of such complexes in live systems. Confocal microscopy revealed the influence of the alkyl chain length on the cellular internalisation and thus complexes **79**, **82**, **80** and **83**, containing long alkyl chains, were shown to be rapidly taken up into the cells with a preliminary localisation in the cell membrane while **78** and **81** were not internalised by the cells. Furthermore, cellular toxicity studies showed that complexes **79**, **82** and **83** displayed moderate phototoxicity against HeLa cells in contrast to **80** which exhibited significant light-dependent cytotoxicity with IC_{50} values of *ca.* 13 μM in dark and 0.5 μM after exposure to light irradiation, displaying a good therapeutic window for their use in PDT. Intracellular ROS generation studies using the ROS indicator DCFH-DA showed that the high phototoxicity observed for this complex is probably due to $^1\text{O}_2$ or other ROS production despite Φ_A values not being determined at low complex concentration. These results confirmed the increasing cellular uptake of Ru(II) polypyridyl complexes containing lipophilic ligands and suggested a possible toxicity modulation with the alkyl chain length.

Due to the lipid resemblance of some of the ruthenium complexes studied in this chapter, future work of this project will look at their interaction with other structures of biological relevance such as liposomes with a view to further investigate their potential to be used in the biophysical characterisation and imaging of lipid membranes.^{388,389,394,438} Furthermore, the lipophilicity and ability to self-assembly into supramolecular structures of some these complexes could make them powerful luminescent tools to effectively induce DNA condensation and be used in gene delivery and transfection applications.^{401,439}

Building on preliminary work conducted within the Gunnlaugsson group,^{264,271} the next chapter will focus on the synthesis of new Ru(II) functionalised gold nanoparticles by using a 2,2'-bipyridine-based ligand to attach the Ru(II) complex to the gold surface in contrast to the 1,10-phenanthroline derivative ligand used previously in the group with the aim to study the photophysical properties and biological applications of the resulting nanomaterial.

Chapter 5

Ruthenium(II) Polypyridyl

Functionalised Gold Nanoparticles for

Cellular Imaging

5.1 Introduction

As was introduced in Section 1.7, research into gold nanoparticles (AuNPs) has received increasing interest in recent years due to their unique size- and shape-dependent optoelectronic properties, biocompatibility and ease of functionalisation with a variety of ligands.^{245,246} Such features provide them with enormous potential to be used in a broad range of applications including sensing,^{440,441} catalysis,⁴⁴² light energy conversion and,⁴⁴³ of relevance to the work described over this thesis, in bioimaging and medicine.²⁴²⁻²⁴⁶ In this context, luminophores have been attached to AuNPs and used as probes for non-invasive biomolecular imaging.^{244,444} Furthermore, the conjugation of photosensitisers to AuNPs has emerged as an alternative to classic PDT agents.²⁵⁸ The resulting photosensitiser-AuNP conjugates offer several advantages over classic PDT agents, such as an increase of the local photosensitiser concentration at the target cells, prevention of nonspecific accumulation in normal tissues, or tumour-targeted delivery of the photosensitiser due to an enhanced permeability and retention (EPR) effect of the particle scaffold.²⁵⁸

In previous chapters, the attractive photophysical properties and selective photochemistry of Ru(II) polypyridyl complexes have been intensively demonstrated. In addition, their ability to be used in a biological context as DNA photoprobes, cellular imaging agents and light-activated anticancer drugs has played a major role in the development of the ruthenium-based systems described throughout this thesis and in the literature.^{2,62,63,93} Therefore, the combination of the advantageous properties of both gold nanoparticles and Ru(II) polypyridyl complexes has resulted in attractive systems for application in cellular imaging or photothermal therapy (PTT) in the treatment of cancer, as was shown in previous work developed in the Gunnlaugsson group and in a few other examples in the literature.^{264,266,270,271}

With this in mind, the aim of this chapter consists of expanding the research work carried out previously in the Gunnlaugsson group in the development of surface modified AuNPs with luminescent Ru(II) polypyridyl complexes.^{264,271} Thus, the work presented here will deal with the synthesis of a new alkyl disulphide functionalised bipyridine based ligand (**89**) and its coordination to a Ru(II) centre containing either **phen** or **TAP** as ancillary ligands. The purpose of the disulphide group was to enable subsequent covalent attachment of the resulting Ru(II) complexes to the surface of the AuNPs, while the eleven carbon alkyl chains act as spacer groups to reduce quenching of the Ru(II) luminescence by the AuNPs.^{264,271,445-447} First, the photophysical properties of the free alkyl disulphide functionalised dinuclear Ru(II) complexes **90** and **91** (Figure 5.1) will be investigated,

followed by the evaluation of their cellular uptake and light-dependent toxicity in HeLa cells as free systems. Further functionalisation of AuNPs with complexes **90** and **91** via the

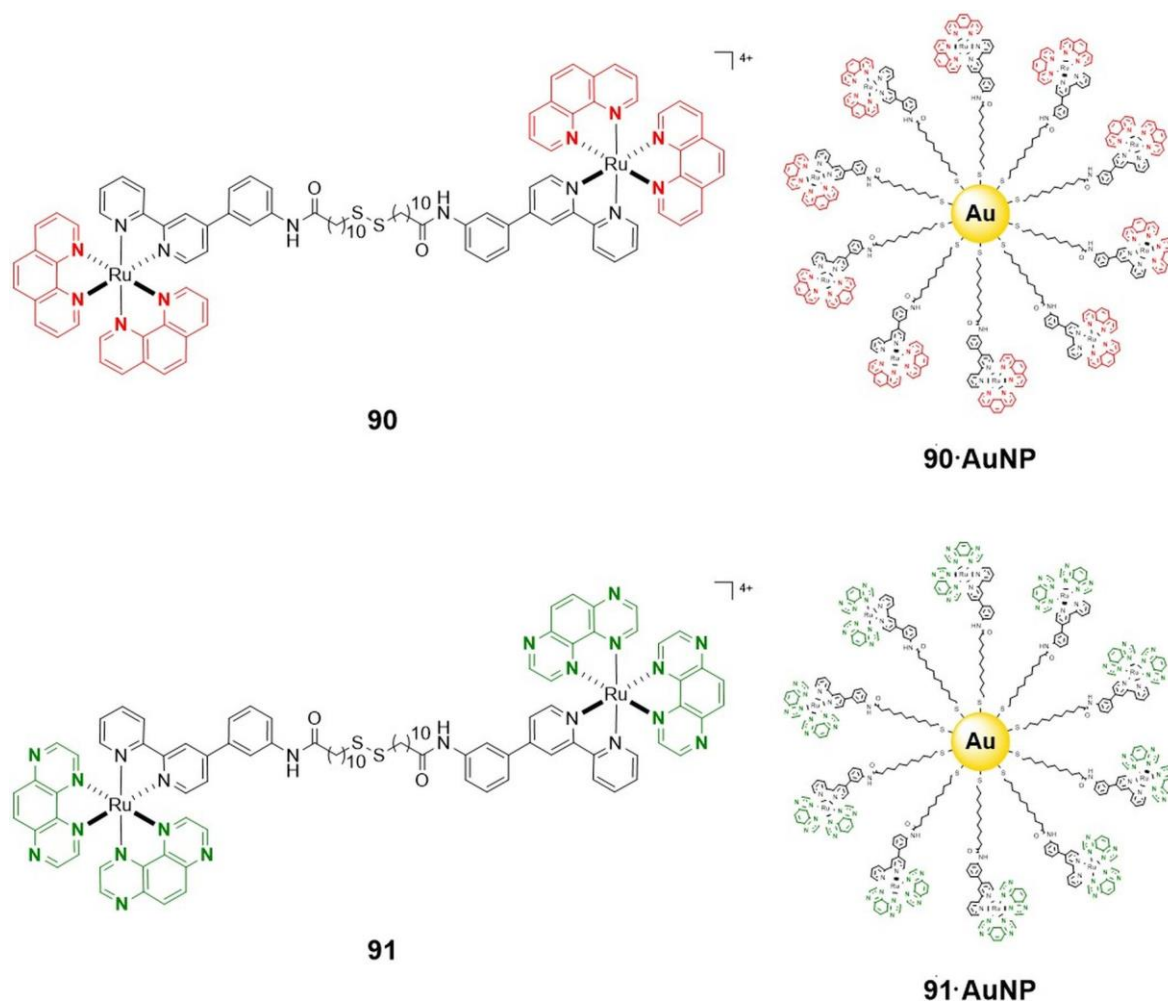


Figure 5.1. Chemical structures of the alkyl disulphide functionalised dinuclear Ru(II) polypyridyl complexes **90** and **91** and their corresponding gold conjugates **90·AuNP** and **91·AuNP** studied in this chapter.

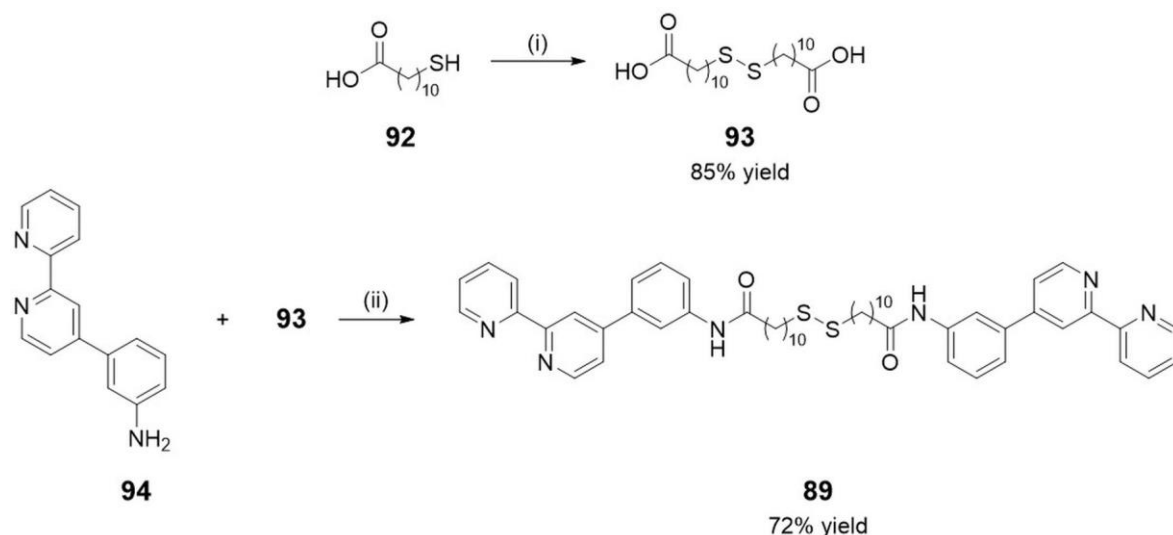
formation of Au-S covalent bonds will result in the Ru(II)-AuNP conjugates **90·AuNP** and **91·AuNP** (Figure 5.1). The new gold nanosystems will be characterised using different techniques including dynamic light scattering (DLS), transmission electron microscopy (TEM) and UV-vis absorption and emission spectroscopy, which also allow for confirmation of the successful functionalisation of the gold surface with the ruthenium complexes. Finally, preliminary *in vitro* studies will be described detailing the cellular uptake and localisation of the systems **90·AuNP** and **91·AuNP** in HeLa cells to probe the effectiveness of the gold nanocarrier to deliver ruthenium complexes into live cells.

5.2 Synthesis of 90·AuNP and 91·AuNP

The new Ru(II) polypyridyl functionalised gold nanoparticles **90·AuNP** and **91·AuNP** were prepared according to synthetic procedures previously used in the Gunnlaugsson group for similar systems.^{264,271} Thus, the synthesis of such gold conjugates consisted of (i) the preparation of the Ru(II) polypyridyl complexes containing an alkyl disulphide moiety **90** and **91** followed by (ii) incorporation of such complexes onto the surface of AuNPs *via* the sulphur atoms to form the systems **90·AuNP** and **91·AuNP**. A detailed description of such synthetic procedures will be next presented.

5.2.1 Synthesis and Characterisation of 90 and 91

The synthesis of alkyl disulphide functionalised dinuclear Ru(II) polypyridyl complexes **90** and **91** was carried out in a manner similar to that described in previous chapters and according to the usual procedures reported in the literature for $[\text{Ru}(\text{L})_2(\text{L}')]^{2+}$ di-heteroleptic complexes, where L = 1,10-phenanthroline (**phen**) or 1,4,5,8-tetraazaphenanthrene (**TAP**), and L' = 11,11'-disulfanediyldis(*N*-(3-([2,2'-bipyridin]-4-yl)phenyl)undecanamide) (**89**).^{170,302} First, ligands **TAP** and **89** were synthesised. The **TAP** ligand was prepared according to the procedure described in Section 2.2 while the synthetic route to produce ligand **89** is shown in Scheme 5.1.



Scheme 5.1. Synthetic pathway for **89**: (i) Br_2 , DMF (anh.), 0 °C, 3 h; (ii) EDC, DMAP, CH_2Cl_2 , r.t., 2 days.

The first step involved oxidation of the thiol group of 11-mercaptoundecanoic acid (**92**) to the corresponding disulphide using bromine in anhydrous DMF at 0 °C for 3 h. Removal of the solvent under reduced pressure followed by washing with NaHCO_3 (aq), 1 M HCl and H_2O yielded 11,11'-disulfanediyldiundecanoic acid (**93**) as a white solid in 85%

yield. Successful formation of the disulphide bond was confirmed by measuring the melting points of both starting material and product, as thiols and their disulphides analogues are known to melt at different temperatures.^{448,449} The melting point of **92** was found to be 50–51 °C while **93** exhibited a melting point of 88–92 °C. Formation of the disulphide provides protection of the thiol group which can otherwise undergo nucleophilic attack with the carbonyl group under the conditions required for the next synthetic step. Previous experiments have demonstrated no formation, or formation in a low yield, of the desired product when **92** was used instead of **93**.

The reagent 3-([2,2'-bipyridin]-4-yl)aniline (**94**) needed for the next step was prepared by PhD student Hannah Dalton and thus, the detailed synthetic procedure used to produce such compound will be reported in the PhD Thesis of Ms. Dalton. A coupling reaction between **94** and **93** was then performed in dry DCM using *N*-ethyl-*N'*-(3-dimethylaminopropyl)carbodiimide hydrochloride (EDC) in the presence of 4-dimethylaminopyridine (DMAP).²⁶⁴ The ligand **89** was obtained as a beige solid in 72% yield after precipitation with H₂O and washing with MeCN. Successful formation of the novel ligand **89** was supported by the ¹H NMR spectrum (400 MHz, DMSO-*d*₆) shown in Figure 5.2, from which the characteristic NH signal was clearly visible at 10.08 ppm,

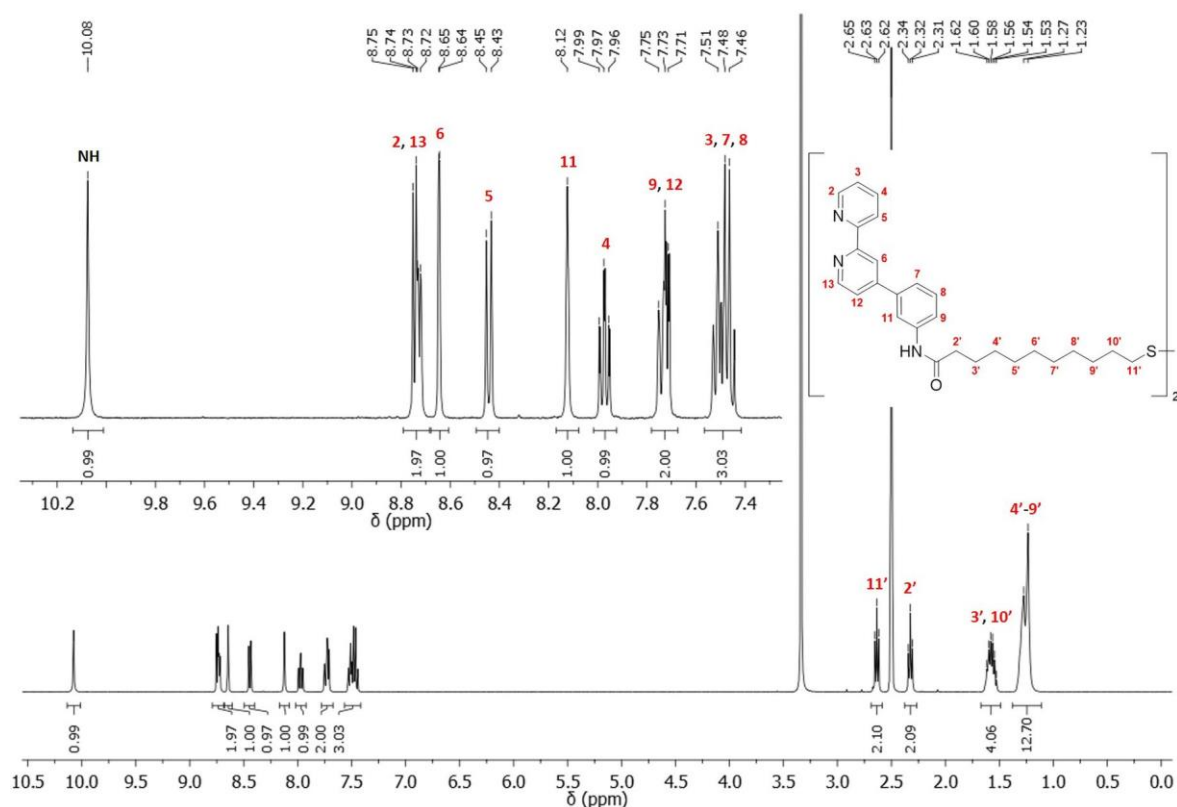
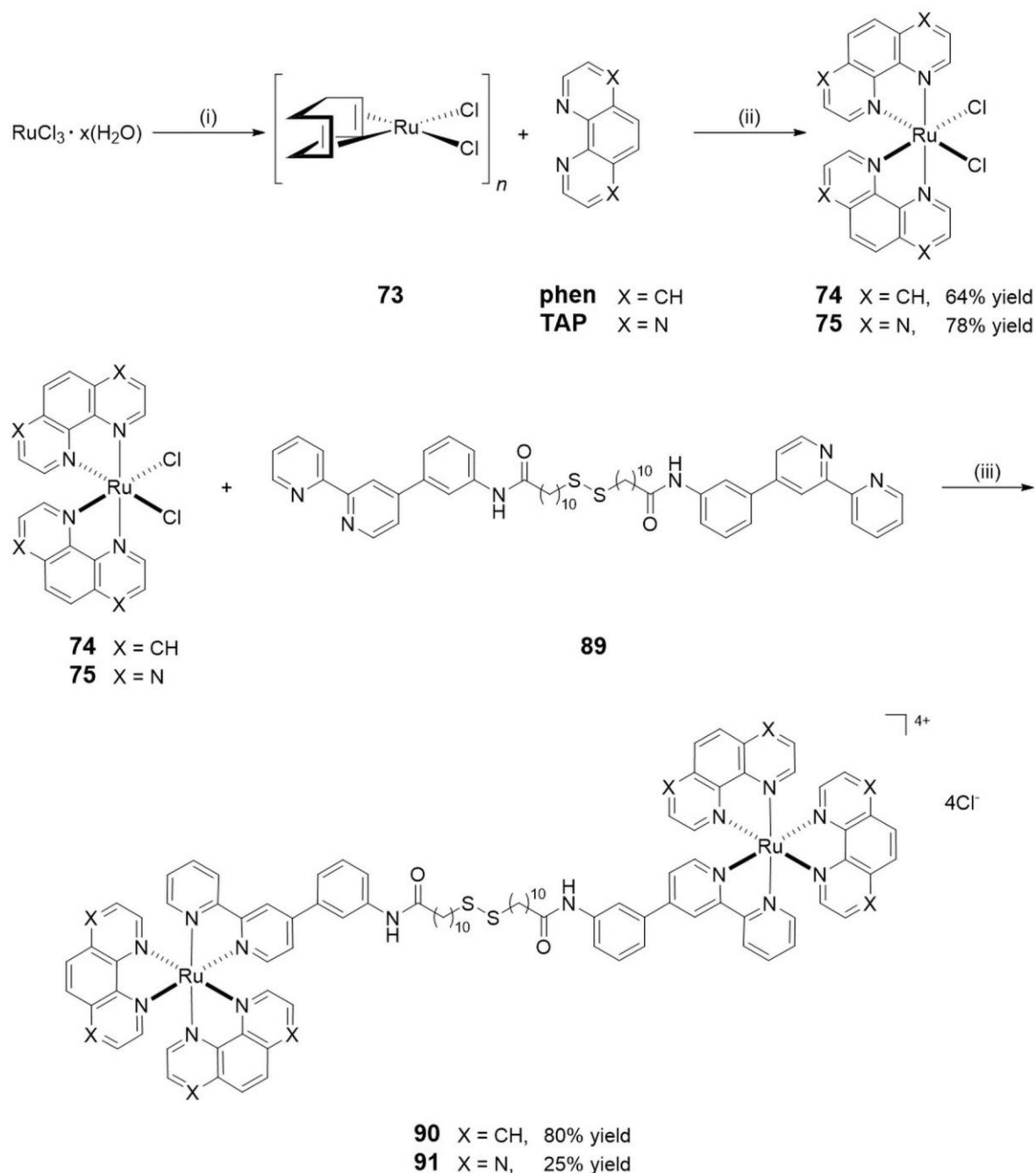


Figure 5.2. ¹H NMR (400 MHz, DMSO-*d*₆) spectrum of **89**.

indicating formation of the amide bond. Furthermore, eleven protons in the aromatic region between 7.4 and 10.2 ppm were identified and assigned to the bipyridine-aniline moiety of the ligand. The remaining twenty protons observed in the aliphatic region between 1.0 and 3.0 ppm corresponded to the ten carbon alkyl chain in ligand **89**. The ligand **89** is dimeric in nature and thus the integration is expected to be double that shown in Figure 5.2.



Scheme 5.2. Synthetic pathway for **90** and **91**: (i) 1,5-cyclooctadiene, EtOH, reflux, 3 days; (ii) DMF, microwave reaction, 140 °C, 40 min; (iii) EtOH/H₂O (1:1), microwave reaction, 140 °C, 40 min (**90**) or 30 min (**91**).

MALDI⁺-HRMS also confirmed the formation of ligand **89**, as evidenced by the peak observed at m/z 893.4639 that corresponds to the $[M+H]^+$ ion. In addition to ¹H NMR and HRMS, other conventional techniques including ¹³C NMR, 2D NMR, melting point analysis and IR spectroscopy were employed for full characterisation of ligand **89** and they can be found in Section 7.10.1 of Chapter 7 and Figure A5.1 of the Appendices. All of these techniques are in agreement for the formation and purification of **89**.

In a similar manner to that described previously in Chapters 2 and 4, microwave-assisted synthesis was carried out for the complexation of ligand **89** with the appropriate Ru(II) bispolypyridyl dichloride precursor complex (**74** and **75**) in a mixture of H₂O/EtOH (1:1) at 140 °C for 40 (**90**) or 30 min (**91**) (Scheme 5.2). A slight excess of both **74** and **75** precursors was needed to ensure the complexation of both bipyridine moieties of the symmetrical ligand **89**. Purification by column chromatography on neutral alumina using MeCN/H₂O (10:0 to 9:1) as eluent afforded the chloride salts of the dinuclear Ru(II) complexes **90** and **91** in 80% and 26% yield, respectively.

The two complexes were characterised by ¹H NMR, ¹³C NMR, elemental analysis, HRMS and IR spectroscopy. The ¹H NMR spectrum (400 MHz, DMSO-*d*₆) of **90** is shown

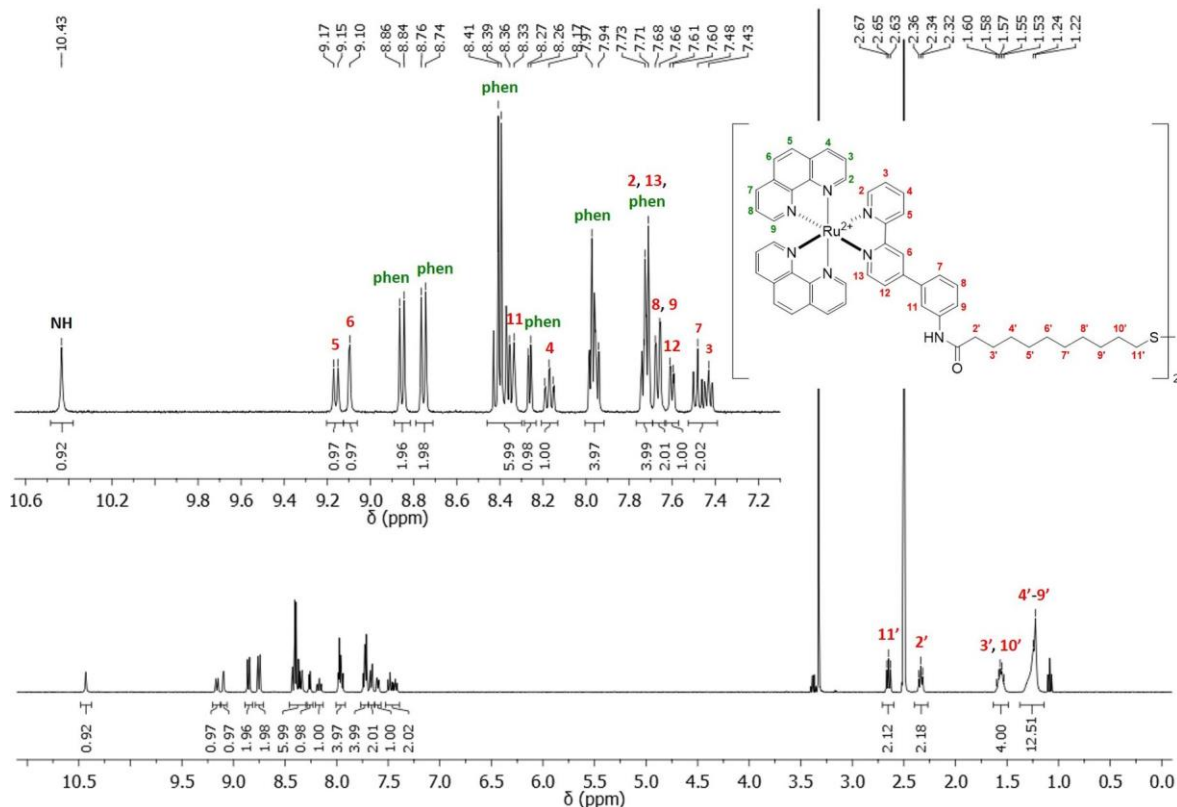


Figure 5.3. ¹H NMR (400 MHz, DMSO-*d*₆) spectrum of **90**. Signals corresponding to **phen** ligands are in green and signals assigned to ligand **89** are in red.

in Figure 5.3 while that of **91** shown in Figure A5.3 of the Appendices. Additional 2D NMR experiments allowed the identification of most of the signals. Twenty-seven protons were observed between 7.2 and 9.4 ppm in the aromatic region and were assigned to the bipyridine-aniline moiety of ligand **89** and to the **phen** ancillary ligands, whereas the signal at 10.43 ppm was attributed to the amide proton. In addition, twenty protons were observed between 1.0 and 3.0 ppm corresponding to the ten carbons alkyl chain in ligand **89**. Thus, a total of forty-eight protons were found which was consistent with the molecular formula of the compound, taking into account that, as previously shown for the ligand itself, only half of the dinuclear ruthenium complex was considered for the signal integration since protons from both halves of the molecule are equivalent.

The successful formation of complexes **90** and **91** was also corroborated by MALDI⁺-HRMS where peaks at m/z 1815.5494 and 1823.5002 were found, which corresponded to their respective $[M-H]^+$ ions. Both complexes showed the expected isotopic profiles, as observed in Figure 5.4 from the comparison of the theoretical and experimental isotopic distribution patterns of **90** and **91**.

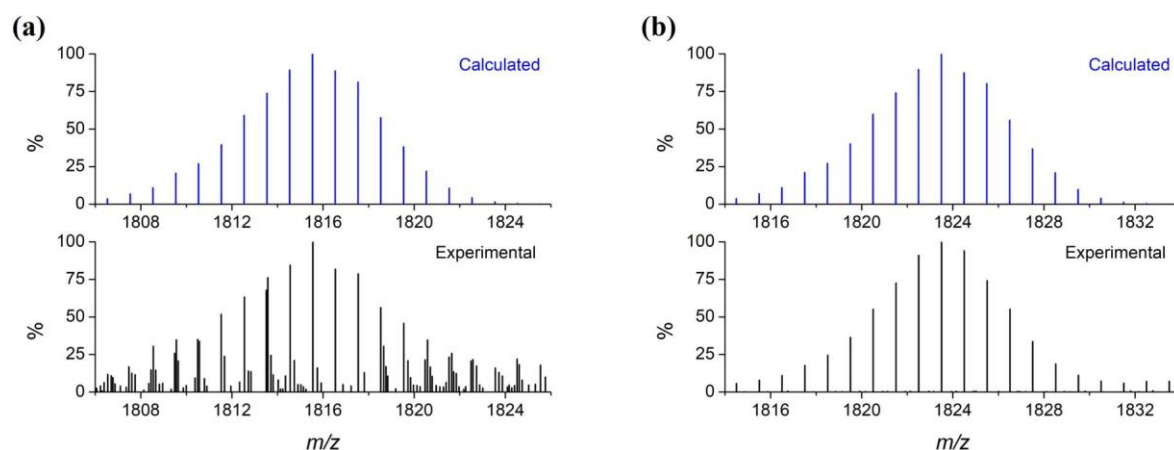


Figure 5.4. Comparison between the calculated (blue) and experimental (black) isotopic distribution pattern for (a) **90** and (b) **91** from matrix-assisted laser desorption/ionisation (positive mode) high resolution mass spectrometry analysis.

More detailed synthetic procedures and characterisation of both ruthenium complexes are given in Section 7.10.2 of Chapter 7 and Figures A5.1–A5.4 of the Appendices. After being successfully synthesised and characterised, both complexes **90** and **91** were used as ligands to functionalise AuNPs. The synthesis and purification of such Ru(II) polypyridyl functionalised AuNPs will be presented in the next section.

5.2.2 Functionalisation of AuNPs with 90 and 91

Due to the growing interest in the potential applications of AuNPs, particularly in nanomedicine as drug delivery systems, a large variety of preparative methods for the synthesis and functionalization of these nanomaterials have been explored and reported in the literature over the last few decades.⁴⁵⁰⁻⁴⁵³ Among these synthetic procedures, the two-phase Brust-Schiffrin method is one of the most popular methods chosen for the formation of thermally- and air-stable AuNPs of controlled size, with a Au(0) metallic core diameter in the range of 1.5 to 5.2 nm.⁴⁵¹

The synthesis of **90·AuNP** and **91·AuNP** was achieved using a modified version of the two-phase Brust-Schiffrin method used previously in the Gunnlaugsson group.^{264,445,446,454} First, a solution of tetraoctylammomium bromide (TOAB) in toluene was added to an aqueous solution of H₂AuCl₄. The two-phase mixture was stirred vigorously for 10 min and H₂AuCl₄ was transferred from the water to the toluene layer. Subsequently,

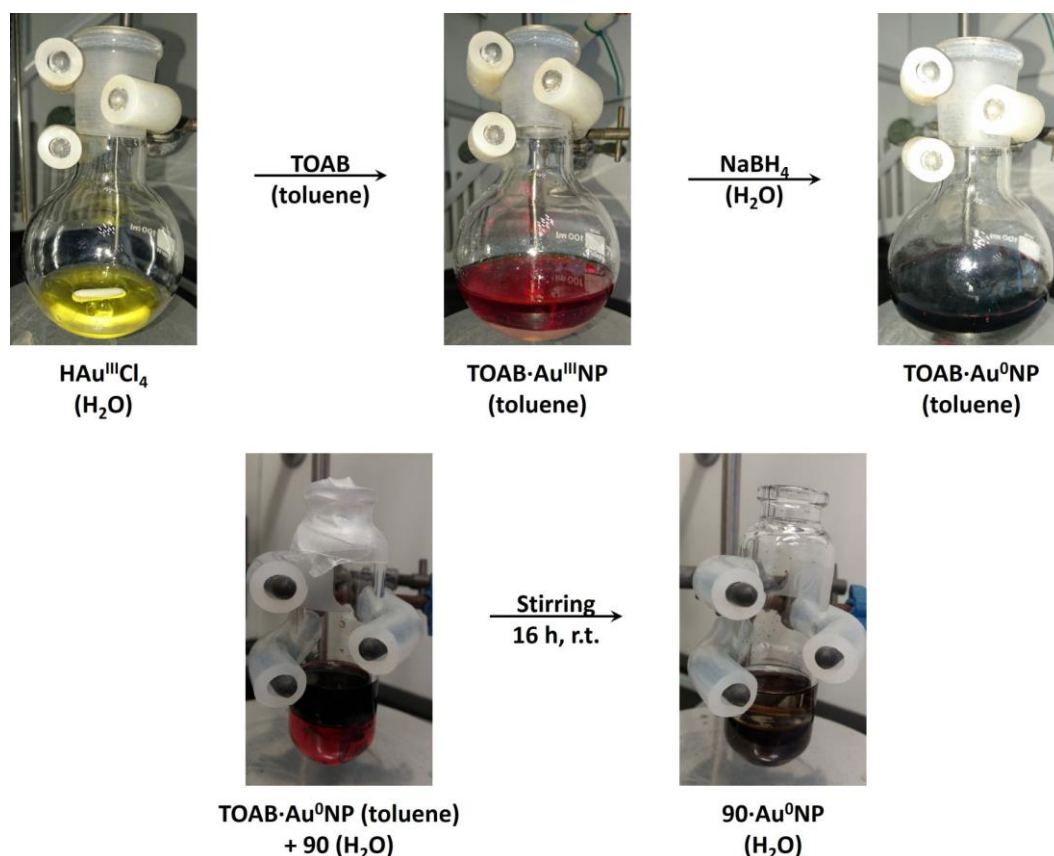


Figure 5.5. Reduction of Au(III) to Au(0) and functionalisation of the resulting TOAB-stabilised AuNPs with **90** using a modified Brust-Schiffrin two-phase method.

an aqueous solution of NaBH₄ was added dropwise into the mixture resulting in the reduction of the Au(III) to Au(0) to give TOAB-stabilised gold nanoparticles (TOAB·AuNP). The fast

colour change of the toluene layer from orange to deep purple after addition of the reducing agent indicated the formation of the colloidal species (Figure 5.5). The mixture was stirred for a further 2 h followed by separation of the toluene layer containing the TOAB·AuNP from the aqueous layer and washing with H₂O, 0.1 M HCl and 0.1 M NaOH.

Functionalisation of the surface of the resulting TOAB-stabilised AuNPs with the Ru(II) complexes was then carried out by exchanging the TOAB stabiliser coat with **90** and **91**. For this purpose, an aqueous solution of the appropriate Ru(II) complex was added to a toluene solution of the previously synthesised TOAB·AuNP and stirred vigorously for 16 h. Complete transfer of the AuNPs from the toluene layer to the aqueous layer was confirmed by the initial orange aqueous layer turning dark brown, indicating functionalisation of the AuNPs with the water-soluble Ru(II) complexes. After separation of the two layers by centrifugation, to remove any aggregates, the aqueous layer containing the Ru(II) polypyridyl functionalised AuNPs was filtered through a PDVF 0.45 µm microsyringe. In order to remove any unbound complex, a series of anion exchange steps based on a method developed by Mayer *et al.* and previously used in the Gunnlaugsson group for similar systems was conducted (Figure 5.6).^{264,271,455}

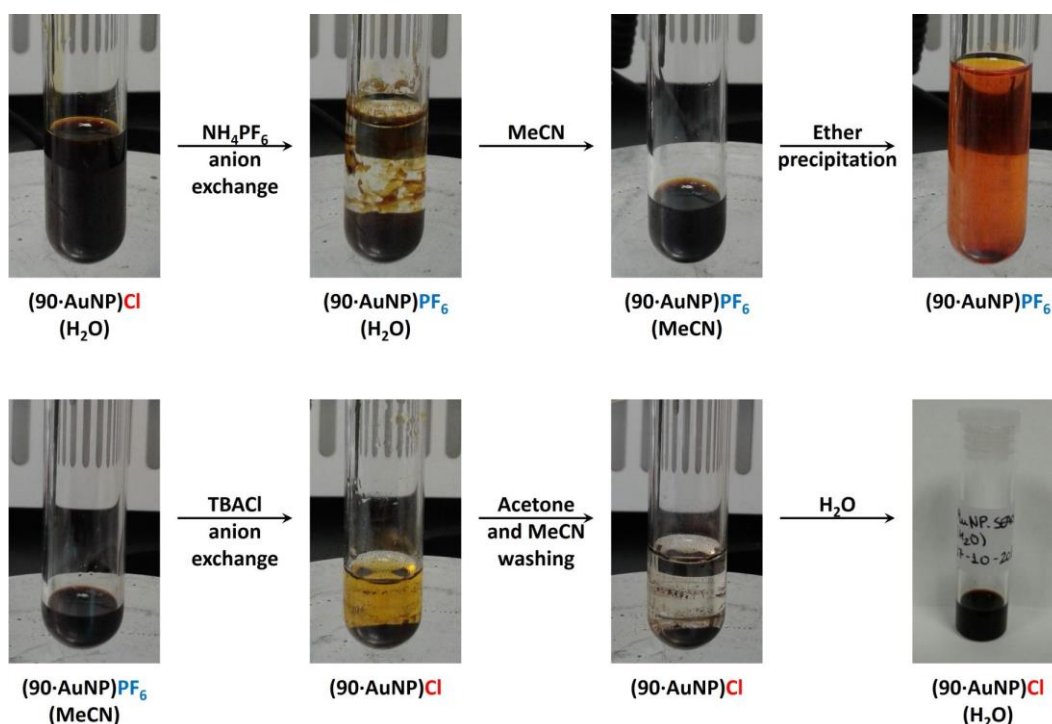


Figure 5.6. Purification of the Ru(II) polypyridyl functionalised AuNPs by several precipitation and anion exchange steps.

First, a saturated aqueous solution of NH₄PF₆ was added to the aqueous solution containing the Ru(II) polypyridyl functionalised AuNPs and the resulting flocculate was

isolated by centrifugation and washed several times with a mixture of H₂O/MeOH (3:1). The obtained solid was dissolved in MeCN and repeatedly precipitated by adding Et₂O until the supernatant, initially bright orange, became colourless. Once the resultant solid was redispersed in MeCN, the next anion exchange step consisted of addition of a concentrated acetone solution of tetrabutylammonium chloride (TBACl), followed by stirring for 1 h. After centrifugation, the dark brown solid obtained was washed several times with acetone and MeCN, dried under vacuum and finally suspended in H₂O to give a dark brown coloured colloidal solution.

The water-soluble systems **90·AuNP** and **91·AuNP** were then characterised by several techniques, including dynamic light scattering (DLS), transmission electron microscopy (TEM) and UV-vis absorption and emission spectroscopy, as presented in the following sections.

5.3 Dynamic Light Scattering Studies of **90·AuNP** and **91·AuNP**

As was shown previously in Section 4.4.2 with the Ru(II) polypyridyl-based surfactants, DLS is a powerful technique to study the size distribution profile of AuNP systems in solution. Therefore, in order to estimate the size of the synthesised Ru(II) polypyridyl functionalised AuNPs, DLS measurements were conducted on aqueous solutions containing **90·AuNP** and **91·AuNP** using a Malvern Zetasizer Instrument. Particle size distribution profiles for both systems are shown in Figure 5.7.

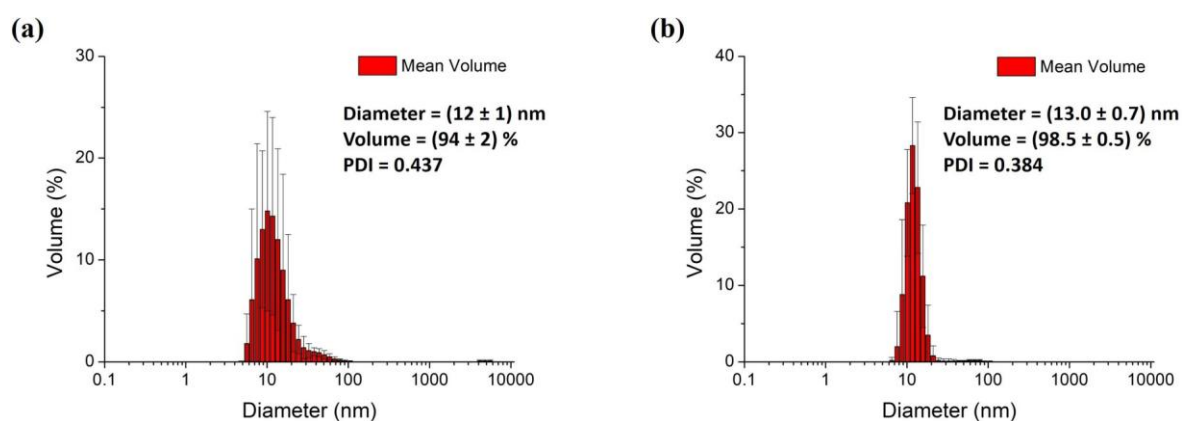


Figure 5.7. Particle size distribution determined by DLS analysis for (a) **90·AuNP** and (b) **91·AuNP** in aqueous solutions at 298 K.

Average hydrodynamic diameters of 12 nm (94% volume) and 13 nm (98% volume) were determined for both gold conjugates **90·AuNP** and **91·AuNP**, respectively. The diameter values obtained by DLS correspond not only to the gold particle core, but also to the capping layer bound to the gold surface.^{264,417,446,456} Interestingly, as was already

observed for the surfactant systems discussed in the previous chapter, similarity in the hydrodynamic diameters of both systems suggests that the presence of **phen** or **TAP** as ancillary ligands in the Ru(II) complexes bound to the surfaces of the AuNPs does not have a significant influence in the size of the resulting Ru(II) polypyridyl functionalised AuNPs. However, the replacement of the N in positions 1 and 8 in the **TAP** ligand by CH in the **phen** ligand was shown to have a clear effect in the aggregation of the gold conjugate. Thus, while the AuNPs functionalised with the Ru(II) **TAP**-based complex **91•AuNP** showed a narrow size distribution in the range of 6.5–24.4 nm, a broader size distribution in the range of 5.6–78.8 nm was observed for the **phen** analogue system **90•AuNP** indicating the presence of much larger species. These results point to a greater tendency of **90•AuNP** to form aggregates when compared to the **TAP** analogue gold conjugate **91•AuNP**. Such behaviour has been previously observed in the Gunnlaugsson group for similar systems and was attributed to the ability of the **TAP** ligand to participate in hydrogen bonding with water which reduces the aggregation of the resulting Ru(II) **TAP** complexes-based systems.²⁷¹

Having studied the size of the gold conjugates **90•AuNP** and **91•AuNP** in solution by DLS, TEM imaging was subsequently employed to further characterise these systems in the solid state and the results obtained will be discussed in the next section.

5.4 Transmission Electron Microscopy Studies of **90•AuNP** and **91•AuNP**

Another technique that is often used to visualise and analyse the size and shape of nanomaterials is TEM. This microscopy technique images a sample by transmitting a beam of electrons through the sample, instead of utilising light as is the case in optical microscopes. Interaction between the electrons and the sample results in generation of an image showing regions of the sample with different levels in darkness according to their density. The smaller de Broglie wavelength of electrons compared with visible light provides transmission electron microscopes with a higher resolution than optical microscopes, making them suitable for imaging at the nanoscale range and as such for the characterisation of AuNP systems.⁴⁵⁷

In this context, TEM studies were then performed to gain further information on the size, size distribution and morphology of the systems **90•AuNP** and **91•AuNP**. These studies were carried out by the Gunnlaugsson team member Dr Aramballi J. Savyasachi in the CRANN - Advanced Microscopy Laboratory (AML) at Trinity College Dublin. A drop of the appropriate AuNP solution (250 μ M) was adsorbed onto a 200-mesh formvar film stabilised with carbon copper grid before being imaged using a Jeol 2100 transmission

electron microscope. TEM images obtained for both **90**·AuNP and **91**·AuNP and their corresponding size distribution profile are given in Figure 5.8.

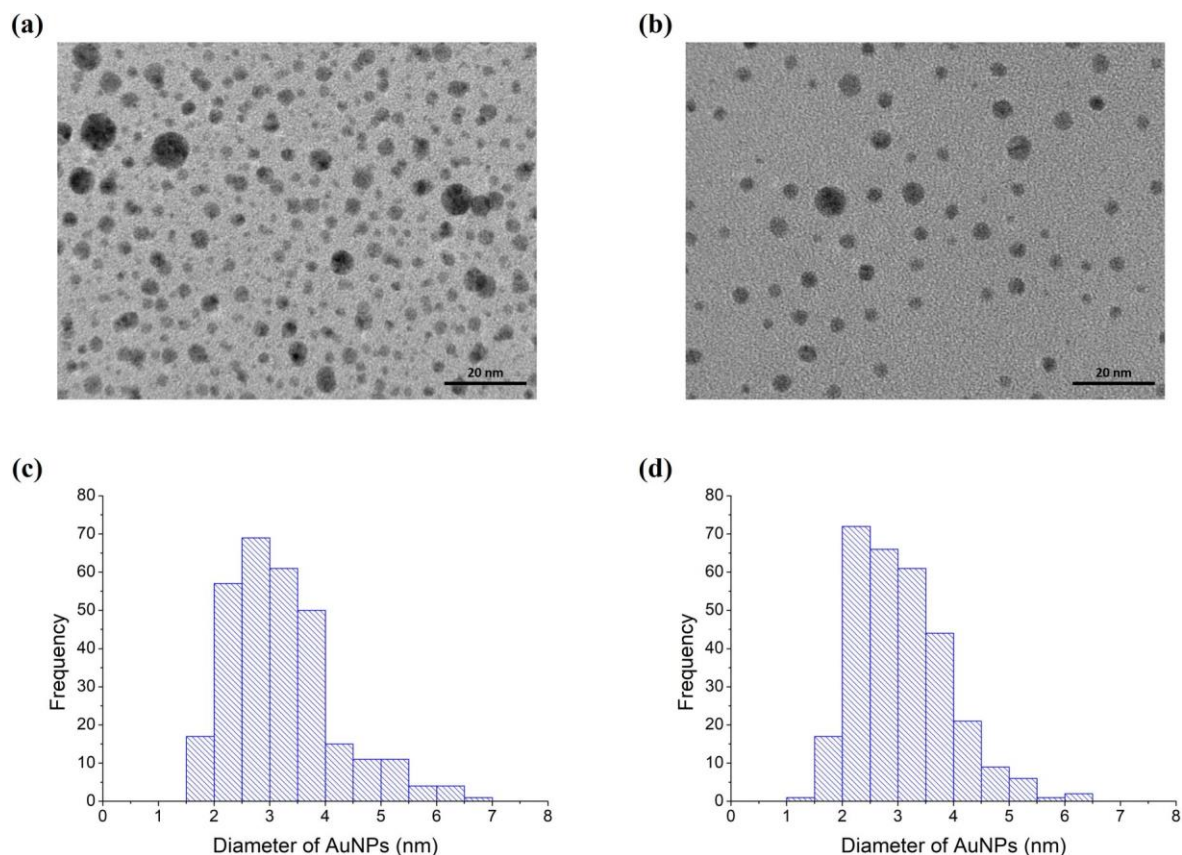


Figure 5.8. TEM images of (a) **90**·AuNP (250 μ M) and (b) **91**·AuNP (250 μ M) after deposition onto formvar stabilised carbon coated copper grids and the particle size distribution profile calculated from analysing the TEM images for (c) **90**·AuNP and (d) **91**·AuNP.

TEM images revealed spherical nanoparticles (Figures 5.8a and 5.8b) with diameters in the range of 1.5–7.0 nm for the system **90**·AuNP and 1.0–6.5 nm for the system **91**·AuNP, which are consistent with the synthetic procedure employed.⁴⁵¹ Interestingly, aggregation was found to be more important in the case of the nanoparticles functionalised with the **phen** containing Ru(II) complex **90**·AuNP, with no major evidence of aggregates formation by the **TAP** conjugate **91**·AuNP. These observations are in agreement with the DLS studies discussed previously. Furthermore, analysis of the particle size of *ca.* 300 nanoparticles from different regions of TEM images showed that the majority of the AuNPs functionalised with **90** displayed an average gold core diameter between 2.5 and 3.0 nm (Figure 5.8c). However, a slightly smaller average gold core diameter was observed for the majority of the AuNPs functionalised with the **TAP** analogue complex **91** with diameters values between 2.0 and 2.5 nm (Figure 5.8d). It should be noticed that, while the particle size determined by DLS measurements includes the alkyl disulphide functionalised Ru(II) complex bound to the gold

surface, TEM analysis only depends on the size of the particle gold core. Thus, smaller diameter values are expected when employing TEM imaging, which is consistent with the results showed in this section.

DLS and TEM studies provided information about the size and shape of both systems **90·AuNP** and **91·AuNP**. However, confirmation that the surface of the AuNPs was functionalised with the corresponding Ru(II) complexes was achieved by evaluating the photophysical properties of **90·AuNP** and **91·AuNP** as will be discussed in the next section. Photophysical characterisation of the free complexes **90** and **91** was also assessed for comparison.

5.5 Photophysical Characterisation of **90**, **91**, **90·AuNP** and **91·AuNP**

The photophysical properties of the free dinuclear complexes **90** and **91**, as well as the systems resulting from their attachment onto the surface of AuNPs (**90·AuNP** and **91·AuNP**), were evaluated in 10 mM sodium phosphate-buffered aqueous solution at pH 7.4. UV-vis absorption, emission and excitation spectra of complexes **90** and **91** are shown in Figure 5.9 and those corresponding to **90·AuNP** and **91·AuNP** are given in Figure 5.10.

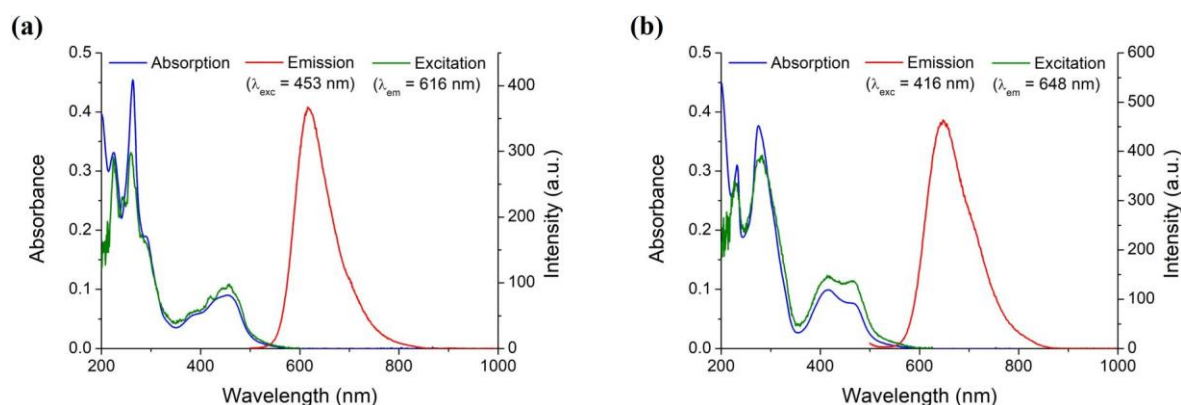


Figure 5.9. UV-vis absorption, excitation and emission spectra of (a) **90** and (b) **91** in 10 mM sodium phosphate-buffered aqueous solution at pH 7.4, at 298 K. Note that different emission and excitation slits widths were used for both complexes due to the poor emission of **91** when compared to **90**, and as such emission intensities of complexes cannot be compared.

As was already discussed for similar Ru(II) polypyridyl complexes in previous chapters, three main absorption maxima were observed for complex **90** at 225, 262 and 453 nm. Bands at 225 and 263 nm were attributed to π - π^* intra-ligand transitions within the ancillary **phen** ligands while the broad band centred at 453 nm was characteristic of the MLCT transition of the Ru(II) centre. Likewise, complex **91** showed intense absorption bands at 232 and 275 nm that correspond to π - π^* intra-ligand transitions in the **TAP** ligand, and a broad band centred at 416 nm assigned to the MLCT transition of the Ru(II) centre. A

summary of the molar absorptivity values determined at these absorption maxima for these complexes is given in Table 5.1.

Table 5.1. Absorption properties of **90** and **91** in 10 mM sodium phosphate-buffered aqueous solution at pH 7.4, at 298 K.

Complex	Absorbance λ_{max} , nm (ϵ , $10^4 \text{ M}^{-1}\text{cm}^{-1}$) ^[a]		
	π - π^* IL	π - π^* IL	MLCT
90	225 (13.0 \pm 0.3)	263 (18.1 \pm 0.5)	453 (3.6 \pm 0.1)
91	232 (12.2 \pm 0.4)	275 (14.8 \pm 0.5)	416 (3.9 \pm 0.1)

^[a] Molar absorptivity values correspond to the mean \pm SEM.

Functionalisation of AuNPs with complexes **90** and **91** resulted in the appearance of a broad shoulder in their MLCT absorption bands extending to *ca.* 700 nm and attributed to the SPR band characteristic of metallic nanoparticles. The presence of the SPR band confirms the successful attachment of the Ru(II) complexes on the AuNP surface.

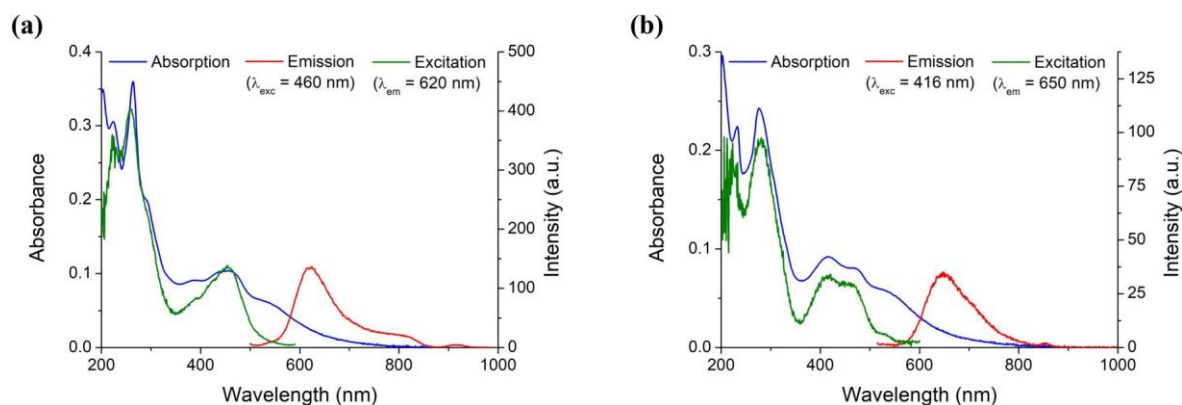


Figure 5.10. UV-vis absorption, excitation and emission spectra of (a) **90**-AuNP and (b) **91**-AuNP in 10 mM sodium phosphate-buffered aqueous solution at pH 7.4, at 298 K.

Interestingly, no major changes were observed in the π - π^* intra-ligand and MLCT bands position when compared to those shown by the free complexes **90** and **91** (Figure 5.11). However, a 31% hypochromism of the π - π^* intra-ligands absorption bands was observed upon attachment of the free complexes to AuNPs in relation to their MLCT absorption bands. This is most likely due to the overlap of both MLCT and SPR bands. Such overlap also makes it difficult to identify any shifts in the position of the SPR band after incorporation of the Ru(II) complexes onto the gold surface. The absorption maximum and bandwidth of the SPR band has been shown to be sensitive to the size, shape and composition of the nanoparticle.²⁴⁸ As a result of these spectral perturbations, determination of accurate

concentrations of the resulting gold conjugates **90·AuNP** and **91·AuNP** is not possible by using the molar absorptivity values obtained for the free complexes **90** and **91**.

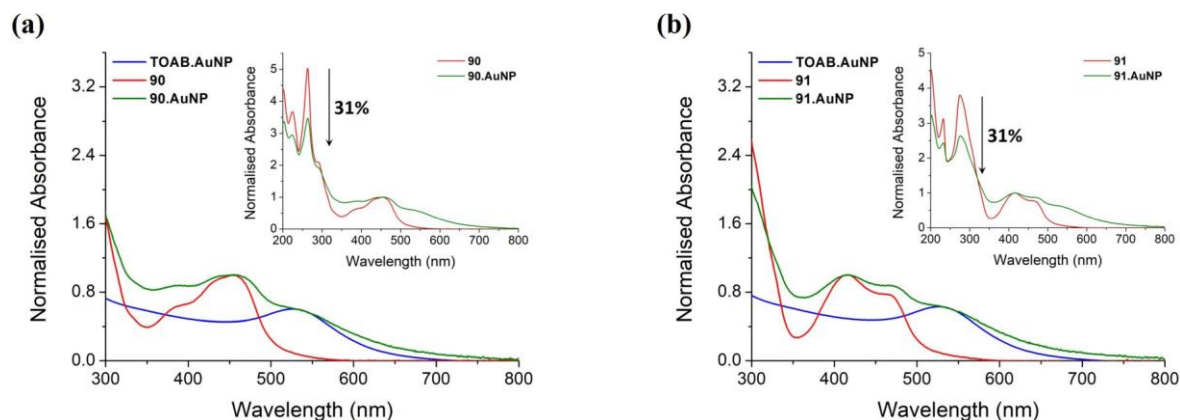


Figure 5.11. UV-vis absorption spectra (normalised absorbance at the MLCT band) showing the comparison between (a) the TOAB-stabilised AuNPs, the free complex **90** and the gold conjugate **90·AuNP**, and (b) the TOAB-stabilised AuNPs, the free complex **91** and the gold conjugate **91·AuNP**, in 10 mM sodium phosphate-buffered aqueous solution at pH 7.4, at 298 K. Inset: Hypochromism underwent by the π - π^* intra-ligand transitions within the ancillary ligands upon attachment to AuNPs in relation to the MLCT absorption band.

The emission properties of the free complexes **90** and **91** and their gold conjugates **90·AuNP** and **91·AuNP** in 10 mM sodium phosphate-buffered aqueous solution at pH 7.4 are summarised in Table 5.2. Excitation into the MLCT bands of the free complexes resulted

Table 5.2. Emission properties of **90**, **91**, **90·AuNP** and **91·AuNP** in 10 mM sodium phosphate-buffered aqueous solution at pH 7.4, at 298 K. Complexes **95** and **96** are included for comparison.

Complex	λ_{max}^{em} (nm) buffer	$\Phi_{em}^{[a]}$ buffer (air)	τ_{em} (ns) buffer (air)	τ_{em} (ns) buffer (N ₂)
95	615 ^[b]	-	784 ^[c]	-
96 ^[d]	649	0.040	778	-
90	616	0.048	804 ^[e]	1237 ^[e]
91	648	0.007	254 ^[f]	253 ^[f]
90·AuNP	624	0.002	827 ^[e]	999 ^[e]
91·AuNP	649	0.001	303 ^[e]	421 ^[e]

^[a] Air-saturated aqueous solution of [Ru(bpy)₃]Cl₂ as reference ($\Phi_{em} = 0.028$).³⁰⁸ Estimated errors $\pm 2\%$.

^[b] From reference 458. The reported values are in aqueous solution.

^[c] From reference 459. The reported values are in aqueous solution.

^[d] From reference 122. The reported values are in aqueous solution.

^[e] The luminescence decays are monoexponential. Estimated errors $\pm 5\%$.

^[f] The luminescence decays are bi-exponential; reported data correspond to the pre-exponential weighted mean lifetimes (τ_M).³²⁹ Estimated errors $\pm 5\%$.

in broad bands centred at 616 nm for **90** and 648 nm for **91**. Interestingly, **91** exhibited lower emission intensity when compared with **90** in the same conditions. However, it must be noted

that, in order to measure a well resolved emission spectrum, the emission of **91** reported in Figure 5.9b was recorded using wider emission and excitation slits than those employed in the acquisition of the emission spectrum of the **phen** analogue. Thus, the emission intensities of both complexes cannot be compared. Similarly, the excitation spectra recorded for **90** and **91** were found to be identical to their absorption spectra.

The difference in the emission intensities observed for complexes **90** and **91** was in agreement with the luminescence quantum yields and lifetimes measured for these complexes in aerated 10 mM sodium phosphate-buffered aqueous solution at pH 7.4. Luminescence quantum yields values of 0.048 and 0.007 were calculated for complexes **90** and **91**, respectively, using the optically dilute solution method and $[\text{Ru}(\text{bpy})_3]\text{Cl}_2$ as reference compound, with the reported values taken as an average of a minimum of three independent measurements.³⁰⁸ Luminescence lifetimes of 804 and 254 ns were determined by single-photon timing (SPT) ($\lambda_{\text{exc}} = 458 \text{ nm}$, $A_{\text{MLCT}} = 0.05$) for **90** and **91**, respectively, in aerated 10 mM sodium phosphate-buffered aqueous solution at pH 7.4. The data was best fitted to a monoexponential (**90**) or bi-exponential (**91**) decay function, with χ^2 values close to 1 and the reported lifetime values corresponding to the average of a minimum of two measurements for each complex. In the case of **90**, this value is similar to that reported in the literature for the complex $[\text{Ru}(\text{phen})_2\text{bpy}]^{2+}$ (**95**),⁴⁵⁹ whereas **91** exhibited a much lower luminescence lifetime than its analogue complex $[\text{Ru}(\text{TAP})_2\text{bpy}]^{2+}$ (**96**).¹²² As has been discussed in previous chapters, the presence of the electron-withdrawing **TAP** ligands confers an oxidizing character to the excited state of the resulting Ru(II) complex (*e.g.* the reduction potential of **96** in the excited state is +1.10 V/SCE).¹²² Therefore, the ³MLCT excited state of **TAP** containing Ru(II) complexes would be sufficiently photooxidizing to extract one electron from reductant molecules resulting in a quenching of their luminescence. On the other hand, sulphur containing molecules such as H₂S or cysteine have shown to be efficient reductants.⁴⁶⁰ In this context, the low quantum yield and lifetime values observed for **91** could be explained by an intramolecular photoinduced electron transfer from the alkyl disulphide moiety to the oxidizing Ru(TAP)₂ core. Such intramolecular quenching was not observed for the **phen** analogue as the electron accepting character of complex **91** is due to the π -deficient **TAP** ancillary ligands.

When the solution was deaerated, significant increase of the lifetime of complex **90** was observed, indicating a quenching of the excited state by dissolved oxygen in solution. In contrast, no change in the lifetime was observed for **91** in deaerated solution which is consistent with the behaviour exhibited for the **TAP** complexes described in previous

chapters, indicating that the excited state of these complexes seems to be less affected by the presence of dissolved oxygen than their **phen** analogues.^{197,211,212,404}

Concerning the emission properties of the AuNP conjugates **90·AuNP** and **91·AuNP** in the same conditions employed for the free complexes, broad emission bands were observed at 624 and 649 nm, respectively, upon excitation into their MLCT absorption bands, as was shown for complexes **90** and **91**. Likewise, excitation spectra of **90·AuNP** and **91·AuNP** were shown to be identical to those of the corresponding free complexes indicating no contribution to the observed luminescence from the AuNP SPR band. Luminescence quantum yields of both systems were found to be significantly low in comparison to those determined for the free complexes, with Φ_{em} values of 0.002 and 0.001 determined for **90·AuNP** and **91·AuNP**, respectively. This behaviour was not unexpected, as quenching of the Ru(II) complex luminescence by an energy-transfer mechanism resulting from the interaction with the AuNP surface has already been reported in the literature.^{267,461}

In addition, lifetime values of 827 and 303 ns were measured in aerated 10 mM sodium phosphate-buffered aqueous solution at pH 7.4 for the gold conjugates **90·AuNP** and **91·AuNP**, respectively. These values are similar to those observed for their free complex counterparts in the same conditions and are likely due to the unquenched complexes bound to the gold surface. These values correspond to the average of a minimum of two independent measurements for which the luminescence decays were fitted to a monoexponential function with χ^2 values close to 1. Moreover, **90·AuNP** and **91·AuNP** showed lifetimes values of 999 and 421 ns in deaerated 10 mM sodium phosphate-buffered aqueous solution which are only slightly larger values than those measured in aerated solutions. This behaviour is in contrast to that showed by the free complex **90** for which a more significant increase of the lifetime was observed when the solution was deaerated. It could be presumed that, in a similar way to the behaviour observed for the surfactant complex **80** in the previous chapter, the attachment of a large number of complex molecules around the gold surface would keep them close to each other resulting in the protection of their excited state from oxygen quenching. Thus, deaeration of the solution would not have a major effect as complexes molecules would be already protected in their new arrangement around the gold core. In the case of the **TAP** containing gold conjugate **91·AuNP**, results are consistent with those observed for the free complex and thus similarity in lifetime values measured in both aerated and deaerated conditions would be due to the negligible contribution of dissolved oxygen to the quenching of the excited state of **TAP** containing Ru(II) complexes.^{197,211,212,404}

In summary, the free complexes **90** and **91** and their corresponding AuNP conjugates **90·AuNP** and **91·AuNP** have shown attractive photophysical properties in aqueous solution which may be suitable for their use in biological imaging and therapeutic applications. Thus, *in vitro* studies of these systems were next conducted in order to assess their potential to be used in a biological environment.

5.6 *In vitro* Studies of **90**, **91**, **90·AuNP** and **91·AuNP**

With the aim of investigating the applicability of the new systems in biological imaging and diagnostics, cellular uptake studies in HeLa cells were first conducted on both the free complexes **90** and **91** and their gold conjugates **90·AuNP** and **91·AuNP**. In addition, toxicity studies in HeLa cells were also performed on the free complexes **90** and **91**, while those involving the nanoparticles systems are still in progress and as such are not presented here. It should be noted that, in the case of the gold conjugates, the Ru(II) complex concentrations reported are only an estimation and were calculated using the π - π^* intra-ligand absorption bands and the molar absorptivity values determined for such transitions in the free complexes. Further experiments such as inductively coupled plasma mass spectrometry (ICP-MS) will be necessary to determine the number of ruthenium complexes per AuNP and give more accurate concentration values.

5.6.1 Cellular Uptake Studies of **90**, **91**, **90·AuNP** and **91·AuNP**

Cellular uptake and localisation of the free complexes **90** and **91**, as well as their gold counterparts **90·AuNP** and **91·AuNP**, in HeLa cells were investigated by confocal fluorescence microscopy. HeLa cells were incubated either with **90** and **91** (20 μ M) or with **90·AuNP** and **91·AuNP** (~20 μ M Ru(II) complex concentration which corresponds to Au concentrations of ~60 nM and ~68 nM for the conjugates **90·AuNP** and **91·AuNP**, respectively)⁴⁶² at 37 °C for 2, 4 and 24 h. Cells were then treated with the nuclear stain Hoechst 33258 and imaged using a Leica SP8 gated STED confocal microscope with a 40x oil immersion lens with an NA (numerical aperture) of 1.30. Confocal fluorescence images showing the cellular uptake of both **90** and **91** over time are shown in Figure 5.12.

Both free complexes seemed to localise in the cytoplasm of HeLa cells with a time dependant cellular uptake and thus an increase of the emission intensity of **90** and **91** was detected over time, with almost negligible emission after 2 h incubation, and then more significant emission intensity after 4 and 24 h incubation. The fast uptake of both compounds was not unexpected since these complexes can be considered to be similar Ru(II) dinuclear versions of complexes **79** and **82**, presented in the previous chapter, which were observed to

be quickly taken up by the cells. However, complex **91** seemed to be less emissive inside the cells when compared with complex **90**. This is in agreement with the photophysical properties displayed by these complexes and shown in Section 5.5 of this chapter where complex **90** was found to be much more emissive than complex **91** as a likely result of an intramolecular photoinduced electron transfer from the alkyl disulphide moiety to the oxidizing Ru(TAP)₂ core. On the other hand, lipophilicity studies performed in the previous

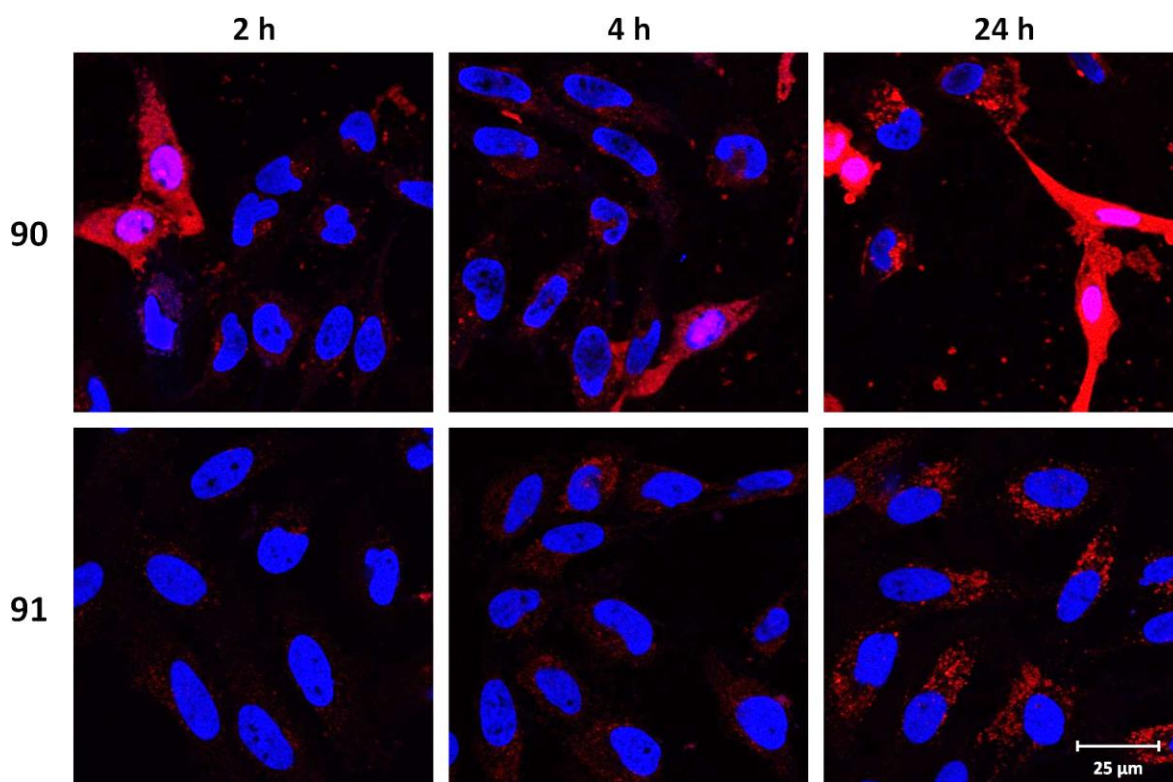


Figure 5.12. Confocal fluorescence microscopy images of HeLa cells showing the uptake of **90** and **91** (red) at 20 μM after 2, 4 and 24 h incubation. The nucleus is stained blue with Hoechst 33258.

chapter revealed that complexes containing **phen** as ancillary ligands were more lipophilic than their **TAP** analogues and thus a lower intracellular concentration can be expected for complex **91** than for complex **90** resulting in a lower emission intensity inside the cells when treated with the **TAP** complex. In addition, luminescence intensity of **TAP** complexes can be quenched by reductant biomolecules such as the nucleobase guanine and the amino acid tryptophan through a photoelectron transfer process, as has been fully discussed in previous chapters.^{203,231}

Interestingly, partial nuclear localisation of complex **90** was observed after 24 h incubation. Confocal fluorescence microscopy images with a clearer visualisation of such nuclear uptake are shown in Figure 5.13.

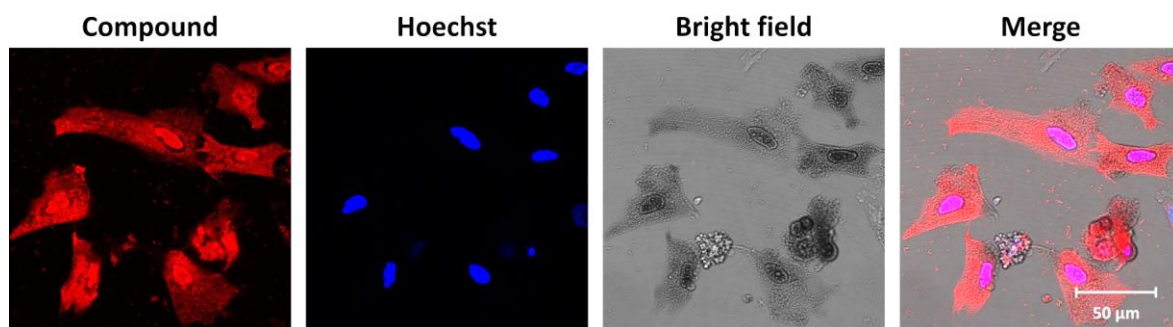


Figure 5.13. Confocal fluorescence microscopy images of HeLa cells showing the nuclear uptake of **90** (red) at 20 μM after 24 h incubation. The nucleus is stained blue with Hoechst 33258.

Overlap of the fluorescence from the nuclear stain Hoechst 33258 (blue) with the luminescence emanated from the Ru(II) complex (red) confirmed the nuclear uptake of **90** in some cells. Furthermore, nuclear localisation was also seen in the bright field image where cells exhibited a darker appearance as a result of the high overload of **90** inside the cells. However, it must be noted that the cell morphology of the HeLa cells treated with **90** for 24 h suggests that this complex is more toxic than its **TAP** analogue. Therefore, nuclear localisation could also be a sign of cell damage after long exposure to **90**.

Concerning the cellular uptake of the gold conjugates **90**·AuNP and **91**·AuNP, confocal fluorescence images in the same conditions as those employed for the corresponding free complexes are given in Figure 5.14. As was previously observed for complexes **90** and **91**, an increase in cellular uptake over time was observed for both systems **90**·AuNP and **91**·AuNP. After 2 to 4 h of incubation, both gold conjugates seemed to mainly localise in the cell membrane. However, brighter luminescent emission from **90**·AuNP and **91**·AuNP appeared in the cytoplasm of the cells after 24 h incubation. Moreover, cellular internalisation of the gold systems was also observed in the bright field images with the appearance of the AuNPs as dense dark areas (Figure A5.5 of the Appendices). The effective cellular internalisation of the AuNPs conjugates was further confirmed by Z-stack studies as shown in Figure 5.15. An aqueous solution of fluorescein sodium salt (5 μM) was also added to the cells as it is a water-soluble fluorescent dye which is not taken up by live cells, and so makes the extracellular medium fluorescent. Thus, by fluorescent saturation of the extracellular medium, the contrast between the inside and the outside of the cells is maximised resulting in better definition of the outline of the cells. Both systems **90**·AuNP and **91**·AuNP were clearly localised in the cytoplasm of the cells around the nuclei as observed from the red emission from the ruthenium-based nanomaterials. Thus, these results gave further evidence of the successful internalisation of the gold conjugates **90**·AuNP and

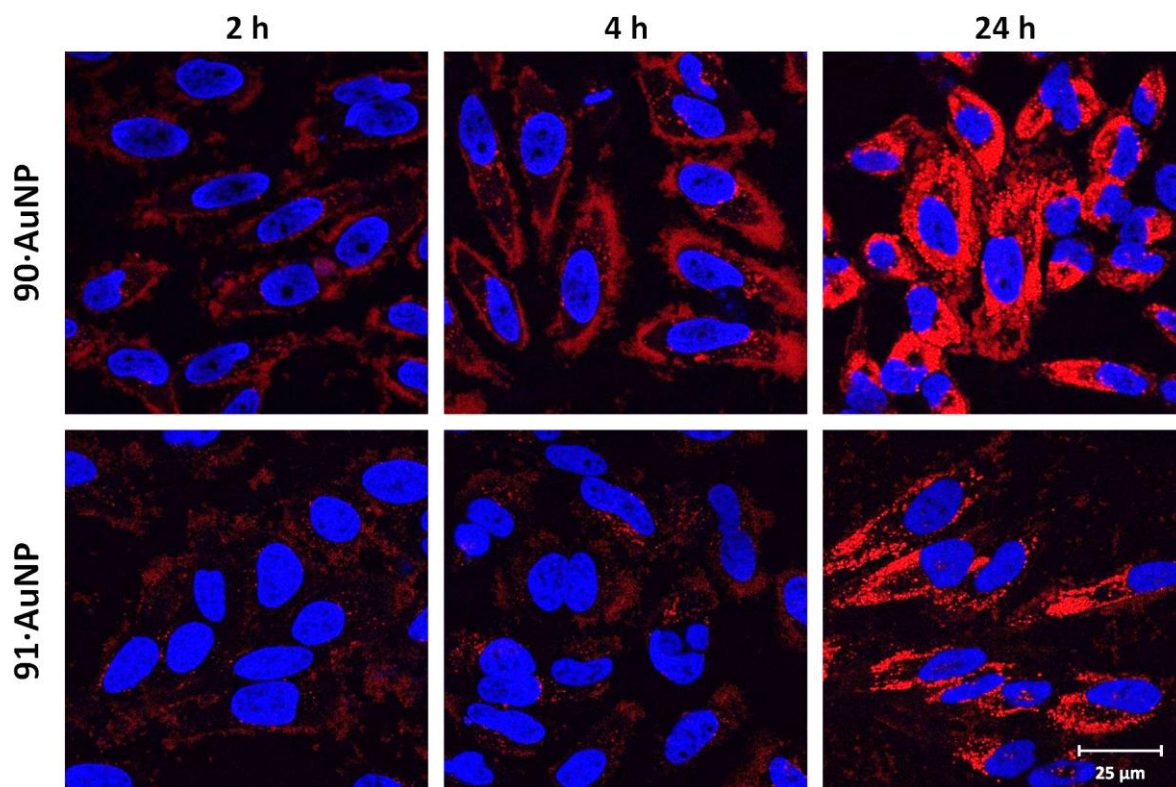


Figure 5.14. Confocal fluorescence microscopy images of HeLa cells showing the uptake of **90·AuNP** and **91·AuNP** (red) at ca. $20 \mu\text{M}$ Ru(II) complex concentration after 2, 4 and 24 h incubation. The nucleus is stained blue with Hoechst 33258.

91·AuNP in HeLa cells. Further experiments must be performed in order to elucidate the mechanism by which the free complexes **90** and **91**, or the AuNP conjugates **90·AuNP** and **91·AuNP** are taken up by the cells. In the particular case of the nanoparticles, the cellular uptake effectiveness and mechanism has shown to be dependent on the size, shape and surface charge of the nanomaterial.^{246,250,463} This may occur through receptor-mediated endocytosis as has been described in the literature for many other AuNP conjugates.^{246,250,271,463} Such an uptake mechanism can be supported by the punctate appearance of the gold systems **90·AuNP** and **91·AuNP** inside the cells.

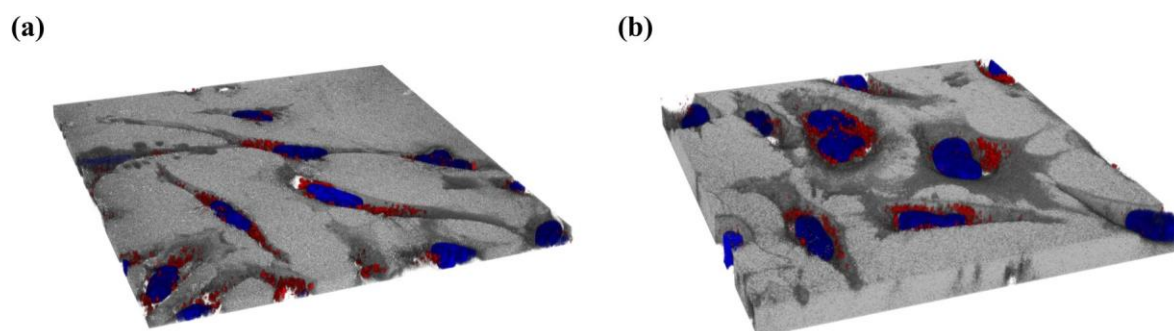


Figure 5.15. 3D confocal fluorescence microscopy images generated from Z-stack studies showing the cytoplasm effective internalisation of (a) **90·AuNP** and (b) **91·AuNP** (red) at ca. $20 \mu\text{M}$ Ru(II) complex concentration in HeLa cells after 24 h incubation. The nucleus is stained blue with Hoechst 33258.

Interestingly, cell morphology showed that the gold conjugate **90**·AuNP was better tolerated by HeLa cells than its free complex counterpart **90** after 24 h incubation, suggesting a lower toxicity of this complex when bound to the gold surface. In the next section, the potential of the free complexes **90** and **91** to induce cell death will be investigated in both dark conditions and after light activation. Unfortunately, cytotoxicity studies on the gold conjugates **90**·AuNP and **91**·AuNP are still in progress and will not be discussed.

5.6.2 Cellular Toxicity Studies of **90** and **91**

Having demonstrated that both **90** and **91** were successfully taken up by HeLa cells, their toxicity against the same cancer cell line was evaluated using the Alamar Blue cytotoxicity assay in the same way as described in previous chapters. Although $^1\text{O}_2$ production has not still been quantified for these complexes, their ability to be light-activated was also investigated based on the potential of Ru(II) polypyridyl complexes to be used as PDT agents reported in the literature and the results presented in previous chapters with similar complexes.^{62,63,93} For this purpose, HeLa cells were treated with different concentrations of **90** and **91** and incubated for 24 h at 37 °C before being exposed to 18 J cm^{-2} of light for 1 h using a Hg-Xe arc lamp equipped with a NaNO_2 filter or kept in dark. Cells were then incubated for a further 24 h and treated then with the Alamar Blue reagent. After 4 h incubation, toxicity under both light and dark conditions was assessed. Toxicity profiles of **90** and **91** under the previously mentioned conditions are shown in Figure 5.16 and the corresponding IC_{50} values can be found in Table 5.3. The reported values correspond to the average of triplicate treatments performed on three independent days.

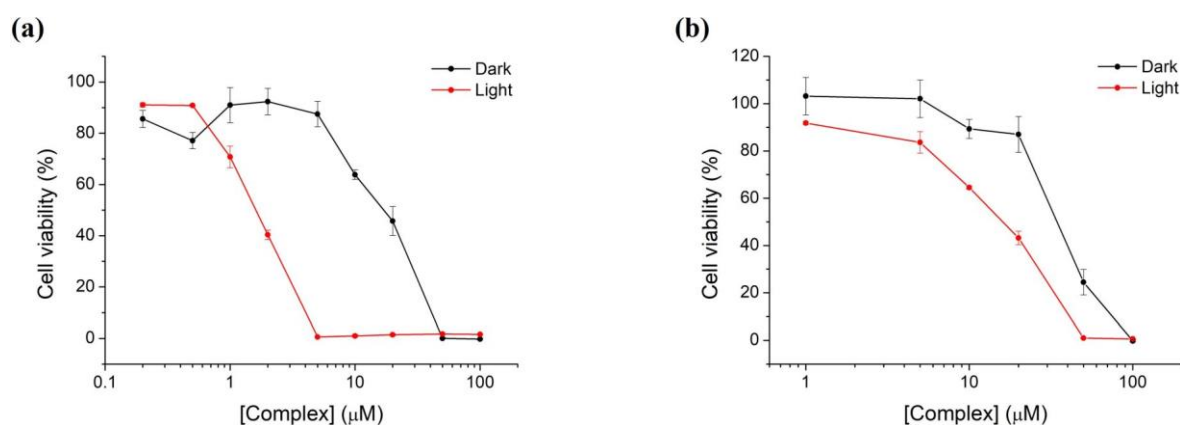


Figure 5.16. Toxicity profiles of (a) **90** and (b) **91** in HeLa cells. HeLa cells were treated with the indicated concentrations of the required complexes and incubated for 24 h followed by either exposure to light for 1 h or maintenance in the dark and followed by further 24 h incubation. Cells were then incubated with the Alamar Blue dye for 4 h and assessed for cellular viability. Note that a logarithmic scale is used for clarity.

Results revealed that both complexes displayed modest toxicity against HeLa cells in dark conditions. However, complex **90** was shown to be twice as toxic as **91** with IC₅₀ values of 19 μM and 38 μM, respectively. This is most likely due to a higher lipophilicity of **90** when compared to its **TAP** analogue which results in larger intracellular concentration. The decrease of the lipophilicity of Ru(II) polypyridyl complexes when the ancillary **phen** ligands are replaced by **TAP** was discussed in the previous chapter for similar mononuclear versions of these complexes. In addition, complex **90** was shown to be significantly more photo-toxic than **91** displaying IC₅₀ values of 1.77 μM and 17.1 μM, respectively, upon light irradiation and resulting in PI values of 11 and 2, respectively. An explanation for this behaviour could be that ¹O₂ generation by **90** is larger than by **91**, which is in accordance with larger quantum yields of ¹O₂ production determined in air-saturated H₂O for **phen** complexes when compared with their **TAP** analogues in the previous chapter. Further experiments must be carried out in order to discern the mechanism by which these complexes particularly **90** exhibit light-activated toxicity against HeLa cells.

Table 5.3. IC₅₀ values for the cytotoxicity of **90** and **91** in HeLa cells in the dark and exposed to light.

Complex	IC ₅₀ dark (μM) ^[a]	IC ₅₀ light (μM) ^[a]	PI ^[b]
90	19 ± 2	1.77 ± 0.05	11
91	38 ± 2	17.1 ± 0.8	2

^[a] IC₅₀ values correspond to the mean ± SEM.

^[b] Phototoxic index (PI) is defined as the ratio of the IC₅₀ value in the dark to the IC₅₀ value upon light irradiation.

These results highlighted once again the potential of Ru(II) polypyridyl complexes to be used as light-activated compounds and the importance of the ligands coordinated to the ruthenium centre when designing Ru(II)-based therapeutic agents. Furthermore, although the cytotoxicity of these complexes when bound to the surface of gold nanoparticles has not still been assessed, the morphology of the cells observed by confocal microscopy after 24 h incubation with the gold conjugate **90**·**AuNP** pointed to a lower toxicity of this system when compared to its free complex analogue **90**. Thus, it should be also taken into account the influence of the delivery of such complexes attached to nanomaterials into cells not only in their imaging applications but also in their cytotoxic potential.

5.7 Conclusion and Future Perspectives

This chapter presented the synthesis, photophysical characterisation and biological evaluation of novel dinuclear Ru(II) polypyridyl complexes, along with their subsequent

incorporation onto the surface of AuNPs with a view to explore their potential as cellular imaging and therapeutic agents. Two new alkyl disulphide functionalised dinuclear Ru(II) polypyridyl complexes containing either **phen** (**90**) or **TAP** (**91**) as ancillary ligands were successfully synthesised and characterised. An investigation of their photophysical properties, followed by the study of their potential to be used in biological applications, gave indications about their behaviour as free complexes prior to their attachment onto the surface of the gold nanomaterial. Both complexes **90** and **91** showed the distinctive absorption and emission properties associated with Ru(II) polypyridyl complexes that has made them attractive candidates to be explored as conjugates for AuNPs. Furthermore, their ability to be rapidly taken up by HeLa cells with mainly localisation in the cell cytoplasm was confirmed by confocal microscopy studies. Such quick cellular uptake is most likely due to a combination of their high positive charge, and the presence of relatively long alkyl chains, which again highlighted the important role that lipophilicity plays in the capability of a compound to cross the cell membrane. Additional cytotoxicity studies demonstrated that while both complexes were only moderately toxic when kept in the dark, their illumination with visible light resulted in an increase in toxicity, in particular for the **phen** derivative **90**. Although the origin of such photoactivation has not yet been investigated for these particular complexes, based on previous observations along this thesis and the work reported in the literature, singlet oxygen production could be one of the major pathways by which these complexes become toxic after light activation.^{62,63,296}

Once the properties of **90** and **91** as free complexes were investigated, functionalisation of AuNPs (average diameter of *ca.* 2.5 nm) with these complexes was performed in order to obtain the corresponding Ru(II)-AuNP conjugates **90·AuNP** and **91·AuNP**. Characterisation of the new nanomaterials by DLS measurement and TEM imaging provided information about the size and shape of the resulting gold conjugates. Interestingly, the system functionalised with the **phen** containing Ru(II) complex was observed to be more susceptible to aggregation than that with the **TAP** analogue and it is most likely due to the ability of the **TAP** ligand to form hydrogen bonds with protic solvents which would reduce the tendency of the gold conjugate **91·AuNP** to aggregate.²⁷¹ Successful functionalisation of the AuNPs with the Ru(II) complexes was further confirmed by the investigation of their photophysical properties. Both nanosystems showed absorption properties characteristic of both the AuNP SPR and the Ru(II) complex MLCT absorption bands. On the other hand, the emissive behaviour of the Ru(II)-AuNPs conjugates is due to the Ru(II) MLCT excited state, although a lower quantum yield was observed when

compared to the free complexes as a consequence of energy-transfer quenching of the Ru(II) luminescence by interaction with the gold surface.^{267,461} Despite their diminished luminescence, cellular uptake studies in HeLa cells were performed on both **90·AuNP** and **91·AuNP** systems with a view to evaluating their potential applicability as cellular imaging agents as their conjugation to the gold platform was expected to deliver larger concentrations of Ru(II) complex into the cell. Indeed, **90·AuNP** and **91·AuNP** were found to be successfully internalised into HeLa cells with localisation in the cytoplasm. These results represent a contribution to the potential bioimaging applications of the nanomaterial resulting from the combination of Ru(II) polypyridyl complexes and AuNPs.

Future work will focus on improving the emission properties of the Ru(II)-AuNP conjugates in order to produce highly luminescent nanoparticles that will be more suitable for imaging applications. Luminescence quenching by the surface plasmon of AuNPs can be controlled by varying the distance between the gold core and the luminophore, and also depends on the method employed to attach the luminescent molecule to the gold surface.^{266,269,270} For example, Pikramenou and co-workers have shown that the emission properties of different size Ru(II) polypyridyl functionalised AuNPs, precoated with a fluorinated surfactant, are distance-dependent and can be enhanced over their free counterparts.^{266,269} In addition, the DNA binding ability of **90·AuNP** and **91·AuNP** to be used as photoprobes of the genetic material will be investigated in line with the work described in previous chapters of this thesis and with similar systems developed recently in the Gunnlaugsson group.^{264,271} Furthermore, the therapeutic potential of these Ru(II)-AuNP conjugates will be explored with a view to be used in simultaneous photodynamic and photothermal therapy taking advantage of the properties displayed by both the Ru(II) centre (PDT) and the gold nanocore (PTT) which may contribute to the design of new nanomaterials with applications on light activated therapies.

Chapter 6

Conclusions

Conclusions

In this work, a series of systems based on Ru(II) polypyridyl complexes have been synthesised and studied for use in biological applications. In particular, the versatility of these types of complexes has been extensively demonstrated in the four results chapters that compose this thesis, where they have been employed as DNA photoprobes, cellular imaging agents and photosensitisers in photodynamic therapy. The biological potential of Ru(II) polypyridyl complexes lies in their attractive photophysical and chemical properties that can be modulated by the nature of the ligands coordinated to the Ru(II) centre.^{2,62,63,93} Therefore, an understanding of the effects that different ligands have on the properties of the resulting complexes has been essential for the rational design of compounds with a particular biological application. For example, the strength and the binding mode by which the complexes interact with DNA can be modified by selecting the appropriate ligand coordinated to the Ru(II) centre. Thus, in addition to an electrostatic interaction between the negatively charged DNA phosphate bone and the positively charged Ru(II) complex, the incorporation of extended aromatic ligands such as the well-known **dppz**, has been proved to confer the resulting complex with an intercalative binding mode.¹⁴⁰ This is the case of complexes **63** and **64** discussed in *Chapter 2*, which contain the **dppz** derivative ligand **dtp** and either **phen** and **TAP** as ancillary ligands. Different techniques, including UV-vis absorption and emission spectroscopy, DNA thermal denaturation, circular dichroism and viscosity measurements showed that both complexes displayed high affinities for DNA with K_b values of *ca.* 10^7 and 10^6 M⁻¹ at low and high ionic strength, respectively. Viscosity studies confirmed that the interaction between the DNA double helix and **63** and **64** occurred by intercalation of the extended aromatic ligand between the DNA base pairs.

The nature of the ancillary ligands coordinated to the Ru(II) centre also plays an important role in the photophysical properties of complexes containing **dppz** derivatives. For example, complex **63**, containing **phen** ancillary ligands, showed no emission in aqueous solution while complex **64**, in which the **phen** ligands were replaced by **TAP**, was highly emissive in aqueous solution. This behaviour could be explained by the existence of different excited states in **63** and **64**, in the same way that occurs for the extensively studied **dppz** analogues **29** and **30**.¹³⁷⁻¹³⁹ Moreover, as is the case for **29**,¹⁶⁵ complex **63** showed the well-known “light-switch effect” upon binding to DNA wherein recovery of its luminescence was observed. However, similarly to **30**,¹⁶⁶ a quenching of the luminescence was observed for **64** in the presence of DNA-containing guanine due to a photoinduced-electron transfer from the nucleobase to the excited state of the complex.

The different photophysical properties displayed by both **phen** and **TAP** complexes **63** and **64**, respectively, also had an effect on the ability of the complexes to produce singlet oxygen, a reactive oxygen species which is known to be involved in the PDT activity of photosensitisers.^{9,62,63} Complex **63** was shown to produce no $^1\text{O}_2$ in air-saturated aqueous solution as a consequence of its short luminescence lifetime in that solvent. In contrast, complex **64** displayed a quantum yield of singlet oxygen generation of 0.19 in the same conditions. Neither **63** nor **64** were found to produce significant amounts of $^1\text{O}_2$ in the presence of DNA, most likely due to their strong DNA binding that protected them from interacting with molecular oxygen. These results highlighted the importance of the cellular localisation of compounds in the exercise of their PDT activity. In this context, despite both complexes being able to be internalised by HeLa cells and localising in the cytoplasm, only **64** showed an increase in its toxicity after being illuminated with visible light (PI value of 16), as expected from its ability to produce $^1\text{O}_2$. Therefore, while **63** could be used for DNA and cellular imaging, complex **64** showed potential to be used as a PDT agent, demonstrating the important role that the ancillary ligands coordinated to the Ru(II) centre play in their biological activity.

In addition, the use of **TAP** as ancillary ligands has also been shown to have consequences in the DNA binding mode of Ru(II) polypyridyl complexes.^{202,203} The π -deficient character of this ligand confers a high photooxidation power to the excited state of the Ru(II) complex, which provides the complex with the ability to covalently bind to reducing biomolecules such as the DNA base guanine.^{202,203} Thus, when π -deficient Ru(II) polyaaromatic complexes such as **38** are illuminated in the presence of guanine-containing molecules like GMP in the appropriate conditions, a photoreaction between both moieties can take place, resulting in the formation of a covalent photoadduct.^{202,203} The ability of these complexes to bind covalently to DNA can be exploited as a therapeutic tool to induce photocontrolled DNA damage by irreversible crosslinking of the two strands of the genetic material. However, the photoadduct **43**, formed by addition of one molecule of GMP to **38**, is not emissive and as such, its ability to react with a second molecule of GMP and be involved in DNA photocrosslinkings is intriguing. The mechanism by which **43** can incorporate a second GMP unit under further illumination only at pH 5–6, despite its non-emissive character, was the research topic of *Chapter 3*. An extensive spectroscopic study on both the ground and excited states of the mono-phototoadduct at different pH values lead to the proposal of a plausible photophysical mechanism based on the existence of different ground and excited states depending on the solution pH. While experiments carried out on

the ground state of **43** showed that the protonation state the photoadduct is different at pH 5 and 8, transient spectroscopic studies suggested the formation of different excited states at those pH values as the origin of the pH-dependent photoreactivity of **43**. Thus, reactive MLCT excited states that lead to the formation of a long-lived species with a lifetime of hundreds of nanoseconds would be produced at pH 5, while unreactive LLCT/ILCT excited states that decay to the ground state after hundreds of picoseconds would be formed at pH 8. Therefore, the work presented in *Chapter 3* contributes to the understanding of the photoreactivity of π -deficient Ru(II) polyaaromatic complexes towards DNA and highlights the importance of the conditions for such covalent binding to occur.

Another advantage of Ru(II) polypyridyl complexes is that the ligands coordinated to the Ru(II) centre are easy to modify and as such, it is possible to build more complex systems from simple structures. In *Chapter 4*, the incorporation of a ligand containing a hydrophobic tail (twenty one carbon alkyl chain) to the hydrophilic Ru(II) centre was shown to induce self-assembly of the resulting complexes **80** and **83** (**phen** and **TAP** as ancillary ligands, respectively) into micellar structures with sizes of *ca.* 10.5 nm. In addition, a concentration effect on the luminescence lifetimes of complexes **80** and **83** was observed due to their surfactant behaviour. Furthermore, the variation of the length of the alkyl chain was found to have an effect not only on the emission properties and the ability to produce $^1\text{O}_2$ of the resulting complexes, but also on the DNA binding affinity. Thus, while complexes **78** and **81** (**phen** and **TAP** as ancillary ligands, respectively), containing only a methyl group, interacted with the DNA helical structure through a combination of an electrostatic attraction and partial intercalation of the ancillary ligands, complexes **79** and **82** (**phen** and **TAP** as ancillary ligands, respectively), with ten carbon alkyl chains, displayed an additional hydrophobic interaction due to their hydrophobic tails.

An important consequence from the addition of alkyl chains to the ligands coordinated to the Ru(II) centre was an enhancement of the lipophilicity of the complexes which affected their cellular uptake and localisation within the cells. Specifically, complexes **79**, **80**, **82** and **83**, containing long alkyl chains, were shown to be rapidly taken up by HeLa cells, with preliminary localisation in the cell membrane. Furthermore, the phototoxic potential of the complexes was shown to be alkyl chain length-dependent, with complex **80**, containing the longest alkyl chain and **phen** as ancillary ligands, displaying the highest phototoxicity (PI value of 27). This is most likely due to a combination of an increase in the intracellular concentration as a result of enhanced lipophilicity (dark toxicity), as well as the complex's ability to produce $^1\text{O}_2$ or other ROS (light toxicity). Thus, by combining these

features complex **80** was found to be the most promising PDT agent. This work highlights the importance of considering additional properties to the photophysics of the Ru(II) complexes, with the lipophilicity that the incorporation of hydrophobic chains confers to the resulting complexes observed here clearly playing an important role in the capacity of the Ru(II) polypyridyl complexes to be taken up into a cellular environment.

Modification of the ligands coordinated to the Ru(II) centre also offers the possibility of functionalising Ru(II) complexes with other entities with a view to combining the advantageous properties of both moieties. For example, the systems resulting from the attachment of Ru(II) polypyridyl complexes onto the surface of AuNPs (average diameter of *ca.* 2.5 nm) were investigated in *Chapter 5*. Disappointingly, the incorporation of the Ru(II) moieties onto the gold nanomaterial was found to have a negative effect on the emission properties of the resulting systems **90·AuNP** and **91·AuNP** (**phen** and **TAP** as ancillary ligands, respectively), with these conjugates displaying lower quantum yields than those determined for the free complexes **90** and **91**. This behaviour was explained by energy-transfer quenching of the Ru(II) luminescence by interaction with the gold surface. Nevertheless, despite their diminished luminescence, **90·AuNP** and **91·AuNP** were found to exhibit successful internalisation within HeLa cells, and were found to localise in the cytoplasm. Therefore, these studies showed that AuNPs are suitable platforms for the delivery of larger concentrations of Ru(II) complex into the cell than would be achieved with direct treatment with free Ru(II) complexes.

In conclusion, the work presented in this thesis provides a powerful demonstration of the potential Ru(II) polypyridyl complexes have for use in biological applications as well as further insight into the key parameters that control their therapeutic activity. It was shown that exercising special care over the design of the ligands coordinated to the Ru(II) centre can allow for careful control over the photophysical and photochemical properties, DNA binding (non-covalent and covalent binding modes), and lipophilicity of the Ru(II) polypyridyl complexes. Thus, the work described herein shows the potential for designing Ru(II) polypyridyl complexes for targeted use in specific biological or therapeutic applications simply by selecting appropriate coordination ligands with suitable physical or chemical features.

Chapter 7

Experimental

7.1 General Experimental Apparatus and Techniques

Nuclear Magnetic Resonance (NMR) Spectroscopy: All NMR spectra were recorded using either a 400 MHz Bruker Avance III 400 NMR spectrometer operating at 400 MHz for ^1H NMR, 101 MHz for ^{13}C NMR and 162 MHz for ^{31}P NMR, a 600 MHz Bruker Avance II 600 NMR spectrometer operating at 600 MHz for ^1H NMR and 151 MHz for ^{13}C NMR, or a 800 MHz Agilent Technologies DD2 NMR spectrometer equipped with a 5 mm triple resonance ColdProbe and operating at 800 MHz for ^1H NMR and 201 MHz for ^{13}C NMR. Chemical shifts (δ) were referenced relative to the internal solvent signals. All NMR spectra were carried out at 25.0 °C except for those performed at 800 MHz where temperature values of 20.0 °C or 5.0 °C were employed depending on the experiment.

Mass Spectrometry: Electrospray ionisation (ESI) mass spectra were recorded on a Micromass LCT spectrometer or a MALDI QToF Premier, running Mass Lynx NT V 3.4 on a Waters 600 controller connected to a 996 photodiode array detector using HPLC-grade solvents. High resolution (HR) mass spectra were determined by a peak matching method, using leucine enkephaline (Tyr-Gly-Gly-Phe-Leu) as the standard reference ($m/z = 556.2771$). All accurate mass values were reported within ± 5 ppm.

Infrared Spectroscopy: Infrared spectra were recorded on a Perkin Elmer Spectrum One FT-IR spectrometer fitted with a Universal ATR Sampling Accessory for solid samples. Solution samples were loaded into a demountable solution IR cell (Harrick Scientific Products Inc., New York) fitted with 25 mm diameter CaF_2 windows (Crystran Ltd, UK), separated by Teflon spacers of 150 μm path length and recorded in a N_2 flushed Transmission Accessory. Sample preparation was carried out in a glove bag filled with N_2 to avoid moisture. Each spectrum is the average of 256 scans and a fresh background of the solvent was recorded prior to each sample. The baseline was subtracted from the FTIR spectra to allow clear visualisation of the bands of the molecules under investigation.

Melting Points: Melting points were determined using an IA9000 digital melting point apparatus.

Elemental Analysis: Elemental analyses were either conducted at the Microanalytical Laboratory, School of Chemistry, University College Dublin (UCD) or Department of Chemistry, Maynooth University.

Microwave Reactions: Reactions in which microwave irradiation was used were carried out using a Biotage[®] Initiator microwave synthesizer.

X-ray crystallography: X-ray diffraction data were collected on a Bruker APEX 2 DUO CCD diffractometer using graphite-mono-chromatized Mo-K α (0.71073 Å). Crystals were mounted in a cryoloop/MiTeGen micromount and collected at (100 \pm 2) K using an Oxford Cryosystems Cobra low temperature device. Data were collected using omega and phi scans and were corrected for Lorentz and polarization effects. Structures were solved with SHELXS-2014 and further refined with SHELXL-2014.⁴⁶⁴

Dynamic Light Scattering (DLS): DLS measurements were performed at 298 K with a Malvern Instruments Zetasizer Nano ZS provided with a 633 nm He-Ne laser (4 mW) as the light source. Prior to each measurement, fresh aqueous solutions containing the appropriate Ru(II) complex-based surfactant were prepared and left to equilibrate for 16 h before being passed through a syringe filter (0.45 μ m pore size, hydrophilic polyethersulfone membrane, PALL Acrodisc[®]). In the case of the AuNP, the appropriate Ru(II) polypyridyl functionalised AuNP sample ($A_{SPR} \approx 0.03$) was centrifuged for 60 min at 3900 rpm before each measurement to break up any possible aggregates.

Transmission Electron Microscopy (TEM): TEM analysis were conducted in the CRANN - Advanced Microscopy Laboratory (AML) at Trinity College Dublin using a Jeol 2100 transmission electron microscope operating at 200 kV. Samples were prepared by adsorbing a drop of the appropriate Ru(II) polypyridyl functionalised AuNP solution (250 μ M) onto a 200-mesh formvar film stabilised with carbon copper grid, with the excess solution being wicked off using filter paper after 10 min of adsorption time.

Surface Tension Measurements: Surface tension was measured with a Kibron Inc. EZ-PI Plus Surface Tensiometer for automatic measurement of surface and interfacial tension provided with a 0.5 mm diameter metallic rod (Kibron DyneProbe) and a polypropene sample cup. Individual aqueous solutions (3 mL) at different surfactant concentrations were prepared and left equilibrated for 16 h before surface tension was measured at 20 °C.

Partition Coefficients (log *P*): Partition coefficients were determined by using the "shake-flask" method.⁴²³ The appropriate ruthenium complex was dissolved in 1 mL of water (pre-saturated with 1-octanol) and the concentration was determined by UV-vis absorption spectroscopy. An equivalent volume of 1-octanol (pre-saturated with water) was added and

both phases were shaken for 1 h. The mixture was centrifuge for 1 h at 3000 rpm in order to separate the phases and then equilibrated for a further 16 h. The concentration of the complex in the aqueous phase was determined by UV-vis absorption spectroscopy. The $\log P$ values were calculated according to equation (7.1):

$$\log P = \log \left(\frac{c_t - c_{water}}{c_{water}} \right) \quad (7.1)$$

Where c_t is the total concentration of complex in the aqueous phase before adding 1-octanol and c_{water} is the concentration of complex in the aqueous phase after adding 1-octanol and shaking.

High-performance Liquid Chromatography (HPLC): Monitoring of photoreactions and purification of photoadducts were performed on a Varian 920-LC analytical high-performance liquid chromatograph provided with a quaternary gradient solvent delivery system, autosampler, UV-vis detector (deuterium and quartz halogen as the light source for UV and visible, respectively) and column heater. Phenomenex C18 columns were used (Jupiter[®] 5 μm C18 300 \AA , LC Column 250 \times 4.6/10.0 mm for analytical and semi-preparative HPLC, respectively). The system was controlled by Varian Galaxie[™] Chromatography Software.

7.2 Photophysical and Photochemical Characterisation

UV-vis Absorption Spectroscopy: UV-vis absorption spectra were recorded in an optical path 0.5 or 1 cm quartz cuvette (0.5 and 3 mL, respectively) on a Varian CARY 50 spectrophotometer with a wavelength range of 200–900 nm and a scan rate of 600 nm min^{-1} . Baseline correction measurements were used for all spectra.

Molar Absorption Coefficients: Molar absorption coefficients were determined by measuring the absorption spectra of the corresponding ruthenium complex at different concentrations. The appropriate absorption maxima (typically $\pi\text{-}\pi^*$ IL and MLCT transitions) were plotted versus concentration of complex and absorption coefficients were calculated from the slope of the best linear regression according to the Bouguer-Lambert-Beer law (equation (7.2)):

$$A(\lambda) = \log \frac{I_0}{I} = \varepsilon(\lambda) \times c \times l \quad (7.2)$$

Where A is the absorbance, I_0 is the intensity of light passing through the reference cell, I is the intensity of light passing through the sample cell, ε is the molar absorption coefficient ($\text{M}^{-1} \text{cm}^{-1}$), c is the concentration (M) and l is the path length (cm).

Luminescence Spectroscopy: Luminescence measurements were performed in an optical path 0.5 or 1 cm quartz cuvette (0.5 and 3 mL, respectively) on a Varian Carey Eclipse Fluorimeter. Emission and excitation spectra were obtained with 10 nm excitation and 10 nm emission slit widths.

Luminescence Quantum Yields: Luminescence quantum yields were calculated from the average of three measurements relative to the reference value of $[\text{Ru}(\text{bpy})_3]\text{Cl}_2$ (0.028 in air-saturated aqueous solution)³⁰⁸ with the same absorbance at the wavelength of excitation (436 nm) of both samples based on the equation (7.3):

$$\Phi_{em}^i = \frac{F^i A^{ref} \eta_i^2}{F^{ref} A^i \eta_{ref}^2} \times \Phi_{em}^{ref} \quad (7.3)$$

Where i and ref refer to the sample and reference, respectively, Φ_{em} is the quantum yield of emission, F is the integrated intensities of the luminescence spectra, A is the absorbance at the wavelength of excitation for luminescence measurements and η is the refractive index of the solvent.

Time-resolved Luminescence: Luminescence lifetimes were measured by single-photon timing (SPT) either on a Horiba Fluoromax-4TC-SPC (UCM Optical Chemosensors & Applied Photochemistry Group) or a Fluorolog FL 3-22 equipped with a FluoroHub v2.0 single-photon timing module using a sub-ns 405 nm pulsed diode laser (Horiba N-405L) or a 458 nm pulsed nanosecond light-emitting diode (Horiba N-460) as excitation source, respectively. The emission lifetimes were the average values obtained from a minimum of three replicate decay measurements with 10,000 counts at the peak channel. The decays were analysed using the Horiba DAS6 software, and the data were fitted to a sum of the minimum number of exponentials (n , equation (7.4)), employing a proprietary grid-search error minimization algorithm,

$$I_{em}(t) = \sum_{i=1}^n a_i \exp\left(-\frac{t}{\tau_i}\right) \quad (7.4)$$

Where $I_{em}(t)$ is the luminescence intensity at time t , a_i is the i^{th} pre-exponential factor and τ_i is the i^{th} emission lifetime.

For multi-exponential decays, the contribution of each component to the initial emission intensity (% A_i) was calculated according to equation (7.5):

$$\%A_i = \left[\frac{a_i}{\sum_{i=1}^n a_i} \right] \times 100 \quad (7.5)$$

The pre-exponential weighted mean lifetime, τ_M is given by equation (4.2):³²⁹

$$\tau_M = \sum_{i=1}^n \frac{a_i}{\sum_{i=1}^n a_i} \tau_i \quad (4.2)$$

The goodness-of-the-fit was assessed by the chi-squared value (always better than 1.1) as well as the symmetric distribution of the weighted residuals about the zero axis.

Luminescence lifetimes of surfactant complexes at different concentrations were measured at the UCM Optical Chemosensors & Applied Photochemistry Group (GSOLFA) of Universidad Complutense de Madrid (UCM) by SPT on an Edinburgh Instruments (UK) FLS980-xD2-T photoluminescence spectrometer equipped with the 405 nm laser diode source mentioned above and a 1200 grooves mm^{-1} 500 nm-blazed double monochromator in the emission channel. A 405 nm narrow bandpass interference filter was used to polish the laser diode violet emission. Luminescence from the dye solutions was detected at the wavelength of the emission maximum of each Ru(II) complex with a red-sensitive photomultiplier tube (Hamamatsu R928P), thermoelectrically cooled at -21 °C. The emission lifetimes were extracted from the exponential raw decay data (1024 channels) by using the manufacturer FAST Advanced Analysis software package based on proprietary data processing algorithms for multi-exponential decay analysis.

Singlet Oxygen ($^1\text{O}_2$) Luminescence Measurements: Quantum yields of singlet oxygen production were measured at the UCM Optical Chemosensors & Applied Photochemistry Group (GSOLFA) of Universidad Complutense de Madrid (UCM) using an Edinburgh Instruments (UK) LP-900 laser kinetic spectrometer system equipped with a frequency-doubled Nd:YAG laser (Minilite II, Continuum, CA) for excitation at 532 nm, and a Hamamatsu H10330-45 NIR PMT module for the singlet oxygen emission monitoring at 1265 nm (Bentham TM300 monochromator with 600 grooves mm^{-1} NIR grating). The PMT is fitted with a 10 K Ω resistor at the signal output for proper amplification of the signal. A pyroelectric Gentec QE12LP-S-MB energy meter was employed to monitor the energy of

the laser pulse, which was varied from 100 to 1000 $\mu\text{J pulse}^{-1}$ to avoid partial saturation of the $^1\text{O}_2$ emission signal and keep it in the linear region.

Absorbance-matched ($A_{532} \approx 0.40$) solutions of the ruthenium complex and the reference photosensitiser $[\text{Ru}(\text{phen})_3]\text{Cl}_2$ ($\Phi_A = 0.39 \pm 0.03$ in O_2 -saturated D_2O at room temperature)³²⁷ were prepared in D_2O . The solutions were then saturated by sparging with O_2 from a cylinder (Extrapure oxygen 4X, Praxair) for a minimum of 30 min. The NIR emission from the sample was monitored at a 90° angle with respect to the excitation pathway and detected with the NIR PMT after passing through an interference filter centered at 1265 nm (77-nm FWHM, Roithner-laser, AT). Typically, 60 laser shots were averaged for each signal to improve the s/n ratio.

For the samples where the singlet oxygen production was measured in the presence of stDNA (25 eq. base pairs), the native genetic material was dissolved in D_2O and sheared with ultrasounds (SONICS Vibra-cell VCX130, 75% power, 20 min in 30 s intervals on ice) to obtain fragments of *ca.* 200 base pairs. Then it was extensively dialysed against D_2O (Spectra/Por[®] 3 RC dialysis tubing). Due to the poor singlet oxygen production by the sample complexes in the presence of DNA, the slits were opened enough to detect the singlet oxygen emission and a metal mesh optical attenuator (1.52% transmittance at 1265 nm) was used when the reference was measured to avoid saturation of the NIR PMT detector keeping the same slits width as the samples.

The $^1\text{O}_2$ luminescence decay profiles were fitted to a single exponential function after excluding the fast (sub- μs) decay due to the residual Ru(II) sensitiser emission even under O_2 saturation of the solution. The quality of the D_2O solvent used was checked by measuring the $^1\text{O}_2$ luminescence lifetime of the sensitiser solutions (*ca.* 65 μs).^{327,465} After extrapolating the intensities of the $^1\text{O}_2$ signal at zero time within each exponential decay curve, the intercept values were plotted as a function of the laser energy. The slope values (m) obtained from the linear regression plots of the sample and reference sensitiser dyes were used to calculate the quantum yields of singlet oxygen production (Φ_A) for the different Ru(II) complexes in O_2 -saturated D_2O according to equation (2.5):

$$\Phi_{\Delta, \text{D}_2\text{O}, \text{O}_2}^{\text{complex}} = \Phi_{\Delta, \text{D}_2\text{O}, \text{O}_2}^{\text{ref}} \frac{m_{\text{complex}}}{m_{\text{ref}}} \quad (2.5)$$

From the experimental data obtained in D_2O it was possible to calculate the Φ_A values in air-equilibrated H_2O taking into account equations (2.6) and (2.7):³²⁶

$$P_{O_2}^T = \tau k_q [O_2] = 1 - \frac{\tau}{\tau_0} \quad (2.6)$$

$$\Phi_{\Delta} = \Phi_T P_{O_2}^T f_{\Delta}^T \quad (2.7)$$

Where $P_{O_2}^T$ is the proportion of triplet excited states quenched by O_2 , k_q is the O_2 quenching rate constant, τ and τ_0 are the emission lifetimes in the presence and in the absence of O_2 , respectively, Φ_T is the quantum yield of triplet excited-state formation (intersystem crossing), and f_{Δ}^T is the fraction of excited triplet states quenched by O_2 yielding 1O_2 .

Knowing that Φ_T is considered to be equal to 1 for these types of complexes,³²⁶ and assuming that f_{Δ}^T is the same in O_2 -saturated D_2O and air-saturated H_2O , Φ_{Δ} values in air-equilibrated H_2O were calculated according to equation (2.8):

$$\Phi_{\Delta, H_2O, air}^{complex} = \Phi_{\Delta, D_2O, O_2}^{complex} \left(1 - \frac{\tau_{H_2O, air}}{\tau_{H_2O, Ar}} \right) / \left(1 - \frac{\tau_{D_2O, O_2}}{\tau_{D_2O, Ar}} \right) \quad (2.8)$$

Indirect Detection of Singlet Oxygen (1O_2): Quantum yields of singlet oxygen production were also evaluated using the water soluble 1O_2 trap 9,10-anthracenediyl-bis(methylene)dimalonic acid (ABDA).⁴²⁴ Aqueous solutions containing the ruthenium complex photosensitiser ($A_{470} \approx 0.01$) and ABDA (2 μ M, stock solution in 10 mM sodium phosphate-buffered aqueous solution) were irradiated in a 1 \times 1 cm quartz cuvette under continuous stirring using a 470 nm pE-2 fluorescence LED (100% intensity) as the illumination source. The disappearance of the emission band of ABDA at 405 nm ($\lambda_{exc} = 380$ nm) was monitored at different irradiation times. The complex $[Ru(bpy)_3]Cl_2$ ($\Phi_{\Delta} = 0.18$ in air-equilibrated H_2O at room temperature) was used as the reference.⁴²⁵ The emission intensity of ABDA was plotted as a function of the irradiation time and the slope values (m) obtained from the linear regression plots of the sample and reference sensitiser complexes were used to calculate Φ_{Δ} of the different Ru(II) complexes in air-saturated H_2O according to equation (2.5).

Transient Experimental Apparatus and Techniques: ps-TrA and ps-TRIR measurements were performed on the ULTRA apparatus at the Central Laser Facility (STFC Rutherford Appleton Laboratories, Harwell, UK), which is described in detail elsewhere.^{466,467} Briefly, the TRIR spectrometer comprises of a 10 kHz repetition rate titanium sapphire amplifier (Thales), producing 0.8 mJ output with 40 fs pulse duration, at 800 nm. Optical parametric amplifiers (Light Conversion, TOPAS) and second harmonic generation of the 800 nm created the mid-infrared radiation and 373 nm femtosecond pump pulses used in these

experiments. The polarization of the pump pulses at the sample were at the magic angle relative to the probe, with an energy of 1 μJ . The IR probe beam was split to form reference and signal beams which were passed through spectrographs onto MCT array detectors (IR Associates). The 400 nm pump beam was mechanically chopped down to 5 kHz, focused ($\sim 100\ \mu\text{m}$ spot sizes) and overlapped with the probe beam ($\sim 80\ \mu\text{m}$ spot size) in the sample cell. High speed data acquisition systems (Quantum Detectors) allowed 10 kHz acquisition and processing of the probe and reference pulses to generate a pump-on pump-off infrared absorption difference signal. For the ps-TrA measurements, part of the titanium sapphire laser output beam was used to generate a white light continuum (WLC) in a CaF_2 plate. The WLC was dispersed through the grating monochromator and detected using a linear silicon array (Quantum Detectors). In front of the monochromator, a 400 nm notch filter was placed in order to remove scatter from the excitation beam. The polarization of the pump pulses at the sample was at the magic angle relative to the probe, with an energy of 1 μJ and a spot size *ca.* 100–150 μm .

The ns-TRIR experiments were carried out on the LIFETIME apparatus.^{468,469} This uses an 100 kHz dual amplifier ytterbium potassium gadolinium tungstate (Yb:KGW) laser in place of titanium sapphire laser used in ULTRA and also employs two OPAs to generate the probe beams. The pump beam energy at 400 nm was set at 800 nJ. As before, signals from the sample and reference beams were detected on MCT detectors.

Photoadduct samples were prepared in the appropriate potassium phosphate-buffered aqueous solution and dropped (*ca.* 40 μL) in a demountable liquid cell (Harrick Scientific Products Inc., New York) between two 25 mm diameter CaF_2 plates (Crystran Ltd, UK) separated by a PTFE spacer (typically 100 μm). During experiments the samples were raster scanned in the *x* and *y* directions to minimise photo-damage and re-excitation effects. UV-vis absorption spectra of each sample were recorded before and after each experiment to ensure no degradation of the complexes during the course of the measurements.

Data were processed on the in-house Ultraview software provided by the STFC. TrA spectra were calibrated from pixel to wavelength using five band-pass filters, while TRIR spectra were calibrated from pixel to wavenumber using the characteristic polystyrene absorption lines. Single wavelength/wavenumber data were fitted to mono-exponential or bi-exponential growth/decay functions using OriginPro 8.5 software, which uses the Levenberg-Marquardt algorithm.

Photochemical Reactions: Photoreactions were performed in a LightBATH-405 advanced laser photoreactor manufactured by the UCM Optical Chemosensors & Applied Photochemistry Group (GSOLFA) of Universidad Complutense de Madrid (UCM). The device is equipped with eight 405-nm diode lasers as the excitation source, with each having an average radiant power of (33 ± 4) mW, inserted into an aluminium block and powered by a 3 VDC power supply. The solution (25 mL) containing the photoactive compound to be irradiated was placed in the optical glass bottle reactor, tightly closed with a rubber septum, and placed in the tailored pit between the illumination sources. An aluminium lid fitted with a central hole was employed in order to allow argon sparging (to remove the dissolved oxygen) and also for the removal of sample for spectroscopic monitoring of the photochemical reaction progress.

7.3 DNA Binding Studies Techniques

UV-vis Absorption and Emission DNA Titrations: UV-vis absorption and emission titrations were carried out on samples of the dye at $(1 \pm 0.5) \times 10^{-5}$ M at 298 K by monitoring changes in the absorption and emission spectra of the complexes in 10 mM sodium phosphate buffer (pH 7.4) upon successive additions of aliquots of stDNA. The results are quoted using the concentration of stDNA expressed as a nucleotide phosphate to dye ratio (P/D ratio).

Binding constants (K_b) and binding size (n) were determined using equation (2.3) obtained from a reorganisation of the original Bard *et al.* equation.³¹⁰ K_b values represent the mean \pm S.E.M. of three independent experiments.

$$\varepsilon_a = \frac{b - (b^2 - 2K_b^2 C_t [DNA]/n)^{1/2}}{2K_b C_t} \times (\varepsilon_b - \varepsilon_f) + \varepsilon_f \quad (2.3)$$

$$b = 1 + K_b C_t + K_b [DNA]/2n$$

Circular Dichroism (CD) Spectroscopy: CD spectra were recorded on a Jasco J-810-150S CD spectropolarimeter in a quartz cuvette with optical path lengths of 1 cm. A concentration corresponding to an optical density of approximately 1.0 for the DNA absorbance (150 μ M) at 260 nm, in buffered solutions, was used. CD measurements were acquired between 600–200 nm at a data pitch of 1 nm, scanning speed of 200 nm min⁻¹, a response of 1 s, bandwidth of 1 nm, and averaging over three scans. When appropriated, $\Delta\varepsilon$ values were calculated according to equation (7.6):

$$\Delta\varepsilon = \frac{m\theta}{32980 \times c \times l} \quad (7.6)$$

Where $m\theta$ is the ellipticity (mdeg), c is the concentration (M) and l is the path length (cm).

Thermal Denaturation: Thermal denaturation experiments were performed on a thermoelectrically coupled Perkin Elmer LAMBDA 25 UV/Vis Spectrophotometer. Buffered solutions containing 150 μ M concentration of stDNA (optical density of approximately 1.0 for the DNA absorbance at 260 nm) were used. The temperature in the cell was ramped from 30 to 90 °C, at a rate of 1 °C min⁻¹ and the absorbance at 260 nm was measured every 0.2 °C. The melting temperature value was obtained from the maximum of the first derivative of the absorbance (dA/dT).

Viscosity: Viscosity was measured with a Cannon-Manning semimicro viscometer at 298 K. Constant stDNA concentration of 1.2 mM and a total sample volume of 1 mL were used. DNA was sheared with ultrasounds (Jencons Ultrasonic Processor, 100% power, 20 min in 30 s intervals on ice) to obtain fragments of *ca.* 200 base pairs. Ruthenium/nuclear phosphate concentration ratios (D/P) ranging from 0.02 to 0.25 were measured. Viscosity (η) was calculated as sample flow time minus buffer flow time and $(\eta/\eta_0)^{1/3}$ values (where η_0 is the viscosity of stDNA alone) were plotted against D/P.⁴⁷⁰

7.4 General Biological Procedures

Cell Culture: HeLa cells were grown in a cell culture flask using Dulbecco's Modified Eagle Medium supplemented with 10% fetal bovine serum, 1% penicillin/streptomycin and 0.2% plasmocin at 37 °C in a humidified atmosphere of 5% CO₂.

Confocal Microscopy: Confocal microscopy experiments were carried out using HeLa cells seeded at a density of 5×10^4 cells/mL and treated as indicated. Cells were then washed twice with fresh medium and stained blue with Hoechst 33258 (10 μ g/mL) when appropriate before being imaged by live microscopy using either an Olympus FV1000 point scanning microscope with a 60x oil immersion lens with an NA (numerical aperture) of 1.42, or a Leica SP8 gated STED confocal microscope with a 40x oil immersion lens with an NA (numerical aperture) of 1.30. A 405 nm diode laser was used to excite both Hoechst and the appropriate ruthenium complex and emission was measured at 415–505 nm and 610–

715 nm, respectively. The software used to collect images were FluoView Version 7.1 software or Leica Application Suite X (LAS X), respectively.

For the experiments where the intracellular ROS generation was evaluated, HeLa cells were incubated with the appropriate ruthenium complex at 37 °C for 30 min before the ROS indicator 2,7-dichlorofluorescein diacetate (DCFH-DA) was added. After a further 30 min incubation, cells were washed twice with fresh medium and irradiated using a 405 nm diode laser (1.6% intensity) attached to a Leica SP8 scanning confocal microscope. Images were taken every 1.3 s over a 3 min period time. A 498 nm white light laser (4.5% intensity) was used to excite the DCFH-DA and emission was measured at 510–570 nm.

Viability Assays: Viability assays were undertaken by seeding of 2.5×10^3 cells/mL in a 96-well plate and treated as indicated. Each well was then treated with 20 μ L of Alamar Blue (BioSource) and left to incubate at 37 °C in the dark for 4 h. Fluorescence was read using a fluorescence microplate reader (SpectraMax Gemini XS, Molecular Devices) at 590 nm (excitation at 544 nm). The data were analysed using the SoftMax® Pro Software. The background fluorescence of the media without cells plus Alamar Blue was taken away from each group, and the control untreated cells represented 100% cell viability. Data points represent the mean \pm S.E.M. of triplicate treatments performed on three independent days with activity expressed as percentage cell viability compared to vehicle treated controls. For photoactivation studies, cells were subjected to 18 J cm⁻² using a Hamamatsu L2570 200 W HgXe arc lamp equipped with a NaNO₂ filter.

7.5 Materials

Chemicals and Solvents: All chemicals were obtained from Sigma-Aldrich, TCI, Alfa Aesar or Fluorochem and, unless specified, were used without further purification. Chromatographic columns were run using Aluminium oxide neutral (Brockmann I) 60 Å (50–200 μ m). Analytical thin layer chromatography (TLC) was performed using Merck Kieselgel 60 F254 silica gel or aluminium oxide neutral plates. 1,10-Phenanthroline-5,6-dione (**72**) and 4-(3-aminophenyl)-2,2'-bipyridine (**94**) were synthesised by Dr Bjørn la Cour Poulsen and PhD student Hannah Dalton, respectively. The salmon testes DNA was obtained from Sigma Aldrich as their sodium salts and were stored at -20 °C. Deuterated solvents for NMR use were purchased from Apollo Ltd. Solvents for synthetic purposes were used at general purpose reagent (GPR) grade unless otherwise stated. Dry solvents were obtained from a solvent purification system (SPS) purchased from Innovative Technology Incorporated.

Phosphate Buffered Solutions: Phosphate buffered solutions were prepared from dilution of the appropriate amount of sodium or potassium monobasic (XH_2PO_4 , X = Na or K) and dibasic (X_2HPO_4 , X = Na or K) in millipore water (sodium buffer) or D_2O (deuterated potassium buffer). The pH of the sodium phosphate-buffered aqueous solution was adjusted to 7.4 by addition of NaOH using a pH-meter. Deuterated potassium phosphate-buffered solutions used in Chapter 3 were prepared according to Table 7.1:

Table 7.1. Buffer composition of the potassium phosphate-buffered D_2O solutions used in Chapter 3 and their corresponding experimental pH and calculated pD values.

Terms used in this thesis	Buffer composition $\text{KH}_2\text{PO}_4/\text{K}_2\text{PO}_4$	pH ^[a]	pD ^[b]
“pH 5”	10:0	4.50	4.90
“pH 6”	10:1	5.90	6.30
“pH 7”	10:10	6.87	7.27
“pH 8”	1:10	7.84	8.24

^[a] Values measured by Dr Frederico Baptista using a pH-meter.

^[b] Values calculated according to equation (7.7): $\text{pD} = \text{pH} + 0.40$ (7.7).⁴⁷¹

DNA Solutions: Solutions of DNA were prepared by shaking stDNA (about 20 mg) in 10 mM sodium phosphate-buffered aqueous solution (pH 7.4, 10 mL). The stDNA solution was then stored at 4 °C for 16 h and passed through a syringe filter (0.45 μm pore size, hydrophilic polyethersulfone membrane, PALL Acrodisc®). Solutions of stDNA gave a ratio of UV absorbance at 260 and 280 nm of 1.86:1, indicating that the DNA was sufficiently free of protein. The concentration of the stDNA solution was determined spectrophotometrically using the molar absorptivity value of $6600 \text{ M}^{-1} \text{ cm}^{-1}$ (nucleotide) at 260 nm.

7.6 General Synthetic Procedures

7.6.1 Procedure 1: Synthesis of Polypyridyl Alkylamide Ligands

The appropriate amine (5-amino-1,10-phenanthroline (**88**) or 4-(3-aminophenyl)-2,2'-bipyridine (**94**), 1 eq.) was dissolved in dry CH_2Cl_2 (10 mL) before the solution was cooled to 0 °C. The required carboxylic acid (undecanoic acid or heneicosanoic acid, 1 eq., or 11,11'-disulfanediyldiundecanoic acid, 0.5 eq.) was added to the solution followed by *N*-ethyl-*N'*-(3-dimethylaminopropyl)carbodiimide hydrochloride (EDC, 2.5 eq.) and, finally, 4-dimethylaminopyridine (DMAP, 1 eq.). The resulting mixture was stirred under inert atmosphere and at 0 °C for 1 h before being allowed to reach room temperature and stirred

for a further 2 days. Solvent was removed under reduced pressure and the resulting orange oil was dried *in vacuo*. H₂O was added causing precipitation of a beige solid which was isolated by centrifugation and washed several times with more H₂O. The resulting solid was redispersed in MeCN, again collected by centrifugation and dried *in vacuo*.

7.6.2 Procedure 2: Synthesis of [Ru(L)₂Cl₂] Complexes⁴⁷²

Ruthenium(III) chloride hydrate (1 eq.) and 1,5-cyclooctadiene (20 eq.) were mixed in ethanol (200 mL). The solution was degassed with argon for 15 min and refluxed for 3 days followed by cooling to room temperature. The brown precipitate was isolated by filtration, washed with ethanol and dried *in vacuo*. The appropriate polypyridyl ligand (**phen** or **TAP**, 2 eq.) and [Ru(η⁴-COD)Cl₂]_n (1 eq.) were suspended in DMF (20 mL). The mixture was degassed with argon for 15 min and the synthesis was carried out at 140 °C for 40 min under microwave irradiation. After the reaction, acetone (20 mL) was added to the reaction mixture and the resulting suspension was cooled to -15 °C for 2 days. The suspension was then centrifuged to yield a dark purple solid which was washed several times with acetone, H₂O and Et₂O and dried *in vacuo*.

7.6.3 Procedure 3: Synthesis of [Ru(L)₂(L')]²⁺ Complexes

The appropriate *cis*-[Ru(L)₂Cl₂] complex (1 eq.) and the required third ligand (L' = dipyrido[3,2-*a*:2'.3'-*c*][1,2,5]thiadiazolo[3,4-*h*]phenazine (**dtp**), 5-acetamido-1,10-phenanthroline (**84**), *N*-1,10-phenanthroline-5-ylundecanamide (**85**) or *N*-1,10-phenanthroline-5-ylhenicosamide (**86**), 1 eq., or 11,11'-disulfanediybis(*N*-(3-([2,2'-bipyridin]-4-yl)phenyl)undecanamide) (**89**), 0.5 eq.) were suspended in a EtOH/H₂O mixture (1:1, 8 mL). The mixture was degassed with argon for 15 min and the synthesis was carried out at 140 °C for 40 min (L = **phen**) or 10 min (L = **TAP**) under microwave irradiation. Solvent was evaporated at reduced pressure and the resulting solid was purified by alumina chromatography using MeCN/H₂O (10:0 to 9:1) as eluent, yielding a red solid which was dried *in vacuo*.

7.6.4 Procedure 4: Synthesis of Ru(II) Stabilised AuNPs^{264,451,455}

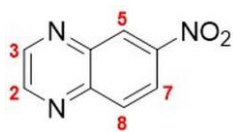
HAuCl₄·3H₂O (0.10 g, 0.25 mmol, 1 eq.) was dissolved in H₂O (10 mL) before TOAB (0.36 g, 0.64 mmol, 2.6 eq.) in toluene (25 mL) was added. The resulting mixture was stirred vigorously at room temperature for 10 min and NaBH₄ (0.12 g, 3.17 mmol, 12.7 eq.) dissolved in H₂O (10 mL) was added drop-wise. The reaction mixture was stirred for a further 2 h. Following successful transfer of the Au(0) into the toluene layer, the organic and

aqueous layers were separated and the toluene layer was washed with H₂O (2 × 20 mL), 0.1 M HCl (2 × 20 mL) and 0.1 NaOH (2 × 20 mL). The TOAB-stabilised AuNPs (5 mL) were added to the appropriate [Ru(L)₄(L')]²⁺ complex (0.5 eq.) in H₂O (5 mL) and the resulting mixture was stirred at room temperature for 16 h. Following successful transfer of the AuNPs into the aqueous layer, the organic and the aqueous layer were separated, and the aqueous layer was subsequently filtered through a PDVF 0.45 μm microsyringe to give a dark brown solution. Any unbound Ru(II) complex was then removed by addition of a saturated aqueous solution of NH₄PF₆ (3 mL) affording flocculation of a dark solid which was collected by centrifugation and washed with a mixture of H₂O/MeOH (3:1, 3 × 5 mL). The solid was redissolved in MeCN (1 mL) and repeatedly precipitated by adding Et₂O. The resulting solid was redispersed in MeCN (1 mL) before addition of an acetone concentrated solution of TBACl (3 mL) resulting in the formation of a dark brown flocculate which was collected by centrifugation, washed with acetone (3 × 5 mL) and dried under high vacuum.

7.7 Synthesis and Characterisation of Compounds Described in Chapter 2

7.7.1 Synthesis and Characterisation of Ligands TAP and dtp

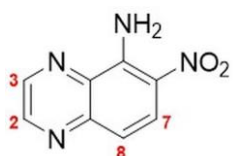
6-Nitroquinoxaline (66)³⁰³



4-Nitro-1,2-benzenediamine (11.5 g, 75.4 mmol, 1 eq.) was dissolved in hot EtOH (100 mL). To this solution, an aqueous solution of glyoxal 40% (16 mL, 140 mmol, 1.8 eq.) was added drop-wise and the resulting

mixture was refluxed and stirred for 16 h. The reaction mixture was cooled to room temperature after which a grey solid precipitated out of solution. The precipitate was filtered and washed with cold MeOH, yielding a grey solid which was dried *in vacuo* (10.4 g, 59.4 mmol, 79%). δ_H (400 MHz, CD₃CN): 9.04 (2H, m, H₃ and H₂), 8.95 (1H, d, H₅, ⁴J = 2.5 Hz), 8.54 (1H, dd, H₇, ³J = 9.2 Hz, ⁴J = 2.5 Hz), 8.29 (1H, d, H₈, ³J = 9.2 Hz).

5-Amino-6-nitroquinoxaline (67)³⁰³

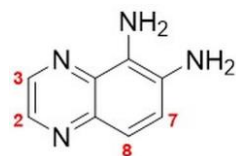


Metallic sodium (4.50 g, 196 mmol, 3.3 eq.) was gently added to MeOH (250 mL). A solution of hydroxylamine hydrochloride (6.16 g, 88.7 mmol, 1.5 eq.) in MeOH (100 mL) was added to this sodium

methanolate solution. The precipitate formed was filtered and the resulting filtrate was added drop-wise to a boiling solution of 6-nitroquinoxaline (10.3 g, 58.7, 1 eq.) in MeOH (500 mL). The dark reaction mixture was refluxed and stirred for 16 h. The mixture was then cooled in the freezer for 2 days and filtered yielding an orange solid which was washed with

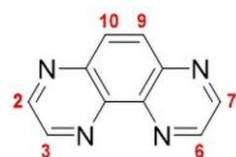
cold MeOH and dried *in vacuo* (5.22 g, 27.5 mmol, 47%). δ_{H} (400 MHz, DMSO- d_6): 9.09 (1H, d, H₃ or H₂, $^3J = 1.9$ Hz), 8.93 (1H, d, H₃ or H₂, $^3J = 1.9$ Hz), 8.50 (2H, s, NH₂), 8.28 (1H, d, H₇, $^3J = 9.7$ Hz), 7.17 (1H, d, H₈, $^3J = 9.7$ Hz).

5,6-Diaminoquinoxaline (68)³⁰³



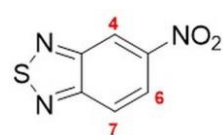
5-Amino-6-nitroquinoxaline (6.24 g, 32.8 mmol, 1 eq.) and 10% Pd/C (1.1 g) were mixed in EtOH (125 mL) and the resulting suspension was refluxed for 1 h. Hydrazine monohydrate 98% (8 mL, 168 mmol, 5.1 eq.) was added drop-wise. The reaction mixture was refluxed and stirred for a further 1 h, after which it was filtered hot through a pad of celite and washed with CH₂Cl₂. Solvent was removed under reduced pressure and the resulting red solid was dried *in vacuo* (4.69 g, 29.3 mmol, 89%). δ_{H} (400 MHz, CD₃CN): 8.58 (1H, d, H₂ or H₃, $^3J = 1.8$ Hz), 8.53 (1H, d, H₂ or H₃, $^3J = 1.8$ Hz), 7.31 (2H, AB q, H₇ and H₈, $^3J = 8.9$ Hz), 4.53 (2H, s, NH₂), 4.29 (2H, s, NH₂).

1,4,5,8-Tetraazaphenanthrene (TAP)³⁰³



5,6-Diaminoquinoxaline (3.99 g, 24.9 mmol, 1 eq.) was dissolved in hot EtOH (40 mL). An aqueous solution of glyoxal 40% (5.7 mL, 49.9 mmol, 2 eq.) was added drop-wise and the resulting mixture was stirred and refluxed for 2 h. After cooling, the reaction mixture was filtered and the resulting brown solid was washed with cold EtOH and dried *in vacuo*. The solid was suspended in CH₂Cl₂, filtered through silica and washed with a mixture CH₂Cl₂/acetone (8:2). Solvent was removed at reduced pressure and the resulting solid was recrystallised from EtOH yielding the product 1,4,5,8-tetraazaphenanthrene as beige needles which were dried *in vacuo* (1.86 g, 10.2 mmol, 41%). m.p. 251–253 °C. Lit. m.p. 249–252 °C.⁴⁷³ δ_{H} (400 MHz, DMSO- d_6): 9.22 (2H, d, H₃ and H₆, $^3J = 1.9$ Hz), 9.19 (2H, d, H₂ and H₇, $^3J = 1.9$ Hz), 8.34 (2H, s, H₉ and H₁₀). δ_{C} (101 MHz, DMSO- d_6): 146.86, 145.64, 143.45 (q), 140.19 (q), 131.50. ν_{max} (ATR)/cm⁻¹: 3018 (aromatic C-H stretch), 1492 (aromatic C=C stretch), 1382 (C-N stretch). ESI⁺-HRMS: m/z calc = 183.0671 for C₁₀H₇N₄; m/z found = 183.0681 [M+H]⁺.

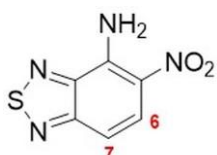
5-Nitro-2,1,3-benzothiadiazole (69)²⁹⁸



A solution of 4-nitro-1,2-benzenediamine (5.00 g, 32.7 mmol, 1 eq.) and triethylamine (7.70 mL, 55.2 mmol, 1.7 eq.) in DMF (50 mL) was cooled to 0 °C. Thionyl chloride (5.7 mL, 78.6 mmol, 2.4 eq.) was added drop-wise and the reaction mixture was stirred at 0 °C for 2 h. The mixture was quenched with

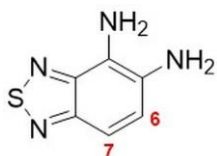
H₂O and extracted with CH₂Cl₂. The organic layer was washed with a saturated solution of NaHCO₃, H₂O and brine and dried with MgSO₄. Solvent was removed at reduced pressure. The obtained solid was purified by silica chromatography using CH₂Cl₂/hexane (1:1) as eluent yielding a yellow solid which was dried *in vacuo* (3.03 g, 16.7 mmol, 51%). δ_{H} (400 MHz, CDCl₃): 8.99 (1H, s, H₄), 8.44 (1H, d, H₆, $^3J = 9.5$ Hz), 8.17 (1H, d, H₇, $^3J = 9.5$ Hz).

4-Amino-5-nitro-2,1,3-benzothiadiazole (70)²⁹⁸



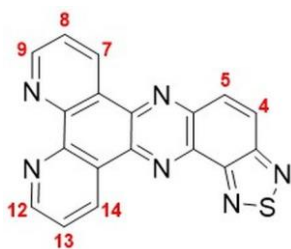
A suspension of 5-nitro-2,1,3-benzothiadiazole (1.01 g, 5.58 mmol, 1 eq.) and hydroxylammonium chloride (1.01 g, 14.6 mmol, 2.6 eq.) in EtOH (50 mL) was cooled to 0 °C. A saturated ethanolic solution of KOH (10 mL) was added drop-wise to the cold mixture. The reaction mixture was stirred for 2 h and then quenched with 36% HCl. The resulting yellow precipitate was filtered, washed with EtOH and used directly in the next reaction. δ_{H} (400 MHz, CDCl₃): 13.60 (2H, s, NH₂), 12.95 (1H, d, H₆, $^3J = 9.9$ Hz), 11.92 (1H, d, H₇, $^3J = 9.9$ Hz).

4,5-Diamine-2,1,3-benzothiadiazole (71)²⁹⁸



To a boiling mixture of 4-amino-5-nitro-2,1,3-benzothiadiazole in H₂O (50 mL), Na₂S₂O₄ (5.24 g, 30.1 mmol) was added slowly. The reaction mixture was stirred for 20 min and then filtered while hot. The filtrate was cooled to room temperature and allowed to stand for 16 h and the resulting red precipitate was washed with cold H₂O and dried *in vacuo* (659 mg, 3.97 mmol, 71%). δ_{H} (400 MHz, DMSO-*d*₆): 7.25 (1H, d, H₆, $^3J = 9.1$ Hz), 7.17 (1H, d, H₇, $^3J = 9.1$ Hz), 5.09 (2H, s, NH₂), 4.93 (2H, s, NH₂).

Dipyrido[3,2-*a*:2',3'-*c*][1,2,5]thiadiazolo[3,4-*h*]phenazine (dtp)²⁹⁸

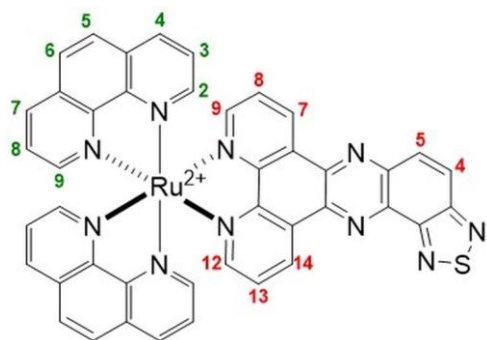


4,5-Diamine-2,1,3-benzothiadiazole (121 mg, 729 μmol , 1 eq.) and 1,10-phenanthroline-5,6-dione (156 mg, 741 μmol , 1 eq.) were suspended in a mixture of EtOH/H₂O (1:1, 20 mL). The mixture was heated in a high-pressure tube at 140 °C and stirred for 16 h followed by cooling to room temperature. The resulting yellow precipitate was filtered, washed with H₂O, EtOH and Et₂O, and dried *in vacuo* (200 mg, 588 μmol , 81%). m.p. > 260 °C. δ_{H} (400 MHz, CDCl₃): 9.87 (1H, dd, H₉ or H₁₂, $^3J = 8.1$ Hz, $^4J = 1.8$ Hz), 9.70 (1H, dd, H₉ or H₁₂, $^3J = 8.1$ Hz, $^4J = 1.8$ Hz), 9.35 (2H, m, H₇ and H₁₄), 8.33 (2H, AB q, H₄ and H₅, $^3J = 9.6$ Hz), 7.88 (1H, dd, H₈ or H₁₃, $^3J = 4.4$ Hz, $^3J = 8.1$ Hz), 7.86 (1H, dd, H₈ or H₁₃, $^3J = 4.4$ Hz, $^3J = 8.1$ Hz). δ_{C} (101 MHz, CDCl₃): 156.21 (q), 152.96 (q),

152.89, 152.81, 144.98 (q), 141.26 (q), 140.16 (q), 137.94 (q), 135.08, 134.63, 132.19, 127.37 (q), 127.32 (q), 125.30, 124.74. ν_{\max} (ATR)/ cm^{-1} : 2980 (aromatic C-H stretch), 1492 (aromatic C=C stretch), 1366 (C-N stretch). ESI⁺-HRMS: $m/z_{\text{calc}} = 341.0609$ for $\text{C}_{18}\text{H}_9\text{N}_6\text{S}$; $m/z_{\text{found}} = 341.0610$ [M+H]⁺.

7.7.2 Synthesis and Characterisation of Complexes **63** and **64**

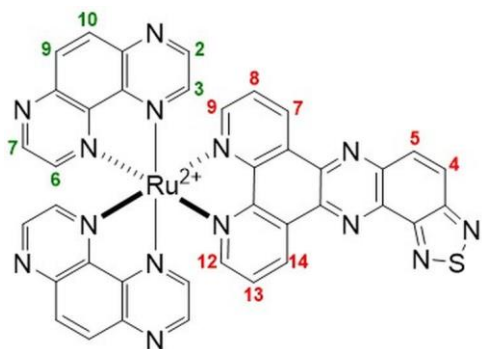
Bis(1,10-phenanthroline)(dipyrido[3,2-*a*:2',3'-*c*][1,2,5]thiadiazolo[3,4-*h*]phenazine) ruthenium(II) chloride (**63**)



Complex **63** was synthesised according to **Procedure 3** using dipyrido[3,2-*a*:2',3'-*c*][1,2,5]thiadiazolo[3,4-*h*]phenazine (69.4 mg, 204 μmol , 1.1 eq.) and $[\text{Ru}(\text{phen})_2\text{Cl}_2]$ (99.4 mg, 187 μmol , 1 eq.), yielding the product as a red solid (134 mg, 154 μmol , 82%). Calculated for $\text{C}_{42}\text{H}_{24}\text{N}_{10}\text{Cl}_2\text{SRu} + 3.5\text{H}_2\text{O}$: C, 53.91; H, 3.34; N, 14.97; S, 3.42; Cl, 7.57. Found: C, 52.40; H, 3.01; N, 14.29; S, 3.94; Cl, 8.03. m.p. > 250 °C. δ_{H} (600 MHz, CD_3CN): 9.73 (1H, dd, H_9^{dtp} or $\text{H}_{12}^{\text{dtp}}$, $^3J = 8.2$ Hz, $^4J = 1.3$ Hz), 9.68 (1H, dd, H_9^{dtp} or $\text{H}_{12}^{\text{dtp}}$, $^3J = 8.2$ Hz, $^4J = 1.3$ Hz), 8.64 (4H, m, H^{phen}), 8.45 (2H, AB q, H_4^{dtp} and H_5^{dtp} , $^3J = 9.6$ Hz), 8.29 (4H, s, H_5^{phen} and H_6^{phen}), 8.23 (2H, 2dd, H^{phen} , $^3J = 5.3$ Hz, $^4J = 1.2$ Hz), 8.18 (2H, 2dd, H_7^{dtp} and $\text{H}_{14}^{\text{dtp}}$, $^3J = 5.3$ Hz, $^4J = 1.3$ Hz), 8.01 (2H, dt, H^{phen} , $^3J = 5.2$ Hz, $^4J = 1.2$ Hz), 7.83 (2H, 2dd, H_8^{dtp} and $\text{H}_{13}^{\text{dtp}}$, $^3J = 8.2$ Hz, $^3J = 5.3$ Hz), 7.66 (4H, m, H^{phen}). δ_{C} (151 MHz, CD_3CN): 157.59 (q), 155.66, 155.58, 154.29, 154.28, 153.98, 153.69 (q), 151.60 (q), 151.55 (q), 148.86 (q), 148.81 (q), 146.76 (q), 141.20 (q), 140.07 (q), 139.67 (q), 137.98, 137.94, 134.55, 132.64, 132.07 (q), 132.05 (q), 131.25 (q), 131.12 (q), 129.07, 128.26, 128.22, 127.58, 126.92, 126.87. ν_{\max} (ATR)/ cm^{-1} : 3047 (aromatic C-H stretch), 1359 (C-N stretch). MALDI⁺-HRMS: $m/z_{\text{calc}} = 802.0950$ for $\text{C}_{42}\text{H}_{24}\text{N}_{10}\text{SRu}$; $m/z_{\text{found}} = 802.0945$ [M]⁺.

Bis(1,4,5,8-tetraazaphenanthrene)(dipyrido[3,2-*a*:2',3'-*c*][1,2,5]thiadiazolo[3,4-*h*]phenazine)ruthenium(II) chloride (**64**)

Complex **64** was synthesised according to **Procedure 3** using dipyrido[3,2-*a*:2',3'-*c*][1,2,5]thiadiazolo[3,4-*h*]phenazine (892 mg, 262 μmol , 1 eq.) and $[\text{Ru}(\text{TAP})_2\text{Cl}_2]$ (140 mg, 262 μmol , 1 eq.), yielding the product as a red solid (100 mg, 114 μmol , 44%). Calculated for $\text{C}_{38}\text{H}_{20}\text{N}_{14}\text{Cl}_2\text{SRu} + 0.5\text{NaCl}$: C, 47.88; H, 2.33; N, 20.57; S, 3.36. Found: C, 46.73; H, 2.09; N, 19.69; S, 6.10. m.p. 162–165 °C (decomp.). δ_{H} (600 MHz, CD_3CN): 9.83

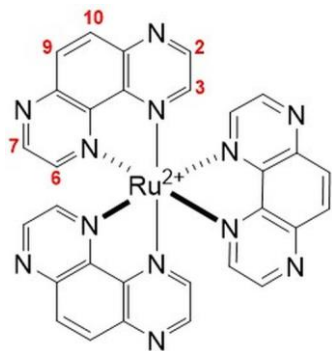


(1H, dd, H₉^{dtp} or H₁₂^{dtp}, ³J = 8.2 Hz, ⁴J = 1.2 Hz), 9.77 (1H, dd, H₉^{dtp} or H₁₂^{dtp}, ³J = 8.2 Hz, ⁴J = 1.2 Hz), 9.01 (2H, 2d, H^{TAP}, ³J = 2.7 Hz), 8.99 (2H, d, H₂^{TAP} or H₇^{TAP}, ³J = 2.7 Hz), 8.62 (4H, s, H₉^{TAP} and H₁₀^{TAP}), 8.46 (2H, AB q, H₄^{dtp} and H₅^{dtp}, ³J = 9.6 Hz), 8.40 (2H, d, H₃^{TAP} or H₆^{TAP}, ³J = 2.7 Hz), 8.39 (2H, 2d, H^{TAP}, ³J = 2.7 Hz), 8.34 (2H, 2dd, H₇^{dtp} and H₁₄^{dtp}, ³J = 5.4 Hz, ⁴J = 1.2 Hz), 7.92 (2H, 2dd, H₈^{dtp} and H₁₃^{dtp}, ³J = 8.2 Hz, ³J = 5.4 Hz). δ_C (151 MHz, CD₃CN): 157.62 (q), 156.74, 156.66, 153.67 (q), 150.73 (q), 150.68 (q), 150.58, 150.57, 150.45, 150.44, 150.07, 146.93 (q), 146.51 (q), 146.50 (q), 146.45 (q), 143.31 (q), 143.30 (q), 143.22 (q), 140.88 (q), 139.83 (q), 139.75 (q), 135.98, 133.81, 133.73, 132.64, 131.44 (q), 131.32 (q), 128.63, 128.59, 127.74. ν_{max} (ATR)/cm⁻¹: 3057 (aromatic C-H stretch), 1486 (aromatic C=C stretch), 1383 (C-N stretch). ESI⁺-HRMS: m/z_{calc} = 806.0760 for C₃₈H₂₀N₁₄SRu; m/z_{found} = 403.0387 [M]²⁺.

7.8 Synthesis and Characterisation of Compounds Described in Chapter 3

7.8.1 Synthesis and Characterisation of Complex 38

Tris(1,4,5,8-tetraazaphenanthrene)ruthenium(II) chloride (38)

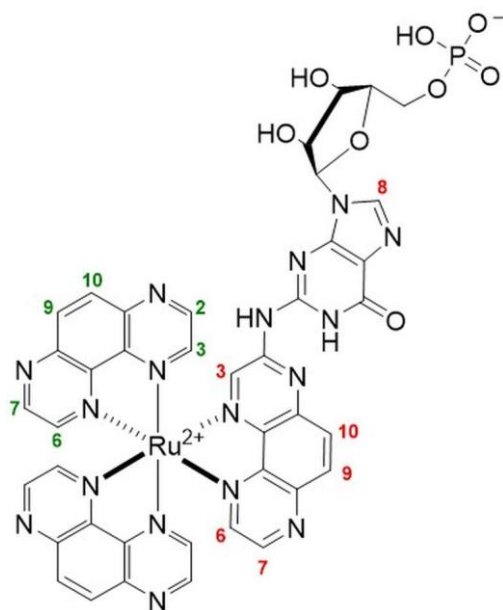


Complex **38** was synthesised according to **Procedure 3** using 1,4,5,8-tetraazaphenanthrene (28.2 mg, 155 μmol, 1.6 eq.) and [Ru(TAP)₂Cl₂] (50.9 mg, 94.9 μmol, 1 eq.), yielding the product as a red solid (33.4 mg, 46.5 μmol, 49%). δ_H (400 MHz, D₂O): 9.09 (2H, d, H₂ and H₇, ³J = 2.8 Hz), 8.72 (2H, s, H₉ and H₁₀), 8.43 (2H, d, H₃ and H₆, ³J = 2.8 Hz). δ_C (101 MHz, D₂O): 149.22, 148.60, 145.20 (q), 141.98 (q), 132.78. ν_{max} (ATR)/cm⁻¹: 3041 (aromatic C-H stretch), 1485 (aromatic C=C stretch), 1384 (C-N stretch). ESI⁺-HRMS: m/z_{calc} = 648.0821 for C₃₀H₁₈N₁₂Ru; m/z_{found} = 324.0419 [M]²⁺.

7.8.2 Photosynthesis of the Photoadduct 43²¹³

Bis(1,4,5,8-tetraazaphenanthrene)((2*S*,3*R*,4*S*,5*S*)-5-(2-(benzo[*f*]quinoxalin-3-ylamino)-6-oxo-1,6-dihydro-9*H*-purin-9-yl)-3,4-dihydroxytetrahydrofuran-2-yl)methyl dihydrogen phosphate)ruthenium(II) chloride (43)

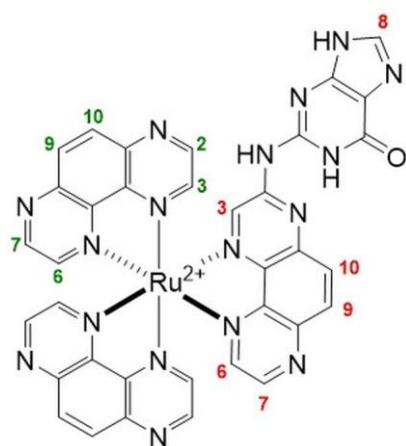
A 25 mL aqueous solution containing **38** (100 μM) and guanosine 5'-monophosphate (3 mM) was prepared and the pH was adjusted to 5 by addition of 0.1 M HCl. The solution was added into an optical glass bottle, closed with a rubber septum and placed in a LightBATH-405



photoreactor. Before irradiation, the solution was purged with Argon for 30 min. The solution was then stirred and irradiated for 8 h. The photoreaction was monitored every hour by UV-vis absorption, emission spectroscopy and HPLC. The reaction was repeated at least five times in order to have enough material. After irradiation, the solvent was removed under reduced pressure and the resulting orange solid was purified by analytical or semi-preparative HPLC using a Jupiter[®] 5 μm C18 300 Å, LC Column 250 \times 4.6/10.0 mm (Phenomenex) with a 1/4 mL/min

flow, respectively, and a gradient elution: 85% H₂O, 10% MeCN and 5% TFA(2%) for 5 min, from 85% H₂O, 10% MeCN and 5% TFA(2%) to 0% H₂O, 95% MeCN and 5% TFA(2%) for 20 min, and 0% H₂O, 95% MeCN and 5% TFA(2%) for 6 min. The solvent of the fraction corresponding to the desired complex was removed under reduced pressure yielding a red solid which was dried *in vacuo*. MALDI⁺-HRMS: m/z calc = 1009.1244 for C₄₀H₃₀N₁₇O₈PRu; m/z found = 1009.1289 [M]⁺.

7.8.3 Acid Hydrolysis of the Ribose-Phosphate Moiety in the Photoadduct **43**²²³ Bis(1,4,5,8-tetraazaphenanthrene)(2-(pyrazino[2,3-f]quinoxalin-3-ylamino)-1,9-dihydro-6H-purin-6-one)ruthenium(II) chloride (**77**)



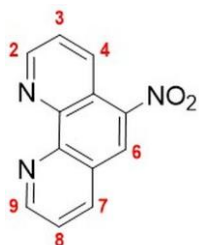
The photoadduct **43** was dissolved in 2 M HCl aqueous solution (5 mL) and heated at 95 °C for 2 h. HCl was removed by vacuum distillation and the resulting orange solid was purified by analytical HPLC using a Jupiter[®] 5 μm C18 300 Å, LC Column 250 \times 4.6 mm (Phenomenex) with a 1 mL/min flow and a gradient elution: 90% H₂O, 5% MeCN and 5% TFA(2%) for 5 min, from 90% H₂O, 5% MeCN and 5% TFA(2%) to 85% H₂O, 10% MeCN and 5% TFA(2%) for 25 min, 85% H₂O, 10% MeCN and 5% TFA(2%) for 5 min, and from 85% H₂O, 10% MeCN and 5% TFA(2%) to 0% H₂O, 95% MeCN and 5% TFA(2%) for 5 min. The solvent of the fraction corresponding to the desired complex was removed under reduced

pressure yielding a yellow solid which was dried *in vacuo*. MALDI⁺-HRMS: m/z calc = 796.1080 for C₃₅H₂₀N₁₇ORu; m/z found = 796.1118 [M-H]⁺.

7.9 Synthesis and Characterisation of Compounds Described in Chapter 4

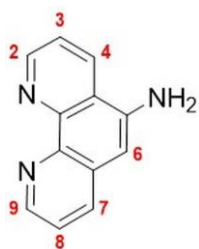
7.9.1 Synthesis and Characterisation of Ligands 84, 85 and 86

5-Nitro-1,10-phenanthroline (87)⁴⁰³



1,10-Phenanthroline (5.02 g, 27.9 mmol) was dissolved in concentrated H₂SO₄ (30 mL). The solution was heated at 160 °C and fuming HNO₃ (15 mL) was added drop-wise. The reaction mixture was stirred at 160 °C for 4 h. The solution was carefully put in an ice bath and neutralized with NaOH. The resulting precipitate was filtered and washed with H₂O yielding a pale-yellow solid which was dried *in vacuo* (4.54 g, 20.2 mmol, 72%). δ_{H} (400 MHz, DMSO-*d*₆): 9.28 (1H, dd, H₉, ³*J* = 4.2 Hz, ⁴*J* = 1.6 Hz); 9.24 (1H, dd, H₂, ³*J* = 4.2 Hz, ⁴*J* = 1.3 Hz); 9.03 (1H, s, H₆); 8.88 (1H, dd, H₇, ³*J* = 8.6 Hz, ⁴*J* = 1.5 Hz); 8.78 (1H, dd, H₄, ³*J* = 8.1 Hz, ⁴*J* = 1.6 Hz); 9.28 (2H, m, H₃ and H₈).

5-Amino-1,10-phenanthroline (88)⁴⁰³



5-Nitro-1,10-phenanthroline (4.54 g, 20.2 mmol, 1 eq.) and 10 % Pd/C (0.93 g) were suspended in EtOH (100 mL). The mixture was refluxed and an ethanolic solution of hydrazine monohydrate 98% (5 mL, 103 mmol, 5.1 eq.) was added drop-wise. The reaction mixture was refluxed and stirred for 16 h. After cooling down, the suspension was filtered on celite and solvent was removed under reduced pressure yielding a yellow solid which was dried *in vacuo* (2.98 g, 15.2 mmol, 76%). δ_{H} (400 MHz, DMSO-*d*₆): 9.05 (1H, dd, H₂, ³*J* = 4.2 Hz, ⁴*J* = 1.6 Hz); 8.67 (2H, m, H₄ and H₉); 8.04 (1H, dd, H₇, ³*J* = 8.2 Hz, ⁴*J* = 1.7 Hz); 7.73 (1H, dd, H₈, ³*J* = 8.2 Hz, ³*J* = 4.2 Hz); 7.50 (1H, dd, H₃, ³*J* = 8.1 Hz, ³*J* = 4.2 Hz); 6.86 (1H, s, H₆); 6.13 (2H, s, NH₂).

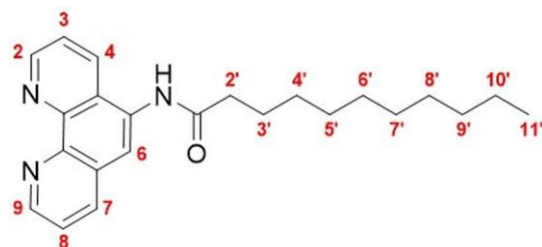
5-Acetamido-1,10-phenanthroline (84)⁴⁰³



5-Amino-1,10-phenanthroline (153 mg, 783 μ mol, 1 eq.) and acetic anhydride (0.75 mL, 7.93 mmol, 10 eq.) were mixed in dry MeCN (25 mL). The reaction mixture was stirred in the dark and under an inert atmosphere at room temperature for 2 days. Solvent was removed under reduced pressure and the resulting beige solid was dried *in vacuo* (114 mg, 482 μ mol, 62%). m.p. 226–231 °C (decomp.) Lit. m.p. 230 °C.⁴⁰³

δ_{H} (400 MHz, DMSO- d_6): 10.14 (1H, s, NH), 9.13 (1H, dd, H₂, $^3J = 4.2$ Hz, $^4J = 1.6$ Hz), 9.03 (1H, dd, H₉, $^3J = 4.3$ Hz, $^4J = 1.7$ Hz), 8.63 (1H, dd, H₄, $^3J = 8.4$ Hz, $^4J = 1.7$ Hz), 8.44 (1H, dd, H₇, $^3J = 8.2$ Hz, $^4J = 1.7$ Hz), 8.17 (1H, s, H₆), 7.82 (1H, dd, H₃, $^3J = 8.4$ Hz, $^3J = 4.3$ Hz), 7.74 (1H, dd, H₈, $^3J = 8.2$ Hz, $^3J = 4.3$ Hz), 6.13 (3H, s, CH₃). δ_{C} (101 MHz, DMSO- d_6): 169.49 (C=O), 149.86, 149.29, 145.85 (q), 143.77 (q), 135.81, 131.86 (q), 131.68, 128.10, 124.59 (q), 123.59, 122.84, 119.86, 23.63 (CH₃). ν_{max} (ATR)/cm⁻¹: 3200 (amide N-H stretch), 3040 (aromatic C-H stretch), 2924 (alkane C-H stretch), 1688 (C=O stretch), 1532 (amide N-H bend), 1476 (aromatic C=C stretch), 1420 (C-N stretch). ESI⁺-HRMS: $m/z_{\text{calc}} = 238.0980$ for C₁₄H₁₂N₃O; $m/z_{\text{found}} = 238.0973$ [M+H]⁺.

N-1,10-phenanthrolin-5-yl-undecanamide (85)

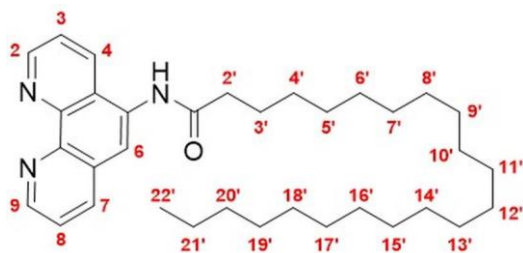


N-1,10-phenanthrolin-5-yl-undecanamide was synthesised according to **Procedure 1** using undecanoic acid (108 μL , 516 μmol , 1 eq.), 5-amino-1,10-phenanthroline (101 mg, 516 μmol , 1 eq.) EDC (246 mg, 1.28 mmol, 2.5 eq.)

and DMAP (62.4 mg, 511 μmol , 1 eq.), yielding the product as a beige solid (107 mg, 295 μmol , 57%). m.p. 83–86 °C. δ_{H} (600 MHz, DMSO- d_6): 10.07 (1H, s, NH), 9.12 (1H, dd, H₂, $^3J = 4.2$ Hz, $^4J = 1.6$ Hz), 9.03 (1H, dd, H₉, $^3J = 4.2$ Hz, $^4J = 1.7$ Hz), 8.59 (1H, dd, H₄, $^3J = 8.4$ Hz, $^4J = 1.6$ Hz), 8.44 (1H, dd, H₇, $^3J = 8.1$ Hz, $^4J = 1.7$ Hz), 8.17 (1H, s, H₆), 7.82 (1H, dd, H₃, $^3J = 8.4$ Hz, $^3J = 4.2$ Hz), 7.74 (1H, dd, H₈, $^3J = 8.1$ Hz, $^3J = 4.2$ Hz), 2.52 (2H, t, H_{2'}, $^3J = 7.3$ Hz), 1.69 (2H, m, H_{3'}), 1.31 (14H, m, H_{4'}–H_{10'}), 0.84 (3H, t, H_{11'}, $^3J = 7.0$ Hz). δ_{C} (151 MHz, DMSO- d_6): 172.44 (C=O), 149.82, 149.26, 145.86 (q), 143.77 (q), 135.75, 131.79 (q), 131.57, 128.09 (q), 124.64 (q), 123.55, 122.78, 119.97, 35.96, 31.30, 28.99, 28.96, 28.81, 28.73, 28.69, 25.22, 22.08, 13.95. ν_{max} (ATR)/cm⁻¹: 3255 (amide N-H stretch), 3046 (aromatic C-H stretch), 2919 and 2849 (alkane C-H stretch), 1655 (C=O stretch), 1543 (amide N-H bend), 1467 (aromatic C=C stretch), 1424 (C-N stretch). ESI⁺-HRMS: $m/z_{\text{calc}} = 386.2203$ for C₂₃H₂₉N₃NaO; $m/z_{\text{found}} = 386.2206$ [M+Na]⁺.

N-1,10-phenanthrolin-5-yl-henicosamide (86)

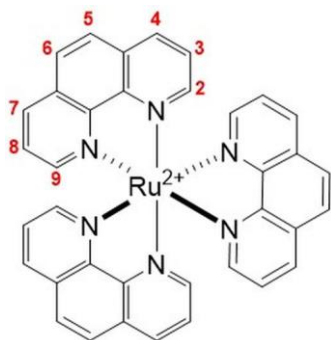
N-1,10-phenanthrolin-5-yl-henicosamide was synthesised according to **Procedure 1** using heneicosanoic acid (179 mg, 525 μmol , 1 eq.), 5-amino-1,10-phenanthroline (101 mg, 515 μmol , 1 eq.) EDC (255 mg, 1.33 mmol, 2.5 eq.) and DMAP (65.0 mg, 532 μmol , 1 eq.), yielding the product as a beige solid (258 mg, 498 μmol , 95%). m.p. 90–93 °C. δ_{H} (600



MHz, CDCl₃): 9.18 (1H, d, H₂), 9.12 (1H, d, H₉), 8.31 (1H, d, H₄, ³J = 8.4 Hz), 8.27 (1H, s, H₆), 8.21 (1H, dd, H₇, ³J = 8.1 Hz, ⁴J = 1.2 Hz), 7.76 (1H, s, NH), 7.64 (1H, 2dd, H₃ and H₈, ³J = 4.2 Hz, ³J = 8.4 Hz, ³J = 4.3 Hz, ³J = 8.1 Hz), 2.58 (2H, m, H_{2'}), 1.84 (2H, m, H_{3'}), 1.36 (36H, m, H_{4'}–H_{21'}), 0.87 (3H, t, H_{22'}, ³J = 6.8 Hz). δ_C (151 MHz, CDCl₃): 172.56 (C=O), 150.31, 149.93, 146.55 (q), 144.42 (q), 136.22, 130.67 (q), 129.84, 128.53 (q), 124.25 (q), 123.68, 122.97, 120.00, 37.82, 32.07, 29.85, 29.82, 29.81, 29.79, 29.67, 29.56, 29.51, 25.91, 22.84. ν_{max} (ATR)/cm⁻¹: 3262 (amide N-H stretch), 3046 (aromatic C-H stretch), 2915 and 2849 (alkane C-H stretch), 1657 (C=O stretch), 1541 (amide N-H bend), 1470 (aromatic C=C stretch), 1422 (C-N stretch). ESI⁺-HRMS: m/z_{calc} = 540.3924 for C₃₄H₅₁N₃NaO; m/z_{found} = 540.3915 [M+Na]⁺.

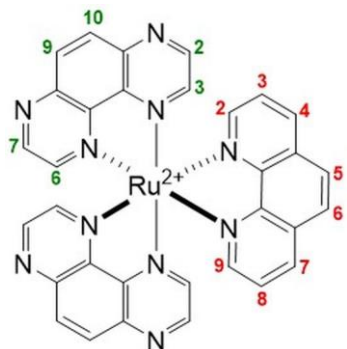
7.9.2 Synthesis and Characterisation of Complexes **42**, **39** and **78–83**

Tris(1,10-phenanthroline)ruthenium(II) chloride (**42**)



Complex **42** was synthesised according to **Procedure 3** using 1,10-phenanthroline (34.2 mg, 190 μmol, 1 eq.) and [Ru(phen)₂Cl₂] (99.7 mg, 187 μmol, 1 eq.), yielding the product as a red solid (70.9 mg, 99.5 μmol, 53%). m.p. > 120 °C (decomp.). δ_H (600 MHz, CD₃CN): 8.61 (6H, dd, H₄ and H₇, ³J = 8.2 Hz, ⁴J = 1.1 Hz), 8.26 (6H, s, H₅ and H₆), 8.03 (6H, dd, H₂ and H₉, ³J = 5.2 Hz, ⁴J = 1.1 Hz), 7.63 (6H, dd, H₃ and H₈, ³J = 8.2 Hz, ³J = 5.2 Hz). δ_C (151 MHz, CD₃CN): 153.91, 148.86 (q), 137.70, 131.92 (q), 128.97, 126.80. ν_{max} (ATR)/cm⁻¹: 3047 (aromatic C-H stretch), 1493 (aromatic C=C stretch), 1426 (C-N stretch). ESI⁺-HRMS: m/z_{calc} = 642.1106 for C₃₆H₂₄N₆Ru; m/z_{found} = 321.0553 [M]²⁺.

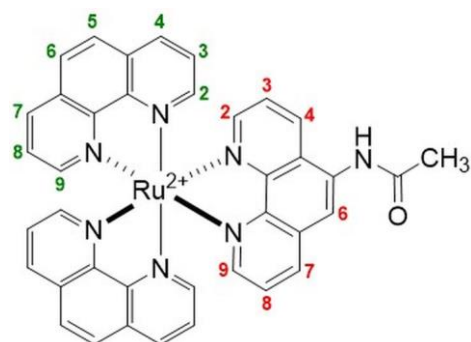
Bis(1,4,5,8-tetraazaphenanthrene)(1,10-phenanthroline)ruthenium(II) chloride (**39**)



Complex **39** was synthesised according to **Procedure 3** using 1,10-phenanthroline (87.5 mg, 486 μmol, 1.4 eq.) and [Ru(TAP)₂Cl₂] (180 mg, 335 μmol, 1 eq.), yielding the product as a red solid (97.6 mg, 136 μmol, 41%). m.p. 147–148 °C (decomp.). δ_H (400 MHz, D₂O): 8.96 (2H, d, H₂^{TAP} or H₇^{TAP}, ³J = 2.9 Hz), 8.92 (2H, d, H₂^{TAP} or H₇^{TAP}, ³J = 2.9 Hz), 8.70 (2H, dd, H₄^{phen} and H₇^{phen}, ³J = 8.3 Hz, ⁴J = 1.2 Hz), 8.62 (4H, s, H₉^{TAP} and H₁₀^{TAP}), 8.37 (2H, d, H₃^{TAP} or H₆^{TAP}, ³J = 2.9 Hz), 8.29 (2H, d, H₃^{TAP} or H₆^{TAP},

$^3J = 2.9$ Hz), 8.26 (2H, s, H^{5phen} and H^{6phen}), 8.08 (2H, dd, H^{2phen} and H^{9phen}, $^3J = 5.3$ Hz, $^4J = 1.2$ Hz), 7.68 (2H, dd, H^{3phen} and H^{8phen}, $^3J = 5.3$ Hz, $^3J = 8.3$ Hz). δ_C (101 MHz, D₂O): 152.58, 148.84, 148.66, 148.48, 148.32, 146.83 (q), 144.94 (q), 144.90 (q), 142.68 (q), 142.66 (q), 138.74, 132.58, 132.50, 131.25 (q), 128.21, 125.96. ν_{\max} (ATR)/cm⁻¹: 3050 (aromatic C-H stretch), 1486 (aromatic C=C stretch), 1384 (C-N stretch). MALDI⁺-HRMS: $m/z_{\text{calc}} = 646.0916$ for C₃₂H₂₀N₁₀Ru; $m/z_{\text{found}} = 646.0927$ [M]⁺.

Bis(1,10-phenanthroline)(N-1,10-phenanthrolin-5-yl-acetamide)ruthenium(II) chloride (78)

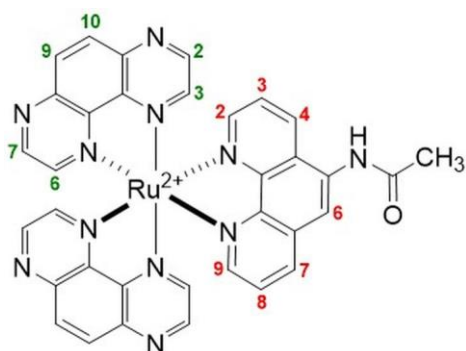


Complex **78** was synthesised according to **Procedure 3** using ligand **84** (66.7 mg, 281 μmol , 1.5 eq.) and [Ru(phen)₂Cl₂] (101 mg, 190 μmol , 1 eq.), yielding the product as a red solid (87.3 mg, 125 μmol , 60%). Calculated for C₃₈H₂₇N₇Cl₂ORu + 2.3H₂O: C, 56.27; H, 3.93; N, 12.09; Cl, 8.74. Found: C, 56.21; H, 3.88; N, 12.12; Cl, 8.20. m.p. 106–109 °C (decomp.). δ_H

(400 MHz, CD₃CN): 11.61 (1H, s, NH), 9.60 (1H, dd, H⁴⁸⁴, $^3J = 8.6$ Hz, $^4J = 1.1$ Hz), 8.64 (1H, s, H⁶⁸⁴), 8.59 (4H, m, H^{phen}), 8.47 (1H, dd, H⁷⁸⁴, $^3J = 8.3$ Hz, $^4J = 1.1$ Hz), 8.25 (2H, s, H^{5phen} or H^{6phen}), 8.24 (2H, s, H^{5phen} or H^{6phen}), 8.09 (1H, dd, H²⁸⁴, $^3J = 5.2$ Hz, $^4J = 1.1$ Hz), 8.02 (4H, m, H^{phen}), 7.89 (1H, dd, H⁹⁸⁴, $^3J = 5.2$ Hz, $^4J = 1.1$ Hz), 7.62 (5H, m, H³⁸⁴ and H^{phen}), 7.52 (1H, dd, H⁸⁸⁴, $^3J = 8.3$ Hz, $^3J = 5.2$ Hz), 2.45 (3H, s, CH₃). δ_C (101 MHz, CD₃CN): 171.81 (C=O), 154.17, 153.97, 153.85, 153.80, 153.68, 152.27, 148.87 (q), 137.62, 137.59, 136.94, 135.46, 131.93 (q), 131.88 (q), 128.97, 128.91, 126.85, 126.83, 126.76, 126.74, 126.64, 125.76, 119.79, 24.40 (CH₃). ν_{\max} (ATR)/cm⁻¹: 3234 (amide N-H stretch), 3046 (aromatic C-H stretch), 2994 (alkane C-H stretch), 1683 (C=O stretch), 1533 (amide N-H bend), 1480 (aromatic C=C stretch), 1424 (C-N stretch). ESI⁺-HRMS: $m/z_{\text{calc}} = 699.1321$ for C₃₈H₂₇N₇ORu; $m/z_{\text{found}} = 349.5676$ [M]²⁺.

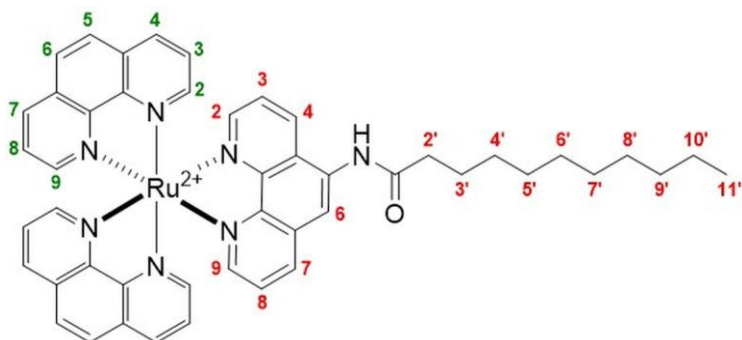
Bis(1,4,5,8-tetraazaphenanthrene)(N-1,10-phenanthrolin-5-yl-acetamide)ruthenium(II) chloride (81)

Complex **81** was synthesised according to **Procedure 3** using ligand **84** (44.1 mg, 186 μmol , 1.1 eq.) and [Ru(TAP)₂Cl₂] (90.8 mg, 169 μmol , 1 eq.), yielding the product as a red solid (67.5 mg, 87.2 μmol , 52%). Calculated for C₃₄H₂₃N₁₁Cl₂ORu + 5.2H₂O + 0.2NaCl: C, 46.46; H, 3.83; N, 17.53; Cl, 8.87. Found: C, 46.27; H, 3.17; N, 16.89; Cl, 8.66. m.p. 162–164 °C



(decomp.). δ_{H} (400 MHz, DMSO- d_6): 10.71 (1H, s, NH), 9.06 (5H, m, H₄⁸⁴ and H^{TAP}), 8.80 (1H, d, H₇⁸⁴, ³*J* = 8.2 Hz), 8.66 (5H, s, H₆⁸⁴, H₉^{TAP} and H₁₀^{TAP}), 8.51 (1H, d, H^{TAP}, ³*J* = 2.8 Hz), 8.48 (1H, d, H^{TAP}, ³*J* = 2.8 Hz), 8.30 (1H, d, H₂⁸⁴, ³*J* = 5.3 Hz), 8.24 (2H, m, H^{TAP}), 8.17 (1H, d, H₉⁸⁴, ³*J* = 5.3 Hz), 7.82 (1H, dd, H₃⁸⁴, ³*J* = 5.3 Hz, ³*J* = 8.5 Hz), 7.73 (1H, dd, H₈⁸⁴, ³*J* = 5.3 Hz, ³*J* = 8.2 Hz), 2.32 (3H, s, CH₃). δ_{C} (101 MHz, DMSO- d_6): 169.82 (C=O), 153.94, 152.66, 149.65, 149.50, 148.67, 148.62, 146.82 (q), 144.52 (q), 144.51 (q), 144.48 (q), 144.06 (q), 141.98 (q), 141.93 (q), 141.91 (q), 137.36, 133.92, 132.41, 132.28, 130.34 (q), 126.45 (q), 126.34, 125.64, 119.01, 23.80 (CH₃). ν_{max} (ATR)/cm⁻¹: 3220 (amide N-H stretch), 3052 (aromatic C-H stretch), 2979 (alkane C-H stretch), 1681 (C=O stretch), 1528 (amide N-H bend), 1485 (aromatic C=C stretch), 1383 (C-N stretch). MALDI⁺-HRMS: *m/z* calc = 703.1131 for C₃₄H₂₃N₁₁ORu; *m/z* found = 703.1135 [M]⁺.

Bis(1,10-phenanthroline)(*N*-1,10-phenanthroline-5-ylundecanamide)ruthenium(II) chloride (**79**)

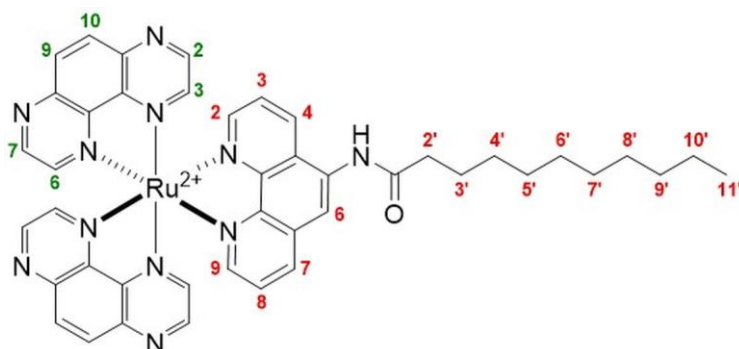


Complex **79** was synthesised according to **Procedure 3** using ligand **85** (109 mg, 300 μmol , 1 eq.) and [Ru(phen)₂Cl₂] (164 mg, 307 μmol , 1 eq.), yielding the product as a red solid (161 mg, 99.0 μmol , 60%).

Calculated for C₄₇H₄₅N₇Cl₂ORu + 2.6H₂O: C, 59.88; H, 5.37; N, 10.40; Cl, 7.52. Found: C, 59.57; H, 5.08; N, 10.37; Cl, 7.18. m.p. 220–223 °C (decomp.). δ_{H} (400 MHz, CD₃CN): 11.33 (1H, s, NH), 9.48 (1H, dd, H₄⁸⁵, ³*J* = 8.6 Hz, ⁴*J* = 1.0 Hz), 8.64 (1H, s, H₆⁸⁵), 8.60 (4H, m, H^{phen}), 8.47 (1H, dd, H₇⁸⁵, ³*J* = 8.3 Hz, ⁴*J* = 1.0 Hz), 8.25 (4H, 2s, H₅^{phen} and H₆^{phen}), 8.09 (1H, dd, H₂⁸⁵, ³*J* = 5.2 Hz, ⁴*J* = 1.0 Hz), 8.02 (4H, m, H^{phen}), 7.90 (1H, dd, H₉⁸⁵, ³*J* = 5.2 Hz, ⁴*J* = 1.0 Hz), 7.62 (5H, m, H₃⁸⁵ and H^{phen}), 7.53 (1H, dd, H₈⁸⁵, ³*J* = 8.3 Hz, ³*J* = 5.2 Hz), 2.79 (2H, t, H₂⁸⁵, ³*J* = 7.4 Hz), 1.71 (2H, m, H₃⁸⁵), 1.34 (14H, m, H₄⁸⁵–H₁₀⁸⁵), 0.84 (3H, t, H₁₁⁸⁵, ³*J* = 6.7 Hz). δ_{C} (101 MHz, CD₃CN): 175.03 (C=O), 154.18, 153.99, 153.88, 153.73, 152.34, 148.89 (q) 137.67, 136.99, 136.08 (q), 135.40, 131.93 (q), 129.03, 128.97, 128.13 (q), 126.91, 126.81, 126.71, 125.85, 119.95, 37.41, 32.61, 30.31, 30.22, 30.03, 26.60, 23.36,

14.37. ν_{\max} (ATR)/ cm^{-1} : 3243 (amide N-H stretch), 3043 (aromatic C-H stretch), 2922 and 2851 (alkane C-H stretch), 1688 (C=O stretch), 1535 (amide N-H bend), 1457 (aromatic C=C stretch), 1424 (C-N stretch). ESI⁺-HRMS: m/z _{calc} = 825.2729 for C₄₇H₄₅N₇ORu; m/z _{found} = 412.6378 [M]²⁺.

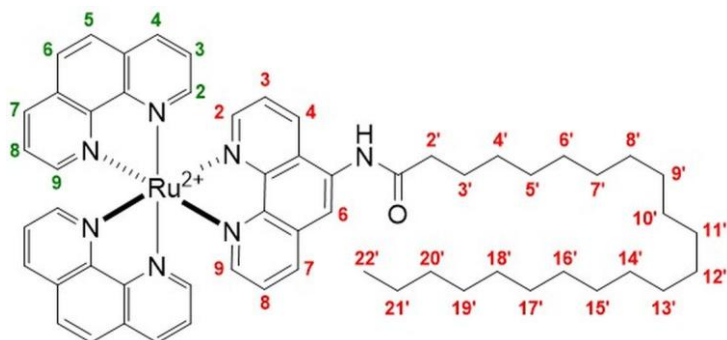
Bis(1,4,5,8-tetraazaphenanthrene)(*N*-1,10-phenanthrolin-5-yl-undecanamide)ruthenium(II) chloride (82)



Complex **82** was synthesised according to **Procedure 3** using ligand **85** (82.5 mg, 227 μmol , 1.2 eq.) and [Ru(TAP)₂Cl₂] (101 mg, 192 μmol , 1 eq.), yielding the product as a red solid (73.0 mg, 81.1 μmol , 43%).

Calculated for C₄₃H₄₁N₁₁Cl₂ORu + 4.6H₂O + 0.1NaCl: C, 52.24; H, 5.12; N, 15.59; Cl, 7.53. Found: C, 51.89; H, 4.45; N, 15.34; Cl, 6.93. m.p. 150–151 °C (decomp.). δ_{H} (400 MHz, CD₃CN): 11.67 (1H, s, NH), 9.71 (1H, d, H₄⁸⁵, ³J = 8.5 Hz), 8.94 (4H, m, H^{TAP}), 8.69 (1H, s, H₆⁸⁵), 8.58 (5H, s, H₇⁸⁵, H₉^{TAP} and H₁₀^{TAP}), 8.29 (1H, d, H^{TAP}, ³J = 2.7 Hz), 8.27 (1H, d, H^{TAP}, ³J = 2.7 Hz), 8.20 (1H, d, H^{TAP}, ³J = 2.7 Hz), 8.16 (1H, d, H^{TAP}, ³J = 2.7 Hz), 8.14 (1H, d, H₂⁸⁵, ³J = 5.1 Hz), 7.99 (1H, d, H₉⁸⁵, ³J = 5.1 Hz), 7.70 (1H, dd, H₃⁸⁵, ³J = 5.1 Hz, ³J = 8.5 Hz), 7.60 (1H, dd, H₈⁸⁵, ³J = 5.1 Hz, ³J = 8.5 Hz), 2.84 (2H, t, H₂⁸⁵, ³J = 7.4 Hz), 1.74 (2H, m, H₃⁸⁵), 1.33 (14H, m, H₄⁸⁵–H₁₀⁸⁵), 0.86 (3H, t, H₁₁⁸⁵, ³J = 7.0 Hz). δ_{C} (101 MHz, CD₃CN): 175.04 (C=O), 154.69, 153.19, 150.38, 150.33, 150.30, 150.14, 150.09, 149.84, 149.70, 148.30 (q), 146.38 (q), 146.34 (q), 146.31 (q), 146.28 (q), 145.33 (q), 143.31 (q), 143.28 (q), 143.26 (q), 138.34, 136.99, 136.24 (q), 133.72, 133.55, 132.11 (q), 128.29 (q), 126.90, 125.98, 119.90, 37.31, 32.56, 30.27, 30.17, 30.00, 29.98, 26.55, 23.32, 14.32. ν_{\max} (ATR)/ cm^{-1} : 3247 (amide N-H stretch), 3048 (aromatic C-H stretch), 2923 and 2852 (alkane C-H stretch), 1671 (C=O stretch), 1535 (amide N-H bend), 1485 (aromatic C=C stretch), 1422 (C-N stretch). ESI⁺-HRMS: m/z _{calc} = 829.2539 for C₄₃H₄₁N₁₁ORu; m/z _{found} = 414.6258 [M]²⁺.

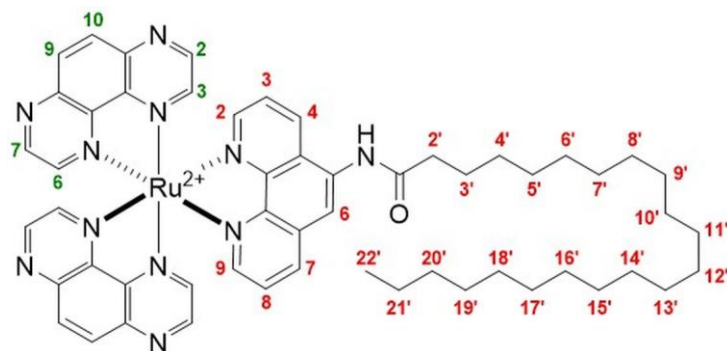
Bis(1,10-phenanthroline)(*N*-1,10-phenanthrolin-5-yl-henicosamide)ruthenium(II) chloride (80)



Complex **80** was synthesised according to **Procedure 3** using ligand **86** (145 mg, 281 μmol , 1.5 eq.) and $[\text{Ru}(\text{phen})_2\text{Cl}_2]$ (102 mg, 192 μmol , 1 eq.), yielding the product as a red solid (101 mg, 96.0 μmol , 50%). Calculated for

$\text{C}_{58}\text{H}_{67}\text{N}_7\text{Cl}_2\text{ORu} + 2.7\text{H}_2\text{O} + 0.1\text{NaCl}$: C, 63.06; H, 6.61; N, 8.88; Cl, 6.74. Found: C, 63.00; H, 6.08; N, 8.88; Cl, 6.70. m.p. 248–251 $^\circ\text{C}$ (decomp.). δ_{H} (600 MHz, $\text{DMSO-}d_6$): 10.51 (1H, s, NH), 8.93 (1H, dd, H_{4}^{86} , $^3J = 8.6$ Hz, $^4J = 1.0$ Hz), 8.77 (4H, m, H^{phen}), 8.71 (1H, dd, H_{7}^{86} , $^3J = 8.3$ Hz, $^4J = 0.8$ Hz), 8.66 (1H, s, H_{6}^{86}), 8.39 (4H, s, $\text{H}_{5}^{\text{phen}}$ and $\text{H}_{6}^{\text{phen}}$), 8.08 (4H, m, H^{phen}), 8.05 (1H, dd, H_{2}^{86} , $^3J = 5.2$ Hz, $^4J = 1.0$ Hz), 7.96 (1H, dd, H_{9}^{86} , $^3J = 5.2$ Hz, $^4J = 0.8$ Hz), 7.77 (5H, m, H_{3}^{86} and H^{phen}), 7.69 (1H, dd, H_{8}^{86} , $^3J = 8.3$ Hz, $^3J = 5.2$ Hz), 2.60 (2H, t, H_{22}^{86} , $^3J = 7.4$ Hz), 1.69 (2H, m, H_{3}^{86}), 1.29 (36H, m, $\text{H}_{4'}\text{--H}_{21'}^{86}$), 0.84 (3H, t, H_{22}^{85} , $^3J = 7.0$ Hz). δ_{C} (151 MHz, $\text{DMSO-}d_6$): 172.79 (C=O), 152.74, 151.51, 147.59 (q), 147.22 (q), 147.20 (q), 147.18 (q), 144.82 (q), 136.83, 136.19, 133.87 (q), 132.64, 130.44 (q), 130.23 (q), 128.04, 126.35, 126.28, 125.53 (q), 119.07, 36.05, 31.27, 29.00, 28.97, 28.94, 28.82, 28.68, 25.19, 22.07, 13.94. ν_{max} (ATR)/ cm^{-1} : 3185 (amide N-H stretch), 3044 (aromatic C-H stretch), 2920 and 2848 (alkane C-H stretch), 1698 (C=O stretch), 1541 (amide N-H bend), 1458 (aromatic C=C stretch), 1424 (C-N stretch). ESI⁺-HRMS: $m/z_{\text{calc}} = 979.4451$ for $\text{C}_{58}\text{H}_{67}\text{N}_7\text{ORu}$; $m/z_{\text{found}} = 489.7232$ [M]²⁺.

Bis(1,4,5,8-tetraazaphenanthrene)(*N*-1,10-phenanthrolin-5-yl-henicosamide)ruthenium(II) chloride (83)



Complex **83** was synthesised according to **Procedure 3** using ligand **86** (122 mg, 236 μmol , 1.2 eq.) and $[\text{Ru}(\text{TAP})_2\text{Cl}_2]$ (103 mg, 192 μmol , 1 eq.), yielding the product as a red solid (84.4 mg, 80.0 μmol , 42%).

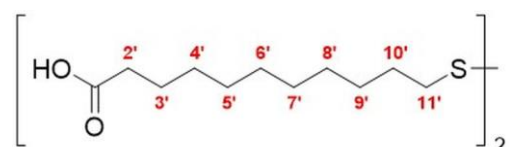
Calculated for $\text{C}_{54}\text{H}_{63}\text{N}_{11}\text{Cl}_2\text{ORu} + 4.7\text{H}_2\text{O} + 0.1\text{NaCl}$: C, 56.66; H, 6.38; N, 13.46; Cl, 6.50.

Found: C, 56.50; H, 5.82; N, 13.45; Cl, 6.38. m.p. 171–172 °C (decomp.). δ_{H} (400 MHz, CD_3CN): 11.63 (1H, s, NH), 9.71 (1H, dd, H_4^{86} , $^3J = 8.6$ Hz, $^4J = 1.1$ Hz), 8.93 (4H, m, H^{TAP}), 8.70 (1H, s, H_6^{86}), 8.60 (5H, m, H_7^{86} , H_9^{TAP} and $\text{H}_{10}^{\text{TAP}}$), 8.27 (1H, d, H^{TAP} , $^3J = 2.8$ Hz), 8.26 (1H, d, H^{TAP} , $^3J = 2.8$ Hz), 8.19 (1H, d, H^{TAP} , $^3J = 2.8$ Hz), 8.14 (2H, m, H^{TAP} and H_2^{86}), 7.99 (1H, dd, H_9^{86} , $^3J = 5.2$ Hz, $^4J = 1.2$ Hz), 7.71 (1H, dd, H_3^{86} , $^3J = 5.2$ Hz, $^3J = 8.6$ Hz), 7.60 (1H, dd, H_8^{86} , $^3J = 5.2$ Hz, $^3J = 8.3$ Hz), 2.84 (2H, t, H_2^{86} , $^3J = 7.4$ Hz), 1.75 (2H, m, H_3^{86}), 1.32 (36H, m, $\text{H}_4\text{--H}_{21}^{86}$), 0.87 (3H, t, H_{22}^{86} , $^3J = 7.0$ Hz). δ_{C} (101 MHz, CD_3CN): 174.97 (C=O), 154.70, 153.20, 150.36, 150.32, 150.30, 150.08, 150.04, 149.79, 149.64, 146.37 (q), 146.34 (q), 146.32 (q), 145.37 (q), 143.33 (q), 143.27 (q), 138.39, 136.86, 136.19 (q), 133.75, 133.58, 132.14 (q), 128.31 (q), 126.93, 126.03, 119.95, 37.34, 32.56, 30.31, 30.29, 30.18, 29.99, 26.53, 23.32, 14.32. ν_{max} (ATR)/ cm^{-1} : 3245 (amide N-H stretch), 3050 (aromatic C-H stretch), 2920 and 2851 (alkane C-H stretch), 1686 (C=O stretch), 1535 (amide N-H bend), 1485 (aromatic C=C stretch), 1423 (C-N stretch), 1384 (C-N stretch). MALDI⁺-HRMS: $m/z_{\text{calc}} = 983.4261$ for $\text{C}_{54}\text{H}_{63}\text{N}_{11}\text{ORu}$; $m/z_{\text{found}} = 983.4290$ [M]⁺.

7.10 Synthesis and Characterisation of Compounds Described in Chapter 5

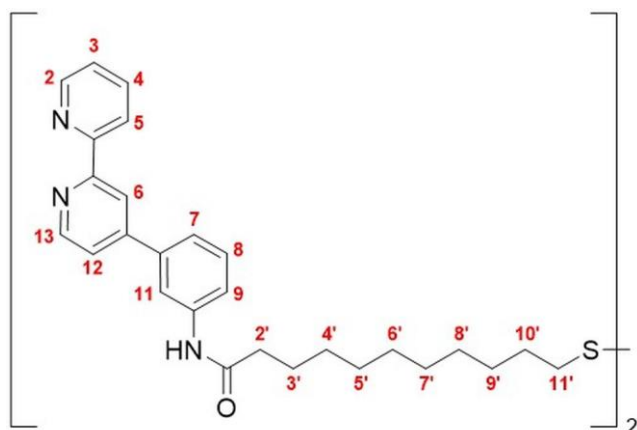
7.10.1 Synthesis and Characterisation of the Ligand 89

11,11'-Disulfanediyldiundecanoic acid (93)

 11-Mercaptoundecanoic acid (1.01 g, 4.62 mmol, 1 eq.) was dissolved in anhydrous DMF (15 mL) and cooled to 0 °C. To this solution, bromine (140 μL , 2.73 mmol, 0.6 eq.) was added drop-wise and the resulting mixture was stirred at 0 °C and under argon for 3 h. Solvent was removed at reduced pressure and the resulting solid was washed with NaHCO_3 (aq), 1 M HCl and H_2O yielding a white solid which was dried *in vacuo* (858 mg, 1.97 mmol, 85%). m.p. 88–92 °C. Lit. m.p. 93–97 °C.⁴⁴⁹ δ_{H} (400 MHz, $\text{DMSO-}d_6$): 2.68 (2H, t, H_{11}' , $^3J = 7.2$ Hz), 2.17 (2H, t, H_2' , $^3J = 7.4$ Hz), 1.60 (2H, m, H_{10}'), 1.47 (2H, m, H_3'), 1.31 (12H, m, $\text{H}_4\text{--H}_9'$).

11,11'-Disulfanediyldis(*N*-(3-([2,2'-bipyridin]-4-yl)phenyl)undecanamide) (89)

Ligand **89** was synthesised according to **Procedure 1** using 11,11'-disulfanediyldiundecanoic acid (77.6 mg, 178 μmol , 0.5 eq.), 3-([2,2'-bipyridin]-4-yl)aniline (88.2 mg, 357 μmol , 1 eq.) EDC (181 mg, 942 μmol , 2.6 eq.) and DMAP (53.2 mg, 436 μmol , 1.2 eq.), yielding the product as a beige solid (115 mg, 129 μmol , 72%). m.p. 85–87 °C. δ_{H} (400 MHz, $\text{DMSO-}d_6$): 10.08 (1H, s, NH), 8.75 (1H, d, H_{13} , $^3J = 5.2$ Hz), 8.73 (1H,

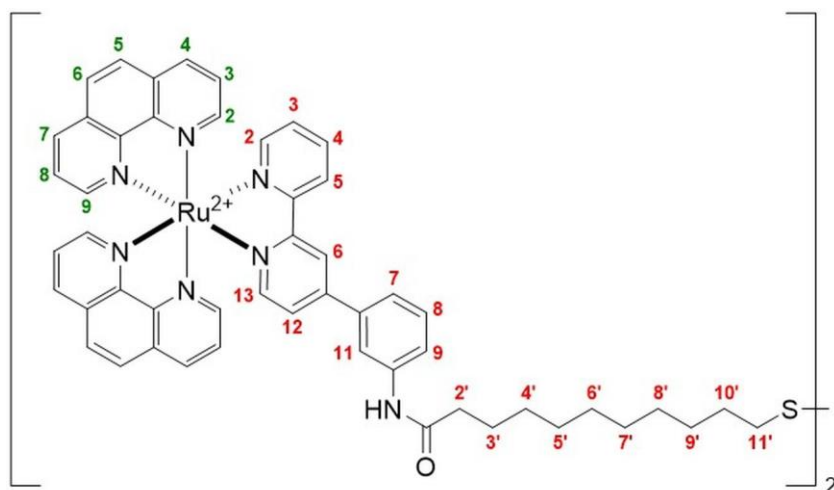


ddd, H₂, ³J = 4.8 Hz, ⁴J = 1.8 Hz, ⁴J = 0.8 Hz), 8.65 (1H, d, H₆, ⁴J = 1.8 Hz), 8.44 (1H, d, H₅, ³J = 7.9 Hz), 8.12 (1H, s, H₁₁), 7.97 (1H, td, H₄, ³J = 7.9 Hz, ⁴J = 1.8 Hz), 7.74 (1H, d, H₉, ³J = 8.3 Hz), 7.72 (1H, dd, H₁₂, ³J = 5.2 Hz, ⁴J = 1.8 Hz), 7.49 (3H, m, H₃, H₇ and H₈), 2.63 (2H, t, H_{11'}, ³J = 7.2 Hz), 2.32 (2H, t,

H_{2'}, ³J = 7.3 Hz), 1.57 (4H, m, H_{3'} and H_{10'}), 1.25 (12H, m, H_{4'}–H_{9'}). δ_c (101 MHz, DMSO-*d*₆): 171.59 (C=O), 155.95 (q), 155.04 (q), 150.10, 149.29, 148.12 (q), 140.28 (q), 137.68 (q), 137.41, 129.74, 124.40, 121.48, 121.34, 120.65, 119.81, 117.38, 117.03, 37.88, 36.48, 28.83, 28.81, 28.74, 28.64, 28.51, 28.48, 27.68, 25.05. ν_{max} (ATR)/cm⁻¹: 3283 (amide N-H stretch), 3061 (aromatic C-H stretch), 2918 and 2848 (alkane C-H stretch), 1656 (C=O stretch), 1543 (amide N-H bend), 1464 (aromatic C=C stretch), 1425 (C-N stretch). MALDI⁺-HRMS: m/z_{calc} = 893.4610 for C₅₄H₆₅N₆O₂S₂; m/z_{found} = 893.4639 [M+H]⁺.

7.10.2 Synthesis and Characterisation of Complexes 90 and 91

Tetra(1,10-phenanthroline)(11,11'-disulfanediylbis(*N*-(3-((2,2'-bipyridin-4-yl)phenyl)undecanamide))diruthenium(II) chloride (90)

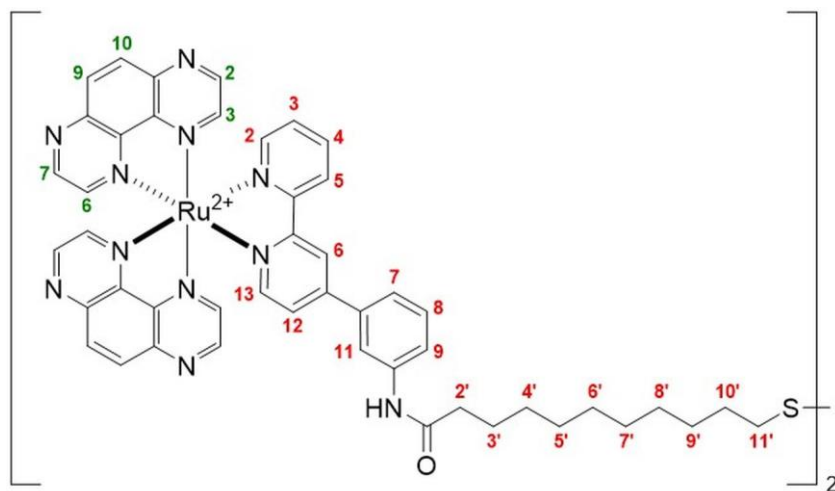


Complex **90** was synthesised according to **Procedure 3** using ligand **89** (38.6 mg, 43.2 μmol, 1 eq.) and [Ru(phen)₂Cl₂] (50.5 mg, 94.8 μmol, 2.2 eq.), yielding the product as a red solid (65.6 mg, 34.8 μmol, 80%). Calculated

for C₁₀₂H₉₆N₁₄Cl₄O₂S₂Ru₂ + 16H₂O: C, 54.54; H, 5.74; N, 8.73. Found: C, 54.04; H, 5.21; N, 9.07. δ_H (400 MHz, DMSO-*d*₆): 10.43 (1H, s, NH), 9.16 (1H, d, H₅^{pbpySS}, ³J = 8.2 Hz), 9.10 (1H, d, H₆^{pbpySS}, ⁴J = 1.4 Hz), 8.85 (2H, d, H^{phen}, ³J = 8.2 Hz), 8.75 (2H, dt, H^{phen}, ³J = 8.3 Hz, ⁴J = 1.1 Hz), 8.38 (5H, m, H₅^{phen} and H₆^{phen}, H^{phen}), 8.33 (1H, s, H₁₁^{pbpySS}), 8.26 (1H, dd, H^{phen}, ³J = 5.2 Hz, ⁴J = 1.1 Hz), 8.17 (1H, td, H₄^{pbpySS}, ³J = 8.2 Hz, ⁴J = 1.3 Hz),

7.96 (4H, m, H^{phen}, H₂^{pbpySS} and H₁₃^{pbpySS}), 7.73 (4H, m, H^{phen}), 7.67 (2H, dd, H₈^{pbpySS} and H₉^{pbpySS}, ³J = 8.0 Hz, ⁴J = 1.7 Hz), 7.60 (1H, dd, H₁₂^{pbpySS}, ³J = 6.0 Hz, ⁴J = 1.4 Hz), 7.48 (1H, t, H₇^{pbpySS}, ³J = 8.0 Hz), 7.43 (1H, m, H₃^{pbpySS}), 2.65 (2H, t, H_{11'}^{pbpySS}, ³J = 7.2 Hz), 2.34 (2H, t, H₂^{pbpySS}, ³J = 7.4 Hz), 1.57 (4H, m, H_{3'}^{pbpySS} and H_{10'}^{pbpySS}), 1.23 (12H, m, H_{4'}–H_{9'}^{pbpySS}). δ_C (101 MHz, DMSO-*d*₆): 171.68 (C=O), 157.40 (q), 157.00 (q), 152.72, 152.58, 152.44, 152.40, 151.86, 151.70, 152.44, 152.40, 148.56 (q), 147.17 (q), 147.15 (q), 146.91 (q), 146.89 (q), 140.36 (q), 137.78, 136.93, 136.91, 136.80, 135.73 (q), 130.53 (q), 130.49 (q), 130.43 (q), 129.61, 128.07, 127.79, 126.46, 126.35, 124.78, 124.61, 121.97, 121.54, 120.88, 117.82, 37.79, 36.32, 28.86, 28.85, 28.79, 28.65, 28.54, 28.48, 27.69, 25.04. ν_{max} (ATR)/cm⁻¹: 3247 (amide N-H stretch), 3053 (aromatic C-H stretch), 2923 and 2851 (alkane C-H stretch), 1665 (C=O stretch), 1550 (amide N-H bend), 1469 (aromatic C=C stretch), 1426 (C-N stretch). MALDI⁺-HRMS: m/z_{calc} = 1815.5331 for C₁₀₂H₉₅N₁₄O₂S₂Ru; m/z_{found} = 1815.5494 [M-H]⁺.

Tetra(1,4,5,8-tetraazaphenanthrene)(11,11'-disulfanediylbis(*N*-(3-([2,2'-bipyridin]-4-yl)phenyl)undecanamide))diruthenium(II) chloride (91)



Complex **91** was synthesised according to **Procedure 3** using ligand **89** (84.1 mg, 94.1 μmol, 1 eq.) and [Ru(TAP)₂Cl₂] (104 mg, 193 μmol, 2.1 eq.), yielding the product as a red solid (48.1 mg, 24.5

μmol, 26%). Calculated for C₉₄H₈₈N₂₂Cl₄O₂S₂Ru₂ + 16.5H₂O: C, 49.88; H, 5.39; N, 13.62. Found: C, 49.22; H, 4.62; N, 13.37. δ_H (400 MHz, DMSO-*d*₆): 10.58 (1H, s, NH), 9.22 (3H, m, H₅^{pbpySS} and H^{TAP}), 9.13 (1H, d, H₆^{pbpySS}, ⁴J = 1.7 Hz), 9.02 (2H, d, H^{TAP}, ³J = 2.8 Hz), 8.66 (4H, m, H₉^{TAP} and H₁₀^{TAP}), 8.52 (1H, d, H^{TAP}, ³J = 2.9 Hz), 8.44 (2H, m, H^{TAP}), 8.38 (2H, m, H₁₁^{pbpySS} and H^{TAP}), 8.26 (1H, td, H₄^{pbpySS}, ³J = 7.9 Hz, ⁴J = 1.2 Hz), 7.91 (2H, m, H₂^{pbpySS} and H₁₃^{pbpySS}), 7.71 (2H, m, H₇^{pbpySS} and H₉^{pbpySS}), 7.60 (1H, dd, H₁₂^{pbpySS}, ³J = 6.1 Hz, ⁴J = 1.7 Hz), 7.49 (2H, m, H₃^{pbpySS} and H₈^{pbpySS}), 2.66 (2H, t, H_{11'}^{pbpySS}, ³J = 7.2 Hz), 2.34 (2H, t, H₂^{pbpySS}, ³J = 7.5 Hz), 1.58 (4H, m, H_{3'}^{pbpySS} and H_{10'}^{pbpySS}), 1.26 (12H, m, H_{4'}–H_{9'}^{pbpySS}). δ_C (101 MHz, DMSO-*d*₆): 171.74 (C=O), 156.76 (q), 156.37 (q), 152.94,

152.85, 149.78, 149.76, 149.29, 149.25, 148.62, 148.52, 144.55 (q), 144.50 (q), 141.88 (q), 141.59 (q), 140.46 (q), 139.00, 135.22 (q), 132.49, 132.44, 132.32, 129.64, 128.05, 124.96, 124.69, 122.02, 121.71, 121.04 (q), 121.03, 117.88, 37.81, 36.33, 28.87, 28.81, 28.68, 28.55, 28.49, 27.70, 25.07. ν_{\max} (ATR)/ cm^{-1} : 3244 (amide N-H stretch), 3052 (aromatic C-H stretch), 2922 and 2851 (alkane C-H stretch), 1665 (C=O stretch), 1536 (amide N-H bend), 1485 (aromatic C=C stretch), 1406 (C-N stretch). MALDI⁺-HRMS: $m/z_{\text{calc}} = 1823.4911$ for $\text{C}_{94}\text{H}_{87}\text{N}_{22}\text{O}_2\text{S}_2\text{Ru}_2$; $m/z_{\text{found}} = 1823.5002$ [M-H]⁺.

Chapter 8

References

References

1. Neidle, S. *Nucleic Acid Structure and Recognition*; 1st ed.; Oxford University Press, 2002.
2. Gill, M. R.; Thomas, J. A. *Chem. Soc. Rev.* **2012**, *41*, 3179–3192.
3. Cancer Research UK. <https://www.cancerresearchuk.org/> (accessed January 2019).
4. Hanahan, D.; Weinberg, R. A. *Cell* **2000**, *100*, 57–70.
5. Arruebo, M.; Vilaboa, N.; Sáez-Gutierrez, B.; Lambea, J.; Tres, A.; Valladares, M.; González-Fernández, Á. *Cancers* **2011**, *3*, 3279–3330.
6. Baudino, T. A. *Curr. Drug Discovery Technol.* **2015**, *12*, 3–20.
7. Persidis, A. *Nat. Biotechnol.* **1999**, *17*, 94–95.
8. Kostova, I. *Curr. Med. Chem.* **2006**, *13*, 1085–1107.
9. Triesscheijn, M.; Baas, P.; Schellens, J. H.; Stewart, F. A. *Oncologist* **2006**, *11*, 1034–1044.
10. Dolmans, D. E. J. G. J.; Fukumura, D.; Jain, R. K. *Nat. Rev. Cancer* **2003**, *3*, 380–387.
11. Dougherty, T. J.; Gomer, C. J.; Henderson, B. W.; Jori, G.; Kessel, D.; Korbelik, M.; Moan, J.; Peng, Q. *J. Natl. Cancer Inst.* **1998**, *90*, 889–905.
12. Das, S. K.; Menezes, M. E.; Bhatia, S.; Wang, X.-Y.; Emdad, L.; Sarkar, D.; Fisher, P. B. *J. Cell. Physiol.* **2015**, *230*, 259–271.
13. Amer, M. H. *Mol. Cell. Ther.* **2014**, *2*, 27.
14. Hurley, L. H. *Nat. Rev. Cancer* **2002**, *2*, 188–200.
15. Neidle, S. *Principles of Nucleic Acid Structure*; 1st ed. Academic Press: London, 2008.
16. Watson, J. D.; Crick, F. H. C. *Nature* **1953**, *171*, 737–738.
17. Breslauer, K. J.; Frank, R.; Blöcker, H.; Marky, L. A. *Proc. Natl. Acad. Sci. U. S. A.* **1986**, *83*, 3746–3750.
18. Gotoh, O.; Tagashira, Y. *Biopolymers* **1981**, *20*, 1033–1042.
19. Yanson, I. K.; Teplitsky, A. B.; Sukhodub, L. F. *Biopolymers* **1979**, *18*, 1149–1170.
20. Shindo, H.; Simpson, R. T.; Cohen, J. S. *J. Biol. Chem.* **1979**, *254*, 8125–8128.
21. Dickerson, R. E.; Drew, H. R. *Proc. Natl. Acad. Sci. U. S. A.* **1981**, *78*, 7318–7322.
22. Privé, G. G.; Yanagi, K.; Dickerson, R. E. *J. Mol. Biol.* **1991**, *217*, 177–199.
23. Price, M. A.; Tullius, T. D. *Methods in Enzymology*; Elsevier, 1992; Vol. 212.
24. Maehigashi, T.; Hsiao, C.; Kruger Woods, K.; Moulai, T.; Hud, N. V.; Dean Williams, L. *Nucleic Acids Res.* **2012**, *40*, 3714–3722.
25. Bansal, M. *Curr. Sci.* **2003**, *85*, 1556–1563.

26. Baikalov, I.; Grzeskowiak, K.; Yanagi, K.; Quintana, J.; Dickerson, R. E. *J. Mol. Biol.* **1993**, *231*, 768–784.
27. Privé, G. G.; Heinemann, U.; Chandrasegaran, S.; Kan, L. S.; Kopka, M. L.; Dickerson, R. E. *Science* **1987**, *238*, 498–504.
28. Shui, X.; Sines, C. C.; McFail-Isom, L.; VanDerveer, D.; Williams, L. D. *Biochemistry* **1998**, *37*, 16877–16887.
29. Franklin, R. E.; Gosling, R. G. *Nature* **1953**, *171*, 740–741.
30. Hall, J. P.; Sanchez-Weatherby, J.; Alberti, C.; Quimper, C. H.; O’Sullivan, K.; Brazier, J. A.; Winter, G.; Sorensen, T.; Kelly, J. M.; Cardin, D. J.; Cardin, C. J. *J. Am. Chem. Soc.* **2014**, *136*, 17505–17512.
31. Pohl, F. M.; Jovin, T. M. *J. Mol. Biol.* **1972**, *67*, 375–396.
32. Wang, A. H. J.; Quigley, G. J.; Kolpak, F. J.; Crawford, J. L.; van Boom, J. H.; van der Marel, G.; Rich, A. *Nature* **1979**, *282*, 680–686.
33. Kelly, J. M.; Tossi, A. B.; McConnell, D. J.; OhUigin, C. *Nucleic Acids Res.* **1985**, *13*, 6017–6034.
34. Igarashi, K.; Kashiwagi, K. *Int. J. Biochem. Cell Biol.* **2010**, *42*, 39–51.
35. Lown, J. W. *J. Mol. Recognit.* **1994**, *7*, 79–88.
36. Kielkopf, C. L.; White, S.; Szewczyk, J. W.; Turner, J. M.; Baird, E. E.; Dervan, P. B.; Rees, D. C. *Science* **1998**, *282*, 111–115.
37. Takeda, Y.; Ohlendorf, D. H.; Anderson, W. F.; Matthews, B. W. *Science* **1983**, *221*, 1020–1026.
38. Pabo, C. O.; Sauer, R. T. *Annu. Rev. Biochem* **1984**, *53*, 293–321.
39. Neidle, S. *Nat. Prod. Rep.* **2001**, *18*, 291–309.
40. Kim, S. K.; Nordén, B. *FEBS Lett.* **1993**, *315*, 61–64.
41. Fornander, L. H.; Wu, L.; Billeter, M.; Lincoln, P.; Nordén, B. *J. Phys. Chem. B* **2013**, *117*, 5820–5830.
42. Lerman, L. S. *J. Mol. Biol.* **1961**, *3*, 18–30.
43. Dedon, P. C. *Curr. Protoc. Nucleic Acid Chem.* **2000**, 8.1.1–8.1.13.
44. Blackburn, G. M.; Gait, M. J.; Loakes, D.; Williams, D. M. *Nucleic Acids in Chemistry and Biology*; 3rd ed.; Royal Society of Chemistry, 2006.
45. Wassermann, K.; Markovits, J.; Jaxel, C.; Capranico, G.; Kohn, K. W.; Pommier, Y. *Mol. Pharmacol.* **1990**, *38*, 38–45.
46. Binaschi, M.; Farinosi, R.; Borgnetto, M. E.; Capranico, G. *Cancer Res.* **2000**, *60*, 3770–3776.

47. Canals, A.; Purciolas, M.; Aymami, J.; Coll, M. *Acta Crystallogr., Sect. D: Biol. Crystallogr.* **2005**, *61*, 1009–1012.
48. Vann, K. R.; Ergün, Y.; Zencir, S.; Oncuoglu, S.; Osheroff, N.; Topcu, Z. *Bioorg. Med. Chem. Lett.* **2016**, *26*, 1809–1812.
49. Gilman, A.; Philips, F. S. *Science* **1946**, *103*, 409–436.
50. Goldacre, R. J.; Loveless, A.; Ross, W. C. J. *Nature* **1949**, *163*, 667–669.
51. Decatris, M. P.; Sundar, S.; O’Byrne, K. J. *Cancer Treat. Rev.* **2004**, *30*, 53–81.
52. Wang, D.; Lippard, S. J. *Nat. Rev. Drug Discovery* **2005**, *4*, 307–320.
53. Bellon, S. F.; Coleman, J. H.; Lippard, S. J. *Biochemistry* **1991**, *30*, 8026–8035.
54. Bancroft, D. P.; Lepre, C. A.; Lippard, S. J. *J. Am. Chem. Soc.* **1990**, *112*, 6860–6871.
55. Takahara, P. M.; Rosenzweig, A. C.; Frederick, C. A.; Lippard, S. J. *Nature* **1995**, *377*, 649–652.
56. Jamieson, E. R.; Lippard, S. J. *Chem. Rev.* **1999**, *99*, 2467–2498.
57. von Tappeiner, H.; Jesionek, A. *Munch. Med. Wochenschr.* **1903**, *47*, 2042–2044.
58. van Straten, D.; Mashayekhi, V.; de Bruijn, S. H.; Oliveira, S.; Robinson, J. D. *Cancers* **2017**, *9*, 19.
59. Wilson, B. C.; Patterson, M. S. *Phys. Med. Biol.* **2008**, *53*, R61.
60. Bonnett, R.; Martínez, G. *Tetrahedron* **2001**, *57*, 9513–9547.
61. Moylan, C.; Scanlan, E. M.; Senge, M. O. *Curr. Med. Chem.* **2015**, *22*, 2238–2348.
62. Mari, C.; Pierroz, V.; Ferrari, S.; Gasser, G. *Chem. Sci.* **2015**, *6*, 2660–2686.
63. Poynton, F. E.; Bright, S. A.; Blasco, S.; Williams, D. C.; Kelly, J. M.; Gunnlaugsson, T. *Chem. Soc. Rev.* **2017**, *46*, 7706–7756.
64. Pineiro, M.; Pereira, M. M.; Formosinho, S. J.; Arnaut, L. G. *J. Phys. Chem. A* **2002**, *106*, 3787–3795.
65. Ding, H.; Yu, H.; Dong, Y.; Tian, R.; Huang, G.; Boothman, D. A.; Sumer, B. D.; Gao, J. *J. Control. Release* **2011**, *156*, 276–280.
66. Castano, A. P.; Demidova, T. N.; Hamblin, M. R. *Photodiagn. Photodyn. Ther.* **2004**, *1*, 279–293.
67. Kuimova, M. K.; Yahioğlu, G.; Ogilby, P. R. *J. Am. Chem. Soc.* **2009**, *131*, 332–340.
68. Nonell, S.; Flors, C. *Singlet Oxygen: Applications in Biosciences and Nanosciences*; Royal Society of Chemistry, 2016; Vol. 2.
69. Quasthoff, S.; Hartung, H. P. *J. Neurol.* **2002**, *249*, 9–17.
70. Allison, R. R.; Downie, G. H.; Cuenca, R.; Hu, X.-H.; Childs, C. J. H.; Sibata, C. H. *Photodiagn. Photodyn. Ther.* **2004**, *1*, 27–42.

71. Ormond, A.; Freeman, H. *Materials* **2013**, *6*, 817.
72. Zhu, W.; Gao, Y.-H.; Song, C.-H.; Lu, Z.-B.; Namulinda, T.; Han, Y.-P.; Yan, Y.-J.; Wang, L.-X.; Chen, Z.-L. *Photochem. Photobiol. Sci.* **2017**, *16*, 1623–1630.
73. Ndagi, U.; Mhlongo, N.; Soliman, M. E. *Drug Des., Dev. Ther.* **2017**, *11*, 599–616.
74. Rosenberg, B.; Van Camp, L.; Krigas, T. *Nature* **1965**, *205*, 698–699.
75. Rosenberg, B.; Vancamp, L.; Trosko, J. E.; Mansour, V. H. *Nature* **1969**, *222*, 385–386.
76. Ott, I.; Gust, R. *Arch. Pharm.* **2007**, *340*, 117–126.
77. Bruijninx, P. C. A.; Sadler, P. J. *Curr. Opin. Chem. Biol.* **2008**, *12*, 197–206.
78. Jaouen, G.; Metzler-Nolte, N. *Medicinal Organometallic Chemistry*; 1 ed.; Springer-Verlag Berlin Heidelberg, 2010.
79. Weidmann, A. G.; Komor, A. C.; Barton, J. K. *Comments Inorg. Chem.* **2014**, *34*, 114–123.
80. Zhang, P.; Chiu, C. K. C.; Huang, H.; Lam, Y. P. Y.; Habtemariam, A.; Malcomson, T.; Paterson, M. J.; Clarkson, G. J.; O'Connor, P. B.; Chao, H.; Sadler, P. J. *Angew. Chem. Int. Ed.* **2017**, *56*, 14898–14902.
81. Jia, P.; Ouyang, R.; Cao, P.; Tong, X.; Zhou, X.; Lei, T.; Zhao, Y.; Guo, N.; Chang, H.; Miao, Y.; Zhou, S. *J. Coord. Chem.* **2017**, *70*, 2175–2201.
82. Florea, A.-M.; Büsselberg, D. *Cancers* **2011**, *3*, 1351–1371.
83. Johnstone, T. C.; Suntharalingam, K.; Lippard, S. J. *Chem. Rev.* **2016**, *116*, 3436–3486.
84. Monneret, C. *Ann. Pharm. Fr.* **2011**, *69*, 286–295.
85. Bhargava, A.; Vaishampayan, U. N. *Expert Opin. Invest. Drugs* **2009**, *18*, 1787–1797.
86. Bednarski, P. J.; Grünert, R.; Zielzki, M.; Wellner, A.; Mackay, F. S.; Sadler, P. J. *Chem. Biol.* **2006**, *13*, 61–67.
87. Olszewski, U.; Claffey, J.; Hogan, M.; Tacke, M.; Zeillinger, R.; Bednarski, P. J.; Hamilton, G. *Invest. New Drugs* **2011**, *29*, 607–614.
88. Jaouen, G.; Vessières, A.; Top, S. *Chem. Soc. Rev.* **2015**, *44*, 8802–8817.
89. Jackson, B. A.; Barton, J. K. *J. Am. Chem. Soc.* **1997**, *119*, 12986–12987.
90. Ernst, R. J.; Song, H.; Barton, J. K. *J. Am. Chem. Soc.* **2009**, *131*, 2359–2366.
91. Thota, S.; Rodrigues, D. A.; Crans, D. C.; Barreiro, E. J. *J. Med. Chem.* **2018**, *61*, 5805–5821.
92. Monro, S.; Colón, K. L.; Yin, H.; Roque, J.; Konda, P.; Gujar, S.; Thummel, R. P.; Lilje, L.; Cameron, C. G.; McFarland, S. A. *Chem. Rev.* **2018**.

93. Jakubaszek, M.; Goud, B.; Ferrari, S.; Gasser, G. *Chem. Commun.* **2018**, *54*, 13040–13059.
94. Lin, K.; Zhao, Z.-Z.; Bo, H.-B.; Hao, X.-J.; Wang, J.-Q. *Front. Pharmacol.* **2018**, *9*.
95. Bergamo, A.; Messori, L.; Piccioli, F.; Cocchietto, M.; Sava, G. *Invest. New Drugs* **2003**, *21*, 401–411.
96. Alessio, E.; Mestroni, G.; Bergamo, A.; Sava, G. *Curr. Top. Med. Chem.* **2004**, *4*, 1525–1535.
97. Debreczeni, J. É.; Bullock, A. N.; Atilla, G. E.; Williams, D. S.; Bregman, H.; Knapp, S.; Meggers, E. *Angew. Chem. Int. Ed.* **2006**, *45*, 1580–1585.
98. Feng, L.; Geisselbrecht, Y.; Blanck, S.; Wilbuer, A.; Atilla-Gokcumen, G. E.; Filippakopoulos, P.; Kräling, K.; Celik, M. A.; Harms, K.; Maksimoska, J.; Marmorstein, R.; Frenking, G.; Knapp, S.; Essen, L.-O.; Meggers, E. *J. Am. Chem. Soc.* **2011**, *133*, 5976–5986.
99. Juris, A.; Balzani, V.; Barigelletti, F.; Campagna, S.; Belser, P.; von Zelewsky, A. *Coord. Chem. Rev.* **1988**, *84*, 85–277.
100. Balzani, V.; Juris, A.; Venturi, M.; Campagna, S.; Serroni, S. *Chem. Rev.* **1996**, *96*, 759–834.
101. Vos, J. G.; Kelly, J. M. *Dalton Trans.* **2006**, 4869–4883.
102. Puntoriero, F.; Nastasi, F.; Cavazzini, M.; Quici, S.; Campagna, S. *Coord. Chem. Rev.* **2007**, *251*, 536–545.
103. Konduri, R.; Ye, H.; MacDonnell, F. M.; Serroni, S.; Campagna, S.; Rajeshwar, K. *Angew. Chem. Int. Ed.* **2002**, *41*, 3185–3187.
104. Sens, C.; Romero, I.; Rodríguez, M.; Llobet, A.; Parella, T.; Benet-Buchholz, J. *J. Am. Chem. Soc.* **2004**, *126*, 7798–7799.
105. Buda, M.; Kalyuzhny, G.; Bard, A. J. *J. Am. Chem. Soc.* **2002**, *124*, 6090–6098.
106. Wardle, B. *Principles and Applications of Photochemistry*; 1st ed.; Wiley, 2009.
107. Dixon, I. M.; Lebon, E.; Sutra, P.; Igau, A. *Chem. Soc. Rev.* **2009**, *38*, 1621–1634.
108. Burstall, F. H. *J. Chem. Soc.* **1936**, 173–175.
109. Durham, B.; Caspar, J. V.; Nagle, J. K.; Meyer, T. J. *J. Am. Chem. Soc.* **1982**, *104*, 4803–4810.
110. Caspar, J. V.; Meyer, T. J. *J. Am. Chem. Soc.* **1983**, *105*, 5583–5590.
111. Lewis, G. N.; Lipkin, D.; Magel, T. T. *J. Am. Chem. Soc.* **1941**, *63*, 3005–3018.
112. Lewis, G. N.; Kasha, M. *J. Am. Chem. Soc.* **1945**, *67*, 994–1003.

113. Turro, N. J.; Ramamurthy, V.; Scaiano, J. C. *Principles of Molecular Photochemistry: An Introduction*; 1st ed.; University Science Books, 2009.
114. Marian, C. M. *Wiley Interdiscip. Rev.: Comput. Mol. Sci.* **2012**, *2*, 187–203.
115. Caspar, J. V.; Sullivan, B. P.; Kober, E. M.; Meyer, T. J. *Chem. Phys. Lett.* **1982**, *91*, 91–95.
116. Allen, G. H.; White, R. P.; Rillema, D. P.; Meyer, T. J. *J. Am. Chem. Soc.* **1984**, *106*, 2613–2620.
117. Vining, W. J.; Caspar, J. V.; Meyer, T. J. *J. Phys. Chem.* **1985**, *89*, 1095–1099.
118. Barqawi, K. R.; Llobet, A.; Meyer, T. J. *J. Am. Chem. Soc.* **1988**, *110*, 7751–7759.
119. Barqawi, K. R.; Murtaza, Z.; Meyer, T. J. *J. Phys. Chem.* **1991**, *95*, 47–50.
120. Thompson, D. W.; Ito, A.; Meyer, T. J. *Pure Appl. Chem.* **2013**, *85*, 1257–1305.
121. Liu, Y.; Hammitt, R.; Lutterman, D. A.; Joyce, L. E.; Thummel, R. P.; Turro, C. *Inorg. Chem.* **2009**, *48*, 375–385.
122. Masschelein, A.; Jacquet, L.; Kirsch-De Mesmaeker, A.; Nasielski, J. *Inorg. Chem.* **1990**, *29*, 855–860.
123. Salierno, M.; Marceca, E.; Peterka, D. S.; Yuste, R.; Etchenique, R. *J. Inorg. Biochem.* **2010**, *104*, 418–422.
124. Garner, R. N.; Gallucci, J. C.; Dunbar, K. R.; Turro, C. *Inorg. Chem.* **2011**, *50*, 9213–9215.
125. Respondek, T.; Garner, R. N.; Herroon, M. K.; Podgorski, I.; Turro, C.; Kodanko, J. *J. Am. Chem. Soc.* **2011**, *133*, 17164–17167.
126. Howerton, B. S.; Heidary, D. K.; Glazer, E. C. *J. Am. Chem. Soc.* **2012**, *134*, 8324–8327.
127. Wachter, E.; Heidary, D. K.; Howerton, B. S.; Parkin, S.; Glazer, E. C. *Chem. Commun.* **2012**, *48*, 9649–9651.
128. Palmer, A. M.; Peña, B.; Sears, R. B.; Chen, O.; El Ojaimi, M.; Thummel, R. P.; Dunbar, K. R.; Turro, C. *Philos. Trans. R. Soc., A* **2013**, *371*, 20120135.
129. Sgambellone, M. A.; David, A.; Garner, R. N.; Dunbar, K. R.; Turro, C. *J. Am. Chem. Soc.* **2013**, *135*, 11274–11282.
130. Hidayatullah, A. N.; Wachter, E.; Heidary, D. K.; Parkin, S.; Glazer, E. C. *Inorg. Chem.* **2014**, *53*, 10030–10032.
131. Respondek, T.; Sharma, R.; Herroon, M. K.; Garner, R. N.; Knoll, J. D.; Cueny, E.; Turro, C.; Podgorski, I.; Kodanko, J. *J. ChemMedChem* **2014**, *9*, 1306–1315.

132. Sainuddin, T.; McCain, J.; Pinto, M.; Yin, H.; Gibson, J.; Hetu, M.; McFarland, S. A. *Inorg. Chem.* **2016**, *55*, 83–95.
133. Cuello-Garibo, J.-A.; Meijer, M. S.; Bonnet, S. *Chem. Commun.* **2017**, *53*, 6768–6771.
134. White, J. K.; Schmehl, R. H.; Turro, C. *Inorg. Chim. Acta* **2017**, *454*, 7–20.
135. Li, A.; Turro, C.; Kodanko, J. J. *Chem. Commun.* **2018**, *54*, 1280–1290.
136. Chambron, J. C.; Sauvage, J. P.; Amouyal, E.; Koffi, P. *Nouv. J. Chim.* **1985**, *9*, 527–529.
137. Olson, E. J. C.; Hu, D.; Hörmann, A.; Jonkman, A. M.; Arkin, M. R.; Stemp, E. D. A.; Barton, J. K.; Barbara, P. F. *J. Am. Chem. Soc.* **1997**, *119*, 11458–11467.
138. Olofsson, J.; Önfelt, B.; Lincoln, P. *J. Phys. Chem. A* **2004**, *108*, 4391–4398.
139. Coates, C. G.; Callaghan, P.; McGarvey, J. J.; Kelly, J. M.; Jacquet, L.; Kirsch-De Mesmaeker, A. *J. Mol. Struct.* **2001**, *598*, 15–25.
140. Lincoln, P.; Nordén, B. *J. Phys. Chem. B* **1998**, *102*, 9583–9594.
141. Friedman, A. E.; Kumar, C. V.; Turro, N. J.; Barton, J. K. *Nucleic Acids Res.* **1991**, *19*, 2595–2602.
142. Hartshorn, R. M.; Barton, J. K. *J. Am. Chem. Soc.* **1992**, *114*, 5919–5925.
143. Hiort, C.; Lincoln, P.; Norden, B. *J. Am. Chem. Soc.* **1993**, *115*, 3448–3454.
144. Tuite, E.; Lincoln, P.; Nordén, B. *J. Am. Chem. Soc.* **1997**, *119*, 239–240.
145. McKinley, A. W.; Lincoln, P.; Tuite, E. M. *Coord. Chem. Rev.* **2011**, *255*, 2676–2692.
146. McKinley, A. W.; Lincoln, P.; Tuite, E. M. *Dalton Trans.* **2013**, *42*, 4081–4090.
147. Dupureur, C. M.; Barton, J. K. *J. Am. Chem. Soc.* **1994**, *116*, 10286–10287.
148. Greguric, A.; Greguric, I. D.; Hambley, T. W.; Aldrich-Wright, J. R.; Collins, J. G. *J. Chem. Soc., Dalton Trans.* **2002**, 849–855.
149. Coates, C. G.; Jacquet, L.; McGarvey, J. J.; Bell, S. E. J.; Al-Obaidi, A. H. R.; Kelly, J. M. *Chem. Commun.* **1996**, 35–36.
150. Coates, C. G.; Jacquet, L.; McGarvey, J. J.; Bell, S. E. J.; Al-Obaidi, A. H. R.; Kelly, J. M. *J. Am. Chem. Soc.* **1997**, *119*, 7130–7136.
151. Coates, C. G.; Olofsson, J.; Coletti, M.; McGarvey, J. J.; Önfelt, B.; Lincoln, P.; Norden, B.; Tuite, E.; Matousek, P.; Parker, A. W. *J. Phys. Chem. B* **2001**, *105*, 12653–12664.
152. Önfelt, B.; Lincoln, P.; Nordén, B.; Baskin, J. S.; Zewail, A. H. *Proc. Natl. Acad. Sci. U. S. A.* **2000**, *97*, 5708–5713.
153. Westerlund, F.; Pierard, F.; Eng, M. P.; Nordén, B.; Lincoln, P. *J. Phys. Chem. B* **2005**, *109*, 17327–17332.

154. Mårtensson, A. K. F.; Lincoln, P. *Dalton Trans.* **2015**, *44*, 3604–3613.
155. Liu, J. G.; Ye, B. H.; Zhang, Q. L.; Zou, X. H.; Zhen, Q. X.; Tian, X.; Ji, L. N. *JBIC, J. Biol. Inorg. Chem.* **2000**, *5*, 119–128.
156. Hall, J. P.; O’Sullivan, K.; Naseer, A.; Smith, J. A.; Kelly, J. M.; Cardin, C. J. *Proc. Natl. Acad. Sci. U. S. A.* **2011**, *108*, 17610–17614.
157. Niyazi, H.; Hall, J. P.; O’Sullivan, K.; Winter, G.; Sorensen, T.; Kelly, J. M.; Cardin, C. J. *Nat. Chem.* **2012**, *4*, 621–628.
158. Song, H.; Kaiser, J. T.; Barton, J. K. *Nat. Chem.* **2012**, *4*, 615–620.
159. Hall, J. P.; Cook, D.; Morte, S. R.; McIntyre, P.; Buchner, K.; Beer, H.; Cardin, D. J.; Brazier, J. A.; Winter, G.; Kelly, J. M.; Cardin, C. J. *J. Am. Chem. Soc.* **2013**, *135*, 12652–12659.
160. Hall, J. P.; Beer, H.; Buchner, K.; Cardin, D. J.; Cardin, C. J. *Philos. Trans. R. Soc., A* **2013**, *371*, 20120525.
161. Hall, J. P.; Beer, H.; Buchner, K.; Cardin, D. J.; Cardin, C. J. *Organometallics* **2015**, *34*, 2481–2486.
162. Hall, J. P.; Keane, P. M.; Beer, H.; Buchner, K.; Winter, G.; Sorensen, T. L.; Cardin, D. J.; Brazier, J. A.; Cardin, C. J. *Nucleic Acids Res.* **2016**, *44*, 9472–9482.
163. Jenkins, Y.; Friedman, A. E.; Turro, N. J.; Barton, J. K. *Biochemistry* **1992**, *31*, 10809–10816.
164. Andersson, J.; Fornander, L. H.; Abrahamsson, M.; Tuite, E.; Nordell, P.; Lincoln, P. *Inorg. Chem.* **2013**, *52*, 1151–1159.
165. Friedman, A. E.; Chambron, J. C.; Sauvage, J. P.; Turro, N. J.; Barton, J. K. *J. Am. Chem. Soc.* **1990**, *112*, 4960–4962.
166. Ortmans, I.; Elias, B.; Kelly, J. M.; Moucheron, C.; Kirsch-DeMesmaeker, A. *Dalton Trans.* **2004**, 668–676.
167. Moucheron, C.; Kirsch-De Mesmaeker, A. *J. Phys. Org. Chem.* **1998**, *11*, 577–583.
168. Ghizdavu, L.; Pierard, F.; Rickling, S.; Aury, S.; Surin, M.; Beljonne, D.; Lazzaroni, R.; Murat, P.; Defrancq, E.; Moucheron, C.; Kirsch-De Mesmaeker, A. *Inorg. Chem.* **2009**, *48*, 10988–10994.
169. Ambroise, A.; Maiya, B. G. *Inorg. Chem.* **2000**, *39*, 4256–4263.
170. Cloonan, S. M.; Elmes, R. B. P.; Erby, M.; Bright, S. A.; Poynton, F. E.; Nolan, D. E.; Quinn, S. J.; Gunnlaugsson, T.; Williams, D. C. *J. Med. Chem.* **2015**, *58*, 4494–4505.
171. Luo, Z.; Yu, L.; Yang, F.; Zhao, Z.; Yu, B.; Lai, H.; Wong, K.-H.; Ngai, S.-M.; Zheng, W.; Chen, T. *Metallomics* **2014**, *6*, 1480–1490.

172. Gill, M. R.; Garcia-Lara, J.; Foster, S. J.; Smythe, C.; Battaglia, G.; Thomas, J. A. *Nat. Chem.* **2009**, *1*, 662–667.
173. Deepika, N.; Kumar, Y. P.; Shobha Devi, C.; Reddy, P. V.; Srishailam, A.; Satyanarayana, S. *JBIC, J. Biol. Inorg. Chem.* **2013**, *18*, 751–766.
174. Véry, T.; Ambrosek, D.; Otsuka, M.; Gourlaouen, C.; Assfeld, X.; Monari, A.; Daniel, C. *Chem. Eur. J.* **2014**, *20*, 12901–12909.
175. Wragg, A.; Gill, M. R.; Turton, D.; Adams, H.; Roseveare, T. M.; Smythe, C.; Su, X.; Thomas, J. A. *Chem. Eur. J.* **2014**, *20*, 14004–14011.
176. Han, B.-J.; Jiang, G.-B.; Yao, J.-H.; Li, W.; Wang, J.; Huang, H.-L.; Liu, Y.-J. *Spectrochim. Acta, Part A* **2015**, *135*, 840–849.
177. Wenzel, M.; de Almeida, A.; Bigaeva, E.; Kavanagh, P.; Picquet, M.; Le Gendre, P.; Bodio, E.; Casini, A. *Inorg. Chem.* **2016**, *55*, 2544–2557.
178. Puckett, C. A.; Barton, J. K. *J. Am. Chem. Soc.* **2007**, *129*, 46–47.
179. Mari, C.; Pierroz, V.; Rubbiani, R.; Patra, M.; Hess, J.; Spingler, B.; Oehninger, L.; Schur, J.; Ott, I.; Salassa, L.; Ferrari, S.; Gasser, G. *Chem. Eur. J.* **2014**, *20*, 14421–14436.
180. Svensson, F. R.; Matson, M.; Li, M.; Lincoln, P. *Biophys. Chem.* **2010**, *149*, 102–106.
181. Matson, M.; Svensson, F. R.; Nordén, B.; Lincoln, P. *J. Phys. Chem. B* **2011**, *115*, 1706–1711.
182. Schatzschneider, U.; Niesel, J.; Ott, I.; Gust, R.; Alborzinia, H.; Wölfl, S. *ChemMedChem* **2008**, *3*, 1104–1109.
183. O'Reilly, F.; Kelly, J.; Kirsch-De Mesmaeker, A. *Chem. Commun.* **1996**, 1013–1014.
184. O'Reilly, F. M.; Kelly, J. M. *New J. Chem.* **1998**, *22*, 215–217.
185. O'Reilly, F. M.; Kelly, J. M. *J. Phys. Chem. B* **2000**, *104*, 7206–7213.
186. Pisani, M. J.; Weber, D. K.; Heimann, K.; Collins, J. G.; Keene, F. R. *Metallomics* **2010**, *2*, 393–396.
187. Pisani, M. J.; Fromm, P. D.; Mulyana, Y.; Clarke, R. J.; Körner, H.; Heimann, K.; Collins, J. G.; Keene, F. R. *ChemMedChem* **2011**, *6*, 848–858.
188. Gorle, A. K.; Feterl, M.; Warner, J. M.; Wallace, L.; Keene, F. R.; Collins, J. G. *Dalton Trans.* **2014**, *43*, 16713–16725.
189. Li, X.; Gorle, A. K.; Ainsworth, T. D.; Heimann, K.; Woodward, C. E.; Collins, J. G.; Keene, F. R. *Dalton Trans.* **2015**, *44*, 3594–3603.
190. Rajput, C.; Rutkaite, R.; Swanson, L.; Haq, I.; Thomas, J. A. *Chem. Eur. J.* **2006**, *12*, 4611–4619.

191. Puckett, C. A.; Barton, J. K. *J. Am. Chem. Soc.* **2009**, *131*, 8738–8739.
192. Puckett, C. A.; Barton, J. K. *Biorg. Med. Chem.* **2010**, *18*, 3564–3569.
193. Cosgrave, L.; Devocelle, M.; Forster, R. J.; Keyes, T. E. *Chem. Commun.* **2010**, *46*, 103–105.
194. Blackmore, L.; Moriarty, R.; Dolan, C.; Adamson, K.; Forster, R. J.; Devocelle, M.; Keyes, T. E. *Chem. Commun.* **2013**, *49*, 2658–2660.
195. Joshi, T.; Pierroz, V.; Ferrari, S.; Gasser, G. *ChemMedChem* **2014**, *9*, 1419–1427.
196. Mari, C.; Pierroz, V.; Leonidova, A.; Ferrari, S.; Gasser, G. *Eur. J. Inorg. Chem.* **2015**, *2015*, 3879–3891.
197. Marcélis, L.; Kajouj, S.; Ghesquière, J.; Fettweis, G.; Coupienne, I.; Lartia, R.; Surin, M.; Defrancq, E.; Piette, J.; Moucheron, C.; Kirsch-De Mesmaeker, A. *Eur. J. Inorg. Chem.* **2016**, *2016*, 2902–2911.
198. Burke, C. S.; Byrne, A.; Keyes, T. E. *J. Am. Chem. Soc.* **2018**, *140*, 6945–6955.
199. Burke, C. S.; Byrne, A.; Keyes, T. E. *Angew. Chem. Int. Ed.* **2018**, *57*, 12420–12424.
200. Le Gac, S.; Foucart, M.; Gerbaux, P.; Defrancq, E.; Moucheron, C.; Kirsch-De Mesmaeker, A. *Dalton Trans.* **2010**, *39*, 9672–9683.
201. Copeland, K. D.; Fitzsimons, M. P.; Houser, R. P.; Barton, J. K. *Biochemistry* **2002**, *41*, 343–356.
202. Elias, B.; Kirsch-De Mesmaeker, A. *Coord. Chem. Rev.* **2006**, *250*, 1627–1641.
203. Marcélis, L.; Ghesquière, J.; Garnir, K.; Kirsch-De Mesmaeker, A.; Moucheron, C. *Coord. Chem. Rev.* **2012**, *256*, 1569–1582.
204. Fukuzumi, S.; Miyao, H.; Ohkubo, K.; Suenobu, T. *J. Phys. Chem. A* **2005**, *109*, 3285–3294.
205. Harriman, A. *J. Phys. Chem.* **1987**, *91*, 6102–6104.
206. Moucheron, C.; Kirsch-De Mesmaeker, A.; Kelly, J. M. *J. Photochem. Photobiol., B* **1997**, *40*, 91–106.
207. Kelly, J. M.; McConnell, D. J.; OhUigin, C.; Tossi, A. B.; Kirsch-De Mesmaeker, A.; Masschelein, A.; Nasielski, J. *J. Chem. Soc., Chem. Commun.* **1987**, 1821–1823.
208. Blasius, R.; Moucheron, C.; Kirsch-De Mesmaeker, A. *Eur. J. Inorg. Chem.* **2004**, *2004*, 3971–3979.
209. Kelly, J. M.; Feeney, M. M.; Tossi, A. B.; Lecomte, J.-P.; Kirsch-De Mesmaeker, A. *Anti-Cancer Drug Des.* **1990**, *5*, 69–75.
210. Kirsch-De Mesmaeker, A.; Orellana, G.; Barton, J. K.; Turro, N. J. *Photochem. Photobiol.* **1990**, *52*, 461–472.

211. Lecomte, J.-P.; Kirsch-De Mesmaeker, A.; Feeney, M. M.; Kelly, J. M. *Inorg. Chem.* **1995**, *34*, 6481–6491.
212. Lecomte, J.-P.; Kirsch-De Mesmaeker, A.; Kelly, J. M.; Tossi, A. B.; Görner, H. *Photochem. Photobiol.* **1992**, *55*, 681–689.
213. Marcélis, L.; Rebarz, M.; Lemaur, V.; Fron, E.; De Winter, J.; Moucheron, C.; Gerbaux, P.; Beljonne, D.; Sliwa, M.; Kirsch-De Mesmaeker, A. *J. Phys. Chem. B* **2015**, *119*, 4488–4500.
214. Tan-Sien-Hee, L.; Kirsch-De Mesmaeker, A. *J. Chem. Soc., Dalton Trans.* **1994**, 3651–3658.
215. Candeias, L. P.; Steenken, S. *J. Am. Chem. Soc.* **1989**, *111*, 1094–1099.
216. Steenken, S. *Free Radical Res. Commun.* **1992**, *16*, 349–379.
217. Reynisson, J.; Steenken, S. *Phys. Chem. Chem. Phys.* **2002**, *4*, 527–532.
218. Elias, B.; Creely, C.; Doorley, G. W.; Feeney, M. M.; Moucheron, C.; Kirsch-De Mesmaeker, A.; Dyer, J.; Grills, D. C.; George, M. W.; Matousek, P.; Parker, A. W.; Towrie, M.; Kelly, J. M. *Chem. Eur. J.* **2008**, *14*, 369–375.
219. Feeney, M. M.; Kelly, J. M.; Tossi, A. B.; Kirsch-De Mesmaeker, A.; Lecomte, J.-P. *J. Photochem. Photobiol., B* **1994**, *23*, 69–78.
220. Lewis, F. D.; Wu, T.; Liu, X.; Letsinger, R. L.; Greenfield, S. R.; Miller, S. E.; Wasielewski, M. R. *J. Am. Chem. Soc.* **2000**, *122*, 2889–2902.
221. Orlova, G.; Goddard, J. D. *J. Org. Chem.* **2001**, *66*, 4026–4035.
222. Weinberg, D. R.; Gagliardi, C. J.; Hull, J. F.; Murphy, C. F.; Kent, C. A.; Westlake, B. C.; Paul, A.; Ess, D. H.; McCafferty, D. G.; Meyer, T. J. *Chem. Rev.* **2012**, *112*, 4016–4093.
223. Jacquet, L.; Kelly, J. M.; Kirsch-De Mesmaeker, A. *J. Chem. Soc., Chem. Commun.* **1995**, 913–914.
224. Tossi, A. B.; Kelly, J. M. *Photochem. Photobiol.* **1989**, *49*, 545–556.
225. Herman, L.; Ghosh, S.; Defrancq, E.; Kirsch-De Mesmaeker, A. *J. Phys. Org. Chem.* **2008**, *21*, 670–681.
226. Armitage, B. *Chem. Rev.* **1998**, *98*, 1171–1200.
227. Rebarz, M.; Ghesquière, J.; Boisdenghien, A.; Defrancq, E.; Moucheron, C.; Kirsch-De Mesmaeker, A. *Inorg. Chem.* **2010**, *49*, 10867–10874.
228. Blasius, R.; Nierengarten, H.; Luhmer, M.; Constant, J.-F.; Defrancq, E.; Dumy, P.; van Dorsselaer, A.; Moucheron, C.; Kirsch-DeMesmaeker, A. *Chem. Eur. J.* **2005**, *11*, 1507–1517.

229. Jacquet, L.; Davies, R. J. H.; Kirsch-De Mesmaeker, A.; Kelly, J. M. *J. Am. Chem. Soc.* **1997**, *119*, 11763–11768.
230. Perrier, S.; Mugeniwabagara, E.; Kirsch-De Mesmaeker, A.; Hore, P. J.; Luhmer, M. *J. Am. Chem. Soc.* **2009**, *131*, 12458–12465.
231. Estalayo-Adrián, S.; Garnir, K.; Moucheron, C. *Chem. Commun.* **2018**, *54*, 322–337.
232. Zeng, L.; Gupta, P.; Chen, Y.; Wang, E.; Ji, L.; Chao, H.; Chen, Z.-S. *Chem. Soc. Rev.* **2017**, *46*, 5771–5804.
233. Lincoln, R.; Kohler, L.; Monro, S.; Yin, H.; Stephenson, M.; Zong, R.; Chouai, A.; Dorsey, C.; Hennigar, R.; Thummel, R. P.; McFarland, S. A. *J. Am. Chem. Soc.* **2013**, *135*, 17161–17175.
234. Palmer, A. M.; Peña, B.; Sears, R. B.; Chen, O.; El Ojaimi, M.; Thummel, R. P.; Dunbar, K. R.; Turro, C. *Philos. Trans. R. Soc., A* **2013**, *371*, 20120135/20120131–20120135/20120110.
235. Peña, B.; David, A.; Pavani, C.; Baptista, M. S.; Pellois, J.-P.; Turro, C.; Dunbar, K. R. *Organometallics* **2014**, *33*, 1100–1103.
236. Ghosh, G.; Colón, K. L.; Fuller, A.; Sainuddin, T.; Bradner, E.; McCain, J.; Monro, S. M. A.; Yin, H.; Hetu, M. W.; Cameron, C. G.; McFarland, S. A. *Inorg. Chem.* **2018**, *57*, 7694–7712.
237. Fong, J.; Kasimova, K.; Arenas, Y.; Kaspler, P.; Lazic, S.; Mandel, A.; Lilge, L. *Photochem. Photobiol. Sci.* **2015**, *14*, 2014–2023.
238. Arenas, Y.; Monro, S.; Shi, G.; Mandel, A.; McFarland, S.; Lilge, L. *Photodiagn. Photodyn. Ther.* **2013**, *10*, 615–625.
239. Shi, G.; Monro, S.; Hennigar, R.; Colpitts, J.; Fong, J.; Kasimova, K.; Yin, H.; DeCoste, R.; Spencer, C.; Chamberlain, L.; Mandel, A.; Lilge, L.; McFarland, S. A. *Coord. Chem. Rev.* **2015**, *282–283*, 127–138.
240. Intravesical Photodynamic Therapy (PDT) in BCG Refractory High-Risk Non-muscle Invasive Bladder Cancer (NMIBC) Patients. <https://clinicaltrials.gov/ct2/show/NCT03053635> (accessed January 2019).
241. Kalinina, S.; Breymayer, J.; Reeß, K.; Lilge, L.; Mandel, A.; Rück, A. *J. Biophotonics* **2018**, *11*, e201800085.
242. Rosi, N. L.; Mirkin, C. A. *Chem. Rev.* **2005**, *105*, 1547–1562.
243. Boisselier, E.; Astruc, D. *Chem. Soc. Rev.* **2009**, *38*, 1759–1782.
244. Giljohann, D. A.; Seferos, D. S.; Daniel, W. L.; Massich, M. D.; Patel, P. C.; Mirkin, C. A. *Angew. Chem. Int. Ed.* **2010**, *49*, 3280–3294.

245. Dreaden, E. C.; Mackey, M. A.; Huang, X.; Kang, B.; El-Sayed, M. A. *Chem. Soc. Rev.* **2011**, *40*, 3391–3404.
246. Dreaden, E. C.; Alkilany, A. M.; Huang, X.; Murphy, C. J.; El-Sayed, M. A. *Chem. Soc. Rev.* **2012**, *41*, 2740–2779.
247. Eustis, S.; El-Sayed, M. A. *Chem. Soc. Rev.* **2006**, *35*, 209–217.
248. Daniel, M. C.; Astruc, D. *Chem. Rev.* **2004**, *104*, 293–346.
249. Davis, M. E.; Chen, Z.; Shin, D. M. *Nat. Rev. Drug Discovery* **2008**, *7*, 771–782.
250. Chithrani, B. D.; Ghazani, A. A.; Chan, W. C. W. *Nano Lett.* **2006**, *6*, 662–668.
251. Jiang, W.; Kim, B. Y. S.; Rutka, J. T.; Chan, W. C. W. *Nature Nanotechnology* **2008**, *3*, 145–150.
252. Ghosh, P.; Han, G.; De, M.; Kim, C. K.; Rotello, V. M. *Adv. Drug Delivery Rev.* **2008**, *60*, 1307–1315.
253. Dhar, S.; Daniel, W. L.; Giljohann, D. A.; Mirkin, C. A.; Lippard, S. J. *J. Am. Chem. Soc.* **2009**, *131*, 14652–14653.
254. Ding, Y.; Jiang, Z.; Saha, K.; Kim, C. S.; Kim, S. T.; Landis, R. F.; Rotello, V. M. *Mol. Ther.* **2014**, *22*, 1075–1083.
255. Mendes, R.; Fernandes, A. R.; Baptista, P. V. *Genes* **2017**, *8*, 94.
256. Gharatape, A.; Davaran, S.; Salehi, R.; Hamishehkar, H. *RSC Adv.* **2016**, *6*, 111482–111516.
257. Riley, R. S.; Day, E. S. *Wiley Interdiscip. Rev.: Nanomed. Nanobiotechnol.* **2017**, *9*, e1449.
258. Lucky, S. S.; Soo, K. C.; Zhang, Y. *Chem. Rev.* **2015**, *115*, 1990–2042.
259. García Calavia, P.; Bruce, G.; Pérez-García, L.; Russell, D. A. *Photochem. Photobiol. Sci.* **2018**, *17*, 1534–1552.
260. Hone, D. C.; Walker, P. I.; Evans-Gowing, R.; FitzGerald, S.; Beeby, A.; Chambrier, I.; Cook, M. J.; Russell, D. A. *Langmuir* **2002**, *18*, 2985–2987.
261. Wieder, M. E.; Hone, D. C.; Cook, M. J.; Handsley, M. M.; Gavrilovic, J.; Russell, D. A. *Photochem. Photobiol. Sci.* **2006**, *5*, 727–734.
262. Camerin, M.; Magaraggia, M.; Soncin, M.; Jori, G.; Moreno, M.; Chambrier, I.; Cook, M. J.; Russell, D. A. *Eur. J. Cancer* **2010**, *46*, 1910–1918.
263. Pramod, P.; Sudeep, P. K.; Thomas, K. G.; Kamat, P. V. *J. Phys. Chem. B* **2006**, *110*, 20737–20741.
264. Elmes, R. B. P.; Orange, K. N.; Cloonan, S. M.; Williams, D. C.; Gunnlaugsson, T. *J. Am. Chem. Soc.* **2011**, *133*, 15862–15865.

265. Zedler, L.; Theil, F.; Csáki, A.; Fritzsche, W.; Rau, S.; Schmitt, M.; Popp, J.; Dietzek, B. *RSC Adv.* **2012**, *2*, 4463–4471.
266. Rogers, N. J.; Claire, S.; Harris, R. M.; Farabi, S.; Zikeli, G.; Styles, I. B.; Hodges, N. J.; Pikramenou, Z. *Chem. Commun.* **2014**, *50*, 617–619.
267. Leung, F. C.-M.; Tam, A. Y.-Y.; Au, V. K.-M.; Li, M.-J.; Yam, V. W.-W. *ACS Appl. Mater. Interfaces* **2014**, *6*, 6644–6653.
268. Moreau, J.; Lux, F.; Four, M.; Olesiak-Banska, J.; Matczyszyn, K.; Perriat, P.; Frochot, C.; Arnoux, P.; Tillement, O.; Samoc, M.; Ponterini, G.; Roux, S.; Lemercier, G. *Phys. Chem. Chem. Phys.* **2014**, *16*, 14826–14833.
269. Osborne, S. A. M.; Pikramenou, Z. *Faraday Discuss.* **2015**, *185*, 219–231.
270. Zhang, P.; Wang, J.; Huang, H.; Yu, B.; Qiu, K.; Huang, J.; Wang, S.; Jiang, L.; Gasser, G.; Ji, L.; Chao, H. *Biomaterials* **2015**, *63*, 102–114.
271. Martínez-Calvo, M.; Orange, K. N.; Elmes, R. B. P.; la Cour Poulsen, B.; Williams, D. C.; Gunnlaugsson, T. *Nanoscale* **2016**, *8*, 563–574.
272. Ryan, G. J.; Quinn, S.; Gunnlaugsson, T. *Inorg. Chem.* **2008**, *47*, 401–403.
273. Elmes, R. B. P.; Gunnlaugsson, T. *Tetrahedron Lett.* **2010**, *51*, 4082–4087.
274. Elmes, R. B. P.; Kitchen, J. A.; Williams, D. C.; Gunnlaugsson, T. *Dalton Trans.* **2012**, *41*, 6607–6610.
275. Elmes, R. B. P.; Erby, M.; Bright, S. A.; Williams, D. C.; Gunnlaugsson, T. *Chem. Commun.* **2012**, *48*, 2588–2590.
276. Kitchen, J. A.; Boyle, E. M.; Gunnlaugsson, T. *Inorg. Chim. Acta* **2012**, *381*, 236–242.
277. Ryan, G. J.; Poynton, F. E.; Elmes, R. B. P.; Erby, M.; Williams, D. C.; Quinn, S. J.; Gunnlaugsson, T. *Dalton Trans.* **2015**, *44*, 16332–16344.
278. Shanmugaraju, S.; la Cour Poulsen, B.; Arisa, T.; Umadevi, D.; Dalton, H. L.; Hawes, C. S.; Estalayo-Adrián, S.; Savyasachi, A. J.; Watson, G. W.; Williams, D. C.; Gunnlaugsson, T. *Chem. Commun.* **2018**, *54*, 4120–4123.
279. Keane, P. M.; Poynton, F. E.; Hall, J. P.; Sazanovich, I. V.; Towrie, M.; Gunnlaugsson, T.; Quinn, S. J.; Cardin, C. J.; Kelly, J. M. *Angew. Chem. Int. Ed.* **2015**, *54*, 8364–8368.
280. Keane, P. M.; Poynton, F. E.; Hall, J. P.; Clark, I. P.; Sazanovich, I. V.; Towrie, M.; Gunnlaugsson, T.; Quinn, S. J.; Cardin, C. J.; Kelly, J. M. *Faraday Discuss.* **2015**, *185*, 455–469.

281. Keane, P. M.; Poynton, F. E.; Hall, J. P.; Clark, I. P.; Sazanovich, I. V.; Towrie, M.; Gunnlaugsson, T.; Quinn, S. J.; Cardin, C. J.; Kelly, J. M. *J. Phys. Chem. Lett.* **2015**, *6*, 734–738.
282. Hall, J. P.; Poynton, F. E.; Keane, P. M.; Gurung, S. P.; Brazier, J. A.; Cardin, D. J.; Winter, G.; Gunnlaugsson, T.; Sazanovich, I. V.; Towrie, M.; Cardin, C. J.; Kelly, J. M.; Quinn, S. J. *Nat. Chem.* **2015**, *7*, 961–967.
283. Poynton, F. E.; Hall, J. P.; Keane, P. M.; Schwarz, C.; Sazanovich, I. V.; Towrie, M.; Gunnlaugsson, T.; Cardin, C. J.; Cardin, D. J.; Quinn, S. J.; Long, C.; Kelly, J. M. *Chem. Sci.* **2016**, *7*, 3075–3084.
284. Keane, P. M.; Hall, J. P.; Poynton, F. E.; Poulsen, B. C.; Gurung, S. P.; Clark, I. P.; Sazanovich, I. V.; Towrie, M.; Gunnlaugsson, T.; Quinn, S. J.; Cardin, C. J.; Kelly, J. M. *Chem. Eur. J.* **2017**, *23*, 10344–10351.
285. Turro, C.; Bossmann, S. H.; Jenkins, Y.; Barton, J. K.; Turro, N. J. *J. Am. Chem. Soc.* **1995**, *117*, 9026–9032.
286. Nair, R. B.; Cullum, B. M.; Murphy, C. J. *Inorg. Chem.* **1997**, *36*, 962–965.
287. Coates, C. G.; Callaghan, P. L.; McGarvey, J. J.; Kelly, J. M.; Kruger, P. E.; Higgins, M. E. *J. Raman Spectrosc.* **2000**, *31*, 283–288.
288. Brennaman, M. K.; Alstrum-Acevedo, J. H.; Fleming, C. N.; Jang, P.; Meyer, T. J.; Papanikolas, J. M. *J. Am. Chem. Soc.* **2002**, *124*, 15094–15098.
289. Olofsson, J.; Önfelt, B.; Lincoln, P.; Nordén, B.; Matousek, P.; Parker, A. W.; Tuite, E. *J. Inorg. Biochem.* **2002**, *91*, 286–297.
290. Önfelt, B.; Olofsson, J.; Lincoln, P.; Nordén, B. *J. Phys. Chem. A* **2003**, *107*, 1000–1009.
291. Brennaman, M. K.; Meyer, T. J.; Papanikolas, J. M. *J. Phys. Chem. A* **2004**, *108*, 9938–9944.
292. Daniel, C. *Coord. Chem. Rev.* **2015**, *282–283*, 19–32.
293. Gao, X.; Shi, S.; Yao, J.-L.; Zhao, J.; Yao, T.-M. *Dalton Trans.* **2015**, *44*, 19264–19274.
294. Chambron, J.-C.; Sauvage, J.-P. *Chem. Phys. Lett.* **1991**, *182*, 603–607.
295. Coates, C. G.; McGarvey, J. J.; Callaghan, P. L.; Coletti, M.; Hamilton, J. G. *J. Phys. Chem. B* **2001**, *105*, 730–735.
296. Knoll, J. D.; Turro, C. *Coord. Chem. Rev.* **2015**, *282–283*, 110–126.
297. Huang, H.; Zhang, P.; Chen, H.; Ji, L.; Chao, H. *Chem. Eur. J.* **2015**, *21*, 715–725.

298. da Silva Miranda, F.; Signori, A.; Vicente, J.; de Souza, B.; Priebe, J. P.; Szpoganicz, B.; Gonçalves, N. S.; Neves, A. *Tetrahedron* **2008**, *64*, 5410–5415.
299. Schäfer, S.; Ott, I.; Gust, R.; Sheldrick, W. S. *Eur. J. Inorg. Chem.* **2007**, *2007*, 3034–3046.
300. Lee, Y.-R.; Chen, T.-C.; Lee, C.-C.; Chen, C.-L.; Ahmed Ali, A. A.; Tikhomirov, A.; Guh, J.-H.; Yu, D.-S.; Huang, H.-S. *Eur. J. Med. Chem.* **2015**, *102*, 661–676.
301. Wang, P.; Zhu, G. *Chin. J. Chem.* **1999**, *17*, 502–507.
302. Rau, S.; Schäfer, B.; Grüßing, A.; Schebesta, S.; Lamm, K.; Vieth, J.; Görls, H.; Walther, D.; Rudolph, M.; Grummt, U. W.; Birkner, E. *Inorg. Chim. Acta* **2004**, *357*, 4496–4503.
303. Nasielski-Hinkens, R.; Benedek-Vamos, M.; Hautain, Y.; Nasielski, J. *Bull. Soc. Chim. Belg.* **1976**, *85*, 781–786.
304. Shaver, R. J.; Rillema, D. P. *Inorg. Chem.* **1992**, *31*, 4101–4107.
305. Finck, S.; Issenhuth, J.-T.; Despax, S.; Sirlin, C.; Pfeffer, M.; Poidevin, C.; Gourlaouen, C.; Boeglin, A.; Daniel, C. *J. Organomet. Chem.* **2014**, *760*, 248–259.
306. Wachter, E.; Howerton, B. S.; Hall, E. C.; Parkin, S.; Glazer, E. C. *Chem. Commun.* **2014**, *50*, 311–313.
307. Williams, A. T. R.; Winfield, S. A.; Miller, J. N. *Analyst* **1983**, *108*, 1067–1071.
308. Brouwer, A. M. *Pure Appl. Chem.* **2011**, *83*, 2213–2228.
309. Danilov, V. I.; Volkov, S. N. *Biopolymers* **1975**, *14*, 1205–1212.
310. Carter, M. T.; Rodriguez, M.; Bard, A. J. *J. Am. Chem. Soc.* **1989**, *111*, 8901–8911.
311. Poulsen, B. C.; Estalayo-Adrián, S.; Blasco, S.; Bright, S. A.; Kelly, J. M.; Williams, D. C.; Gunnlaugsson, T. *Dalton Trans.* **2016**, *45*, 18208–18220.
312. McKinley, A. W.; Andersson, J.; Lincoln, P.; Tuite, E. M. *Chem. Eur. J.* **2012**, *18*, 15142–15150.
313. Thomas, R. *Gene* **1993**, *135*, 77–79.
314. Wilson, B. C.; Tanious, F. A.; Fernandez-Saiz, M.; Rigl, C. T. In *Drug-DNA Interaction Protocols. Methods in Molecular Biology*TM; Humana Press: Totowa, NJ, 1997; Vol. 90, p 219–240.
315. Mergny, J.-L.; Lacroix, L. *Oligonucleotides* **2003**, *13*, 515–537.
316. Waring, M. J. *J. Mol. Biol.* **1965**, *13*, 269–282.
317. Fiel, R. J.; Howard, J. C.; Mark, E. H.; Gupta, N. D. *Nucleic Acids Res.* **1979**, *6*, 3093–3118.

318. Nair, R. B.; Teng, E. S.; Kirkland, S. L.; Murphy, C. J. *Inorg. Chem.* **1998**, *37*, 139–141.
319. Peng, B.; Chen, X.; Du, K.-J.; Yu, B.-L.; Chao, H.; Ji, L.-N. *Spectrochim. Acta, Part A* **2009**, *74*, 896–901.
320. Nordén, B.; Kurucsev, T. *J. Mol. Recognit.* **1994**, *7*, 141–155.
321. Nordén, B.; Rodger, A.; Dafforn, T. *Linear dichroism and circular dichroism: a textbook on polarized-light spectroscopy*; Royal Society of Chemistry: Cambridge, United Kingdom, 2010.
322. Garbett, N. C.; Ragazzon, P. A.; Chaires, J. B. *Nat. Protoc.* **2007**, *2*, 3166–3172.
323. Chang, Y.-M.; Chen, C. K.-M.; Hou, M.-H. *Int. J. Mol. Sci.* **2012**, *13*, 3394–3413.
324. Maheswari, P. U.; Rajendiran, V.; Palaniandavar, M.; Parthasarathi, R.; Subramanian, V. *J. Inorg. Biochem.* **2006**, *100*, 3–17.
325. Satyanarayana, S.; Dabrowiak, J. C.; Chaires, J. B. *Biochemistry* **1992**, *31*, 9319–9324.
326. García-Fresnadillo, D.; Georgiadou, Y.; Orellana, G.; Braun, A. M.; Oliveros, E. *Helv. Chim. Acta* **1996**, *79*, 1222–1238.
327. Hergueta-Bravo, A.; Jiménez-Hernández, M. E.; Montero, F.; Oliveros, E.; Orellana, G. *J. Phys. Chem. B* **2002**, *106*, 4010–4017.
328. Gomes, A.; Fernandes, E.; Lima, J. L. F. C. *J. Biochem. Biophys. Methods* **2005**, *65*, 45–80.
329. Carraway, E. R.; Demas, J. N.; DeGraff, B. A. *Anal. Chem.* **1991**, *63*, 332–336.
330. Zhu, B.-Z.; Chao, X.-J.; Huang, C.-H.; Li, Y. *Chem. Sci.* **2016**, *7*, 4016–4023.
331. Stewart, M. P.; Langer, R.; Jensen, K. F. *Chem. Rev.* **2018**, *118*, 7409–7531.
332. Jiménez-Hernández, M. E.; Orellana, G.; Montero, F.; Portolés, M. T. *Photochem. Photobiol.* **2000**, *72*, 28–34.
333. Sanmartín, C.; Plano, D.; Sharma, A. K.; Palop, J. A. *Int. J. Mol. Sci.* **2012**, *13*, 9649.
334. Pang, Y.; An, B.; Lou, L.; Zhang, J.; Yan, J.; Huang, L.; Li, X.; Yin, S. *J. Med. Chem.* **2017**, *60*, 7300–7314.
335. An, B.; Wang, B.; Hu, J.; Xu, S.; Huang, L.; Li, X.; Chan, A. S. C. *J. Med. Chem.* **2018**, *61*, 2571–2588.
336. An, B.; Zhang, S.; Hu, J.; Pan, T.; Huang, L.; Tang, J. C.-o.; Li, X.; Chan, A. S. C. *Org. Biomol. Chem.* **2018**, *16*, 4701–4714.
337. Zhao, Z.; Gao, P.; You, Y.; Chen, T. *Chem. Eur. J.* **2018**, *24*, 3289–3298.
338. Vanderlinden, W.; Blunt, M.; David, C. C.; Moucheron, C.; Kirsch-De Mesmaeker, A.; De Feyter, S. *J. Am. Chem. Soc.* **2012**, *134*, 10214–10221.

339. Knobloch, B.; Sigel, H.; Okruszek, A.; Sigel, R. K. O. *Org. Biomol. Chem.* **2006**, *4*, 1085–1090.
340. McGovern, D. A.; Doorley, G. W.; Whelan, A. M.; Parker, A. W.; Towrie, M.; Kelly, J. M.; Quinn, S. J. *Photochem. Photobiol. Sci.* **2009**, *8*, 542–548.
341. Troian-Gautier, L.; Mugeniwabagara, E.; Fusaro, L.; Moucheron, C.; Kirsch-De Mesmaeker, A.; Luhmer, M. *Inorg. Chem.* **2017**, *56*, 1794–1803.
342. Cardin, C. J.; Kelly, J. M.; Quinn, S. J. *Chem. Sci.* **2017**, *8*, 4705–4723.
343. Keane, P. M.; Kelly, J. M. *Coord. Chem. Rev.* **2018**, *364*, 137–154.
344. Gicquel, E.; Boisdenghien, A.; Defrancq, E.; Moucheron, C.; Kirsch-De Mesmaeker, A. *Chem. Commun.* **2004**, 2764–2765.
345. Gauthier, N.; De Winter, J.; Gerbaux, P.; Moucheron, C.; Luhmer, M.; Kirsch-De Mesmaeker, A. *Inorg. Chem.* **2010**, *49*, 6796–6798.
346. Ghesquière, J.; Gauthier, N.; De Winter, J.; Gerbaux, P.; Moucheron, C.; Defrancq, E.; Kirsch-De Mesmaeker, A. *Chem. Eur. J.* **2012**, *18*, 355–364.
347. Kirsch-De Mesmaeker, A.; Nasielski-Hinkens, R.; Maetens, D.; Pauwels, D.; Nasielski, J. *Inorg. Chem.* **1984**, *23*, 377–379.
348. Herman, L.; Elias, B.; Pierard, F.; Moucheron, C.; Kirsch-De Mesmaeker, A. *J. Phys. Chem. A* **2007**, *111*, 9756–9763.
349. Wang, Z.; Pakoulev, A.; Pang, Y.; Dlott, D. D. *J. Phys. Chem. A* **2004**, *108*, 9054–9063.
350. Zhang, Y.; Improta, R.; Kohler, B. *Phys. Chem. Chem. Phys.* **2014**, *16*, 1487–1499.
351. Ghana, R.; Walss, C.; Walmsley, J. A. *J. Biomol. Struct. Dyn.* **1996**, *14*, 101–110.
352. Guzmán, M. R.; Liquier, J.; Brahmachari, S. K.; Taillandier, E. *Spectrochim. Acta, Part A* **2006**, *64*, 495–503.
353. Goncharova, I.; Novotná, J.; Urbanová, M. J. A.; Chemistry, B. *Anal. Bioanal. Chem.* **2012**, *403*, 2635–2644.
354. Pakhomov, S.; Hammer, R. P.; Mishra, B. K.; Thomas, B. N. *Proc. Natl. Acad. Sci. U. S. A.* **2003**, *100*, 3040.
355. Wang, Y.; Zhou, D.; Li, H.; Li, R.; Zhong, Y.; Sun, X.; Sun, X. *J. Mater. Chem. C* **2014**, *2*, 6402–6409.
356. Anuradha; La, D. D.; Al Kobaisi, M.; Bhosale, S. V. *Sci. Rep.* **2015**, *5*, 15652.
357. Anuradha; La, D. D.; Al Kobaisi, M.; Gupta, A.; Bhosale, S. V. *Chem. Eur. J.* **2017**, *23*, 3950–3956.

358. Kypr, J.; Kejnovská, I.; Renčiuk, D.; Vorlíčková, M. *Nucleic Acids Res.* **2009**, *37*, 1713–1725.
359. del Villar-Guerra, R.; Trent, J. O.; Chaires, J. B. *Angew. Chem. Int. Ed.* **2018**, *57*, 7171–7175.
360. Panda, M.; Walmsley, J. A. *J. Phys. Chem. B* **2011**, *115*, 6377–6383.
361. Pinnavaia, T. J.; Miles, H. T.; Becker, E. D. *J. Am. Chem. Soc.* **1975**, *97*, 7198–7200.
362. Pinnavaia, T. J.; Marshall, C. L.; Mettler, C. M.; Fisk, C. L.; Miles, H. T.; Becker, E. D. *J. Am. Chem. Soc.* **1978**, *100*, 3625–3627.
363. Borzo, M.; Detellier, C.; Laszlo, P.; Paris, A. *J. Am. Chem. Soc.* **1980**, *102*, 1124–1134.
364. Petersen, S. B.; Led, J. J.; Johnston, E. R.; Grant, D. M. *J. Am. Chem. Soc.* **1982**, *104*, 5007–5015.
365. Wong, A.; Ida, R.; Spindler, L.; Wu, G. *J. Am. Chem. Soc.* **2005**, *127*, 6990–6998.
366. Wu, G.; Kwan, I. C. M. *J. Am. Chem. Soc.* **2009**, *131*, 3180–3182.
367. Wu, G.; Kwan, I. C. M.; Yan, Z.; Huang, Y.; Ye, E. *J. Nucleic Acids* **2017**, *2017*, 1–7.
368. McGovern, D. A.; Quinn, S.; Doorley, G. W.; Whelan, A. M.; Ronayne, K. L.; Towrie, M.; Parker, A. W.; Kelly, J. M. *Chem. Commun.* **2007**, 5158–5160.
369. McCusker, J. K. *Acc. Chem. Res.* **2003**, *36*, 876–887.
370. Wallin, S.; Davidsson, J.; Modin, J.; Hammarström, L. *J. Phys. Chem. A* **2005**, *109*, 4697–4704.
371. Sun, Q.; Dereka, B.; Vauthey, E.; Lawson Daku, L. M.; Hauser, A. *Chem. Sci.* **2017**, *8*, 223–230.
372. Thompson, D. W.; Wishart, J. F.; Brunschwig, B. S.; Sutin, N. *J. Phys. Chem. A* **2001**, *105*, 8117–8122.
373. Damrauer, N. H.; McCusker, J. K. *J. Phys. Chem. A* **1999**, *103*, 8440–8446.
374. Yeh, A. T.; Shank, C. V.; McCusker, J. K. *Science* **2000**, *289*, 935–938.
375. De Armond, M. K.; Myrick, M. L. *Acc. Chem. Res.* **1989**, *22*, 364–370.
376. Yersin, H.; Humbs, W.; Strasser, J. *Coord. Chem. Rev.* **1997**, *159*, 325–358.
377. Shimizu, O.; Watanabe, J.; Naito, S. *Chem. Phys. Lett.* **2000**, *332*, 295–298.
378. Smith, B. C. *Infrared Spectral Interpretation: A Systematic Approach*; 1st ed. Taylor & Francis, 1998.
379. Kuimova, M. K.; Cowan, A. J.; Matousek, P.; Parker, A. W.; Sun, X. Z.; Towrie, M.; George, M. W. *Proc. Natl. Acad. Sci. U. S. A.* **2006**, *103*, 2150–2153.

380. Parker, A. W.; Lin, C. Y.; George, M. W.; Towrie, M.; Kuimova, M. K. *J. Phys. Chem. B* **2010**, *114*, 3660–3667.
381. Cao, Q.; Creely, C. M.; Davies, E. S.; Dyer, J.; Easun, T. L.; Grills, D. C.; McGovern, D. A.; McMaster, J.; Pitchford, J.; Smith, J. A.; Sun, X.-Z.; Kelly, J. M.; George, M. W. *Photochem. Photobiol. Sci.* **2011**, *10*, 1355–1364.
382. Bucher, D. B.; Pilles, B. M.; Carell, T.; Zinth, W. *Proc. Natl. Acad. Sci. U. S. A.* **2014**, *111*, 4369–4374.
383. Lecomte, J.-P.; Kirsch-De Mesmaeker, A.; Kelly, J. M.; Tossi, A. B.; Görner, H. *Photochemistry and Photobiology* **1992**, *55*, 681–689.
384. Zhang, C.; Xie, L.; Ding, Y.; Sun, Q.; Xu, W. *ACS Nano* **2016**, *10*, 3776–3782.
385. Farrer, N. J.; Salassa, L.; Sadler, P. J. *Dalton Trans.* **2009**, 10690–10701.
386. Johnson, I. D. Probes for Lipids and Membranes. In *Molecular Probes Handbook: A Guide to Fluorescent Probes and Labeling Technologies*; 11th ed.; Thermo Fisher Scientific: 2010.
387. Li, L.; Szmecinski, H.; Lakowicz, J. R. *Anal. Biochem.* **1997**, *244*, 80–85.
388. Svensson, F. R.; Li, M.; Nordén, B.; Lincoln, P. *J. Phys. Chem. B* **2008**, *112*, 10969–10975.
389. Mechler, A.; Stringer, B. D.; Mubin, M. S. H.; Doeven, E. H.; Phillips, N. W.; Rudd-Schmidt, J.; Hogan, C. F. *Biochim. Biophys. Acta, Biomembr.* **2014**, *1838*, 2939–2946.
390. Kašćáková, S.; Giuliani, A.; Lacerda, S.; Pallier, A.; Mercère, P.; Tóth, É.; Réfrégiers, M. *Nano Res.* **2015**, *8*, 2373–2379.
391. Verwilt, P.; Park, S.; Yoon, B.; Kim, J. S. *Chem. Soc. Rev.* **2015**, *44*, 1791–1806.
392. Arroyo, I. Z.; Gomez, C.; Alarcon, H.; Jimenez, A.; Pardo, A.; Montañó, G.; Armijos, R. X.; Noveron, J. C. *J. Drug Delivery* **2018**, *2018*, 11.
393. Griffiths, P. C.; Fallis, I. A.; Chuenpratoom, T.; Watanesk, R. *Adv. Colloid Interface Sci.* **2006**, *122*, 107–117.
394. Lo, K. K.-W.; Lee, P.-K.; Lau, J. S.-Y. *Organometallics* **2008**, *27*, 2998–3006.
395. Chu, B. W.-K.; Yam, V. W.-W. *Inorg. Chem.* **2001**, *40*, 3324–3329.
396. Goedheijt, M. S.; Hanson, B. E.; Reek, J. N. H.; Kamer, P. C. J.; van Leeuwen, P. W. N. M. *J. Am. Chem. Soc.* **2000**, *122*, 1650–1657.
397. Jervis, H. B.; Bruce, D. W.; Raimondi, M. E.; Seddon, J. M.; Maschmeyer, T.; Raja, R. *Chem. Commun.* **1999**, 2031–2032.
398. Danks, M. J.; Jervis, H. B.; Nowotny, M.; Zhou, W.; Maschmeyer, T. A.; Bruce, D. W. *Catal. Lett.* **2002**, *82*, 95–98.

399. Nagaraj, K.; Ambika, S.; Rajasri, S.; Sakthinathan, S.; Arunachalam, S. *Colloids Surf., B* **2014**, *122*, 151–157.
400. Komatsu, H.; Yoshihara, K.; Yamada, H.; Kimura, Y.; Son, A.; Nishimoto, S.-i.; Tanabe, K. *Chem. Eur. J.* **2013**, *19*, 1971–1977.
401. Lebrón, J. A.; Ostos, F. J.; Moyá, M. L.; López-López, M.; Carrasco, C. J.; López-Cornejo, P. *Colloids Surf., B* **2015**, *135*, 817–824.
402. Nagaraj, K.; Murugan, K. S.; Thangamuniyandi, P.; Sakthinathan, S. *RSC Adv.* **2014**, *4*, 56084–56094.
403. Lecomte, J. P.; Kirsch-De Mesmaeker, A.; Demeunynck, M.; Lhomme, J. *J. Chem. Soc., Faraday Trans.* **1993**, *89*, 3261–3269.
404. Kajouj, S.; Marcélis, L.; Lemaur, V.; Beljonne, D.; Moucheron, C. *Dalton Trans.* **2017**, *46*, 6623–6633.
405. García-Fresnadillo, D.; Marazuela, M. D.; Moreno-Bondi, M. C.; Orellana, G. *Langmuir* **1999**, *15*, 6451–6459.
406. García-Fresnadillo, D.; Orellana, G. *Helv. Chim. Acta* **2001**, *84*, 2708–2730.
407. Scholz, N.; Behnke, T.; Resch-Genger, U. *J. Fluoresc.* **2018**, *28*, 465–476.
408. Thongngam, M.; McClements, D. J. *Langmuir* **2005**, *21*, 79–86.
409. Palladino, P.; Ragone, R. *Langmuir* **2011**, *27*, 14065–14070.
410. Fuguet, E.; Rafols, C.; Roses, M.; Bosch, E. *Anal. Chim. Acta* **2005**, *548*, 95–100.
411. Chakraborty, T.; Chakraborty, I.; Ghosh, S. *Arabian J. Chem.* **2011**, *4*, 265–270.
412. Lotfi, M.; Nejib, M.; Naceur, M. Chapter 8. In *Advances in Biomaterials Science and Biomedical Applications* 2013.
413. Padday, J. F.; Pitt, A. R.; Pashley, R. M. *J. Chem. Soc., Faraday Trans. 1* **1975**, *71*, 1919–1931.
414. Bowers, J.; Amos, K. E.; Bruce, D. W.; Webster, J. R. P. *Langmuir* **2005**, *21*, 1346–1353.
415. Bowers, J.; Amos, K. E.; Bruce, D. W.; Heenan, R. K. *Langmuir* **2005**, *21*, 5696–5706.
416. Valcárcel, M.; López-Lorente, Á. *Gold Nanoparticles in Analytical Chemistry*; Elsevier, 2014; Vol. 66.
417. Berne, B. J.; Pecora, R. *Dynamic Light Scattering: With Applications to Chemistry, Biology, and Physics*; Dover Publications, 2013.
418. Haworth, I. S.; Elcock, A. H.; Rodger, A.; Richards, W. G. *J. Biomol. Struct. Dyn.* **1991**, *9*, 553–569.

419. Eriksson, M.; Leijon, M.; Hiort, C.; Norden, B.; Graeslund, A. *Biochemistry* **1994**, *33*, 5031–5040.
420. Husale, S.; Grange, W.; Karle, M.; Bürgi, S.; Hegner, M. *Nucleic Acids Res.* **2008**, *36*, 1443–1449.
421. Guo, L.; Zhang, Z.; Qiao, H.; Liu, M.; Shen, M.; Yuan, T.; Chen, J.; Dionysiou, D. D. *Spectrochim. Acta, Part A* **2015**, *151*, 237–246.
422. Guo, Q.; Zhang, Z.; Song, Y.; Liu, S.; Gao, W.; Qiao, H.; Guo, L.; Wang, J. *Chemosphere* **2017**, *168*, 599–605.
423. Sangster, J. *Octanol-Water Partition Coefficients: Fundamentals and Physical Chemistry*; Wiley, 1997.
424. González-Béjar, M.; Liras, M.; Francés-Soriano, L.; Voliani, V.; Herranz-Pérez, V.; Duran-Moreno, M.; Garcia-Verdugo, J. M.; Alarcon, E. I.; Scaiano, J. C.; Pérez-Prieto, J. *J. Mater. Chem. B* **2014**, *2*, 4554–4563.
425. Wessels, J. M.; Foote, C. S.; Ford, W. E.; Rodgers, M. A. J. *Photochem. Photobiol.* **1997**, *65*, 96–102.
426. Masnovi, J. M.; Seddon, E. A.; Kochi, J. K. *Can. J. Chem.* **1984**, *62*, 2552–2559.
427. Siewert, B.; Langerman, M.; Hontani, Y.; Kennis, J. T. M.; van Rixel, V. H. S.; Limburg, B.; Siegler, M. A.; Talens Saez, V.; Kieltyka, R. E.; Bonnet, S. *Chem. Commun.* **2017**, *53*, 11126–11129.
428. Puckett, C. A.; Barton, J. K. *Biochemistry* **2008**, *47*, 11711–11716.
429. Dobrucki, J. W. *J. Photochem. Photobiol., B* **2001**, *65*, 136–144.
430. Huang, H.; Yu, B.; Zhang, P.; Huang, J.; Chen, Y.; Gasser, G.; Ji, L.; Chao, H. *Angew. Chem. Int. Ed.* **2015**, *54*, 14049–14052.
431. Svensson, F. R.; Abrahamsson, M.; Strömberg, N.; Ewing, A. G.; Lincoln, P. *J. Phys. Chem. Lett.* **2011**, *2*, 397–401.
432. Huang, H.; Zhang, P.; Yu, B.; Chen, Y.; Wang, J.; Ji, L.; Chao, H. *J. Med. Chem.* **2014**, *57*, 8971–8983.
433. Zava, O.; Zakeeruddin, S. M.; Danelon, C.; Vogel, H.; Grätzel, M.; Dyson, P. J. *ChemBioChem* **2009**, *10*, 1796–1800.
434. Sainuddin, T.; Pinto, M.; Yin, H.; Hetu, M.; Colpitts, J.; McFarland, S. A. *J. Inorg. Biochem.* **2016**, *158*, 45–54.
435. Albani, B. A.; Peña, B.; Leed, N. A.; de Paula, N. A. B. G.; Pavani, C.; Baptista, M. S.; Dunbar, K. R.; Turro, C. *J. Am. Chem. Soc.* **2014**, *136*, 17095–17101.

436. Koopman, W. J. H.; Visch, H.-J.; Smeitink, J. A. M.; Willems, P. H. G. M. *Cytometry, Part A* **2006**, *69A*, 1–12.
437. Duvezin-Caubet, S.; Jagasia, R.; Wagener, J.; Hofmann, S.; Trifunovic, A.; Hansson, A.; Chomyn, A.; Bauer, M. F.; Attardi, G.; Larsson, N. G.; Neupert, W.; Reichert, A. *S. J. Biol. Chem.* **2006**, *281*, 37972–37979.
438. Bonnet, S.; Limburg, B.; Meeldijk, J. D.; Gebbink, R. J. M. K.; Killian, J. A. *J. Am. Chem. Soc.* **2011**, *133*, 252–261.
439. Yu, B.; Ouyang, C.; Qiu, K.; Zhao, J.; Ji, L.; Chao, H. *Chem. Eur. J.* **2015**, *21*, 3691–3700.
440. Bunz, U. H. F.; Rotello, V. M. *Angew. Chem. Int. Ed.* **2010**, *49*, 3268–3279.
441. Labande, A.; Ruiz, J.; Astruc, D. *J. Am. Chem. Soc.* **2002**, *124*, 1782–1789.
442. Stratakis, M.; Garcia, H. *Chem. Rev.* **2012**, *112*, 4469–4506.
443. Hasobe, T.; Imahori, H.; Kamat, P. V.; Fukuzumi, S. *J. Am. Chem. Soc.* **2003**, *125*, 14962–14963.
444. Elghanian, R.; Storhoff, J. J.; Mucic, R. C.; Letsinger, R. L.; Mirkin, C. A. *Science* **1997**, *277*, 1078–1081.
445. Massue, J.; Quinn, S. J.; Gunnlaugsson, T. *J. Am. Chem. Soc.* **2008**, *130*, 6900–6901.
446. Comby, S.; Gunnlaugsson, T. *ACS Nano* **2011**, *5*, 7184–7197.
447. Truman, L. K.; Comby, S.; Gunnlaugsson, T. *Angew. Chem. Int. Ed.* **2012**, *51*, 9624–9627.
448. *11-Mercaptoundecanoic acid*; SDS No. 450561; Sigma-Aldrich: Arklow, Wicklow, 21 December 2015.
449. *Bis(10-carboxydecyl)disulfide*; SDS No. 674451; Sigma-Aldrich: Tallaght, Dublin, 7 November 2017.
450. Turkevich, J.; Stevenson, P. C.; Hillier, J. *J. Phys. Chem.* **1953**, *57*, 670–673.
451. Brust, M.; Walker, M.; Bethell, D.; Schiffrin, D. J.; Whyman, R. *J. Chem. Soc., Chem. Commun.* **1994**, 801–802.
452. Perrault, S. D.; Chan, W. C. W. *J. Am. Chem. Soc.* **2009**, *131*, 17042–17043.
453. Fratoddi, I.; Venditti, I.; Cametti, C.; Russo, M. V. *J. Mater. Chem. B* **2014**, *2*, 4204–4220.
454. Comby, S.; Surender, E. M.; Kotova, O.; Truman, L. K.; Molloy, J. K.; Gunnlaugsson, T. *Inorg. Chem.* **2014**, *53*, 1867–1879.
455. Mayer, C. R.; Dumas, E.; Sécheresse, F. *J. Colloid Interface Sci.* **2008**, *328*, 452–457.

456. Tong, L.; Lu, E.; Pichaandi, J.; Cao, P.; Nitz, M.; Winnik, M. A. *Chem. Mater.* **2015**, *27*, 4899–4910.
457. Deepak, F. L.; Mayoral, A.; Arenal, R. *Advanced Transmission Electron Microscopy: Applications to Nanomaterials*; 1st ed.; Springer International Publishing, 2015.
458. Cooke, M. M.; Doeven, E. H.; Hogan, C. F.; Adcock, J. L.; McDermott, G. P.; Conlan, X. A.; Barnett, N. W.; Pfeffer, F. M.; Francis, P. S. *Anal. Chim. Acta* **2009**, *635*, 94–101.
459. Baggott, J. E.; Gregory, G. K.; Pilling, M. J.; Anderson, S.; Seddon, K. R.; Turp, J. E. *J. Chem. Soc., Faraday Trans. 2* **1983**, *79*, 195–210.
460. Urriza-Arsuaga, I.; Bedoya, M.; Orellana, G. *Anal. Chem.* **2019**, *91*, 2231–2238.
461. Huang, T.; Murray, R. W. *Langmuir* **2002**, *18*, 7077–7081.
462. Taton, T. A. *Curr. Protoc. Nucleic Acid Chem.* **2002**, *9*, 12.12.11–12.12.12.
463. Yameen, B.; Choi, W. I.; Vilos, C.; Swami, A.; Shi, J.; Farokhzad, O. C. *J. Control. Release* **2014**, *190*, 485–499.
464. Sheldrick, G. *Acta Crystallogr., Sect. C: Struct. Chem.* **2015**, *71*, 3–8.
465. Martinez, L. A.; Martínez, C. G.; Klopotek, B. B.; Lang, J.; Neuner, A.; Braun, A. M.; Oliveros, E. *J. Photochem. Photobiol., B* **2000**, *58*, 94–107.
466. Greetham, G. M.; Burgos, P.; Cao, Q.; Clark, I. P.; Codd, P. S.; Farrow, R. C.; George, M. W.; Kogimtzis, M.; Matousek, P.; Parker, A. W.; Pollard, M. R.; Robinson, D. A.; Xin, Z.-J.; Towrie, M. *Appl. Spectrosc.* **2010**, *64*, 1311–1319.
467. Greetham, G. M.; Sole, D.; Clark, I. P.; Parker, A. W.; Pollard, M. R.; Towrie, M. *Rev. Sci. Instrum.* **2012**, *83*, 103107.
468. Greetham, G. M.; Donaldson, P. M.; Nation, C.; Sazanovich, I. V.; Clark, I. P.; Shaw, D. J.; Parker, A. W.; Towrie, M. *Appl. Spectrosc.* **2016**, *70*, 645–653.
469. Donaldson, P. M.; Greetham, G. M.; Shaw, D. J.; Parker, A. W.; Towrie, M. *J. Phys. Chem. A* **2018**, *122*, 780–787.
470. Cohen, G.; Eisenberg, H. *Biopolymers* **1969**, *8*, 45–55.
471. Westcott, C. *Ph Measurements*; Elsevier Science, 2012.
472. Doi, T.; Nagamiya, H.; Kokubo, M.; Hirabayashi, K.; Takahashi, T. *Tetrahedron* **2002**, *58*, 2957–2963.
473. Molbase. http://www.molbase.com/en/sds_231-23-2-moldata-553280.html#tabs (accessed January 2019).

Appendices

Appendix 2

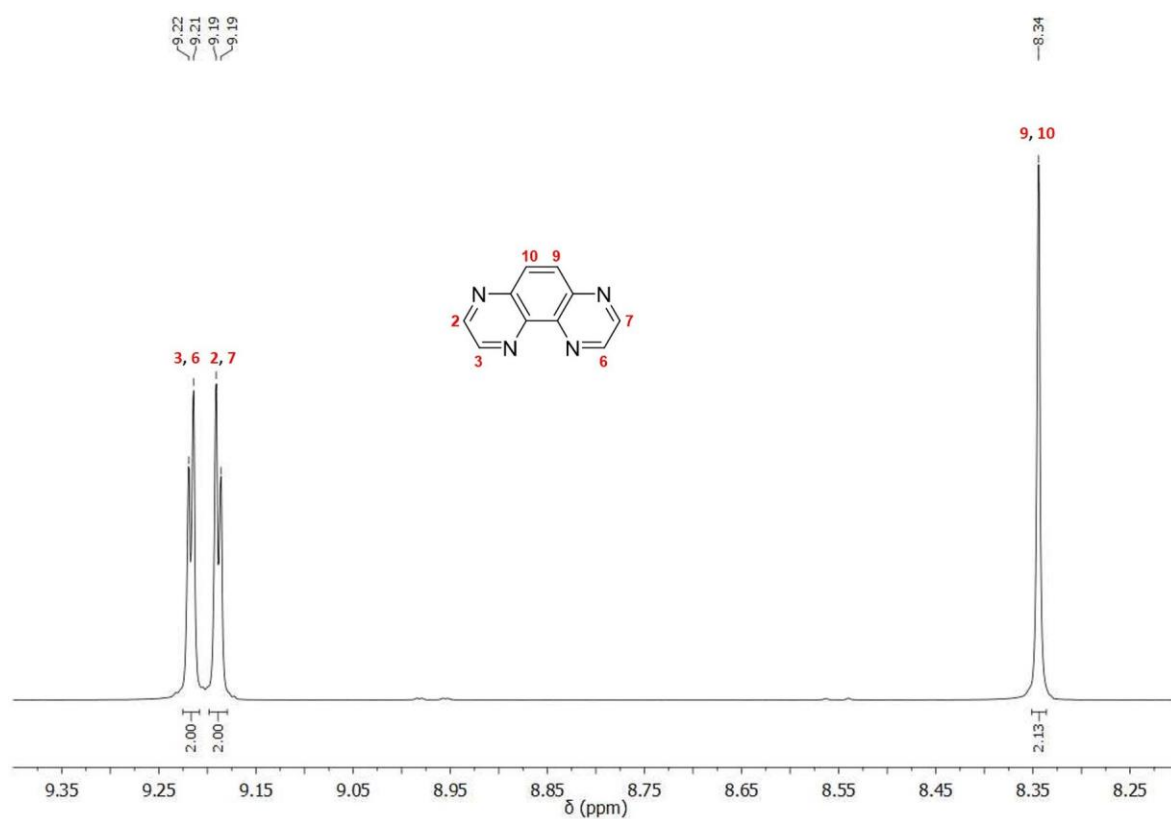


Figure A2.1. ¹H NMR (400 MHz, DMSO-*d*₆) spectrum of TAP.

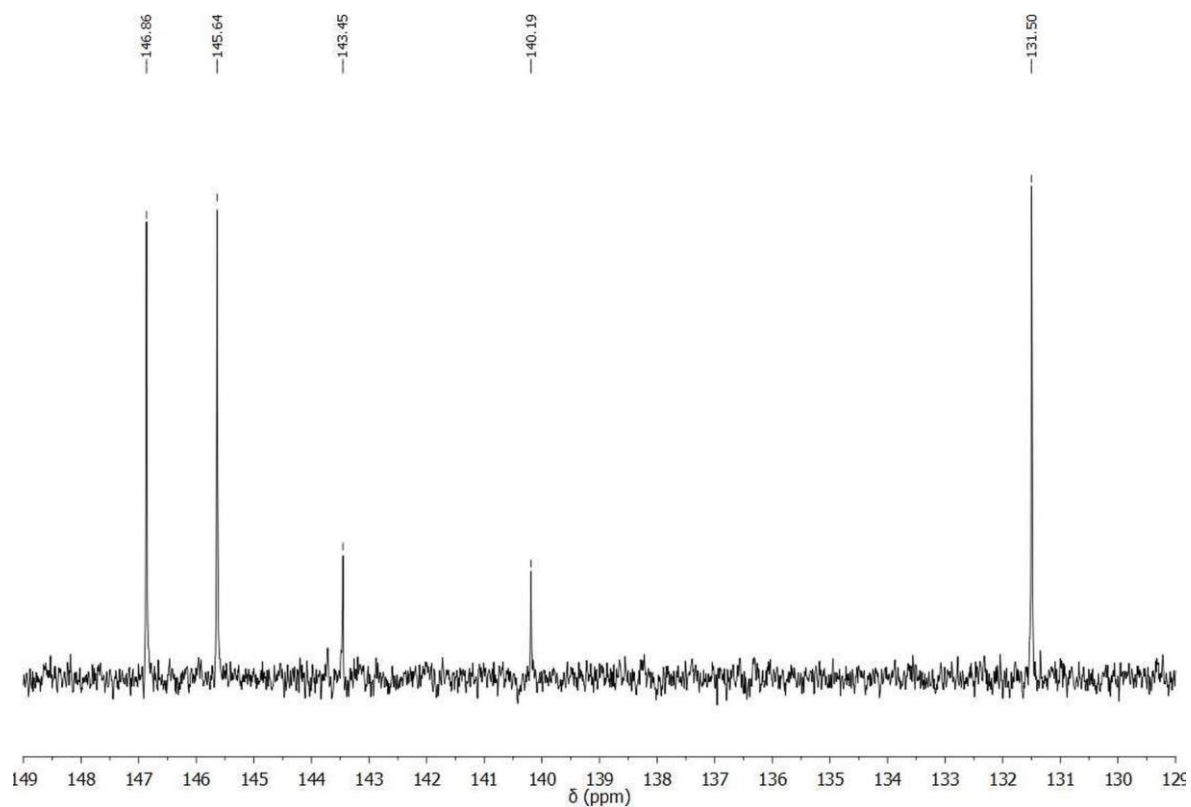


Figure A2.2. ¹³C NMR (101 MHz, DMSO-*d*₆) spectrum of TAP.

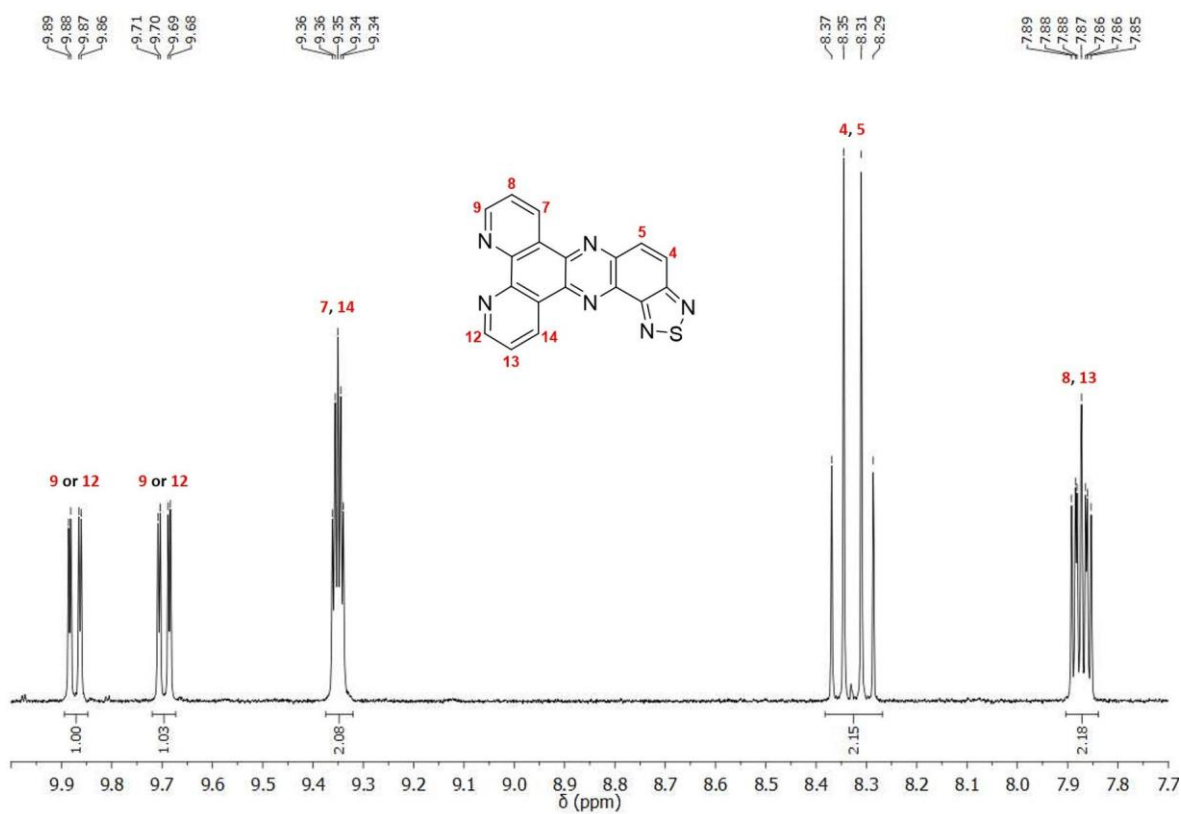


Figure A2.3. ^1H NMR (400 MHz, CDCl_3) spectrum of *dtp*.

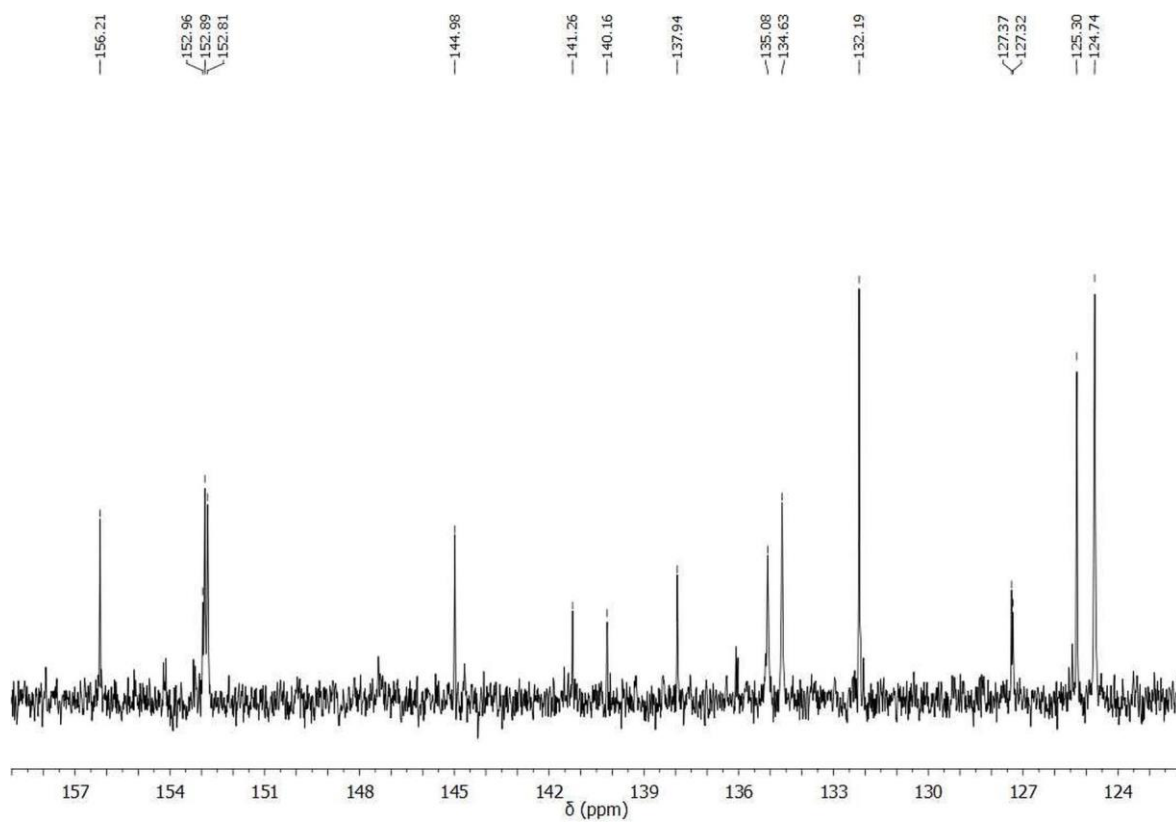


Figure A2.4. ^{13}C NMR (101 MHz, CDCl_3) spectrum of *dtp*.

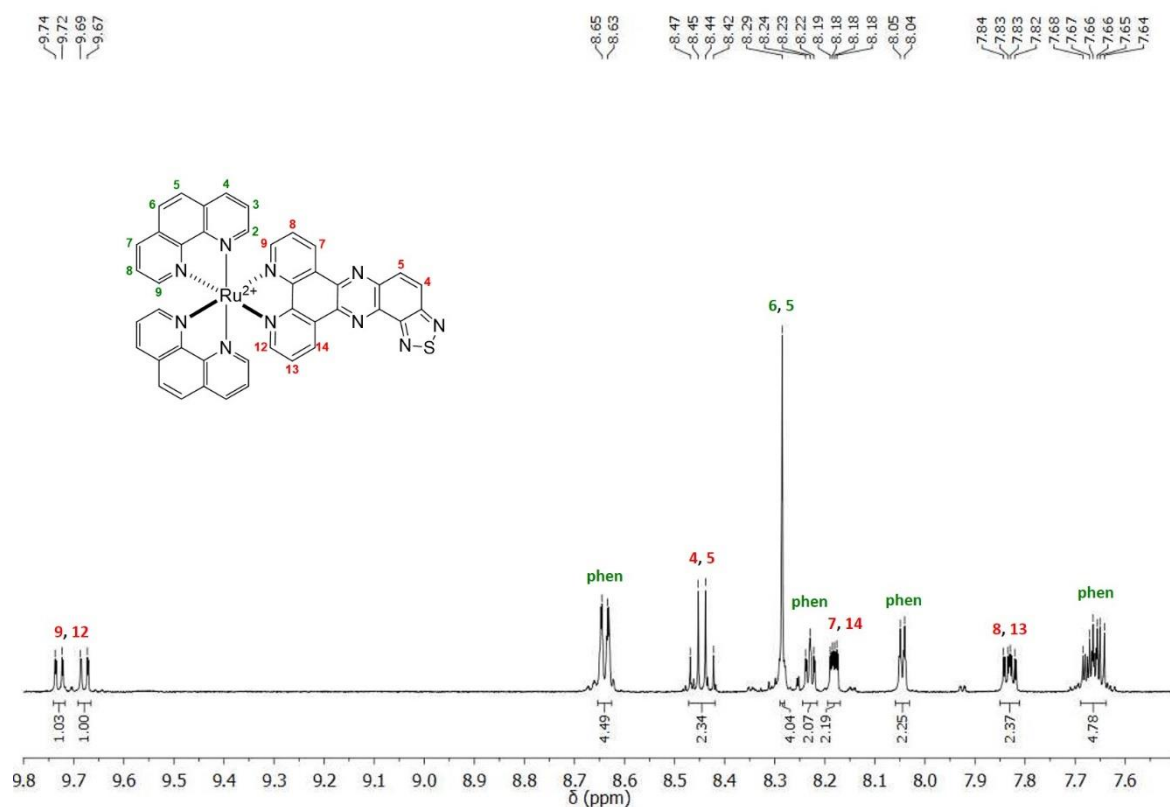


Figure A2.5. ¹H NMR (600 MHz, CD₃CN) spectrum of **63**. Signals corresponding to *phen* ligands are in green and signals assigned to the *dtp* ligand are in red.

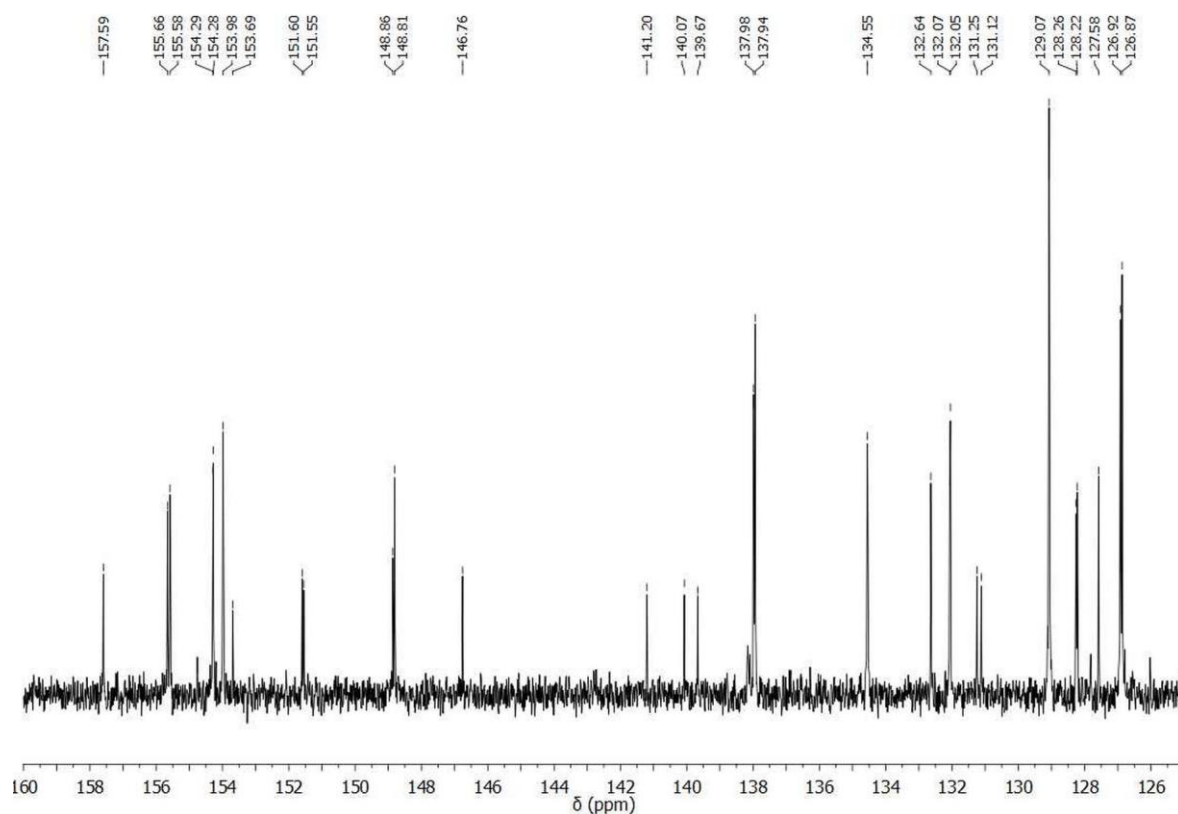


Figure A2.6. ¹³C NMR (151 MHz, CD₃CN) spectrum of **63**.

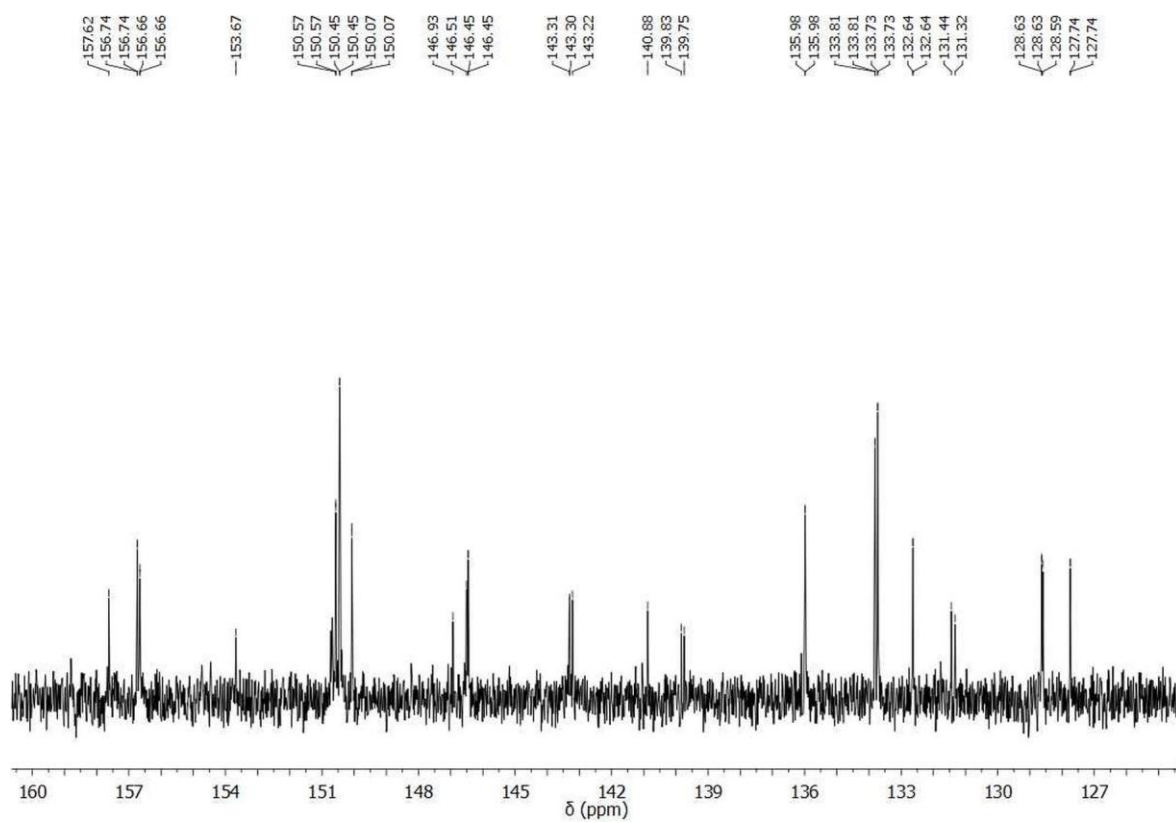


Figure A2.7. ^{13}C NMR (151 MHz, CD_3CN) spectrum of **64**.

Table A2.1. Crystal data and structure refinement for **64**.

Identification code	64
Empirical formula	$C_{38}H_{20}N_{14}RuS \cdot 2Cl \cdot 6H_2O$
Formula weight	984.80
Temperature / K	100
Crystal system	Monoclinic
Space group	$C2/c$
a / Å	14.9292(5)
b / Å	14.9340(6)
c / Å	35.2162(12)
α / °	90
β / °	96.717(2)
γ / °	90
Volume / Å ³	7797.7(5)
Z	8
ρ_{calc} / g cm ⁻³	1.678
μ / mm ⁻¹	5.605
F(000)	4000
Crystal size / mm ³	0.18 × 0.12 × 0.07
Radiation	CuK α ($\lambda = 1.54178$)
2 θ range for data collection / °	8.40 to 108.42
Index ranges	$-15 \leq h \leq 15, -15 \leq k \leq 15, -37 \leq l \leq 34$
Reflections collected	29550
Independent reflections	4756 [$R_{\text{int}} = 0.0603, R_{\text{sigma}} = 0.0412$]
Data/restraints/parameters	4756/24/554
Goodness-of-fit on F^2	1.247
Final R indexes [$I \geq 2\sigma(I)$]	$R_1 = 0.0937, wR_2 = 0.2097$
Final R indexes [all data]	$R_1 = 0.1004, wR_2 = 0.2133$
Largest diff. peak/hole / e Å ⁻³	1.87/-1.20

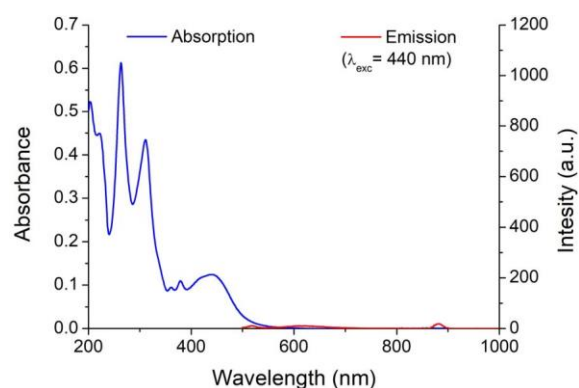


Figure A2.8. UV-vis absorption and emission spectra of **63** in 10 mM sodium phosphate-buffered aqueous solution at pH 7.4, at room temperature (rt).

Table A2.2. Bi-exponential and pre-exponential weighted mean emission lifetimes (τ_M) of **63** and **64** in the presence of DNA in different conditions, at 298 K.

Complex	Conditions	τ_1 (ns)	%A ₁	τ_2 (ns)	%A ₂	τ_3 (ns)	%A ₃	τ_M (ns)
63 + DNA	D ₂ O (O ₂)	169	35	493	47	1179	18	504
	D ₂ O (Ar)	182	37	549	45	1306	18	554
	H ₂ O (Air)	107	46	336	40	842	14	301
	H ₂ O (Ar)	113	46	358	40	876	14	319
64 + DNA	D ₂ O (O ₂)	92	41	362	40	1012	19	374
	D ₂ O (Ar)	180	42	759	39	2173	19	777
	H ₂ O (Air)	75	42	246	42	606	16	232
	H ₂ O (Ar)	91	45	391	38	1147	16	377

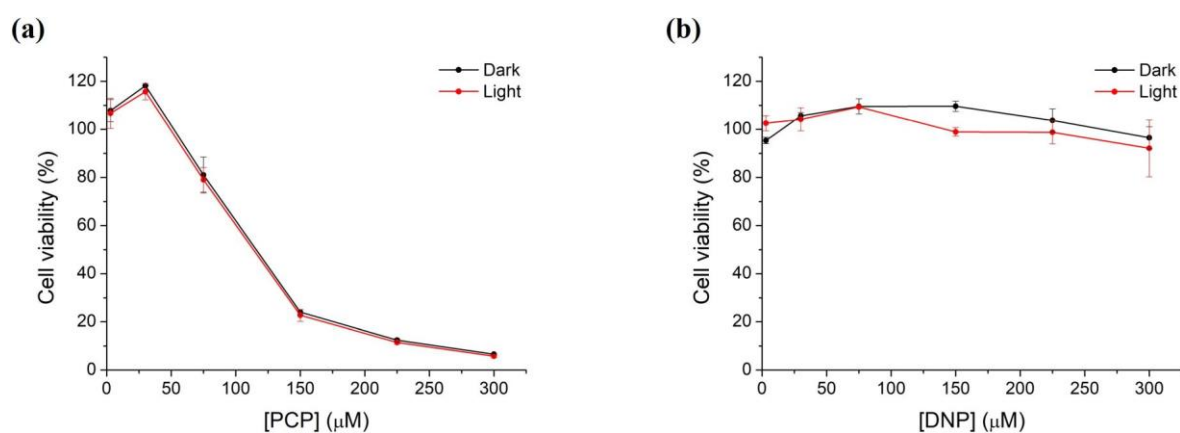


Figure A2.9. Toxicity profiles of (a) PCP and (b) DNP in HeLa cells. HeLa cells were treated with the indicated concentrations of the required complexes and incubated for 24 h followed by either exposure to light for 1 hour or maintenance in the dark and followed by further 24 h incubation. Cells were then incubated with the Alamar Blue dye for 4 h and assessed for cellular viability.

Appendix 3

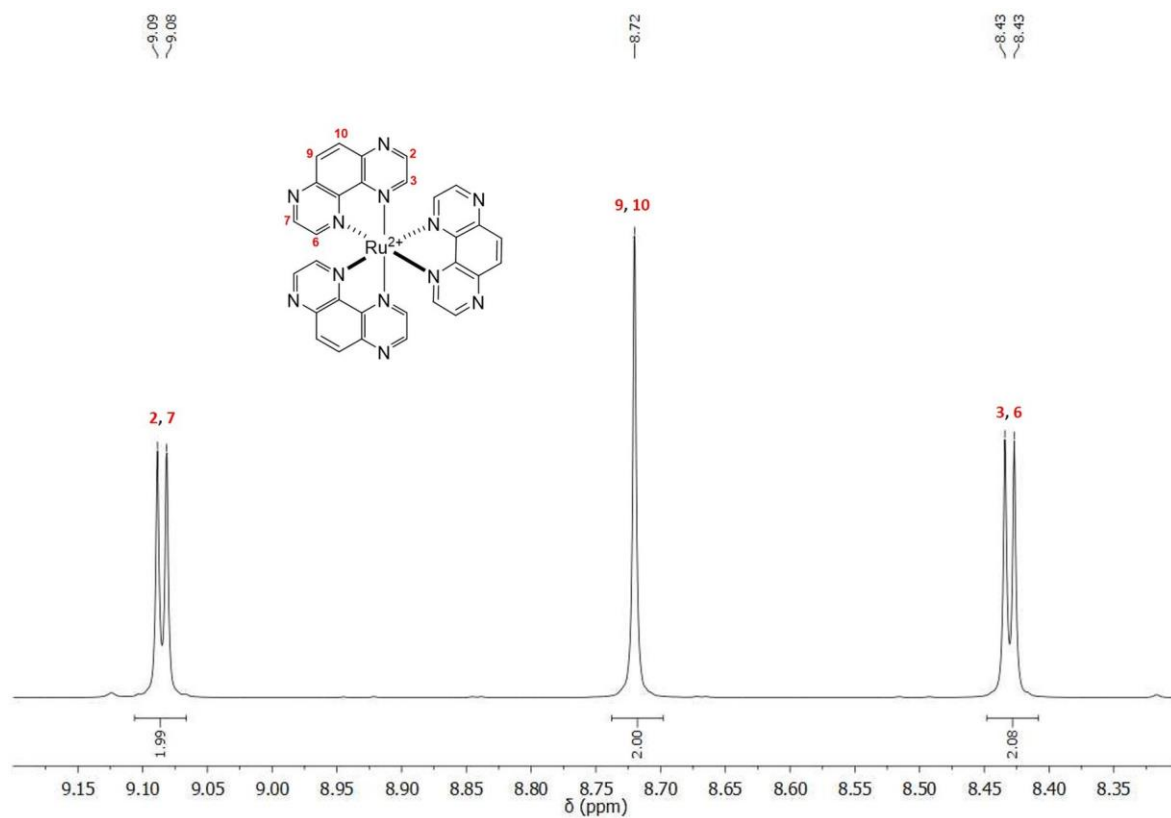


Figure A3.1. ^1H NMR (400 MHz, D_2O) spectrum of 38.

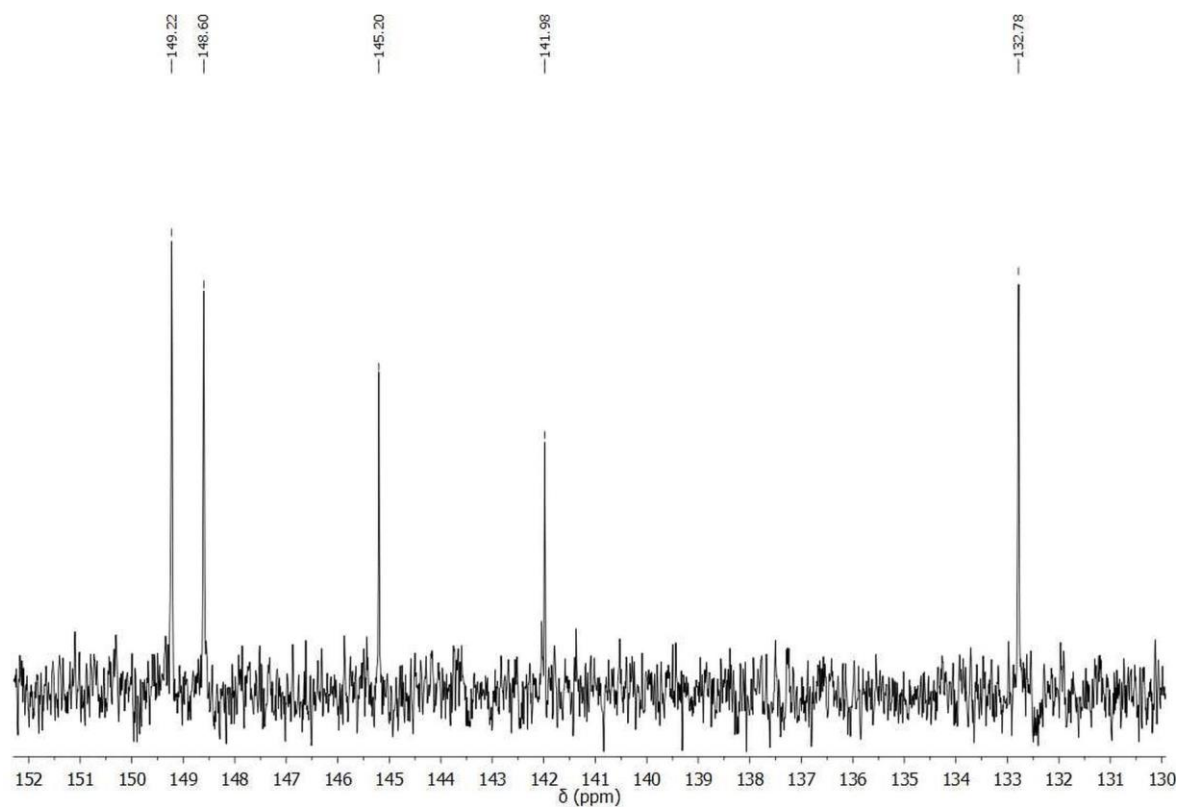


Figure A3.2. ^{13}C NMR (101 MHz, D_2O) spectrum of 38.

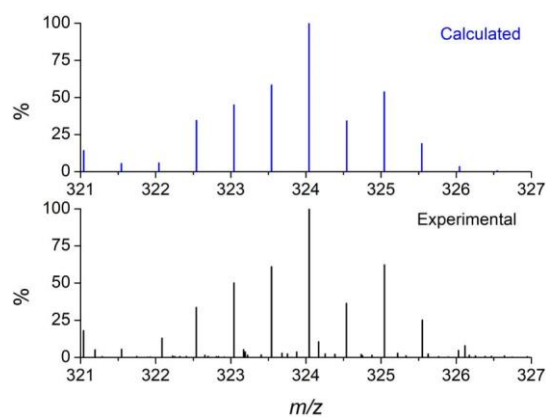


Figure A3.3. Comparison between the calculated (blue) and experimental (black) isotopic distribution pattern for **38** from electrospray ionisation (positive mode) high resolution mass spectrometry analysis.

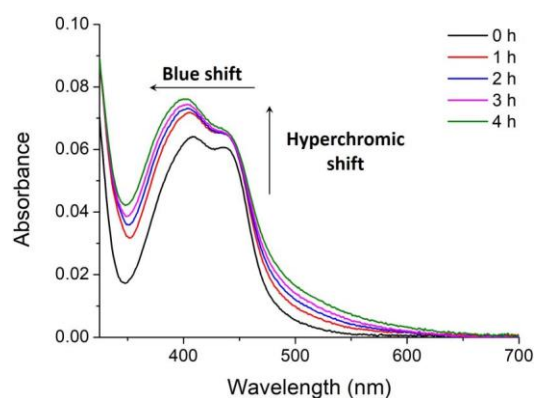


Figure A3.4. Monitoring of the photoreaction progress between **38** ($100\ \mu\text{M}$) and GMP ($10\ \text{mM}$) in deaerated aqueous solution at pH 5 by UV-vis absorption spectroscopy.

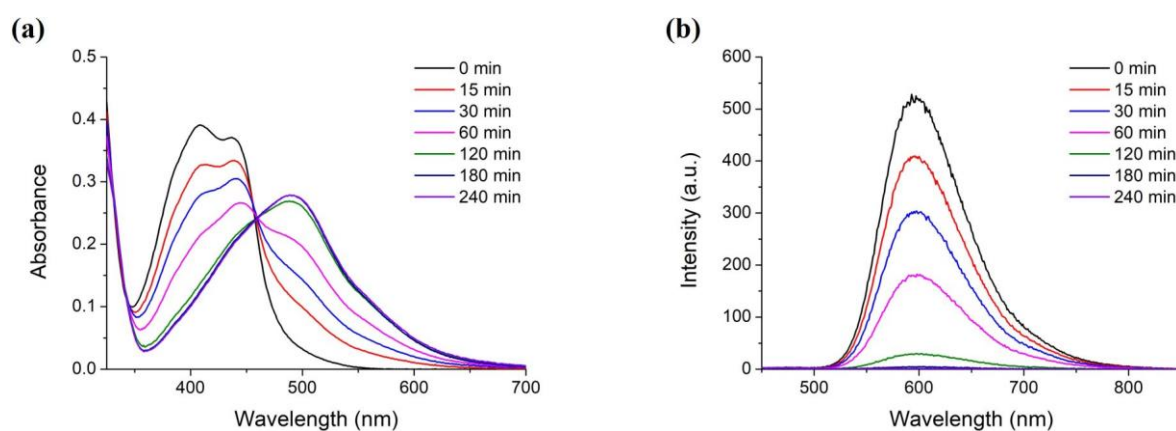


Figure A3.5. Monitoring of the illumination of **38** ($50\ \mu\text{M}$) in the absence of GMP in deaerated aqueous solution at pH 5 by (a) UV-vis absorption and (b) emission spectroscopy ($\lambda_{\text{exc}} = 407\ \text{nm}$) at different irradiation times, at 298 K.

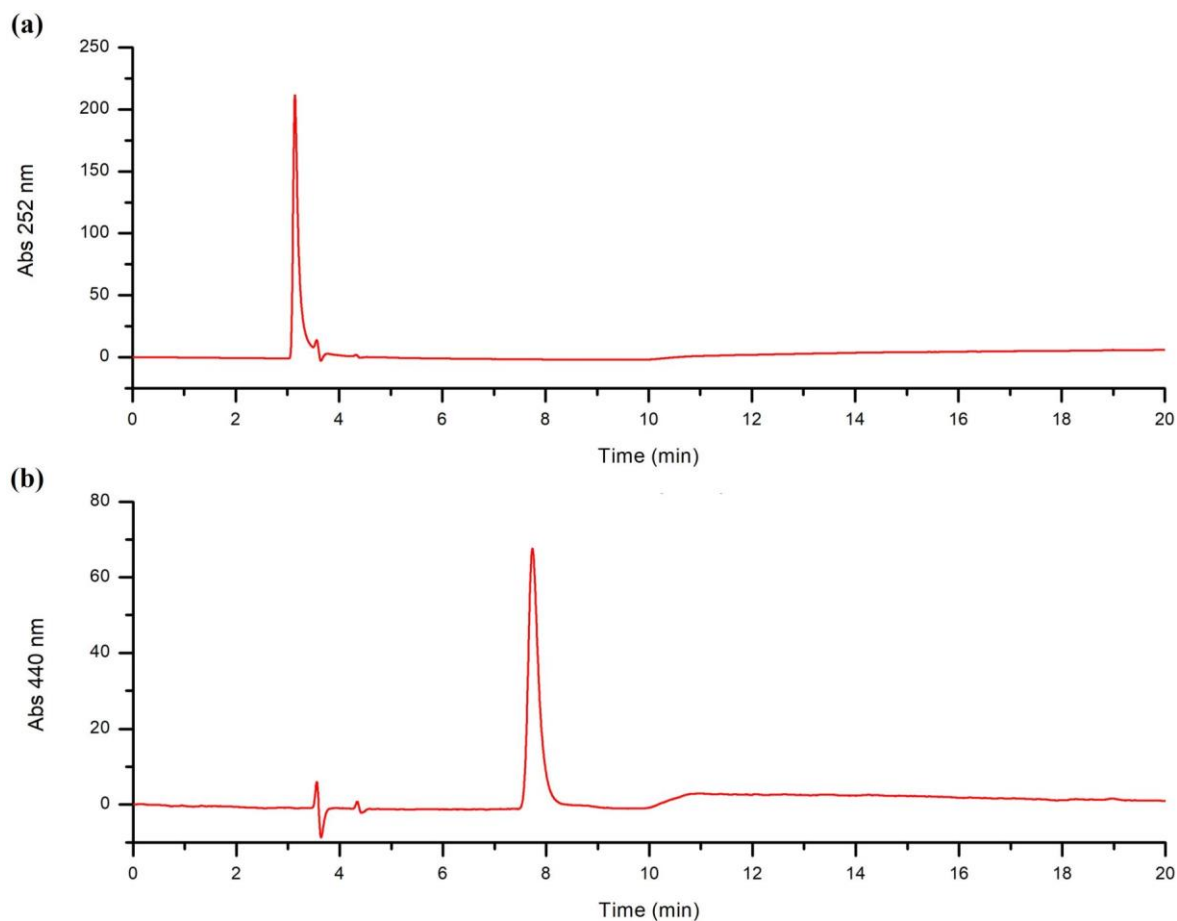


Figure A3.6. HPLC chromatogram ($\lambda_{abs} = 440 \text{ nm}$) of (a) GMP and (b) **38**. Column: Jupiter[®] 5 μm C18 300 \AA , LC Column 250 \times 10.0 mm. Column: Jupiter[®] 5 μm C18 300 \AA , LC Column 250 \times 4.6 mm. Gradient: 0–5 min 85% A, 10% B and 5% C; 5–25 min from 85% A, 10% B and 5% C to 0% A, 95% B and 5% C (A = H₂O, B = MeCN and C = TFA (2%)).

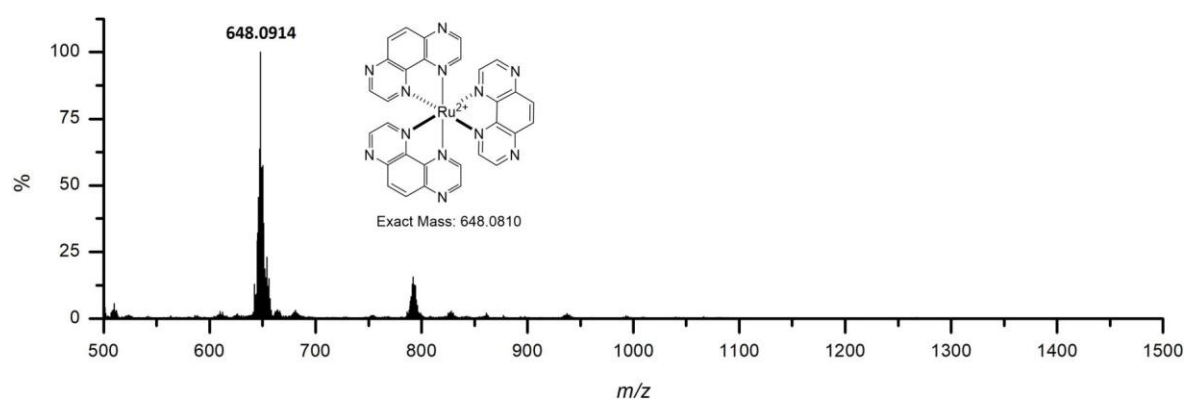


Figure A3.7. Mass spectrum of fraction b obtained by high resolution MALDI-TOF mass spectrometry analysis (α -cyano-4-hydroxycinnamic acid (α -CHCA) matrix, molecular weight 189.17 Da) and corresponding to **38** ($m/z = 648.0810$).

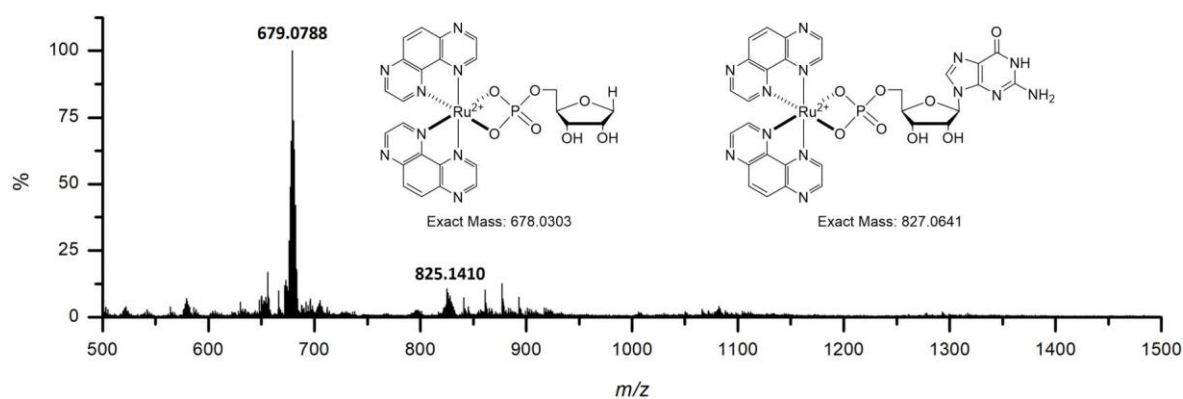


Figure A3.8. Mass spectrum of fraction *c* obtained by high resolution MALDI-TOF mass spectrometry analysis (α -cyano-4-hydroxycinnamic acid (α -CHCA) matrix, molecular weight 189.17 Da) and corresponding to the photoproducts formed by the substitution of a TAP ligand in complex **38** by a GMP, and the loss of the guanine base by such photoproduct (m/z 825.1410 and 679.0788, respectively).

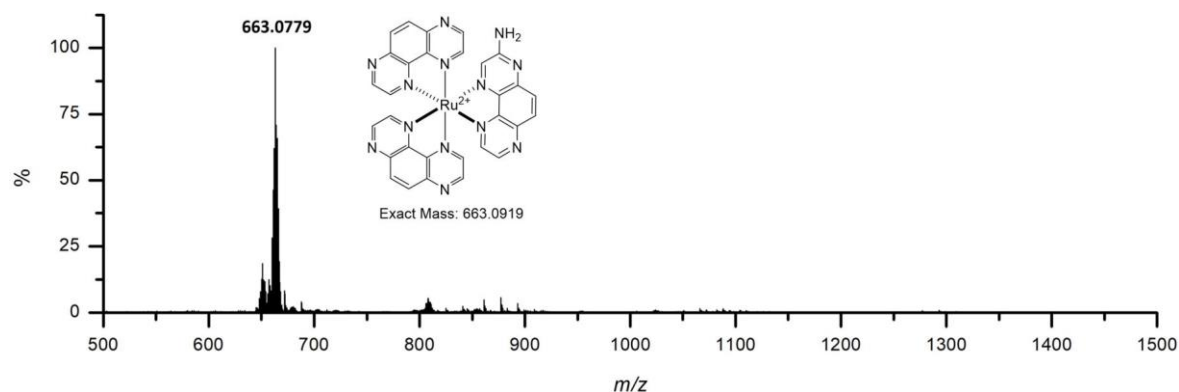


Figure A3.9. Mass spectrum of fraction *d* obtained by high resolution MALDI-TOF mass spectrometry analysis (α -cyano-4-hydroxycinnamic acid (α -CHCA) matrix, molecular weight 189.17 Da) and corresponding to the complex **38** bearing an amino group on one of its TAP ligands (m/z 663.0779).

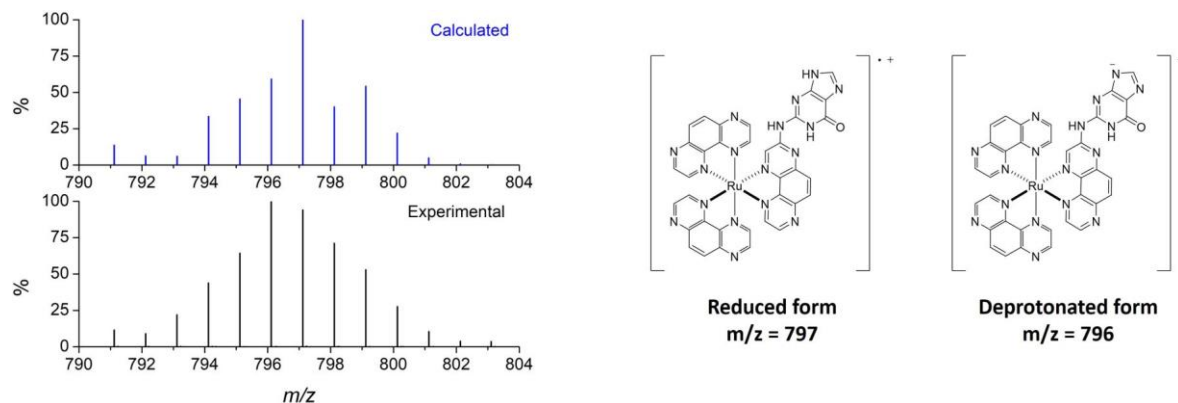


Figure A3.10. Comparison between the calculated (blue) and experimental (black) isotopic distribution pattern for **77** obtained by high resolution MALDI-TOF mass spectrometry analysis.

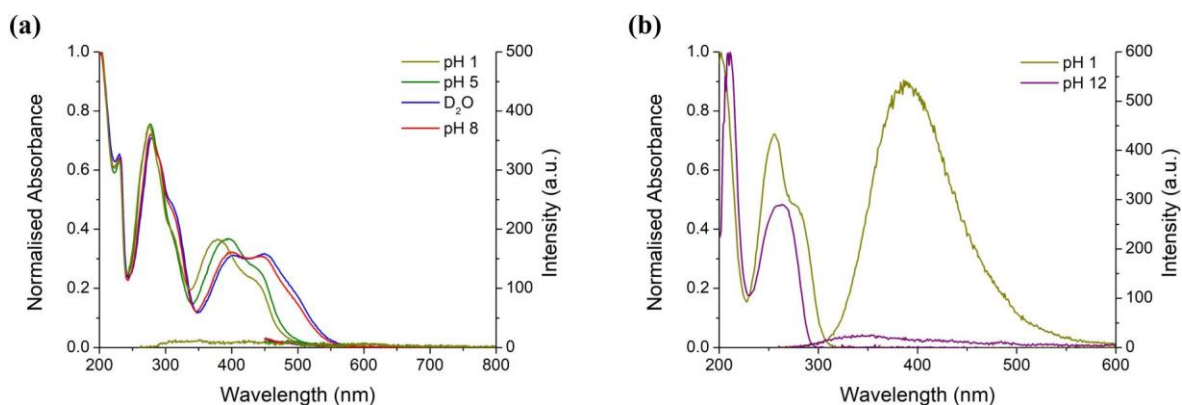


Figure A3.11. UV-vis absorption and emission spectra of (a) **43** in D₂O (blue) and 10 mM potassium phosphate-buffered D₂O solution at pH 1 (dark yellow), 5 (green) and 8 (red), and (b) GMP in 10 mM potassium phosphate-buffered D₂O solution at pH 1 (dark yellow) and 12 (purple), at 298 K.

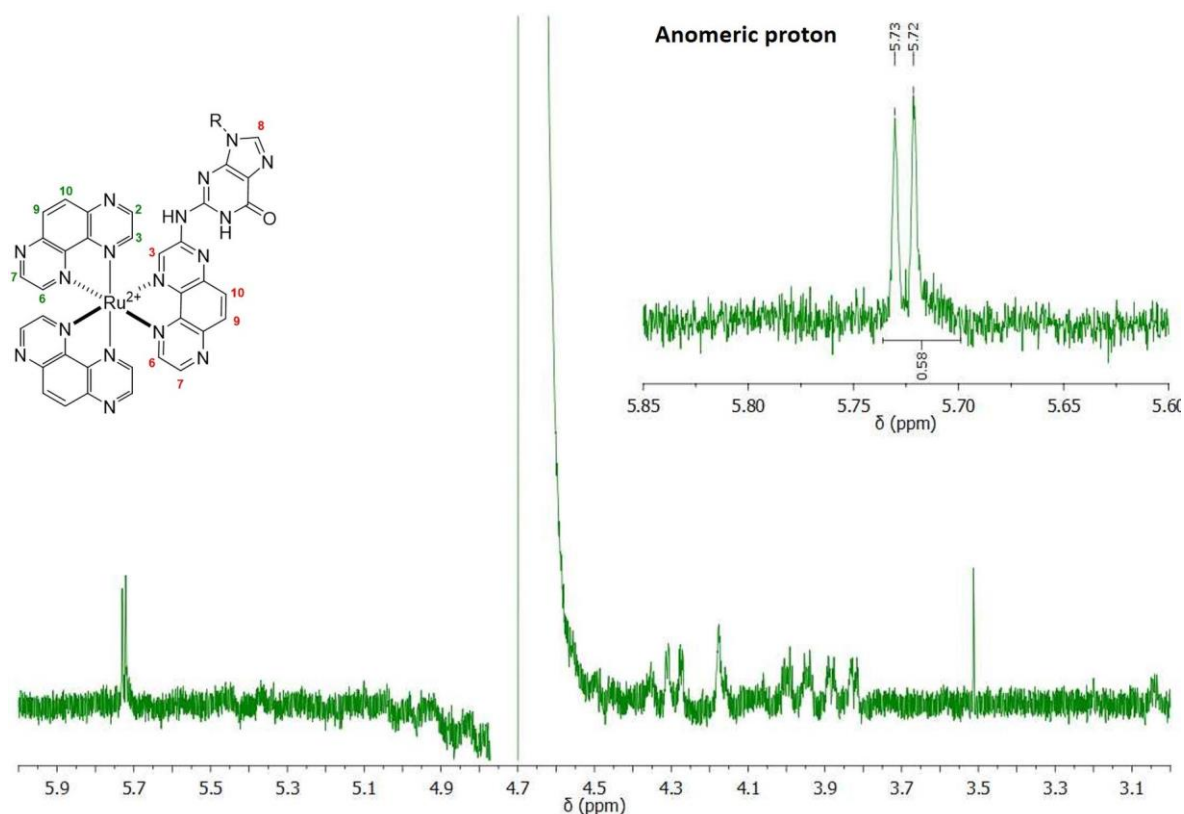


Figure A3.12. ¹H NMR (800 MHz) spectrum of **43** (400 μM, R = ribose-phosphate) in 10 mM potassium phosphate-buffered H₂O/D₂O (95:5) solution at pH 5 and 293 K, showing the sugar protons between 3.0 and 6.0 ppm.

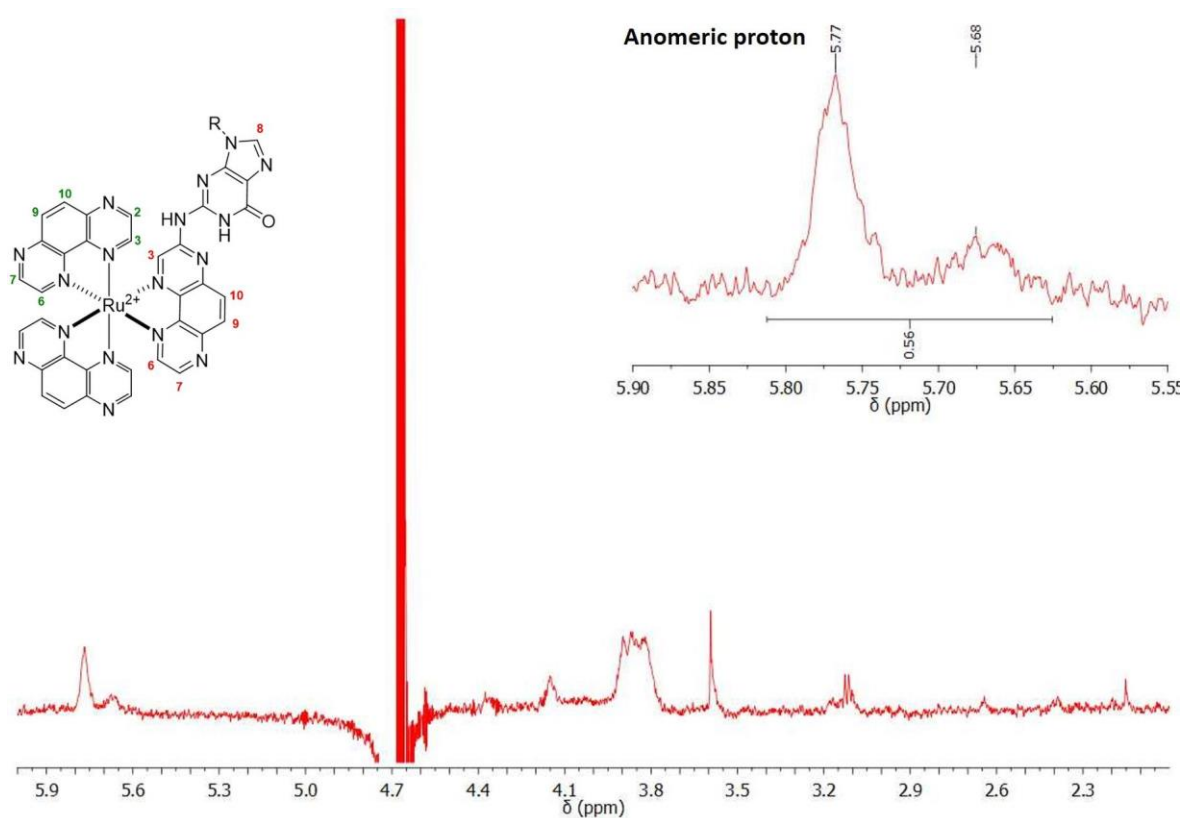


Figure A3.13. ^1H NMR (800 MHz) spectrum of **43** (400 μM , R = ribose-phosphate) in 10 mM potassium phosphate-buffered $\text{H}_2\text{O}/\text{D}_2\text{O}$ (95:5) solution at pH 8 and 293 K, showing the sugar protons between 3.0 and 6.0 ppm.

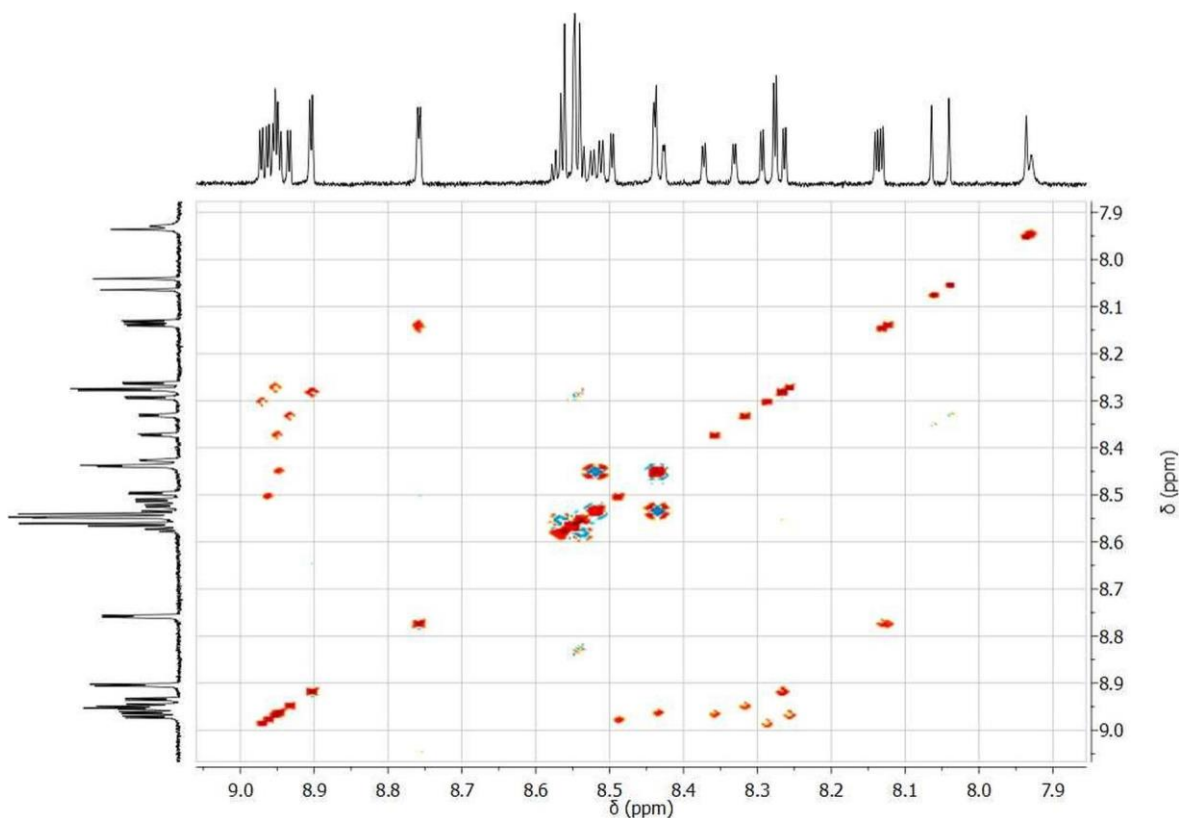


Figure A3.14. TOCSY (600 MHz) spectrum of **43** (200 μM) in 10 mM potassium phosphate-buffered $\text{H}_2\text{O}/\text{D}_2\text{O}$ (95:5) solution at pH 5 and 293 K.

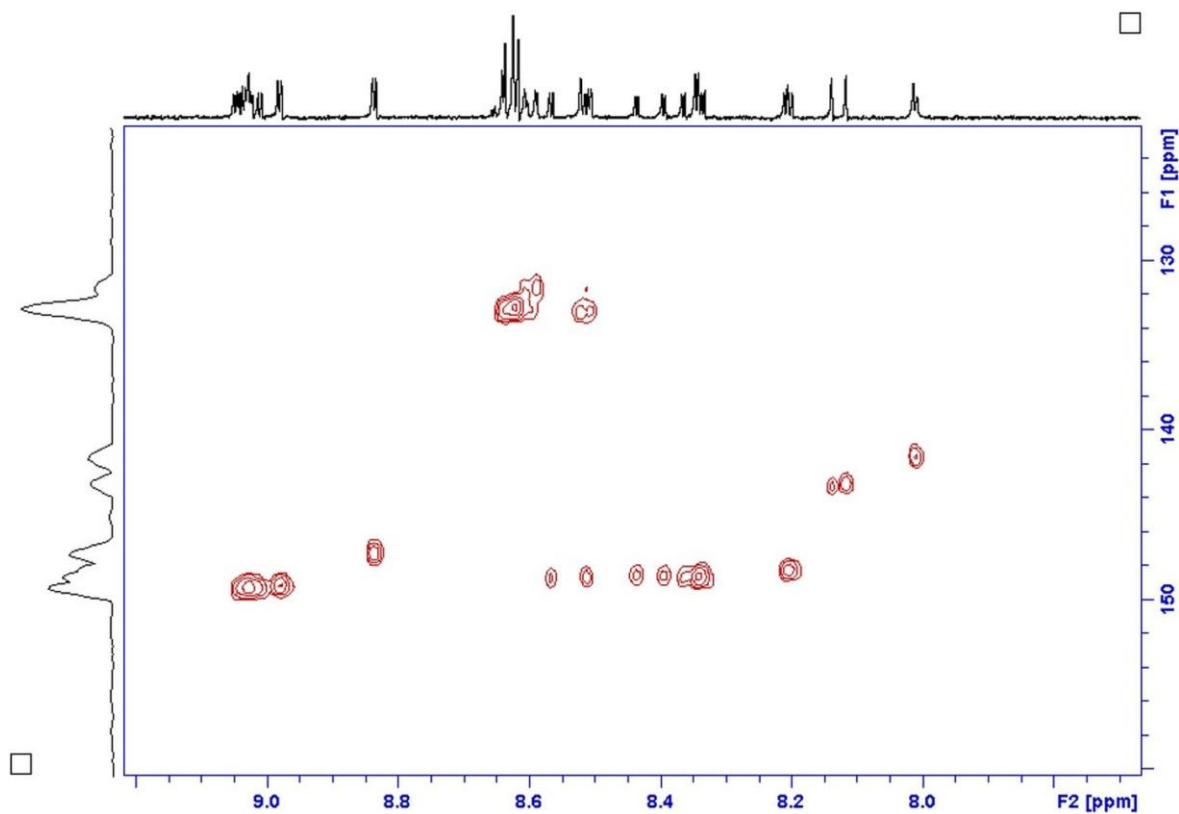


Figure A3.15. HSQC (600 MHz) spectrum of **43** (200 μM) in 10 mM potassium phosphate-buffered $\text{H}_2\text{O}/\text{D}_2\text{O}$ (95:5) solution at pH 5 and 293 K.

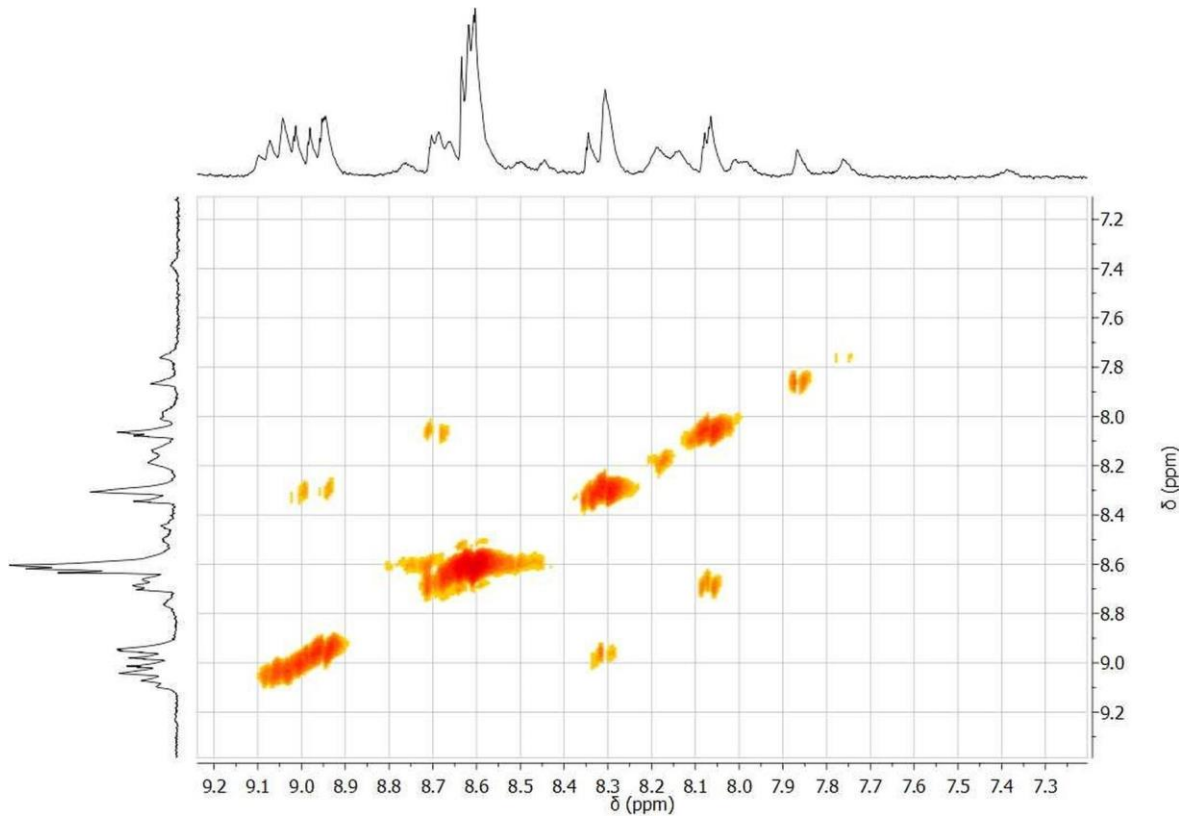


Figure A3.16. COSY (600 MHz) spectrum of **43** (400 μM) in 10 mM potassium phosphate-buffered $\text{H}_2\text{O}/\text{D}_2\text{O}$ (95:5) solution at pH 8 and 293 K.

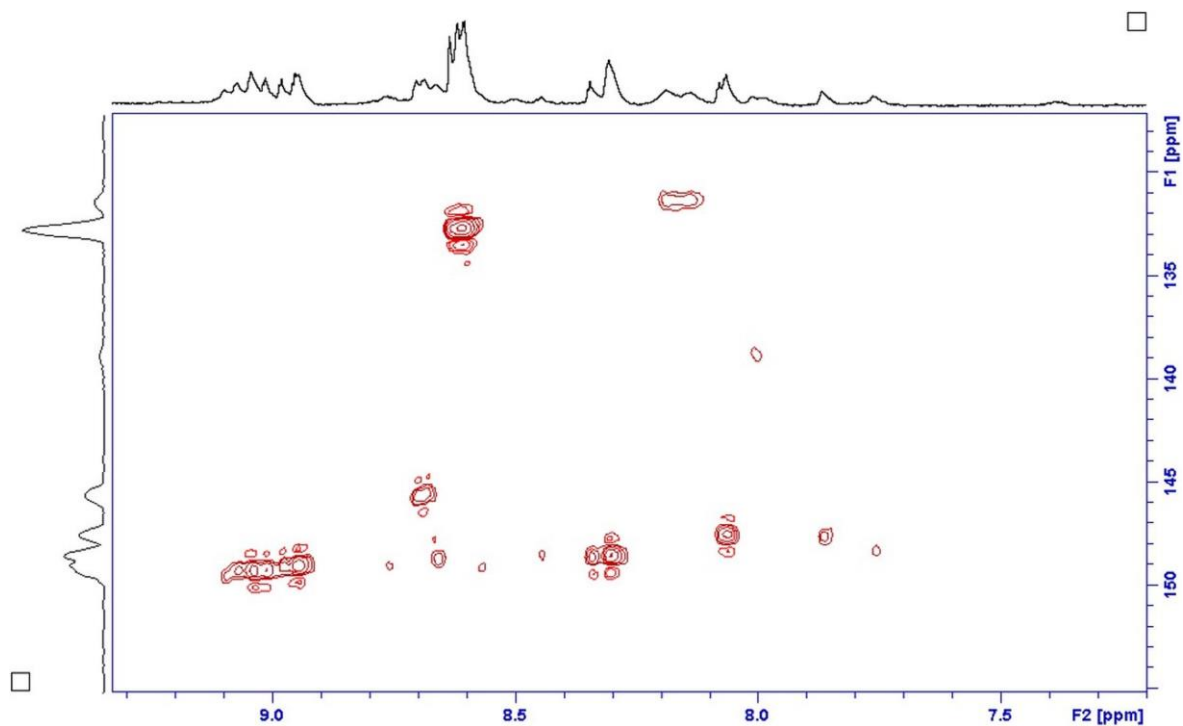


Figure A3.17. HSQC (600 MHz) spectrum of **43** (400 μM) in 10 mM potassium phosphate-buffered $\text{H}_2\text{O}/\text{D}_2\text{O}$ (95:5) solution at pH 8 and 293 K.

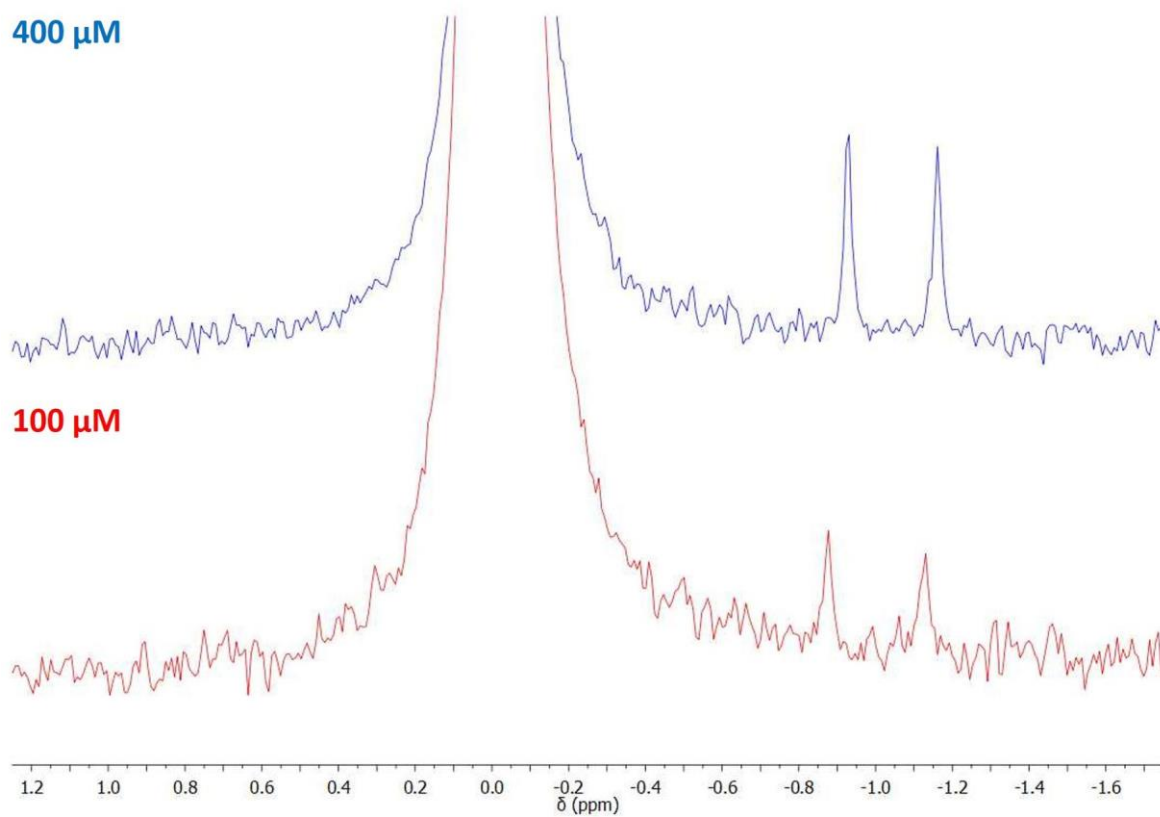


Figure A3.18. ^{31}P NMR (162 MHz) spectrum of **43** at 400 and 200 μM in 10 mM potassium phosphate-buffered $\text{H}_2\text{O}/\text{D}_2\text{O}$ (95:5) solution at pH 5, at 295 K.

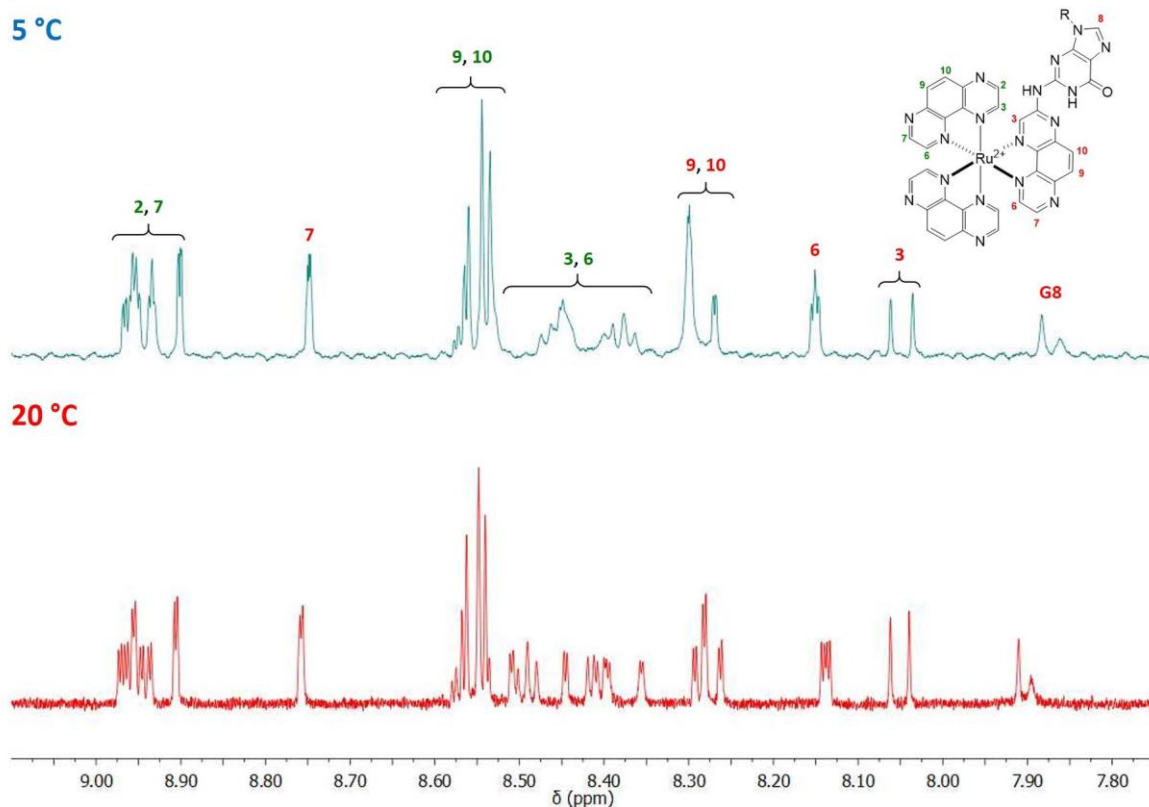


Figure A3.19. ^1H NMR (800 MHz) spectrum of **43** (400 μM) at 5 and 20 °C in 10 mM potassium phosphate-buffered $\text{H}_2\text{O}/\text{D}_2\text{O}$ (95:5) solution at pH 5.

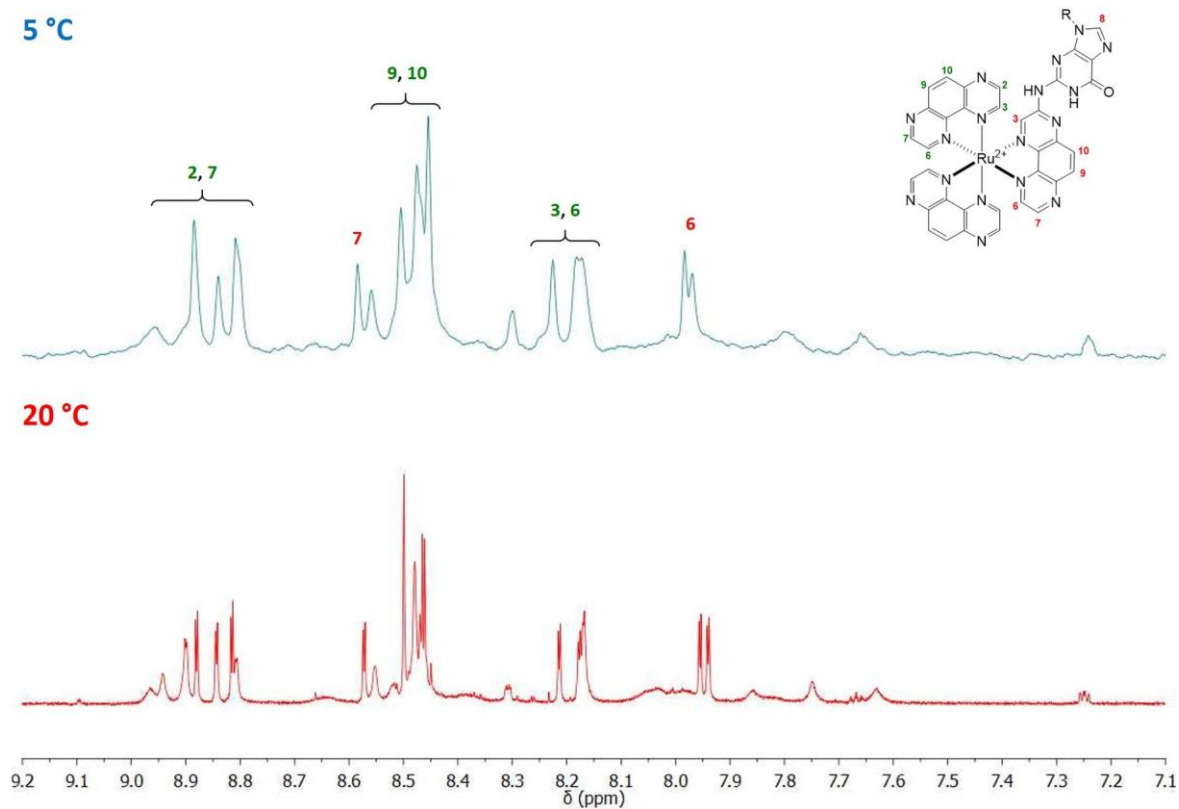


Figure A3.20. ^1H NMR (800 MHz) spectrum of **43** (400 μM) at 5 and 20 °C in 10 mM potassium phosphate-buffered $\text{H}_2\text{O}/\text{D}_2\text{O}$ (95:5) solution at pH 8.

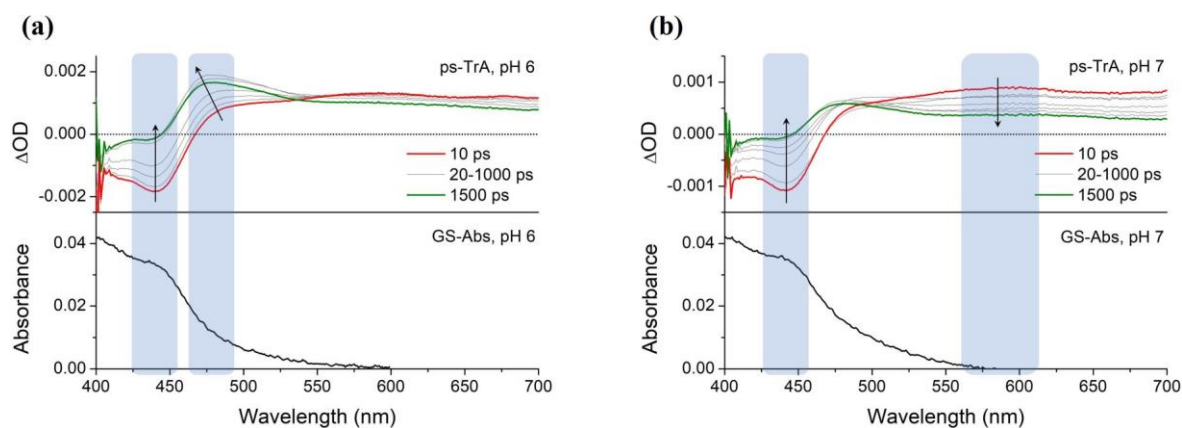


Figure A3.21. ps-TrA spectra recorded at the stated time delays after 373 nm excitation of **43** (400 μM) in 50 mM potassium phosphate-buffered D_2O solution at (a) pH 6 and (b) pH 7, and the corresponding ground-state absorption (GS-Abs) spectra.

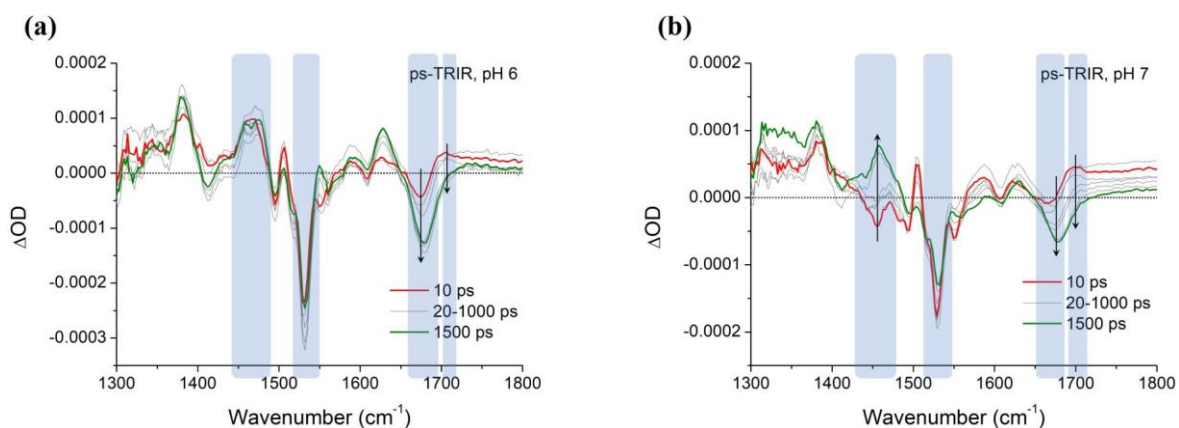


Figure A3.22. ps-TRIR spectra recorded at the stated time delays after 373 nm excitation of **43** (400 μM) in 50 mM potassium phosphate-buffered D_2O solution at (a) pH 6 and (b) pH 7.

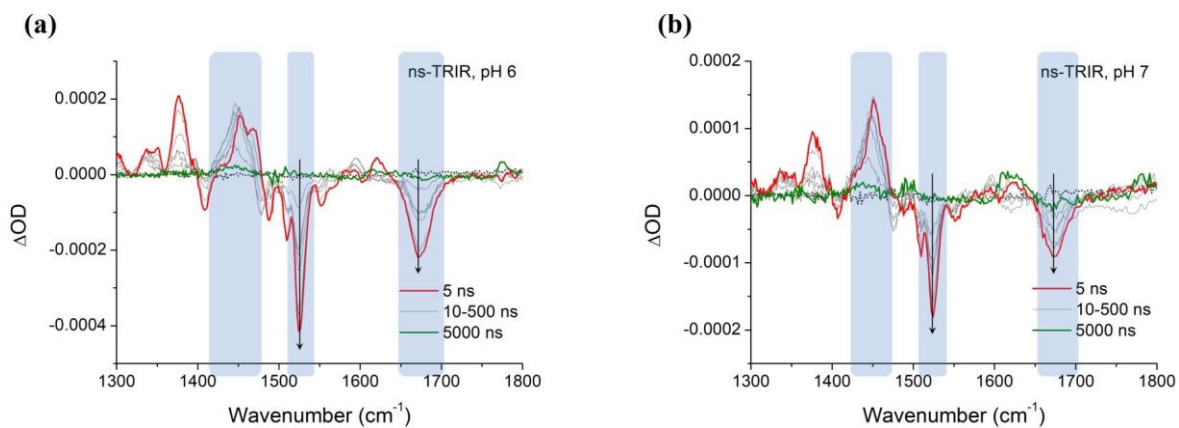


Figure A3.23. ns-TRIR spectra recorded at the stated time delays after 373 nm excitation of **43** (400 μM) in 50 mM potassium phosphate-buffered D_2O solution at (a) pH 6 and (b) pH 7.

Appendix 4

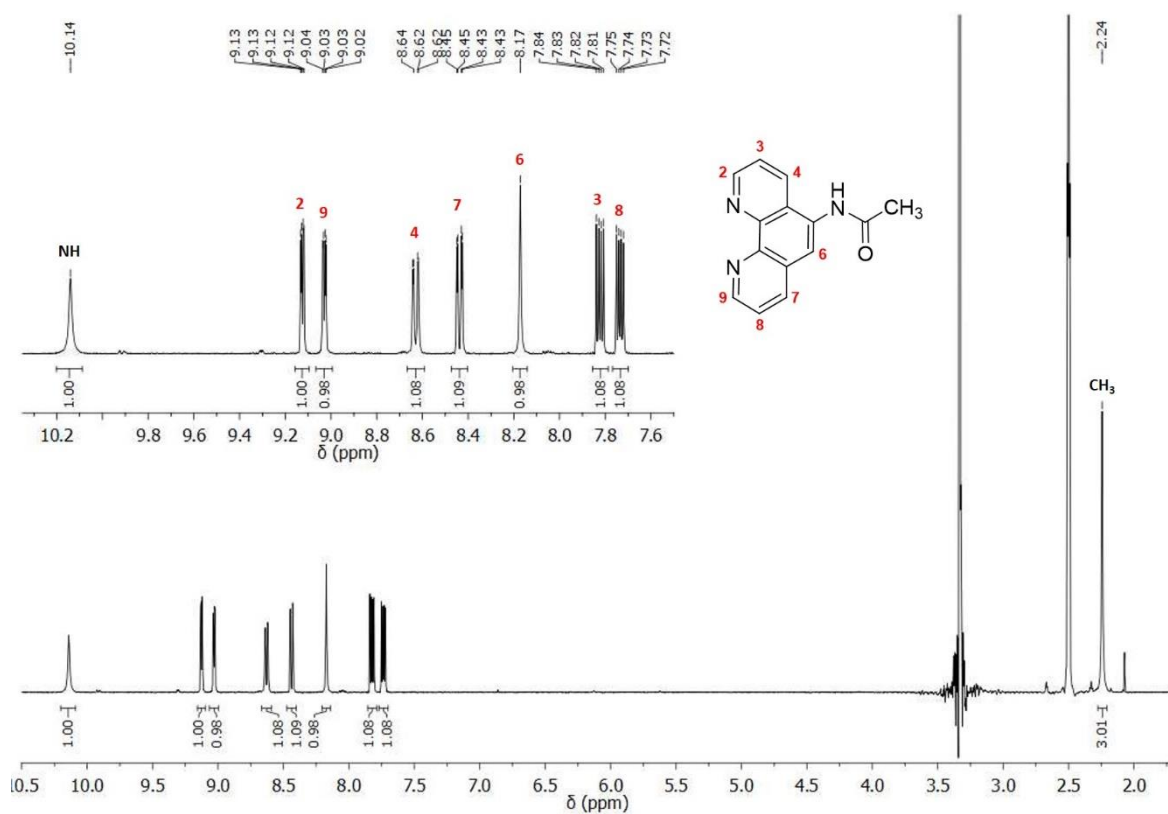


Figure A4.1. ¹H NMR (400 MHz, DMSO-d₆) spectrum of ligand 84.

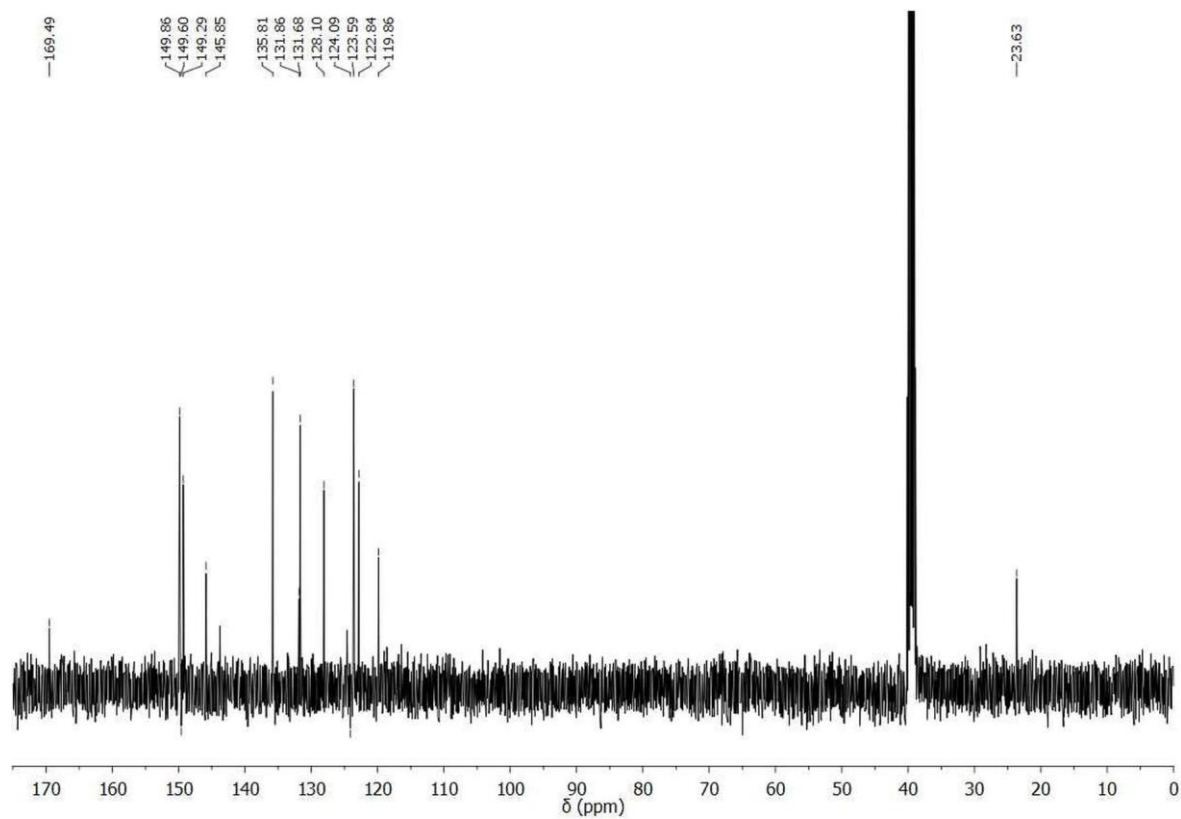


Figure A4.2. ¹³C NMR (101 MHz, DMSO-d₆) spectrum of ligand 84.

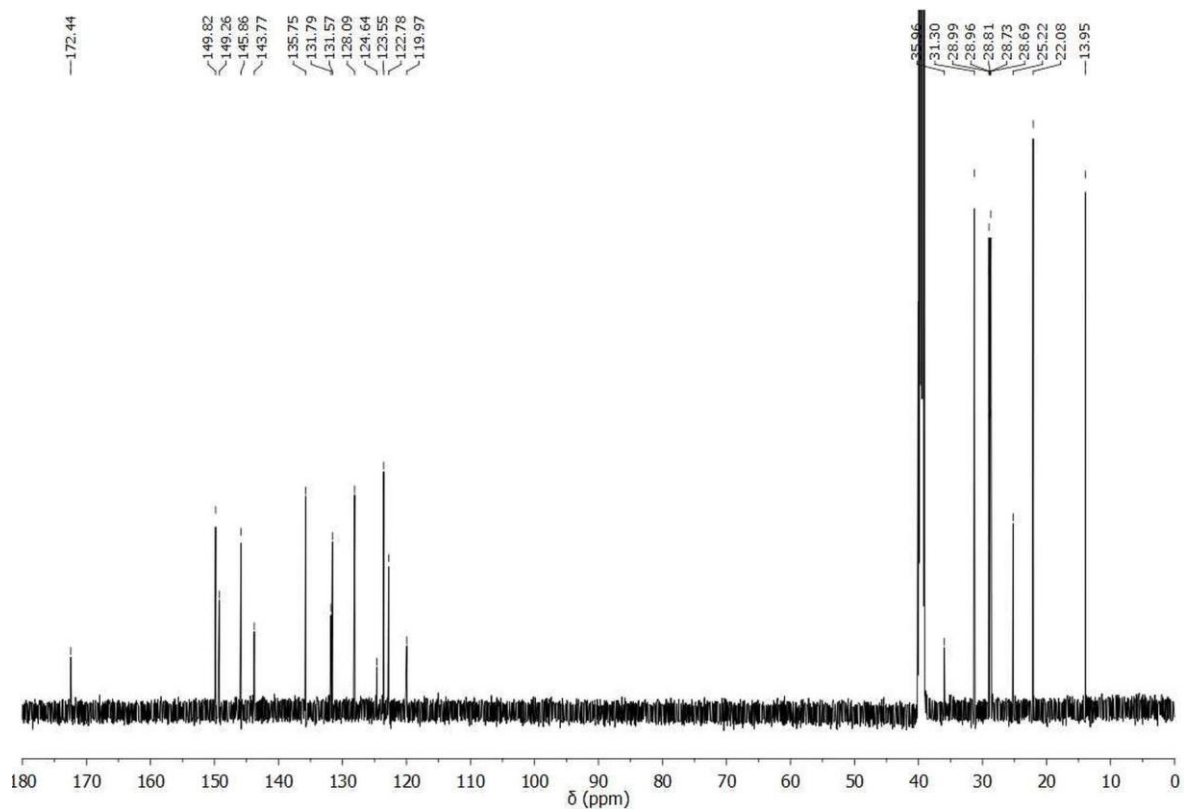


Figure A4.3. ^{13}C NMR (151 MHz, DMSO-d_6) spectrum of ligand 85.

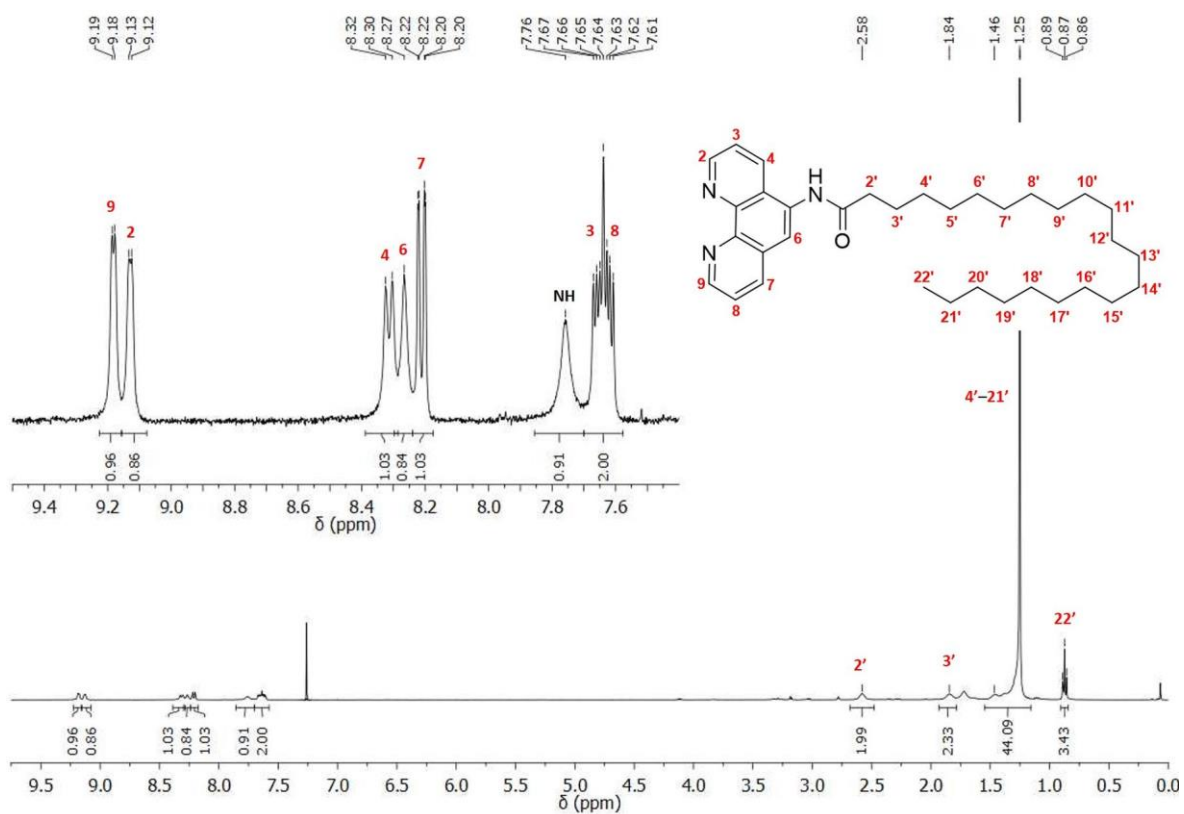


Figure A4.4. ^1H NMR (600 MHz, CDCl_3) spectrum of ligand 86.

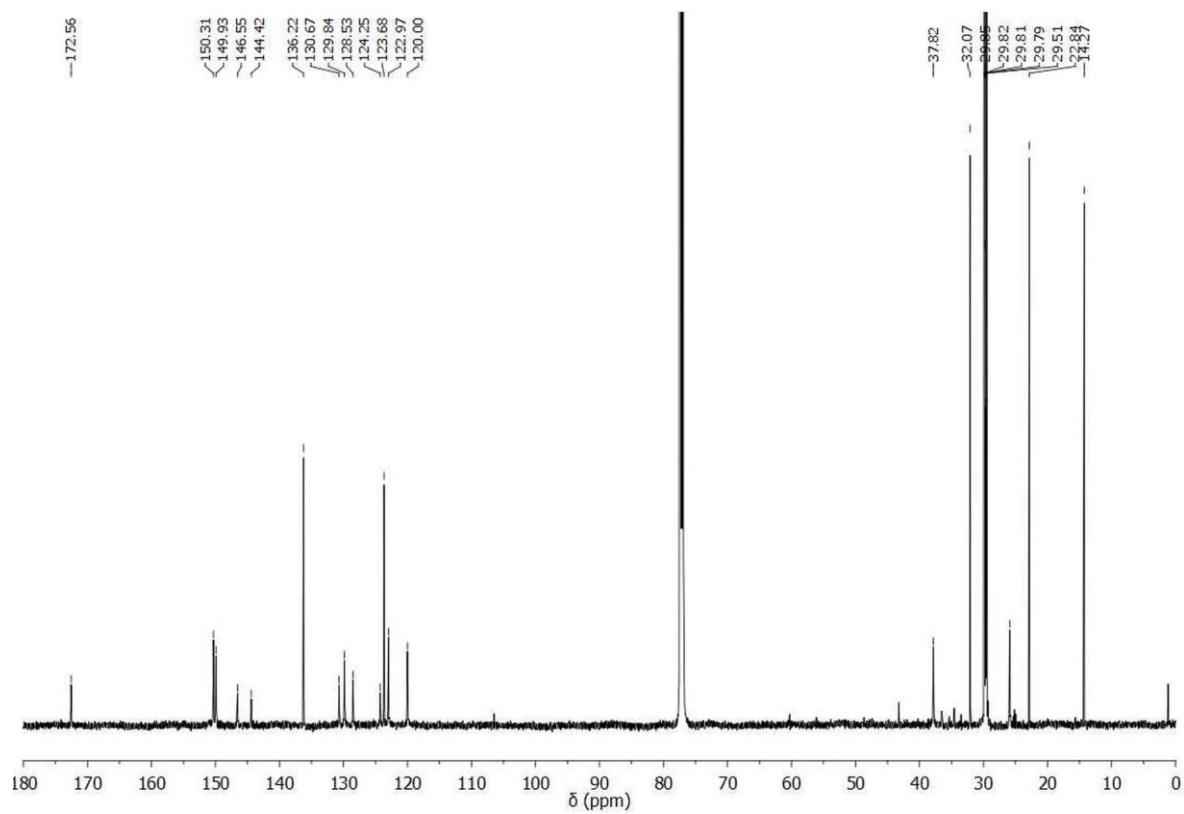


Figure A4.5. ^{13}C NMR (151 MHz, CDCl_3) spectrum of ligand **86**.

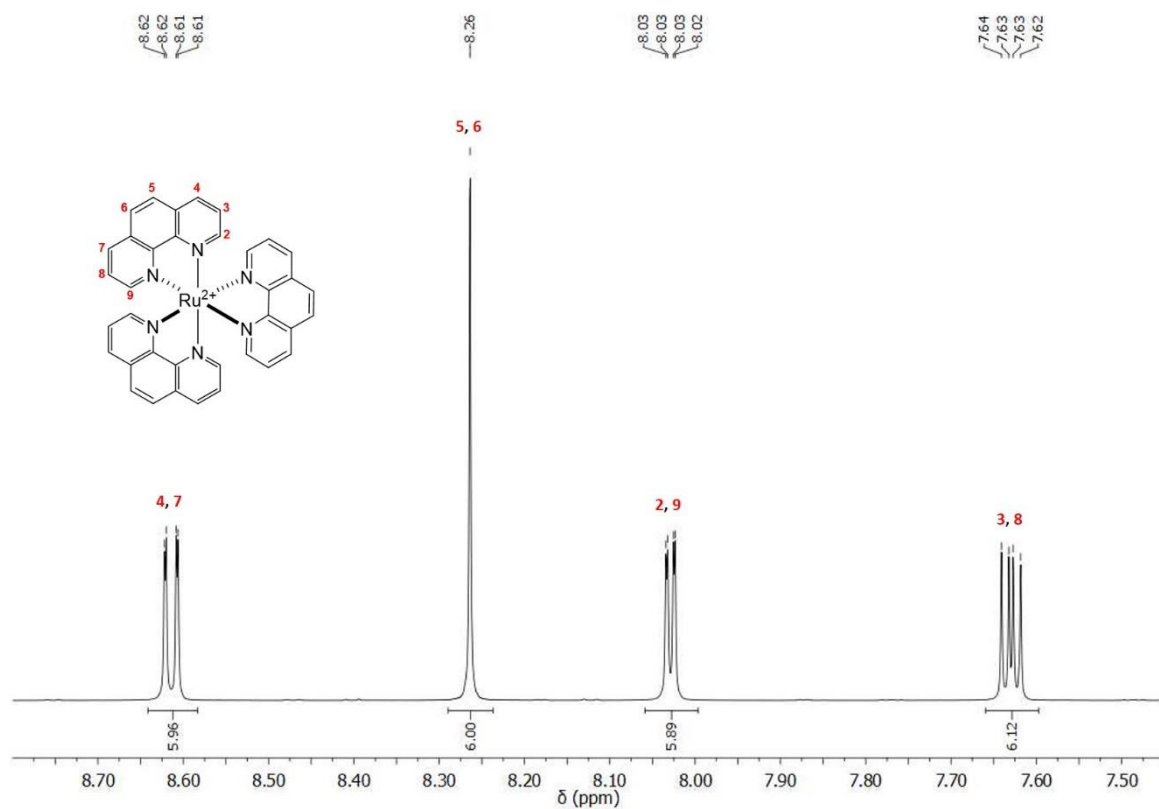


Figure A4.6. ^1H NMR (600 MHz, CD_3CN) spectrum of **42**.

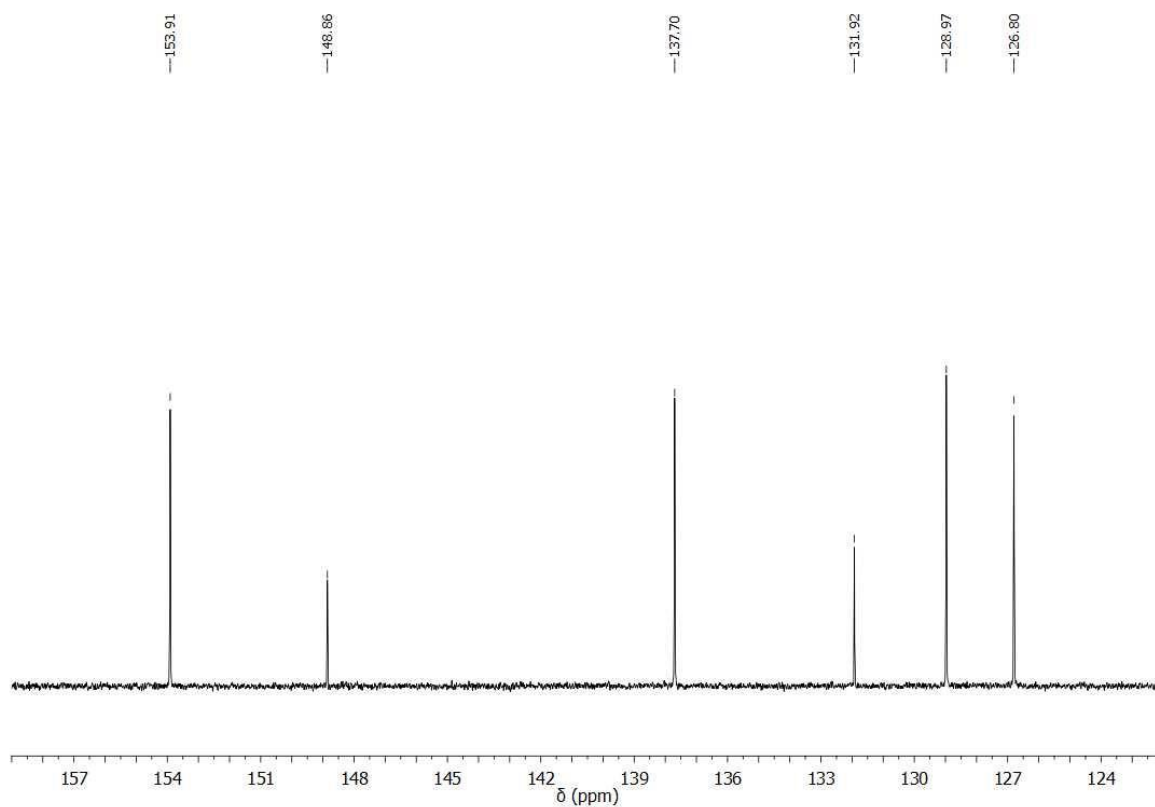


Figure A4.7. ^{13}C NMR (151 MHz, CD_3CN) spectrum of **42**.

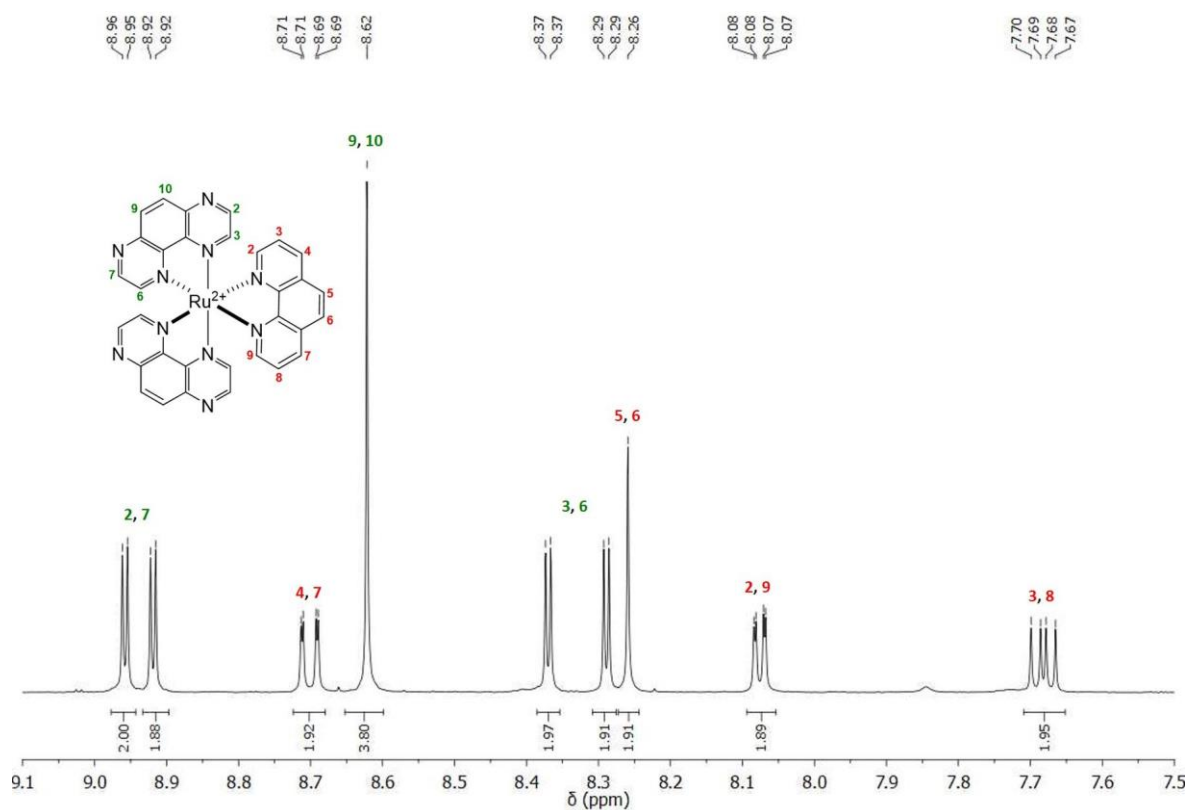


Figure A4.8. ^1H NMR (400 MHz, D_2O) spectrum of **39**. Signals corresponding to **TAP** ligands are in green and signals assigned to the **phen** ligand are in red.

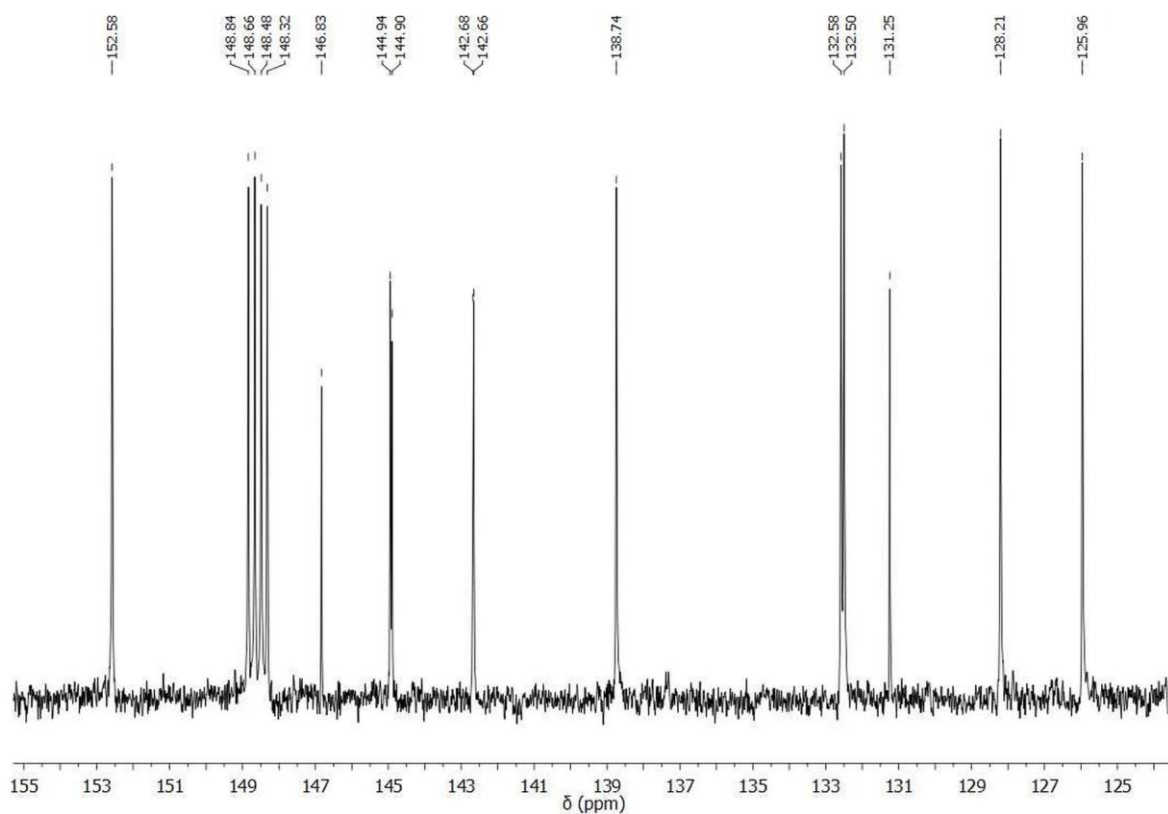


Figure A4.9. ^{13}C NMR (101 MHz, D_2O) spectrum of **39**.

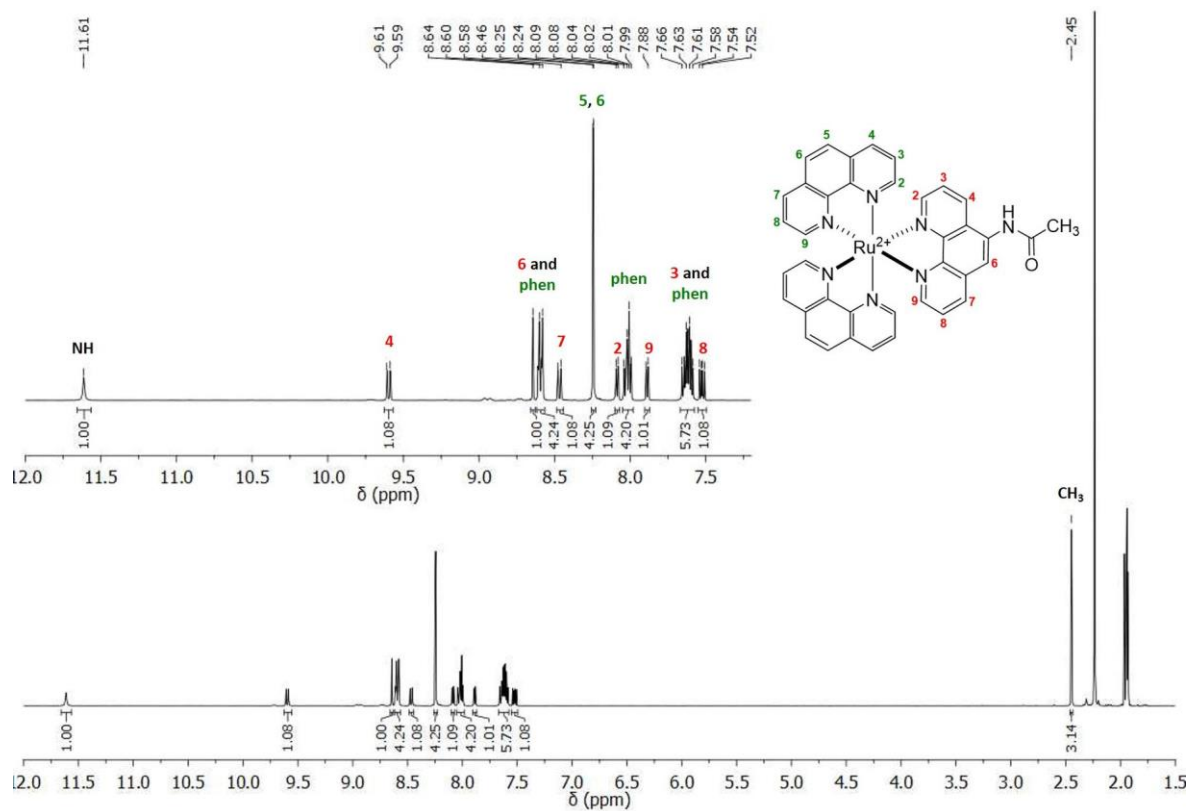


Figure A4.10. ^1H NMR (400 MHz, CD_3CN) spectrum of **78**. Signals corresponding to *phen* ligands are in green and signals assigned to ligand **84** ligand are in red.

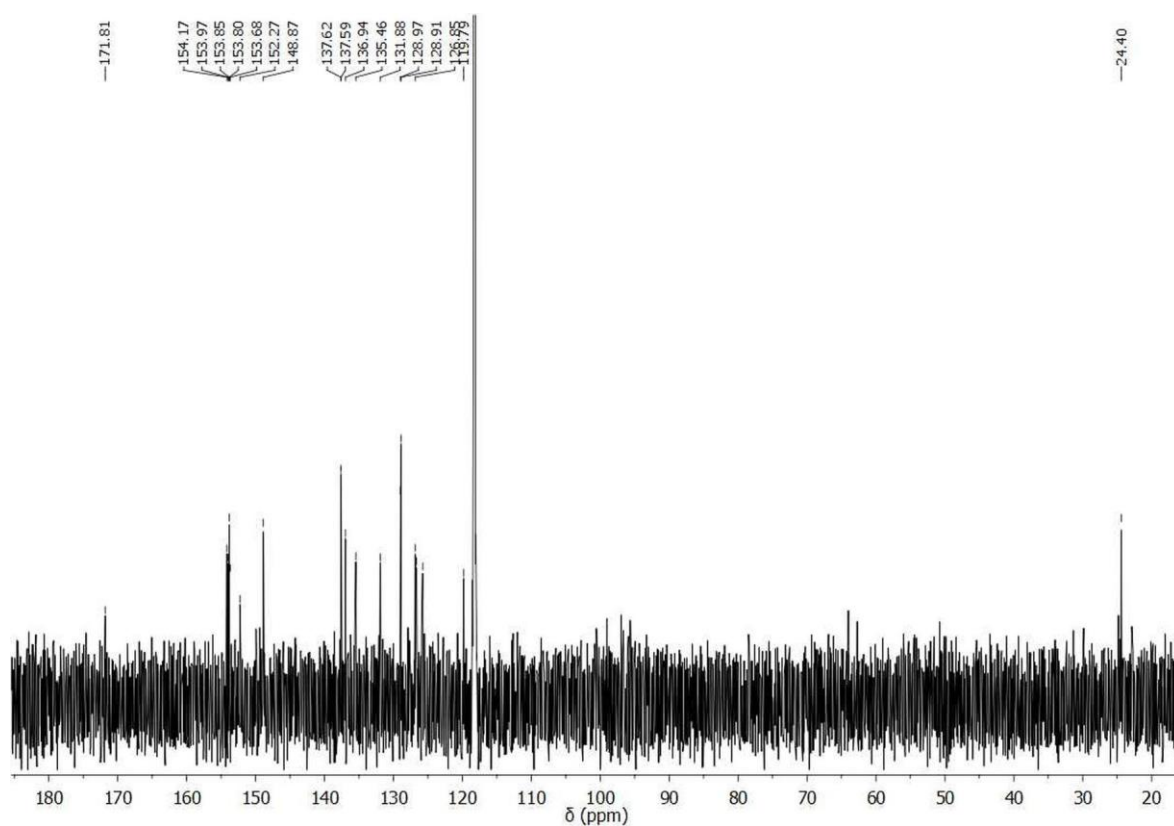


Figure A4.11. ^{13}C NMR (101 MHz, CD_3CN) spectrum of 78.

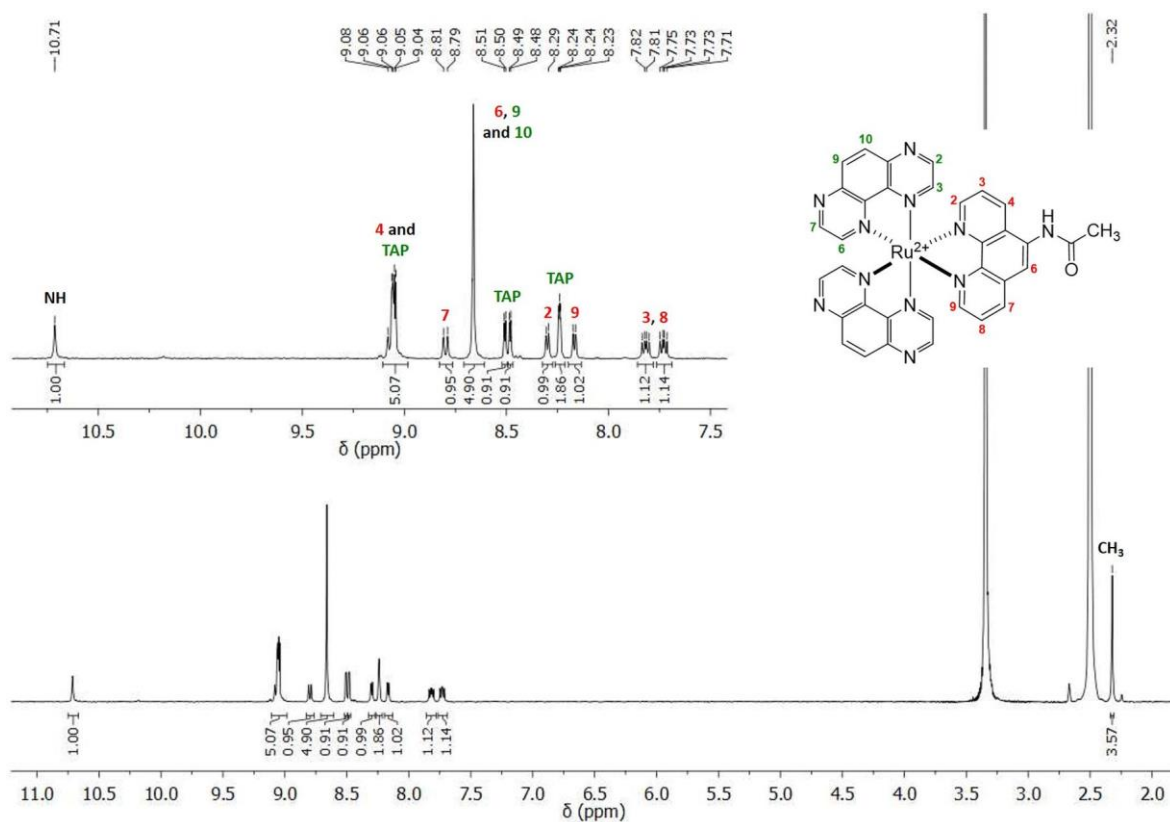


Figure A4.12. ^1H NMR (400 MHz, DMSO-d_6) spectrum of 81. Signals corresponding to TAP ligands are in green and signals assigned to ligand 84 are in red.

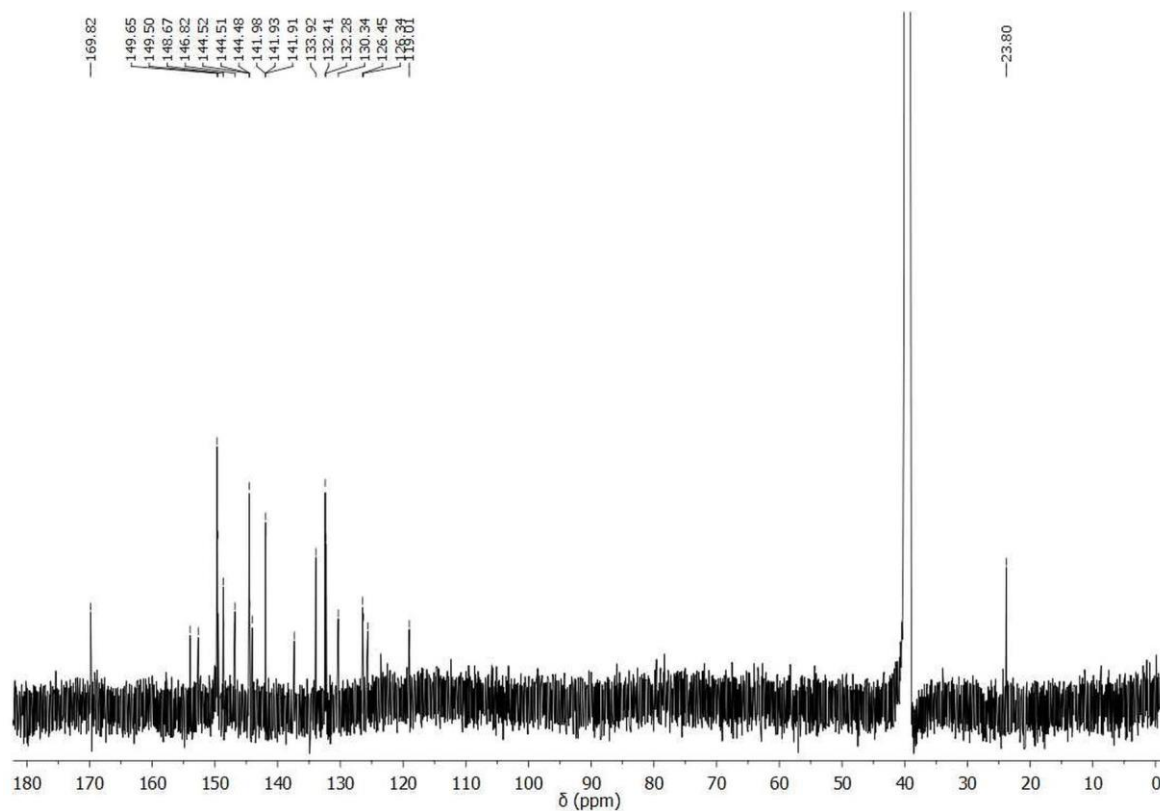


Figure A4.13. ^{13}C NMR (151 MHz, DMSO-d_6) spectrum of **81**.

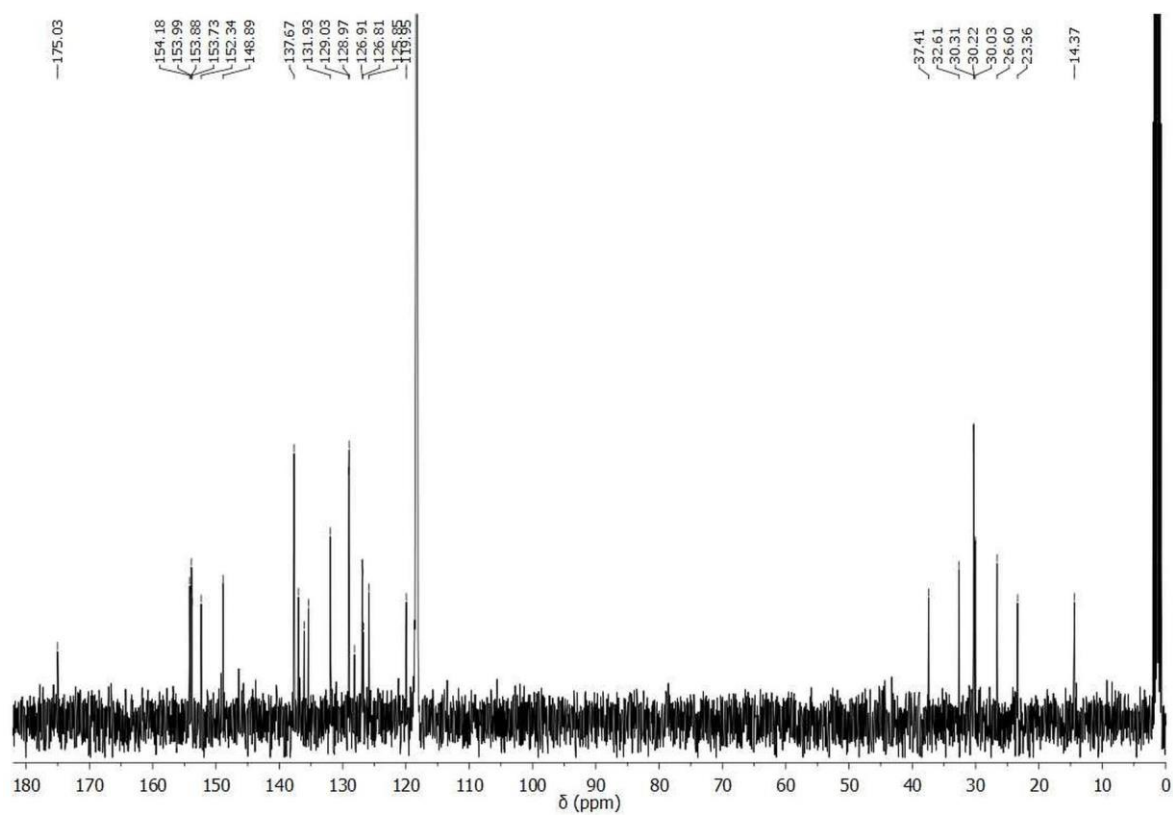


Figure A4.14. ^{13}C NMR (101 MHz, CD_3CN) spectrum of **79**.

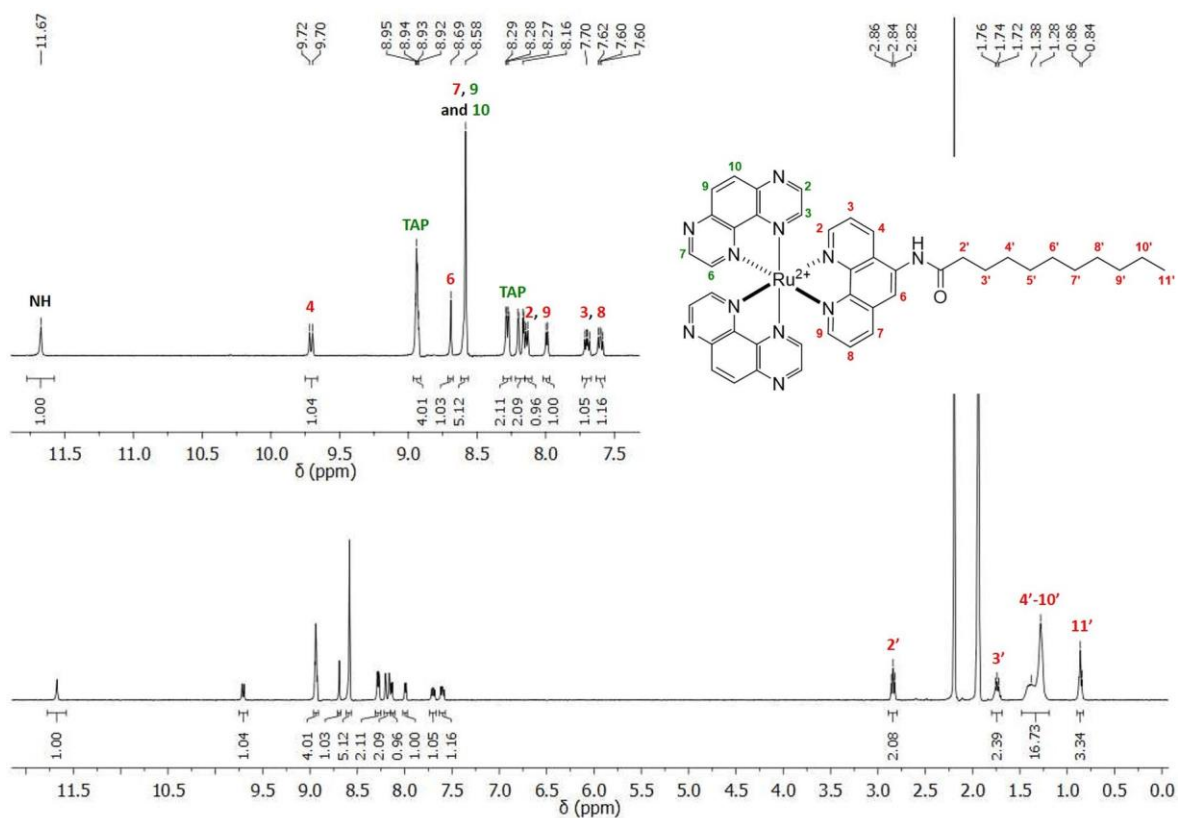


Figure A4.15. ^1H NMR (400 MHz, CD_3CN) spectrum of **82**. Signals corresponding to TAP ligands are in green and signals assigned to ligand **85** are in red.

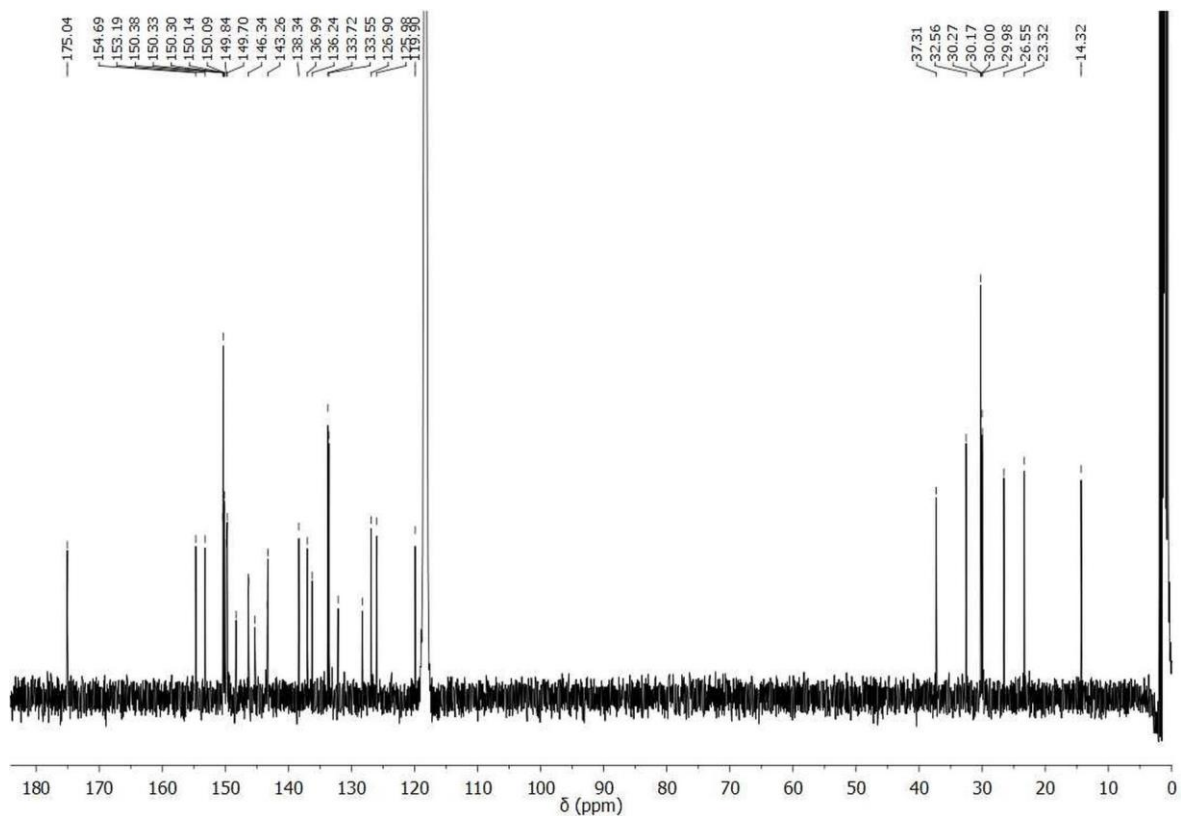


Figure A4.16. ^{13}C NMR (101 MHz, CD_3CN) spectrum of **82**.

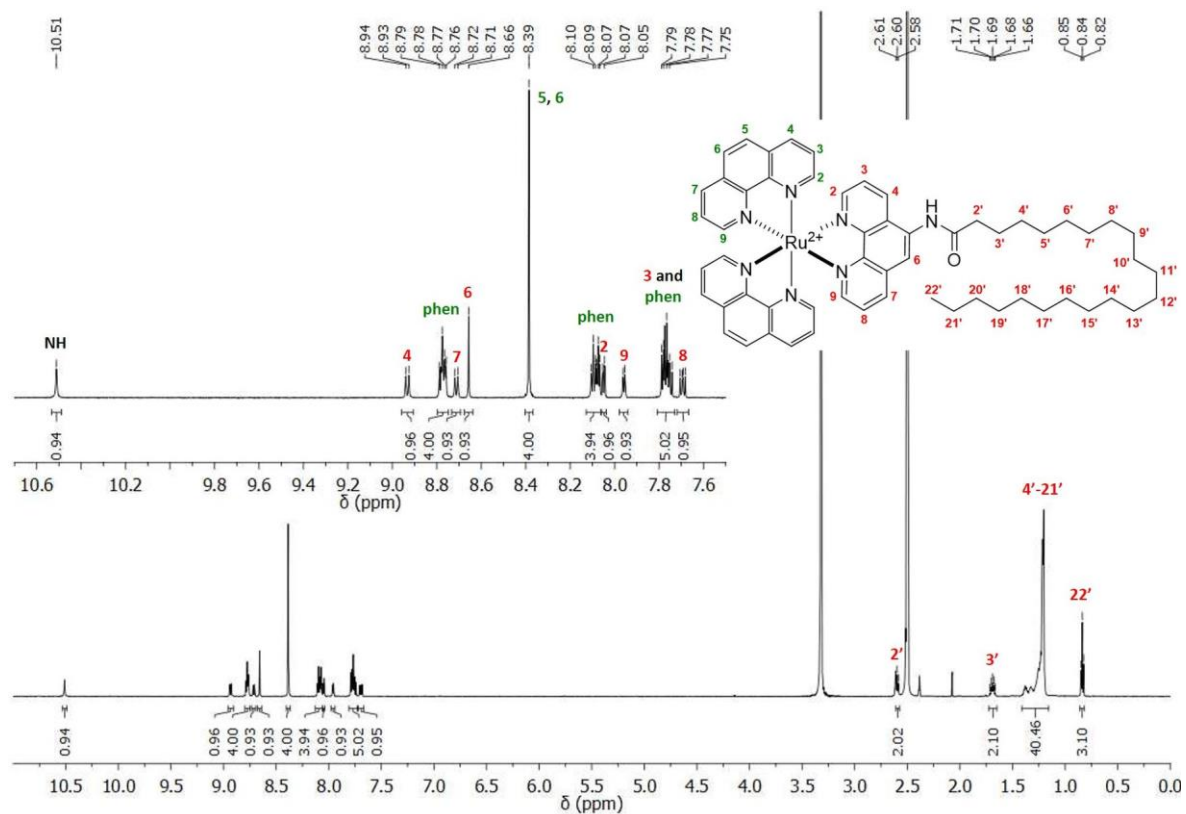


Figure A4.17. ^1H NMR (600 MHz, $\text{DMSO-}d_6$) spectrum of **80**. Signals corresponding to **phen** ligands are in green and signals assigned to ligand **86** ligand are in red.

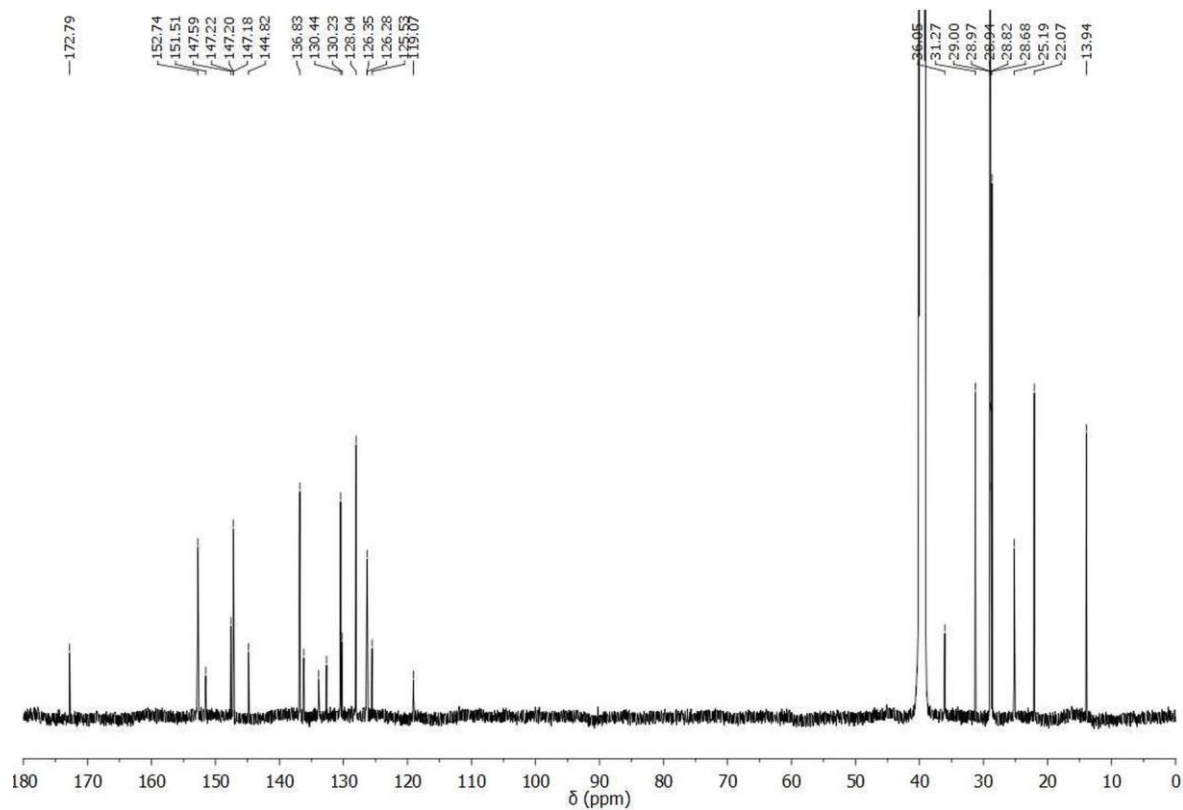


Figure A4.18. ^{13}C NMR (151 MHz, $\text{DMSO-}d_6$) spectrum of **80**.

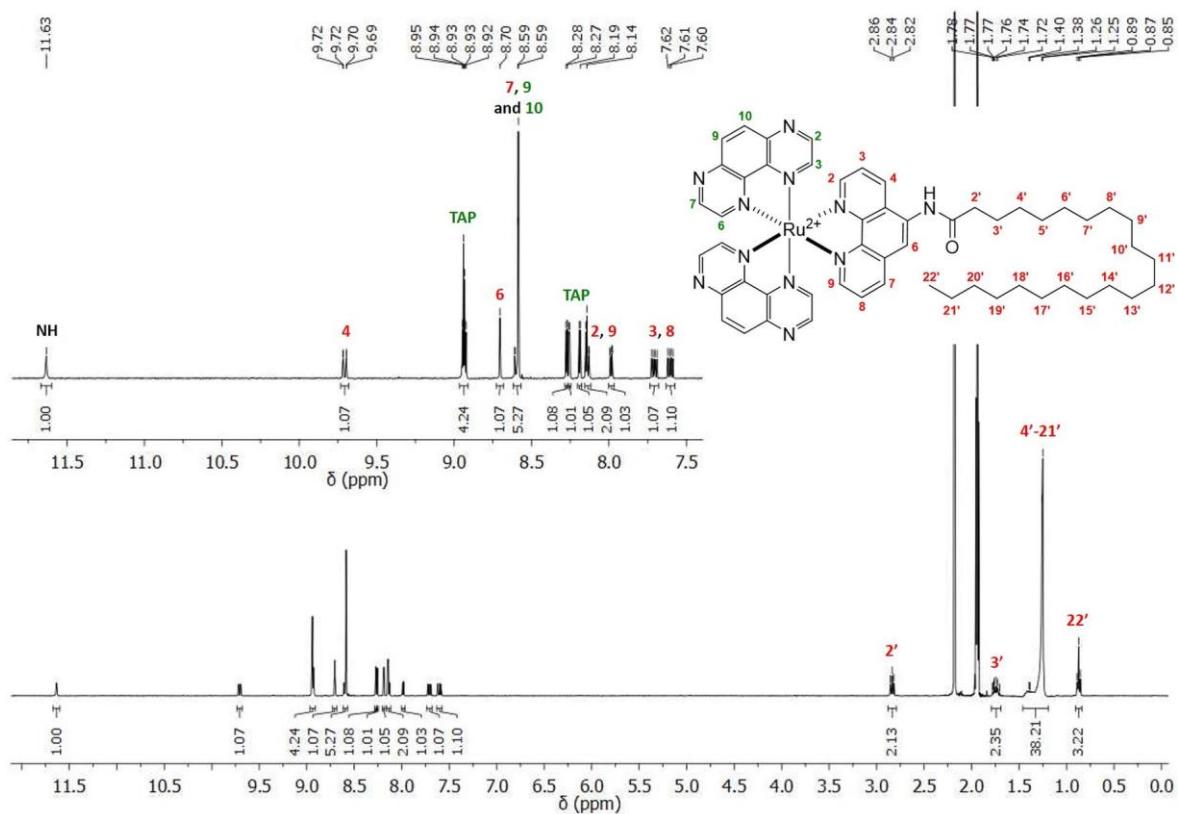


Figure A4.19. ^1H NMR (400 MHz, CD_3CN) spectrum of **83**. Signals corresponding to TAP ligands are in green and signals assigned to ligand **86** are in red.

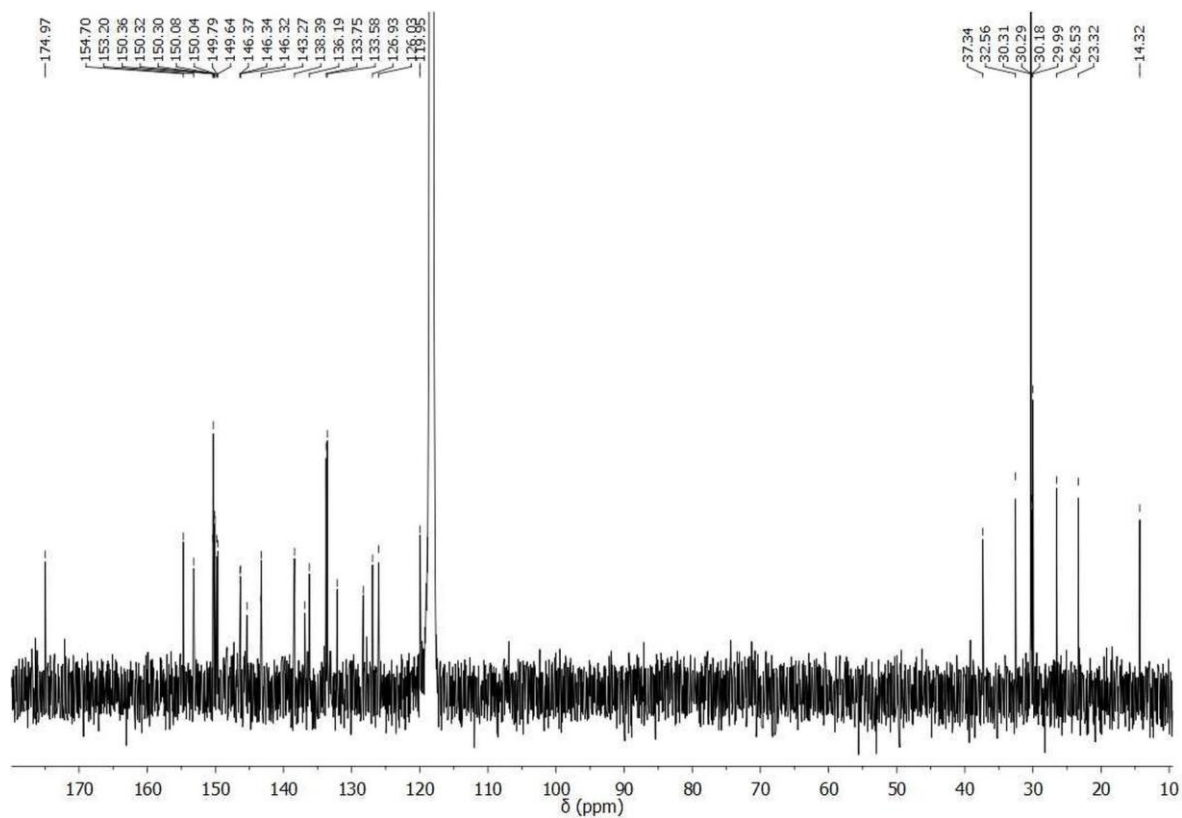


Figure A4.20. ^{13}C NMR (101 MHz, CD_3CN) spectrum of **83**.

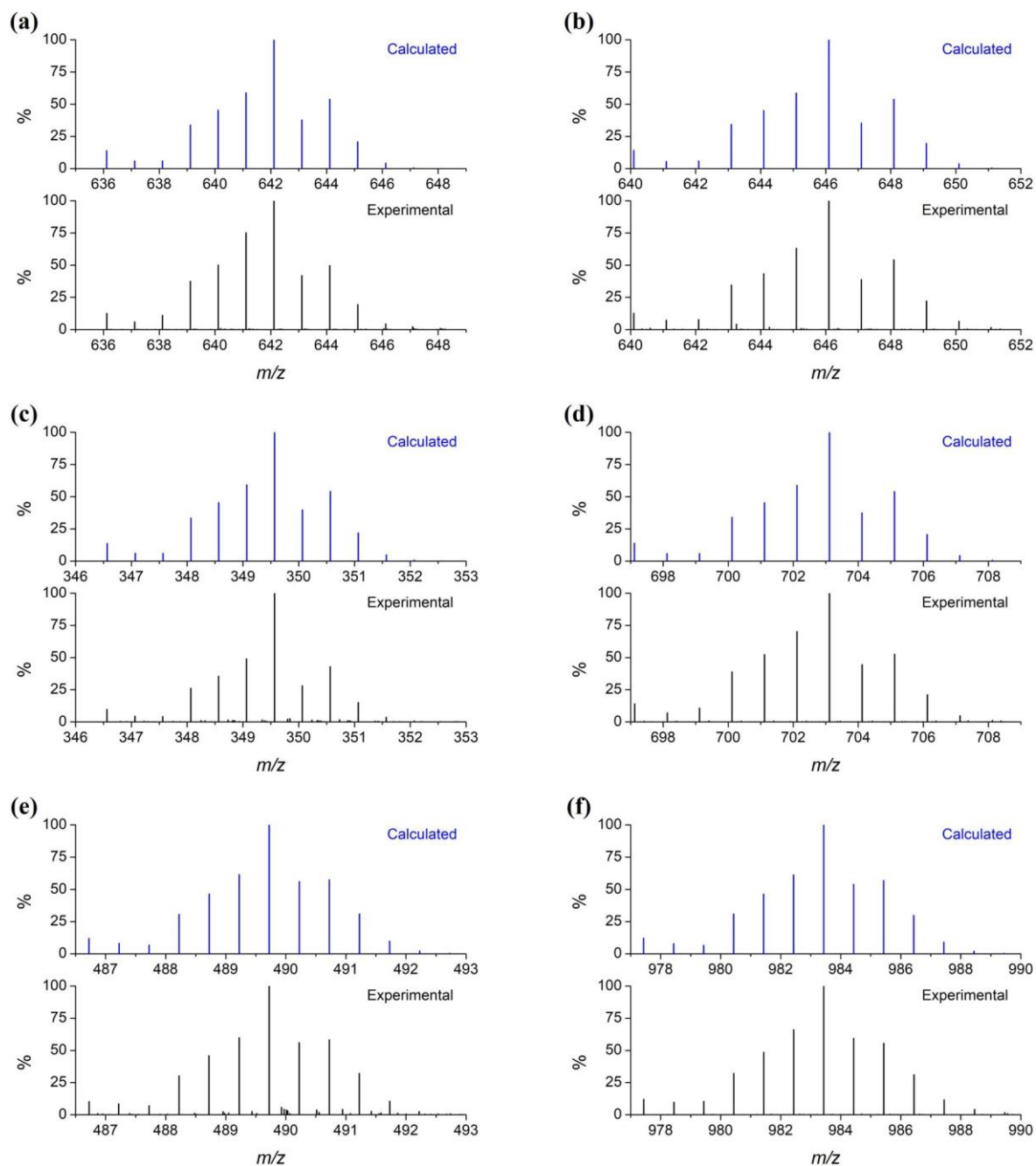


Figure A4.21. Comparison between the calculated (blue) and experimental (black) isotopic distribution pattern for (a) 42, (b) 39, (c) 78, (d) 81, (e) 80 and (f) 83 from electrospray ionisation (positive mode) or matrix-assisted laser desorption/ionisation (positive mode) high resolution mass spectrometry analysis.

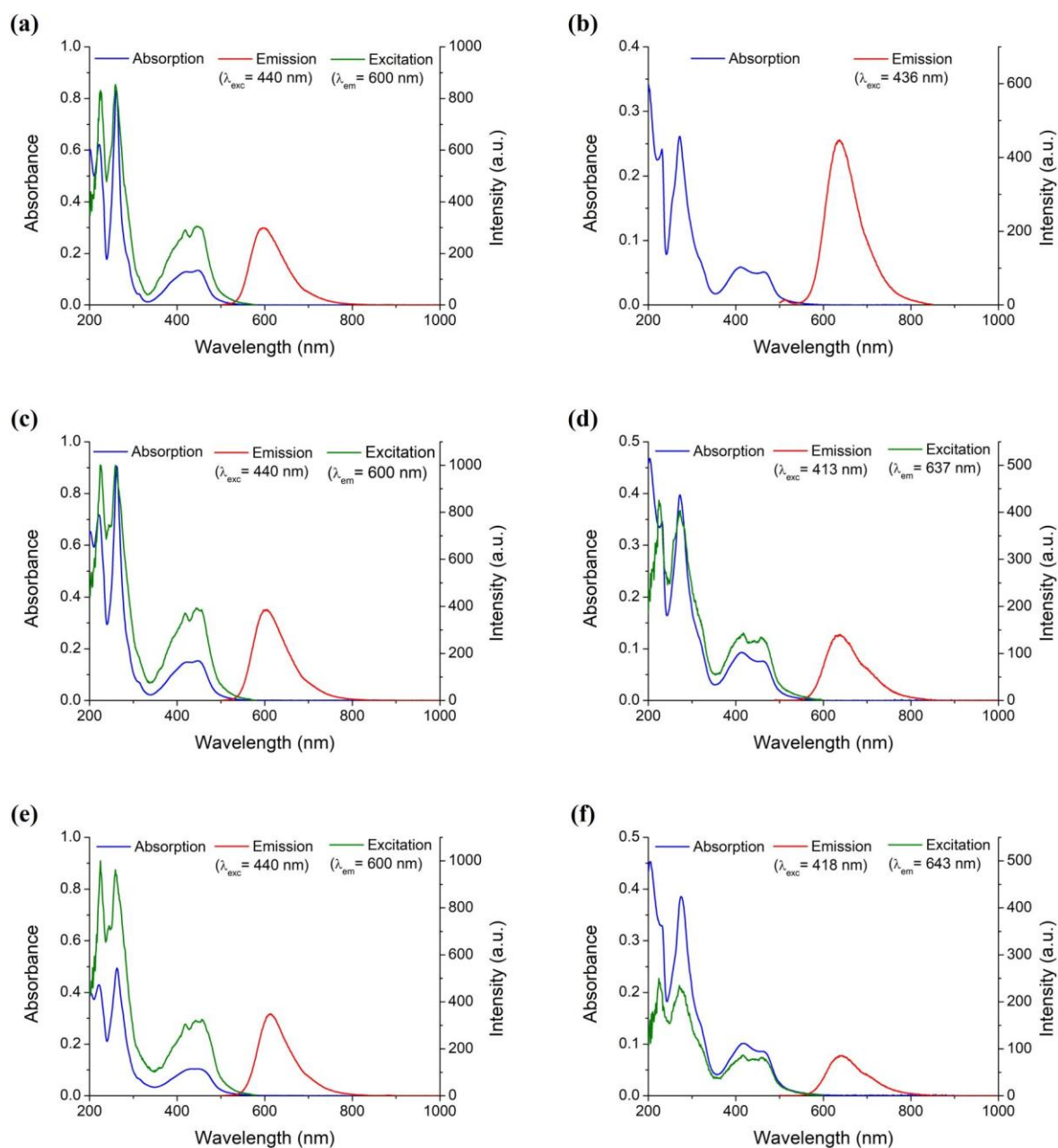


Figure A4.22. UV-vis absorption, excitation and emission spectra of (a) **42**, (b) **39**, (c) **78**, (d) **81**, (e) **80** and (f) **83** in 10 mM sodium phosphate-buffered aqueous solution at pH 7.4, at 298 K.

Table A4.1. Bi-exponential and pre-exponential weighted mean emission lifetimes (τ_M) of **80** and **83** in 10 mM sodium phosphate-buffered aqueous solution at pH 7.4, at 298 K.

Complex	Conditions	τ_1 (ns)	%A ₁	τ_2 (ns)	%A ₂	τ_M (ns)
80	Air	759	55	1490	45	1085
	N ₂	358	49	813	51	587
83	Air	896	46	1752	54	1354
	N ₂	343	42	949	58	696

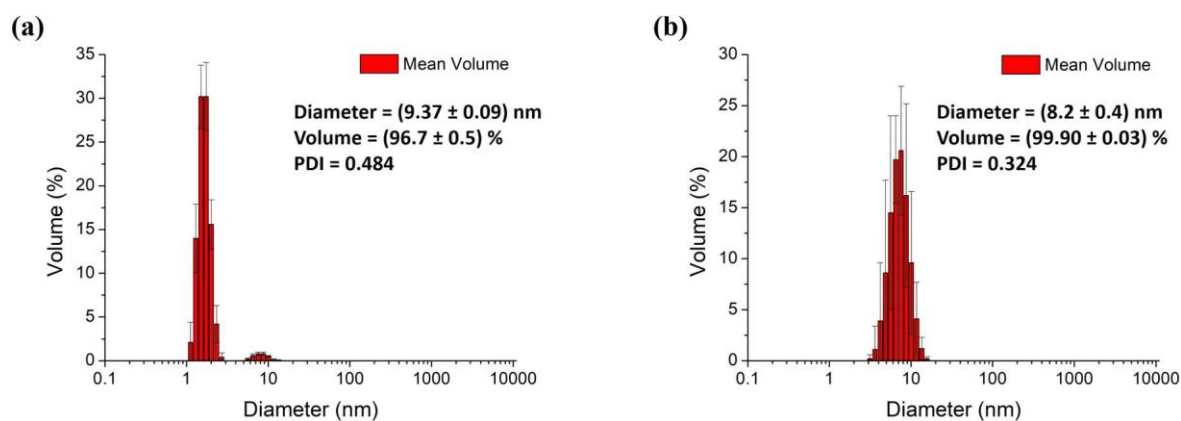


Figure A4.23. Micelle size distribution determined by DLS analysis for (a) **80** at 263 μM (above the cmc) and (b) **83** at 226 μM (above the cmc) in aqueous solutions at 298 K.

Table A4.2. Bi-exponential and pre-exponential weighted mean emission lifetimes (τ_M) of **80** at different concentrations in H_2O at 298 K.

Concentration (μM)	τ_1 (ns)	%A ₁	τ_2 (ns)	%A ₂	τ_M (ns)
5.60	353	41	768	59	597
11.20	307	47	736	53	535
28.00	523	68	784	32	605
56.01	495	50	707	50	602
74.68	526	67	991	33	680
112.01	565	70	1032	30	703
149.35	542	53	907	47	715
186.69	553	52	977	48	756
224.03	498	35	929	65	777
261.36	471	30	953	70	809
336.04	555	37	1081	63	884
429.38	549	31	1151	69	965
522.73	541	28	1137	72	969

Table A4.3. Bi-exponential and pre-exponential weighted mean emission lifetimes (τ_M) of **83** at different concentrations in H_2O at 298 K.

Concentration (μM)	τ_1 (ns)	%A ₁	τ_2 (ns)	%A ₂	τ_M (ns)
6.83	325	5	945	95	916
13.67	412	6	956	94	924
22.78	364	6	950	94	916
34.17	388	5	951	95	923
45.56	427	7	957	93	918
72.90	210	8	946	92	890
100.23	247	6	948	94	906
145.79	265	17	944	83	832
205.02	332	24	946	76	800
250.58	375	21	934	79	814
296.14	434	25	967	75	835
364.48	457	32	977	68	811
432.82	435	32	969	68	799
501.16	403	39	922	61	719

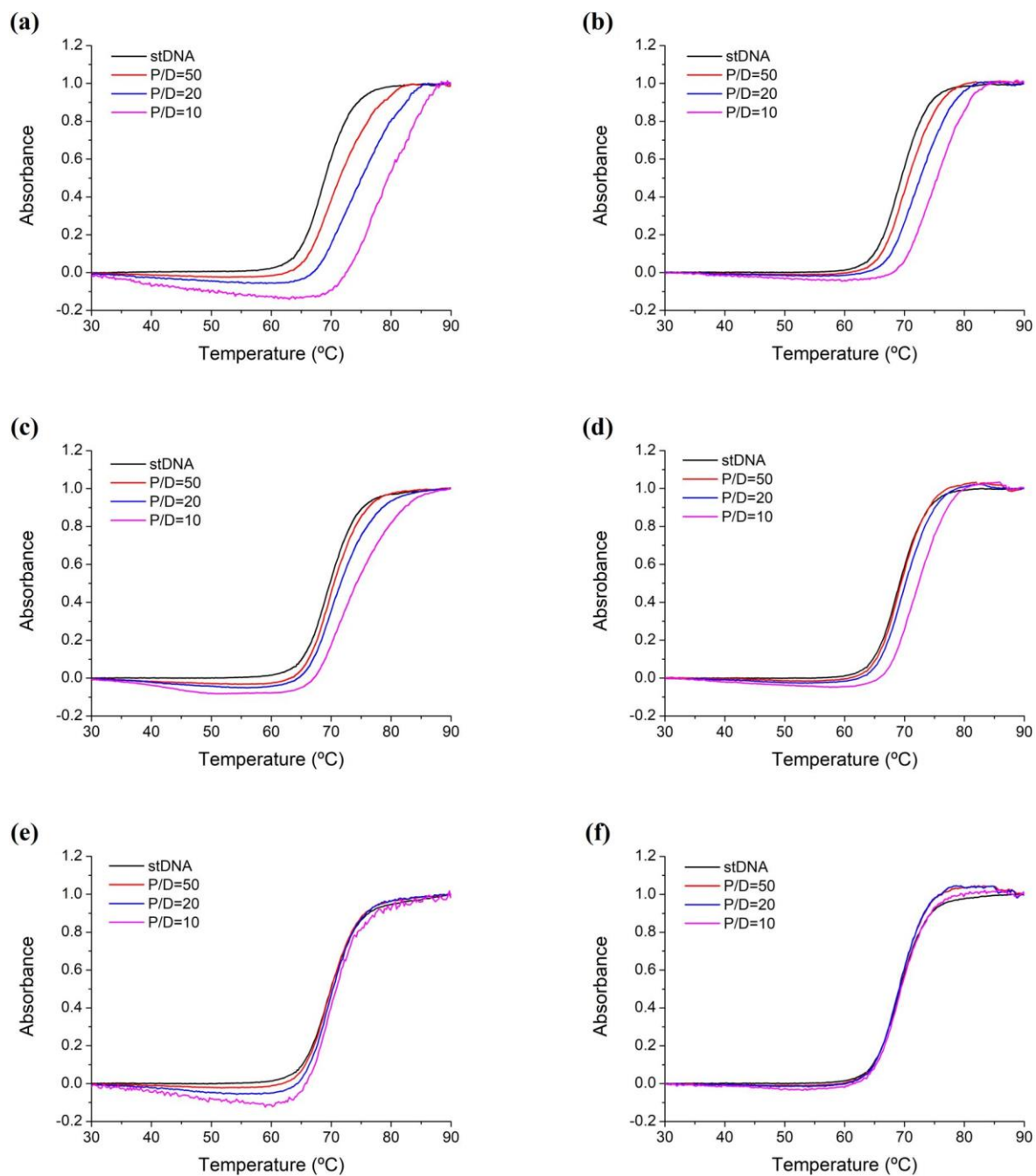


Figure A4.24. Thermal denaturation curves of stDNA ($150 \mu\text{M}$) in 10 mM sodium phosphate-buffered aqueous solution at pH 7.4, in the absence and presence of (a) **78**, (b) **81**, (c) **79**, (d) **82**, (e) **80** and (f) **83** at different P/D ratios.

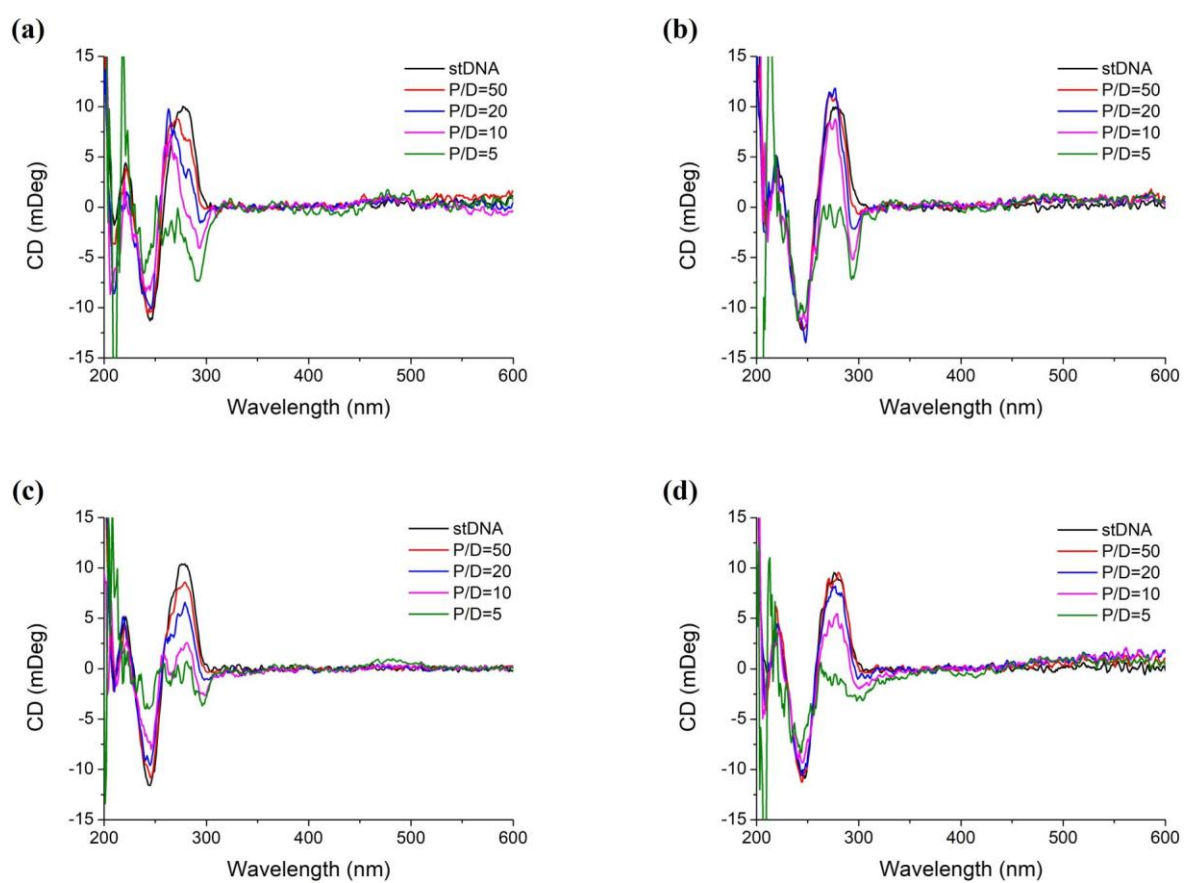


Figure A4.25. Circular dichroism spectra of stDNA ($150 \mu\text{M}$) in 10 mM sodium phosphate-buffered aqueous solution at pH 7.4, in the absence and presence of (a) **78**, (b) **81**, (c) **80** and (d) **83** at different P/D ratios.

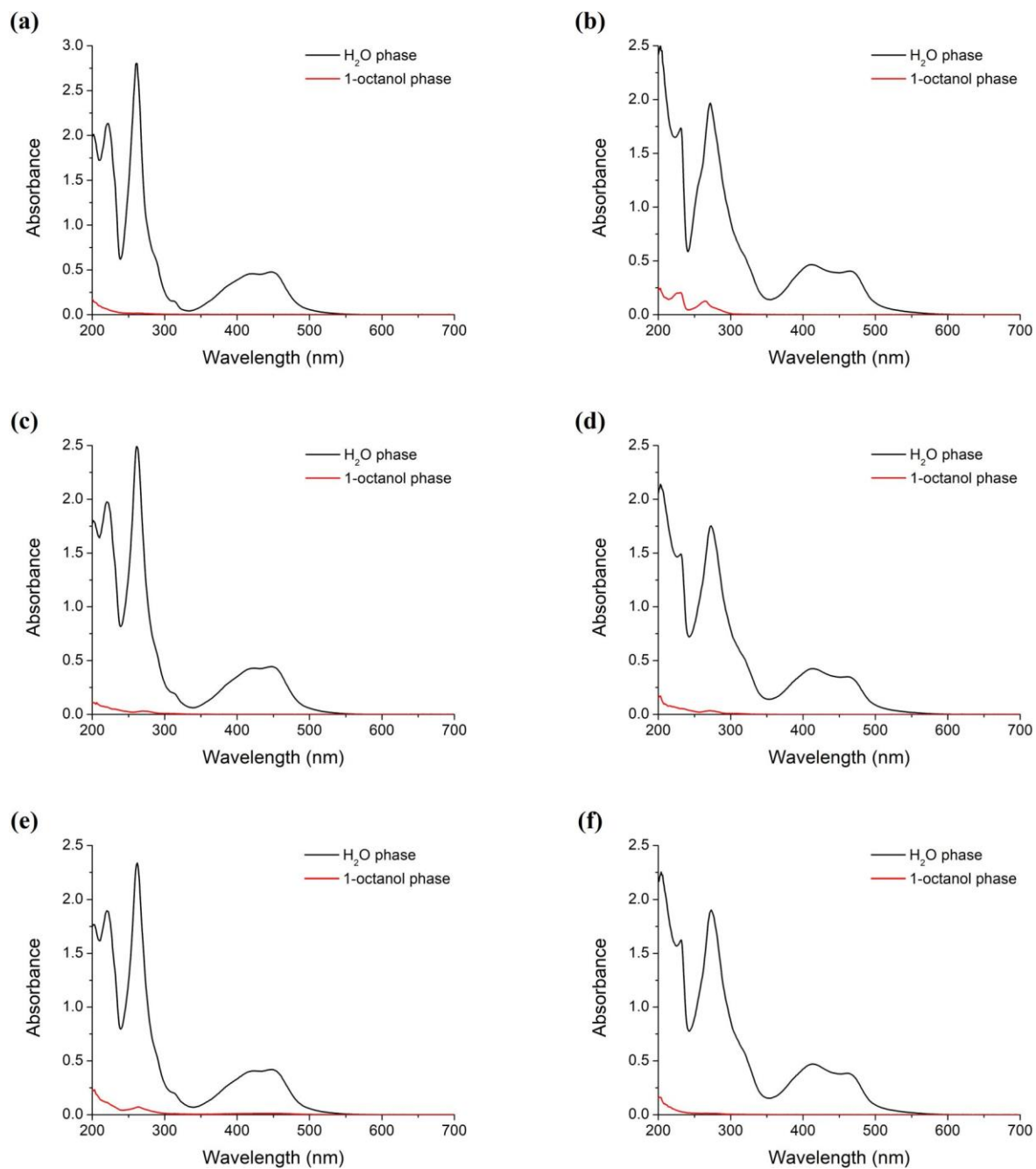


Figure A4.26. UV-vis absorption spectra of (a) **42**, (b) **39**, (c) **78**, (d) **81**, (e) **79** and (f) **82** in water (black) and 1-octanol (red) phases at 298 K, showing the preference of the six complexes by the aqueous phase.

Table A4.4. Bi-exponential, tri-exponential and pre-exponential weighted mean emission lifetimes (τ_M) of **80** and **83** in different conditions, at 298 K.

Complex	Conditions	τ_1 (ns)	%A ₁	τ_2 (ns)	%A ₂	τ_3 (ns)	%A ₃	τ_M (ns)
80	D ₂ O (O ₂)	210	35	441	65	-	-	361
	D ₂ O (Ar)	424	48	991	52	-	-	719
	H ₂ O (Air)	414	25	1030	75	-	-	876
	H ₂ O (Ar)	479	36	1206	64	-	-	947
83	D ₂ O (O ₂)	175	43	719	34	33	24	326
	D ₂ O (Ar)	349	24	2157	41	98	35	985
	H ₂ O (Air)	273	21	903	79	-	-	770
	H ₂ O (Ar)	313	31	1056	69	-	-	825

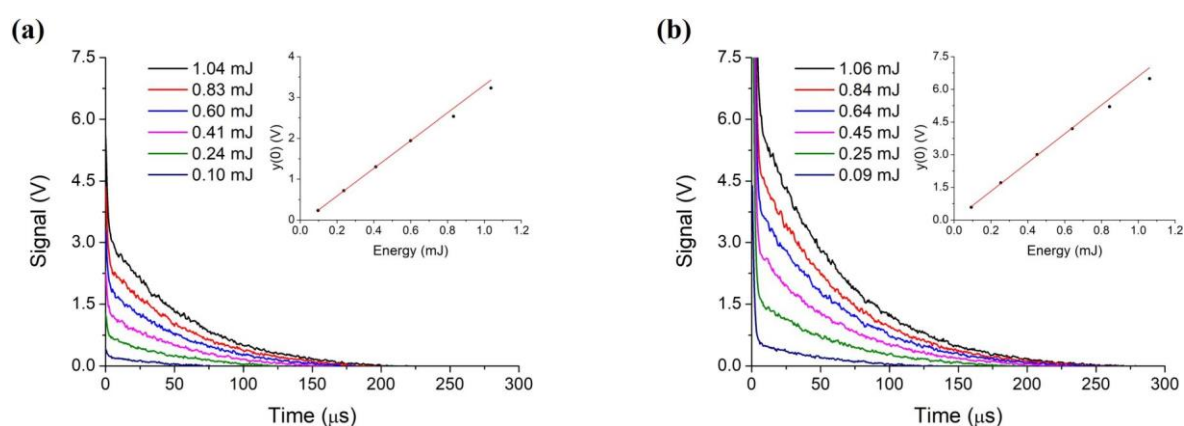


Figure A4.27. Singlet oxygen emission decays at 1270 nm produced by (a) **42** and (b) **39** at different laser energies ($\lambda_{exc} = 532$ nm) in O₂-saturated D₂O solution at 298 K. Inset: Plot of intercept values (V) vs. laser energy (mJ) and the best linear fit of the data.

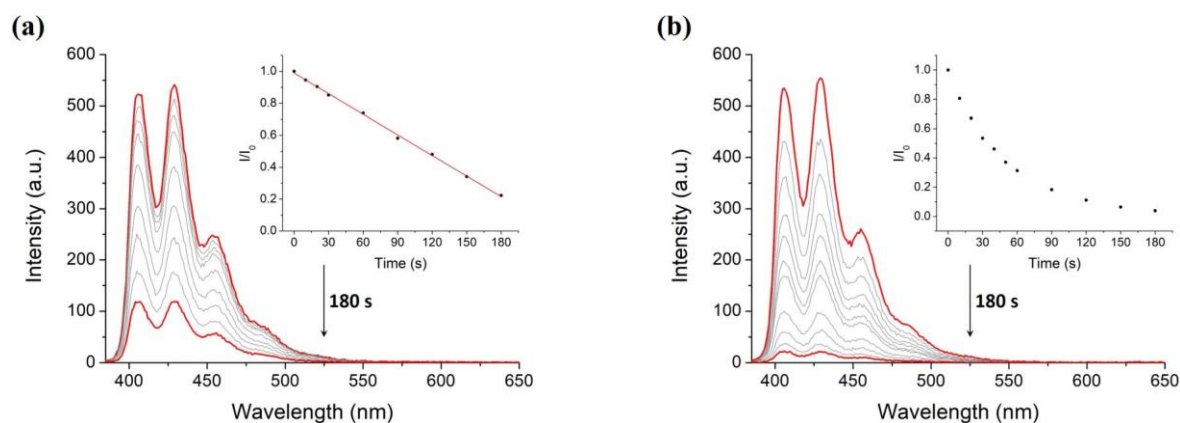


Figure A4.28. Emission spectra of ABDA ($\lambda_{exc} = 380$ nm) in the presence of (a) **42** and (b) **39** ($A_{470} \approx 0.01$) in H₂O at different irradiation times using a 470 nm pE-2 LED illumination system (100% intensity), at 298 K. Inset: Plot of I/I_0 vs. irradiation time (s) and the best linear fit of the data.

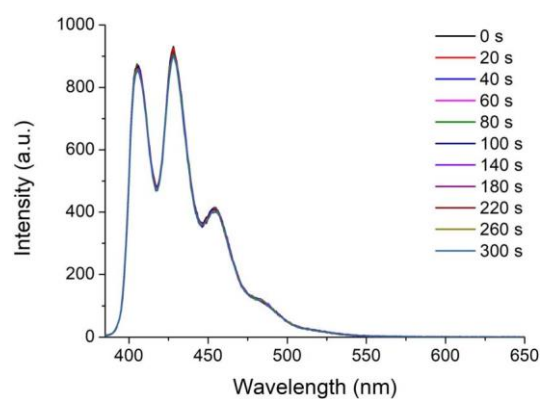


Figure A4.29. Emission spectra of ABDA ($\lambda_{exc} = 380$ nm) in the absence of photosensitiser in H_2O at different irradiation times using a 470 nm pE-2 LED illumination system (100% intensity), at 298 K.

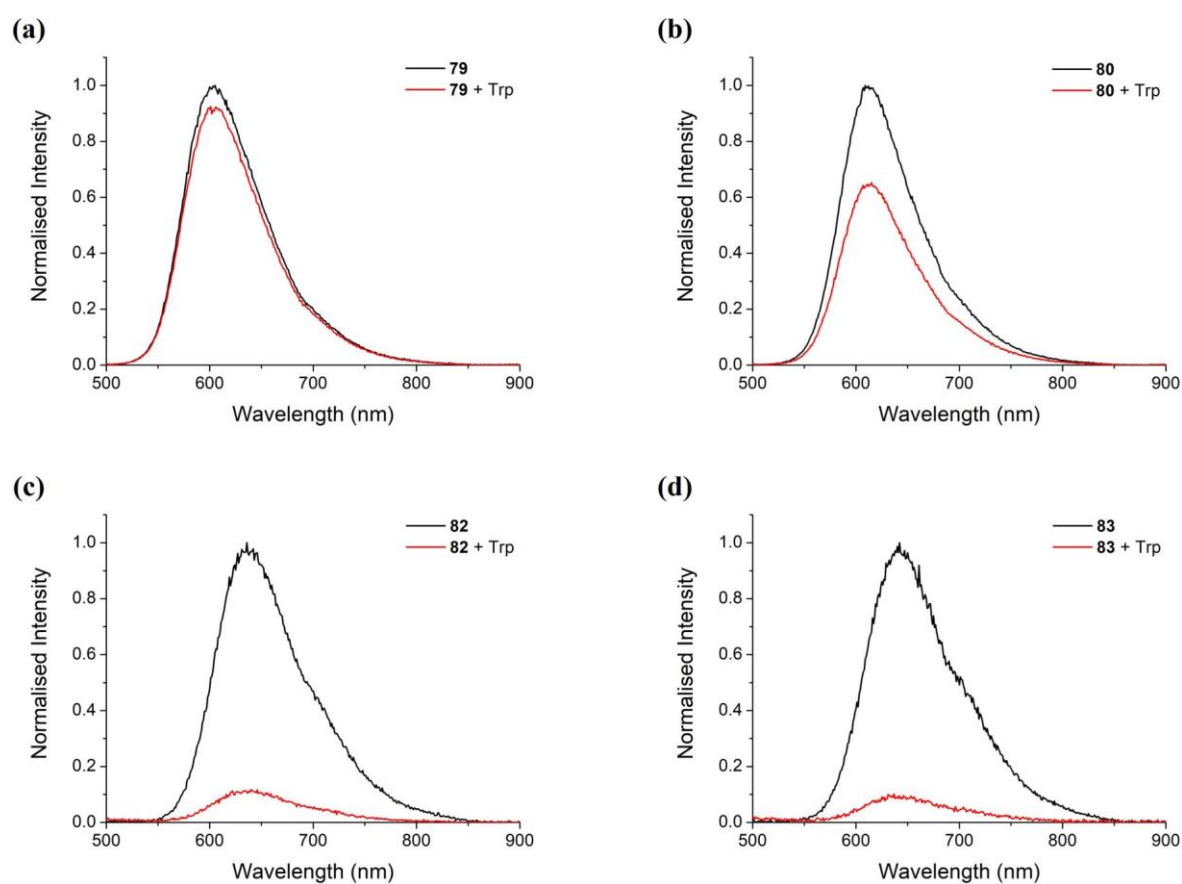


Figure A4.30. Emission spectra of (a) 79, (b) 80, (c) 82 and (d) 83 in the absence (black) and in the presence of L-tryptophan (5 mM) in aqueous solution at 298 K.

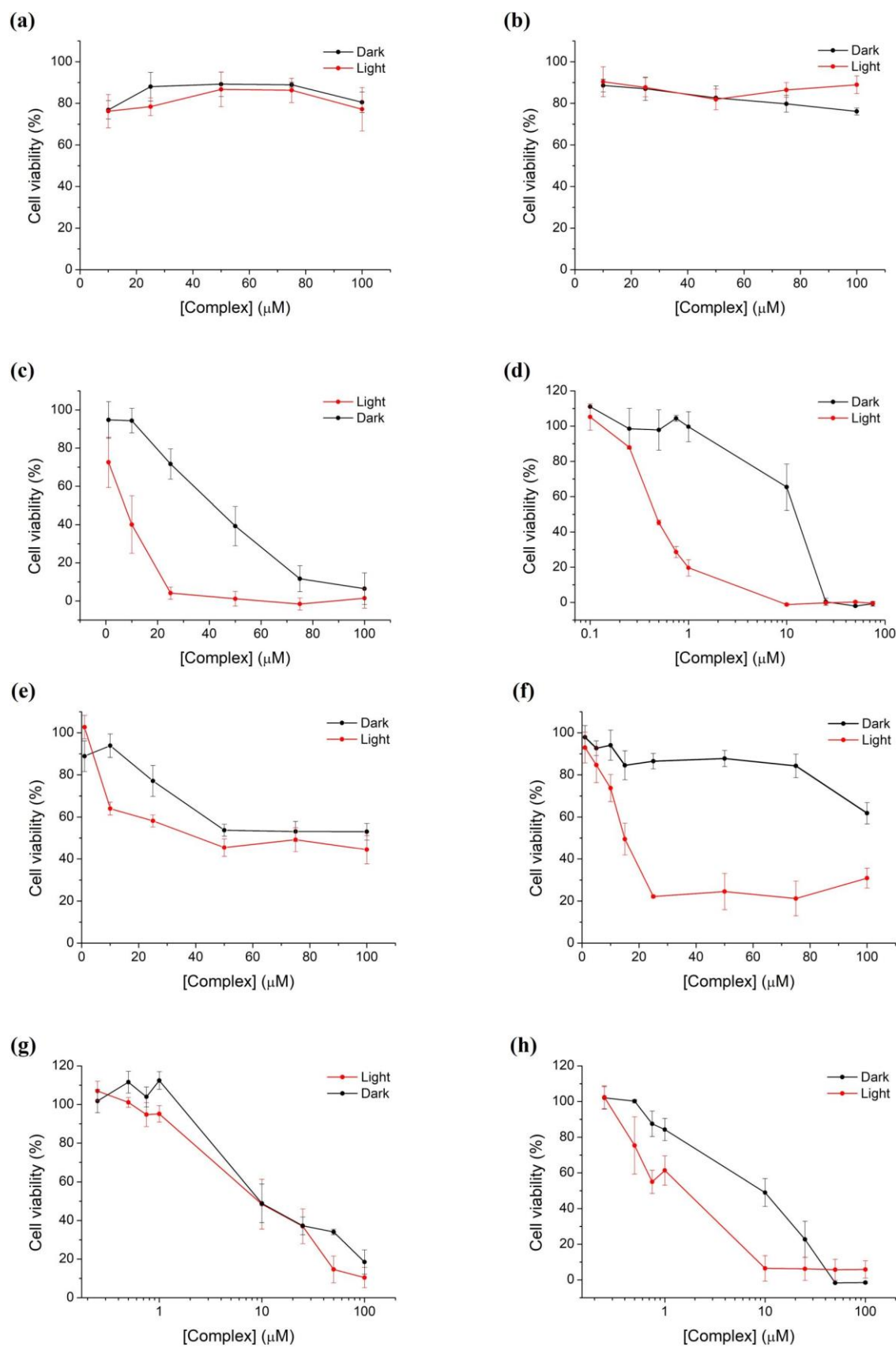


Figure A431. Toxicity profiles of (a) 42, (b) 78, (c) 79, (d) 80, (e) 39, (f) 81, (g) 82 and (h) 83 in HeLa cells. HeLa cells were treated with the indicated concentrations of the required complexes and incubated for 24 h followed by either exposure to light for 1 hour or maintenance in the dark and followed by further 24 h incubation. Cells were then incubated with the Alamar Blue dye for 4 h and assessed for cellular viability. Note that a logarithmic scale is used in graphs (d), (g) and (h) for clarity.

Appendix 5

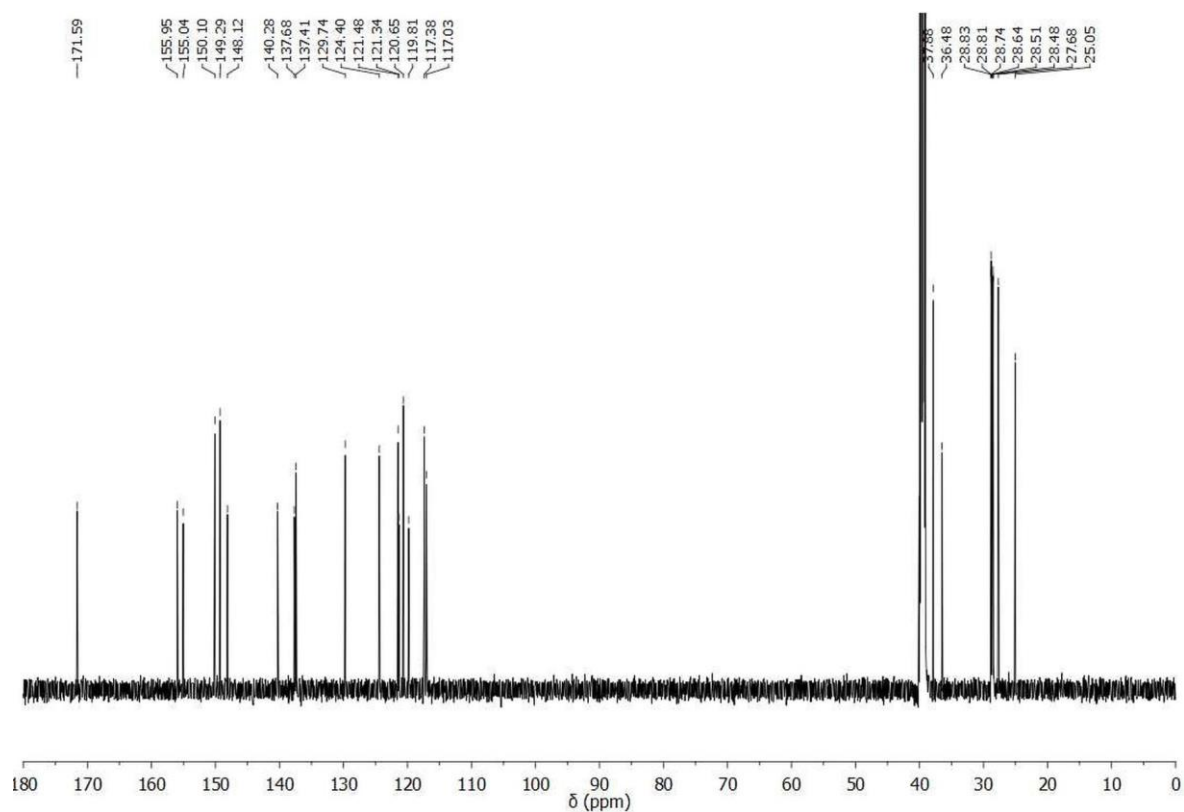


Figure A5.1. ^{13}C NMR (151 MHz, DMSO-d_6) spectrum of ligand 89.

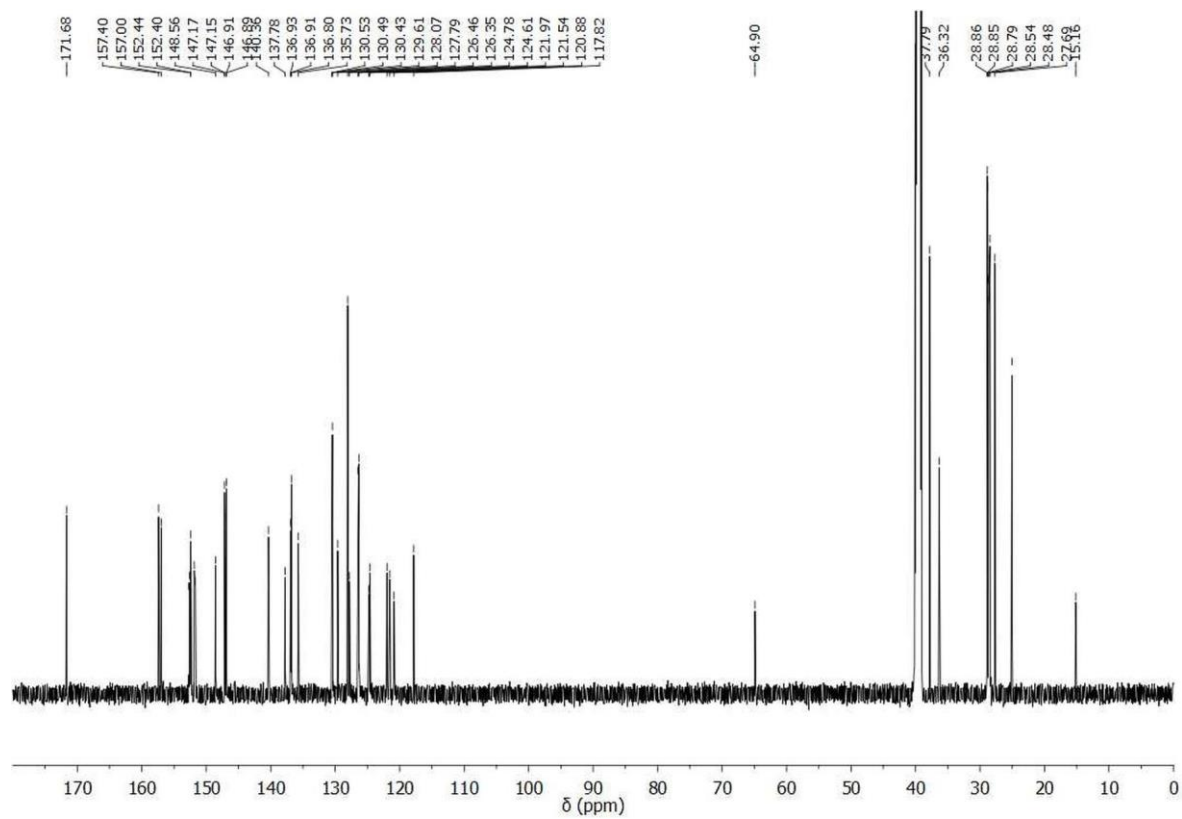


Figure A5.2. ^{13}C NMR (151 MHz, DMSO-d_6) spectrum of 90.

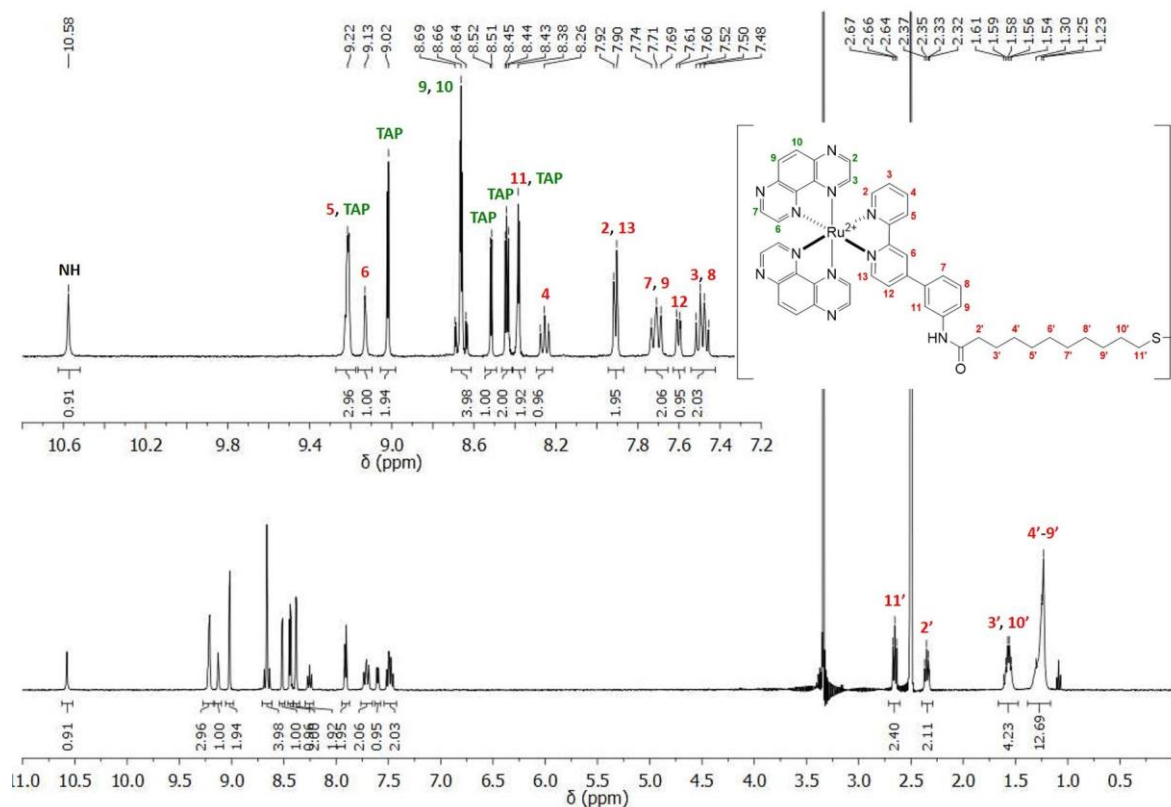


Figure A5.3. ^1H NMR (400 MHz, DMSO-d_6) spectrum of **91**. Signals corresponding to TAP ligands are in green and signals assigned to ligand **89** ligand are in red.

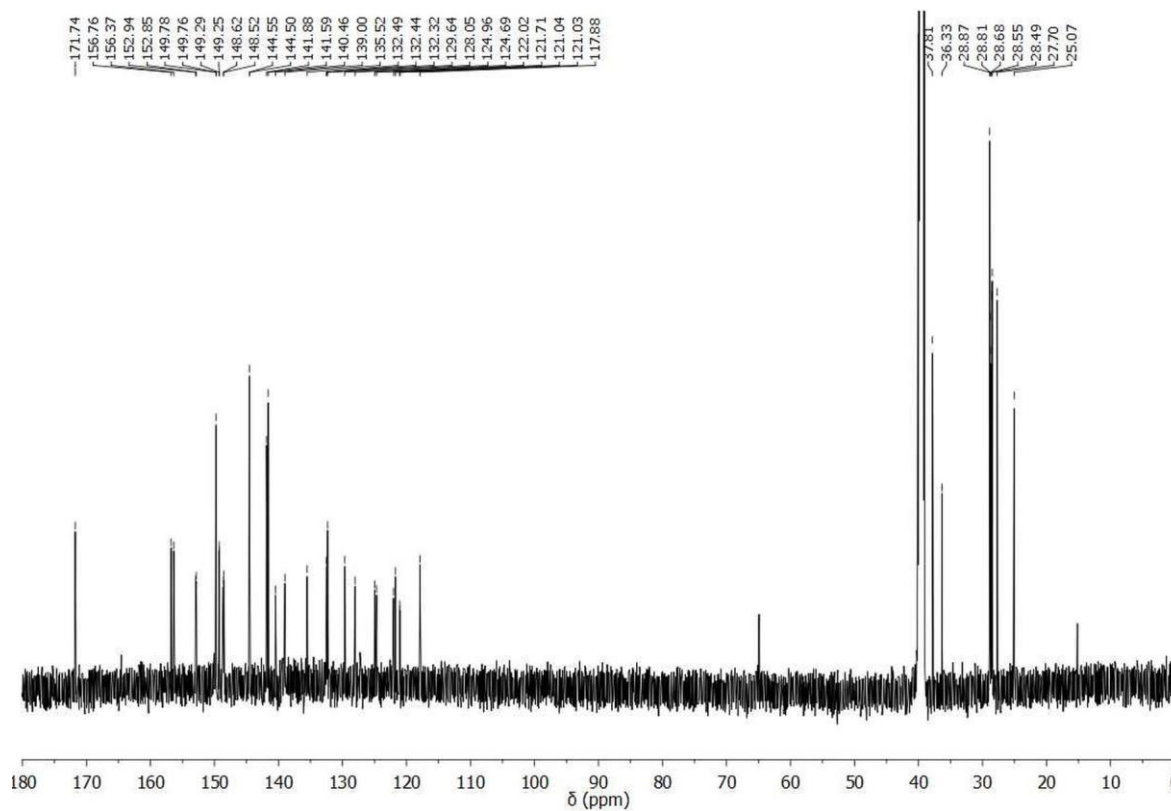


Figure A5.4. ^{13}C NMR (151 MHz, DMSO-d_6) spectrum of **91**.

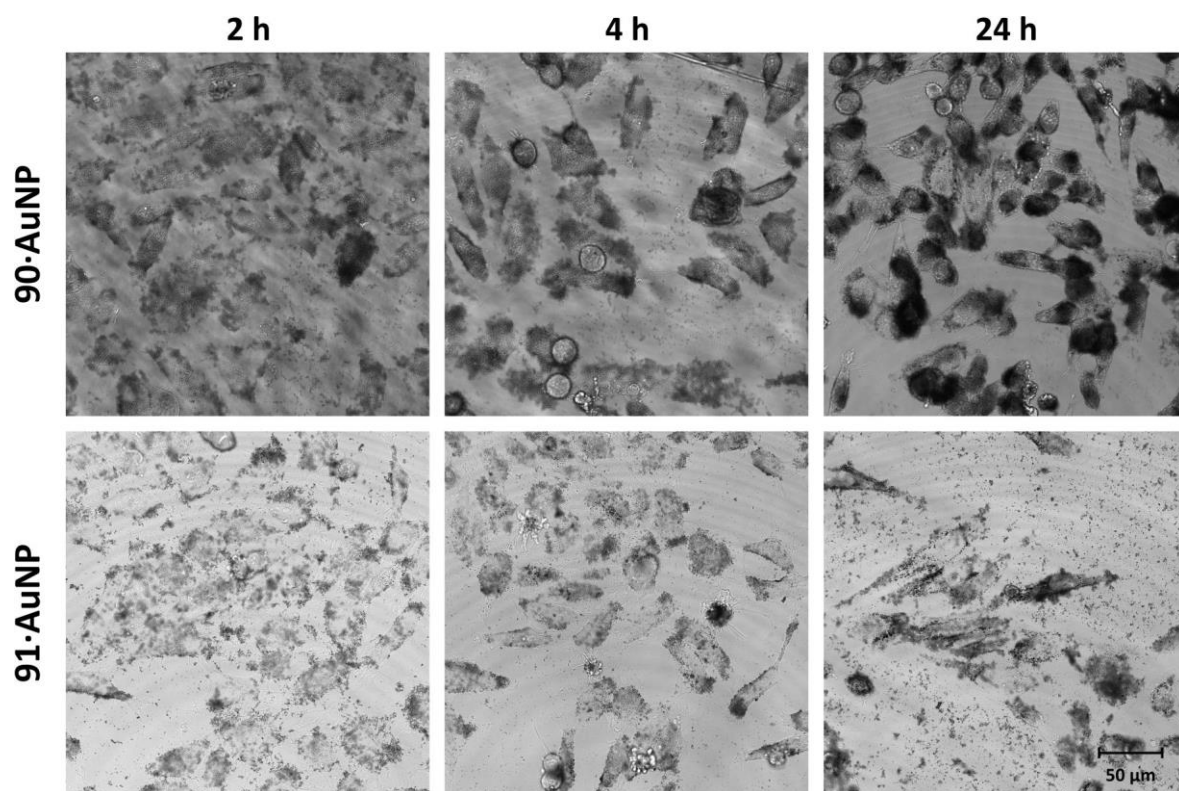


Figure A5.5. Bright field images of HeLa cells showing the uptake of **90-AuNP** and **91-AuNP** at ca. $20 \mu\text{M}$ Ru(II) complex concentration after 2, 4 and 24 h incubation.

Publications



Cite this: *Dalton Trans.*, 2016, **45**, 18208

Luminescent ruthenium polypyridyl complexes with extended 'dppz' like ligands as DNA targeting binders and cellular agents†

Bjørn C. Poulsen,^{‡a} Sandra Estalayo-Adrián,^{‡a} Salvador Blasco,^{‡a} Sandra A. Bright,^{a,b} John M. Kelly,^a D. Clive Williams*^b and Thorfinnur Gunnlaugsson*^a

Four new Ru(II) polypyridyl complexes that contain an extended aromatic moiety derived from pyrazino [2,3-*h*]dipyrido[3,2-*a*:2',3'-*c*]phenazine and either 1,10-phenanthroline (**phen**) or 1,4,5,8-tetraazaphenanthrene (**TAP**) have been synthesized, their solid state X-ray crystal structure determined and their photophysical and biological properties evaluated. Their interactions with DNA have been studied, and they have been tested for their potential as photodynamic therapeutic (PDT) agents in the treatment of cancer. A practical modification of a method by Carter, Rodriguez and Bard has been introduced and used to calculate binding parameters for the complexes which show a strong affinity for DNA with binding constants in the order of 10^7 M^{-1} (in 10 mM phosphate buffer). The complexes containing **phen** as an ancillary ligand become emissive upon binding to DNA ("light switch effect"), but do not show selective cytotoxicity upon light irradiation. On the other hand, the **TAP** complexes, which show an inverse "light switch effect" (emission quenched upon binding to DNA), are strongly photo-toxic suggesting their use in Photodynamic Therapy (PDT). In HeLa cells the best PDT agent shows an IC_{50} value (light) = 4 μM vs. IC_{50} value (dark) = 62 μM .

Received 29th September 2016,
Accepted 21st October 2016

DOI: 10.1039/c6dt03792e

www.rsc.org/dalton

Introduction

Ruthenium (Ru(II)) polypyridyl complexes possess interesting photophysical properties that can have applications in supramolecular chemistry, biology and potentially in medicine.^{1–3} In recent times, such complexes have been developed as nucleic acid binders; the binding mode being shown to be highly dependent on the structure of the coordinating ligands.² Recently the development of Ru(II) complexes that have ligands possessing extended aromatic regions such as dipyrido[3,2-*a*:2',3'-*c*]phenazine (**dppz**) and pyrazino[2,3-*h*]dipyrido[3,2-*a*:2',3'-*c*]phenazine (**pdppz**) have been developed and their ability to intercalate into oligonucleotides has been studied, which includes the use of X-ray crystallography in con-

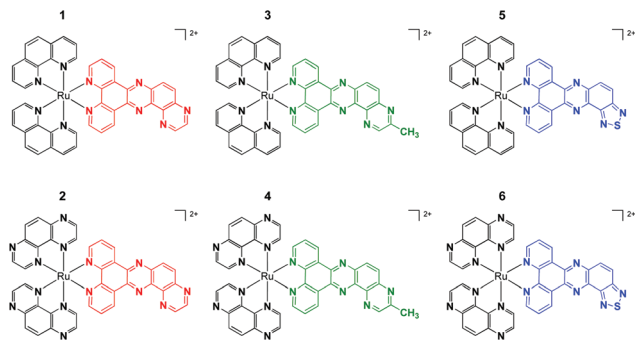
junction with ultra-fast spectroscopy, such as transient IR.³ As the photophysical (*i.e.* absorption/emission, lifetime, and quantum yield, *etc.*) properties of such complexes are usually significantly modulated upon DNA binding, their application as novel photodynamic therapy (PDT) agents has also emerged.^{2a-c} PDT is a strategy to selectively kill cancer cells by modulation in the toxicity of the therapeutic agent upon light irradiation, and has been commonly employed using chemical structures such as porphyrins, azadipyromethenes,⁴ BODIPY based dyes and more recently, Ru(II) polypyridyl complexes,^{5,6} that upon light activation/irradiation can generate reactive species (such as reactive oxidative species) or partake in electron transfer reactions, that results in the onset of apoptosis or necrosis with concomitant cell death. We have recently explored the properties of different Ru(II) complexes as imaging or anti-cancer agents, and detailed biological profiling of two Ru(II) polypyridyl complexes (**1** and **2**, Scheme 1)^{2a} containing **pdppz** as auxiliary ligands which, depends on the nature of the remaining two polypyridyl ligands, function as luminescent cellular probes (**1**) or as novel PDT agents (**2**).^{2a} These results inspired us to make different variations in the structure of these complexes and determine how such changes affect their properties. Moreover, such complexes can be conjugated to surfaces such as gold nanoparticles, as we have recently demonstrated, and employed in cellular applications,

^aSchool of Chemistry and Trinity Biomedical Sciences Institute (TBSI), Trinity College Dublin, The University of Dublin, Dublin 2, Ireland.
E-mail: gunnlaut@tcd.ie

^bSchool of Biochemistry and Immunology and Trinity Biomedical Sciences Institute (TBSI), Trinity College Dublin, The University of Dublin, Dublin 2, Ireland.
E-mail: Clive.Williams@tcd.ie

† Electronic supplementary information (ESI) available: Characterisation, data-fitting and X-ray crystallographic information. CCDC 1489206 and 1489207. For ESI and crystallographic data in CIF or other electronic format see DOI: 10.1039/c6dt03792e

‡ These authors contributed equally to the work herein.



Scheme 1 Structure of the ruthenium complexes: (1–2) 1,10-phenanthroline (**phen**) and 1,4,5,8-tetraazaphenanthrene (**TAP**) ruthenium complexes with pyrazino[2,3-*h*]dipyrido[3,2-*a*:2',3'-*c*]phenazine (**pdppz**). (3–4) **phen** and **TAP** ruthenium complexes with 3-methylpyrazino[2,3-*h*]dipyrido[3,2-*a*:2',3'-*c*]phenazine (**mpdppz**). (5–6) **phen** and **TAP** ruthenium complexes with dipyrido[3,2-*a*:2',3'-*c*][1,2,5]thiadiazolo[3,4-4,3]phenazine (**dtp**).

such as in luminescent imaging and theranostics.^{7,8} Herein we report a new family of Ru(II) complexes that we have prepared with extended aromatic groups derived from **pdppz**, Scheme 1, using either **phen** or **TAP** ligands. We report their characterisation, photophysical properties and anticancer activity towards HeLa cancer cells. We also demonstrate that the interactions of these with nucleic acids (*e.g.* DNA) can be quantified by fitting the spectroscopic data using non-linear regression analysis; this analysis demonstrating very high affinity for the novel Ru(II) complexes presented herein.

Results and discussion

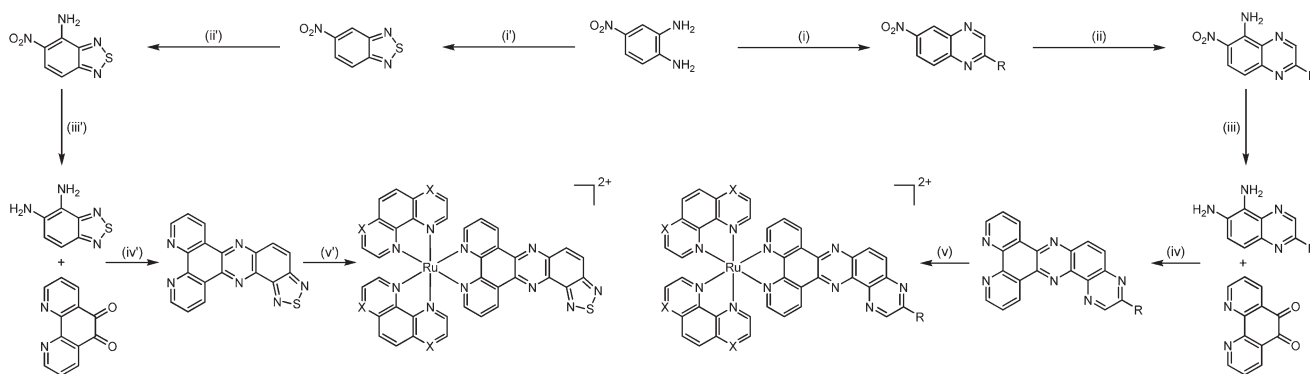
Synthesis of ligands and complexes

The synthesis of the ligand **pdppz**, as well as the complexes 1 and 2 (see Scheme 1), has been previously reported by our research group.^{2,9} The synthesis of 1,10-phenanthroline-5,6-dione,^{10–12} dipyrido[3,2-*a*:2',3'-*c*][1,2,5]thiadiazolo[3,4-4,3]phenazine (**dtp**),¹³ **TAP**,¹⁴ 5-nitro-2,1,3-benzothiadiazole and 4,5-

diamino-2,1,3-benzothiadiazole was by established procedures.¹⁵ Synthesis of complexes 3–6 was achieved by adapting the procedures for 1 and 2, as shown in Scheme 2. The extended polypyridyl ligands 3-methylpyrazino[2,3-*h*]dipyrido[3,2-*a*:2',3'-*c*]phenazine (**mpdppz**) and **dtp** were synthesised by condensation of 1,10-phenanthroline-5,6-dione with 2-methyl-5,6-diaminoquinoxaline or 4,5-diamino-2,1,3-benzothiadiazole, respectively by refluxing in ethanol, yielding **mpdppz** or **dtp** as a white and a yellow solid in 92% and 81% yield, respectively. Microwave reactions of **mpdppz** and **dtp** with the appropriate Ru(II) bispolypyridyl dichloride at 140 °C followed by column chromatographic purification using neutral alumina and MeCN : H₂O (10 : 0 to 9 : 1) as eluent, yielded complexes 3–6 as orange-red solids in 74%, 59%, 30% and 44% yield, respectively. The distinct units of the complexes were readily discerned by NMR (CD₃CN, 400 MHz) (see ESI Fig. S4, S7, S13 and S16†). CHN analysis and mass spectrometry showed the formation of the desired products in high purity.

Photophysical characterisation of Ru(II) complexes

The photophysical properties of 3–6 were studied in 10 mM aqueous sodium phosphate buffer at pH 7.4 for complexes 4 and 6 and in acetonitrile for complexes 3 and 5 (as their chloride salts); these latter complexes were found to be non-emissive in aqueous solution.^{16,17} As has been reported for other related Ru(II) polypyridyl complexes containing extended aromatic ligands, similar characteristic bands were observed in the UV-Vis absorption and the emission spectra of 3–6 (Fig. 1 & ESI†).^{18,19} Complexes 3 and 5 showed two absorption bands at 223 nm and 262 nm ($\epsilon(3) = 12.5 \times 10^4 \text{ M}^{-1} \text{ cm}^{-1}$, $\epsilon(5) = 9.0 \times 10^4 \text{ M}^{-1} \text{ cm}^{-1}$) which can be assigned to π - π^* intra-ligand transitions of the **phen** ligands. An absorption band was also observed at 310 nm ($\epsilon(3) = 7.5 \times 10^4 \text{ M}^{-1} \text{ cm}^{-1}$, $\epsilon(5) = 6.4 \times 10^4 \text{ M}^{-1} \text{ cm}^{-1}$) which is characteristic of π - π^* transitions within the extended aromatic ligand **mpdppz** and **dtp**. Further two absorption bands were observed centred at 360 nm and 380 nm, these being attributed to π - π^* transition within the phenazine part of **mpdppz** and **dtp**. Finally, a broad absorption band centred at 440 nm ($\epsilon(3) = 2.41 \times 10^4 \text{ M}^{-1} \text{ cm}^{-1}$, $\epsilon(5) =$



Scheme 2 Synthesis of Ru(II) complexes 1–6, where R = H or CH₃ and X = N or CH: (i) methylglyoxal, EtOH, Δ , 43%; (ii) NH₂OH·HCl, Na, MeOH, 27%; (iii) NH₂NH₂·H₂O, 10% Pd/C, EtOH, Δ ; (iv and iv') EtOH/H₂O, Δ , 91% and 81%, respectively; (v and v') Ru(L)₂Cl₂ (L = **phen** or **TAP**), EtOH/H₂O, microwave reaction, 140 °C, 40 min; (i') SOCl₂, NEt₃, DMF, 0 °C, 51%; (ii') NH₂OH·HCl, KOH, EtOH, 0 °C; (iii') Na₂S₂O₄, H₂O, Δ , 71%.

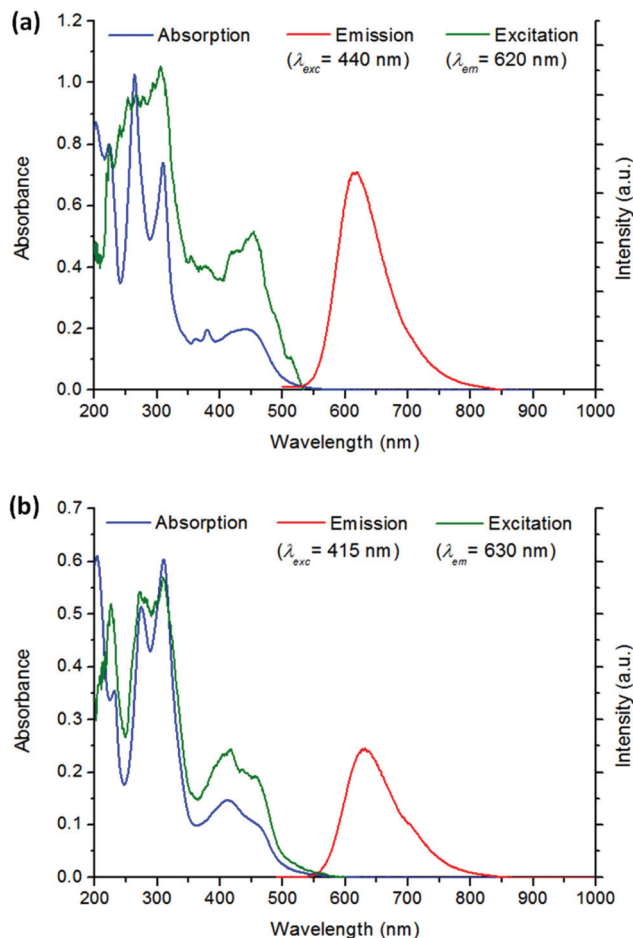


Fig. 1 UV-Vis absorption, emission and excitation spectra of complexes (a) **3** in acetonitrile; (b) **6** in 10 mM phosphate buffered aqueous solution at pH 7.4.

$1.83 \times 10^4 \text{ M}^{-1} \text{ cm}^{-1}$) corresponding to the metal to ligand charge transfer (MLCT) transition of the Ru(II) complex with an electron transfer from the metal centre to the extended ligand was also observed. Complexes **4** and **6** showed an absorption band at 275 nm ($\epsilon(\mathbf{4}) = 8.8 \times 10^4 \text{ M}^{-1} \text{ cm}^{-1}$, $\epsilon(\mathbf{6}) = 6.8 \times 10^4 \text{ M}^{-1} \text{ cm}^{-1}$) characteristic of $\pi\text{-}\pi^*$ intra-ligand transitions of the ancillary TAP ligands; an absorption band at 310 nm ($\epsilon(\mathbf{4}) = 8.7 \times 10^4 \text{ M}^{-1} \text{ cm}^{-1}$, $\epsilon(\mathbf{6}) = 7.9 \times 10^4 \text{ M}^{-1} \text{ cm}^{-1}$) corresponding to $\pi\text{-}\pi^*$ transition within the ligand **mpdppz** and **dtp**; and an absorption band at 412 nm ($\epsilon(\mathbf{4}) = 2.4 \times 10^4 \text{ M}^{-1} \text{ cm}^{-1}$, $\epsilon(\mathbf{6}) = 2.0 \times 10^4 \text{ M}^{-1} \text{ cm}^{-1}$) attributed to the typical MLCT transition of this kind of complex where an electron transfer occurs from the metal centre to the TAP ligands. Concerning the emission properties, luminescence bands were observed with band maxima at 619 nm for complexes **3** and **5** ($\lambda_{\text{exc}} = 440 \text{ nm}$), and at ca. 630 nm for complexes **4** and **6** ($\lambda_{\text{exc}} = 415 \text{ nm}$).

Luminescence quantum yields (ϕ_{em}) and lifetime measurements were undertaken and the results are summarised for each of the complexes in Table 1. The four complexes exhibited similar emission properties compared to **dppz** Ru(II) com-

plexes described in the literature.^{18,19} Complexes **3** and **5**, showed luminescence lifetimes of 166 ns and 169 ns, respectively in air-saturated acetonitrile solution. These values are very close to the reported lifetime of $[\text{Ru}(\text{phen})_2\text{dppz}]^{2+}$ complex (177 ns).²⁰ However, whilst the lifetime of complex **5** (590 ns) in deaerated acetonitrile solution is close to the value of $[\text{Ru}(\text{phen})_2\text{dppz}]^{2+}$ (663 ns), the value obtained for the lifetime of **3** is significantly shorter (324 ns) than the others. However, this value is close to that reported previously by our laboratory for **1** (411 ns).² A possible explanation of this observation could be the existence of more than one luminescent state as has previously been described for the similar complex $[\text{Ru}(\text{phen})_2\text{PHEHAT}]^{2+}$, (**PHEHAT** = 1,10-phenanthroline[5,6-*b*]1,4,5,8,9,12-hexaazatri-phenylene).²¹ For **4** and **6**, which have TAP ligands, the excited electron is located at TAP instead of at the extended aromatic ligand and the luminescent properties should be less influenced by the extended ligand structure. Complexes **4** and **6** showed similar lifetimes values in air-saturated aqueous solution (679 ns and 697 ns, respectively) and in deaerated aqueous solution (801 ns and 864 ns, respectively). These values are slightly smaller than the corresponding reported values of $[\text{Ru}(\text{TAP})_2\text{dppz}]^{2+}$ (820 ns and 1090 ns in air-saturated and deaerated aqueous solution, respectively).²² The quantum yields of the four compounds reported here, **3** and **5** showed values higher than seen for $[\text{Ru}(\text{phen})_2\text{dppz}]^{2+}$ ($\phi_{\text{F}} = 0.0073$ in air-saturated acetonitrile solution), while quantum yields of complexes **4** and **6** are quite close to the corresponding value of the $[\text{Ru}(\text{TAP})_2\text{dppz}]^{2+}$ complex ($\phi_{\text{F}} = 0.035$ in air-saturated aqueous solution).^{20,22} More detailed studies of these complexes are currently being undertaken in our laboratory.

Crystallographic studies

Having synthesised and photophysically characterised the above complexes, we next initiated an investigation into their solid-state structures. Both the TAP complexes (**4** and **6**) were successfully crystallised to give products that were suitable for single crystal X-ray diffraction studies. Unfortunately, the phen analogues (**3** and **5**) gave crystals that were not suitable for such investigations. The crystal structures can be seen in Fig. 2 and 3.

Molecules of **6**·2Cl crystallize in a monoclinic *C2/c* system in which the unit cell contains 8 complexes of **6**, with 16 chloride counterions along with water molecules. The asymmetric unit contains one molecule of complex **6** in which the metal atom is octahedrally coordinated with two TAP ligands and one **dtp** moiety, and this coordination geometry is fairly regular for the bond lengths (see Table 2) with Ru–N bond averaging 2.06 Å. The N–Ru–N angles are not far from 90° and these deviations are imposed by the geometry of the bidentate ligands. None of the external nitrogen atoms of the complex seem to be engaged in hydrogen bonding from the solvent molecules (water) except for N9 which receives one from O6 (*c.f.* CIF file). The rest of the water molecules along with the

§ CCDC numbers: 1489206 and 1489207.

Table 1 Emission properties of complexes **3–6** in acetonitrile and in 10 mM phosphate buffered aqueous solutions at pH 7.4

Complex	$\lambda_{\text{max}}^{\text{em}}$ (nm)	φ_{em}^a buffer	φ_{em}^a MeCN	τ_{em}^b (ns) buffer (air)	τ_{em}^b (ns) buffer (N ₂)	τ_{em}^b (ns) MeCN (air)	τ_{em}^b (ns) MeCN (N ₂)
[Ru(phen) ₂ dppz] ²⁺	607	—	0.0073	—	—	177	663
[Ru(TAP) ₂ dppz] ²⁺	621	0.035	—	820	1090	—	—
1 ^c	625	—	—	—	—	170	411
2 ^c	615	—	—	655	813	557	914
3	619	—	0.018	—	—	166	324
4	627	0.031	0.024	679	801	715	1070
5	619	—	0.016	—	—	169	590
6	631	0.029	0.036	697	864	683	1122

^a Air-saturated aqueous solution of [Ru(bpy)₃]²⁺ as reference ($\varphi_{\text{F}} = 0.028$).¹ Estimated errors $\pm 5\%$. ^b The luminescence decays are monoexponential. Estimated errors $\pm 10\%$. ^c Cloonan *et al.*²

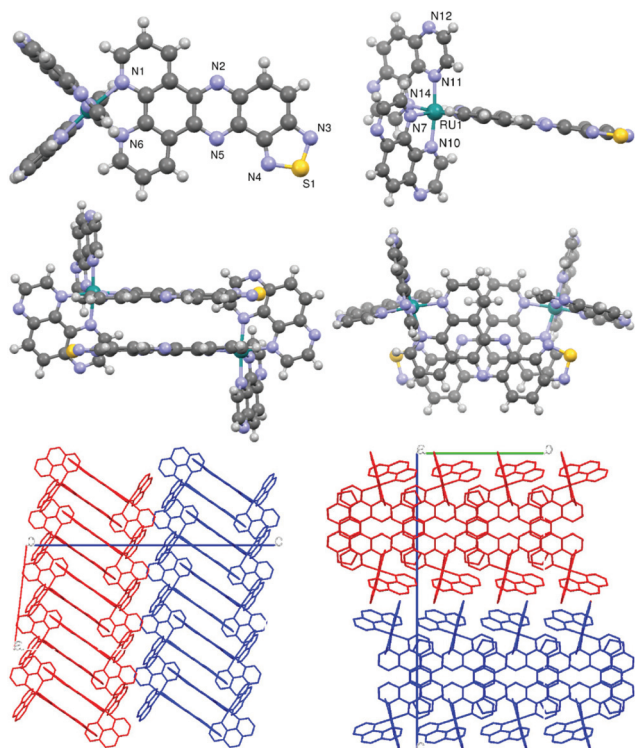


Fig. 2 X-ray crystal structure for complex **6**. (First row) crystal structure for **6** with highlighting of the complex. (Second row) dimeric structure of neighbouring Λ -**6** molecules. Counter ions and solvent molecules are omitted for clarity. (Third row) arrangement of Λ (blue) and Δ (red) domains.

counterions form a hydrogen bond network. The **dtp** moiety is quite flat and it shows face to face π stacking interactions with another **dtp** moiety of a neighbouring complex with the same absolute configuration (see Fig. 2, middle) which results in complexes that are paired together. The mean planes of each **dtp** units are almost parallel and form a narrow angle of 4.01° ; the stacking distances range between 3.12 – 3.67 Å and the shift distance is 1.42 Å. At a higher level these pairs of $\Lambda\Lambda$ or $\Delta\Delta$ complexes pack together forming layers that pile along the *c* crystallographic axis.

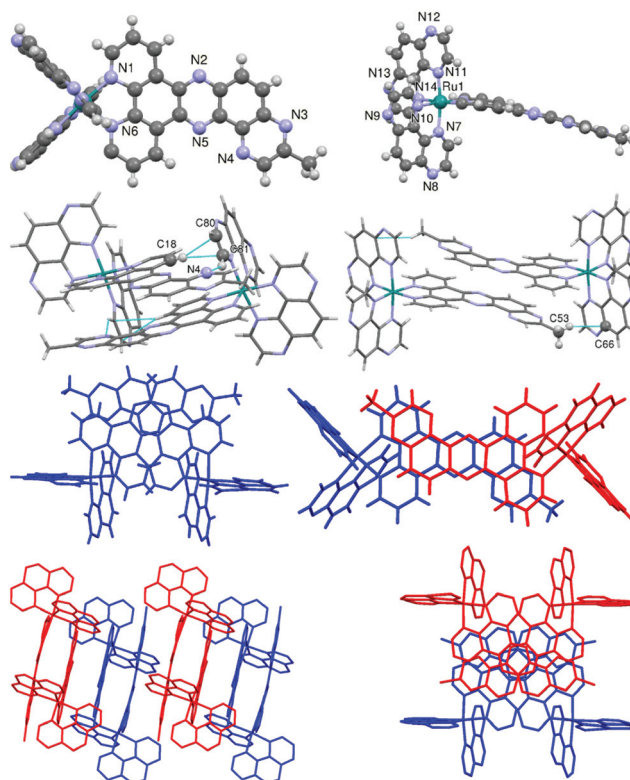


Fig. 3 X-ray crystal structure for complex **4**. (First row) crystal structure for complex **4** with highlighting of the complex and the bending of the **mpdppz** moiety. Only one of the two units is shown. (Second row, left) Details of CH– π and CH–N bonds between neighbouring molecules. (Second row, right) Details of the only interaction, CH₃– π bond between neighbouring molecules. (Third row, left) Stacking mode between neighbouring molecules which form an angle of 87.6° (measured as the torsion angle of Ru atoms and centroids of the central pyrazine within either **mpdppz**). (Third row, right) Complexes are shown in red and blue. (Fourth row) Packing and chirality domains. Hydrogen and chlorine atoms omitted for clarity.

Molecules of **4** crystallized in a triclinic $P\bar{1}$ system with two chlorine counterions. This crystal was rather small, the reflections very weak and the data collection was difficult. Nonetheless the structure could be solved and refined. The

Table 2 Binding parameters obtained from emission data for the binding between the complexes and st-DNA in 10 mM sodium phosphate buffered solution at pH 7.4 and either with or without 160 mM NaCl (high and low ionic strength respectively). The parameters and SEM are for the mean of three replicates. Parameters obtained from the absorption data can be seen in the ESI

Complex	Low ionic strength		High ionic strength	
	K_b (10^6 M $^{-1}$)	n (#bp)	K_b (10^6 M $^{-1}$)	n (#bp)
3	27 ± 4	2.5 ± 0.1	2.6 ± 0.2	2.7 ± 0.1
4	42 ± 9	1.8 ± 0.1	0.33 ± 0.02	1.6 ± 0.1
5	11 ± 0.8	1.8 ± 0.1	1.35 ± 0.1	1.6 ± 0.1
6	28 ± 0.4	1.9 ± 0.1	0.33 ± 0.07	1.8 ± 0.2
1^a	12 ± 3	1.5 ± 0.1	4.6 ± 0.5	2.0 ± 0.1
2^a	5.4 ± 0.4	1.6 ± 0.1	0.84 ± 0.1	1.9 ± 0.1

^a Cloonan *et al.*²

solvent molecules were very disordered and could not be modelled properly. SQUEEZE tool²³ was used to remove electron density from the disordered areas and refinement was continued with the recalculated data. The crystal structure contains four molecules of **4** along with the corresponding chlorine counterions. The asymmetric unit contains two crystallographically different molecules of **4**: one Λ -**4** and one Δ -**4** along with four chlorine atoms that balance the charge and as mentioned some very disordered solvent molecules. In both cases the ruthenium core shows a fairly regular octahedral geometry with N–Ru bond distance ranging from 1.99 to 2.12 Å for Ru1 and 2.03 to 2.12 Å for Ru2. The **mpdppz** moiety is bent with respect to the plane defined by the Ru–N plane. We have tried to quantify this bending as the angle between two planes: (1) the plane defined by the ruthenium and the “phenanthroline” part of the **mpdppz** moiety and (2) the mean planes defined by the “methyl diazine” part of the **mpdppz**. This distortion is 14.13° for the Λ and 14.62° for the Δ enantiomer. The **mpdppz** moieties pile up along the *a* axis forming strands of alternate couples of isomers (see Fig. 3, fourth row) being the relative conformation different depending on whether they are the same enantiomer or two different ones. This can be explained in terms of the different interaction modes between the $\Delta\Lambda$ and $\Delta\Delta/\Lambda\Lambda$ isomers. In Fig. 3 (second and third row) it can be seen that one ArC–H– π bond and one ArC–H...N bond hold the pair of complexes in that particular conformation forming an angle of 87.6° (measured as the torsion angle of the Ru atoms and centroids of the central pyrazine ring within either **mpdppz**). This conformation also explains the bending of the **mpdppz** moiety as these two bonds pull one of the **TAP** moieties in the bending direction. For the $\Delta\Lambda$ stacking, we see that they form an angle of 180° with each other due to an inversion centre between them, and apart from the stacking, there is a CH₃... π bond. These bonds are weak, but their importance is not to be neglected as they might be significant in explaining the overall packing.²⁴ These two features, the bending of the extended aromatic moiety and the pattern of stacking, are missing in the analogous crystal for **2** (CCDC 1012983)² where

the bending angle is 4.98°, the $\Delta\Delta/\Lambda\Lambda$ stacking is missing, and only $\Delta\Lambda$ pairs are present.

Interactions with DNA

To explore the potential biological activity at the genome level the binding of the complexes to DNA was next investigated. Spectroscopic DNA titrations were carried out in 10 mM phosphate buffered solution with pH at 7.4 and either with or without 160 mM NaCl by adding a solution of salmon testes DNA (st-DNA) to the solution of the complexes in a 1 cm emission quartz cuvette and by measuring the absorption and emission after each addition.²⁵ Titrations for all complexes were repeated at least three times for each condition to ensure reproducibility.

The increase in the concentration of st-DNA resulted in a significant change in both the absorption and the emission spectrum (Fig. 4). The general behaviour for complexes **3–6** was similar to that previously reported for **1** and **2**² as well as for other intercalating compounds.^{16,22,25–28} The general trend was an overall decrease in the absorption with increasing concentrations of DNA. The decrease in the absorbance of the MLCT band at 440 nm for complexes **3** and **5**, which contained **phen** as ancillary ligand, was 17% and 18%, respectively, and the decrease in the π – π^* band for the extended aromatic moiety at 310 nm was 44% and 52% for **3** and **5**, respectively (low ionic strength). Similarly for the **TAP** complexes the decrease in the MLCT band at 412 nm was 22% and 19%, and the decrease in the π – π^* band for the extended aromatic moiety at 310 nm was 34% and 41% for **4** and **6**, respectively (low ionic strength). This hypochromic behaviour indicates intercalation where particularly, the large decrease in the absorbance at 310 nm can be explained by a strong interaction between the chromophore of the extended aromatic moiety and the chromophores of the base pairs in the form of π – π stacking.²⁹

We observe a fundamental difference in the change in the emission spectra for complexes that have **phen** (**3** and **5**) and **TAP** (**4** and **6**) as ligands.² Complexes **3** and **5** exhibit the well-known “light switch effect”,^{16,30} as their emissions are fully quenched in aqueous solution, but they become highly emissive upon binding to DNA. This effect is explained by the change in the environment due to the intercalation of the extended aromatic moiety, which prevents solvent molecules from interacting with N-atoms of the phenazine moieties, an interaction that results in quenching of the emission.³¹ The emission showed biphasic behaviour in solutions containing only 10 mM phosphate buffer. In the first phase a strong emission enhancement was observed, while in the second phase the emission intensity began to decrease slowly. A decrease was not observed at high ionic strength (160 mM NaCl). In contrast to **3** and **5**, **TAP** complexes **4** and **6** exhibit 80% and 81% quenching of the emission respectively upon binding to DNA (at low ionic strength). This is common for Ru(**TAP**)₂ complexes as the excited state, instead of undergoing radiative decay, can photo-oxidize guanine residues in DNA resulting in an overall quenching of the emission.^{22,32}

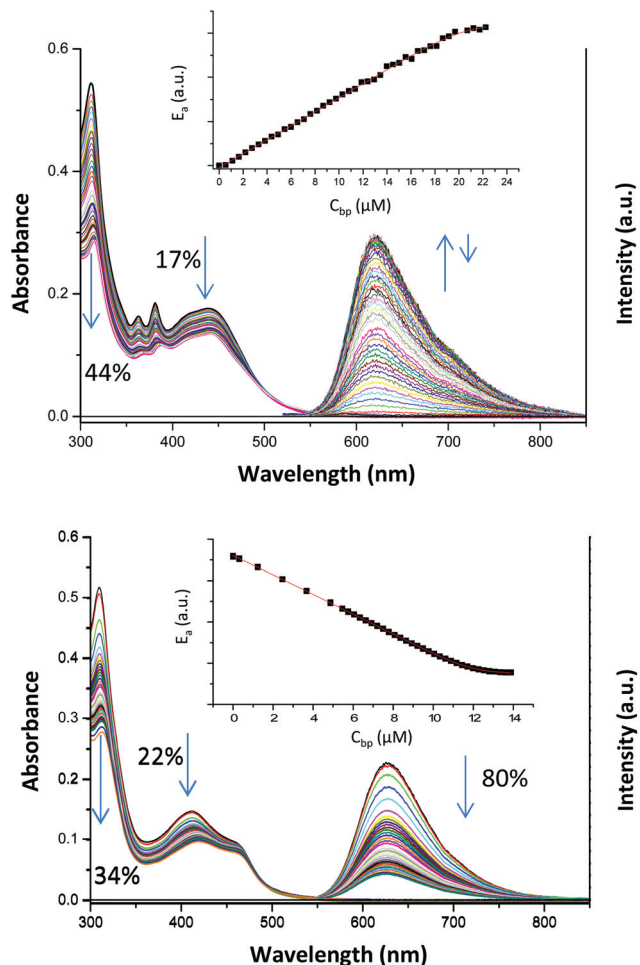


Fig. 4 Changes in the UV-Vis and emission spectra of (top) **3** and (bottom) **4** with the addition of increasing amounts of st-DNA (0–100 μM base pairs) at pH 7.4 (10 mM sodium phosphate). Similar spectra for the titration of **5** and **6** can be seen in the ESI†. Inset: Plot of the concentration corrected emission (E_a) at increasing concentration of DNA base pairs and the corresponding non-linear fit of eqn (S3.5) (see ESI†). Similar plots and fits have been made for the absorption data.

From the spectrophotometric data presented herein, we have quantified the affinity of the complexes for DNA by calculating values for the binding constant (K_b) and for the binding site size (n). For this purpose we used a simple modification of a method by Carter, Rodriguez and Bard.³³ Our method assumes the same binding model, however knowledge of the molar absorbance or emission for bound complex is not needed. A detailed description of the method and the problems addressed by the method are given in the ESI†. The parameters were calculated using the changes in the absorbance of the MLCT band (440 nm or 412 nm) as well as the changes of the integrated emission.

Both the absorption corresponding to the MLCT band and the integrated emission indicated a very strong interaction between the complexes and DNA at low ionic strength (10 mM sodium phosphate) with binding constants in the order of 10^7 M^{-1} (see Tables 2 and S1 in the ESI†). The data showed

that values of n for all complexes except **3** were 1.7 ± 0.2 base pairs (bp). It should be noted that fitting to this binding isotherm is empirical and interpretation is necessarily approximate. It implicitly assumes that the binding of both enantiomers is similar, that the affinity for the ten discrete two base-pair binding sites^{34a} is the same, and that binding occurs only from one of the grooves. In the crystal structures so far reported for $[\text{Ru}(\text{phen})_2\text{dppz}]^{2+}$ and $[\text{Ru}(\text{TAP})_2\text{dppz}]^{2+}$ with DNA the complex intercalates *via* the minor groove,³⁵ although some solution experiments indicate that entry from the major groove is possible.³⁶ Crystal structures have also shown that at the high concentrations present in the crystal semi-intercalation of the ancillary ligand of the lambda-enantiomer is possible. However in solution this binding mode is likely to be much weaker than intercalation. The work of Lincoln and co-workers has shown that the DNA binding of the enantiomers $[\text{Ru}(\text{phen})_2\text{dppz}]^{2+}$ and $[\text{Ru}(\text{bpy})_2\text{dppz}]^{2+}$ is complex. The complexes show some preference for binding to particular sequences and the enantiomers show contrasting behaviour.^{34b} For $[\text{Ru}(\text{phen})_2\text{dppz}]^{2+}$ both cooperative and anti-cooperative interactions have been demonstrated.^{34c} Similar effects may be expected here and could be the reason for the relatively low site size recorded for the complexes here.

Binding constants for the four complexes are still high, in 160 mM NaCl, but decrease by an order of magnitude to about 10^6 M^{-1} (see Table 2) while n -values hardly change. These results indicate a similar binding mode under both conditions, however with a significantly weaker binding at increased ionic strength. A good agreement between the size of the values of K_b and n are seen when the values calculated from the absorption and emission data, respectively, are compared. This indicates a more specific and well-defined mode of binding than the situation at low ionic strength.³⁷ The **phen** complexes **3** and **5**, and **TAP** complexes **4** and **6** show pairwise very similar binding constants where the **phen** complexes bind strongest. The emission data gave K_b for **3** and **5** at 2.6×10^6 and $1.4 \times 10^6 \text{ M}^{-1}$, respectively and K_b was $0.33 \times 10^6 \text{ M}^{-1}$ for both **4** and **6**. A similar trend between **phen** and **TAP** complexes has previously been shown for **1** and **2** in 100 mM NaCl (see Table 2).²

Circular dichroism studies

Circular dichroism (CD) is a powerful spectroscopic technique in the study of binding of ligands (here ruthenium complexes) to DNA with respect to study the binding modes as well as the conformational changes of DNA.³⁸ DNA is an optically active molecule as a result of the chiral sugar-phosphate backbone and its helicity. B-DNA form exhibits a typical CD spectrum characterised by a positive band around 280 nm and a negative band around 245 nm.⁵² In addition chiral and achiral molecules bound to DNA can have induced CD (ICD) signals. Strong ICD indicates groove binding since this will place the molecule close to the chiral sugar backbone, whereas intercalation will place the molecules between the achiral base pairs.³⁹ ICD is known to be an order of magnitude stronger for groove binders than for intercalators.

In order to evaluate the ability of complexes 3–6 to bind to DNA, CD titrations were carried out by keeping the concentration of st-DNA constant (150 μM nucleotide) and measuring the CD spectrum for different concentrations of complex (Fig. 5). Racemic mixtures of the complexes were used in the titrations and therefore they show no optical activity. However, the CD spectra of st-DNA show significant changes in the presence of complexes 3–6. For wavelengths higher than 300 nm some CD signals were observed that could be assigned to ICD of the complexes since this was outside of the range where DNA absorb or that one of the enantiomers (Δ or Λ) is demonstrating preferential binding to DNA.

At short wavelength, the evolution of a strong negative band was observed with a maximum at about 275 nm for complex 3 and 5, and about 295 nm for complex 4 and 6. These bands could be attributed to π - π^* intra-ligand transitions of the ancillary

phen and TAP ligands, respectively and the strong signal indicated that the phen and TAP complexes were positioned in the grooves that also is the expected placement of the auxiliary ligands when mpdppz or dtp are intercalating. At high P/D ratio, a very small negative CD signal was observed for the four complexes at about 415 nm corresponding to the typical MLCT absorption band of the Ru(II) polypyridyl complexes. The exact binding modes cannot be determined from these observations, however the existence of an interaction between complexes 3–6 and the DNA molecule can be concluded. These results are similar to other Ru(II) complexes reported in the literature.^{38–43}

Thermal denaturation studies

Evidence that a compound is bound to DNA can be deduced by an increase in the melting temperature (T_m) of the double-stranded structure, the temperature at which 50% of the duplex has dissociated to a single stranded form.^{41–43} Thereby, thermal denaturation studies are useful to evaluate the ability of a compound to bind to DNA. Thermal denaturation curves of st-DNA (150 μM nuclear phosphates) in the presence of complexes 3–6 in 10 mM phosphate buffer at P/D ratios of 50, 20 and 10 are shown (see ESI†). The T_m was determined as the temperature corresponding to the steepest increase in the absorption by finding the maximum in the first derivative. In the absence of Ru(II) complexes, st-DNA exhibited a T_m of 69.8 $^\circ\text{C}$. At P/D of 50 and 20, there was a small increase in the T_m for the four complexes (Table 3). At P/D ratio of 10, complexes 3–6 displayed an increase of T_m for st-DNA from 69.8 $^\circ\text{C}$ to 76.4 $^\circ\text{C}$, 76.1 $^\circ\text{C}$, 76.5 $^\circ\text{C}$ and 76.3 $^\circ\text{C}$, respectively, indicating stabilisation of the DNA helix by DNA–Ru complex interaction. These values are smaller than those observed for the complex $[\text{Ru}(\text{phen})_2\text{dppz}]^{2+}$ (increase of 9.1 $^\circ\text{C}$) with calf thymus DNA at similar P/D ratio but similar to ΔT_m values determined for other Ru(II) complexes.^{44,45}

Viscometry studies

In order to determine whether the complexes interact with DNA through intercalation we measured the viscosity of st-DNA with increasing ratio of complexes 3–6. The plot of $(\eta/\eta_0)^{1/3}$ against D/P (concentration of ruthenium divided by concentration of nuclear phosphate) gave a straight line with positive slope for all complexes (see Fig. 6) which can be considered a positive proof for intercalation. The slope of this plot quan-

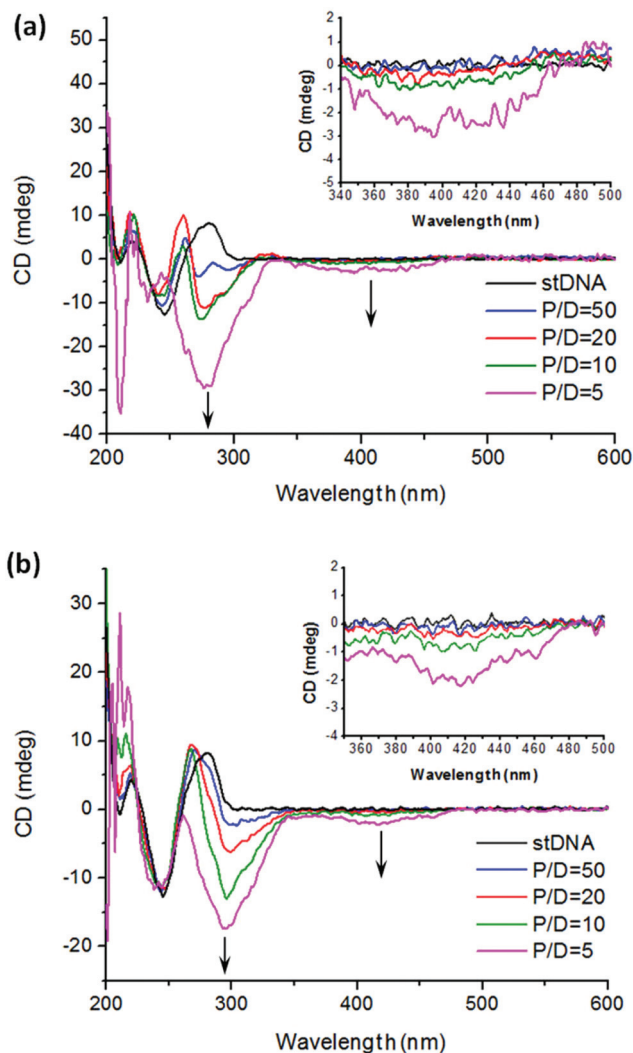


Fig. 5 Circular dichroism spectra of st-DNA (150 μM nuclear phosphate) in 10 mM sodium phosphate buffered aqueous solution at pH 7.4, in the absence and presence of (a) 3 and (b) 6 at different nuclear phosphates to dye (P/D) ratios.

Table 3 Melting temperature values for thermal denaturation of st-DNA (150 μM) in 10 mM phosphate buffered aqueous solution at pH 7.4, in the presence of complexes 3–6 at different P/D ratios

Complex	ΔT_m ($^\circ\text{C}$)		
	P/D = 50	P/D = 20	P/D = 10
3	0.7 ± 0.1	1.2 ± 0.8	6.6 ± 1.3
4	0.3 ± 0.4	2.1 ± 0.1	6.3 ± 0.4
5	1.2 ± 0.8	1.5 ± 0.9	6.7 ± 0.4
6	0.8 ± 0.0	2.3 ± 0.5	6.5 ± 0.5

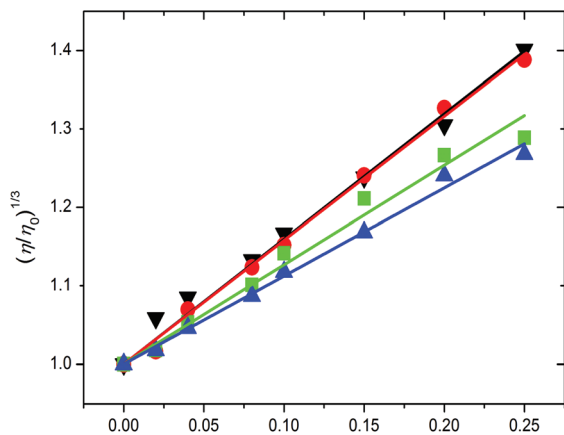


Fig. 6 Viscosity measurements for complexes 3 (▼), 4 (●), 5 (■) and 6 (▲) in 10 mM sodium phosphate buffered aqueous solution at pH 7.4, at different D/P ratios.

tifies the contribution of the intercalator to the elongation of the DNA. For complexes 3 and 4 which contain **mpdppz** as extended aromatic ligand we have found the slopes are almost identical: 1.60 ± 0.05 and 1.58 ± 0.04 respectively. Similarly, for complexes 5 and 6 the values found were 1.27 ± 0.07 and 1.12 ± 0.04 respectively which are also close to each other. It can be seen that the complexes with the same extended aromatic ligand show similar behaviour, which suggests that the intercalation takes place preferentially through that moiety.

Cellular uptake and viability studies

The uptake of the four complexes 3–6 into HeLa (cervical cancer) cells in the dark was investigated using confocal microscopy (see Fig. 7). The results demonstrated that the cells

successfully internalised all complexes at 100 μM within 24 hours. The complexes appeared to localise within the cytoplasm of cells with red fluorescent emission observed outside the nucleus. These results are in agreement with previous results observed for complexes 1 and 2.² Some toxicity against the cells was observed during confocal imaging (the generation of singlet oxygen by 3–6 was not quantified).

Next the complexes were assessed for cytotoxicity against HeLa cells under both dark and visible light (from an UV-filtered HgXe arc lamp) (photoactivated) conditions (see Table 4). 25×10^3 cells per well were seeded into 96-well plates and treated with compound (ruthenium complexes – see Table 4) for 24 hours at 37 °C. Following this, the cells were either irradiated with 18 J cm^{-2} of light for one hour or maintained in the dark. After further 24 hours incubation, each well was treated with 20 μL of Alamar Blue and left to incubate for 4–5 hours. Emission was read at 590 nm (excitation at 544 nm). The chemotherapeutic drug paclitaxel (Taxol®) and

Table 4 Effects of Ru(II) complexes 1–6 on HeLa cervical cancer cells with or without light activation. Results are presented as the mean \pm SEM

Complex	IC ₅₀ , μM	
	Dark	Light
3	37 ± 6	48 ± 8
4	60 ± 15	4.8 ± 0.5
5	34 ± 3	33 ± 6
6	63 ± 8	4.0 ± 1.5
1 ^a	>100	>100
2 ^a	70 ± 6	8.8 ± 2.9
Taxol®	0.0028 ± 0.0005	0.0026 ± 0.0006

^a Cloonan *et al.*²

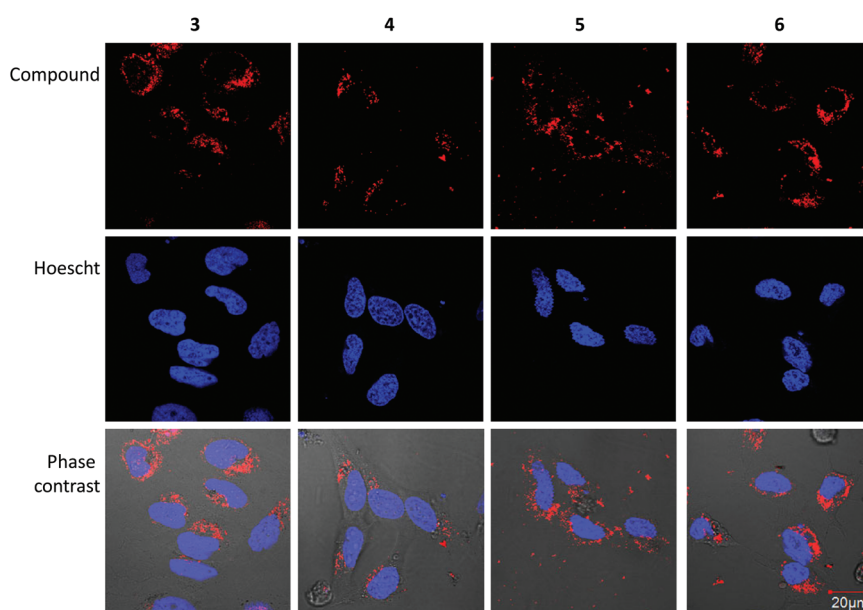


Fig. 7 Complexes were successfully taken up by HeLa cells and localised in the cytoplasm.

the previously studied **phen** complex **1** have been used as references. The studies demonstrated that the **phen** complexes **3** and **5** did not show light-dependent cytotoxicity yielding similar IC_{50} values under both dark and light conditions.

These IC_{50} values were, however, significantly lower than those observed previously for **phen** complex **1**. These results suggest that the introduced modifications of **pdppz** have increased the overall cytotoxicity relative to the **phen** reference complex. This increase in toxicity has been confirmed by comparison of the viability of the cells at 100 μ M. The cell viability in the case of **1** was 35% while for **3** and **5** it was 6% and 5%, respectively. However, light activation resulted in a more than 10 fold increase in the toxicity of the **TAP** complexes **4** and **6**, similar to what is seen for **TAP** complex **2**. The IC_{50} values for **4** and **6** in the dark were 60 μ M and 63 μ M, respectively, decreasing to 5 μ M and 4 μ M after photoactivation. These IC_{50} values following light activation are marginally lower than the value reported for **2** (9 μ M), which possessed a similar toxicity in the dark (IC_{50} value at 70 μ M).

Conclusions

We have reported the synthesis of four new DNA binding and cytotoxic ruthenium polypyridyl complexes with two new ligands derived from **dppz** (**mpdppz** and **dtp**) and **phen** or **TAP** as ancillary ligands. Crystal structures were obtained for two of the complexes that incorporated the **TAP** ancillary ligand (complexes **4** and **6**). Their photophysical properties have been studied, and they have shown MLCT based luminescence properties, which were modulated in the presence of st-DNA. Complexes with **phen** as ancillary ligand (complexes **3** and **5**) have shown no emission in aqueous medium. However, in the presence of DNA the luminescence was switched on, a property known as the "light switch" effect and assigned to intercalation.

The complexes with **TAP** as ancillary ligand (**4** and **6**) have shown the opposite behaviour. In aqueous medium these complexes showed a relatively strong emission that was however almost totally quenched in the presence of DNA. This was assigned to photo-induced oxidation of guanine when the compounds were bound to DNA as has been studied in detail with $[Ru(TAP)_2dppz]^{2+}$. A modification of a method by Carter, Rodriguez and Bard has been used to calculate binding parameters from the spectroscopic data showing binding constants in the order of 10^7 and 10^6 M^{-1} at low and high ionic strength, respectively. The binding was significantly stronger for the **phen** complexes than for the **TAP** complexes. Further, CD spectroscopy and DNA denaturation studies have been used to investigate the interaction between the complexes and DNA. In accordance with previous studies the **phen** and **TAP** complexes show differences in their toxicity upon light activation. The **phen** complexes did not show increased toxicity upon exposure to light while the **TAP** complexes showed a good therapeutic window with a more than 10-fold increase in toxicity upon exposure to light. It was demonstrated with confocal

microscopy that HeLa cells took up the compounds with emission in the cytoplasm outside the nucleus indicating that cell death is unlikely to be due to interaction with nuclear DNA. In conclusion **phen** complexes **3** and **5** have shown to be candidates for use in fluorescence imaging while **TAP** complexes **4** and **6** have shown to be candidates for use in photodynamic therapy.

Experimental

Materials and methods

All chemicals were purchased from Sigma-Aldrich, Acros Organics or TCI and used as received without further purification. The DNA used for all the experiments was double-stranded salmon testes DNA sodium salt purchased from Sigma-Aldrich which was dissolved in a buffered aqueous solution and then filtered to remove insoluble impurities. DNA concentration in base pairs was determined by UV using $\epsilon_{260\text{ nm}} = 13\,200\text{ M}^{-1}\text{ cm}^{-1}$.⁵⁰

NMR spectra were recorded either using a Bruker DPX-400 Avance spectrometer, which operates at 400.13 MHz for ^1H NMR and 100 MHz for ^{13}C NMR, or a Bruker AV-600 spectrometer, operating at 600.1 MHz for ^1H NMR and 150.2 MHz for ^{13}C NMR. Chemical shifts (δ) were referred relative to the internal solvent signals and reported in ppm. Electrospray ionisation (ESI) mass spectra were recorded on a Mass Lynx NT V 3.4 with a Waters 600 controller connected to a 996 photodiode array detector using HPLC-grade acetonitrile, methanol, dichloromethane or chloroform as carrier solvents. All high resolution (HR) masses were reported within ± 10 ppm of the expected mass. Infrared spectra were recorded on a Perkin Elmer Spectrum One FT-IR spectrometer fitted with a Universal ATR Sampling Accessory. Melting points were obtained in an unsealed capillary tube using an Electrothermal 9100 melting point apparatus. Elemental analyses were conducted at the Microanalytical Laboratory, School of Chemistry and Chemical Biology, University College Dublin (UCD).

UV-Vis-NIR and luminescence measurements were done in a 1.0 cm optical path quartz cell at room temperature. The absorption spectra were recorded using a Varian Cary 50 UV-Visible spectrophotometer. The emission and excitation spectra were recorded on a Varian Cary Eclipse fluorescence spectrophotometer. Fluorescence lifetime experiments were carried out on a Horiba Scientific FluoroLog - Modular Spectrofluorometer equipped with Time Correlated Single Photon Counting (TCSPC) capability. Circular Dichroism (CD) spectra were recorded at a concentration corresponding to an optical density of approximately 1.0 for the DNA absorbance at 260 nm (150 μ M) on a Jasco J-810-150S CD spectropolarimeter.⁵¹

X-ray diffraction data were collected on a Bruker APEX 2 DUO CCD diffractometer using graphite-mono-chromatized $\text{Mo-K}\alpha$ (0.71073 \AA). Crystals were mounted in a cryoloop/MiTeGen micromount and collected at 100(2) K using an Oxford Cryosystems Cobra low temperature device. Data were

collected using omega and phi scans and were corrected for Lorentz and polarization effects.⁴⁶ Structures were solved with SHELXS-2014 and further refined with SHELXL-2014.⁴⁷ In the case of the crystal 4·2Cl·xH₂O, highly disordered solvent molecules were removed using SQUEEZE⁴⁸ software and then refined as indicated.

Viscosity was measured with a Cannon-Manning semi-micro viscometer at precisely 25.0 °C. Constant DNA concentration of 1.2 mM and total sample volume of 1 mL were used. DNA was sheared with ultrasound to obtain fragments of ca. 200 bp. Ruthenium/nuclear phosphate concentration ratios (D/P) ranging from 0.02 to 0.25 were measured. Viscosity (η) was calculated as sample flow time minus buffer flow time. Finally (η/η_0)^{1/3} values (where η_0 is the viscosity of DNA alone) were plotted against D/P.⁴⁹

General biological procedures

Cell culture reagents were obtained from Greiner Bio-one and all other chemicals were obtained from Sigma unless otherwise stated.

Cell culture. HeLa cells were grown in a cell culture flask using low-glucose Dulbecco's Modified Eagle Medium supplemented with 10% fetal bovine serum and 50 $\mu\text{g mL}^{-1}$ penicillin/streptomycin at 37 °C in a humidified atmosphere of 5% CO₂.

Viability assay. 25 × 10³ cells per well were seeded in a 96-well plate and treated as indicated. Each well was then treated with 20 μL of Alamar Blue (BioSource) and left to incubate at 37 °C in the dark for 4–5 hour. Fluorescence was read at 590 nm (excitation 544 nm). The background fluorescence of the media without cells + Alamar Blue was taken away from each group, and the control untreated cells represented 100% cell viability. Data points represent the mean ± SEM of triplicate treatments performed on three independent days with activity expressed as percentage cell viability compared to vehicle treated controls. IC₅₀ values for the toxicity of the compounds were calculated for each of the three independent experiments by interpolation to concentration corresponding to 50% viability and this were used to calculate the mean ± SEM. For photoactivation studies, cells were subjected to 18 J cm⁻² using a Hamamatsu L2570 200 W visible light form a HgXe arc lamp equipped with a NaNO₂ filter.

Confocal microscopy. HeLa cells were seeded at a density of 5 × 10⁴ cells per mL and treated as indicated. Cells were then washed two times with fresh media, nuclei were stained blue with Hoechst and cells were imaged by live confocal microscopy using an Olympus FV1000 point scanning microscope with a 60× oil immersion lens with an NA (numerical aperture) of 1.42. The software used to collect images was FluoView Version 7.1 software.

Synthesis of ligands and complexes

3-Methylpyrazino[2,3-*h*]dipyrido[3,2-*a*:2',3'-*c*]phenazine (mpdppz). 2-Methyl-5,6-diaminoquinoxaline (74 mg, 0.43 mmol, 1 eq.) and 1,10-phenanthroline-5,6-dione (94 mg, 0.45 mmol, 1 eq.) were suspended in a mixture of ethanol and H₂O (1 : 1, 25 mL).

The mixture was heated in a high-pressure tube at 140 °C overnight followed by cooling to room temperature. The suspension was filtered, and the grey filter cake was washed with CH₂Cl₂ (25 mL) leaving the product as a white solid that was dried *in vacuo* (137 mg, 92%). Calculated for C₂₁H₁₂N₆ + 2.25H₂O: C, 64.84; H, 3.12; N, 21.60%. Found: C, 64.84; H, 3.41; N, 21.99%. M.p.: >250 °C. ¹H NMR (CDCl₃/TFA, 400 MHz, δ): 10.69 (1H, d, *J* = 7.3 Hz), 10.16 (1H, d, *J* = 8.0 Hz), 9.77 (1H, s), 9.40 (2H, bs), 8.95 (1H, d, *J* = 9.3 Hz), 8.79 (1H, d, *J* = 9.3 Hz), 8.38 (2H, bs), 3.27 (3H, s, CH₃). ¹³C NMR (CDCl₃/TFA, 100 MHz, δ): 158.26, 150.48, 148.91, 145.24, 144.67, 142.06, 141.83, 140.36, 140.27, 140.00, 139.86, 138.52, 136.63, 136.39, 129.59, 129.22, 129.15, 128.14, 127.87, 21.04 (CH₃). IR (ATR, cm⁻¹): 1392 and 1367 (C–N stretches). ESI-HRMS (*m/z*) calculated for C₂₁H₁₃N₆: 349.1196. Found: 349.1202 [M + H]⁺.

Bis(1,10-phenanthroline)(3-methylpyrazino[2,3-*h*]dipyrido[3,2-*a*:2',3'-*c*]phenazine)ruthenium(II) chloride (3). [Ru(phen)₂Cl₂] (160 mg, 0.301 mmol, 1 eq.) and **mpdppz** (105 mg, 0.301 mmol, 1 eq.) were suspended in 8 mL of a 50% mixture EtOH/H₂O. The mixture was degassed by bubbling with Argon for 15 minutes and then heated at 140 °C for 40 min using microwave irradiation. Solvent was evaporated and the resulting red solid was purified by column chromatography with neutral alumina using MeCN:H₂O (10 : 0 to 9 : 1) as eluent. Solvent was removed at reduced pressure yielding a red solid which was dried *in vacuo* (198 mg, 74%). Calculated for C₄₅H₂₈N₁₀RuCl₂ + 1.3NaCl: C, 53.86; H, 3.33; N, 13.96%. Found: C, 53.68; H, 3.33; N, 13.83; Cl, 10.47%. M.p.: >250 °C. ¹H NMR (CD₃CN, 600 MHz, δ): 9.86 (1H, d, *J* = 8.1 Hz), 9.70 (1H, d, *J* = 8.1 Hz), 9.15 (1H, s), 8.63 (2H, bs), 8.61 (2H, bs), 8.58 (1H, d, *J* = 9.4 Hz), 8.47 (1H, d, *J* = 9.4 Hz), 8.27 (5H, bs), 8.26–8.22 (1H, m), 8.16 (2H, d, *J* = 5.2 Hz), 8.05 (2H, d, *J* = 5.2 Hz), 7.85–7.80 (2H, m), 7.68–7.63 (4H, m), 3.59 (3H, s). ¹³C NMR (CD₃CN, 100 MHz, δ): 158.38, 155.48, 155.36, 154.32, 154.23, 153.98, 151.64, 151.58, 148.89, 148.87, 148.81, 145.57, 144.95, 142.42, 141.13, 140.32, 139.43, 137.98, 137.96, 137.92, 135.18, 134.41, 132.20, 132.09, 132.07, 132.05, 131.63, 131.23, 129.10, 129.06, 128.20, 128.14, 126.93, 126.90, 126.87, 22.77 (CH₃). IR (ATR, cm⁻¹): 3059 (aromatic C–H stretch), 1426 and 1361 (C–N stretches). MALDI-HRMS (*m/z*) calculated for C₄₅H₂₈N₁₀Ru: 810.1542. Found: 810.1567 [M]⁺.

Bis(1,4,5,8-tetraazaphenanthrene)(3-methyl-pyrazino[2,3-*h*]dipyrido[3,2-*a*:2',3'-*c*]phenazine)ruthenium(II) chloride (4). [Ru(TAP)₂Cl₂] (93 mg, 173 μmol , 1 eq.) and **mpdppz** (59 mg, 0.169 mmol, 1 eq.) were suspended in a mixture EtOH/H₂O (1 : 1, 8 mL). The mixture was degassed by bubbling with Argon for 15 minutes and then heated at 140 °C for 40 minutes using microwave irradiation. Solvent was evaporated and the resulting red solid was purified by chromatography with neutral alumina using MeCN:H₂O (10 : 0 to 9 : 1) as eluent. Solvent was removed at reduced pressure yielding a red solid which was dried *in vacuo* (88 mg, 59%). Calculated for C₄₁H₂₄Cl₂N₁₄Ru + 2.2H₂O + 2.5NaCl: C, 46.00; H, 2.67; N, 18.32%. Found: C, 46.23; H, 2.67; N, 18.16%. M.p.: >250 °C (decomp). ¹H NMR (CD₃CN, 600 MHz, δ): 9.99 (1H, dd, *J* = 8.3 Hz, 1.1 Hz), 9.82 (1H, dd, *J* = 8.3 Hz, 1.3 Hz), 9.16 (1H, s),

9.00–8.97 (4H, m), 8.63 (4H, s), 8.60 (1H, d, $J = 9.5$ Hz), 8.50 (1H, d, $J = 9.5$ Hz), 8.32–8.30 (2H, m), 8.26–8.23 (4H, m), 7.94–7.89 (2H, m), 2.90 (3H, s). ^{13}C NMR (CD_3CN , 100 MHz, δ): 157.62, 156.74, 156.66, 153.67, 150.73, 150.68, 150.58, 150.57, 150.45, 150.44, 150.07, 146.93, 146.51, 146.50, 146.45, 143.31, 143.30, 143.22, 140.88, 139.83, 139.75, 135.98, 133.81, 133.73, 132.64, 131.44, 131.32, 128.63, 128.59, 127.74. IR (ATR, cm^{-1}): 3058 (aromatic C–H stretch), 1486, 1385 and 1273 (C–N stretches). ESI-HRMS (m/z) calculated for $\text{C}_{45}\text{H}_{28}\text{N}_{10}\text{Ru}$: 407.0676. Found: 407.0679 $[\text{M}]^{2+}$.

Dipyrido[3,2- α :2',3'- c][1,2,5]thiadiazolo[3,4- h]phenazine (dtp). 4,5-Diamine-2,1,3-benzothiadiazole (121 mg, 0.73 mmol, 1 eq.) and 1,10-phenanthroline-5,6-dione (156 mg, 0.74 mmol, 1 eq.) were suspended in a mixture of ethanol and H_2O (1 : 1, 20 mL). The mixture was heated in a high-pressure tube at 140 °C overnight followed by cooling to room temperature. The resulting yellow precipitate was filtered, washed with H_2O , ethanol and diethyl ether, and dried *in vacuo* (200 mg, 81%). M.p.: >250 °C. ^1H NMR (CDCl_3 , 400 MHz, δ): 9.87 (1H, dd, $J = 8.1$ Hz, 1.8 Hz), 9.70 (1H, dd, $J = 8.1$ Hz, 1.8 Hz), 9.35 (2H, m), 8.33 (2H, syst AB), 7.88 (1H, dd, $J = 4.4$ Hz, 8.1 Hz), 7.86 (1H, dd, $J = 4.4$ Hz, 8.1 Hz). ^{13}C NMR (CDCl_3 , 100 MHz, δ): 156.21, 152.96, 152.89, 152.81, 144.98, 141.26, 140.16, 137.94, 135.08, 134.63, 132.19, 127.37, 127.32, 125.30, 124.74. IR (ATR, cm^{-1}): 2984 (aromatic C–H stretch), 1494 (aromatic C=C stretch), 1368 (C=N stretch). ESI-HRMS (m/z) calculated for $\text{C}_{18}\text{H}_9\text{N}_6\text{S}$: 341.0609. Found: 341.0610 $[\text{M} + \text{H}]^+$.

Bis(1,10-phenanthroline)(dipyrido[3,2- α :2',3'- c][1,2,5]thiadiazolo[3,4-4,3]phenazine)ruthenium(II) chloride (5). $[\text{Ru}(\text{phen})_2\text{Cl}_2]$ (0.158 g, 0.297 mmol, 1 eq.) and **dtp** (0.101 g, 0.297 mmol, 1 eq.) were suspended in a mixture EtOH/ H_2O (1 : 1, 8 mL). The mixture was degassed by bubbling with argon for 15 minutes and then heated at 140 °C for 40 minutes using microwave irradiation. Solvent was evaporated and the resulting red solid was purified by chromatography with neutral alumina using MeCN : H_2O (10 : 0 to 9 : 1) as eluent. Solvent was removed at reduced pressure yielding a red solid which was dried *in vacuo* (77 mg, 30%). Calculated for $\text{C}_{41}\text{H}_{24}\text{Cl}_2\text{N}_{14}\text{Ru}$ + 3.5 H_2O : C, 52.40; H, 3.01; N, 14.29; S, 3.94; Cl, 8.03%. Found: C, 53.91; H, 3.34; N, 14.97; S, 3.43; Cl, 7.58%. M.p.: >250 °C. ^1H NMR (CD_3CN , 400 MHz, δ): 9.86 (1H, d, $J = 8.1$ Hz), 9.70 (1H, d, $J = 8.1$ Hz), 9.15 (1H, s), 8.63 (2H, b), 8.61 (2H, m), 8.58 (1H, d, $J = 9.4$ Hz), 8.47 (1H, d, $J = 9.4$ Hz), 8.27 (5H, b), 8.23 (2H, m), 8.16 (2H, d, $J = 5.2$ Hz), 8.05 (2H, d, $J = 5.2$ Hz), 7.85–7.80 (2H, m), 7.68–7.63 (4H, m), 3.59 (3H, s). ^{13}C NMR (CD_3CN , 100 MHz, δ): 157.59, 155.66, 155.58, 154.28, 153.98, 153.69, 151.60, 151.55, 148.86, 148.81, 146.76, 141.20, 140.07, 139.67, 137.98, 137.94, 134.55, 132.64, 132.07, 132.05, 131.25, 131.12, 129.07, 128.26, 128.22, 127.58, 126.92, 126.87; IR (ATR, cm^{-1}): 3066 (aromatic C–H stretch), 1496 (aromatic C=C stretch), 1360, 1336 (C=N stretch). MALDI-HRMS (m/z) calculated for $\text{C}_{42}\text{H}_{24}\text{N}_{10}\text{SRu}$: 802.0950. Found: 802.0957 $[\text{M}]^+$.

Bis(1,4,5,8-tetraazaphenanthrene)(dipyrido[3,2- α :2',3'- c][1,2,5]thiadiazolo [3,4-4,3]phenazine)ruthenium(II) chloride (6). $[\text{Ru}(\text{TAP})_2\text{Cl}_2]$ (140 mg, 262 μmol , 1 eq.) and **dtp** (892 mg, 262 μmol , 1 eq.) were suspended in a mixture EtOH/ H_2O (1 : 1,

8 mL). The mixture was degassed by bubbling with Argon for 15 minutes and then heated at 140 °C for 40 minutes using microwave irradiation. Solvent was evaporated and the resulting red solid was purified by chromatography with neutral alumina using MeCN : H_2O (10 : 0 to 9 : 1) as eluent. Solvent was removed at reduced pressure yielding a red solid which was dried *in vacuo* (100 mg, 44%). Calculated for $\text{C}_{38}\text{H}_{20}\text{N}_{14}\text{Cl}_2\text{SRu}$ + 0.5NaCl: C, 47.88; H, 2.33; N, 20.57; S, 3.36%. Found: C, 46.73; H, 2.09; N, 19.69; S, 6.10%. M.p.: 162–165 (decomp). ^1H NMR (CD_3CN , 600 MHz, δ): 9.83 (1H, dd, $J = 8.2$ Hz, 1.2 Hz), 9.77 (1H, dd, $J = 8.2$ Hz, 1.2 Hz), 9.01 (2H, 2d, $J = 2.8$ Hz), 8.99 (2H, d, $J = 2.7$ Hz), 8.62 (4H, s), 8.46 (2H, syst AB), 8.40 (2H, 2d, $J = 2.9$ Hz), 8.39 (2H, d, $J = 2.7$ Hz), 8.34 (2H, 2dd, $J = 5.4$ Hz, 1.3 Hz), 7.92 (2H, 2dd, $J = 8.3$ Hz, 5.4 Hz). ^{13}C NMR (CD_3CN , 100 MHz, δ): 157.62, 156.74, 156.66, 153.67, 150.73, 150.68, 150.58, 150.57, 150.45, 150.44, 150.07, 146.93, 146.51, 146.50, 146.45, 143.31, 143.30, 143.22, 140.88, 139.83, 139.75, 135.98, 133.81, 133.73, 132.64, 131.44, 131.32, 128.63, 128.59, 127.74. IR (ATR, cm^{-1}): 3075 (aromatic C–H stretch), 1488 (aromatic C=C stretch), 1385, 1362 (C=N stretch). ESI-HRMS (m/z) calculated for $\text{C}_{38}\text{H}_{20}\text{N}_{14}\text{SRu}$: 806.0760. Found: 403.0387 $[\text{M}]^{2+}$.

Acknowledgements

We thank Science Foundation Ireland (SFI PI Awards 10/45 IN.1/B2999 and 13/IA/1865), and the Irish Research Council (IRC); PhD Scholarship B. C. P.), Marie Skłodowska-Curie actions (MSCA, to SB), and Trinity College Dublin (TCD) for financial support. We thank Dr Fergus Poynton and Dr Susan J. Quinn for their help and valuable discussion and guidance during this project. We thank Dr Martin Feeney and Dr Garry Hessman for the help with mass spectrometry studies, and Dr John E. O'Brien and Dr Manuel Ruether for the help with NMR studies.

Notes and references

- (a) F. E. Poynton, J. P. Hall, P. M. Keane, C. Schwarz, I. V. Sazanovich, M. Towrie, T. Gunnlaugsson, C. J. Cardin, D. J. Cardin, S. J. Quinn, C. Long and J. M. Kelly, *Chem. Sci.*, 2016, 7, 3075–3084; (b) A. Byrne, C. S. Burke and T. E. Keyes, *Chem. Sci.*, 2016, 7, 6551–6562; (c) B.-Z. Zhu, X.-J. Chao, C.-H. Huang and Y. Li, *Chem. Sci.*, 2016, 7, 4016–4023; (d) V. Pierroz, R. Rubbiani, C. Gentili, M. Patra, C. Mari, G. Gasser and S. Ferrari, *Chem. Sci.*, 2016, 7, 6115–6124; (e) R. B. P. Elmes, J. A. Kitchen, D. C. Williams and T. Gunnlaugsson, *Dalton Trans.*, 2012, 41, 6607–6610; (f) J. A. Kitchen, E. M. Boyle and T. Gunnlaugsson, *Inorg. Chim. Acta*, 2012, 381, 236–242; (g) A. M. Nonat, C. Allain, S. Faulkner and T. Gunnlaugsson, *Inorg. Chem.*, 2010, 49, 8449–8456; (h) A. M. Brouwer, *Pure Appl. Chem.*, 2011, 83, 2213–2228; (i) M. R. Gill, J. Garcia-Lara, S. J. Foster, C. Smythe, G. Battaglia and J. A. Thomas, *Nat. Chem.*, 2009, 1, 662–667.

- 2 (a) S. M. Cloonan, R. B. P. Elmes, M. Erby, S. A. Bright, F. E. Poynton, D. E. Nolan, S. J. Quinn, T. Gunnlaugsson and D. C. Williams, *J. Med. Chem.*, 2015, **58**, 4494–4505; (b) C. Mari, V. Pierroz, R. Rubbiani, M. Patra, J. Hess, B. Spingler, L. Oehninger, J. Schur, I. Ott, L. Salassa, S. Ferrari and G. Gasser, *Chem. – Eur. J.*, 2014, **20**, 14421–14436; (c) G. J. Ryan, F. E. Poynton, R. B. P. Elmes, M. Erby, D. C. Williams, S. J. Quinn and T. Gunnlaugsson, *Dalton Trans.*, 2015, **44**, 16332–16344; (d) L.-L. Huang, J. Xu, Y.-J. Jin, D.-X. Zhao and H.-Y. Xie, *Analyst*, 2016, **141**, 2948–2954; (e) J. G. Vos and J. M. Kelly, *Dalton Trans.*, 2006, 4869–4883; (f) J. P. Lecomte, A. Kirsch-De Mesmaeker, M. M. Feeney and J. M. Kelly, *Inorg. Chem.*, 1995, **34**, 6481–6491.
- 3 (a) J. P. Hall, F. E. Poynton, P. M. Keane, S. P. Gurung, J. A. Brazier, D. J. Cardin, G. Winter, T. Gunnlaugsson, I. V. Sazanovich, M. Towrie, C. J. Cardin, J. M. Kelly and S. J. Quinn, *Nat. Chem.*, 2015, **7**, 961–967; (b) P. M. Keane, F. E. Poynton, J. P. Hall, I. V. Sazanovich, M. Towrie, T. Gunnlaugsson, S. J. Quinn, C. J. Cardin and J. M. Kelly, *Angew. Chem., Int. Ed.*, 2015, **54**, 8364–8368.
- 4 (a) Y. Ge and D. F. O'Shea, *Chem. Soc. Rev.*, 2016, **45**, 3846–3864; (b) M. Grossi, M. Morgunova, S. Cheung, D. Dimitri Scholz, E. Conroy, M. Terrile, A. Panarella, J. C. Simpson, W. M. Gallagher and D. F. O'Shea, *Nat. Commun.*, 2016, **7**, 10855, DOI: 10.1038/ncomms10855; (c) W. M. Gallagher, L. T. Allen, C. O'Shea, T. Kenna, M. Hall, A. Gorman, J. Killoran and D. F. O'Shea, *Br. J. Cancer*, 2005, **92**, 1702–1710.
- 5 (a) G. Li, L. Sun, L. Ji and H. Chao, *Dalton Trans.*, 2016, **45**, 13261–13276; (b) J. F. Lovell, T. W. B. Liu, J. Chen and G. Zheng, *Chem. Rev.*, 2010, **110**, 2839–2857.
- 6 (a) M. R. Gill and J. A. Thomas, *Chem. Soc. Rev.*, 2012, **41**, 3179–3192; (b) D. E. J. G. J. Dolmans, D. Fukumura and R. K. Jain, *Nat. Rev. Cancer*, 2003, **3**, 380–387.
- 7 R. B. P. Elmes, K. N. Orange, S. M. Cloonan, D. C. Williams and T. Gunnlaugsson, *J. Am. Chem. Soc.*, 2011, **133**, 15862–15865.
- 8 M. Martínez-Calvo, K. N. Orange, R. B. Elmes, B. la Cour Poulsen, D. C. Williams and T. Gunnlaugsson, *Nanoscale*, 2016, **8**, 563–574.
- 9 R. B. Elmes, M. Erby, S. M. Cloonan, S. J. Quinn, D. C. Williams and T. Gunnlaugsson, *Chem. Commun.*, 2011, **47**, 686–688.
- 10 L. Calucci, G. Pampaloni, C. Pinzino and A. Prescimone, *Inorg. Chim. Acta*, 2006, **359**, 3911–3920.
- 11 W. Guo, B. J. Engelman, T. L. Haywood, N. B. Blok, D. S. Beaudoin and S. O. Obare, *Talanta*, 2011, **87**, 276–283.
- 12 N. N. Sergeeva, M. Donnier-Marechal, G. Vaz, A. M. Davies and M. O. Senge, *J. Inorg. Biochem.*, 2011, **105**, 1589–1595.
- 13 F. da Silva Miranda, A. M. Signori, J. Vicente, B. de Souza, J. P. Priebe, B. Szpoganicz, N. S. Gonçalves and A. Neves, *Tetrahedron*, 2008, **64**, 5410–5415.
- 14 R. Nasielski-Hinkens, M. Benedek-Vamos, Y. Hautain and J. Nasielski, *Bull. Soc. Chim. Belg.*, 1976, **85**, 781–786.
- 15 T. Murashima, K.-i. Fujita, K. Ono, T. Ogawa, H. Uno and N. Ono, *J. Chem. Soc., Perkin Trans. 1*, 1996, 1403–1407.
- 16 A. E. Friedman, C. V. Kumar, N. J. Turro and J. K. Barton, *Nucleic Acids Res.*, 1991, **19**, 2595–2602.
- 17 Y. Jenkins, A. E. Friedman, N. J. Turro and J. K. Barton, *Biochemistry*, 1992, **31**, 10809–10816.
- 18 R. M. Hartshorn and J. K. Barton, *J. Am. Chem. Soc.*, 1992, **114**, 5919–5925.
- 19 C. Moucheron and A. Kirsch-De Mesmaeker, *J. Phys. Org. Chem.*, 1998, **11**, 577–583.
- 20 R. B. Nair, B. M. Cullum and C. J. Murphy, *Inorg. Chem.*, 1997, **36**, 962–965.
- 21 L. Troian-Gautier and C. Moucheron, *Molecules*, 2014, **19**, 5028.
- 22 I. Ortman, B. Elias, J. M. Kelly, C. Moucheron and A. Kirsch-DeMesmaeker, *Dalton Trans.*, 2004, 668–676.
- 23 A. L. Spek, *Acta Crystallogr., Sect. C: Cryst. Struct. Commun.*, 2015, **71**, 9–18.
- 24 M. Nishio, *CrystEngComm*, 2004, **6**, 130–158.
- 25 G. J. Ryan, S. Quinn and T. Gunnlaugsson, *Inorg. Chem.*, 2008, **47**, 401–403.
- 26 (a) K. A. O'Donoghue, J. M. Kelly and P. E. Kruger, *Dalton Trans.*, 2004, 13–14; (b) K. O'Donoghue, J. C. Penedo, J. M. Kelly and P. E. Kruger, *Dalton Trans.*, 2005, 1123–1128.
- 27 S. Vasudevan, J. A. Smith, M. Wojdyla, T. McCabe, N. C. Fletcher, S. J. Quinn and J. M. Kelly, *Dalton Trans.*, 2010, **39**, 3990–3998.
- 28 (a) S. Banerjee, S. A. Bright, J. A. Smith, J. Burgeat, M. Martínez-Calvo, D. C. Williams, J. M. Kelly and T. Gunnlaugsson, *J. Org. Chem.*, 2014, **79**, 9272–9283; (b) S. Banerjee, J. A. Kitchen, S. A. Bright, J. E. O'Brien, D. C. Williams, J. M. Kelly and T. Gunnlaugsson, *Chem. Commun.*, 2013, **49**, 8522–8524; (c) S. Banerjee, J. A. Kitchen, T. Gunnlaugsson and J. M. Kelly, *Org. Biomol. Chem.*, 2013, **11**, 5642–5655.
- 29 V. Danilov and S. Volkov, *Biopolymers*, 1975, **14**, 1205–1212.
- 30 A. E. Friedman, J. C. Chambron, J. P. Sauvage, N. J. Turro and J. K. Barton, *J. Am. Chem. Soc.*, 1990, **112**, 4960–4962.
- 31 (a) E. J. C. Olson, D. Hu, A. Hörmann, A. M. Jonkman, M. R. Arkin, E. D. A. Stemp, J. K. Barton and P. F. Barbara, *J. Am. Chem. Soc.*, 1997, **119**, 11458–11467; (b) M. K. Brennaman, J. H. Alstrum-Acevedo, C. N. Fleming, P. Jang, T. J. Meyer and J. M. Papanikolas, *J. Am. Chem. Soc.*, 2002, **124**, 15094–15098; (c) J. Olofsson, B. Önfelt and P. Lincoln, *J. Phys. Chem. A*, 2004, **108**, 4391–4398; (d) A. W. McKinley, P. Lincoln and E. M. Tuite, *Coord. Chem. Rev.*, 2011, **255**, 2676–2692; (e) C. Qian, J. Wu, L. Ji and H. Chao, *Dalton Trans.*, 2016, **45**, 10546–10555.
- 32 (a) P. M. Keane, F. E. Poynton, J. P. Hall, I. P. Clark, I. V. Sazanovich, M. Towrie, T. Gunnlaugsson, S. J. Quinn, C. J. Cardin and J. M. Kelly, *J. Phys. Chem. Lett.*, 2015, **6**, 734–738; (b) L. Marcelis, M. Rebarz, V. Lemaure, E. Fron, J. DeWinter, C. Moucheron, P. Gerbaux, D. Beljonne, M. Sliwa and A. Kirsch-De Mesmaeker, *J. Phys. Chem. B*, 2015, **119**, 4488–4500; (c) P. M. Keane, F. E. Poynton,

- J. P. Hall, I. P. Clark, I. V. Sazanovich, M. Towrie, T. Gunnlaugsson, S. J. Quinn, C. J. Cardin and J. M. Kelly, *Faraday Discuss.*, 2015, **185**, 455–469.
- 33 M. T. Carter, M. Rodriguez and A. J. Bard, *J. Am. Chem. Soc.*, 1989, **111**, 8901–8911.
- 34 (a) A. W. McKinley, J. Andersson, P. Lincoln and E. M. Tuite, *Chem. – Eur. J.*, 2012, **18**, 15142–15150; (b) A. W. McKinley, P. Lincoln and E. M. Tuite, *Dalton Trans.*, 2013, **42**, 4081–4090; (c) J. Andersson, L. H. Fornander, M. Abrahamsson, E. Tuite, P. Nordell and P. Lincoln, *Inorg. Chem.*, 2013, **52**, 1151–1159.
- 35 (a) J. P. Hall, K. O'Sullivan, A. Naseer, J. A. Smith, J. M. Kelly and C. J. Cardin, *Proc. Natl. Acad. Sci. U. S. A.*, 2011, **108**, 17610–17614; (b) H. Niyazi, J. P. Hall, K. O. Sullivan, G. Winter, T. Sorensen, J. M. Kelly and C. J. Cardin, *Nat. Chem.*, 2012, **4**, 621–628; (c) J. P. Hall, D. Cook, S. R. Morte, P. McIntyre, K. Buchner, H. Beer, D. J. Cardin, J. A. Brazier, G. Winter, J. M. Kelly and C. J. Cardin, *J. Am. Chem. Soc.*, 2013, **135**, 12652–12659; (d) H. Song, J. T. Kaiser and J. K. Barton, *Nat. Chem.*, 2012, **4**, 615–620; (e) B. Elias, C. Creely, G. W. Doorley, M. M. Feeney, C. Moucheron, A. Kirsch-De Mesmaeker, J. Dyer, D. C. Grills, M. W. George, P. Matousek, A. W. Parker, M. Towrie and J. M. Kelly, *Chemistry – Eur. J.*, 2008, **14**, 369–375.
- 36 C. M. Dupureur and J. K. Barton, *J. Am. Chem. Soc.*, 1994, **116**, 10286–10287.
- 37 F. H. Stootman, D. M. Fisher, A. Rodger and J. R. Aldrich-Wright, *Analyst*, 2006, **131**, 1145–1151.
- 38 B. Nordén and T. Kurucsev, *J. Mol. Recognit.*, 1994, **7**, 141–155.
- 39 A. K. Mårtensson and P. Lincoln, *Dalton Trans.*, 2015, **44**, 3604–3613.
- 40 P. U. Maheswari, V. Rajendiran, M. Palaniandavar, R. Parthasarathi and V. Subramanian, *J. Inorg. Biochem.*, 2006, **100**, 3–17.
- 41 J. M. Kelly, A. B. Tossi, D. J. McConnell and C. Ohuigin, *Nucleic Acids Res.*, 1985, **13**, 6017–6034.
- 42 M. J. Waring, *J. Mol. Biol.*, 1965, **13**, 269–282.
- 43 R. B. P. Elmes, M. Erby, S. A. Bright, D. C. Williams and T. Gunnlaugsson, *Chem. Commun.*, 2012, **48**, 2588–2590.
- 44 (a) R. B. Nair, E. S. Teng, S. L. Kirkland and C. J. Murphy, *Inorg. Chem.*, 1998, **37**, 139–141; (b) A. M. Nonat, S. J. Quinn and T. Gunnlaugsson, *Inorg. Chem.*, 2009, **48**, 4646–4648.
- 45 B. Peng, X. Chen, K.-J. Du, B.-L. Yu, H. Chao and L.-N. Ji, *Spectrochim. Acta, Part A*, 2009, **74**, 896–901.
- 46 B. A. I. Bruker, *APEX v2012.12-0*, Madison, Wisconsin, USA, 2012.
- 47 G. Sheldrick, *Acta Crystallogr., Sect. C: Cryst. Struct. Commun.*, 2015, **71**, 3–8.
- 48 A. Spek, *Acta Crystallogr., Sect. C: Cryst. Struct. Commun.*, 2015, **71**, 9–18.
- 49 G. Cohen and H. Eisenberg, *Biopolymers*, 1969, **8**, 45–55.
- 50 H. Wei, Y. Du, J. Kang and E. Wang, *Electrochem. Commun.*, 2007, **9**, 1474–1479.
- 51 (a) O. Kotova, S. Blasco, B. Twamley, J. O'Brien, R. D. Peacock, J. A. Kitchen, M. Martínez-Calvo and T. Gunnlaugsson, *Chem. Sci.*, 2015, **6**, 457–471; (b) S. J. Bradberry, A. J. Savyasachi, R. D. Peacock and T. Gunnlaugsson, *Faraday Discuss.*, 2015, **178**, 413–431; (c) J. P. Byrne, M. Martínez-Calvo, R. D. Peacock and T. Gunnlaugsson, *Chem. – Eur. J.*, 2016, **22**, 486–490.
- 52 Y.-M. Chang, C. K.-M. Chen and M.-H. Hou, *Int. J. Mol. Sci.*, 2012, **13**, 3394–3413.